EVOLUTION OF THE WAKE AND PERFORMANCE OF OSCILLATING FOILS IN MULTI-DEGREE OF FREEDOM MOTION

BY

SUYASH VERMA

A THESIS SUBMITTED IN PARTIAL FULFILMENT OF THE REQUIREMENTS FOR THE DEGREE OF DOCTOR OF PHILOSOPHY

DEPARTMENT OF MECHANICAL ENGINEERING

UNIVERSITY OF ALBERTA

ABSTRACT

This dissertation numerically evaluates the wake dynamics of oscillating foils with combined heaving and pitching motion. Spatio-temporal evolution of vortical structures and associated instabilities contributed to transitions in the wake topology. This also coincided with changes in the foil's propulsive performance. A fundamental association of these transitions and foil kinematics is investigated at a range of Reynolds numbers and motion parameters, to ultimately improve understanding of efficient biological swimming practices.

The spatial arrangement of two-dimensional primary rollers changed with transitioning of the foil kinematics from heave- to pitch-dominated motion, or vice-versa. A novel mathematical relationship is modeled to accurately predict these changes at low Reynolds number, which involved relative circulation of coherent paired rollers, and governing foil kinematic settings. Apparent similarities in roller arrangement also coincided with either mean momentum deficit or excess in the wake. Thus, it is demonstrated that transitions of the wake topology may not always possess a direct one-to-one association with propulsive performance.

The three-dimensional wake topology at $Re = 8000$ highlighted spanwise undulations of primary rollers characterized by elliptic instability, and a consequent growth of secondary coherent structures. The latter resembled hairpin and horseshoe formations on a large spatial scale, and spanwise corrugations (valleys and bulges) on a finer scale. The changes in kinematics further reflected a fundamental association with the spanwise instability, and alteration in mechanisms that governed the growth of secondary structures. For the heave dominated kinematics, a paired primary and secondary leading edge vortex triggered elliptic instability, which inherently contributed to the growth of secondary hairpins, and their eventual transformation to ribs. As heave domination weakened, secondary hairpin growth occurred through a deforming trailing edge vortex rather than a secondary leading edge vortex. The onset of pitch domination eventually led to an absence of hairpin structures owing to the decreased circulation of primary rollers. The evolution of secondary structures thus presents a fundamental route to three-dimensional transition in wake topology while showcasing a crucial association with multi-degree of freedom foil kinematics.

PREFACE

This dissertation is the original work of the author under the supervision of Dr. Arman Hemmati. Mr. Benjamin R.S. Freeman collaborated on the research presented in Chapter 4. Dr. Muhammad Saif Ullah Khalid further collaborated and provided valuable inputs with regards to Chapter 6 and Chapter 11. The contents of Chapter 3, 4, 5, 6, 7, 8 and 9 have been published, and their respective citations are:

Verma, S., & Hemmati, A. (2020). Performance of overset mesh in modeling the wake of sharp-edge bodies. *Journal of Computation*, 8 (3), 66.

Verma, S., Freeman, B. R. S., & Hemmati, A. (2022). Effects of Reynolds number and average angle of attack on the laminar scaling of oscillating foils. *Physics of Fluids*, 34(3), 031905.

Verma, S., & Hemmati, A. (2022). Route to transition in propulsive performance of oscillating foil. *Physical Review E*, 105(4), 045102.

Verma S, Khalid M.S.U, Hemmati A (2022). On association of lift generation, wake topology and kinematics of oscillating foils. *International Journal of Micro Air Vehicles*, 14, 17568293211073959.

Verma, S., & Hemmati, A. (2022). Characterization of bifurcated dual vortex streets in the wake of an oscillating foil. *Journal of Fluid Mechanics*, 945, A7.

Verma, S., & Hemmati, A. (2021). Evolution of wake structures behind oscillating hydrofoils with combined heaving and pitching motion. *Journal of Fluid Mechanics*, 927, A23.

Verma, S., Hemmati, A. (2021). Asymmetry in Wake of Oscillating Foils with Combined Pitching and Heaving Motion. In: Örlü, R., Talamelli, A., Peinke, J., Oberlack, M. (eds) *Progress in Turbulence IX*. iTi 2021. Springer Proceedings in Physics, vol 267. Springer, Cham.

Verma, S., Hemmati, A. (2022). Implications of spanwise wake instability on formation of secondary structures behind oscillating foils. *Proceedings of the twelfth International Symposium on Turbulence and Shear Flow Phenomena (TSFP12)* 1-6.

Contents of Chapter 10 and 11 has been submitted for publication and its citation read:

Verma, S., Hemmati, A. (2023). Influence of reduced frequency on evolution of secondary wake structures. *International Journal of Heat and Fluid Flow*.

Verma, S., Khalid M.S.U & Hemmati, A. (2023). On the association of kinematics, spanwise instability and growth of secondary vortex structures in the wake of oscillating foils. *Proceedings of Royal Society A*.

To Maa, Papa, sister and friends,

for all your love, support and patience

ACKNOWLEDGEMENTS

Firstly, I would like to express my deepest appreciation and gratitude to Dr. Arman Hemmati, who provided me an opportunity to pursue the Doctor of Philosophy degree in the field of Mechanical Engineering. Your expertise and perspectives in understanding fluid dynamics and explaining complex mechanisms of interacting vortex structures provided strong roots during the initial stages of this research study. Your constant motivation during my quest to pursue novelty, along with developing the conceptual proofs of hypothesis at successive phases, is highly appreciable. I am extremely grateful for your consistent support in helping me participate and attend various scientific conferences, while connecting me with established research leaders across the fluid dynamics community. I also extend appreciation towards my supervisory committee mentors, Drs. Alexandra Komrakova and Carlos F. Lange, for their valuable contribution in planning and review at several stages of my thesis.

Further, I want to thank all of my colleagues including Dr. Muhammad Saif Ullah Khalid, Mr. Benjamin R.S. Freeman, Shubham Goswami, Ahmet Gungor, Arash Zargar and Stanley John, with whom I had spent an enjoyable four years and gathered fruitful insights during this study. Numerous collaborative efforts on different projects have further provided me great exposure to team work and management skills that will be useful throughout my career. I am extremely grateful for all your assistance. My deepest appreciation also goes to my friends with whom I shared office space, and time during various departmental seminars, and extra-curricular activities.

Finally, I would like to thank Future Energy Systems (FES) and Canada First Research Excellence Fund (CFREF) for their support during my research. My sincere appreciation also goes to the administrative staff of Mechanical Engineering and Faculty of Graduate Studies and Research (FGSR), for helping and supporting me with the orientation, scholarship grants and meeting the program requirements for completing my degree.

This work will reflect my gratefulness to all of you till the quest for knowledge continues.

Contents

Abstract ii

Preface iii

Acknowledgements vi

List of Tables xii

List of Figures xiv

List of Abbreviations, Symbols, and Nomenclature xxxi

1 INTRODUCTION **1**

1.1 The Overview 1

1.2 Motivations and Objectives 10

1.3 Novelty 13

1.4 Structure of the thesis 14

2 BACKGROUND **17**

2.1 Kinematics of Oscillating Foil 18

2.2 Propulsive Performance of Oscillating Foil 21

2.3 Wake of an Oscillating Foil 25

2.3.1 Transitions in Wake Topology & Performance 28

2.3.2 Relationship of Wake, Performance and Kinematics 35

2.4 Three-dimensional Wake Topology 37

2.5 Wake Instabilities and Secondary Structures 41

2.5.1 Mechanisms of Vortex Instabilities . . . 43
2.5.2 Instabilities and Wake of Stationary Bluff Bodies . . . 48
2.5.3 Instabilities and Wake of Oscillating Bluff Bodies . . . 52
2.6 Computational Fluid Dynamics (CFD) Approach . . . 57
2.6.1 Overset Grid Assembly . . . 58
2.6.2 Immersed Boundary Methods . . . 59
2.6.3 Sliding Grid Interface . . . 59
2.6.4 Dynamic Mesh Morphing . . . 60
2.7 Summary . . . 61

3 METHODOLOGY **63**
3.1 Foil Geometry and Kinematics . . . 64
3.2 Numerical Method . . . 64
3.3 Overset Grid Assembly Algorithm . . . 65
3.4 Computational Setup . . . 70
3.4.1 3D Square Panel . . . 70
3.4.2 2D Teardrop Foil . . . 72
3.4.3 3D Teardrop Foil . . . 74
3.5 Verification Studies . . . 76
3.5.1 3D Square Panel . . . 77
3.5.2 2D Teardrop Foil . . . 79
3.5.3 3D Foil . . . 81
3.6 Validation Studies . . . 86
3.6.1 3D Stationary Square Panel . . . 87
3.6.2 3D Pitching Square Panel . . . 91
3.6.3 2D Teardrop Foil . . . 99
3.6.4 3D Teardrop Foil . . . 99
3.7 Scalability Results . . . 100

3.8 Summary . . . 103

4 GENERALIZING THE SCALING OF PROPULSIVE PERFORMANCE 105

4.1 Introduction . . . 105

4.2 Problem Description . . . 107

4.3 Results and Discussion . . . 109

4.3.1 Assessment of laminar scaling . . . 109

4.3.2 Implications of pressure and viscous forces . . . 114

4.3.3 Incorporation of laminar scaling into the existing scaling model . . . 119

4.4 Summary . . . 124

5 ROUTE TO TRANSITION IN PROPULSIVE PERFORMANCE 126

5.1 Introduction . . . 126

5.2 Problem Description . . . 128

5.3 Results and Discussion . . . 129

5.4 Summary . . . 152

6 ON ASSOCIATION OF LIFT GENERATION, WAKE TOPOLOGY AND KINEMATICS 155

6.1 Introduction . . . 155

6.2 Problem Description . . . 157

6.3 Results and Discussion . . . 157

6.3.1 Lift Generation and Wake Topology . . . 158

6.3.2 Vortex Shedding and Lift Variation . . . 160

6.4 Summary . . . 165

7 CHARACTERIZATION OF BIFURCATED DUAL VORTEX STREETS IN THE WAKE 168

7.1 Introduction . . . 168

7.2 Problem Description . . . 170
7.3 Results and Discussion . . . 171
7.3.1 Evaluation of kinematics . . . 171
7.3.2 Evaluation of wake mode transition at $Re = 1000$ . . . 173
7.3.3 Formation mechanism of $2P^D$ pairs and symmetric bifurcation . . . 177
7.3.4 Quantitative assessment of evolution characteristics . . . 180
7.3.5 Evaluation of wake mode transition at $Re = 4000$ . . . 188
7.3.6 Formation mechanism of $rBvK + 2P$ mode and symmetric bifurcations . . . 191
7.3.7 Mean flow development in bifurcated dual vortex street wakes . . . 196
7.4 Summary . . . 200

8 EVOLUTION OF THREE-DIMENSIONAL WAKE STRUCTURES AND FEATURES 204

8.1 Introduction . . . 204
8.2 Problem Description . . . 206
8.3 Results and Discussion . . . 207
8.3.1 Propulsive performance . . . 208
8.3.2 Primary vortex characteristics . . . 209
8.3.3 The wake three-dimensionality . . . 228
8.3.4 Secondary vortex structures . . . 237
8.3.5 Vortex skeleton models for high propulsive performance regimes . . . 248
8.4 Summary . . . 249

9 IMPLICATIONS OF SPANWISE WAKE INSTABILITY ON THE FORMATION OF SECONDARY WAKE STRUCTURES 254

9.1 Introduction . . . 254
9.2 Problem Description . . . 256
9.3 Results and Discussion . . . 257

9.4 Summary 263

10 INFLUENCE OF REDUCED FREQUENCY ON EVOLUTION OF SECONDARY WAKE STRUCTURES **265**

10.1 Introduction 265

10.2 Results and Discussion 267

10.2.1 $St_c = 0.32$ 267

10.2.2 $St_c = 0.40$ 269

10.2.3 $St_c = 0.48$ and 0.56 269

10.3 Summary 275

11 ON THE ASSOCIATION OF KINEMATICS, SPANWISE INSTABILITY AND GROWTH OF SECONDARY VORTEX STRUCTURES **277**

11.1 Introduction 277

11.2 Results and Discussion 280

11.3 Impacts of variation in reduced frequency (St_c) 289

11.4 Summary 293

12 CONCLUSION **296**

13 FUTURE WORK **301**

Bibliography **303**

List of Tables

2.1 Quantitative comparison of spanwise wavelength for secondary vortices in wake of different geometries, motion and Re. Diameter (D), height (h) and chord length (c) for respective geometries were used for normalizing λ_z. 56

3.1 Grid sensitivity investigation. 77

3.2 CPU time requirement for different interpolation schemes employed for 2D stationary panel at $\alpha = 30^{\circ}$. 78

3.3 Grid convergence analysis for oscillating foil. Here, N_{total} represents the sum of hexahedral elements in background and overset grids. 80

3.4 Summary of Grid refinement study. N_{total} represents the sum of hexahedral elements in background grid and overset grid. 82

3.5 Grid refinement details for the current study. N_{total} represents the sum of hexahedral elements in background grid and overset grid. Here, “Ref3D" refers to refined version of 3D grid. 85

3.6 Case studies and relevant parameters for each case. 87

3.7 Case studies and relevant parameters for each case. 91

4.1 Comparison of parameter space employed for the current study and some existing literature. 108

4.2 Results of least squares regression of equation 4.5 over entire parameter space. . . 123

4.3 Results of least squares regression of equation 4.6 over entire parameter space. . . 123

5.1 Parameter space for studies conducted on transitions in performance and wake of oscillating foil. Studies with a fixed ϕ correspond to the coupled motion while others either considered pure pitching or heaving motion. 129

8.1 Parameter space for the current studies and the companion experiments. 207

8.2 Quantitative evaluation of performance, showing $\overline{C_T}$, C_L^{rms}, $\overline{C_P}$, and η for SIM1 and SIM2 respectively. 208

List of Figures

1.1 Schematics representing (a) Benard Von Kármán, (b) reverse Benard Von Kármán and (c) 2P mode in the wake of oscillating foil. 5

2.1 Foil kinematics, geometry and coordinate system. (a) Pure heave, (b) pure pitch and (c) coupled motion. 20

2.2 Time-averaged (a) thrust and (b) power coefficients of heaving foils, as functions of the scaling parameters (Eq. 2.13 of Floryan et al. (2017)) for various $h^* = h_o/c$. Time-averaged (a) thrust and (b) power coefficients of pitching foils, as functions of the scaling parameters (Eq. 2.14 of Floryan et al. (2017)) for various $h^* = h_o/c$. Here, f^* is equivalent to St_c used in our study. (Reprinted with permission from Floryan et al. (2017), Copyright 2017, Cambridge University Press). 23

2.3 Thrust coefficients versus the non-dimensional term $St(St - St_o)$. The dashed black line is a linear curve fit to the current experimental data of Groups II–IV only (Reprinted with permission from Lau and Kelso (2016), Copyright 2016, Elsevier). 25

2.4 Wakes of the pitching foil in simulation (colour) and experiment (greyscale). Red (blue) corresponds to positive (negative) vorticity, and the magenta lines show average velocity profiles four chord lengths downstream of the trailing edge, with the black lines showing the inflow velocity as reference. (a) 2P wake (St_D = 0.08, A_D = 1.14 and $\overline{C_T}$ = -0.12); (b) a 2P wake that evolves to a von Kármán wake (St_D = 0.11, A_D = 1.14 and $\overline{C_T}$ = -0.12); (c) a von Kármán wake (St_D = 0.12, A_D = 1.14 and $\overline{C_T}$ = -0.12); (d) an inverted von Kármán wake (St_D = 0.18, A_D = 1.65 and $\overline{C_T}$ = 0.00). (Reprinted with permission from Andersen et al. (2017), Copyright 2017, Cambridge University Press). 27

2.5 Sketches of the vortex shedding patterns. "P" means a vortex pair and "S" means a single vortex, and each pattern is defined by the number of pairs and single vortices formed per cycle; "Dashed curves" encircle the vortices shed in one complete cycle. (Reprinted with permission from Williamson and Roshko (1988), Copyright 1998 Elsevier). 29

2.6 (a) A_D vs St_D map for Re_D = 255. Experimental points are labeled as *BvK* wake (unfilled square); 2*S* aligned wake (filled square); + depicts reverse *BvK* wake; deflected reverse *BvK* street (triangles); Blue line: transition between *BvK* and reverse *BvK*. Green line: transition between reverse *BvK* and asymmetric wake. The shaded area corresponds to the St_A = 0.3+/−0.1 interval. (b) Contours of mean drag coefficient C_D/C_{D_o}. The black line corresponds to C_D = 0 where the estimated drag-thrust transition occurs. The shaded area represents the estimated error for the C_D = 0 curve due to sensitivity on the choice of the control volume. The gray line is the transition from *BvK* to reverse *BvK*. The dashed line corresponds to St_A = 0.3. (Reprinted with permission from Godoy-Diana et al. (2008), Copyright 2008 by the American Physical Society). 31

2.7 Phase-space diagram depicting vortex synchronization regions across a range of St_D-A_D. The solid line indicate that the amplitude-based Strouhal number is constant with the values $St_A = 0.11$ (blue) and $St_A = 0.18$ (black). The arrow indicates the 2P to 2S transition. The black regions at low frequency and amplitude did not present a synchronized wake. A small ($D = 0.10$ cm) and large ($D = 0.20$ cm) foil were used at $St_D < 0.15$ and $St_D > 0.15$, respectively. (Reprinted with permission from Schnipper et al. (2009), Copyright 2009, Cambridge University Press). 32

2.8 (a) A_D vs St_D map for $Re = 1700$. Computational points are labeled as BvK wake (unfilled square); $2S$ aligned wake (filled square); $+$ depicts reverse BvK wake; deflected reverse BvK street resulting in asymmetric wake (triangles); points with neutral stability (circles). Blue (dotted) line: transition between BvK and reverse BvK. Green (dash-dot) line: transition between reverse BvK and the asymmetric regime.Red (dash-dot-dot) line: transition between 2D and 3D wakes. The shaded area corresponds to the $St_A = 0.3 +/- 0.1$ interval (Reprinted with permission from Deng et al. (2015), Copyright 2015 by the American Physical Society). (b) The wake maps and iso-lines of $\alpha(T/4)$ for a purely heaving foil (Reprinted with permission from Zheng et al. (2019), Copyright 2019 by the American Physical Society). 34

2.9 Experimentally measured η as function of the Strouhal number St. Case 1: $h_o/c = 0.75$, $\alpha_{max} = 21°$, $\phi = 75°$; Case 2: $h_o/c = 0.75$, $\alpha_{max} = 17°$, $\phi = 105°$;Case 3: $h_o/c = 0.25$, $\alpha_{max} = 15°$, $\phi = 90°$; Case 4: $h_o/c = 0.75$, $\alpha_{max} = 5°$, $\phi = 90°$;Case 5: $h_o/c = 0.75$, $\alpha_{max} = 25°$, $\phi = 90°$; Case 6: $h_o/c = 0.75$, $\alpha_{max} = 20°$, $\phi = 90°$;Case 7: $h_o/c = 0.75$, $\alpha_{max} = 10°$, $\phi = 90°$; Case 8: $h_o/c = 0.75$, $\alpha_{max} = 30°$, $\phi = 90°$; (Reprinted with permission from Anderson et al. (1998), Copyright 1998, Cambridge University Press). 36

2.10 Effects of St on evolution of wake structure for a finite span wing: h/h_o = -1, θ_o = 10°, ψ = 90°; (a) St = 0.3, (b) St = 0.4 (Reprinted with permission from von Ellenrieder et al. (2003), Copyright 2003, Cambridge University Press). 37

2.11 Aluminum-flake visualization in cross-sectional view: evidence for the location of streamwise vorticity in the braid shear layer regions between primary vortices. Flow is to the right past the cylinder on the left (Reprinted with permission from Williamson (1996), Copyright 1996, Cambridge University Press). 39

2.12 Identification of vortical structures in the near wake of the stationary circular cylinder using Direct numerical simulations. The structures are visualized by $\lambda_2 = 1.1$ (Reprinted with permission from Mittal and Balachandar (1995), Copyright 1995 by the American Physical Society). 40

2.13 Left and right columns depicts instantaneous spanwise vorticity fields and mean flow (time averaged horizontal velocity) for fixed Strouhal and Reynolds numbers St_D=0.22 and Re=255. A_D from top to bottom varies from A_D = 0.36, 1.77 and 2.8, respectively, for an oscillating foil in pure pitching motion. (Reprinted with permission from Godoy-Diana et al. (2008), Copyright 2008 by the American Physical Society). 42

2.14 Visualization of vortex pair evolution under the combined action of long-wavelength (Crow) and Elliptic instability at Re = 2750. The pair is moving towards the observer. (a) t^* = 1.7, (b) t^* = 5.6, (c) t^* = 6.8 (Reprinted with permission from Leweke and Williamson (1998), Copyright 1998, Cambridge University Press). 43

2.15 (a) Long-wavelength Crow instability of a counter-rotating vortex pair at Re = 1450 (Reprinted with permission from Leweke and Williamson (2011), Copyright 2011, AIP Publishing LLC). (b) Inviscid Vortex filament simulation results depicting evolution of Crow instability (Reprinted with permission from Winckelmans et al. (2005), Copyright 2005, Elsevier). 44

2.16 (a) Illustration of the symmetric displacement mode associated with the Crow Instability, (b) Steps indicating onset of Crow Instability for a counter-rotating vortex pair (Reprinted with permission from Leweke et al. (2016), Copyright 2016, Annual Reviews). (c) and (d) depict results of a Numerical simulation depicting developed Crow instability on vortex rollers of unequal strength (Reprinted with permission from Chatelain et al. (2008), Copyright 2008, Elsevier). 45

2.17 Short-wavelength elliptic instability of (a) counter-rotating vortex pair at Re = 2750, where the pair moving towards observer (Reprinted with permission from Leweke and Williamson (1998), Copyright 1998, Cambridge University Press), (b) co-rotating vortex pair at Re = 4140 (Reprinted with permission from Meunier and Leweke (2001), Copyright 2001, AIP Publishing LLC). 47

2.18 (a) Elliptic instability in the secondary vortex roller and (b) growth of streamwise filaments at $Re = 5{,}200$. Figure reproduced with permission from Duponcheel (2009). 48

2.19 Model for wake instabilities and formation of secondary vortex pair for stationary circular cylinder. (a) primary and (b) secondary vortices in the transitional wake of the cylinder for the two shedding modes A and B. Arrows denote the sense of rotation and dashed lines represent vortex lines (Reprinted with permission from Brede et al. (1996), Copyright 1996, by American Institute of Physics). Mechanisms of (a) Mode A and (b) Mode B instability (Reprinted with permission from Williamson (1996), Copyright 1996, Cambridge University Press). 49

2.20 Secondary vortices of the (a) A, (b) B, and (c) C mode in wake of a stationary circular cylinder. Instantaneous contour plots of the numerically obtained vorticity component ω_y in the xz plane at $Re = 200$, 240, and 210 (top to bottom) (Reprinted with permission from Zhang et al. (1995), Copyright 1995, by American Institute of Physics). 51

2.21 Secondary rib pairs in wake of a stationary BTE airfoil. Isosurface constructions of modified Q-criterion ($Q' = \omega_x Q/|\omega_x|$) in the wake at $x = 2h$ for (a) $Re_h = 3500$ (isosurface at $|Q' = |\ 2000\ s^{-1}$) and (b) $Re_h = 7000$ (isosurface at $|Q' = |\ 18000\ s^{-1}$). Green and gold represent positive and negative rotational directions, respectively (Reprinted with permission from Gibeau et al. (2018), Copyright 2018, Cambridge University Press). 52

2.22 Secondary vortex pairs in wake of a pitching foil. Three-dimensional DNS results for the isosurfaces of streamwise vorticity field ($|\omega_x| = 6$) for the short wavelength mode at $Re = 1500$, $A_D = 2.8$, and $\beta = 30.0$. Five instants during a periodic cycle are shown. Blue (dark gray) and red (light gray) colors denote negative values and positive values respectively of 0.3 of the instantaneous maximum magnitude. Isosurfaces of spanwise vorticity ($|\omega_z| = 6$) are also shown (Reprinted with permission from Deng and Caulfield (2015a), Copyright 2020 by the American Physical Society). 54

2.23 Spanwise undulations on a *LEV*. Isosurfaces of normalized vorticity magnitude $|\omega|c/U_\infty = 13.4$ for $\alpha = 15°$, $St_c = 1.1$, $A/c = 0.5$. Top view of the swept wing with flat-plate cross section (Reprinted with permission from Chiereghin et al. (2020), Copyright 2020 by the American Physical Society). 55

2.24 Illustration of spanwise instability and secondary vortex evolution in wake of a heaving foil. Vortical structures (Q^*=5), colored by spanwise vorticity, from experiments (upper row) and numerical simulations (bottom row) for the airfoil case of St_c =2, A/c=0.5 (Reprinted with permission from Son et al. (2022), Copyright 2022, Cambridge University Press). Flow from top to bottom. 55

3.1 Description of teardrop foil geometry and motion in the current study. 64

3.2 Block structured mesh depicting Overset Grid Assembly. 66

3.3 Overset Grid Assembly (OGA) meshing and cell identification for an oscillating foil and an inclined square panel. (a) Typical overlap of an structured overset grid (black lines), and background grid (white lines) for this study. (b) Representation of Hole cells in white (A), interpolation cell fringe in black (B), and calculated cells in dark grey (C), identified on background grid, respectively. Identification of cells on (c) Overset and (d) Background grid of an inclined square panel. The cell types depict how interpolation weights vary based on their distance from the hole points. 68

3.4 Schematic of the computational domain and boundary conditions. 71

3.5 (a) Merged background and overset grid for stationary panel at $\alpha = 30^{\circ}$ (Case 3). (b) shows the Isometric view for the secondary or "Overset" grid, while (c) represents the chordwise view of the overset grid. 72

3.6 Schematics of the computational domain and foil kinematics. (not to scale) 73

3.7 Schematics of the grid and Overset Grid Assembly method. 74

3.8 Schematics of the computational domain (not to scale). 75

3.9 Depiction of three-dimensional background and Overset Grid. 76

3.10 Variation of C_d with time for 2D stationary panel ($\alpha = 30$ deg), estimated using different overset interpolation techniques. 78

3.11 (a) Domain and (b) boundary condition sensitivity results for C_T. 80

3.12 Comparison of (a) unsteady variation of C_T, and (b) cross-stream velocity profiles at increasing streamwise distance (X^+) for three grids. 81

3.13 Comparison of time histories for thrust and moment coefficients for all grids employed in our study. 82

3.14 Grid sensitivity study using mean streamwise velocity variations along the $y-$direction at (a) $x = 2c$ and (b) $x = 4c$. 83

3.15 Spanwise domain length analysis in terms of λ_z characterizing the spanwise instability of primary *LEV*. 84

3.16 Comparison of (a) unsteady variation of C_T, and (b) cross-stream velocity profiles at increasing streamwise distance (X^+) for three grids. 86
3.17 Variation of $\overline{C_d}$ with α° for 3D stationary panel (Case 1–5). 88
3.18 Contours of spanwise component of vorticity magnitude (ω_z^+) at xy-plane ($z = 0$) for 3D stationary panel at $\alpha = 30^\circ$. 89
3.19 Iso-surfaces of vorticity magnitude ($|\omega^+| = 1.62$, 1.65 and 2.14), for cases of (a) $\alpha = 30^\circ$, (b) 45° and (c) 60°, respectively. 90
3.20 Parametric description of motion of pitching panel (PanelS6–PanelS7). 92
3.21 Contour plots for (**a**) C_{pr} and (**b**) C_f variation across the top surface of pitching panel for $\psi = 0^\circ, 90^\circ, 180^\circ$ and 270°, respectively. The Reynolds number is 500. The bottom plots show the variation of C_{pr} and C_f across the midspan in chordwise direction. Black, red, blue and green correspond to the $\psi = 0^\circ, 90^\circ, 180^\circ$ and 270°, respectively. Colored markers represent the data of Senturk and Smits (2018) at corresponding ψ. 93
3.22 Contour plots for (**a**) C_{pr} and (**b**) C_f variation across the top surface of pitching panel for $\psi = 0^\circ, 90^\circ, 180^\circ$ and 270°, respectively. The Reynolds number is 2000. 94
3.23 Variation of Coefficients of lift (C_l) and drag (C_d) with normalized time t^+, for (**a**) Case 6 and (**b**) Case 7, respectively. 95
3.24 Surface pressure contours of C_{pr}, plotted on top and bottom surface of square panel for (**a**) Case 6, and (**b**) Case 7, respectively, at positions of peak trailing edge amplitudes (i.e., $\psi = 90^\circ$ and 270°). 96
3.25 Iso-surfaces of vorticity magnitude ($|\omega^+| = 1$) in chordwise (**a**) and spanwise direction (**b**) respectively. The Reynolds number is 2000. 97
3.26 Three dimensional isometric view of iso-surfaces corresponding to $|\omega^+| = 1$ (top). Black edges depict the overset grid boundaries. Bottom figures depict two-dimensional Iso-contours for $|\overline{u^+}|$. The *Re* is 2000. 98

3.27 Comparison of numerically obtained variation of $\overline{C_T}$ at $St_c = 0.67$, with experiments of Van Buren et al. (2019). 99
3.28 Comparison of current numerical results with experiments of Van Buren et al. (2019). Variations of mean thrust are compared at $St_c = 1.87$. 100
3.29 Unsteady variations of lift and moment contribution to the total power are compared at (a) ϕ =0° and (b) ϕ =270°. Details of the parameter space are provided in the text. 101
3.30 Variation of Speed-up (S) and total execution time (Tp) for simulation (in seconds), with increase in number of processors (pr). 101
3.31 Variation of efficiency (η_S) with increase in number of processors (pr). 102

4.1 (a) Schematic of motion state of foil and (b) Variation of instantaneous α within one oscillation cycle at increasing ϕ. Black dotted line in (a) represent the heave motion profile of the foil. 108
4.2 Examples of laminar scaling for (a) varying frequency at $a_h = 0.25$, $\phi = 270°$ (b) varying amplitude at $St_c = 0.64$, $\phi = 270°$ (c) varying phase at $a_h = 0.25$, $St_c = 0.48$ and $St_c = 0.64$. Solid lines represent the scaling. 110
4.3 Variation of κ with increasing $\overline{\alpha}$. 112
4.4 R^2 of laminar scaling with varying phase and amplitude. (a) shows the variation with amplitude for $\phi = 270°$ and (b) shows the variations with phase offset for $a_h = 0.25$. 113
4.5 Contributions of pressure and viscous forces to the change in $\overline{C_T}$ between low and high Re cases based on (a) variations in amplitude for $\phi = 270°$ and (b) variations in phase offset for $a_h = 0.25$. 115
4.6 Variation of C_{pr} and C_f at increasing Re and $\phi = 270°$, along the chord for St_c = 0.16 (a,b) and $St_c = 0.32$ (c,d), respectively. 116
4.7 Variation of C_{pr} and C_f at increasing Re and $\phi = 270°$, along the chord for St_c = 0.48 (a,b) and $St_c = 0.64$ (c,d), respectively. 117

4.8 ω_z^+ contours at a range of Re and St_c, corresponding to ϕ =270°. 118

4.9 Variation of C_{pr} and C_f at increasing Re and $\phi = 0°$, along the chord for $St_c = 0.16$ (a,b) and $St_c = 0.32$ (c,d), respectively. 120

4.10 Variation of C_{pr} and C_f at increasing Re and $\phi = 0°$, along the chord for $St_c = 0.48$ (a,b) and $St_c = 0.64$ (c,d), respectively. 121

4.11 ω_z^+ contours at a range of Re and St_c, corresponding to ϕ =0°. 122

4.12 Modification of the scaling relationships for (a) $\overline{C_T}$ and (b) $\overline{C_P}$ proposed by Van Buren et al. (2019), to incorporate a laminar scaling dependence on the Reynolds' number. See Figure 4.3 for symbol interpretation. 123

5.1 The phase-space maps of $\phi - St_c$, depicting the transition of (a) drag to thrust production, and (b) wake modes for $Re = 1000$. Circular and Triangular markers depict the drag and thrust producing cases, respectively. Increasing saturation color levels of filled marker correspond to the increasing the magnitude of thrust or drag. Solid and broken lines represent data points with constant $\overline{C_T}$ and $\overline{C_D}$, respectively. 130

5.2 Contours of ω_z^+ depicting 2P+2S wake mode at (a) $t = 0$, (b) $t = T/4$, (c) $t = T/2$ and (d) $t = 3T/4$. 132

5.3 Wake modes for increasing ϕ at $St_c = 0.16$. (a)-(f) presents ϕ corresponding to 0°, 90°, 180°, 225°, 270° and 315°, respectively. The color codes refer to the phase map of wake modes, represented in the Figure 5.1(b). 133

5.4 Contours for $\overline{u_x}/U_\infty$ for ϕ = (a) 0°, (b) 45° and (c) 90°, corresponding to St_c = 0.16. Variation of $\overline{u_x}/U_\infty$ along the cross-stream direction, at different streamwise locations, are also shown alongside each contour. 135

5.5 Wake modes for increasing ϕ at $St_c = 0.24$. (a)-(f) presents ϕ corresponding to 0°, 90°, 180°, 225°, 270° and 315°, respectively. The color codes refer to the phase map of wake modes, represented in the Figure 5.1(b). 136

5.6 Contours for $\overline{u_x}/U_\infty$ for ϕ = (a) 0°, (b) 45° and (c) 90°, corresponding to St_c = 0.24. Variation of $\overline{u_x}/U_\infty$ along the cross-stream direction, at different streamwise locations, are also shown alongside each contour. 138

5.7 Dynamic interactions of vortex structures identified using contours of non-dimensional spanwise vorticity ($\omega_z^+ = \omega_z c/U_\infty$), in the wake corresponding to (a) $\phi = 0°$, (b) $\phi = 45°$ and (c) $\phi = 90°$. St_c corresponds to 0.24. Red dotted line represents the wake centerline. 140

5.8 Wake modes for increasing ϕ at $St_c = 0.32$. (a)-(f) presents ϕ corresponding to 0°, 90°, 180°, 225°, 270° and 315°, respectively. The color codes refer to the phase map of wake modes, represented in the Figure 5.1(b). 141

5.9 Contours for $\overline{u_x}/U_\infty$ for ϕ = (a) 0°, (b) 45° and (c) 90°, corresponding to St_c = 0.32. Variation of $\overline{u_x}/U_\infty$ along the cross-stream direction, at different streamwise locations, are also shown alongside each contour. 143

5.10 Dynamic interactions of vortex structures identified using contours of non-dimensional spanwise vorticity ($\omega_z^+ = \omega_z c/U_\infty$), in the wake corresponding to (a) $\phi = 0°$, (b) $\phi = 45°$ and (c) $\phi = 90°$. St_c corresponds to 0.32. Red dotted line represents the wake centerline. 145

5.11 Wake modes for increasing ϕ at $St_c = 0.40$. (a)-(f) presents ϕ corresponding to 0°, 90°, 180°, 225°, 270° and 315°, respectively. The color codes refer to the phase map of wake modes, represented in the Figure 5.1(b). 146

5.12 Contours for $\overline{u_x}/U_\infty$ for ϕ = (a) 0°, (b) 45° and (c) 90°, corresponding to St_c = 0.40. Variation of $\overline{u_x}/U_\infty$ along the cross-stream direction, at different streamwise locations, are also shown alongside each contour. 147

5.13 Dynamic interactions of vortex structures identified using contours of non-dimensional spanwise vorticity ($\omega_z^+ = \omega_z c/U_\infty$), in the wake corresponding to (a) $\phi = 0°$, (b) $\phi = 45°$ and (c) $\phi = 90°$. St_c corresponds to 0.4. Red dotted line represents the wake centerline. 149

5.14 Wake modes for increasing ϕ at $St_c = 0.48$. (a)-(f) presents ϕ corresponding to 0°, 90°, 180°, 225°, 270° and 315°, respectively. The color codes refer to the phase map of wake modes, represented in the Figure 5.1(b). 152

6.1 (a) Variation of C_L^{rms} with increasing ϕ and St_c, and (b) Wake mode transition depicted on a $\phi - St_c$ phase space. 158

6.2 Temporal variation of C_L at increasing St_c and ϕ = (a) 0°, (b) 45°, (c) 90°, (d) 120°, (e) 180°, (f) 225°, (g) 270°, (h) 315°. 159

6.3 Snapshots of ω_z^+ depicting wake formation at $St_c = 0.48$ and $\phi = 45°$, at quarter period of oscillation cycle: (a) $t^+ = 0$, (b) $t^+ = 0.25$, (c) $t^+ = 0.5$ and (d) $t^+ = 0.75$. 161

6.4 Snapshots of ω_z^+ depicting wake formation at $St_c = 0.48$ and $\phi = 180°$, at quarter period of oscillation cycle, i.e. (a) $t^+ = 0$, (b) $t^+ = 0.25$, (c) $t^+ = 0.5$ and (d) $t^+ = 0.75$. 163

7.1 Schematics of the foil kinematics and resultant velocity at the leading edge during the motion. 170

7.2 Temporal variation of (a) a_T^+, (b) h^+ and (c) instantaneous $\alpha°$, within one single oscillation cycle. (d) represents variation of peak α with respect to ϕ and St_c. . . . 172

7.3 Phase map representation of identified wake modes on (a) $\phi - St_c$ and (b) $A_c - St_c$ phase-space for $Re = 1000$. 174

7.4 Wake modes at increasing ϕ and $Re = 1000$. (a)-(f) represents ϕ corresponding to 0°, 45°, 90°, 120°, 180° and 225°, respectively, while St_c corresponds to 0.4. 175

7.5 Temporal snapshots representing contours of ω_z^+, and depicting formation of $2P^D$ pair and bifurcation within the $2P$ mode at $St_c = 0.4$, $\phi = 180°$ and $Re = 1000$. . . 178

7.6 Variation of (a) Γ^+ and (b) ζ^+ between counter-rotating and co-rotating vortex structures (highlighted in Figure 7.4), with respect to ϕ. 181

7.7 Scaling of estimated $\Gamma_{TEV}/\Gamma_{LEV}$ and Model (Eq. 7.15) outputs at increasing St_h, St_θ and ϕ. 187

7.8 Phase map representation of identified wake modes on (a) $\phi - St_c$ and (b) $A_c - St_c$ phase-space for $Re = 4000$. 188
7.9 Wake modes at increasing ϕ and $Re = 4000$. (a)-(f) represents ϕ corresponding to 0°, 45°, 90°, 120°, 180° and 225°, respectively, while St_c corresponds to 0.4. 190
7.10 Temporal snapshots representing contours of ω_z^+, and depicting formation of $rBvK + 2P$ mode with bifurcation at $Re = 4000$. 192
7.11 Changes in dynamic shear splitting process with increasing ϕ. 194
7.12 Temporal evolution of wake splitting and merging at $\phi = 120°$. 195
7.13 Contours of $\overline{u_x^+}$ at (a) $\phi = 0°$, (b) $\phi = 90°$, (c) $\phi = 180°$ and (d) $\phi = 225°$, respectively. Solid red lines depict the streamwise locations where cross-stream profiles of $\overline{u_x^+}$ are extracted and shown in Figure 7.14. 197
7.14 Profiles of $\overline{u_x^+}$ along the cross-stream (Y^+) direction at streamwise locations corresponding to (a) $X^+ = 1.5$, (b) $X^+ = 3.5$ and (c) $X^+ = 5.5$, respectively. 198
7.15 Contours of $\overline{u_x^+}$ at (a) $\phi = 225°$, $St_c = 0.48$ and $Re = 1000$ (b) $\phi = 90°$, $St_c = 0.4$ and $Re = 4000$. 199

8.1 Contours of ω_z^+ superimposed by velocity vectors for SIM1. Phases (ψ) of the shedding cycle are (a) $\psi = 0^o$ at $t = 0$, (b) $\psi = 90^o$ at $t = T/4$, (c) $\psi = 180^o$ at $t = T/2$, (d) $\psi = 270^o$ at $t = 3T/4$ and (e) $\psi = 360^o$ at $t = T$. 210
8.2 Variation of force (a,b) and moment (c) in one cycle for SIM1. 212
8.3 C_{pr} distribution on suction side (*top row*) and pressure side (*bottom row*) of the foil at instants (a) 1, (b) 2 and (c) 3 of Figure 8.2. 214
8.4 Contours of ω_z^+ superimposed by velocity vectors for SIM2. Phases (ψ) of the shedding cycle are (a) $\psi = 0^o$ at $t = 0$, (b) $\psi = 90^o$ at $t = T/4$, (c) $\psi = 180^o$ at $t = T/2$, (d) $\psi = 270^o$ at $t = 3T/4$ and (e) $\psi = 360^o$ at $t = T$. 218
8.5 Variation of force (a,b) and moment (c) in one cycle for SIM2. 219
8.6 C_{pr} distribution on suction side (*top row*) and pressure side (*bottom row*) of the foil at instants (a) 1, (b) 2 and (c) 3 of Figure 8.5. 221

8.7 Variation of (a,c) vortex radii, a^+, (b,d) cross-stream coordinate of vortex center, Y^+, and (b,d) separation distance between the paired and coupled vortices, ζ^+, with normalized time scale t^+ , for (a,b) SIM1 and (c,d) SIM2, respectively. 224

8.8 Dislocations of primary structures in the wake for SIM1 using (a) iso-surface of $|\omega_z^+| = 0.5$. The iso-contour of $|\omega_z^+|$ on the $yz-$plane are shown at (b) X^+ =4, and (c) $X^+ = 5$. Here, $\omega_z^+ = +0.5$ is colored in grey and $\omega_z^+ = -0.5$ in black. 229

8.9 Dislocations are highlighted on the iso-surface plots of normalized $Q-$criterion ($Q^+ = Qc^2/U_\infty^2 \approx 0.01$), overlaid with iso-surface of ω_z^+ = 0.5 in grey and ω_z^+ = -0.5 in black shown from spanwise (a) top-view and (b) bottom view. 232

8.10 Dislocations observed for the primary structures in the wake for SIM2 using (a) iso-surface of $|\omega_z^+| = 3$ with valleys and bulges depicted on the $yz-$plane at (b) $X^+ = 5.4$, and (c) $X^+ = 6$. Legends are the same as previous figures. 235

8.11 Dislocations observed for the primary structures in the wake for SIM2 are highlighted in iso-surface plots of normalized $Q-$criterion ($Q^+ = Qc^2/U_\infty^2 \approx 0.09$) overlaid with colored contours corresponding to ω_z^+ = 3 (grey) and ω_z^+ = -3 (black). 236

8.12 (a) Iso-surface of $\omega_z^+ = +0.5$ (grey) and $\omega_z^+ = -0.5$ (black) along with $yz-$planar contour of u' at $X^+ = 4$. (b) The depiction of ribs using iso-surface of $\omega_x^+ = +0.055$ (gray) and $\omega_x^+ = -0.055$ (black) along with the $yz-$planar contour of streamwise vorticity at $X^+ = 4$. 239

8.13 (a) Iso-surface of $\omega_z^+ = +0.5$ (grey) and $\omega_z^+ = -0.5$ (black) along with the $yz-$planar contour of u' at $X^+ = 5$. (b) The depiction of ribs using iso-surface of $\omega_x^+ = +0.055$ (grey) and $\omega_x^+ = -0.055$ (black) along with the $yz-$planar contour of streamwise vorticity at $X^+ = 5$. 240

8.14 Variation of $C(\Delta z)$ with respect to spanwise shift (Δz^+) during (a) 2P wake at $X^+ = 4$ and 5, and (b) 2S wake at $X^+ = 6.65$ and 7.65 for SIM1. 242

8.15 Alignment of streamwise vortex pairs on the $yz-$plane at (a) X^+ =6.65, and (b)X^+ =7.65 for SIM1. 242

8.16 Variation of $\rho(\Delta z)$ obtained from cross-correlations of ω_x^+ between (a) Full and (b) Half shedding cycles for SIM1. 243

8.17 (a) Iso-surface of $\omega_z^+ = +3$ (grey) and $\omega_z^+ = -3$ (black) along with the $yz-$planar contour of u' at $X^+ = 5.4$. (b) The depiction of ribs using iso-surface of $\omega_x^+ = +0.5$ (grey) and $\omega_x^+ = -0.5$ (black) along with the $yz-$planar contour of streamwise vorticity at $X^+ = 5.4$. 244

8.18 (a) Iso-surface of $\omega_z^+ = +3$ (grey) and $\omega_z^+ = -3$ (black) along with the $yz-$planar contour of u' at $X^+ = 6$. (b) The depiction of ribs using iso-surface of $\omega_x^+ = +0.5$ (grey) and $\omega_x^+ = -0.5$ (black) along with the $yz-$planar contour of streamwise vorticity at $X^+ = 6$. 245

8.19 Variation of $C(\Delta z)$ with respect to normalized spanwise shift (Δz^+) in the (a) Near wake and (b) Mid wake of SIM2. 246

8.20 Iso-surface of ω_z^+ with the alignment of streamwise vortex pairs shown on $yz-$plane at (a) $X^+ = 7.4$ and (b) $X^+ = 8.4$. 247

8.21 Variation of $\rho(\Delta z)$ with respect to normalized spanwise shift (Δz^+) based on cross-correlations of ω_x^+ between (a) Full and (b) Half shedding cycles for SIM2. 247

8.22 Vortex skeleton models for (a) SIM1 and (b) SIM2. $+\Gamma$ and $-\Gamma$ denote the circulation for counter-clockwise and clockwise rollers, respectively. $+\Gamma_{RI}$ and $-\Gamma_{RI}$ denote the circulation for counter-clockwise and clockwise ribs, respectively. . . . 250

9.1 Time evolution of *LEVs* for $\phi = 90^\circ$ at (a) $t = 0$, (b) $t = T/4$, (c) $t = T/2$, (d) $t = 3T/4$ and (e) $t = T$. The vortical structures are identified using iso-surfaces of $\lambda_2^+ = \lambda_2 c^2/U_\infty^2 =$ -0.032, colored with spanwise vorticity ($|\omega_z^+| = \omega_z c/U_\infty = 4$). 258

9.2 Surface pressure (C_{pr}) distribution on foil for $\phi = 90^\circ$ at (a) $t = T/4$ and (b) $T/2$. 260

9.3 (a) Variation of $C(\Delta z)$ with $\Delta z^+ = \Delta z/c$ and (b) Depiction of ω_x^+ pairs on spanwise slices at increasing X^+. Here, decreasing opacity of *rib* pairs ensures a complete streamwise and spanwise views in the wake. 261

9.4 Iso-surfaces of λ_2^+ = -0.032 criterion colored with $|\omega_z^+| = 4$, for $\phi = 180^\circ$ (a,d,g,j), 225° (b,e,h,k) and 270° (c,f,i,l). The instantaneous snapshots correspond to $t = T/4, T/2, 3T/4,$ T, respectively. 262

10.1 Stages of wake evolution at $\phi = 90^\circ$ and $St_c = 0.32$. (a-c) correspond to quarter phases of an oscillation cycle, beginning from (a) $t^+ = 0.5$, (b) $t^+ = 0.75$ and (c) $t^+ = 1$. Each stage is represented using iso-surfaces of $\lambda_2^+ = -0.05$, which are colored based on $|\omega_z^+| = 5$. 268

10.2 Stages of wake evolution at $\phi = 90^\circ$ and $St_c = 0.40$. (a-c) correspond to quarter phases of an oscillation cycle, beginning from (a) $t^+ = 0.5$, (b) $t^+ = 0.75$ and (c) $t^+ = 1$. Each stage is represented using iso-surfaces of $\lambda_2^+ = -0.05$, which are colored based on $|\omega_z^+| = 5$. 270

10.3 Stages of wake evolution at $\phi = 90^\circ$ and $St_c = 0.48$. (a-b) correspond to quarter phases of an oscillation cycle, beginning from (a) $t^+ = 0.75$ and (b) $t^+ = 1$. Each stage is represented using iso-surfaces of $\lambda_2^+ = -0.05$, which are colored based on $|\omega_z^+| = 5$. 271

10.4 Stages of wake evolution at $\phi = 90^\circ$ and $St_c = 0.56$. (a-c) correspond to quarter phases of an oscillation cycle, beginning from (a) $t^+ = 0.5$, (b) $t^+ = 0.75$ and (c) $t^+ = 1$. Each stage is represented using iso-surfaces of $\lambda_2^+ = -0.05$, which are colored based on $|\omega_z^+| = 5$. 272

10.5 Vortex skeleton model depicting the transition of wake topology at increasing St_c. 274

11.1 Wakes corresponding to (a) $\phi = 90^\circ$ and (b) $\phi = 180^\circ$, at $St_c = 0.32$. The oscillation time corresponds to $t^+ = 0.75$. Each stage is represented using iso-surfaces of $\lambda_2^+ = -0.05$, which are colored based on $|\omega_z^+| = 5$. 281

11.2 Stages of primary and secondary *LEV* evolution at $\phi = 90^\circ$ and $St_c = 0.32$. Each stage is represented using iso-contours of ω_z^+ at the foil mid-span ($Z^+ = 0$). 282

11.3 Stages of wake evolution at $\phi = 180^\circ$ and $St_c = 0.32$. Each stage is represented using iso-surfaces of $\lambda_2^+ = -0.05$, which are colored based on $|\omega_z^+| = 5$. 283

11.4 Wakes corresponding to (a) $\phi = 225^\circ$ and (b) $\phi = 270^\circ$, at $St_c = 0.32$. The oscillation time corresponds to $t^+ = 0.75$. Each stage is represented using iso-surfaces of $\lambda_2^+ = -0.05$, which are colored based on $|\omega_z^+| = 5$. 286

11.5 $|\Gamma^+|$ variation of primary *LEVs* as they advect in an oscillation cycle corresponding to cases of $\phi = 90^\circ$-270°. 287

11.6 Estimation process of λ_z characterizing the spanwise instability of primary *LEV*. . 288

11.7 Variation of λ_z in an oscillation cycle corresponding to $\phi = 90^\circ$-270°. 288

11.8 Wake snapshots corresponding to $\phi = 90^\circ$, at $St_c = 0.48$. The oscillation time corresponds to (a) $t^+ = 0.5$ and (b) $t^+ = 0.75$. Each stage is represented using iso-surfaces of $\lambda_2^+ = -0.05$, which are colored based on $|\omega_z^+| = 5$. 290

11.9 Wake snapshots corresponding to $\phi = 180^\circ$, at $St_c = 0.48$. The oscillation time corresponds to (a) $t^+ = 0.25$, (b) $t^+ = 0.5$ and (c) $t^+ = 0.75$. Each stage is represented using iso-surfaces of $\lambda_2^+ = -0.05$, which are colored based on $|\omega_z^+| = 5$. 291

11.10 Wake snapshots corresponding to $\phi = 225^\circ$, at $St_c = 0.48$. The oscillation time corresponds to (a)$t^+ = 0.5$ and (b) $t^+ = 0.75$. Each stage is represented using iso-surfaces of $\lambda_2^+ = -0.05$, which are colored based on $|\omega_z^+| = 5$. 294

LIST OF ABBREVIATIONS, SYMBOLS, AND NOMENCLATURE

Latin Symbols

h	heave amplitude
θ	pitch amplitude
h_o	Maximum heave amplitude
a_h	Normalized heave amplitude
A	Trailing edge amplitude
D	Maximum thickness of foil
c	Foil chord
Re	Reynolds number based on foil chord
Re_D	Reynolds number based on Diameter
f	oscillation frequency
St_A	Strohaul number based on trailing edge amplitude
St_D	Strohaul number based on foil diameter
St_c	Strohaul number based on foil chord, or reduced frequency
St_θ	Strohaul number based on pitch amplitude
t	time
u	Cartesian $x-$wise velocity component
p	pressure
pr	processors
X_i	Cartesian coordinate component along the i^{th}
C_{pr}	Coefficient of pressure
C_f	skin friction coefficient

L	length scale for normalization
C_T	Coefficient of thrust
$C_{T,Exp}$	Coefficient of thrust for experiments
C_P	Coefficient of power
C_L	Coefficient of lift
F_y	Transverse force
M_θ	pitching moment
Q	Q-criterion
c_i	empirical constants
R^2	Coefficient of Determination
Co	Courant number
h^*	Normalized heave amplitude (h_o/c)
T_s	CPU time for a serial computation
T_p	CPU time for a parallel computation
S	Speed-up
d_{inv}	Diameter of invariant streamtube

Greek Symbols

η	propulsive efficiency
η_k	Kolmogorov length Scale
η_S	Efficiency for parallel scaling
θ_o	Maximum pitch amplitude
ϕ	phase offset
ψ	phase of oscillation cycle
ε	Turbulent kinetic energy dissipation rate

τ_w	Wall shear stress
Γ	circulation strength
η	Kolmogorov length scale
ρ	density
μ	dynamic viscosity
ν	kinematic viscosity
ω_z	spanwise vorticity
ω_x	streamwise vorticity
Ω	rotation rate tensor
S_{ij}	Strain rate tensor
λ_2	second Eigen value of $S_{ij}S_{ij} + \Omega_{ij}\Omega_{ij}$ tensor
λ_z	Wavelength of spanwise instability
α_{eff}	effective angle of attack
ζ	Separation distance
κ	normalization parameter
δ^*	Ratio of minimum grid cell size to Kolmogorov length scale
ε_T	Relative error of changes in mean thrust coefficient
ε_L^{rms}	Relative error of changes in root-mean-square oflift coefficient

Other Symbols

∇	Gradient operator
$\overline{\square}$	Mean (time-averaged)
∂	Partial derivative
$\square \cdot \square$	Dot product
Δ	Difference

$\approx$	i approximately
$[\ ]^T$	Transpose
$O[\ ]$	Order of

Abbreviations

$2D$	Two-Dimensional
$3D$	Three-Dimensional
CFD	Computational Fluid Dynamics
FVM	Finite Volume Method
DNS	Direct Numerical Simulation
LES	Large Eddy Simulation
DES	Detached Eddy Simulation
$RANS$	Reynolds Averaged Navier Stokes
PIV	Particle Image Velocimetry
CFL	Courant-Friedrichs-Levy Number
$SIMPLE$	Semi-Implicit Method for Pressure Linked // Equations
$PISO$	Pressure Implicit with Splitting of Operators
$rBvK$	reverse Benard Von Kármán
BvK	Benard Von Kármán
$wBvK$	wavy Benard Von Kármán
$2S$	Wake characterized by a single vortex shed per half shedding cycle
$2P$	Wake characterized by a single vortex pair shed per half shedding cycle
$2P+2S$	Wake characterized by an isolated vortex and a pair shed per half shedding cycle

AUV	Autonomous underwater vehicle
MAV	Micro-air vehicle
BTE	Blunt trailing edge
NACA	National Advisory Committee for Aeronautics
AMI	Arbitrary mesh interface
GGI	Generalized Grid Interface
IBM	Immersed Boundary method
PbiCGSTAB	Pre-conditioned biconjugate gradient stablized
PCG	Pre-conditioned conjugate gradient
LEV	Leading edge vortex
TEV	Trailing edge vortex
OGA	Overset Grid Assembly
OpenFOAM	Open-source field operation and manipulation

Chapter 1

INTRODUCTION

This study investigates the wake evolution and vortex dynamics behind an oscillating foil undergoing a coupled heaving and pitching motion. The mechanisms and characteristics of wake topology are explored to understand the underlying flow physics. Particularly, the implication of spanwise wake instability on the growth of secondary vortex structures is highlighted in detail, which provides a key fundamental advancement relevant to evolution of the wake behind oscillating foils.

1.1 The Overview

Wakes are prominent aspect of laminar, transitional and turbulent flows. They are observable in various engineering applications, including high speed turbo-machinery compressors, mixing vessels, flow over aircraft wings and countless other man-made processes (Fazle Hussain, 1986; Jeong and Hussain, 1995; Hussain, 1998). Oceanic winds, tidal waves and ocean currents present useful avenues for harnessing renewable energy from wakes which therefore provide positive prospects for understanding wakes, and its features associated with nature (Wang et al., 2017). Fluid dynamicists are specifically intrigued by the repetitive patterns, both in quantitative and qualitative sense, that particularly reflect the underlying order within random fluid motion associated with wakes. These recognizable forms are usually referred to as coherent structures. The definition of coherent structure, as proposed by Fazle Hussain (1986), suggested that any large scale organized compo-

nent of phase correlated vorticity, that accompanied irregular and random vorticity fluctuations, essentially reflected a coherent structure. These were the primary focus of many jet and wake studies over the years, dating back to the pioneering work of Corrsin (1944) and Roshko (1954b). The occurrence of quasi-periodic coherent structures in turbulent shear layers was further analyzed through flow visualization experiments of Kline et al. (1967). Fazle Hussain (1986) indicated that the coherent structures were responsible for transporting mass, momentum and heat in myriad of industrial processes mentioned above. Therefore, the importance of understanding and characterizing every facet of coherent structures in turbulent wakes is one of the major areas of research in modern fluid dynamics.

Free shear layer or mixing layer is another classic problem in fluid mechanics, where coherent structures are observed in terms of streamwise ribs and spanwise rollers (Durbin and Reif, 2010). The spanwise rollers were commonly observed in two-dimensional Kelvin Helmholtz instability (Friedlander and Lipton-Lifschitz, 2003), while the ribs formed in the braid region between two consecutive spanwise rollers. These were represented by elongated and paired streamwise vorticity structures on account of the intense straining of braid shear layers (Mittal and Balachandar, 1995). Such coherent vorticity formations were prominent in flows around stationary cylinders (Zhang et al., 1995; Brede et al., 1996; Mittal and Balachandar, 1995; Williamson, 1996; Robichaux et al., 1999), and airfoils with varying trailing edge shape (Ryan et al., 2005; Gibeau et al., 2018). Oscillating bluff body wakes further depicted the formation of vortex streets that were mainly characterized by shedding of spanwise rollers (Williamson and Roshko, 1988; Koochesfahani, 1989). The onset of three-dimensionality in such cases was linked to the formation of streamwise vortical structures, which originate from the perturbations induced on spanwise rollers (Williamson, 1996).

Several studies employed Floquet stability analysis to quantitatively assess the characteristic spanwise instabilities that trigger the formation of streamwise or secondary vortex structures in the wake of oscillating bluff bodies (Ryan et al., 2005; Deng et al., 2015; Deng and Caulfield, 2015b; Sun et al., 2018; Son et al., 2022). Qualitative evolution of these flow mechanisms also revealed the complex process of vortex interactions and merging, which linked growth of the insta-

bility and evolution of the secondary vortical structures in the wake (Mittal and Balachandar, 1995; Williamson, 1996). However, there is still a lack of knowledge in understanding the wake formation, interactions and developments behind oscillating bodies. Experimental and computational assessments have focused on simpler kinematics of foils, such as pure heaving or pitching (Deng et al., 2015; Sun et al., 2018; Chiereghin et al., 2020; Son et al., 2022). However, there is only a limited understanding of characteristics relevant to the wake topology and three-dimensionality behind foils oscillating in multi-degree of freedom motion.

Besides advancing our fundamental understanding of fluid mechanics and wake dynamics for oscillating rigid bodies, this study contributes to the development of energy harvesting technologies, such as propulsors employed for tidal and wave energy generators (Wang et al., 2017), man-made marine swimmers for biological monitoring of flora and fauna found in seas and oceans (Van Buren et al., 2019), and macro- or micro-robotic swimmers for geophysical resource mining (Ma et al., 2017). The physical flow concepts investigated and explored here also enable development of flow manipulation and control technologies that are capable of reducing drag production through oscillating foil propulsors (Van Buren et al., 2019). Considering the wake three-dimensionality, including assessment of vortex instabilities and secondary structures, this dissertation can provide insights into the unique physical mechanisms that can be capable of controlling vortex disintegration (Leweke et al., 2016). These can ultimately reduce noise propagation in man-made flying and swimming vehicles (Ortega and Savas, 2001), which can otherwise have detrimental effects on biological swarms of marine fauna. The reduction of noise can also be helpful during jet aircraft operations near townships and cities.

Decreasing accidents associated with trailing wake of commercial aircraft is further desirable. Usually, a lower time for disintegration of shed vortices, before they interact with the trailing aircraft, can be helpful in preventing such accidents (Ortega et al., 2003). An elaborate discussion with regards to these applications are included in this section.

Carangiform and Anguiliform constitute two commonly observed and documented biological swimming types in marine species (Smits, 2019). Carangiform type was associated with a finite

amplitude lateral movement of the posterior body part, commonly termed as the caudal fin (Videler, 1993). This mode is believed to be highly efficient considering the biological swimmers do not spend power in moving their entire body (observed for anguiliform mode) for thrust generation (Smits, 2019). The fundamental science and understanding of these biological swimmers have been extensively investigated in recent decades so that efficient swimming robots can be developed for engineering applications (Triantafyllou et al., 1993, 2000, 2004; Schnipper et al., 2009; Dewey et al., 2012; Senturk and Smits, 2019a; Van Buren et al., 2019).

Propulsive performance, wake features and kinematics were often evaluated concurrently for efficient oscillatory swimming motion (Triantafyllou et al., 1993; Blondeaux et al., 2005; Anderson et al., 1998; Triantafyllou et al., 2000). Triantafyllou et al. (1993) assessed the propulsive performance of fish species, such as breams and sharks, and found that their efficient performance coincided with a Strohaul number range of $0.2 - 0.35$. The frequency of oscillating tail is often increased by some biological swimmers in order to gain speed, although they keep the motion amplitude approximately constant (Smits, 2019). Such behaviors motivated researchers to evaluate the coincident wake formation that eventually revealed the presence of reverse Von Kármán vortex streets in most thrust-generating swimmers (Müller et al., 2001; Godoy-Diana et al., 2008). Other typical wake topologies, characterized by shedding of vortex pairs, were referred to as $2P$, which were observed in the wake of swimming alligators (Fish and Lauder, 2013) and depicted highly efficient performance under cruising conditions. Figure 1.1 depicts classical wake models of Benard Von Kármán (2S or BvK), reverse Benard Von Kármán ($rBvK$) and 2P modes behind a rigid oscillating foil that mimic a biological fin motion of a marine swimmer. Such vivid links between the kinematics of oscillating fins and wake topology led to a deeper assessment of there swimming habits.

Evolution in biological fin geometries of marine swimmers further accelerated their performance improvement over time, which thus offers more insightful prospects for developing high efficiency man-made underwater swimming technologies. However, the flow manipulation techniques employed by several marine swimmers are still difficult to understand currently, within

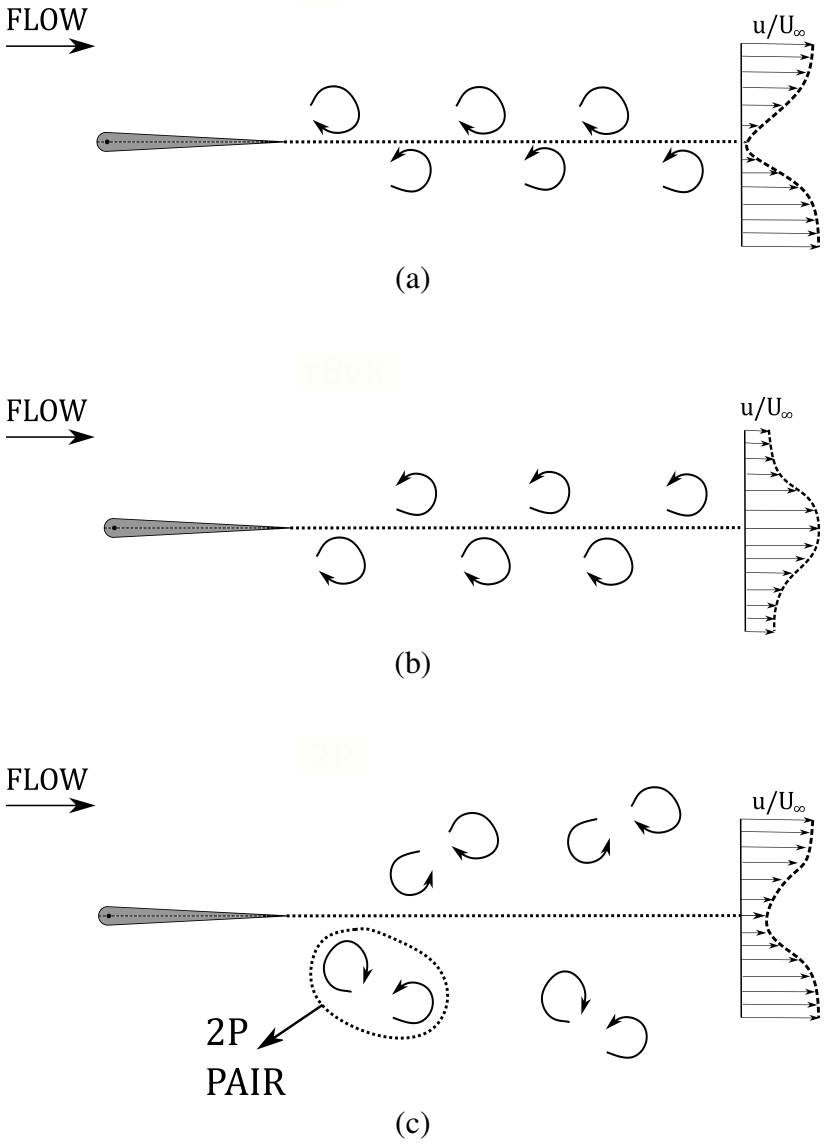

Figure 1.1: Schematics representing (a) Benard Von Kármán, (b) reverse Benard Von Kármán and (c) 2P mode in the wake of oscillating foil.

biological fluid dynamics. For example, the flow often encounters a laminar to turbulent transition in the realm of oscillating foils that relate to engineering applications. Understanding this dynamics is critical for achieving an uninterrupted and efficient thrust generation (Xu et al., 2018). Even greater complexity arose when the modes of transition varied based on the flow Reynolds number (Re), design and kinematic motion parameters (e.g. changing angle of attack for the oscillating foil). Three major transition modes were natural transition due to inherent laminar boundary layer instabilities, bypass transition based on the convection-diffusion process of surrounding freestream turbulence, and the separation induced transition (Xu et al., 2018). Since the occurrence of these modes depended on the flow and motion parameters of an oscillating foil, it was therefore apparent that a vivid analysis of the flow physics, mainly in terms of vortex dynamics, was needed to address the desirable advancements in developing man-made propulsors.

Researchers utilized various foil designs that closely resembled and operated based on caudal fin movement in biological swimmers (Smits, 2019). Their use and development has been studied rigorously since the early 1860s. Some documents suggested that a boat's rear frame should consist of spanwise installation of three airfoil cross-section blades, which was tested in Surrey canal of England (Vagianos, 1970). Observations indicated an increased lift and a lowered drag (achieved through trimming), which therefore highlighted the capability in thrust generation and maneuvering. Significance of oscillating foil was also described in terms of its lift and stability provisions. This, particularly, reflected the use of heaving foils, which were installed and operated on sea planes and boats (Vagianos, 1970). Some examples include British's "Tractor Avro biplane", that employed a system of foil cascades, American seaplane "Flying Fish", which was developed by the Michigan Steel Boat company, and demonstrated a functioning chord foil capable of lifting the entire plane at a speed of 70 miles per hour (Vagianos, 1970).

Autonomous underwater vehicles ($AUVs$) employ oscillating foils in underwater marine surveillance and wave energy harvesting through tidal generators in recent years (Wang et al., 2017). The bionic oscillating foil technology that is extensively utilized in extracting hydro-kinetic energy from flowing water succeeded by overcoming some limitations associated with horizontal

axis water turbines (Kim et al., 2017). This included their operational capability in shallow water channels without producing much noise (on account of their operation underwater). The energy contained in the unsteady flow that consists of strong rotational vortex structures was efficiently extracted by bionic flapping foils (Mannam et al., 2017; Sitorus and Ko, 2019; Mo et al., 2022). Multiple foil patterns were also configured to maximize power extraction from a given resource area (Ma et al., 2017).

The mechanism of energy generation through the oscillatory motion of foils is dominated by vortex dynamics, specifically the formation and advection of leading edge vortex (LEV) structures (Kim et al., 2017). As the LEV sheds, Kim et al. (2017) observed a decrease in the transverse force produced on account of the heaving motion of the foil. To maintain a continuous energy production, a pitching motion was then added to the kinematics to generate another opposite sign LEV. It was thus apparent that a coupled heaving and pitching motion is efficient for energy extraction through an oscillating foil. Despite such observed performance enhancements with the combined oscillatory motion of foils, there still remains imminent knowledge gaps that must be investigated. These specifically revolve around the onset of three-dimensionality in the wake of oscillating foils.

Spanwise instabilities associated with vortex rollers has often indicated the onset of three-dimensionality in the wake of stationary bluff bodies (Williamson, 1996). The resulting growth of streamwise vortical structures contributes towards disintegration of spanwise rollers (Leweke and Williamson, 1998; Bristol et al., 2004). In modern air transportation, trailing wake accidents have put considerable limitations on the number of aircraft that can take-off and land on runaways within a given time-frame (Leweke et al., 2016). Thus, airline industry often fails to meet the growing demand of air traffic. Such accidents usually occur on account of the extreme downwash by trailing vortex rollers in the aircraft wake, which induces sudden and severe vibration loading on the aircraft that is taking off just after its predecessor airplane (Leweke et al., 2016). Co-rotating configuration of vortical structures were also observed in the near wake of flaps installed on aircraft, which could induce unwanted rolling moments (Meunier and Leweke, 2005). The

spanwise instabilities can be effective in early disintegration of these trailing vortex rollers, thereby reducing the time lag between consecutive take-off and landing of airplanes (Ortega et al., 2003).

The role of secondary vortex structures and their link with the developed spanwise instability is not yet fully understood. These can be further exploited to achieve a faster and efficient decay of strong coherent rollers. Oscillating flaps, installed in tandem with the airplane wing cross-section, can be a useful means to control the vortex disintegration timing, thereby reducing the chance of wake hazards. However, we have a limited understanding of the characterization of secondary wake structures and their association with oscillating foil kinematics. The current work addresses this important problem for both practical engineering systems, and elementary mechanisms of vortex interaction.

The roller instabilities were not only evident for fixed wing engineering system, but also remained prominent for flapping or rotating wing/foil technologies (Visbal, 2009; Chiereghin et al., 2020; Son et al., 2022; Hammer et al., 2022). These include micro-air vehicles ($MAVs$), rotorcraft and wind turbines (Chiereghin et al., 2020). Such low or high aspect ratio wing, and flapping foils, experience the formation of dynamic stall vortices on the leading edge that grow in size and advect over the boundary. These vortices experience instability development, which coincided with unwarranted fluctuations in force and moments generated through flapping (Son et al., 2022). In some cases, such dynamic stall vortices also interact with trailing edge vortex (TEV), which thus embark a positive or detrimental effect on account of the spanwise instability. Negative consequences include the deterioration of propulsive performance, whereas the positive effects are revealed in terms of noise canceling mechanisms (through early vortex dissipation and degradation). The latter case is often needed during underwater operations of robotic vehicles, i.e. $AUVs$, such that a smaller disturbance is imposed on the surrounding biological habitat. Similar noise-canceling scenarios were presented as the essential design requirement for submarines, such that a high degree of stealth was achievable during subsea surveillance purposes (Ortega et al., 2003). Owing to such vast engineering needs, an important contribution of this work relates to understanding the association of spanwise instabilities, secondary vortex growth and kinematics of flapping or os-

cillating foils in complex multi-degree of freedom motion. The findings also address the existing knowledge gaps associated with fluid flow manipulation through vortex dynamics.

This dissertation explores the wake evolution behind oscillating foils with two-degree of freedom motion, i.e. heaving (or plunging) and pitching, coupled such that the heaving lags pitching with an assumed phase offset (ϕ). Geometry of the foil resembles a teardrop shape, which closely mimic the oscillating tail fins of biological marine swimmers such as fish, whales and dolphins (Van Buren et al., 2018, 2019). The Re for this study varies in the range of $1000 \leq Re \leq 8000$, which follows with the biological swimming characteristics extracted from marine swimmers (Floryan et al., 2017; Senturk and Smits, 2019a; Smits, 2019). Two-dimensional wakes are particularly observed at $Re \leq 4000$. They present a better prospect to assess the association of propulsive performance and spatio-temporal arrangement of vortex structures (Godoy-Diana et al., 2008; Schnipper et al., 2009). This also enables a comparative evaluation of the wake with other prominent studies of oscillating foils with a single degree of freedom motion (Godoy-Diana et al., 2008, 2009; Schnipper et al., 2009; Deng et al., 2015; Sun et al., 2018; Zheng et al., 2019).

At $Re = 8000$, the flow becomes fully turbulent behind an oscillating foil, and is devoid of major transitional effects in the shear layer (Visbal, 2009; Lagopoulos et al., 2019; Chiereghin et al., 2020; Son et al., 2022). Using three dimensional numerical simulations of an infinite span teardrop foil geometry that oscillates in a coupled heaving and pitching motion, this dissertation examines the evolution of spanwise instabilities and coherent pairs of counter-rotating streamwise vortex structures (also referred to as secondary vortex structures in this study).

Existing literature on wake evolution behind stationary cylinders suggest growing intermediary hairpin-like vortices, whose legs eventually extend to form *rib* pairs (Mittal and Balachandar, 1995). However, extensive research on the presence of hairpin vortical structures, and the origin of ribs, is still required in the wake of foils undergoing complex oscillatory kinematics. Thus, the major foundation laid here comprises the assessment of spanwise instability features of leading (LEV) and TEV rollers, and their association with the growth of secondary vortex structures in the wake of oscillating foils. The influence of changing kinematics on the characteristics of insta-

bilities and secondary structures is also evaluated in this dissertation, which present the universal applicability of this work to three-dimensional wake of oscillating foils.

This study advances the conceptual understanding in modification of wake dynamics using variation in foil kinematics. These can promote desirable extraction of energy from the fluid flow around the foil with low input power requirement, which could therefore improve the propulsive efficiency. The association of changes in the spatial arrangement of primary vortices with variations in kinematics is addressed, and coincident performance features are evaluated. Vortex interactions and merger are then linked with the mean wake characteristics such that the kinematics can be tuned for promoting such mechanisms during operational purposes. A mathematical framework is further developed such that the strength of shed vortices can be efficiently controlled. The wake instability mechanisms are evaluated to control disintegration of vortical structures (either early or delayed) based on the need to reduce far wake effects that are responsible for noise reduction.

1.2 Motivations and Objectives

Investigation of the wake dynamics and turbulence associated with flow around bluff-bodies have motivated several studies in the recent past. These include flow around stationary rigid bodies, such as circular cylinder (Williamson, 1996; Mittal and Balachandar, 1995), blunt trailing edge (BTE) airfoil (Ryan et al., 2005; Gibeau et al., 2018), cylinder with square or rectangular cross-section (Robichaux et al., 1999), and normal thin flat plates of high and low aspect ratio (Najjar, 1998; Hemmati et al., 2016). The generation of propulsive forces (thrust, lift and side-force), enhancement and dissipation of turbulence through manipulation of coherent structures, and interaction of flow with rigid or flexible solids, are some of the aspects which hold an inherent dependence on the wake behavior (Leweke et al., 2016), and thus presents a crucial motivation for researchers.

In case of oscillating rigid bodies, such as a foil geometry (NACA series or teardrop), characterization of the spatial topology of coherent rollers in the wake has been of major interest (Godoy-Diana et al., 2008; Schnipper et al., 2009). The main reason was modeling the net momentum

deficit or excess produced in the wake, which could ultimately result in either propulsive thrust generation or drag production. Studies also conducted stability analysis to gather insights into quantitative features of dominant and unstable instability modes that govern the onset of three-dimensionality in the wake (Deng et al., 2015; Moriche et al., 2016; Sun et al., 2018). However, our knowledge is still limited in characterizing two- and three-dimensional wake of oscillating foils in combined heaving and pitching motion. Studies have proven that a substantial increase in propulsive efficiency occurs when a coupled heaving and pitching motion is employed rather than a single degree of freedom kinematics, i.e. pitching or heaving (Anderson et al., 1998). However, aspects related to coincident transitions in the wake topology at varying kinematics parameters, and the three-dimensional evolution of coherent structures, are still not clear.

This dissertation aims to address the knowledge gaps based on the following objectives:

(A) *To understand and characterize the transition in propulsive performance and wake topologies of oscillating foils in combined heaving and pitching motion, at varying kinematics and Re.* The variation of Strouhal number (St_A), peak heave or pitch amplitude, *Re*, pitch axis location and overall foil geometry impose positive or degrading effects on propulsive performance. Such implications can be modeled through a scaling relationship, which highlights dependence on all kinematic and flow parameters. Several models have been evaluated for foils in either pure pitching or heaving motion (Floryan et al., 2017; Senturk and Smits, 2019a; Smits, 2019). However, advancement of similar models for foils executing coupled oscillatory motion is addressed here. Verification of a prominent laminar scaling model (Senturk and Smits, 2019a), deemed accurate in characterizing the propulsive thrust and power of pitching foils, is conducted. Implications of vortex shedding are evaluated, particularly, to understand the distribution of pressure and viscous forces. Assessment and characterization of performance transition with respect to changes in wake topology is also evaluated. Specifically, the mechanism of drag to thrust transition (or vice-versa) can be associated with changes in the arrangement of coherent structures shed in the wake. Understanding their topology and the coincident momentum change in the wake forms an integral part of this objective.

(B) *Establish a governing relationship between aspects of vortex shedding in the wake, and kinematics of oscillating foil using first principles.* This relationship can provide a mathematical framework to establish a physical association between foil kinematics and transitions in wake topology, which inherently depends on the strength ratio of leading and trailing edge structures. Strength of the coherent structures in the wake, which is quantifiable in terms of circulation or size, is often observed to govern the interaction mechanisms during their spatio-temporal evolution (Schnipper et al., 2009). Formulation of such a model, therefore, provides a unique capability to predict the spatio-temporal transition of wake topologies *a priori*, while allowing engineers to control the circulation of leading and trailing edge structures through tuning of motion settings.

(C) *Characterize the three-dimensional wake evolution behind an oscillating foil executing combined heaving and pitching motion.* Dynamics of three-dimensional instabilities associated with coherent structures in the wake of a stationary or oscillating bluff body presents a crucial importance since they govern the three-dimensional nature of the wake (Williamson, 1996; Deng et al., 2015). Their characteristics also influence the temporal variation of force generation, and topological transition of the wake. Recent studies conducted for purely heaving foils observed dominant spanwise undulations of *LEV*, although the origins of such instability feature remained unclear (Chiereghin et al., 2020). The quantitative assessments of perturbation modes for purely pitching foils also lacked details including association between the instability growth on rollers and secondary vortex pairs (Deng and Caulfield, 2015b). Visbal (2009) also hinted that the interaction of rollers with the moving foil boundary induce strong spanwise instabilities. However, their association with the growth of secondary vortex structures remains unclear.

Experimental visualization techniques, i.e. Particle Image Velocimetry (PIV), employed for understanding wake mechanics of stationary bluff bodies have provided reasonable accuracy in identifying and characterizing coherent structures in detail, specifically the rollers and rib pairs (Williamson, 1996; Gibeau et al., 2018). However, these techniques encounter difficulties in case of oscillating bodies while extracting information on the instability onset, resolving vortex bound-

ary interactions and physics, growth of secondary and intermediate vortical structure formation. These aspects collectively govern the three dimensional wake features.

Directly simulating the flow is a useful computational tool that provides detailed flow data for understanding the formation and evolution mechanisms of intermediate secondary structures, and associated roller instabilities. Access to three-dimensional velocity and vorticity fields allows extensive quantification (in terms of circulation strength and size of vortical structures) for analytical modeling. These simulations also allow for an accurate detection of surface pressure fields that enable clarity with respect to onset and evolution of spanwise instabilities. Such observations are well established in cases that concerned wakes of normal thin flat plates, rectangular cylinders and oscillating square panels (Hemmati et al., 2016, 2019a; Hemmati and Smits, 2019), respectively. The current study directly solves the Navier-Stokes equations (hereby referred to as DNS) on non-homogeneous computational grids, for meeting the objectives outlined above.

1.3 Novelty

The novelty of this work belongs to the wake dynamics of oscillating foils, which can be briefly highlighted as:

(1) Establishing a physics based scaling of the propulsive performance of oscillating foils with combined heaving and pitching motion based on $Re-$variation, and comparing its validity relative to the models of purely heaving or pitching foils.

(2) Investigating the association of transitions in 2D wake topology and propulsive performance towards providing a vivid physical explanation for a lack of direct correspondence between wake structures and performance characteristics of foils.

(3) Identifying the mechanisms of transitions from thrust to drag production for oscillating foils through changes in phase offset between the heaving and pitching motion. Also, characterizing the transitions in wake topology that coincide with either heave- or pitch dominated regimes of kinematics.

(4) Providing a mathematical relationship between kinematics parameters (reduced frequency, Strouhal numbers, ϕ) and strength of shed vortex structures to predict the transitions in wake topology outlined in (3).

(5) Establishing and characterizing three-dimensional wake topology that coincide with high efficiency and large thrust generation. Characterizing the spanwise instability of rollers and the growth of intermediate secondary vortex structures that influence the transition to three-dimensional wake behavior.

(6) Identifying the mechanisms for onset of spanwise instabilities and their changes triggered on account of variation in kinematics. Further, establishing their links with growth and evolution of secondary wake structures.

1.4 Structure of the thesis

This dissertation begins with an elaborate review of the research conducted on the wake of stationary and oscillating bluff bodies, specifically hydro- and aerofoils, in Chapter 2. This chapter describes various experimental and computational strategies utilized for examining and characterizing coherent structures. A vivid description of the computational methodology employed for this study is provided in Chapter 3. The numerical algorithm, computational domain setup, boundary and initial condition that accurately capture and model the wake of foils and bluff bodies (stationary and moving) are explained in detail. The verification and validation assessment of the numerical tool is also included, which provides sufficient confidence in the numerical tools utilized for simulating the wake of an oscillating foil with complex multi-degree of freedom motion (i.e. simultaneous heaving and pitching).

Chapter 4 provides a comprehensive evaluation of the laminar scaling model for the oscillating foils in combined heaving and pitching motion, at a range of kinematic parameters and Re. The assessments based on two-dimensional numerical simulations include insights gained via examining spatial variation of pressure and viscous forces, which provide an appropriate physical reasoning

behind deterioration of the laminar scaling within selective regimes of motion kinematics and *Re*. An adequate improvement to the propulsive thrust and power scaling is finally expressed, which incorporates the dependence of performance metric (thrust and power) on *Re*. An association of performance, kinematics and vortex formation features (strength and location from leading edge) are investigated in the following chapters.

The findings discussed in Chapter 4 highlight some of the unique features relevant to the scaling of propulsive thrust performance of an oscillating foil at varying kinematics. The coincident vortex interaction mechanisms that reasonably associate with the changes of a thrust dominated propulsive performance to a drag domination, are evaluated in Chapter 5. The findings reveal novel transitions in wake topology that coincide with changes in performance, at a range of kinematic parameters. The *Re* is fixed at 1000 in order to have a comparable evaluation with oscillating foils in pure pitching motion. Chapter 6 substantiate the performance evaluation by including the nature of transitions experienced by lift force, within a similar range of motion settings and *Re* assumed in Chapter 5. The findings presented here elaborates on the lift generation features that remain specific to heave and pitch dominated kinematics, respectively. A major contribution of this study in the form of proposition and validation of a new mathematical model, that predicts the wake topology transition based on the changing foil kinematics, is ultimately discussed in Chapter 7. The observations reported at moderate *Re* of 1000 and 4000 further reveal unique dipole bifurcations that can be utilized for manipulating features of fluid-structure interaction around an oscillating foil. Chapters 4, 5, 6 and 7 collectively address the objectives *A* and *B* highlighted in Section 1.2. At $Re > 5000$, three-dimensional onset of spanwise roller instability and secondary wake structures is evident. Therefore, the subsequent chapters establish the three-dimensional wake topology and its association with varying foil kinematics.

Chapter 8 establish novel wake models that coincide with high performance kinematic settings, while showcasing unique insights into onset mechanisms of leading edge vortex instabilities. The coincident features concerning growth of secondary vortex pairs are also evaluated. The contents discussed in this chapter majorly focus on comprehensive evaluation of the three-dimensional

wake, with an aim to characterize the spanwise instabilities on vortex rollers, and secondary wake structures, behind oscillating foils executing coupled heaving and pitching motion. An infinite span teardrop foil geometry is assumed for this assessment, to avoid incorporating effects associated with tip vortex usually observed in wakes of finite aspect ratio geometries. Qualitative evidence of a relatively larger influence of strong amplitude vortex dislocations on spatial features of secondary vortex pairs, compared to their temporal periodicity in the wake of oscillating foils, is also provided in this chapter. Besides identifying and characterizing the three-dimensional instabilities and secondary structures for high performance wakes, their crucial inter-linked dynamics and fundamental association with kinematics also need further investigation.

Chapters 9, 10 and 11 provide fundamental insights into the association of spanwise vortex instability, growth of secondary wake structures and kinematics of oscillating foils. The observations suggests a consistent appearance of hairpin-horseshoe intermediate structures, and high amplitude of vortex undulations, within prescribed heave dominated kinematics. Chapter 10, particularly, presents implications of the increasing reduced frequency on the growth of secondary wake structures. Chapter 11 advances the investigation of Chapter 10 by evaluating the effects of increasing ϕ such that the motion transitions from a heave- to pitch-dominated oscillation. Chapters 8, 9, 10 and 11 collectively address the objective 'C' highlighted in Section 1.2.

The summary of several important contributions and findings of this work is presented in Chapter 12. The prospects of extending this research, particularly, by incorporating effects of flexibility in rigid foils is also highlighted here. Primarily, the advancement in terms of developing a coupled overset numerical solver and solid deformation can provide a major contribution to CFD and fluid dynamics community for numerous applications. Moreover, the influence of flexibility on three-dimensional evolution of instability and secondary wake structures still remains unknown for infinite span oscillating foils. Thus, the wake observations from simulations can reveal deeper insights into the actual swimming and flying mechanics of biological species including fish, birds and reptiles. This knowledge could ultimately re-engineer new and cleaner energy harvesting and bio-inspired propulsion systems.

Chapter 2

BACKGROUND

Wakes are an essential part of the study of turbulence. The flow around any bluff or blunt body results in the formation of energetic motions through the vortex shedding phenomenon, which can be either periodic or quasi-steady in nature (Pope, 2000). A collection of energetic eddies that constitute a highly rotational flow is a common characteristic of all wake flows. The mutual interaction between several groups of eddies can further govern the unruly behavior of the flow, and hence promote turbulence. However, the organized component of a wake flow presents major interest since its spatio-temporal topology associate with the forces generated on the body, and the net momentum created within a specific region around the body (Fazle Hussain, 1986). In case of oscillating foils, particularly hydro- or airfoils, wakes are characterized by spatial arrangement of primary vortex, also referred to as rollers (Williamson, 1996). The spatial arrangement and temporal shedding of these primary vortex structures are essentially responsible for propulsive force generation, useful for various engineering applications (Anderson et al., 1998). The dynamic interaction of rollers can further contribute to differences in the mean flow features (Godoy-Diana et al., 2008).

Despite the role of rollers, the onset of three-dimensionality through secondary vortex formation process strongly govern the fundamental nature of turbulence in the wake. Formation of secondary vortex is associated with the generation of spanwise instability on the rollers that impose

vortex dislocations at specific spatial locations (Williamson, 1996). As the evolution progresses, these dislocations contribute to spanwise arrangement of counter-rotating streamwise vortex pairs, commonly referred as ribs. Interaction of these rib pairs with additional vorticity within the braid region can also lead to intermediate secondary structures (Mittal and Balachandar, 1995), which further promote turbulence production and entrainment of surrounding undisturbed freestream (Durbin and Reif, 2010). A complex interplay between the primary and secondary vortex structures presents an intriguing concept in fluid dynamics of oscillating foils.

This chapter provides a comprehensive review on several areas of flow physics and fluid mechanics behind oscillating foils, which mainly concerns with propulsive performance and its association with primary wake structures. A review of previous studies on the physics and evolution of three-dimensional secondary structures in the wake of stationary bluff bodies (e.g. circular and square cylinder, blunt trailing edge airfoil) and oscillating foils (pure pitching or heaving) is also discussed in this chapter.

2.1 Kinematics of Oscillating Foil

The advent of research on oscillating foils emerged in the 20^{th} century, which has led to the development of novel propeller technologies for underwater propulsion. The operational insights largely came from the biological swimming and flying styles adopted by fish and birds, respectively (Triantafyllou et al., 1993). For example, within biological underwater locomotion practices, numerous swimming styles have been explored by researchers in addition to body morphologies of different species. Some of the widely known types of motion in nature include undulation, oscillatory, pulsatile and drag-based locomotion (Smits, 2019). In undulatory mechanism, the swimmer generates a traveling wave across its body and thereby exerts a push force on the fluid. Oscillatory swimming involves a periodic movement of a fin, which constitutes a segment within the posterior part of the swimmer's body. Pulsatile swimming requires ingestion and discharge of water to generate a periodic thrust. Finally, drag-based swimming uses a rigid flipper to generate forward locomotion.

The principle modes that are generally followed for several foil designs include undulatory and oscillatory forms of swimming, where the latter has been more extensively investigated due to its relatively higher efficiency and thrust generation capabilities (Smits, 2019).

Two generic types of oscillating foil kinematics have been vastly considered in literature. These are namely purely pitching (Figure 2.1(b)) and heaving (Figure 2.1(a)) kinematics, respectively. The coupled form that constitutes simultaneous heave and pitch oscillations (Figure 2.1(c)) further hold a special importance due to its increased capability of achieving highly propulsive performance during cruising conditions (Van Buren et al., 2019). The case of pitching motion involves a foil that rotates around a point located near to the leading edge. Considering the maximum foil angle as θ_o, oscillating frequency as f, the equation for pitching ($\theta(t)$) can be directly defined in terms of a sinusoidal motion as:

$$\theta(t) = \theta_0 \sin(2\pi f t) \tag{2.1}$$

The heaving motion is characterized by a transverse movement of the entire foil's chord. The function ($h(t)$) is expressed in terms of peak heave amplitude (h_o) and f representative motion given by:

$$h(t) = h_0 \sin(2\pi f t) \tag{2.2}$$

A coupled heaving and pitching motion is achieved when the former lags by ϕ, relative to the heave motion. $\theta(t)$ in this case can be represented as:

$$\theta(t) = \theta_0 \sin(2\pi f t + \phi) \tag{2.3}$$

The oscillatory kinematics is governed by several normalized parameters. The St describes the frequency of oscillation, and is defined as:

$$St = \frac{fL}{U_\infty} \tag{2.4}$$

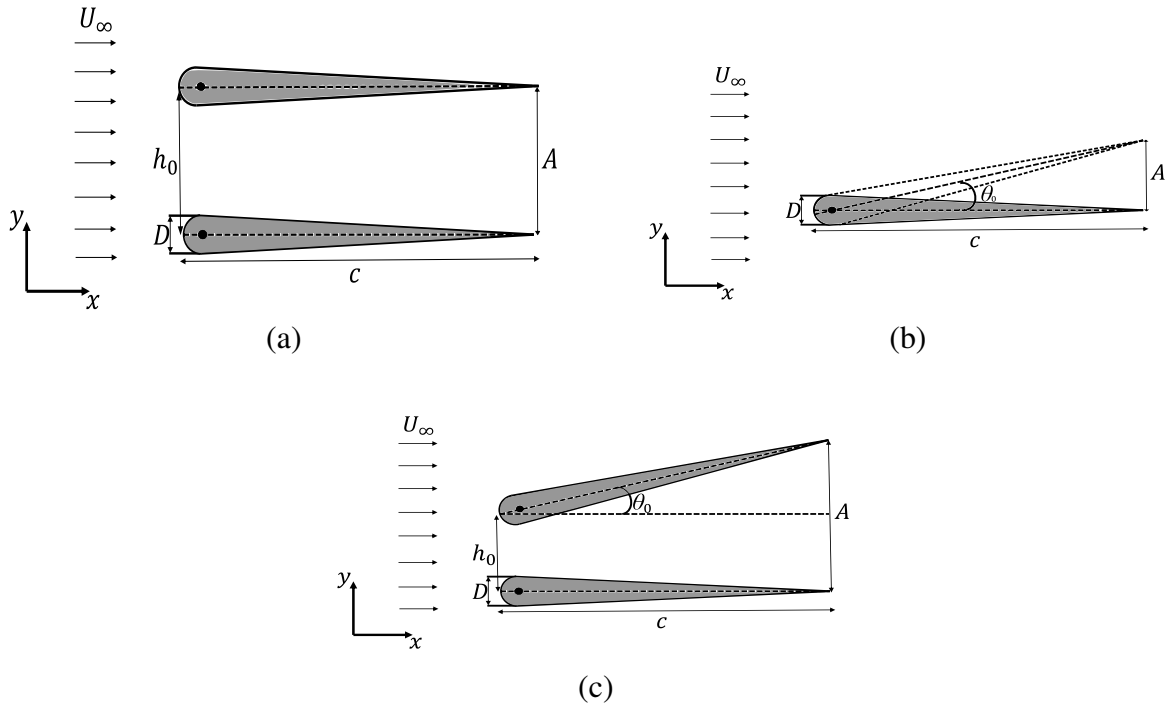

Figure 2.1: Foil kinematics, geometry and coordinate system. (a) Pure heave, (b) pure pitch and (c) coupled motion.

The length scale (L) employed for St can include foil's chord (c) or diameter (D), and maximum trailing edge amplitude (A) achievable within one oscillation cycle. St_c is also termed as reduced frequency of the foil motion. These definitions can be written as below:

$$St_c = \frac{fc}{U_\infty}, \;\; St_D = \frac{fD}{U_\infty}, \;\; St_A = \frac{2fA}{U_\infty} \tag{2.5}$$

The trailing and leading edge amplitudes can be further written in their non-dimensional form as:

$$A_D = \frac{A}{D}, \;\; A_c = \frac{A}{c} \tag{2.6}$$

$$h = \frac{h_0}{c} \tag{2.7}$$

For coupled heave and pitch motion, effective angle of attack (α_{eff}) is treated as another important kinematic parameter for propulsive performance assessments and leading edge vortex dynamics. It

is defined by the summation of instantaneous pitch angle and heave-induced angle of attack. This is represented by the following expression:

$$\alpha_{eff} = \theta_0 \sin(2\pi ft + \phi) - \tan^{-1}\left[\frac{h_0 2\pi f \cos(2\pi ft)}{U_\infty}\right] \tag{2.8}$$

The pivot location of the foil is also marked in Figures 2.1(a-c). Its distance from the leading edge can also influence the behavior of vortex shedding and force generation of the oscillating foil.

2.2 Propulsive Performance of Oscillating Foil

It is well recognized that the physical mechanisms of propulsion depend on various motion and flow parameters: leading/trailing edge amplitude, oscillation frequency (expressed in terms of St_A, St_D or St_c), parameters associated with multi-degree of freedom motion (such as ϕ between heaving and pitching), and Re. Geometrical constraints, i.e. ratio of D to c, can also be added to the list. An understanding of linear and non-linear dependence of the performance metrics on these parameters is required to develop highly propulsive and efficient swimming systems (Floryan et al., 2017). These metrics primarily include lift and thrust coefficient (C_L and C_T), input power coefficient (C_P) and propulsive efficiency (η). The mathematical definitions of these parameters can be written in following forms;

$$C_L = \frac{F_y}{\frac{1}{2}\rho U_\infty^2 A_{ref}}, \quad C_T = \frac{F_x}{\frac{1}{2}\rho U_\infty^2 A_{ref}}, \quad C_P = \frac{F_y\dot{h} + M\dot{\theta}}{\frac{1}{2}\rho U_\infty^3 A_{ref}} \qquad (2.9a\text{–}c).$$

Here, F_x is the thrust force, F_y is the lift force, and M is the pitch moment. Moreover, A_{ref} denotes the reference area calculated as the product of foil span (S) and c. ρ is the density of the fluid medium. We can also represent the time-averaged version of forces, e.g. $\overline{F_x}$, which can be calcu-

lated from the instantaneous force component in the streamwise direction and oscillation period (τ) as:

$$\overline{F_x} = \frac{1}{\tau}\int_0^{\tau} F_x(t)\mathrm{d}t \tag{2.10}$$

Similarly, $\overline{P}$ can be calculated based on the instantaneous transverse force, pitching moment and time derivatives of heaving and pitching motion, respectively. This is represented by:

$$\bar{P} = \frac{1}{\tau}\left[\int_0^{\tau} F_y(t)\frac{\mathrm{d}h(t)}{\mathrm{d}t}\,\mathrm{d}t + \int_0^{\tau} M_\theta(t)\frac{\mathrm{d}\theta(t)}{\mathrm{d}t}\,\mathrm{d}t\right] \tag{2.11}$$

The propulsive efficiency is calculated based on the $\overline{C_T}$ and $\overline{C_P}$, such that:

$$\eta = \frac{\overline{C_T}}{\overline{C_P}} \tag{2.12}$$

Fundamental theories dedicated to modeling oscillating foil propulsion in the mid-20th century (Theodorsen, 1935; Garrick, 1936; Sedov et al., 1965) were limited to inviscid flows. Since these proved unsuccessful in capturing variations of performance characteristics under a broad range of kinematic regimes (Triantafyllou et al., 1993), scaling parameters such as St_A and St_c were identified. As highlighted before, these parameters depicted optimum performance characteristics within a narrow range of f (Triantafyllou et al., 1993) . Triantafyllou et al. (2005) further attributed the amplitude-to-chord ratio, maximum angle of attack and vortex-ring formation-time as other relevant scaling parameters for steadily flapping and maneuvering foils. Increased speed of the foil also has a role in drag-to-thrust transition, which was investigated for different gaits by Lagopoulos et al. (2019). They found that foil propulsion occurred due to a propulsive jet that forms when the induced velocity of the foil exceeds freestream velocity. Similarly, Chao et al. (2021) investigated the dependence of asymmetric pitching motions on drag-to-thrust transition. They empirically determined that the asymmetry parameter is related to the square of transitional St. The corresponding increase in thrust was attributed to the increased pitching speed early in

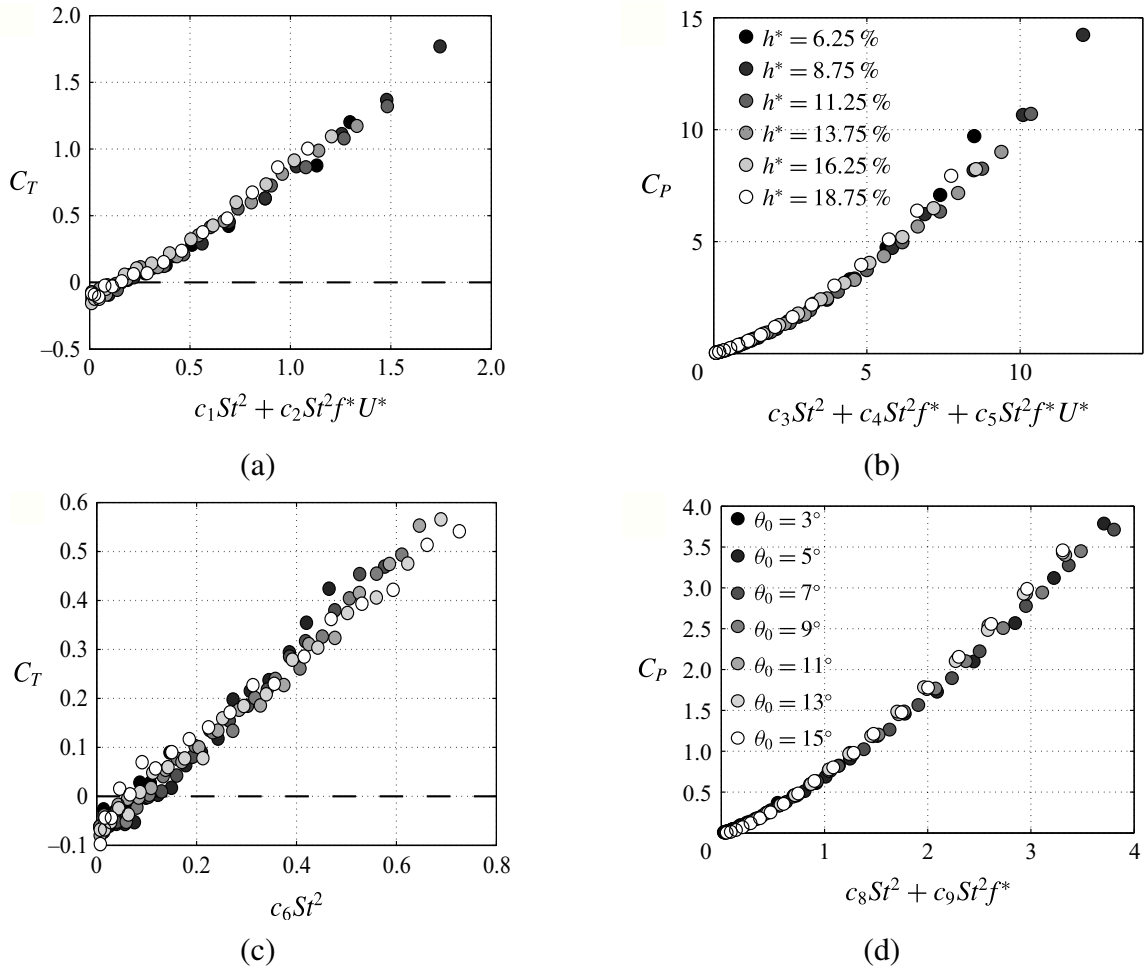

Figure 2.2: Time-averaged (a) thrust and (b) power coefficients of heaving foils, as functions of the scaling parameters (Eq. 2.13 of Floryan et al. (2017)) for various $h^* = h_o/c$. Time-averaged (a) thrust and (b) power coefficients of pitching foils, as functions of the scaling parameters (Eq. 2.14 of Floryan et al. (2017)) for various $h^* = h_o/c$. Here, f^* is equivalent to St_c used in our study. (Reprinted with permission from Floryan et al. (2017), Copyright 2017, Cambridge University Press).

the motion. These individual scaling parameters, however, were found insufficient for appropriate characterization of performance for pitching and heaving foils across a wide range of operating conditions (Floryan et al., 2017). Thus, the dependence of performance characteristics on multiple scaling parameters were examined both experimentally and numerically (Floryan et al., 2017; Van Buren et al., 2019; Senturk and Smits, 2019a; Ayancik et al., 2019; Simsek et al., 2020).

Floryan et al. (2017) employed quasi-steady analysis for lift based and added mass forces to derive scaling laws for both purely pitching and heaving foils, respectively (see Figures 2.2(a-

d)). The experimental results along with biological observations depicted consistent dependence of performance characteristics on both St and St_c. Van Buren et al. (2019) further extended the analysis for a foil undergoing combined heaving and pitching motion at $Re = 8000$, wherein a critical dependence on ϕ was observed. Their experimental results encompassed a wide parameter space in terms of St, St_c, h_o, θ_o, and ϕ. However, their study only considered a single Re.

The influence of Re on propulsive performance of oscillating foils was generally observed in terms of reduction in drag, as discussed briefly by Triantafyllou et al. (2005). Experimental and numerical studies on pitching or heaving foils (Das et al., 2016; Floryan et al., 2017; Senturk and Smits, 2019a) and finite aspect ratio panels (Senturk and Smits, 2018) have also observed the importance of Re as a scaling parameter. However, their analyses were based on a series of assumptions. For example, the quasi-steady model developed by Lau and Kelso (2016) for an oscillating foil in combined pitching and heaving motion depicted an over-estimated propulsive efficiency for $1,500 < Re < 12,500$. Inaccurate modeling of unsteady boundary layer effects reduced the effective drag, thus deviating their predicted results from the Quasi-steady model (see Figure 2.3), especially at high pitching amplitudes (Lau and Kelso, 2016). Das et al. (2016) also stated that their proposed scaling law for drag estimation in pitching foil was inaccurate at high St regimes due to significant wake deflections. This effect resulted in a high pressure drag, which was not accounted for in their approximation. Numerical results of Senturk and Smits (2019a) depicted an inverse square root dependence of the offset drag term, previously introduced by Floryan et al. (2017), on Re for a pitching foil. They further referred to such dependence on Re, in the form of $Re^{-0.5}$, as a laminar flow scaling (Senturk and Smits, 2019a). Recently, Simsek et al. (2020) reported a similar dependence in cases of in-line pitching foils operating in tandem. This was expanded on by Gungor and Hemmati (2021), who developed scaling relations for the performance of pitching parallel (side-by-side) foils, which revealed that laminar scaling worked well for both thrust generation and efficiency at a range of Reynolds numbers, reduced frequencies and phase offsets. Taking a different view of the foil performance, Das et al. (2022) looked at scaling the speed of self-propelled swimmers with respect to Reynolds number. The thrust-scaling relation

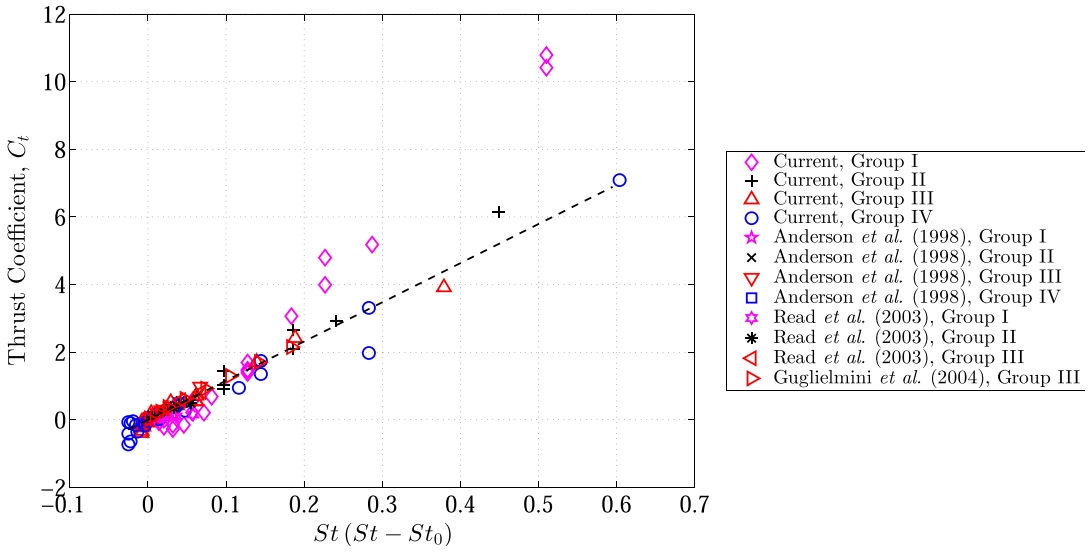

Figure 2.3: Thrust coefficients versus the non-dimensional term $St(St - St_o)$. The dashed black line is a linear curve fit to the current experimental data of Groups II–IV only (Reprinted with permission from Lau and Kelso (2016), Copyright 2016, Elsevier).

that forms the basis of their scaling takes the form $C_D\,Re^{-0.56}$, which is close to that found in the laminar scaling literature (Senturk and Smits, 2018; Simsek et al., 2020). Outside of the rigid foil domain, laminar scaling also applies to undulating anguiliform and carangiform swimmers (Yu and Huang, 2021), including those undergoing braking (Hu and Yu, 2021). These studies were either limited to a single degree of motion (i.e., pitching or heaving) or evaluated the variation of performance characteristics at a range of low *Re*.

2.3 Wake of an Oscillating Foil

The study of flow over stationary bluff bodies has been a classic problem in fluid mechanics, which dates back to the pioneering work of Kármán (Kármán, 2013), in modeling the drag production for a body moving in a quiescent fluid. The stability analysis performed by Kármán (2013) further demonstrated that the instability induced by symmetric arrangement of shed vortices imposed an oscillatory motion in the wake. This was visually confirmed through experimental studies as well (Kármán, 2013). The literature has laid out the foundation for general characteristics of wake around stationary bodies such as flat plates of finite and infinite span, circular cylinders and air-

foils of varying cross-sectional shape (Fage and Johansen, 1927; Roshko, 1954a, 1961). Fage and Johansen (1927) provided an in depth understanding of the vortex shedding phenomenon in the wake of inclined flat plates at different angles of attack. Flow features such as the size of vortex structures, rate at which they are shed, their separation from the body and their movement in the wake, were particularly explored in their study (Fage and Johansen, 1927). Experimental and numerical studies on circular cylinder and normal thin flat plates suggested fundamental insights into coherent structures that dominated the wake at low *Re*. Building upon these insights, experiments on oscillating circular cylinder (Williamson and Roshko, 1988) formed the basis for understanding mechanisms of flow induced vibrations by the flow around a bluff body.

The experiments of Williamson and Roshko (1988) for transversely oscillating cylinder were conducted at a range of increasing amplitude and wavelength (λ). Here, λ was calculated based on the trajectory covered by sine wave of the amplitude function during one complete cycle. Across the wavelength-amplitude plane, several regimes of vortex synchronization were identified based on shedding of vortex structures. In the fundamental lock-in region, two pairs constituting opposite signed vorticity were shed in the wake that led to either momentum excess or deficit. However, below a critical wavelength, similar-signed vortex structures coalesce and formed a typical Kármán type vortex street. Above this threshold, a 2P mode was observed characterized by shed pairs of counter-rotating vortices.

On the experiments that concerned the wakes of oscillating foils, Bratt (1950) conducted one of the first series of smoke flow visualization experiments for a sinusoidal pitching airfoil. The study suggested that the vorticity contained in the wake can be modeled as a system of discrete vortex structures with alternating sense of circulation. Delaurier and Harris (1982) considered a superimposed heaving and pitching motion of a finite span wing, to develop an experimental facility and compare the thrust prediction with theoretical studies and formulations. It was found that the thrust varied linearly with reduced frequency while the best performance was noted within a ϕ ranging from 90° to 120° (Delaurier and Harris, 1982). Extensive investigation into the wake began with experiments of Koochesfahani (1989), who evaluated the influence of sinusoidal and

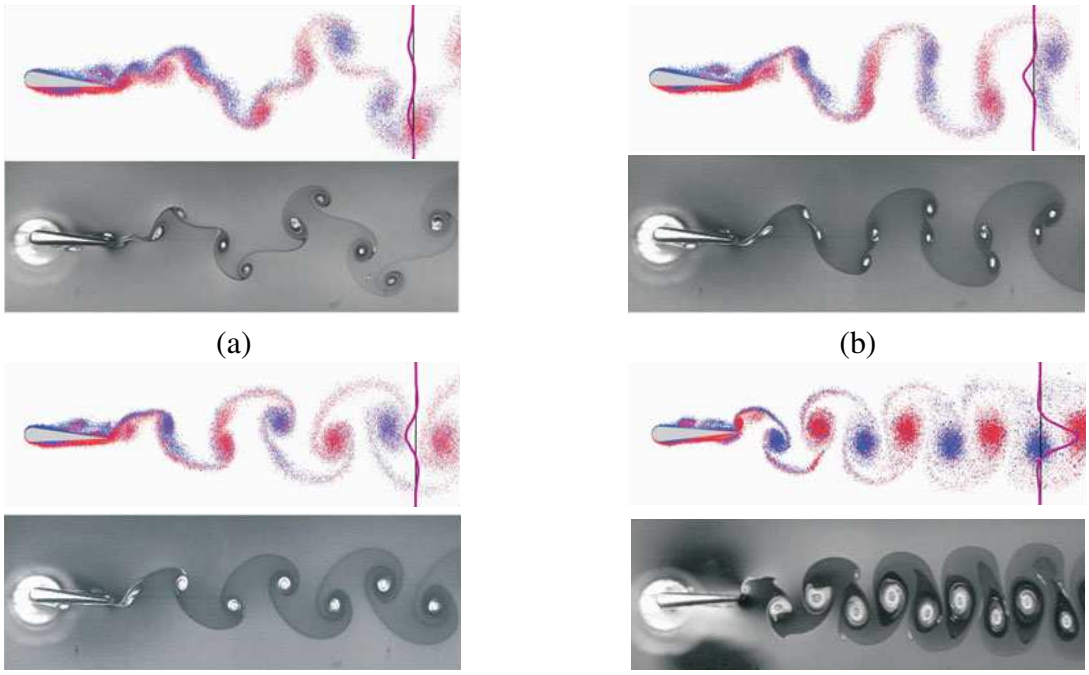

Figure 2.4: Wakes of the pitching foil in simulation (colour) and experiment (greyscale). Red (blue) corresponds to positive (negative) vorticity, and the magenta lines show average velocity profiles four chord lengths downstream of the trailing edge, with the black lines showing the inflow velocity as reference. (a) 2P wake (St_D = 0.08, A_D = 1.14 and $\overline{C_T}$ = -0.12); (b) a 2P wake that evolves to a von Kármán wake (St_D = 0.11, A_D = 1.14 and $\overline{C_T}$ = -0.12); (c) a von Kármán wake (St_D = 0.12, A_D = 1.14 and $\overline{C_T}$ = -0.12); (d) an inverted von Kármán wake (St_D = 0.18, A_D = 1.65 and $\overline{C_T}$ = 0.00). (Reprinted with permission from Andersen et al. (2017), Copyright 2017, Cambridge University Press).

non sinusoidal waveform on the vortex shedding behind a pitching foil. At several combinations of oscillation frequency, amplitude and the waveform shape, different shedding patterns and vortex arrangements were observed in the wake. With a sinusoidal waveform, oscillations at lower frequency depicted Kármán type vortex street, similar to the observations of Bratt (1950). The results also depicted wakes that constituted shed vortex structures of similar sign in one half oscillation cycle. However, at higher frequencies, reverse Von Kármán street became evident that showed a thrust producing wake feature. Ohmi et al. (1990) conducted experimental and numerical analysis for an oscillating foil in simultaneous heaving and pitching motion. The major objective was to determine the effects of amplitude, oscillation frequency, *Re*, mean incidence and angular amplitude, on the wake. The results suggested that at lower St_c (i.e. $St_c = 0.1$), the heave motion is the

primary contributor to the formation of wake structures. However, at higher $St_c = 0.5$, this wake mechanism was found to be directly associated with the pitching motion. The transverse motion of leading and trailing edges contributed to periodic shedding of vortex structures (Ohmi et al., 1991).

2.3.1 Transitions in Wake Topology & Performance

The first major experimental study to discuss vortex arrangements in wake of an oscillating cylinder was conducted by Williamson and Roshko (1988). The observations depicted vortex formation and transitions in the wake at varying amplitudes and body trajectories. They identified several regions of different spatial vortex synchronization, that is 2S, P+S, 2P, P, $2P^*$ at low magnitudes of body trajectory (or λ) and 2P+2S at higher λ and amplitudes. These wake modes were termed based on the number of vortex structures that shed in a single oscillation cycle (see Figure 2.5). For example, 2S mode was characterized by shedding of two single vortices per oscillation period, while 2P mode involved shedding of two pairs of counter-rotating vortices per oscillation cycle. P+S wake mode involved shedding of a single pair and one independent vortex, while 2P+2S consisted of two pairs and two independent vortices being shed per oscillation cycle. They further described the process of vortex pairing, which caused sudden transition between the identified modes (Williamson and Roshko, 1988). They elaborated on a correlation between the observed transitions and sharp differences in temporal force variation (Bishop and Hassan, 1964).

Many studies have focused on the oscillatory kinematics associated with the optimum amplitude and *St* (Triantafyllou et al., 1993; Anderson et al., 1998). The propulsive wake modes corresponding to such optimum motion settings are critical in fundamental understanding of vortical formations in the wake (Koochesfahani, 1989; Triantafyllou et al., 1993; Anderson et al., 1998). It has been well recognized that a *rBvK* vortex street is associated with an excess velocity behind the oscillating foil, which thereby constitutes a thrust generating jet(Koochesfahani, 1989; Jones et al., 1996). However, such a wake configuration is achievable only when the amplitude and *St* is above a threshold (Godoy-Diana et al., 2008).

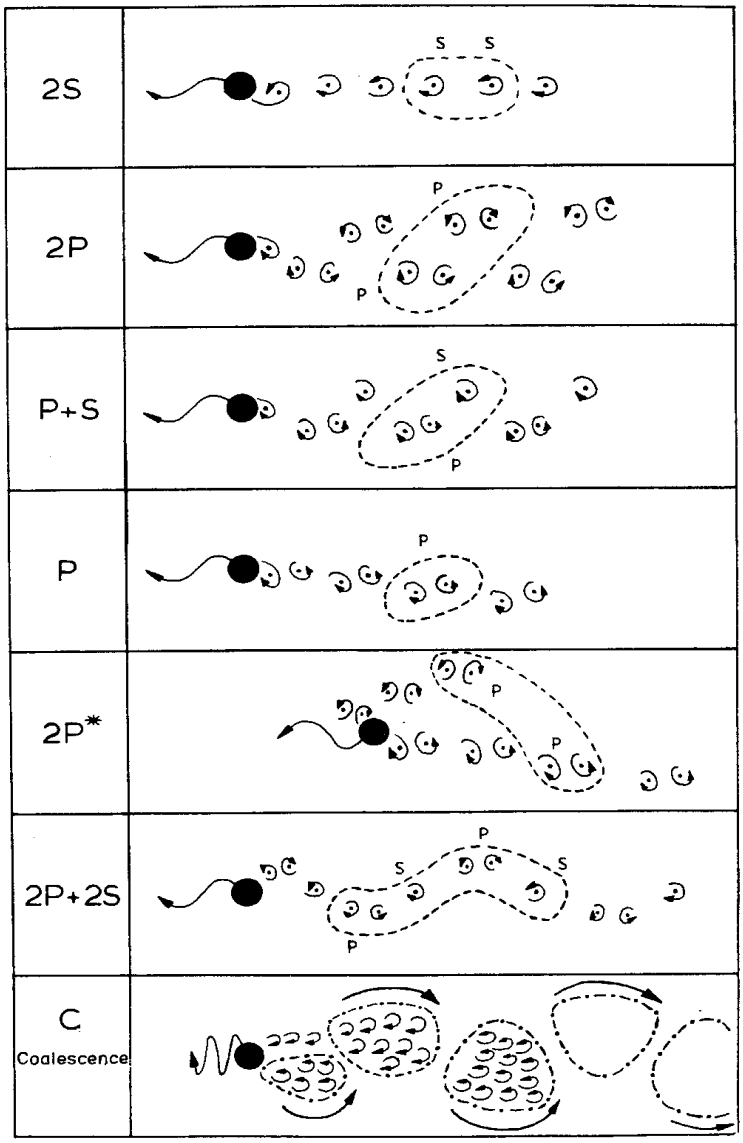

Figure 2.5: Sketches of the vortex shedding patterns. "P" means a vortex pair and "S" means a single vortex, and each pattern is defined by the number of pairs and single vortices formed per cycle; "Dashed curves" encircle the vortices shed in one complete cycle. (Reprinted with permission from Williamson and Roshko (1988), Copyright 1998 Elsevier).

Phase-space diagrams have been previously used (Godoy-Diana et al., 2008; Schnipper et al., 2009) to characterize the implications of different kinematic settings on both performance and wake transition, e.g., transition thresholds (see Figure 2.6). Particularly, these diagrams depicted mapped regions (kinematic settings), where the oscillatory motion begins to produce thrust. Identifying the wake modes and their transition using such phase space diagrams enabled establishing a correlation between performance transition and apparent changes in the vortex synchronization (Godoy-Diana et al., 2008; Schnipper et al., 2009). However, Smits (2019) reported in a recent review study that a propulsively efficient swimming performance could not always correspond to a specific wake pattern. A comparative assessment between the wakes of an American eel, robotic lamprey, dolphins and alligator (Drucker and Lauder, 2001; Fish and Lauder, 2013; Fish et al., 2014) indicated different near wake patterns that possessed similar propulsive performance characteristics.

Godoy-Diana et al. (2008) experimentally examined the hydrodynamics of a pitching foil at a chord based $Re = 1173$. They identified the transition of propulsive performance along with a coincident change in the standard *Bvk* mode configuration to a *rBvK* vortex street. This was further followed by a transition to an asymmetric wake (Godoy-Diana et al., 2008). These transitions were mapped on a phase-space diagram, which was defined by translating amplitude of the A_D and St_D. Here, A_D represented the translating amplitude of trailing edge normalized by the D. Godoy-Diana et al. (2008) also represented the iso-contour lines of mean drag coefficient, which revealed that a transition of standard *BvK* wake to a reverse *BvK* wake occurs before the drag-thrust transition (see Figure 2.6(b)). They attributed this observation to the existence of skin friction drag, which appeared to limit the thrust production even when the wake had transitioned to a *rBvK* mode.

Schnipper et al. (2009) also represented a phase diagram that particularly mapped transitions of vortex synchronization or wake modes on $St_D - A_D$ phase space (see Figure 2.7). Their results indicated the existence of a 2P mode (Williamson and Roshko, 1988) within $0.155 \leq St_D \leq 0.195$. Beyond this range of St_D, a typical 2S wake was dominant with more exotic wakes, such as 2P+2S, 4P+2S and 8P, formed at much lower St_D (below 0.05). Wake modes with paired structures (i.e.,

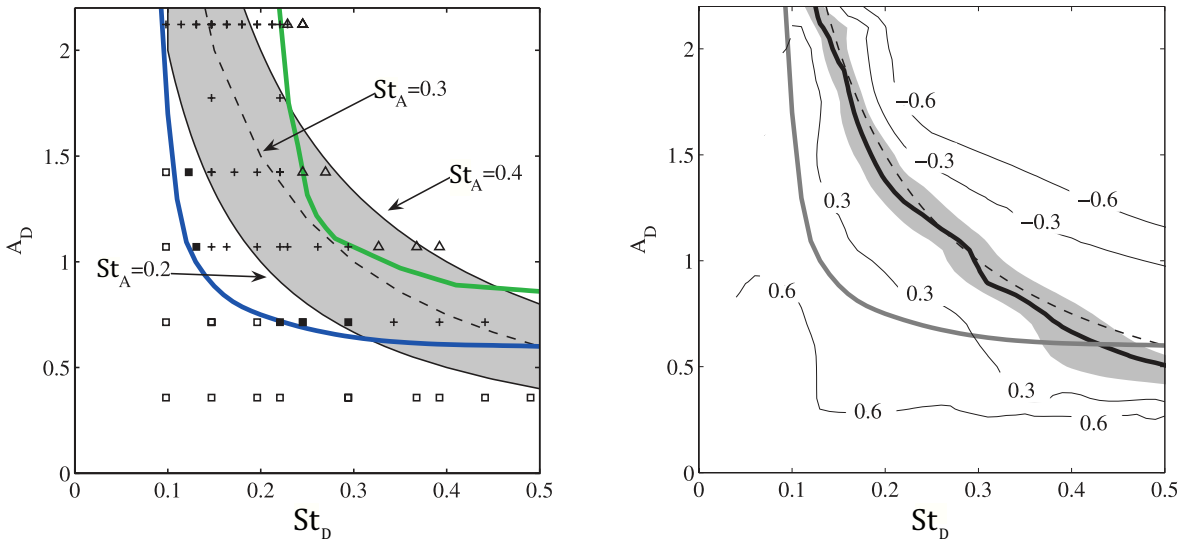

(a) (b)

Figure 2.6: (a) A_D vs St_D map for Re_D = 255. Experimental points are labeled as *BvK* wake (unfilled square); 2*S* aligned wake (filled square); + depicts reverse *BvK* wake; deflected reverse *BvK* street (triangles); Blue line: transition between *BvK* and reverse *BvK*. Green line: transition between reverse *BvK* and asymmetric wake. The shaded area corresponds to the $St_A = 0.3+/-0.1$ interval. (b) Contours of mean drag coefficient C_D/C_{D_o}. The black line corresponds to $C_D = 0$ where the estimated drag-thrust transition occurs. The shaded area represents the estimated error for the $C_D = 0$ curve due to sensitivity on the choice of the control volume. The gray line is the transition from *BvK* to reverse *BvK*. The dashed line corresponds to $St_A = 0.3$. (Reprinted with permission from Godoy-Diana et al. (2008), Copyright 2008 by the American Physical Society).

2P) were suggested to be important propulsively for zebra fish larva and eels in free swimming conditions (Müller et al., 2001, 2008). However, spatial configuration of the pair was still important in terms of the resulting induced velocity component. Schnipper et al. (2009) indicated that only the 2P modes with a downstream pointed orientation yield thrust, while those with an upstream pointed pair only produced drag. The observations of Hultmark et al. (2007) also revealed 2P vortex modes for a robotic lamprey model under steady swimming conditions, wherein two vortices were shed per half cycle. Phase-averaged vorticity fields showed that vortex pairs of 2P mode had a major mutual advection velocity pointing away from the wake centerline, although a minor component of velocity existed along the streamwise direction. This generated a net positive thrust close to the tail (Hultmark et al., 2007).

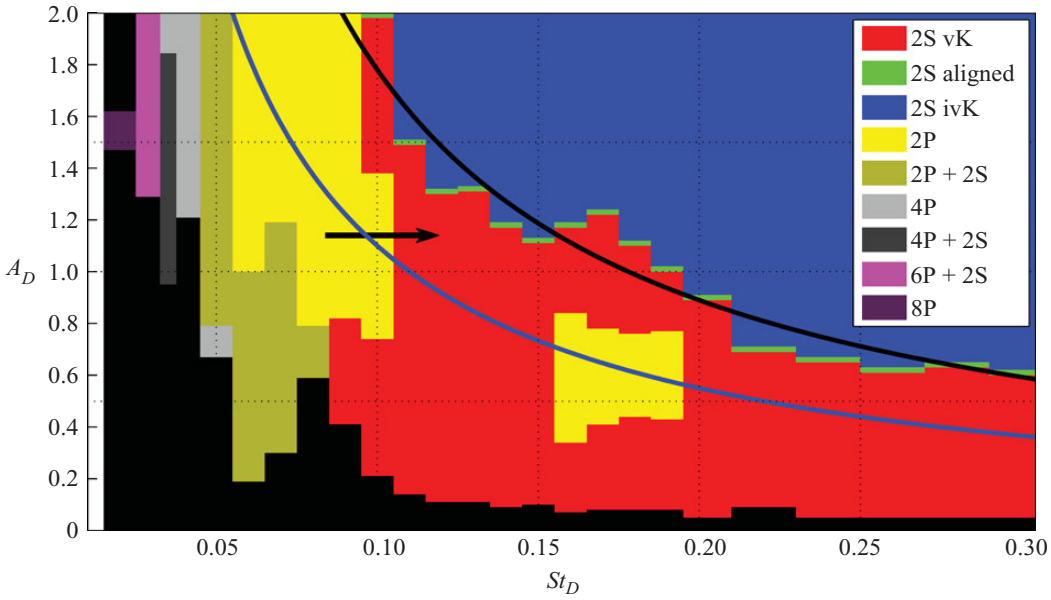

Figure 2.7: Phase-space diagram depicting vortex synchronization regions across a range of St_D-A_D. The solid line indicate that the amplitude-based Strouhal number is constant with the values $St_A = 0.11$ (blue) and $St_A = 0.18$ (black). The arrow indicates the 2P to 2S transition. The black regions at low frequency and amplitude did not present a synchronized wake. A small ($D = 0.10$ cm) and large ($D = 0.20$ cm) foil were used at $St_D < 0.15$ and $St_D > 0.15$, respectively. (Reprinted with permission from Schnipper et al. (2009), Copyright 2009, Cambridge University Press).

Cleaver et al. (2011) discussed the existence of three distinct wake modes due to the shed vortices behind a plunging airfoil. Mode-1 field was observed at $St_c = 2$, which depicted a vortex formation mechanism similar to that observed for a typical 2P wake. However, vortical interactions and merger that occurred near the trailing edge led to the formation of a dipole within one half oscillation cycle, which further advected above the wake centerline. The mean velocity field also depicted a region of very low velocity excess behind the foil. Dewey et al. (2012) later explored the efficient propulsive nature of 2P wakes, which occurred for three-dimensional flexible fins within certain wavelengths of spanwise curvature, mimicking bio-locomotion of a batoid. Interestingly, the increase in trailing edge phase delay at lower wavelengths of actuation switched the 2P mode of the wake to 2S mode (Dewey et al., 2012). The wake configuration was also sensitive to St. For example, increasing St beyond 0.2 led to the dominance of 2S mode in the wake instead of 2P wake that was observed at St =0.15 (Dewey et al., 2012).

Asymmetric wake modes were also discussed extensively by Cleaver et al. (2012) and Calderon et al. (2014). Both studies confirmed that there exists a correspondence between asymmetric wakes formed by a heaving foil and its initial oscillatory direction at the very first cycle, the transverse amplitude and reduced frequency. The findings of Godoy-Diana et al. (2009) had identified earlier a definite transition from a reverse Von Kàrmàn wake to an asymmetric wake with positive thrust generation, which aquatic animals utilize for propulsive maneuvering purposes during swimming. Cleaver et al. (2012) further highlighted aspects of lift generation, and their association with wake modes, mostly in cases of oscillating foils with a single degree of freedom motion (such as plunging). Growth of the *LEV* and its dynamic interactions with trailing edge vorticity held some uniqueness compared to a purely pitching motion, which was dominated by *TEV* shedding (Koochesfahani, 1989; Anderson et al., 1998).

Kozłowski and Kudela (2014) computationally studied transitions in the wake of a purely heaving foil at $100 < Re < 500$. Their phase maps were depicted in an A_c-St phase-space. The wake modes clearly showed transitions from a *BvK* to an aligned *BvK* configuration. These were further followed by asymmetric and chaotic wakes, respectively (Kozłowski and Kudela, 2014). Deng et al. (2015) described the transitions in terms of induction of three-dimensionality in the wake at $Re = 1500$. Similar to previous phase-map depictions (Godoy-Diana et al., 2008; Schnipper et al., 2009), Deng et al. (2015) used a $St_D - A_D$ phase-space diagram to report that a transition to three-dimensional flow in the wake eventually occurred when the wake became asymmetric along the centerline (see Figure 2.8(a)). Cros et al. (2018) further discussed transitions in vortex modes of a pitching foil at a range of aspect ratios and frequencies, while the pitch amplitude was kept constant. They noted several vortex patterns downstream, such as 2P, 2S, $2\overline{S}$, 2S$'$, *rBvK* and P+S. In a more recent study, Zheng et al. (2019) also conducted a numerical study at $Re = 1100$, which mapped different wake modes for a flapping foil on two phase-space representations (see Figure 2.8(b)). Each corresponded to a variation in amplitudes of pitch and heave, along with increase in frequency of oscillation, respectively (Zheng et al., 2019). However, ϕ between the coupled heave and pitch motion was kept fixed at 90°. The different wake modes identified included standard

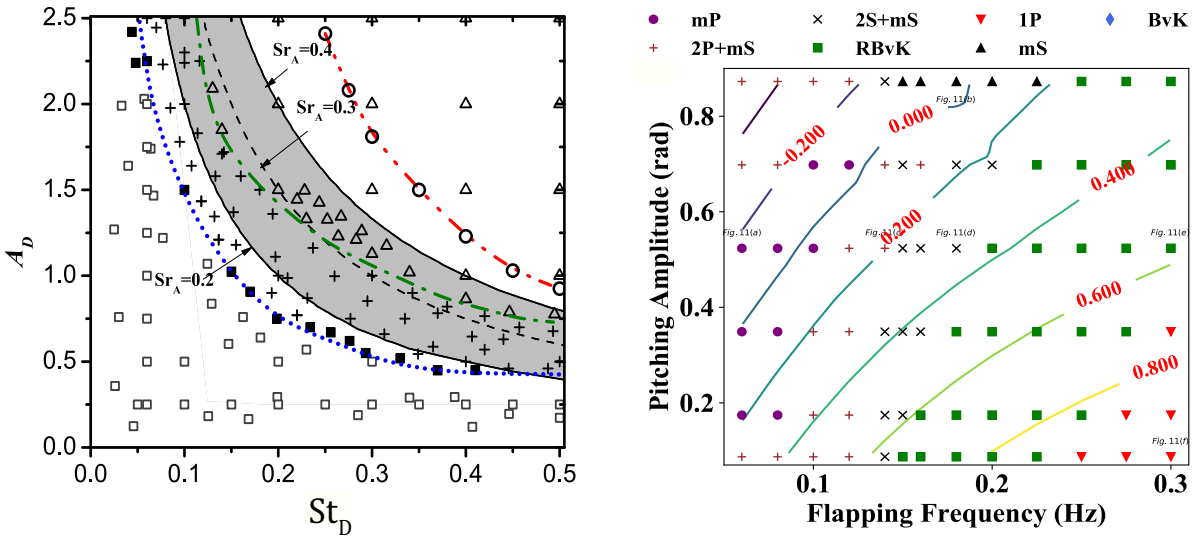

(a) (b)

Figure 2.8: (a) A_D vs St_D map for Re = 1700. Computational points are labeled as *BvK* wake (unfilled square); 2*S* aligned wake (filled square); + depicts reverse *BvK* wake; deflected reverse *BvK* street resulting in asymmetric wake (triangles); points with neutral stability (circles). Blue (dotted) line: transition between *BvK* and reverse *BvK*. Green (dash-dot) line: transition between reverse *BvK* and the asymmetric regime.Red (dash-dot-dot) line: transition between 2D and 3D wakes. The shaded area corresponds to the $St_A = 0.3 +/- 0.1$ interval (Reprinted with permission from Deng et al. (2015), Copyright 2015 by the American Physical Society). (b) The wake maps and iso-lines of $\alpha(T/4)$ for a purely heaving foil (Reprinted with permission from Zheng et al. (2019), Copyright 2019 by the American Physical Society).

BvK, *rBvK*, 2S+mS, 2P+mS, mS, mP and an asymmetric 1P wake configuration. They further described that the angle of attack ($\alpha^{T/4}$) at the quarter phase of the oscillation cycle could characterize the wake mode transition. For example, increasing the magnitude of $\alpha^{(T/4)}$ depicted the wake mode transition from mP to 2S+mS, which was then followed by the *rBvK* mode. This *rBvK* configuration also transitioned to a 1P mode by increasing the magnitude of $\alpha^{(T/4)}$.

Lagopoulos et al. (2019) also described transitions of a flapping foil in a pure pitching, heaving and coupled oscillatory motion at a $\phi = 90^{\circ}$. Analyses at $Re = 1173$ and 11730 depicted universality of Strohaul number, based on trajectory (St_τ), to effectively model and represent the transitions in propulsive performance and wake modes for various motion configurations of a flapping foil. Changes in the drag-to-thrust transition, evolution of wake structures, production of momentum excess and vortex strength in the wake of pitching foil have also been considered recently. For

example, Chao et al. (2021) evaluated the effects of introducing asymmetric oscillations on the wake development at $Re = 1173$. Several forms of P+S (mode 1 and mode 2) and deflected *rBvK* modes were identified on the $St_D - A_D$ phase-space diagrams for both symmetric and asymmetric pitching foils.

2.3.2 Relationship of Wake, Performance and Kinematics

The recurrent observations on association of the wake dynamics and performance motivated researchers to study the biological fin kinematics observed for marine swimmers. Triantafyllou et al. (1993) performed experiments on heaving foils, the results of which indicated that the optimal propulsive efficiency is achieved within a St range of 0.25 to 0.35. The thrust generation through a jet profile was further linked with the formation of reverse Von Kármán wake. It was also confirmed in subsequent experiments that the optimal jet formation is only unstable within a small range of oscillation frequencies that correspond to maximum amplification (Triantafyllou et al., 2000). The observations were found to be supported with data obtained from natural swimmers, i.e. fish and cetaceans, which demonstrated an optimal propulsive efficiency within $St = 0.25$ - 0.35. Anderson et al. (1998) conducted a parametric analysis for an oscillating foil with combined heaving and pitching motion at $Re = 1100$, while St, h_o/c and α_o varied within a specified range (Figure 2.9). The force assessments and coinciding wake topology (mapped on a $St - \alpha$ plot) showed that a high efficiency propulsion is achieved when a moderately strong LEV constructively interacted with a TEV, thereby forming a reverse Von Kármán street. Read et al. (2003) also conducted water tunnel experiments for an oscillating foil in pure heaving motion. The influence of kinematic parameters (St, h_o and α) were assessed, which depicted that a superimposed pitch motion greatly improved the generation of side forces, which could be useful for maneuvering force production.

The Digital PIV technique employed by Birch and Dickinson (2001) described the influence of shed vortices from the previous flapping strokes on the force generation by an oscillating robotic wing. The overall effects of wing-wake interaction was hence summarized in terms of an early augmentation and a subsequent attenuation of forces generated by the wing. Parker et al. (2003)

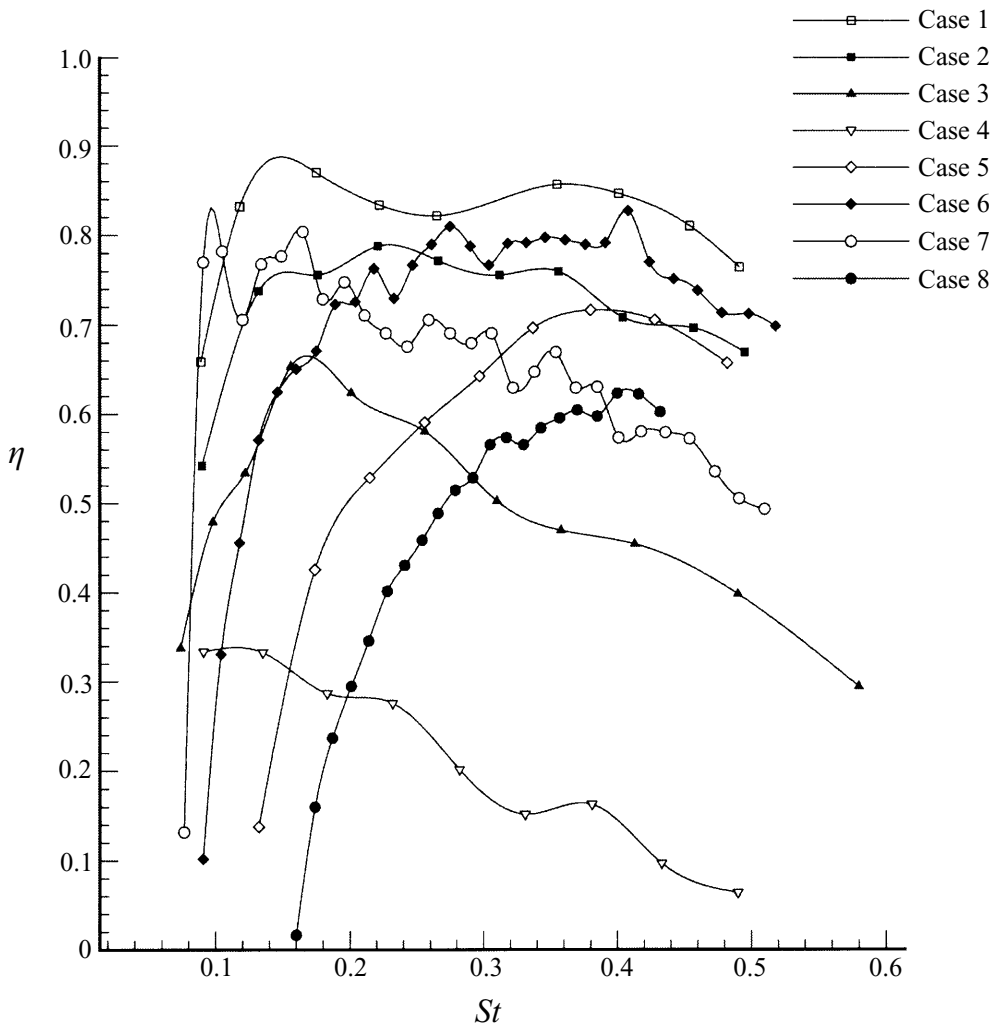

Figure 2.9: Experimentally measured η as function of the Strouhal number St. Case 1: $h_o/c = 0.75$, $\alpha_{max} = 21°$, $\phi = 75°$; Case 2: $h_o/c = 0.75$, $\alpha_{max} = 17°$, $\phi = 105°$;Case 3: $h_o/c = 0.25$, $\alpha_{max} = 15°$, $\phi = 90°$; Case 4: $h_o/c = 0.75$, $\alpha_{max} = 5°$, $\phi = 90°$;Case 5: $h_o/c = 0.75$, $\alpha_{max} = 25°$, $\phi = 90°$; Case 6: $h_o/c = 0.75$, $\alpha_{max} = 20°$, $\phi = 90°$;Case 7: $h_o/c = 0.75$, $\alpha_{max} = 10°$, $\phi = 90°$; Case 8: $h_o/c = 0.75$, $\alpha_{max} = 30°$, $\phi = 90°$; (Reprinted with permission from Anderson et al. (1998), Copyright 1998, Cambridge University Press).

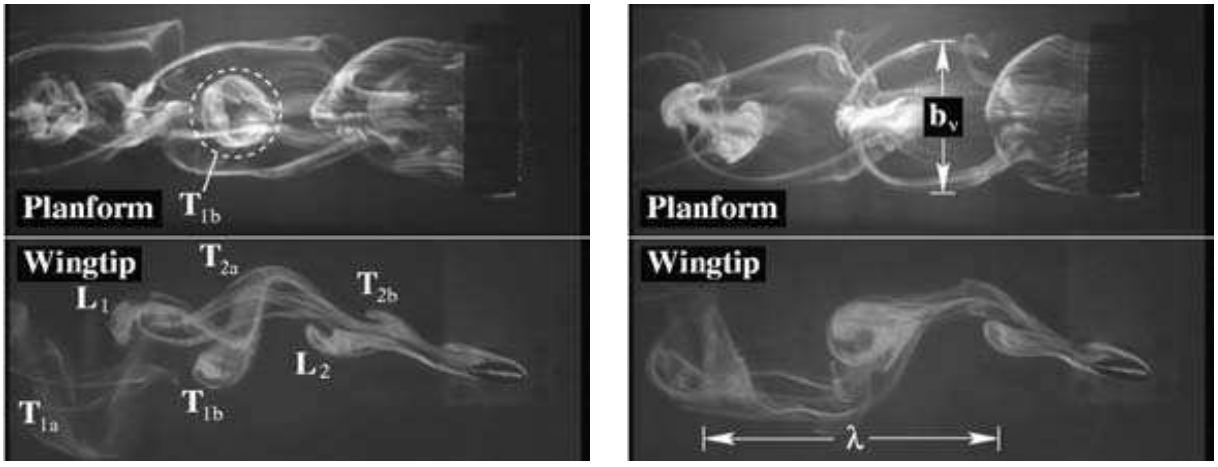

(a) (b)

Figure 2.10: Effects of St on evolution of wake structure for a finite span wing: h/h_o = -1, θ_o = 10°, ψ = 90°; (a) $St = 0.3$, (b) $St = 0.4$ (Reprinted with permission from von Ellenrieder et al. (2003), Copyright 2003, Cambridge University Press).

conducted dye flow visualization for a symmetric foil oscillating in combined heaving and pitching motion. The effects of changes in pitch amplitude on the evolutionary features of *LEV s* influenced the force generation. Ellenrieder (2003) also employed the dye flow visualization to expand and confirm the influence of St, pitch amplitude and phase offset of a harmonically oscillating wing, on the wake structure (see Figure 2.10). Although these studies employed a finite span foil section, a general idea on the influence of kinematics on the wake topology and propulsive forces was vivid. Experiments of Srigrarom and Vincent (2008) provided additional insights into the effects of freestream velocity, rotational angular velocity of the foil, amplitude and St, on the propulsive performance and wake features. A decrease in propulsive efficiency coincided with increasing amplitude and angular velocity of the foil.

2.4 Three-dimensional Wake Topology

The early investigation into the wakes of circular cylinder at low Re revealed the existence of three major components: the boundary layer flow near the cylinder surface, mixing layer flow that separates from sides of the cylinder, and the main wake flow downstream (Durbin and Reif,

2010). The coherent structures observed in the three-dimensional wake comprise of rollers that are represented by iso-surfaces of spanwise vorticity, and ribs, which are dominant structures in the braid region between two consecutive spanwise rollers (see Figure 2.11). The ribs are formed in pairs of counter-rotating streamwise vorticity that align across the spanwise extent of the wake. These components have been well investigated in experiments and numerical simulations that study mixing and free shear layer flows. The arrangement of rollers and ribs in the wake of a bluff-body mainly characterize its three-dimensional topology, which inherently influences the mean and turbulent features of the flow. For boundary layer flows, existence of hairpin and horseshoe vortex structures is well-established. These structures mostly impact the momentum transfer between inner and outer layers, thus helping in production of turbulence (Durbin and Reif, 2010).

Some studies have elaborated on the topological characteristics of plane wakes (Grinstein et al., 1991). For example, in case of plane wake behind a stationary flat plate, amplification of small-scale streamwise vorticity at the trailing edge results in the formation of rib pairs, which further interact with spanwise rollers and result in three-dimensional instabilities. This sort of mechanism is slightly different from the one already discussed in the wake of circular cylinder, where the rollers undergo localized deformation and the subsequent braid vorticity straining resulted in the formation of rib pairs. Several DNS studies have supported the experimental findings related to plane and bluff-body wakes. Mittal and Balachandar (1995) reported the presence of localized deformations on the shed rollers in the wake of stationary elliptic and circular cylinders. The deformation temporally evolved to form horseshoe vortex structures, whose legs subsequently formed a rib pair (see Figure 2.12(a-b)). Thus, the presence of intermediate vortical structures, i.e. hairpin or horseshoe vortices, further characterize the topology of three-dimensional wakes.

Besides the fundamental constituents of the 3D wake discussed thus far, it is also important to understand the temporal shedding and topological arrangements of the primary vortex roller. It can have an influence on the onset of three-dimensionality in the wake. Experiments on the flapping foil have revealed quasi-2D wake behavior when the kinematic and flow parameters, i.e. amplitude, oscillation frequency and *Re*, remain below a certain threshold (Koochesfahani, 1989;

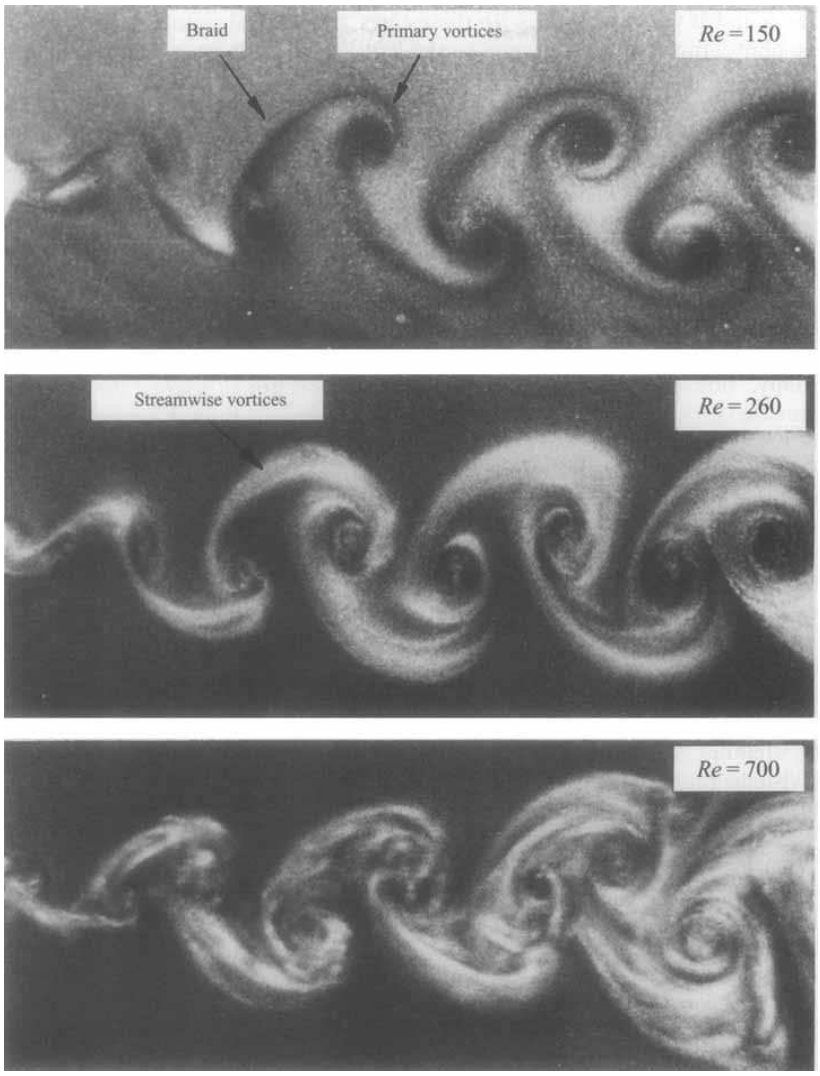

Figure 2.11: Aluminum-flake visualization in cross-sectional view: evidence for the location of streamwise vorticity in the braid shear layer regions between primary vortices. Flow is to the right past the cylinder on the left (Reprinted with permission from Williamson (1996), Copyright 1996, Cambridge University Press).

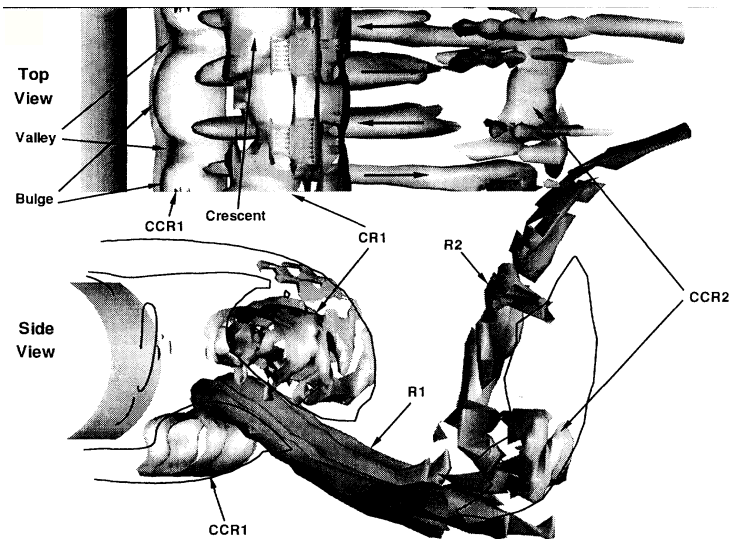

(a)

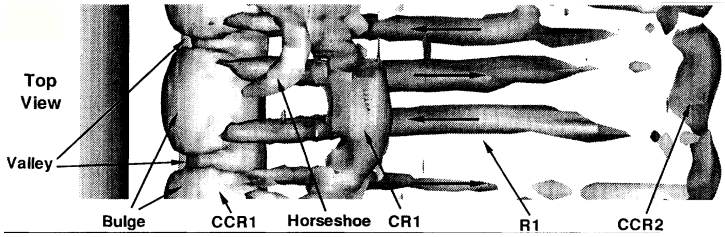

(b)

Figure 2.12: Identification of vortical structures in the near wake of the stationary circular cylinder using Direct numerical simulations. The structures are visualized by $\lambda_2 = 1.1$ (Reprinted with permission from Mittal and Balachandar (1995), Copyright 1995 by the American Physical Society).

Jones et al., 1996, 1998). These scenarios further help in understanding the mean and turbulent fields that characterize the wake.

Godoy-Diana et al. (2008) showed that for low amplitude pitching foil, a Benard Von Kármán street became evident where the vortex structures formed by boundary layer roll-up, and arrange along the same side of the symmetry line in the wake where they were formed. The mean wake therefore characterize a momentum deficit region behind the oscillating foil (see Figure 2.13(a-b)). As the amplitude increased, the vortex structures began to shed and arrange on the opposite side of the symmetry line, and thus depict a reverse Von Kármán wake arrangement (see Figure 2.13(c-d)). The mean wake in this case showed a momentum excess which provide forward thrust to the oscillating foil. A loss in two-dimensional wake nature was eventually observed as the amplitude was further increased beyond $A_D = 1.77$. In such conditions, a strong dipole pair advects at an

angle to the wake centerline, while a weaker isolated structure sheds below the symmetry line (see Figure 2.13(e-f)). Such deflected wake topology coincided with transition of 2D to 3D wake (Deng and Caulfield, 2015a). Numerical simulations conducted in conjunction with Floquet stability analysis depicted the existence of some unstable instability modes that promoted the formation of secondary streamwise vortical structures, the details of which will be covered in upcoming sections. The mean thrust jet observed for the case of asymmetric wake topologies is also deflected in either upwards or downward directions, which thus reveal a major lift contribution in propulsive performance of the oscillating foil (Cleaver et al., 2012).

2.5 Wake Instabilities and Secondary Structures

Vortex decay processes requires fundamental understanding of their formation and advection. These involved assessments of equal or unequal strength counter-rotating vortical pairs (Leweke and Williamson, 1998; Ortega et al., 2003; Bristol et al., 2004; Meunier and Leweke, 2005). The observations suggested novel interaction mechanisms of paired structures that eventually developed wavy undulations in spanwise direction (see Figure 2.14), which were then characterized by a particular wavelength and periodicity (Ortega et al., 2003; Meunier and Leweke, 2005).

Detailed theoretical and evolution aspects of vortex instabilities had been considered, which helped in understanding the disintegration of vortical structures in wakes (Dizès and Laporte, 2002). On a similar note, origins of wake instabilities garnered sufficient attention besides characterizing their spatio-temporal development stages during the evolution process (Williamson, 1996). This further revealed intricate physical connection to the formation of secondary vortical structures as well (Mittal and Balachandar, 1995), whose role in promoting wake three-dimensionality was immense.

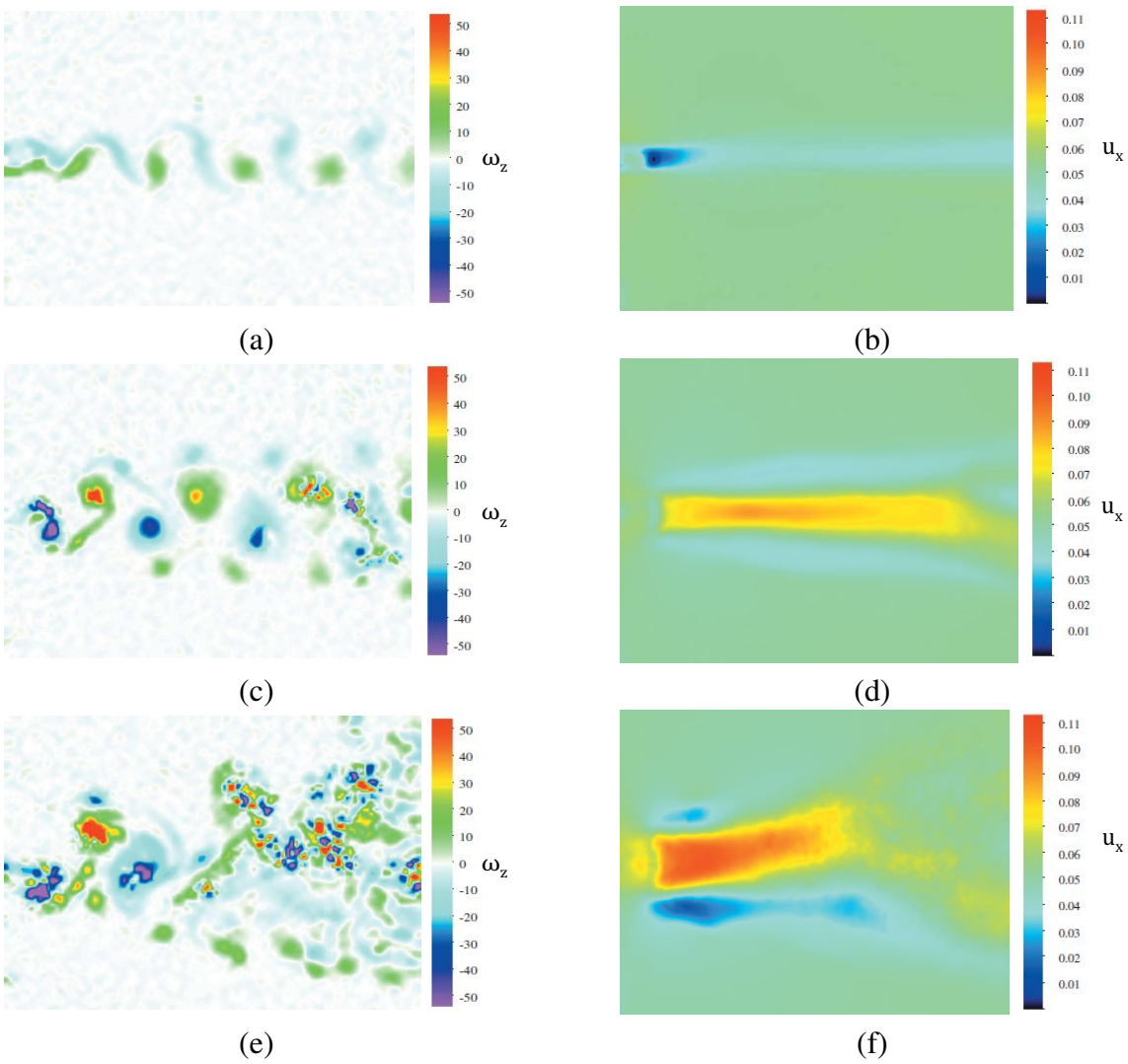

Figure 2.13: Left and right columns depicts instantaneous spanwise vorticity fields and mean flow (time averaged horizontal velocity) for fixed Strouhal and Reynolds numbers St_D=0.22 and Re=255. A_D from top to bottom varies from A_D = 0.36, 1.77 and 2.8, respectively, for an oscillating foil in pure pitching motion. (Reprinted with permission from Godoy-Diana et al. (2008), Copyright 2008 by the American Physical Society).

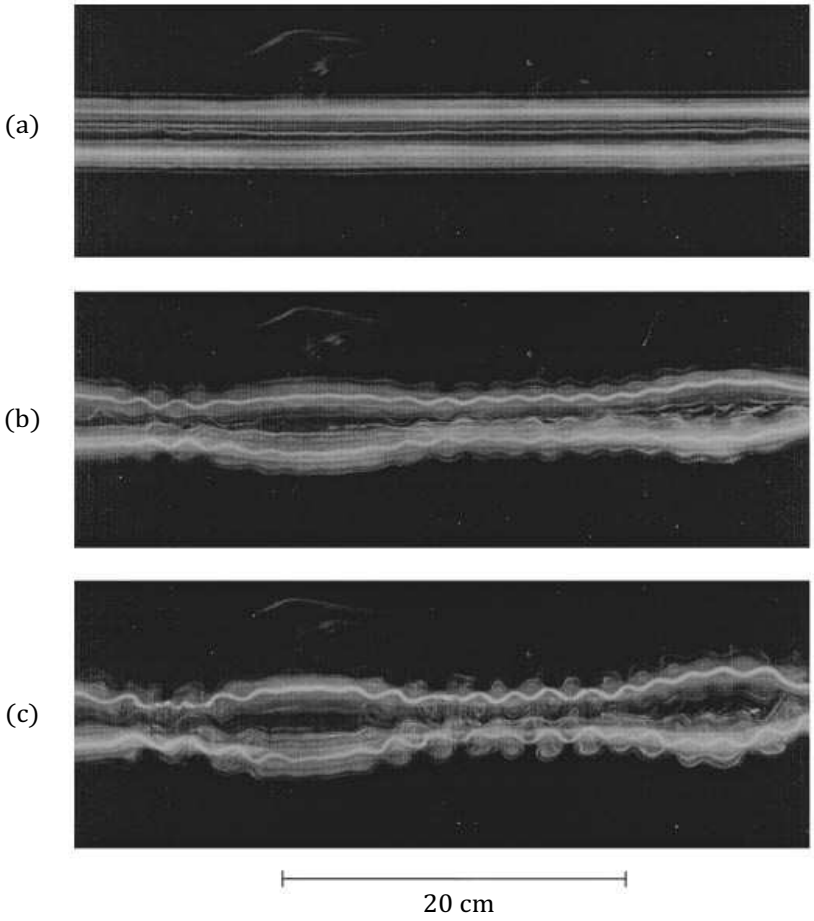

Figure 2.14: Visualization of vortex pair evolution under the combined action of long-wavelength (Crow) and Elliptic instability at Re = 2750. The pair is moving towards the observer. (a) t^* = 1.7, (b) t^* = 5.6, (c) t^* = 6.8 (Reprinted with permission from Leweke and Williamson (1998), Copyright 1998, Cambridge University Press).

2.5.1 Mechanisms of Vortex Instabilities

Experimental and numerical studies that examined wake instabilities focused on isolated pair of vortices, wherein the temporal evolution of spatial dislocations on rollers was quite vivid (Leweke and Williamson, 1998; Ortega et al., 2003; Bristol et al., 2004; Meunier and Leweke, 2005). Two major mechanisms were found to clearly explain the onset of three-dimensionality in the wake. The first mechanism, namely the Crow's instability, entitled displacement of the complete vortex structure locally without any core deformation (see Figure 2.15 and 2.16). However, the second mechanism, termed as Elliptic instability (Kerswell, 2002), was characterized by short wavelength

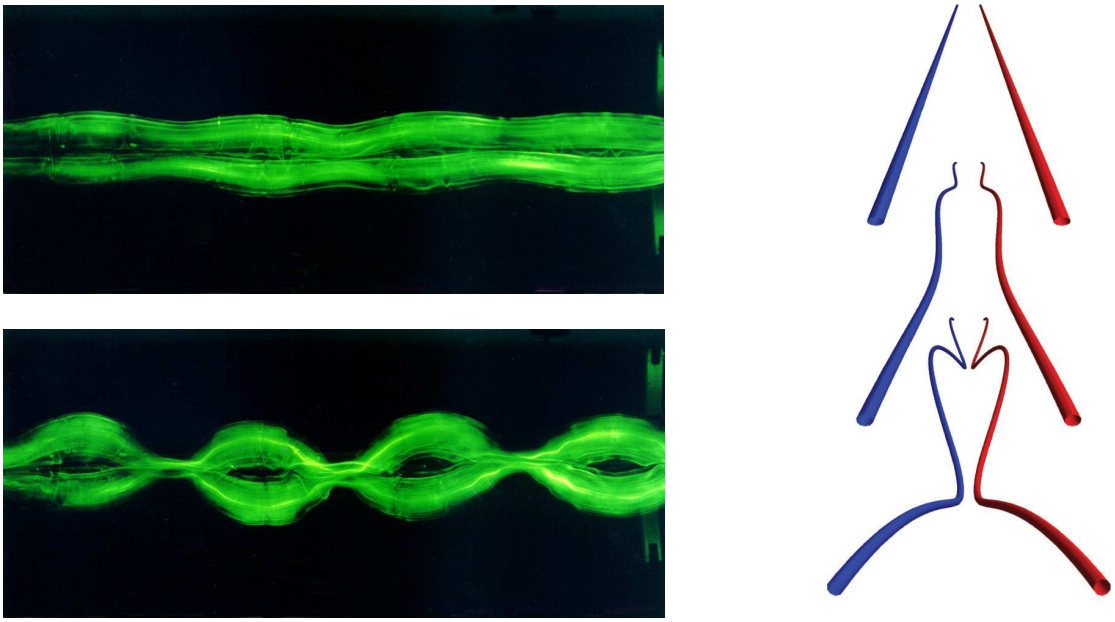

(a) (b)

Figure 2.15: (a) Long-wavelength Crow instability of a counter-rotating vortex pair at Re = 1450 (Reprinted with permission from Leweke and Williamson (2011), Copyright 2011, AIP Publishing LLC). (b) Inviscid Vortex filament simulation results depicting evolution of Crow instability (Reprinted with permission from Winckelmans et al. (2005), Copyright 2005, Elsevier).

perturbations within the vortex core. Each of these instability mechanisms involved different stages that are described below.

The first stage of Crow's instability begin with a self-induced rotation of a sinusoidal perturbation on a straight vortex filament. The sign of this rotation is opposite to that of the core fluid. In the second stage, a secondary motion is induced by the other neighboring vortex that constitutes a plane stagnation point flow. The maximum stretching for this point flow occurs at 45° to the rotational axis of the vortex. In the final stage, the coupled effect of the perturbation induces a motion that comprise of simultaneous rotation and radia stretching. The stages were qualitatively explained in Leweke et al. (2016), and also shown in Figure 2.16(b). Crow's linear stability model effectively described the nature of equal strength counter-rotating vortex pair (Crow, 1970), where the early growth phase of instability coincided with vortex pair merger at specific spanwise intervals. This subsequently led to vortex ring-like arrangement (Crow, 1970). The unstable wavelength, which precisely represented the spanwise intervals, scaled in the range of 6 to 10

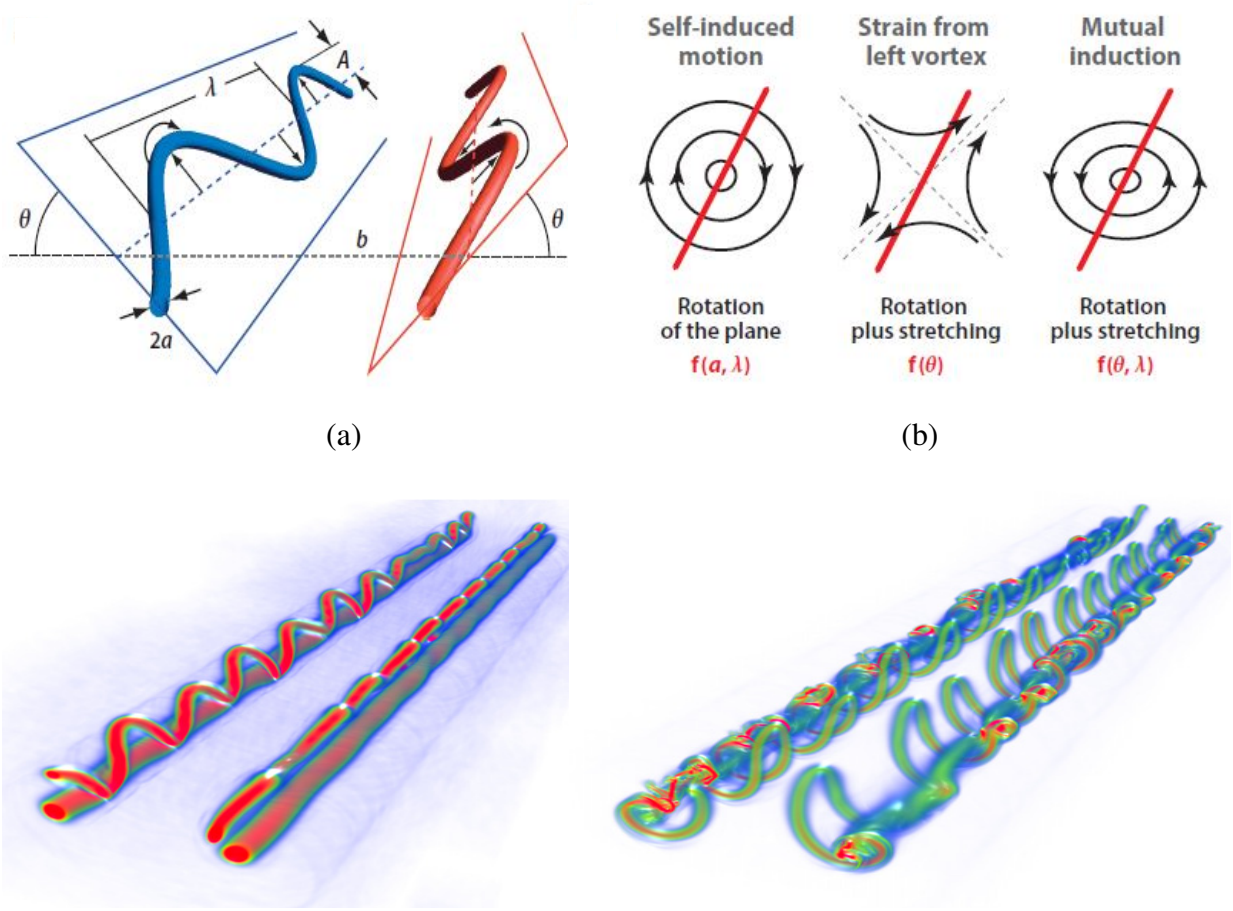

(a) (b)

(c) (d)

Figure 2.16: (a) Illustration of the symmetric displacement mode associated with the Crow Instability, (b) Steps indicating onset of Crow Instability for a counter-rotating vortex pair (Reprinted with permission from Leweke et al. (2016), Copyright 2016, Annual Reviews). (c) and (d) depict results of a Numerical simulation depicting developed Crow instability on vortex rollers of unequal strength (Reprinted with permission from Chatelain et al. (2008), Copyright 2008, Elsevier).

times the distance between neighboring vortex structures. This model was further extended to a system of multiple rollers, including pairs that constituted unequal strength counter-rotating spanwise coherent structures (Ortega et al., 2003). The wavelength observed in some studies on the unequal-strength paired structures scaled with the order of the separation distance. Klein et al. (1995) assessed the wrapping mechanism for a weak vortex filament around the stronger paired roller, which eventually resulted in a vortex loop formation. Stability analysis for paired vortices was conducted by Ortega and Savas (2001), wherein, the qualitative observations supported the previous analysis of Klein et al. (1995). A follow-up study also provided a quantitative assessment, in terms of circulation strength (Γ), internal strain-field distribution, and evolution mechanisms of sinusoidal instability. This revealed a spatial wavelength that had a lower magnitude (Ortega et al., 2003), compared to Crow's estimation for equal-strength vortex pair (Crow, 1970).

Elliptic instability has been primarily associated with counter-rotating pairs of spanwise coherent structures (or rollers), either with equal- or unequal-strength (Leweke and Williamson, 1998; Ortega et al., 2003; Meunier and Leweke, 2005). Bristol et al. (2004) extended this analysis to a co-rotating vortex pair that depicted the formation of vorticity bridges on account of the elliptic instability that subsequently contributed to vortex merger in the wake. Studies that assessed the onset of elliptic instability determined that an initial resonance mechanisms sets in between the two Kelvin modes of the vortex cores. At the same time, base flow within the core is further modified by strain induced on account of the paired vortex structure. The resonance mechanism itself can lead to sudden amplification of the Kelvin modes, thereby leading to the elliptic instability of the vortex core (see Figure 2.17). This characteristic instability has also been referred to as Moore-Saffman-Tsai-Widnall instability or Widnall instability (Leweke et al., 2016).

The interaction of vortex structures with wall or ground is important since configurations were prominent in aircraft take off and landing, junction, and bounded flows, where vortical rollers advect near the wall (Leweke et al., 2016). Studies of Lamb (1945); Dee et al. (1968); Hakvey and Perry (2012); Peace and Riley (1983) reported and explained the formation of a secondary vorticity region with opposite sign circulation, beneath the main vortex, which caused a rebound mechanism

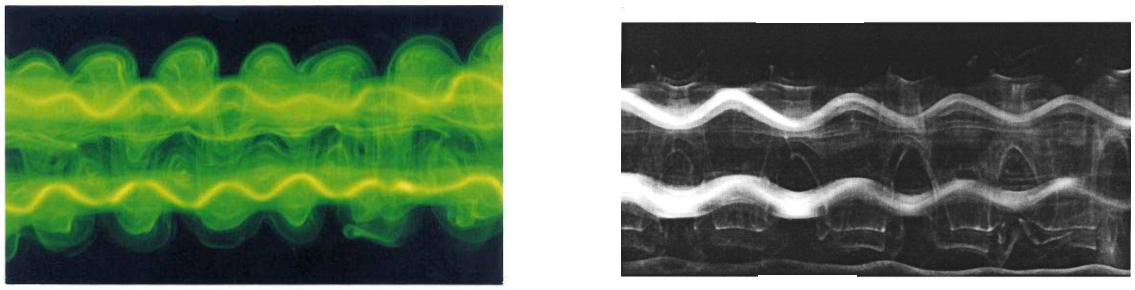

(a) (b)

Figure 2.17: Short-wavelength elliptic instability of (a) counter-rotating vortex pair at Re = 2750, where the pair moving towards observer (Reprinted with permission from Leweke and Williamson (1998), Copyright 1998, Cambridge University Press), (b) co-rotating vortex pair at Re = 4140 (Reprinted with permission from Meunier and Leweke (2001), Copyright 2001, AIP Publishing LLC).

that displaced the main vortex away from the wall. The instability aspects of this secondary vortex was linked with the characteristics of Crow's and elliptic instability, respectively. Luton and Ragab (1994) conducted a numerical investigation on a vortex-wall interaction at $Re = 2196$. The observations indicated that the instability features resembled Crow's displacement bending mode. However, numerical simulations of Duponcheel (2009) at $Re = 5200$ revealed an elliptic instability type for the observed perturbations of secondary vortex filament. The analysis was further extended to different configurations of secondary vortex, paired with a strong primary vortex (see Figure 2.18). The inviscid analysis (Harris and Williamson, 2012) showed an unstable wavelength that corresponded to a displacement mode of Crow's instability. In contrast, Williamson et al. (2014) highlighted that both elliptic and displacement mode wavelengths become apparent for the viscous case. It was convincingly revealed that the narrower peak of the growth rate curve in the case of elliptic instability explain its higher dominance in triggering the onset of perturbation of the secondary vortex. With further temporal evolution, however, Crow's displacement mode eventually dominates the elliptic instability. Simultaneous existence of both major instability mechanisms, therefore, became evident in the case of primary and secondary vortex pairs.

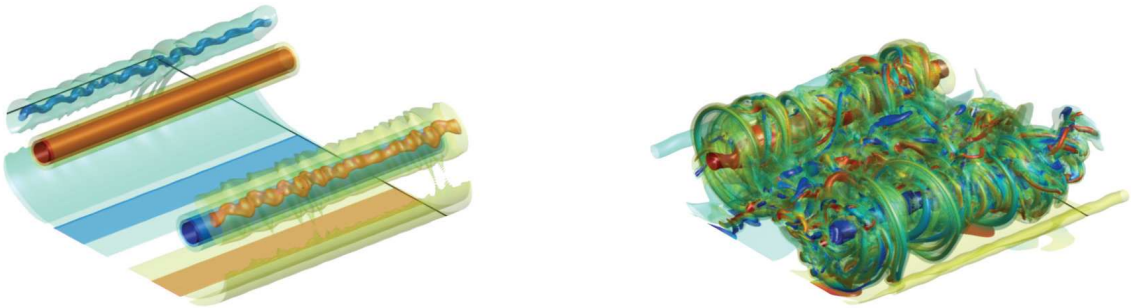

(a) (b)

Figure 2.18: (a) Elliptic instability in the secondary vortex roller and (b) growth of streamwise filaments at $Re = 5{,}200$. Figure reproduced with permission from Duponcheel (2009).

2.5.2 Instabilities and Wake of Stationary Bluff Bodies

Dominant contribution of spanwise instabilities of isolated vortex pairs to wake three-dimensionality has been well observed for stationary bluff bodies, such as a circular cylinder (Williamson, 1996; Barkley and Henderson, 1996; Brede et al., 1996) or the blunt trailing edge airfoil (Ryan et al., 2005; Gibeau et al., 2018). Experimental visualizations suggested that the growth of streamwise coherent structures (ribs), were also associated with spanwise instability modes that possessed different spatio-temporal characteristics (Williamson, 1996). Mode A, in case of stationary cylinder, was characterized by core vorticity outflux from the rollers that consequently led to tongue-like dislocations in the wake Williamson (1996); Mittal and Balachandar (1995). These later elongated into pairs of counter-rotating streamwise filaments with alternating periodicity and a spanwise wavelength (λ_z) equal to four times the cylinder diameter (Williamson, 1996). Mode B, in contrast, featured streamwise filaments characterized by λ_z on the order of cylinder diameter (Williamson, 1996). These thin strands were associated with the straining of streamwise vorticity that existed in the braid region between two consecutive rollers (Williamson, 1996; Brede et al., 1996). Figure 2.19(a,b) demonstrates the schematic representations of Mode A and Mode B, as provided by Brede et al. (1996) and Williamson (1996).

Zhang et al. (1995) observed an instability (later named Mode C) that dominated the wake at Reynolds number of 170 to 270 using an in-house finite difference numerical solver. The characteristic spanwise wavelength of Mode C was approximately two cylinder diameters (Zhang et al.,

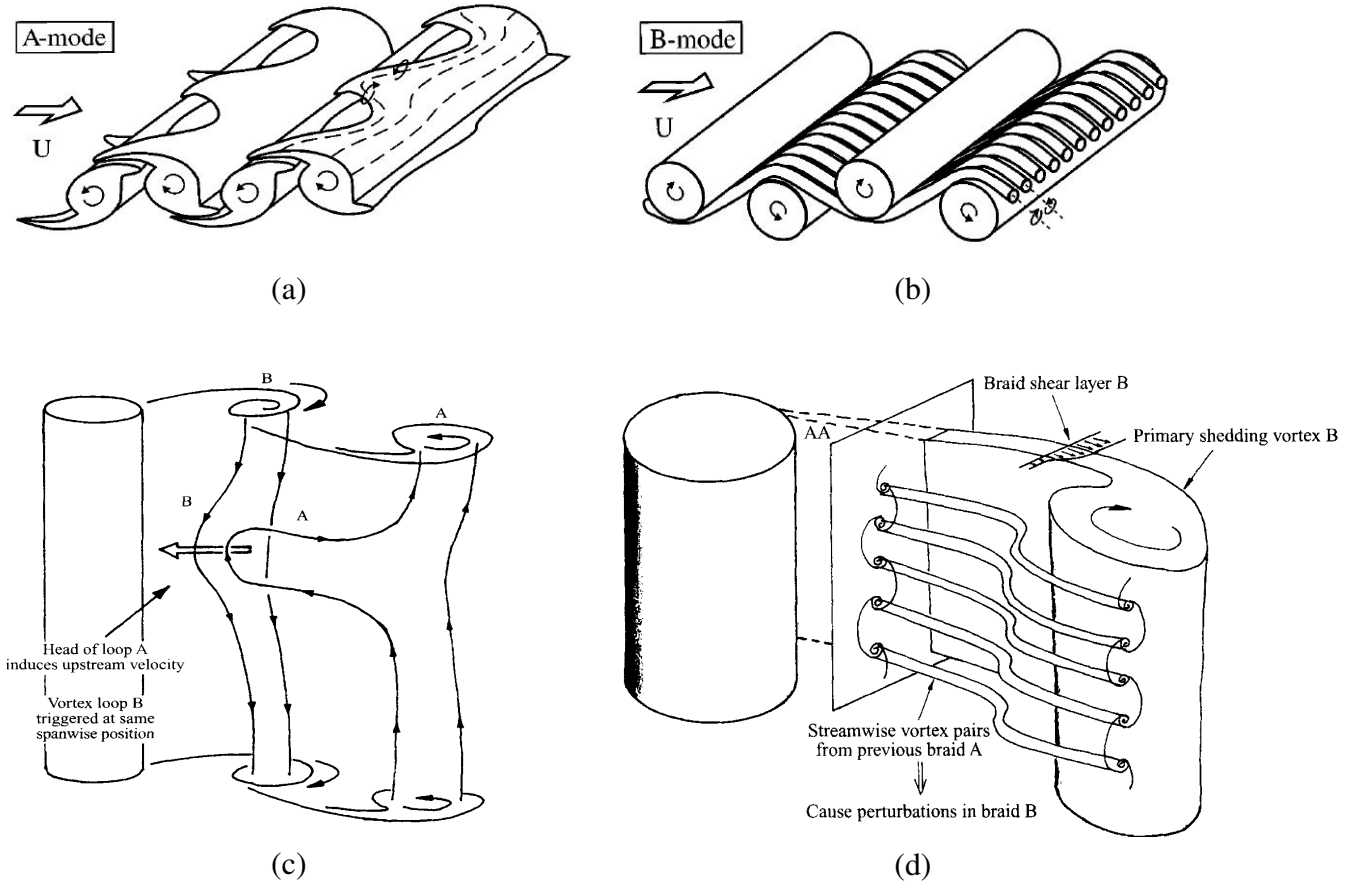

Figure 2.19: Model for wake instabilities and formation of secondary vortex pair for stationary circular cylinder. (a) primary and (b) secondary vortices in the transitional wake of the cylinder for the two shedding modes A and B. Arrows denote the sense of rotation and dashed lines represent vortex lines (Reprinted with permission from Brede et al. (1996), Copyright 1996, by American Institute of Physics). Mechanisms of (a) Mode A and (b) Mode B instability (Reprinted with permission from Williamson (1996), Copyright 1996, Cambridge University Press).

1995). Further assessment of the spatial distribution of Mode C showed that secondary vortices aligned in parallel-pairing in the near and far wake, which is similar to Mode A, but in contrast to Mode B (see Figure 2.20). The latter mostly concentrated in the near wake region (Zhang et al., 1995). Mittal and Balachandar (1995) highlighted the formation of secondary hairpin-like structures that also appeared as spatial dislocation on spanwise rollers, shed in the wake of stationary circular cylinder. Upon evolution, these dislocated formations elongated and formed rib pairs Mittal and Balachandar (1995). These studies (Williamson, 1996; Mittal and Balachandar, 1995) therefore confirmed that the intermediary structures play a pivotal role in governing three-dimensionality of the wake.

Extension of this work on cylinders with varying cross-sections (i.e.square) also exhibited other instability modes (Robichaux et al., 1999), while characterizing their association with secondary vortex pairs. Even for the wake of a blunt trailing edge (BTE) airfoil (see Figure 2.21), experiments (Gibeau et al., 2018) and computational (Ryan et al., 2005) studies utilizing Floquet stability analysis, highlighted the existence of unique instability modes whose spatio-temporal features of secondary wake structures were different compared to previously identified modes (Williamson, 1996). Amongst these was the Mode S instability, which featured a spanwise wavelength of approximately 2.8 cylinder diameters and a periodicity twice that of the primary shedding period for Kàrmàn rollers (Robichaux et al., 1999). A detailed description of the spatio-temporal rib configuration was provided by space-time reconstructed models for all the dominant modes identified by Robichaux et al. (1999). A similar Floquet study was also performed by Ryan et al. (2005) on a blunt trailing edge cylinder. The configuration of ribs observed in this study was referred to as Mode B$'$ with characteristics that partly differed from Mode B previously identified for circular cylinders (Zhang et al., 1995; Williamson, 1996). Specifically, the spanwise wavelength of the ribs was similar to that identified in the wake of circular cylinder. However, a sign swap in streamwise vorticity occurred every half shedding cycle, which was not observed for circular cylinders (Ryan et al., 2005).

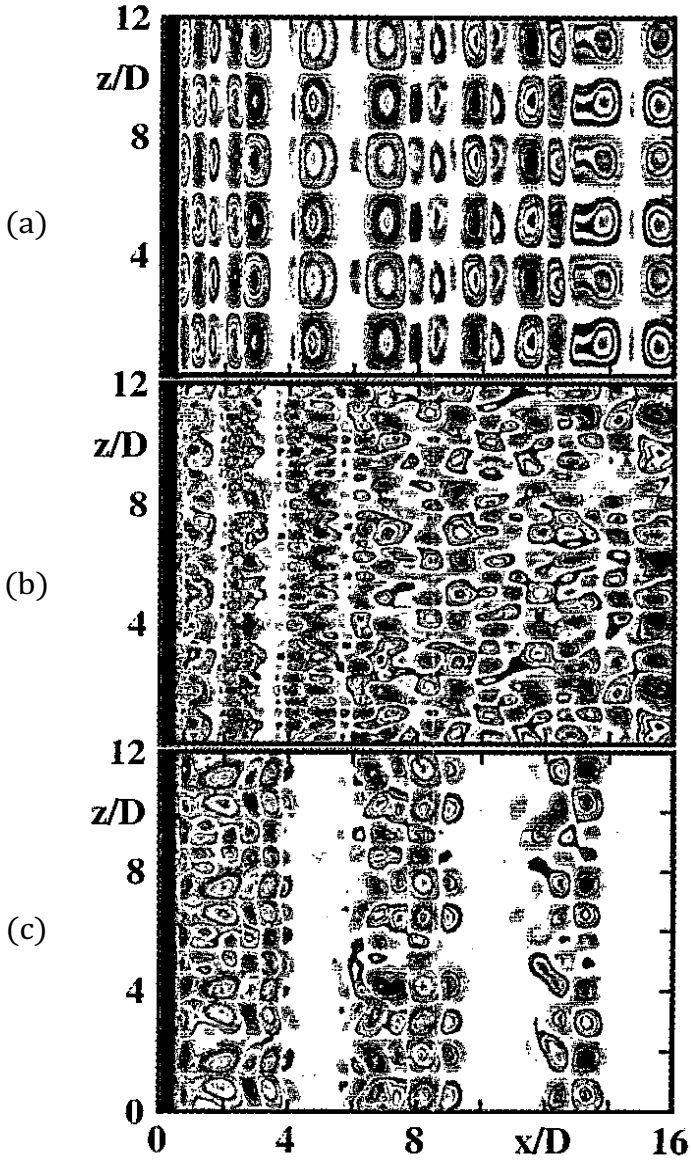

Figure 2.20: Secondary vortices of the (a) A, (b) B, and (c) C mode in wake of a stationary circular cylinder. Instantaneous contour plots of the numerically obtained vorticity component ω_y in the xz plane at Re = 200, 240, and 210 (top to bottom) (Reprinted with permission from Zhang et al. (1995), Copyright 1995, by American Institute of Physics).

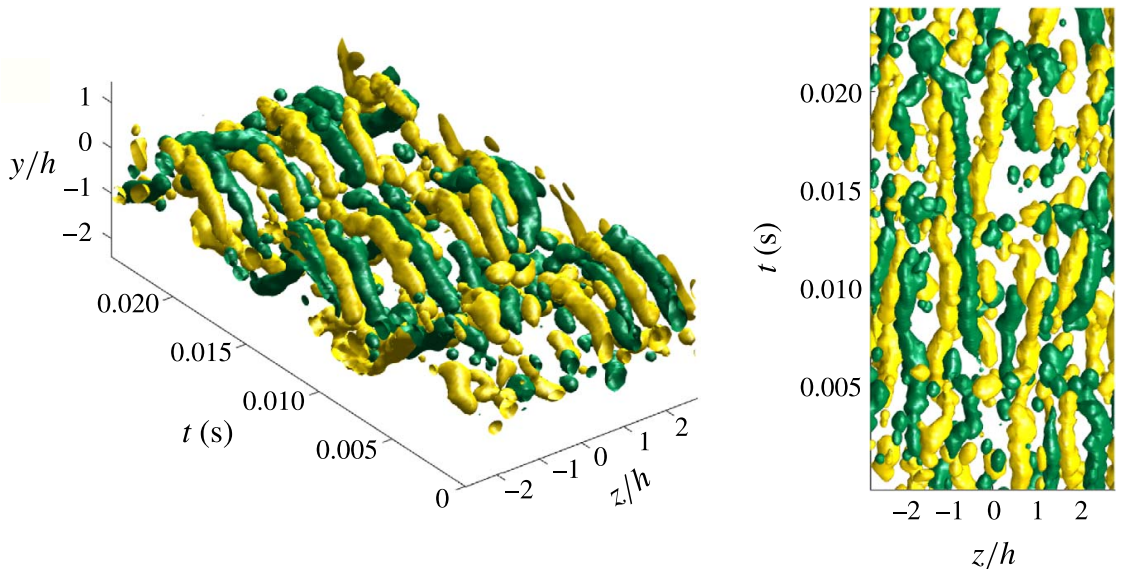

Figure 2.21: Secondary rib pairs in wake of a stationary BTE airfoil. Isosurface constructions of modified Q-criterion ($Q' = \omega_x Q/|\omega_x|$) in the wake at $x = 2h$ for (a) $Re_h = 3500$ (isosurface at $|Q' = |\ 2000\ s^{-1}$) and (b) $Re_h = 7000$ (isosurface at $|Q' = |\ 18000\ s^{-1}$). Green and gold represent positive and negative rotational directions, respectively (Reprinted with permission from Gibeau et al. (2018), Copyright 2018, Cambridge University Press).

2.5.3 Instabilities and Wake of Oscillating Bluff Bodies

Extensive knowledge and understanding of the wake dynamics behind stationary bluff bodies motivated fluid dynamicists to expand the instability assessments into rigid bodies that perform prescribed oscillations (Visbal, 2009; Nazarinia et al., 2009; Deng et al., 2015; Deng and Caulfield, 2015b; Sun et al., 2018; Son et al., 2022). These outlined different aspects of secondary wake structures and how they influenced the wake three-dimensional features. Kinematics prescribed on foils generally included single degree of freedom oscillations in the form of either pitching or heaving motion (Ellenrieder, 2003; Dong et al., 2006; Visbal, 2009; Calderon et al., 2014; Deng et al., 2015; Deng and Caulfield, 2015b; Sun et al., 2018; Chiereghin et al., 2020). Initially, three-dimensional wakes of pitching foils with low aspect ratios were examined (Dong et al., 2006; Calderon et al., 2014; Ellenrieder, 2003). Visbal (2009), then expanded to the secondary vorticity outflux observed near the leading edge of a heaving foil at high Reynolds numbers ($Re \approx 10^4$). Existence of long and short wavelength instability modes and the associated secondary vortex arrangement were also

examined (Deng et al., 2015; Deng and Caulfield, 2015b), where the spatio-temporal features of modes differed in terms of spanwise wavelength and streamwise periodicity. Deng et al. (2015) performed Floquet analysis on pitching foils, which highlighted a direct correspondence of secondary vortex pair formation and asymmetric arrangement of primary rollers shed behind the foil (see Figure 2.22). Sun et al. (2018) discussed features of Modes A, B, and S for a heaving foil that were characterized by $\lambda_z \approx 1.05$, 0.2, and 0.39, respectively.

Some studies also presented limited assessments of foils with combined pitching and heaving oscillations (Moriche et al., 2016). Floquet stability analysis of Moriche et al. (2016) on a foil with combined heaving and pitching motion provided details on the three-dimensional wake transition, along with associated impacts on force generation. Although the observations showed minimal effects on forces, the onset of three-dimensionality on the infinite span oscillating wing was linked to the bending of TEV (Moriche et al., 2016). Chiereghin et al. (2020) observed the existence of sinusoidal undulation on the shed LEV filament in the wake of a high aspect ratio heaving swept wing (see Figure 2.23). The origins, however, remained unclear and they were speculated to be either an instability of oscillating shear flow, mixing layer, or the vortex filament itself (Chiereghin et al., 2020). It was also noted by Chiereghin et al. (2020) that increasing circulation of LEV at high St_c led to stronger deformations, which also coincided with significant effects on lift and bending moments. The presence of secondary structures and their association with the LEV dynamics was, however, not evident in the study of Chiereghin et al. (2020).

Son et al. (2022) recently provided comparative assessments of LEV dynamics on an oscillating finite aspect ratio wing, and an airfoil of infinite span, with prescribed heaving motion at $Re =$ 10,000. Their experimental and computational observations suggested that the counter-rotating rollers were responsible for the resulting spanwise undulations of LEV filament (see Figure 2.24). Son et al. (2022) also found a dependence of LEV spanwise undulations on the reduced frequency, which contributed to differences in circulation ratio of LEV and TEV within one oscillation cycle. This coincided with the occurrence of Crow's instability mechanism (Crow, 1970) triggered by either a $LEV - TEV$ pair (at $St_c = 2$ and 3), or an LEV paired with its image LEV that was formed on

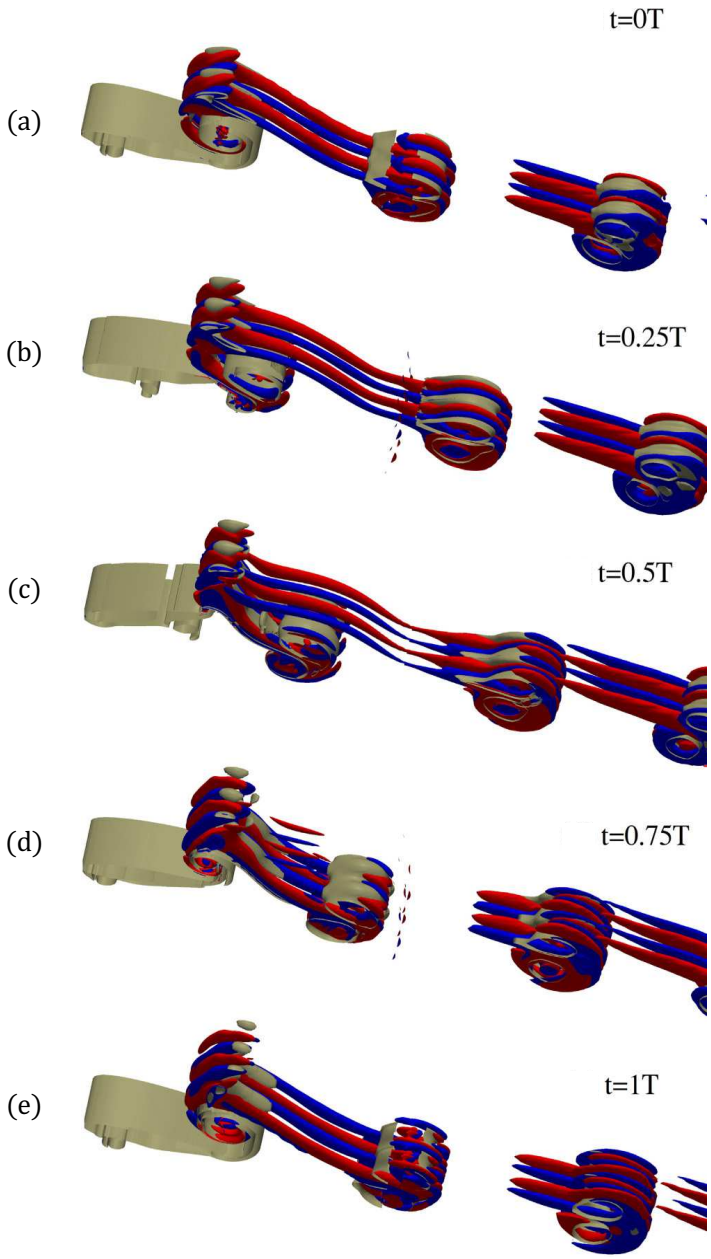

Figure 2.22: Secondary vortex pairs in wake of a pitching foil. Three-dimensional DNS results for the isosurfaces of streamwise vorticity field ($|\omega_x| = 6$) for the short wavelength mode at Re = 1500, $A_D = 2.8$, and $\beta = 30.0$. Five instants during a periodic cycle are shown. Blue (dark gray) and red (light gray) colors denote negative values and positive values respectively of 0.3 of the instantaneous maximum magnitude. Isosurfaces of spanwise vorticity ($|\omega_z| = 6$) are also shown (Reprinted with permission from Deng and Caulfield (2015a), Copyright 2020 by the American Physical Society).

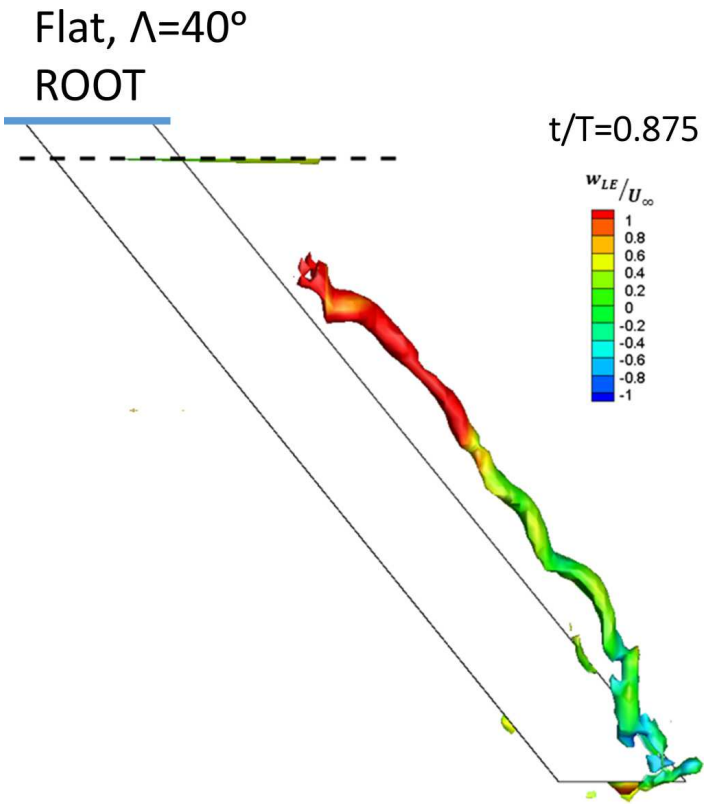

Figure 2.23: Spanwise undulations on a *LEV*. Isosurfaces of normalized vorticity magnitude $|\omega|c/U_\infty = 13.4$ for $\alpha = 15°$, $St_c = 1.1$, $A/c = 0.5$. Top view of the swept wing with flat-plate cross section (Reprinted with permission from Chiereghin et al. (2020), Copyright 2020 by the American Physical Society).

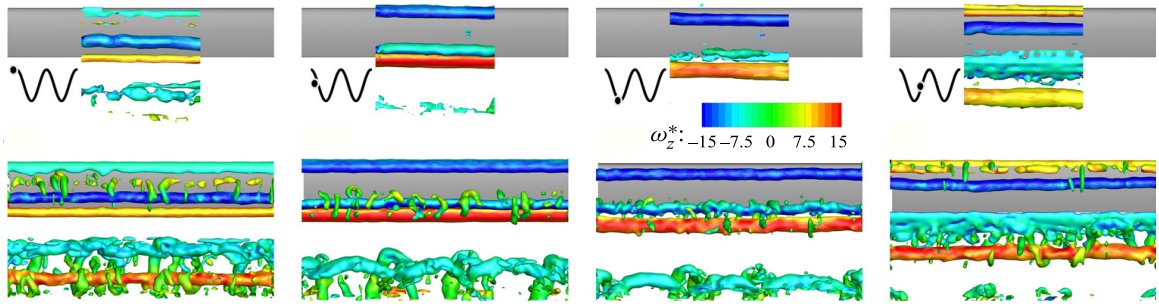

Figure 2.24: Illustration of spanwise instability and secondary vortex evolution in wake of a heaving foil. Vortical structures (Q^*=5), colored by spanwise vorticity, from experiments (upper row) and numerical simulations (bottom row) for the airfoil case of St_c =2, A/c=0.5 (Reprinted with permission from Son et al. (2022), Copyright 2022, Cambridge University Press). Flow from top to bottom.

Table 2.1: Quantitative comparison of spanwise wavelength for secondary vortices in wake of different geometries, motion and Re. Diameter (D), height (h) and chord length (c) for respective geometries were used for normalizing λ_z.

Motion	Geometry	Study	Re	λ_z	Mode
Stationary	Circular Cylinder	Williamson (1996)	170-260	$1D, 4D$	A,B
	Circular Cylinder	Zhang et al. (1995)	160-230	$1D, 2D, 4D$	A,B,C
	Square Cylinder	Robichaux et al. (1999)	200-300	$2.8D$	S
	BTE Cylinder	Ryan et al. (2005)	100-700	$2.2h, 1h$	B',S'
	BTE Cylinder	Gibeau et al. (2018)	3500-7000	$0.7h - 0.8h$	B
Pitching	NACA 0012 airfoil	Deng & Caulfield (2015)	1700	$0.21c$	Short
Pitching	NACA 0012 airfoil	Deng & Caulfield (2015)	1700	$1c$	Long
Heaving	NACA 0012 airfoil	Sun et al. (2018)	1700	$1.05c, 0.393c,$ $0.196c, 0.217c$	A,S, B,QP

account of vortex-foil interaction (Visbal, 2009; Son et al., 2022). A similar qualitative assessment of changes in *LEV* instability features that were associated with strong vortex-foil interaction, with an increase in the aspect ratio (AR) of the heaving foil, was recently completed by Hammer et al. (2022) at $Re = 200{,}000$. Despite this higher Re, the qualitative and quantitative observations were in agreement with instability aspects reported at lower Re (Visbal, 2009; Chiereghin et al., 2020; Son et al., 2022). The effects were dominant as AR increased from 4 to 8, but above 8, the changes were not noticeable. Although an association of *LEV* instability with St_c and AR were apparent in Son et al. (2022) and Hammer et al. (2022), respectively, they were limited to heaving and a single motion or geometrical parameter (i.e. St_c or AR). A summary of studies that outline the instabilities and secondary vortex features in wake of stationary and oscillating bluff bodies is provided in Table 2.1.

2.6 Computational Fluid Dynamics (CFD) Approach

Computational fluid dynamics is proven as a major tool in assessment of fluid and vortex dynamics for both stationary and moving bodies. Particularly, numerical techniques that assesses wakes of stationary cylinders with varying cross-section (i.e. circular, square and prismatic) include DNS, LES, DES and unsteady RANS based solvers (Mittal and Balachandar, 1995; Dong et al., 2006; Hemmati et al., 2019a). The wake assessments for oscillating rigid bodies that execute either single or multiple degree of freedom motion have also been reported using different numerical tools. Although the governing physical equations are the same, but solving them follow different numerical algorithms and techniques.

Some of the most prominent dynamic modeling techniques in CFD simulations include mesh morphing, sliding grid interface, overset or chimera grid assembly and immersed boundary methods. Each of these techniques have their strength and weaknesses, and they can prove robust under specific motion types. For example, oscillatory pitching or heaving at low amplitudes of leading or trailing edge can be effectively modeled using mesh morphing technique. However, at larger displacements, mesh morphing can result in grid cells of relatively high skewness and large aspect ratio near the body. These issues result in numerical divergence or non-physical artifacts in the solution of governing equations. Overset grid assembly and Immersed boundary methods are highly stable and feasible under large amplitudes and high frequency oscillatory motions. They have been employed in simulating moving bodies with a broad engineering applications, including rotating turbines as well as floating oscillatory bodies in fluids (Panahi and Shafieefar, 2009; Chandar, 2019). Blondeaux's study on in-line and transverse oscillating cylinders (Blondeaux et al., 2005) highlighted the capabilities of numerical simulations in explaining the features of vortex shedding. These results were further validated by Senturk et al. (2017) using immersed boundary method to model the wake of moving and oscillating bodies. The changes in the vortex dynamics around pitching square panels at different Reynolds numbers was also explored by Senturk and Smits (2018). Using a modified solver based on OpenFOAM, Senturk and Smits (2018) provided insights into unsteady pressure variations on the panel surfaces.

2.6.1 Overset Grid Assembly

Major challenges in modeling complex body motions in different CFD simulations involve maintaining the grid cell quality, non-orthogonality and skewness. These issues remain dominant in traditional methods such as dynamic mesh morphing, where the entire mesh changes in order to conform movement of the body. Overset grid methods overcomes this difficulty using multiple meshes. Motion of the body is only performed on the overlapping mesh, while the background mesh remains stationary. The solution is interpolated between the overlapping and background mesh at each time-step. This methodology allows for large amplitude motion of the body without any comprise on the grid cell quality.

The concept of Overset mesh has been implemented in some rotorcraft (Shenoy et al., 2014) and hydrodynamic applications (Zhang, 2018; Wang, 2017). Liu et al. (2010) detailed the functionality of an in-house CFD solver, which implemented an unstructured overset meshing capability. This overset methodology applied to both viscid and inviscid flows, including dynamic motion cases, such as a moving valve, pitching airfoil and more complex flows around butterfly valves. The results of the new method compared well with the corresponding experimental observations (Morris, 1987). Shenoy et al. (2014) demonstrated a new in-house Overset implementation for exploring the complex aerodynamic wake interactions between stationary fuselage and a rotating blade of a Rotorcraft. The adaptive overset methodology was able to provide insight into the vortex-fuselage impingement phenomenon (Shenoy et al., 2014), which was not observed using any existing dynamic mesh methods. Chandar (2016) discussed and compared three dynamic grid techniques in OpenFOAM, namely arbitrary mesh interface (AMI), generalized grid interface (GGI), and an in-house Overset method. Chandar (2016) identified that Overset method offered comparable results to other established techniques with better efficiency in parallel computing. Other applications of the overset techniques include modeling ship motion due to large waves (Carrica et al., 2007), parachute inflation (Xia et al., 2009) and simulation of insect flight (Liu, 2009).

2.6.2 Immersed Boundary Methods

Immersed Boundary Method (IBM) represents a robust technique over the boundary fitted methods (i.e. mesh morphing) for modeling flow around bodies with complex oscillations. Continuous and Discrete forcing IBM methods are the most prominent tools that have been well validated and verified against experimental studies. Within continuous forcing IBM, the Navier-Stokes equation is modified before the discretization, such that the forcing is implemented in the form of a source term. Near the boundaries, this term is substituted by a discrete Dirac Delta function that smears the value of boundary fields (Senturk et al., 2017). For discrete forcing or sharp-interface IBM techniques, the forcing is conducted after the discretization. This allows a local reconstruction based on the underlying grid cell and boundary fields themselves. The approximation of interface is more accurate in this technique compared to the continuous forcing method (Senturk et al., 2017).

IBM often encounter accuracy deterioration near the boundary of solid body, although recent developments have attempted to overcome this issue using higher order reconstruction of velocity dependent terms in the Navier-Stokes equation. Furthermore, Finite-volume based IBM method is more suitable compared to finite difference based solvers since an appropriate mass and momentum conservation is guaranteed for the former (Aarnes et al., 2020). Open source software packages like foam-extend 4.1 have provided recent implementation of discrete forcing IBM method, although stability issues were reported at highly refined grids (Senturk et al., 2017).

2.6.3 Sliding Grid Interface

Sliding Mesh Interface technique is commonly used for computational modeling of rotating geometries, such as propeller fan and compressor blade operation. It also represents a class of methods where the mesh cells are not deformed based on the movement of body within a computational domain. This process involves subdivision of a single grid into regions of static and moving cells. The sliding interface is identified in the region separating two regions while the surface elements belonging to this interface are accessible from both connected region (i.e. static and moving). At

each timestep, the rotating mesh slides and a list containing the vertex map is computed to implicitly couple the static and moving regions of the mesh (Mcnaughton et al., 2014). Solution fields (pressure and velocity) are ultimately interpolated across the interface to provide the final solution.

Examples of utilizing sliding grid interface methodology include modeling multi-phase stirred reactors (Yang and Mao, 2014), hybrid aero-acoustics assessment of automotive blowers (Piellard and Coutty, 2011), blade deformation and transient fan modeling of truck cooling systems (Gullberg et al., 2013; Hobeika et al., 2014) and simulating vertical axis wind turbines for hydro-kinetic applications (Mcnaughton et al., 2014). In the case of vertical axis wind turbines, it was recently observed that although sliding grid interface method required 10% less computational time compared to overset technique with similar grid size, the convergence rate was slower and the computed wake dynamics had greater inaccuracies. The sliding grid interface further presents difficulties in modeling complex curved geometries, where the interfaces encounter large non-conformity of cells belonging to sliding and static regions.

2.6.4 Dynamic Mesh Morphing

Dynamic mesh morphing represent a classic CFD tool to model oscillatory motion of solid bodies. The methodology is completely different from those of the overset, IBM and sliding grid interface techniques since it does not involve any additional overlapping grid or identification of segregated regions within the computational grid. Instead, it involves updating the position of grid cell vertices, such that it exactly follows the boundary of the moving solid body. This is achieved by a complete re-meshing of the grid at each time step. This method ensures that while the topology of the mesh changes, the connectivity between boundary faces of body and fluid patch, respectively, is always maintained. The equation of motion is written in arbitrary Lagrangian-Eulerian formulation, while an additional equation is solved for the point displacement. Although the method represents a fully mass conservative approach, it is not proven effective for highly curved geometries (Senturk et al., 2017). This is due to the high non-orthogonality of cells associated with the structured meshing approach. Even for large amplitude oscillatory motion cases, it is quite hard

for the solver to avoid skewness of morphed cells during re-meshing of the grid at a new time step. This subsequently leads to stability and divergence issues during the simulation. The additional computing time needed for remeshing leads to more demanding computational resources, which subsequently reduces its applicability for highly refined three-dimensional geometries Aarnes et al. (2020).

2.7 Summary

Immense research has been conducted for oscillating foils in either heaving or pitching kinematics. These primarily represent a single degree of freedom motion. However, potential gaps in terms of understanding propulsive performance, transition mechanisms of primary wake topology, and three-dimensional secondary instabilities does exist for foils oscillating in complex multi-degree of freedom motion, i.e. combined heaving and pitching. Scaling of propulsive thrust generation and efficiency have been conducted recently for only fixed Reynolds number. Extending these scaling relations to multi-motion oscillations at different Reynolds numbers will eventually improve the existing propulsive scaling models by reflecting a better physical relationship. Besides propulsive performance, insights relevant to transitions in the wake topology, including shedding and spatial arrangement of primary vortex structures, for foils in mixed motion are rather limited. The detailed mechanisms of vortical interactions, merging and bifurcations could hint at a fundamental association with propulsive performance.

Transitions in the wake topology of purely pitching or heaving foils have been best represented on phase maps that include an appropriate wake mode depicting an increasing range of amplitude, reduced frequency or Strouhal number. Such diagrams are available for single degree of freedom oscillatory foils, which also highlighted changes in propulsive nature of the wake. A similar depiction, however, lacks in case of foils with mixed pitching and heaving motion. These not only provide a vivid picture for the existence of novel wake modes, but it could also reveal coincident performance features peculiar to few specific wake modes. Besides, studies had revealed that cer-

tain transitions in wake modes (usually in case of pitching foils) can be mathematically modeled by analyzing circulation strength for shed vortex structures. These models, however, lack the inclusion of heave velocity in their analysis, which becomes a dominant component in cases of foils with coupled heaving and pitching motion. Such gaps must be addressed to get better fundamental understanding of the relationship between kinematics, performance and wake topology.

With regards to three-dimensional wake characteristics of foils oscillating in mixed motion, it is apparent that a coherent discussion on evolution of spanwise instability and secondary wake structures is still required. Majority of studies have dealt with onset of instabilities in the wake of stationary bluff bodies. Quantitative and qualitative characterization of the wake, in terms of instability wavelength, periodicity of secondary structures, their interaction with primary rollers and contribution towards vortex dislocations, provided a clear view of physical mechanisms that govern the three-dimensionality in wake. However, the existence of secondary structures and differences in their fundamental characteristics compared to stationary bluff bodies is unknown. It was also evident how different modes of instability exist in cases of purely heaving or pitching foils. However, there is no specific clarity on the mechanisms of secondary structure evolution. A definitive association between changes in the kinematics of oscillating foil, and the onset of secondary instability, should be well understood to better our knowledge of the wake dynamics behind oscillating foils.

Chapter 3

METHODOLOGY[†]

This chapter details the foil geometrical description and kinematic settings in this dissertation (Section 3.1). Details on the Overset Grid Assembly within OpenFOAM are also provided to outline the numerical methodology for the simulations. Governing equations and a brief overview of this numerical method is described in Section3.2, followed by a discussion of OGA algorithm in Section 3.3. The computational setup, boundary and initial conditions, and discretization schemes that were utilized for simulating the flow around oscillating foils are explained in Section 3.4. Extensive verification and validation analysis are presented in Sections 3.5 and 3.6, respectively. Investigation into parallel scalability features further outline the effective functionality of the Overset grid assembly technique in OpenFOAM with respect to parallel processing and modeling of the wake dynamics resembling an efficient swimmer. The details are provided in Section 3.7.

[†]The content of this chapter has been published in whole or part, in *Journal of Computations (Verma and Hemmati, 2020), Journal of Fluid Mechanics (Verma and Hemmati, 2021b, 2022a), Physics of Fluid (Verma et al., 2022a) and Physical Review E (Verma and Hemmati, 2022b),* under citations:
"Verma, S. & Hemmati, A. (2020). Performance of overset mesh in modeling the wake of sharp-edge bodies. Computations 8 (3), 66."
"Verma, S. & Hemmati, A. (2021). Evolution of wake structures behind oscillating hydrofoils with combined heaving and pitching motion. Journal of Fluid Mechanics 927, A23."
"Verma, S., & Hemmati, A. (2022) Characterization of bifurcated dual vortex streets in the wake of an oscillating foil. Journal of Fluid Mechanics 945, A7."
"Verma, S., Freeman, B.R.S. & Hemmati, A. (2022). Effects of Reynolds number and average angle of attack on the laminar scaling of oscillating foils. Phys. Fluids 34 (3), 031905."
"Verma, S. & Hemmati, A. (2022). Route to transition in propulsive performance of oscillating foil. Phys. Rev. E 105 (4), 045102."

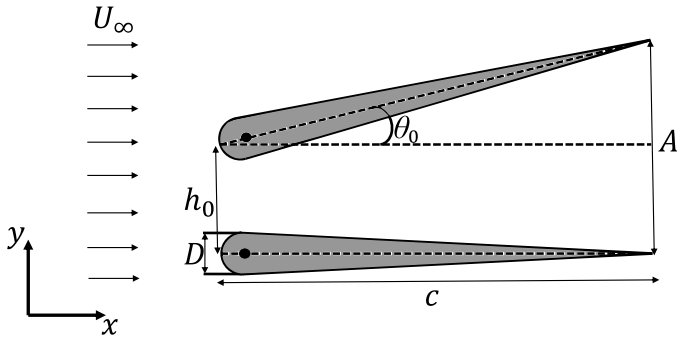

Figure 3.1: Description of teardrop foil geometry and motion in the current study.

3.1 Foil Geometry and Kinematics

A teardrop foil undergoing a combined pitching and heaving oscillation (Figure 3.1) is numerically studied at a range of Re. The D/c ratio for the foil is 0.1. The choice of teardrop foil geometry falls in line with recent experimental studies that evaluated scaling relationships for propulsive thrust, power and efficiency at a constant Re (Floryan et al., 2017; Van Buren et al., 2019). The foil exhibited the oscillatory motion about a point located at 0.05c from its leading edge, following a sinusoidal profile described using Eq. 2.2 and 2.3 in Section 2.2.

3.2 Numerical Method

This work employs OGA technique to examine the wake of oscillating foils. The requirement of smaller grids in overset technique, as seen in a study by Aarnes et al. (2020) for simulating flows over two dimensional bodies, highlighted its potentially better computational efficiency compared to other techniques, such as IBM (Senturk et al., 2017; Taira, 2009). This, particularly, allow modeling complex multi degree of freedom kinematics wherein the oscillation frequency, peak leading and trailing edge amplitudes and phase offset between the heaving and pitching motion can be varied over a larger parameter space.

The Overset Grid Assembly involves merging two spatial grids, which are referred to as the *Background Grid* and *Overset Grid* (see Figure 3.2). The latter contains the moving body, whereas the former grid represents a homogeneous fluid domain. The oscillatory motion dynamics of the body is modeled by moving the *Overset Grid* using prescribed kinematic formulations outlined in Chapter 2. The *Background Grid* remains stationary throughout the simulation. This eliminates the need for deforming the spatial grid per time step.

The three-dimensional incompressible Navies–Stokes and continuity equations were solved using the finite volume discretization method implemented in OpenFOAM:

$$\frac{\partial u_i}{\partial x_i} = 0 \tag{3.1}$$

$$\frac{\partial u_i}{\partial t} + u_j \frac{\partial u_i}{\partial x_j} = -\frac{1}{\rho}\frac{\partial p}{\partial x_i} + \nu \frac{\partial^2 u_i}{\partial x_j x_j} \tag{3.2}$$

Here, u_i is the velocity, p is pressure, ρ is density and υ is the kinematic viscosity of the fluid. All the flow parameters are normalized using the freestream velocity (U_∞) and chord length of the body (c). The velocity and pressure fields are calculated by solving the governing equations based on the interpolation of the solution transferred between the *Background* and *Overset* cells, which are located at the overlapping regions of the merged grid. The resulting flow fields on the *Background Grid* are then utilized for simulation analysis.

3.3 Overset Grid Assembly Algorithm

The OGA algorithm involves identifying three major categories of grid cells: Holes, Interpolated and Calculated. These are updated for every time step in an unsteady simulation. The geometrical profile of the body is represented by the Hole cells, where no field quantities are solved or interpolated. The Interpolated cell pairs, also known as donor-acceptor cells according to Petra (2019),

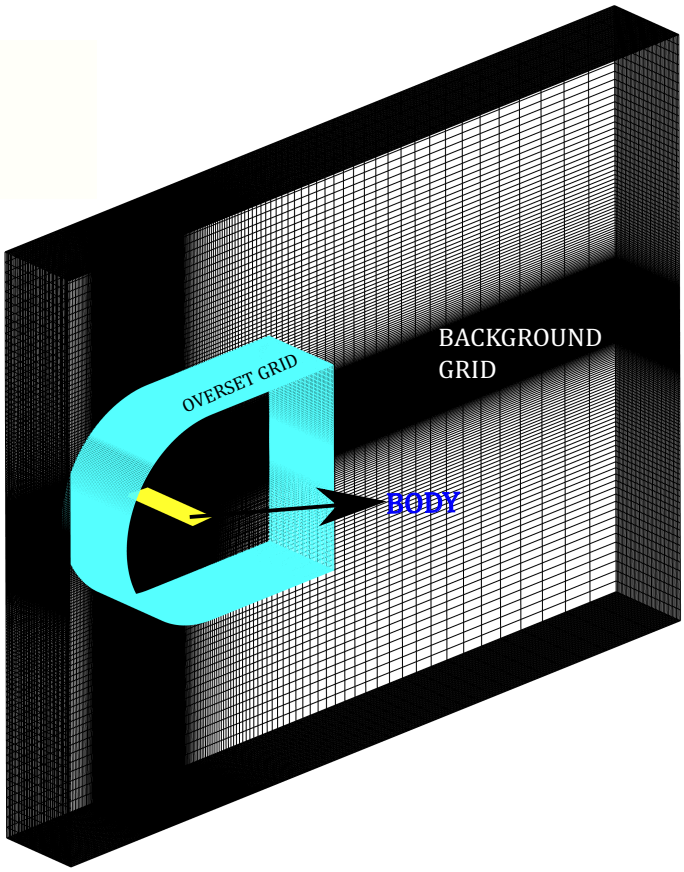

Figure 3.2: Block structured mesh depicting Overset Grid Assembly.

are then utilized for interpolation and transfer of the solution between the two grids, respectively. The steps are briefly explained below and detailed algorithm is provided by Petra (2019):

1. All cells that act as neighbors (donors) to an acceptor cell are referred to by employing their index number defined within the mesh. The solver also identifies the fields (pressure, velocity and turbulence quantities) that are required for data interpolation in acceptor cells on Background and Overset grids.

2. Hole, Interpolated and Calculated cells are then set by the solver. Hole cells are generally identified in the underlying Background or Overset grid, which could be stationary or prescribed to execute a motion. These cells governed by the secondary (overlapping) grid, which approximates the representation of wall boundary of the moving body. The flow field is not solved within these cells. Interpolated cells require interpolation from donor cells that

exist in the overlapping regions of the mesh, i.e., Interpolated cells lying on the background grid have their donors on overset grid and vice-versa. All the remaining cells that are not identified as Interpolated or Hole cells are assigned as Calculated cells.

3. The interpolation scheme specified by the user is used by the solver to perform interpolation from field values of identified donor cells. For instance, if the scheme is specified to be inverse distance, a corresponding list of donor cells and their weights (calculated based on the distance between centroid of acceptor and donor cell) is supplied for each interpolated cell.

Figure 3.3 demonstrates the identified cells by the OGA algorithm for two separate cases. In case of an oscillating foil, Figure 3.3(a) depicts a coarse representation of the merged background and overset grids, colored in white and black, respectively. Figure 3.3(b) shows the Hole and Calculated cells on the Background Grid, along with the Interpolated cell fringe located on and around the foil. Figures 3.3(c) and 3.3(d) show the planar cross-section of an inclined rigid square panel where the latter depicts cells identified on the overset grid, while the former marks representative cells on the background grid.

The “inverse distance" technique is implemented for interpolating velocity and pressure data, which had previously been validated for refined grids (Chandar, 2019). The interpolation function for the Inverse Distance Scheme is

$$\varsigma_D = \sum_{i}^{n} w_i \varsigma_i, \tag{3.3}$$

where, ς_D is the interpolated value obtained from n neighboring donor cells with value of ς_i, and w_i is the weighting function (Chandar, 2019). w_i is obtained by using the distance between a given cell, for which interpolation is performed (acceptor), and its neighboring donor cells (d_i). The formulation is given by:

$$w_i = \frac{\frac{1}{|d_i|}}{\sum_i^n \frac{1}{|d_i|}}. \tag{3.4}$$

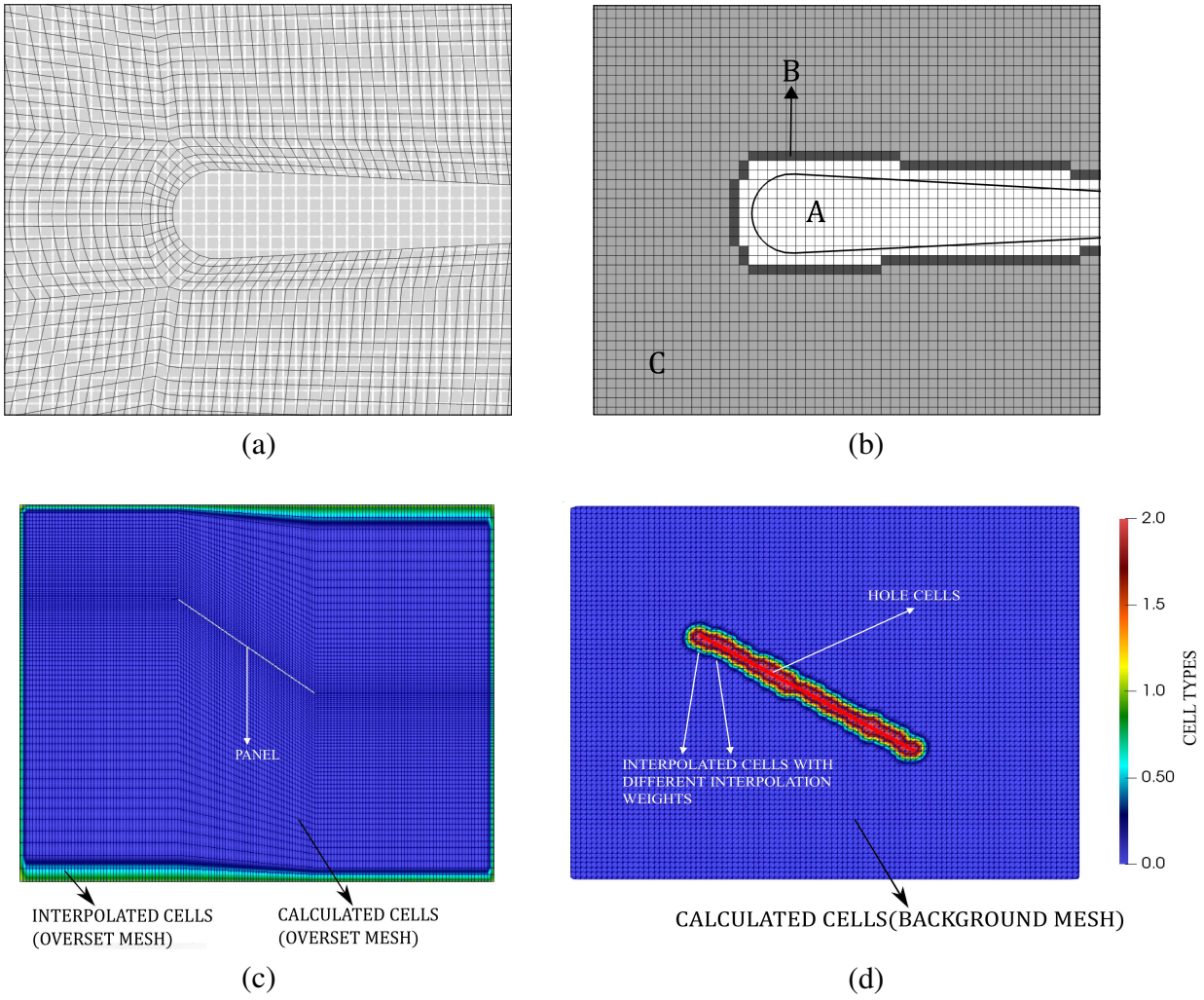

Figure 3.3: Overset Grid Assembly (OGA) meshing and cell identification for an oscillating foil and an inclined square panel. (a) Typical overlap of an structured overset grid (black lines), and background grid (white lines) for this study. (b) Representation of Hole cells in white (A), interpolation cell fringe in black (B), and calculated cells in dark grey (C), identified on background grid, respectively. Identification of cells on (c) Overset and (d) Background grid of an inclined square panel. The cell types depict how interpolation weights vary based on their distance from the hole points.

Several schemes are available for the overset interpolation process, some of which offer higher accuracy according to Chandar (2019). These, however, are not available in OpenFOAM unlike commercial software packages and in-house codes, such as Opera (Chandar, 2019) and SUGGAR++ (Noack, 2009). The Inverse-Distance scheme in OpenFOAM-v1712 Is selected for the overset interpolation. Potentially higher conservation errors in this method are compensated for using a refined overlapping grid and temporal grid, based on the recommendation of Chandar (2019).

In OpenFOAM, OGA method is integrated with the solver based on Pressure-Implicit with Splitting of Operators, called "overPimpleDyMFoam". The PIMPLE algorithm itself is used in various numerical studies concerning high Reynolds number unsteady turbulent flows (Hemmati et al., 2019a; Kim and Xie, 2016). Particularly, Kim and Xie (2016) has shown that implementing the PIMPLE formulation accurately solves the turbulent features of the flow using coarser time steps in unsteady simulations. The multiple corrector loop is executed using PISO method per outer iteration, while the momentum equations are solved repeatedly in the outer iterations using the SIMPLE algorithm. Three corrector loops are applied for the current simulations, which are determined to be the optimum number within the solver tolerance of 10^{-8} for both velocity and pressure. The pressure Poisson formulation for the OGA method is further written as:

$$\nabla^2 p = \nabla \cdot \Phi + \varphi, \tag{3.5}$$

where, φ denotes the source term given by $\varphi = -\nabla \cdot \phi + \nabla^2 p$. Here, p and ϕ represent the pressure and mass flux defined for the cells lying on the interface of overlapping grids. Further details on the Poisson equation in the Overset Grids can be found in Chandar (2019).

3.4 Computational Setup

The computational setup for an overset solver generally consists of a primary solution domain and either a single or multiple secondary grids, which are overlapping the primary domain (Background Grid). This allows for meshing multiple complex geometries separately, and then merging those secondary meshes to the primary background grid for solving the dynamics of a complete system. This technique also provides capabilities to model different forms of motion for each secondary grid, or even assigning them as motion free.

Several rigid body wakes are considered for this initial set of studies. Initially, the flow around three-dimensional finite and thin square panels ($AR = 1$) is simulated. These include both stationary and pitching panel cases. Finite AR panels allow the onset of tip vortices from the side edges early on during evolution of the wake. Thus, the stability and accuracy of overset solver can be tested as early as the first vortex shedding cycle is completed in the simulation. The availability of several published experimental and computational studies further allowed the comparative assessment of the wake of 3D square panels. This is followed by two- and three-dimensional infinite span oscillating foils that addressed the major objectives of this dissertation.

3.4.1 3D Square Panel

A rectangular computational domain is created with the size of $20c \times 16c \times 6.28c$ in the $X-$ (streamwise), $Y-$ (cross-flow) and $Z-$ (spanwise) directions, respectively (Figure 3.4). This domain size ensures that 2 or 3 vortex pairs are captured in the wake, while minimizing the effects of side and top boundaries on the wake characteristics (Najjar, 1998; Hemmati et al., 2016). This domain size follows past numerical studies that investigate the three-dimensional wake characteristics behind normal thin flat plates (Najjar, 1998; Hemmati et al., 2016) and flapping foils (Dong et al., 2006; Deng and Caulfield, 2015a; Deng et al., 2015).

The spatial grid is inhomogeneous with finer mesh around the body and coarser mesh closer to the domain boundaries (Figure 3.5). A secondary grid is set over the Background Grid, which

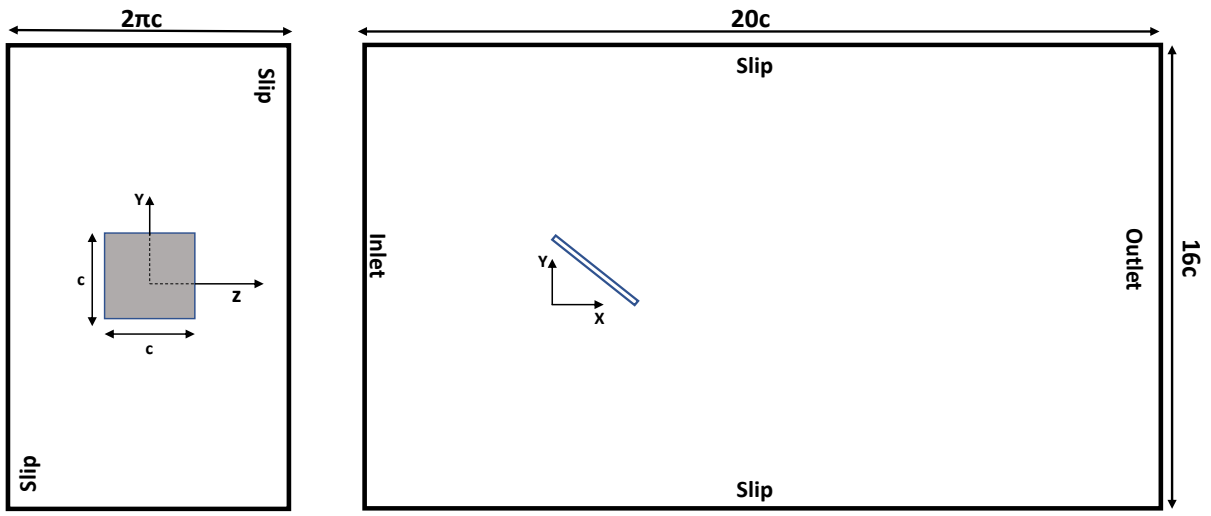

Figure 3.4: Schematic of the computational domain and boundary conditions.

has a mesh spacing equal to the corresponding spacing observed in the background mesh. Grids used in the current simulations requires finer resolution near the flat panel, since the critical wake features dominate the flow (Figure 3.5). The secondary or “Overset" mesh consists of the panel geometry. The panel is modeled as infinitely thin with its thickness equal to the minimum spatial grid element size, which resembles the shape of a beveled panel, following the simulations of Najjar (1998), Narasimhamurthy and Andersson (2009), Hemmati et al. (2018), and Hemmati and Smits (2019).

The Inlet boundary is located at $-5c$ from the body with a uniform velocity of $u = U_\infty$. The normal gradient of pressure at the inlet is set to zero similar to Najjar (1998). At the outlet, a zero gradient (Neumann) velocity boundary condition is used to allow for the shed vortices to freely convect across the boundary. Yet, the pressure is constant, similar to many numerical studies of wakes in literature (Deng and Caulfield, 2015a; Deng et al., 2015; Hemmati et al., 2016). It is located $15c$ downstream of the panel leading edge. The side and top boundaries are assigned the slip boundary condition, which was also used by Senturk et al. (2017) and Hemmati et al. (2019a) for their 3D simulations of oscillating panels. The wall boundary condition for the panel is set to a “moving” no slip wall condition, which is used in dynamic motion study of rigid bodies

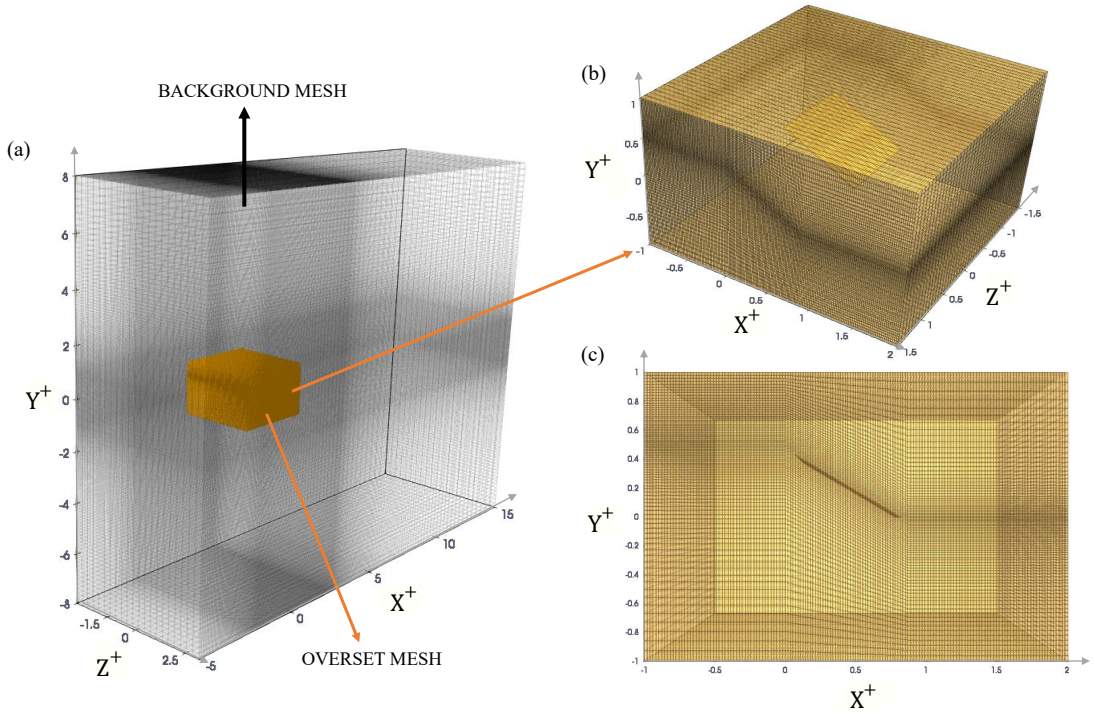

Figure 3.5: (a) Merged background and overset grid for stationary panel at $\alpha = 30°$ (Case 3). (b) shows the Isometric view for the secondary or "Overset" grid, while (c) represents the chordwise view of the overset grid.

(Kim and Xie, 2016). Flow is initialized with a uniform streamwise velocity equal to that at the inlet. The second order backward Euler scheme is used for time discretization. The spatial discretization is second order, and gradients and divergence terms are calculated using a second order accurate method.

3.4.2 2D Teardrop Foil

The oscillatory 2D teardrop foil is modeled based on a stationary Background grid and a moving Overset grid that are merged prior to running the simulation. The details with respect to OGA method had already been described in detail (Sections 3.2 and 3.3).

The computational domain is depicted in Figure 3.6, which highlights the C-type overset boundary. The domain extends a unit grid cell spacing in the spanwise ($Z-$) direction similar to previous studies in literature using OpenFOAM (Senturk and Smits, 2018; Simsek et al., 2020).

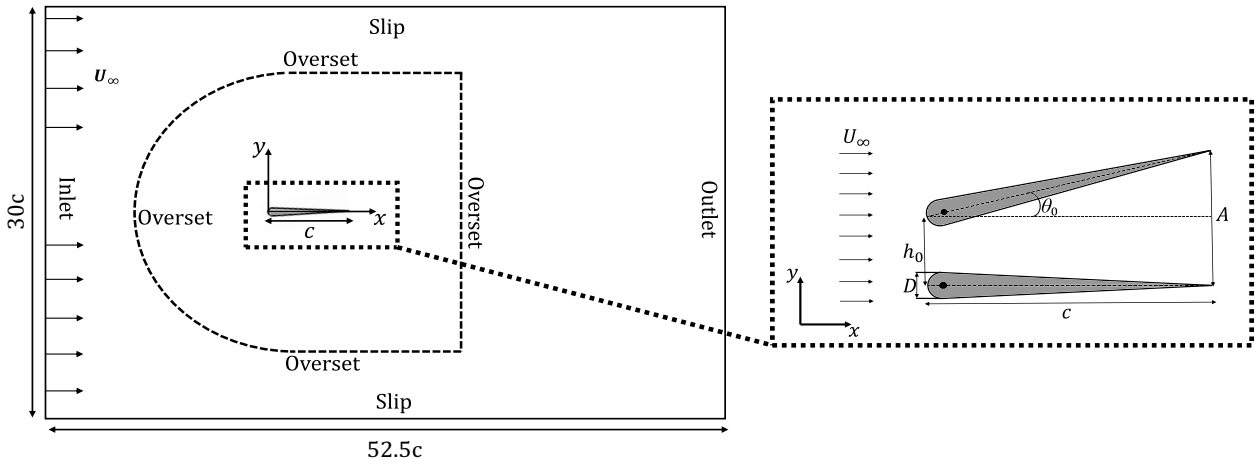

Figure 3.6: Schematics of the computational domain and foil kinematics. (not to scale)

This leads to the generation of hexahedral cell type for the two-dimensional flow assumed here. The streamwise (X^+) and cross-stream (Y^+) lengths are 53 and 30, respectively, which follow closely with numerical assessments of 2D oscillating foils (Deng et al., 2015; Simsek et al., 2020). Figure 3.7 depicts the non-homogeneous hexahedral (structured) grid comprising of a C-type grid (that models the foil geometry and motion), which overlaps a rectangular Background grid. Higher refinement is provided in the critical overlapping regions, such that the near body vortex shedding and performance characteristics are accurately captured. The grid further expands towards the domain boundaries at an expansion factor of less than 1.02.

The boundary conditions at the inlet are uniform fixed velocity (Dirichlet) and zero normal pressure gradient (Neumann). At the outlet, a zero-gradient outflow boundary condition is implied (Deng et al., 2015). The top and bottom boundaries are prescribed a slip boundary condition that effectively models the open surface flows and closely resembled the experimental conditions (Van Buren et al., 2019; Hemmati et al., 2019a). At the foil boundary, a no-slip wall condition is ensured. Flow is initialized with a uniform streamwise velocity equal to that at the inlet.

Second order accurate backward and central difference schemes are employed for temporal and spatial discretizations, respectively (Senturk and Smits, 2018). The momentum equations are specifically solved using Preconditioned Biconjugate Gradient (PbiCGSTAB) method, whereas

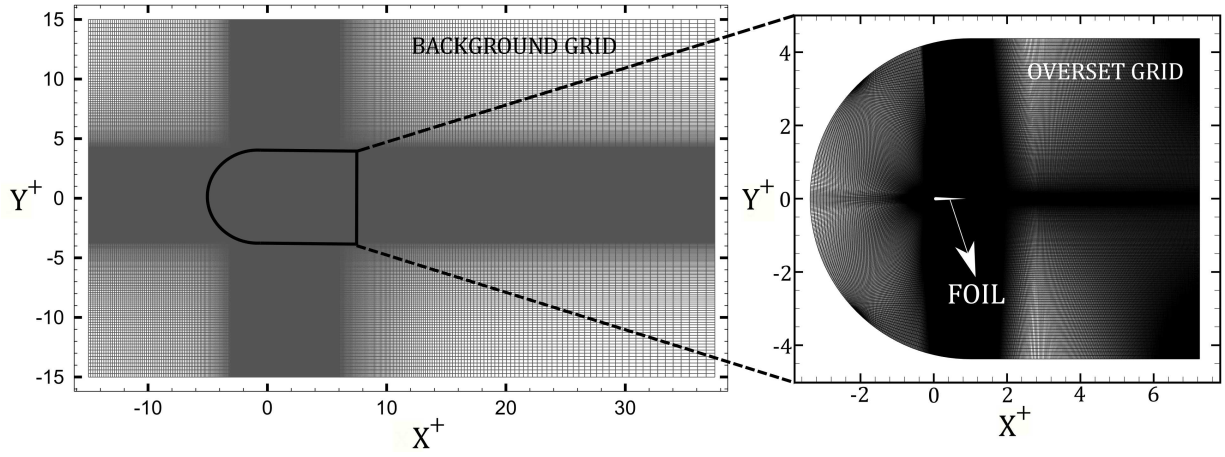

Figure 3.7: Schematics of the grid and Overset Grid Assembly method.

Preconditioned Conjugate Gradient (PCG) method is employed for pressure poisson equation (Deng et al., 2015; Zheng et al., 2019).

3.4.3 3D Teardrop Foil

The computational domain is shown in Figure 3.8, where the center of the coordinate system is at the leading edge of the foil. The $X-$direction is aligned with the streamwise, $Y-$direction with the cross-stream, and $Z-$direction with the spanwise direction of the flow. The domain extended by $20c$ in the streamwise direction with the inlet placed $5c$ from the foil leading edge. The crossflow width of the domain is $16c$ with the foil located in the middle. The domain design is consistent with previous studies on wake characterization of flapping foil, mainly Dong et al. (2006), Deng and Caulfield (2015b), and Zheng and Wei (2012). The domain width in the spanwise direction was $2\pi c$, which is sufficient to accurately capture at least four pairs of streamwise vortex ribs formed along the span of the foil (Robichaux et al., 1999; Barkley and Henderson, 1996; Hemmati et al., 2016).

The inlet boundary is assigned the uniform streamwise velocity condition: $u = U_\infty$ and $v = w = p = 0$. The Neumann outflow boundary condition is imposed at the outlet, which is proven reliable for wake simulations to prevent backward flow or reflection into the domain (Dong et al., 2006). A slip wall condition is imposed on the top and bottom boundaries, which closely resembles

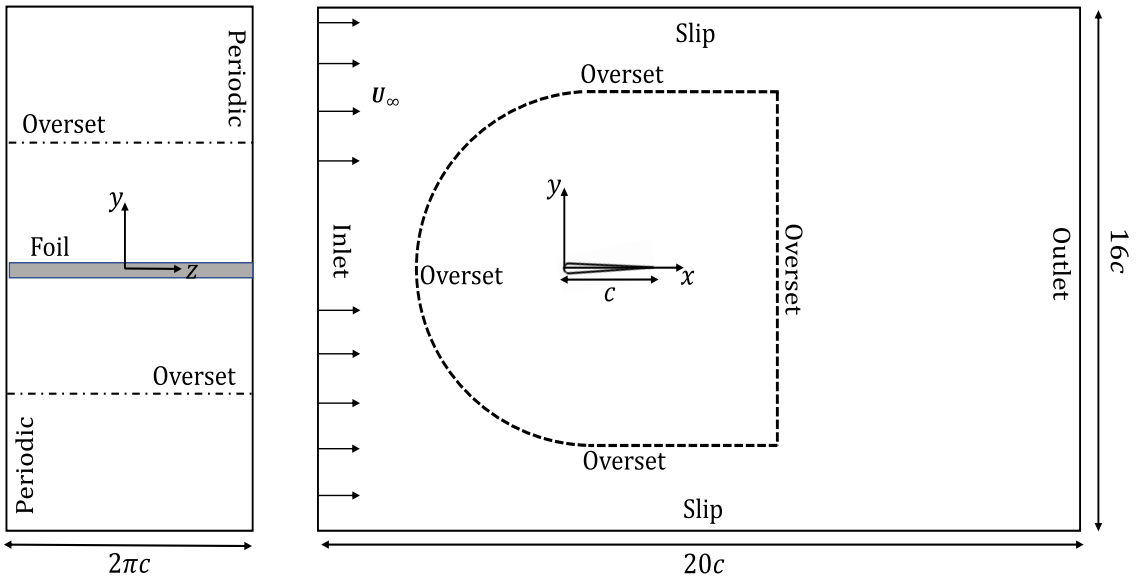

Figure 3.8: Schematics of the computational domain (not to scale).

experimental conditions (Van Buren et al., 2019; Hemmati et al., 2019a). For the side boundaries, a periodic condition is applied, similar to the study of Deng and Caulfield (2015b). The No-slip wall condition for the velocity and a Neumann condition for pressure is imposed on the foil boundary. Flow is initialized with a uniform streamwise velocity equal to that at the inlet.

A non-homogeneous structured grid (Figure 3.9) is constructed with a total of 2.2×10^7 hexahedral elements. Refined grid is used close to the foil, and it extends $5c$ downstream of the trailing edge. This ensures that numerical diffusion effects are minimum and the wake three-dimensionality is accurately captured. The grid transitions to a coarser mesh at the boundaries, while the maximum expansion ratio remains below 1.01. The Overset grid representing the foil is in the form of C-type grid, which is shown in Figure 3.9. The aspect ratio of hexahedral elements on the Overset grid is kept relatively the same as that of the underlying elements on the Background grid. This minimizes the interpolation errors and detection of orphan cells (Roget and Sitaraman, 2014).

Timestep is selected such that the maximum Courant number is maintained below 0.5. The convergence criteria is set as 10^{-6} for the residual of the velocity and pressure components of the momentum equation. The implicit Backward Euler and Central Differences methods are used for

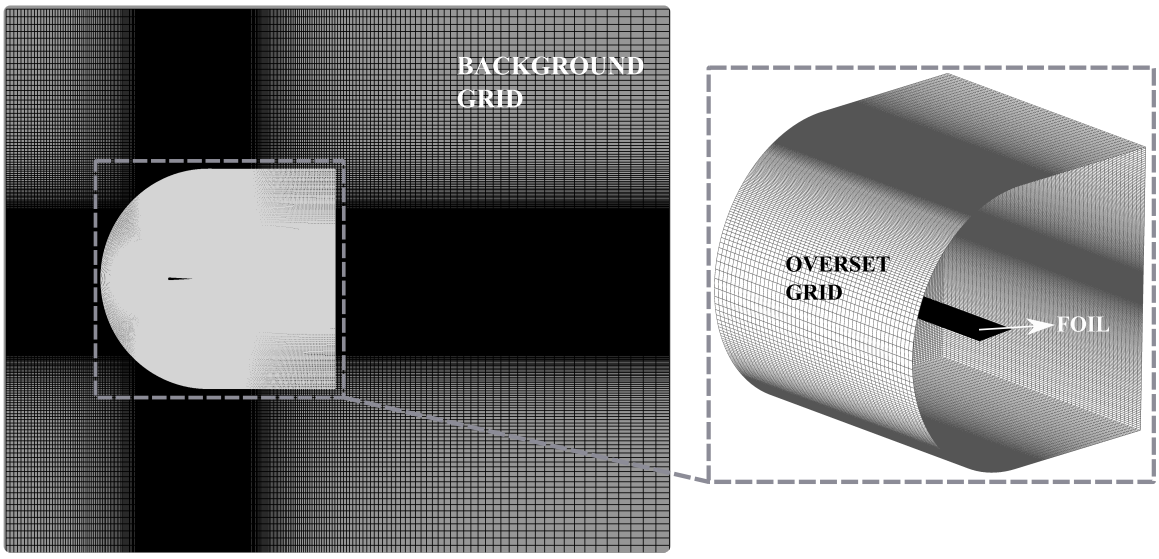

Figure 3.9: Depiction of three-dimensional background and Overset Grid.

temporal and spatial discritization of the governing equations, respectively. These methods are second order accurate (Senturk and Smits, 2018).

A refined version of the computational setup is also constructed to resolve the dynamical features of vortical interaction in near foil and wake region. Particularly, the streamwise and cross-stream lengths of the critical region correspond to $X^+ = 4$ and $Y^+ = 4$, respectively. Spanwise length of the domain is further reduced from $2\pi c$ to πc such that a higher mesh resolution is possible along the spanwise ($Z-$) direction. Since other details of the numerical setup, including the boundary and initial conditions, discretization schemes, structured hexahedral grid closely replicated the nominal 3D foil setup (described above), the readers are referred to discussion associated with Figure 3.8 and 3.9, respectively.

3.5 Verification Studies

Verification studies are performed with regards to domain size, boundary conditions, grid quality and time-step. Specific attention is given for 2D and 3D foil setups, respectively, since this work concerns the performance and wake dynamics of oscillating foils.

Table 3.1: Grid sensitivity investigation.

Study	**Method**	$N_{total,background}$	$N_{total,overset}$	$\overline{C_d}$	**Relative Error**	$\Delta\overline{C_d}$ **(Meshes)**
PanelGrid-1	Direct	1.05×10^6	3.89×10^5	0.612	9.50%	-
PanelGrid-2	Direct	2.60×10^6	5.91×10^5	0.589	5.40%	3.7%
PanelGrid-3	Direct	5.85×10^6	2.09×10^6	0.563	0.89%	4.44%
PanelGrid-4	Direct	1.47×10^7	6.86×10^6	0.56	0.35%	0.5%
Taira (2009)	Direct	2.25×10^6	-	0.558	-	-

3.5.1 3D Square Panel

In order to have an optimum size for the grid and to sufficiently resolve the flow characteristics, grid independence analysis is also completed for the angle of attack (α) of 30°. Four different grids are constructed and the ratio of minimum grid sizes in the streamwise ($X-$) direction is kept constant, i.e., $\delta X_1/\delta X_2 \approx 1.5$ (δX_2 is the minimum grid size for a fine mesh, while δX_1 is the minimum grid size for the coarse mesh). The thickness of the panel is not altered for any cases, in which all panels constitute a zero-thickness plate. The four grids correspond to PanelGrid-1, PanelGrid-2, PanelGrid-3 and PanelGrid-4. The number of grid elements and mesh spacing parameters are defined in Table 3.1, where relative error shows the discrepancy with respect to Taira (2009). $\Delta\overline{C_d}$ is calculated with respect to $\overline{C_d}$ for a coarse grid, and for its subsequent finer grid. The mean drag coefficient ($\overline{C_d}$) from PanelGrid-4 compares well with that obtained by Taira (2009). The relative error is less than 2%. The relative difference between the mean drag for two subsequent studies is shown in Table 3.1. The difference is less than 1% for PanelGrid-3 and PanelGrid-4. Spatial convergence is also obtained with respect to the mean drag, when comparing results in Table 3.1. Therefore, the domain and overset mesh parameters of PanelGrid-4 are sufficient for accurately simulating the wake.

The accuracy of different overset interpolation schemes is studied using a two-dimensional inclined stationary panel at $\alpha = 30°$. Four main schemes are tested: Inverse-Distance, CellVolumeWeight, LeastSquares and trackingInverse-Distance. These are selected based on their total simulation time for completion and prediction accuracy. For simplicity, we compare the coeffi-

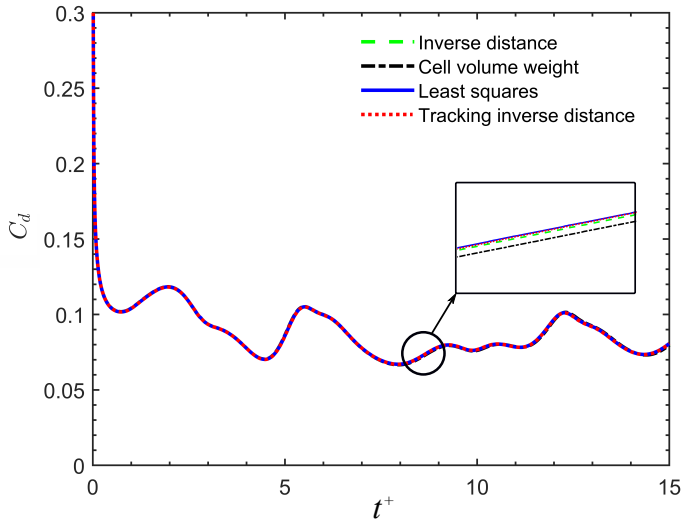

Figure 3.10: Variation of C_d with time for 2D stationary panel ($\alpha = 30$ deg), estimated using different overset interpolation techniques.

Table 3.2: CPU time requirement for different interpolation schemes employed for 2D stationary panel at $\alpha = 30^\circ$.

Sim. No.	**Technique**	**CPU Time**(s)
1	InverseDistance	11330.14
2	CellVolumeWeight	40779.31
3	LeastSquares	15361.44
4	TrackingInverseDistance	12619.05

cients of drag (C_D) estimated for a two-dimensional stationary panel at $\alpha = 30^\circ$. The details for CPU time (s) required for each scheme is shown in Table 3.2, while the variation of C_d with respect to non-dimensional time $t^+ = tU_\infty/c$ is depicted in Figure 3.10.

The Inverse-Distance scheme incorporates the least amount of CPU time as observed in Table 3.2. Particularly, the CellVolumeWeight scheme, although conservative, required 72% more CPU time compared to Inverse-Distance. The CPU time required for LeastSquares and TrackingInverseDistance schemes is also longer by 26% and 10%, respectively. Despite the higher order of accuracy offered by LeastSquares, we suspect that the time requirement is even higher for three-

dimensional cases with more refined grids. The estimated C_d using different interpolation schemes is also within 0.01% (Figure 3.10), which suggest that using the Inverse-Distance scheme is appropriate for all the three-dimensional cases.

3.5.2 2D Teardrop Foil

For domain sensitivity analysis in case of 2D teardrop foil simulations, 2 domains are created based on the setup explained in Section 3.4. These are named as LD (Long Domain) and SD (Short Domain), whose streamwise (X^+) and cross-stream (Y^+) lengths were $[X^+, Y^+] = [93, 75]$ and $[53, 30]$. The kinematics settings for this sensitivity study correspond to $Re = 8000$, $h_o/c = 0$, θ_o =15°, ϕ =270° and $St_c = 1.87$. Variation of coefficient of thrust (C_T) is assessed for the end cycles after a statistical convergent state was achieved. The results for C_T in Figure 3.11a show a good overlap of results for both domains. We therefore employ the Short Domain (SD) for our analysis.

The boundary condition sensitivity focus on the pressure gradient at the Outlet boundary. The fixed pressure (p =0) and zero gradient ($\frac{dp}{dx}$ =0) conditions are utilized for studies BC1 and BC2, respectively. The results for C_T are assessed to compare their performances. The variation of C_T shown in Figure 3.11b depict almost identical results for the two boundary conditions evaluated here.

A spatial convergence analysis is completed at Re =8000, h_o/c =0.25, θ_o =15°, ϕ =270° and St_c =0.67. This enable a comparative evaluation with experiments of Van Buren et al. (2019). Table 3.3 and Figure 3.12a summarize the grid convergence results involving three grids, wherein the ratio (δ^*) of minimum grid size element (Δx) to Kolmogorov scale (η_k) is kept below 10 in the critical region near the foil. Here, Kolmogorov scale is calculated based on kinematic viscosity (ν) and the dissipation rate of turbulence kinetic energy (ε), given by the relation $\eta \approx (\nu^3/\varepsilon)^{0.25}$ (Pope, 2000). The $\overline{C_T}$, which is averaged over the final 10 oscillating cycles following the statistical convergence, is used as a quantitative estimate for spatial grid convergence. The relative error ($\varepsilon_T = |\overline{C_{T,exp}} - \overline{C_T}|/\overline{C_{T,exp}}$) calculated with respect to the experimental results (Van Buren et al.,

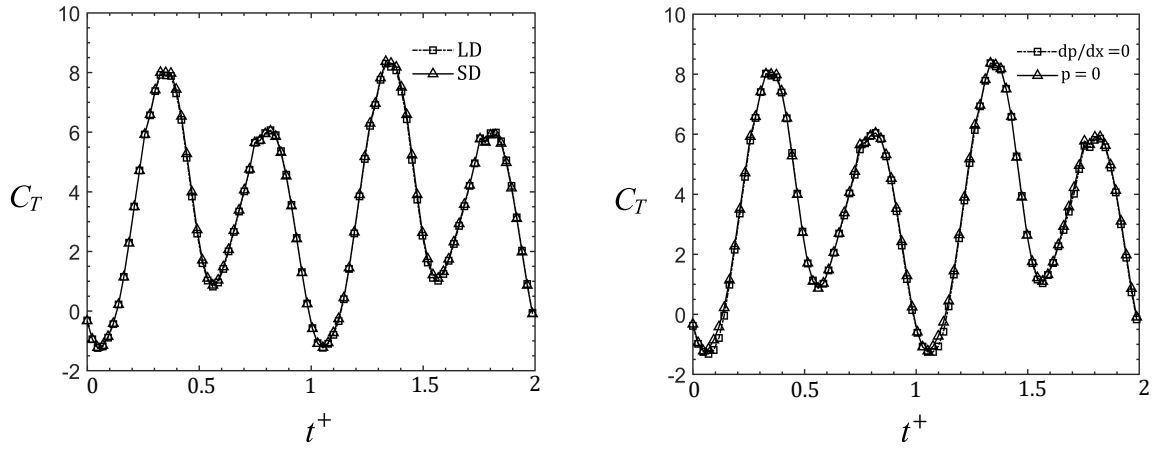

Figure 3.11: (a) Domain and (b) boundary condition sensitivity results for C_T.

Table 3.3: Grid convergence analysis for oscillating foil. Here, N_{total} represents the sum of hexahedral elements in background and overset grids.

Study	N_{total}	$\overline{C_T}$	$\Delta\overline{C_T}$	ε_T	$X =$	$1c$	$2.5c$	$5c$
2DFoilGrid1	4.67×10^5	1.22	0.070	0.117	$\delta^* =$	4.29	4.41	6.18
2DFoilGrid2	8.49×10^5	1.14	0.046	0.044	$\delta^* =$	2.53	3.39	6.36
2DFoilGrid3	1.72×10^6	1.09	-	0.002	$\delta^* =$	1.58	2.03	3.16
Van Buren et al. (2019)	-	1.092	-	-	-	-	-	-

2019) is below 5% for 2DFoilGrid2. This provides sufficient confidence to use this grid for our analysis. All performance and wake observations, and their discussions, are primarily focused on the case of Re =1000, which results in much smaller δ^* compared to the case of Re = 8000 (see Table 3.3).The latter is utilized for verification and validation of the simulations. This provides an additional assurance that the grid resolution is sufficiently fine for the entire paramter space considered in this study. The time-step size (δt) is also set such that the Courant number (Co) is maintained below 0.5, similar to the simulations of Hemmati et al. (2019a).

Figure 3.12 shows the instantaneous C_T variation and cross-stream distribution of mean streamwise velocity ($\overline{u_x^+}$) at increasing streamwise distance (X^+) for the three grids discussed in Table 3.3. These results clearly show that the propulsive performance and wake characteristics of the foil

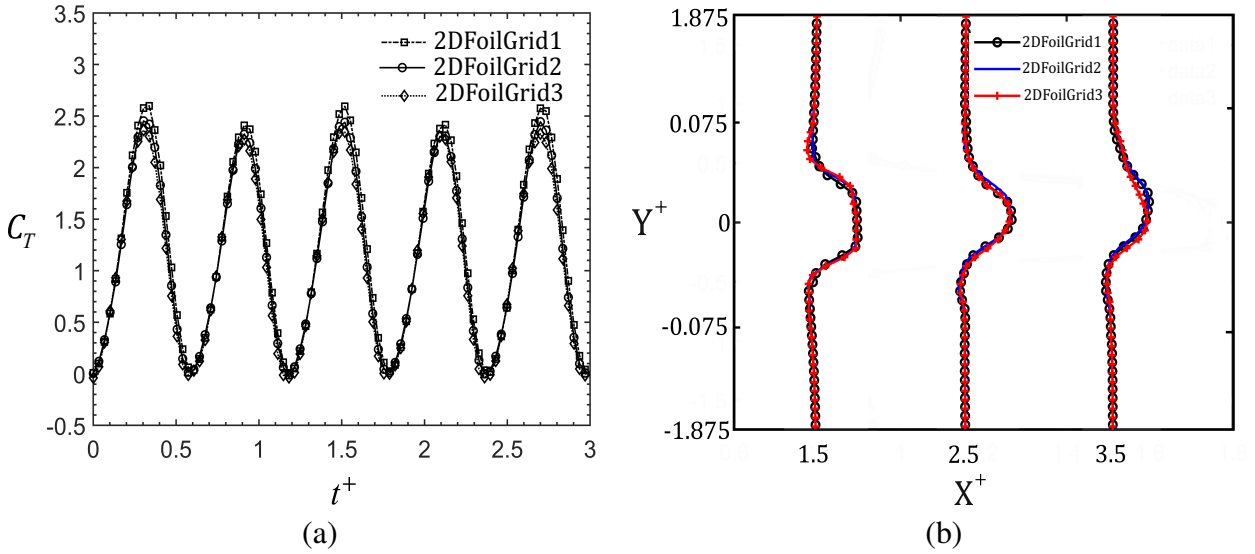

Figure 3.12: Comparison of (a) unsteady variation of C_T, and (b) cross-stream velocity profiles at increasing streamwise distance (X^+) for three grids.

are not sensitive to the spatial grid resolution. This further provides sufficient confidence for using 2DFoilGrid2 for our analysis.

3.5.3 3D Foil

The computational setup, including domain size, grid quality and boundary conditions can impact the accuracy of numerical results. We have completed a thorough investigation of all relevant parameters that affect numerical solutions. It is established that the final setup minimizes all adverse effects. The boundary conditions are set following various previous studies, including Hemmati et al. (2018), Senturk and Smits (2018), and Hemmati et al. (2019a), which have carried out extensive studies on the effect of boundary conditions. Mainly, the outlet boundary is located sufficiently far ($15c$) from the foil, so that there are no adverse effects on the flow in the critical region behind the foil. The sensitivity analysis with respect to the domain size is carried out following previous work of Hemmati et al. (2018).

The propulsive performance of the foils are used as parameters for determining the adverse effects of computational setup on numerical solutions. Mainly, the variations in time-averaged C_T,

Table 3.4: Summary of Grid refinement study. N_{total} represents the sum of hexahedral elements in background grid and overset grid.

Study	N_{total}	$\overline{C_T}$	C_L^{RMS}	ε_T	$\varepsilon_{L_{RMS}}$	$x=$	$1c$	$2.5c$	$5c$
3DFoilGrid1	3.0×10^6	4.05	21.24	0.18	0.037	$\delta^*=$	11.3	10.4	55.2
3DFoilGrid2	9.0×10^6	4.74	22.16	0.05	0.004	$\delta^*=$	5.6	6.2	44.0
3DFoilGrid3	2.2×10^7	4.97	22.06	-	-	$\delta^*=$	3.3	4.4	13.5

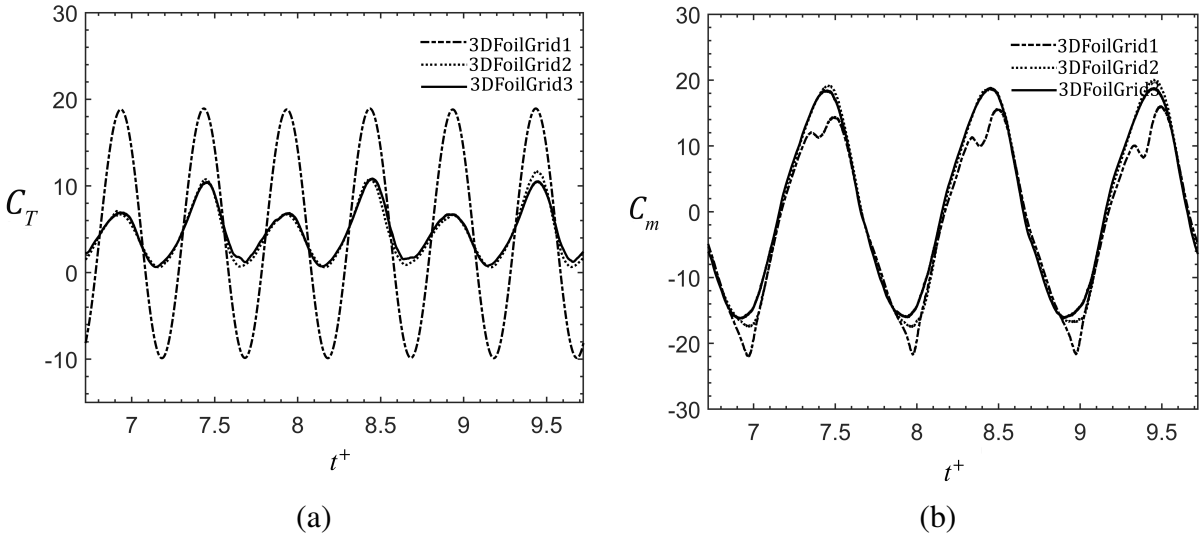

Figure 3.13: Comparison of time histories for thrust and moment coefficients for all grids employed in our study.

C_P and C_L are considered. The mean performance and wake results are time averaged over 10 cycles following the statistical convergence of the simulations with over 2500 timesteps per cycle. The timestep (δt) is set such that the maximum Courant number is below 0.5. This is consistent with common practices in numerical studies for oscillating rigid panels and foils (Senturk and Smits, 2018; Hemmati et al., 2019b).

The effect of grid quality on numerical solutions is examined using the traditional grid sensitivity study and grid-size comparison with Kolmogorov length scales. The analysis begins by assessing the time histories of C_T and moment (C_m), and comparing the $\overline{C_T}$ and C_L^{rms} for the foil using three grids, details of which are outlined in Table 3.4. The flow and motion parameters for all grids correspond to Re =8000, h_o/c =0.375, θ_o =15°, ϕ =330° and St_c =0.8. For each grid,

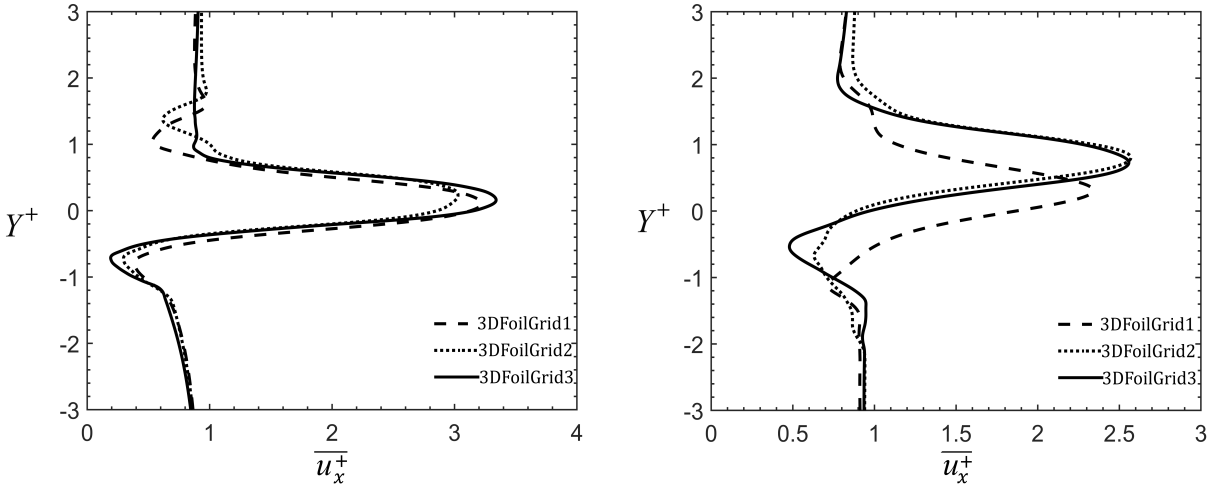

Figure 3.14: Grid sensitivity study using mean streamwise velocity variations along the $y-$direction at (a) $x = 2c$ and (b) $x = 4c$.

the ratio of δx to η_k is presented at three streamwise locations in the wake. The length scale ratios are below 10 in the critical flow region for 3DFoilGrid2 and 3DFoilGrid3, which based on the recommendations of Moin and Mahesh (1998) is sufficiently small for the simulations to capture the main turbulent flow features. In Table 3.4, the ε_T and ε_L are calculated with respect to the results obtained from the finest grid (3DFoilGrid3).

Evidently, time-histories of C_T and C_m for 3DFoilGrid2 and 3DFoilGrid3 depict a relatively consistent variation in Figure 3.13. The relative errors are less than 5% between 3DFoilGrid2 and 3DFoilGrid3 for both ε_T and ε_L. This small relative error showed that the grid quality is sufficient for capturing the main features of both mean and fluctuating flow fields. The effect of grid resolution on the wake developments are also assessed in Figure 3.14, where the profiles of time-averaged streamwise velocities are shown at $X = 2c$ and $4c$. From these results, and others not shown for brevity, it is evident that the difference between wake profiles are negligible ($< 5\%$), especially between 3DFoilGrid2 and 3DFoilGrid3. This further provides confidence in the accuracy of our numerical setup.

The spanwise domain independence analysis is performed by changing the spanwise length of the setup from $2\pi c$ to πc. Spanwise instability of the *LEV* roller is used for this assessment. The

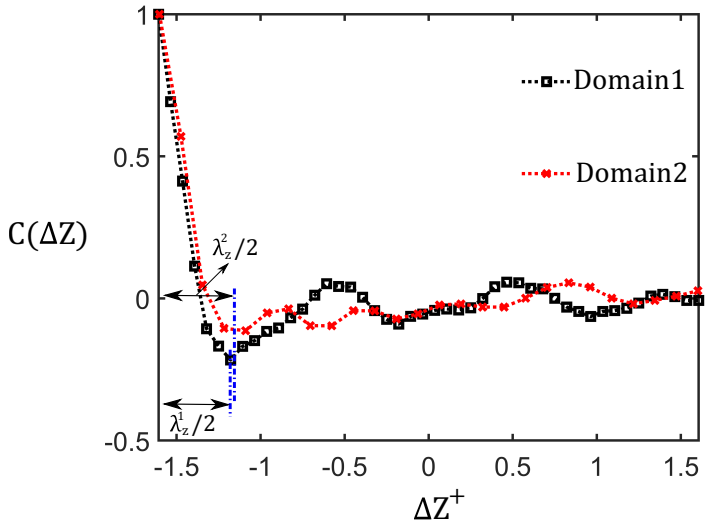

Figure 3.15: Spanwise domain length analysis in terms of λ_z characterizing the spanwise instability of primary *LEV*.

kinematic parameters corresponded to $\phi = 90°$, St_c =0.32, $h_o/c = 0.02$ and $\theta_o = 10°$. In order to calculate the wavelength ($\lambda_z^+ = \lambda_z/c$), a spatial autocorrelation coefficient, $C(\Delta z)$, is calculated with respect to the streamwise vorticity (ω_x^+) distribution on a planar spanwise slice that passes through the core of primary *LEV*. $C(\Delta z)$ is defined as:

$$C(\Delta z) = \frac{\langle \omega_x^+(y_0, z_0, t_i) \cdot \omega_x^+(y_0, z_0 + \Delta z, t_i) \rangle}{\omega_{x,rms}^+(y_0, z_0, t_i)\, \omega_{x,rms}^+(y_0, z_0 + \Delta z, t_i)}, \tag{3.6}$$

where, t_i corresponds to the snapshot of ω_x^+ distribution collected from ith oscillation cycle. For each planar slice, $C(\Delta z)$ is calculated with respect to spanwise lag or shift given as Δz. The results of $C(\Delta z)$ are then averaged over 5 consecutive oscillation cycles. The estimated distance to the first minima of $C(\Delta z)$ is $\lambda_z^+/2$, which characterize the spanwise instability. More details of the calculation process and flow physics are discussed in Chapters 8 and 11, respectively. Figure 3.15 depicts the variation of $C(\Delta z)$ for Domain1 (πc) and Domain2 ($2\pi c$), respectively. The instability wavelength estimated for the primary *LEV* is approximately λ_z^1 =0.70 and λ_z^2 =0.72, for Domain1 and Domain2, respectively. The estimated wavelengths depict a difference of less than 3% and closely follow the cooperative elliptic instability observed recently, for oscillating foils (Deng and Caulfield, 2015b; Sun et al., 2018; Chiereghin et al., 2020; Son et al., 2022). Domain1 is used for

Table 3.5: Grid refinement details for the current study. N_{total} represents the sum of hexahedral elements in background grid and overset grid. Here, "Ref3D" refers to refined version of 3D grid.

Study	N_{total}	$\overline{C_T}$	C_L^{rms}	ε_T	ε_L^{rms}	$X =$	$1c$	$2.5c$	$5c$
Ref3DGrid1	8.4×10^6	0.64	2.86	0.084	0.010	$\delta^* =$	7.3	16.9	55.2
Ref3DGrid2	1.7×10^7	0.60	2.84	0.017	0.003	$\delta^* =$	3.7	8.5	15.8
Ref3DGrid3	3.1×10^7	0.59	2.83	0.001	-	$\delta^* =$	1.8	4.2	7.9
Exp.	-	0.59	-	-	-	$\delta^* =$	-	-	-

the final setup as it allows for a greater resolution of grid elements in spanwise ($Z-$) direction. This domain size also follow closely with recommendations of Zurman-Nasution et al. (2020).

A spatial convergence analysis is further completed at Re =8000, h_o/c =0.25, θ_o =15°, ϕ =270° and St_c =0.67. This enables comparative evaluation of the numerical results with respect to experiments of Van Buren et al. (2019).

Table 3.5 and Figure 3.16 summarize the grid convergence results involving three grids, Ref3DGrid1, Ref3DGrid2 and Ref3DGrid3. The ratio δ^* is kept below 10 in the critical region near the foil ($x < 2.5c$) for Ref3DGrid2 and Ref3DGrid3 (see Table 3.5), where the origin of spanwise instability and secondary structures are speculated to emerge and grow as the wake evolves (Son et al., 2022). The coefficient of thrust and root-mean-square (rms) of lift coefficient, averaged over the final 10 oscillating cycles following the statistical convergence, are used as a quantitative estimate for spatial grid convergence. The relative error in prediction of $\overline{C_T}$ is below 5% for Ref3DGrid2. Similarly, ε_L^{rms}, is calculated with respect to the finest grid (Ref3DGrid3) and it is below 0.1%. The corresponding experimental results for C_L are not available in literature for comparison.

Figure 3.16(a) shows the instantaneous C_T for three grids, which demonstrates the insensitivity of propulsive performance to the spatial grid resolution. Similar agreement also held in terms of wake characteristics, where the cross-stream distribution of $\overline{u_x^+}$ at an increasing streamwise distance (X^+) (Figure 3.16b) are relatively similar for the successively refined grids. This provides sufficient confidence to use Ref3DGrid2 for these analysis. Extensive details for verification and

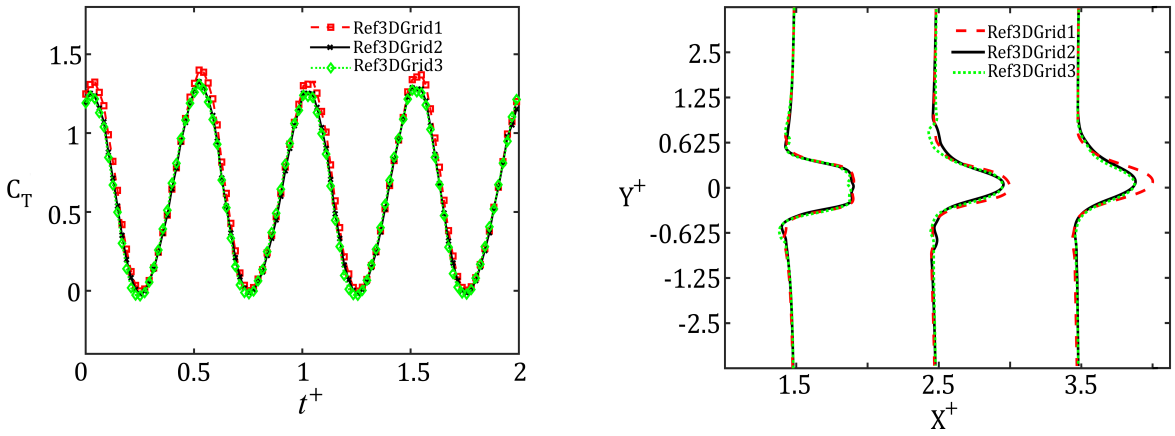

Figure 3.16: Comparison of (a) unsteady variation of C_T, and (b) cross-stream velocity profiles at increasing streamwise distance (X^+) for three grids.

validation of the numerical solver with respect to the domain size, spatial and temporal grid, OGA solver and boundary conditions can be found in Hemmati et al. (2019a).

3.6 Validation Studies

The verification studies described in the previous section provided an accurate and optimized computational setup to evaluate the propulsive performance and wake dynamics of oscillating foils in complex multi-degree of freedom motion. However, validation of overset solver with respect to experimental findings is still necessary to benchmark the numerical discretization and solver algorithm. Particularly, a series of comparative studies evaluated the prediction of mean and instantaneous performance coefficients for 2D and 3D oscillating foils. Experiments of Van Buren et al. (2019) are used for the validation purposes. The quantitative and qualitative results of finite aspect ratio square panels (both stationary and pitching) are also compared with the observations of some established numerical techniques (Taira, 2009; Senturk et al., 2017) and other experiments Buchholz (2006).

Table 3.6: Case studies and relevant parameters for each case.

Case	Motion Description	α°	θ_o°	Re	St
PanelS1	Stationary	0	-	300	-
PanelS2	Stationary	15	-	300	-
PanelS3	Stationary	30	-	300	-
PanelS4	Stationary	45	-	300	-
PanelS5	Stationary	60	-	300	-

3.6.1 3D Stationary Square Panel

The initial case studies comprise of flow past a 3D stationary square panel. Five cases are considered (Table 3.6), in which the panel is kept at angles varying from 0° to 60° (in intervals of 15°), to the incoming freestream flow. The Reynolds number is 300. This Re is similar to the cases studied by Taira (2009) and Senturk et al. (2017). The quantitative analysis of the wake of stationary panel is based on measuring the mean drag coefficient.

We begin by looking at the wake of stationary panels (PanelS1–PanelS5). Numerous experimental studies had provided insight into the characteristics concerning circulation and flow separation, which provides a standard dataset for validation.

Figure 3.17 presents the mean coefficient of drag for stationary panel at different angles of attack. A good agreement is observed in $\overline{C_d}$ for all angles of attack, compared to Taira (2009). The maximum deviation is for the panel at $\alpha = 60^\circ$, although the value is within 6.5% error margin. A good agreement is also observed between the current results for $\overline{C_d}$ (Figure 3.17) and the data obtained by Senturk et al. (2017) using the IBM technique. This indicates that OGA implementation yields a similar accuracy in terms of modeling wake characteristics compared to other techniques. Aarnes et al. (2020) further showed that for the study of two dimensional flow over a circular cylinder using IBM implementation, the domain required an approximately 18 times more grid points than that used in the Overset method for a similar accuracy (Aarnes et al., 2020). The cost and time requirements for the computations would therefore increase, as was observed in another study by Tay et al. (2013) for flapping airfoil simulations. They showed that using the

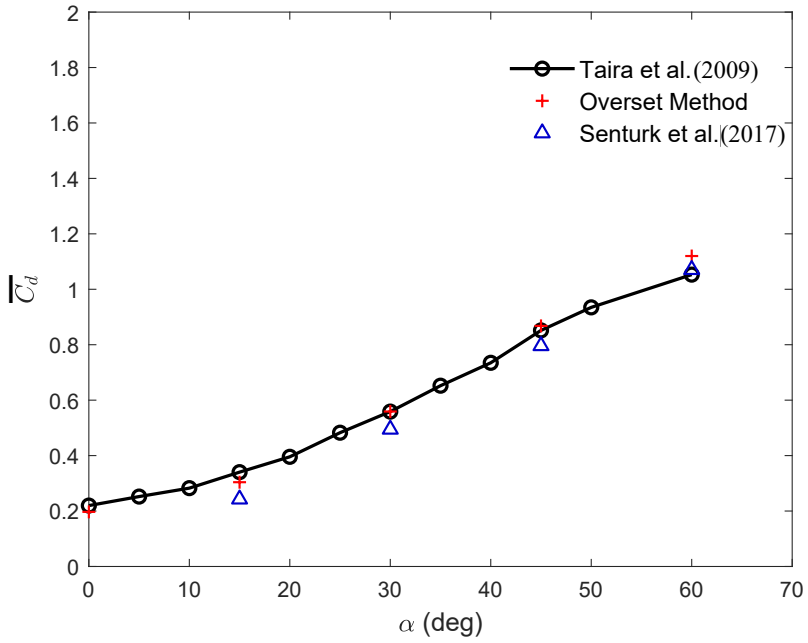

Figure 3.17: Variation of $\overline{C_d}$ with α° for 3D stationary panel (Case 1–5).

Overset grid conforming method (Tay et al., 2013), total number of required cores (or processors) was reduced, along with a reduction in computational time compared to IBM (Tay et al., 2013).

Wake visualizations further provides insight into the vortex features that may affect the drag characteristics of inclined stationary panels. Figure 3.18 presents contours of the ω_z^+ for the panel at 30° (PanelS3). Snapshots at $t^+ = 1, 5$ and 10 are presented. At $t^+ = 1$, the formation of trailing edge and leading edge vortices are clearly identifiable. The viscosity and shear effects are high at $Re = 300$. This lead to a smeared distribution at later times near the surface of the panel. This characteristic is also well captured by Taira (2009) for flow over a panel at the same Re. The plots at $t^+ = 5$ and 10 are similar, and the latter corresponds to flow after reaching statistical convergence.

The generation and interaction of vortices are shown using iso-surfaces of vorticity magnitude in Figure 3.19. The results correspond to PanelS3, PanelS4 and PanelS5, where the stationary panel is fixed at $\alpha = 30^\circ, 45^\circ$ and 60°, respectively. The iso-surface of vorticity magnitude enables detection of a vortex sheet formed and separated from the panel surface (Taira, 2009). The results are well captured at $t^+ = 1$, 5 and 10, respectively.

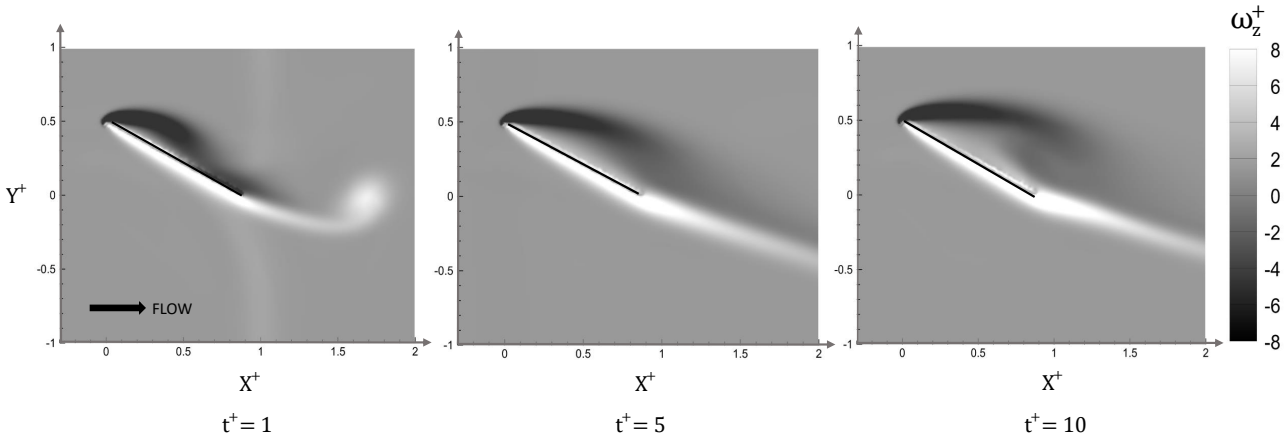

Figure 3.18: Contours of spanwise component of vorticity magnitude (ω_z^+) at xy-plane ($z = 0$) for 3D stationary panel at $\alpha = 30^\circ$.

The iso-surfaces in Figure 3.19a ($\alpha = 30^\circ$) indicates that $LEV1$ is first formed at $t^+ = 1$. A similar vortex structure is also noted by Taira (2009). Over time, the transient effects are overcome by viscosity, and the entire visible span of the panel is dominated by a pair of tip vortices ($TEV1$). Tip vortices are counter rotating and appear to be very similar in structural configuration. The downward velocity induced by tip vortices retains the leading edge vortex sheet from detachment. Figure 3.19b depicts the formation of leading and trailing edge vortices, $LEV2$ and $TEV2$ respectively, for the panel at $\alpha = 45^\circ$. The $TEV2$ structure in Figure 3.19a at $t^+ = 1$ is quite similar in configuration to $TEV1$ in Figure 3.19a. The difference is observed at $t^+ = 5$, wherein $TEV2$ expands to form a horseshoe vortex, retaining its coherence close to the panel. At $t^+ = 10$, the horseshoe vortex $TEV2$ in Figure 3.19b breaks down to form two counter rotating tip vortices. The results for the panel at $\alpha = 60^\circ$ are also presented in Figure 3.19c. At $t^+ = 1$, the generation of a leading edge vortex $LEV3$ is similar to $LEV2$ in Figure 3.19b, although a difference in the wake features is observed with respect to the trailing edge vortices. The horseshoe vortex $TEV3$ at $t^+ = 1$ appear to be forming closer to the panel surface compared to $TEV2$ and $TEV1$, which emerged at $\alpha = 45^\circ$ and 30° respectively, thereby leading to higher drag. With further advection

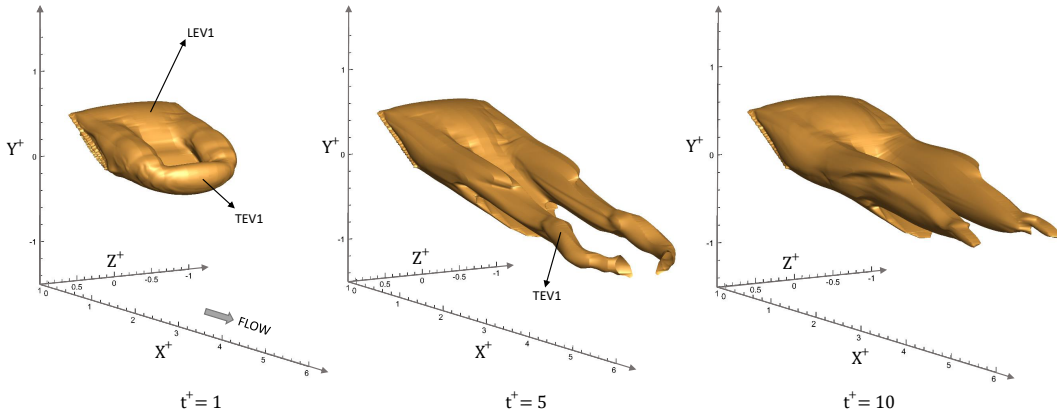

(a)

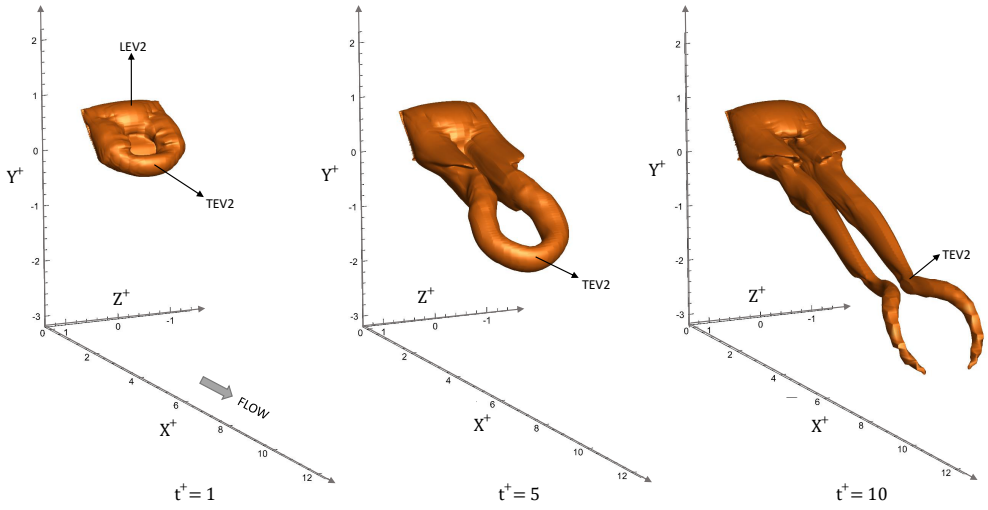

(b)

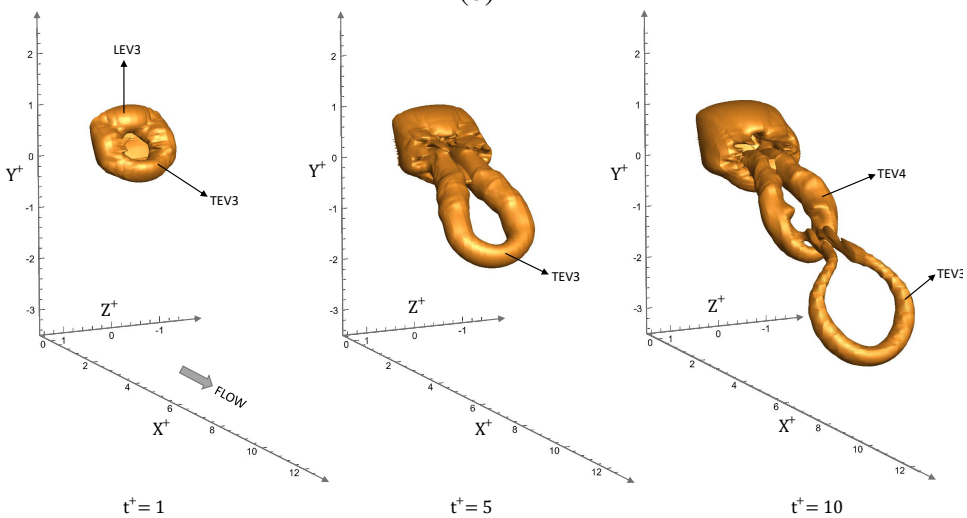

(c)

Figure 3.19: Iso-surfaces of vorticity magnitude ($|\omega^+| = 1.62$, 1.65 and 2.14), for cases of (a) $\alpha = 30°$, (b) 45° and (c) 60°, respectively.

Table 3.7: Case studies and relevant parameters for each case.

Case Number	Motion Description	α°	θ_o°	Re	St
PanelS6	Pitching	-	8	500	0.2
PanelS7	Pitching	-	8	2000	0.2

of vorticity downstream, the newly formed $TEV4$ entrains the $TEV3$ at $t^+ = 10$, leading to an interconnected structure.

This interconnection is also attributed to the high shear effects experienced at low Re, due to which the vortices counteract breakage and separation, in localized regions, such as the trailing edge tips of the panel (Buchholz, 2006).

3.6.2 3D Pitching Square Panel

The wake of a pitching square panel is simulated at Reynolds number of 500 and 2000 (Table 3.7). These Reynolds numbers allow for a direct comparison of results with Senturk and Smits (2018); Senturk et al. (2017), which simulated the flow using a viscous flow solver and Immersed Boundary method (IBM) in OpenFOAM. The Strouhal number ($St = 2fA/U_\infty$), where f and A are the oscillation frequency and the wake width, respectively is kept constant at 0.2. This generally promotes production of drag force instead of thrust (Buchholz, 2006; Senturk et al., 2017). The pitching motion is modeled as a sinusoidal function about a point located at 0.1c downstream of the panel's leading edge, as explained in Section 2.1.

A general description of motion is also depicted in Figure 3.20. The centre of oscillation is 0.1c from the leading edge of the panel. Two cases corresponding to Re of 500 (PanelS6), and 2000 (PanelS7), are selected. Since higher Re are generally associated with an unstable shear layer, and therefore greater turbulence effects near the panel surface, this study proceeded at a moderate $Re = 2000$. Senturk et al. (2017) determined this Re to inhibit turbulence effects.

The net propulsive or Froude efficiency of the panel (η) depends on the force characteristics of the pitching panel. First, the pressure and shear stress distribution are presented on the top surface

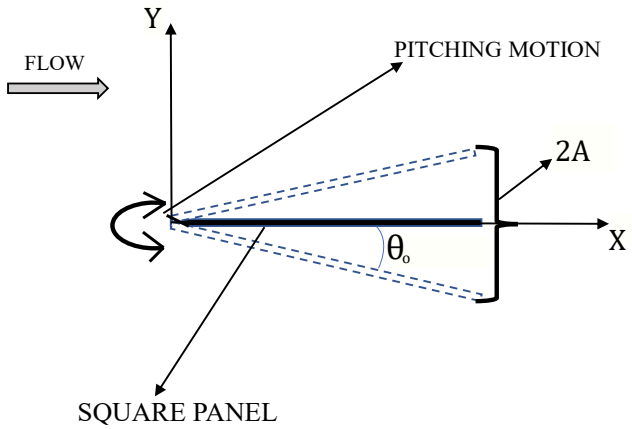

Figure 3.20: Parametric description of motion of pitching panel (PanelS6–PanelS7).

of the square panel, in Figure 3.21a,b and Figure 3.22, for Re = 500 and 2000, respectively. Four instances are selected based on the phase angle of the panel (ψ) in its pitching cycle. The phases correspond to 0°, 90°, 180°, and 270°, respectively. The panel positions at these phases are also shown for clarity. The pressure coefficient, C_{pr}, and shear stress coefficient, C_f, are calculated based on:

$$C_{pr} = \frac{p - p_{ref}}{\frac{1}{2}\rho U_\infty^2} \tag{3.7}$$

$$C_f = \frac{\tau_w}{\frac{1}{2}\rho U_\infty^2} \tag{3.8}$$

Here, p is the pressure on the surface of panel, p_{ref} is the reference pressure and τ_w is the wall shear stress on the surface of the panel. C_{pr} distribution for $\psi = 0°$, indicate a higher pressure at the top surface, except for the extremities of panel where the shear stress distribution was maximum. This trend compares well with the observation of Senturk and Smits (2018), who performed a similar parametric study at Re = 500. The regions of high pressure gradients are concentrated along the panel extremities, which is responsible for the thrust generation (Senturk and Smits, 2018; A.J., 2008). A difference in magnitude of C_f is noted in the cases corresponding to Re = 500 and 2000, respectively. Due to reduced viscous effects, the contributions of pressure to drag increases with increasing Re.

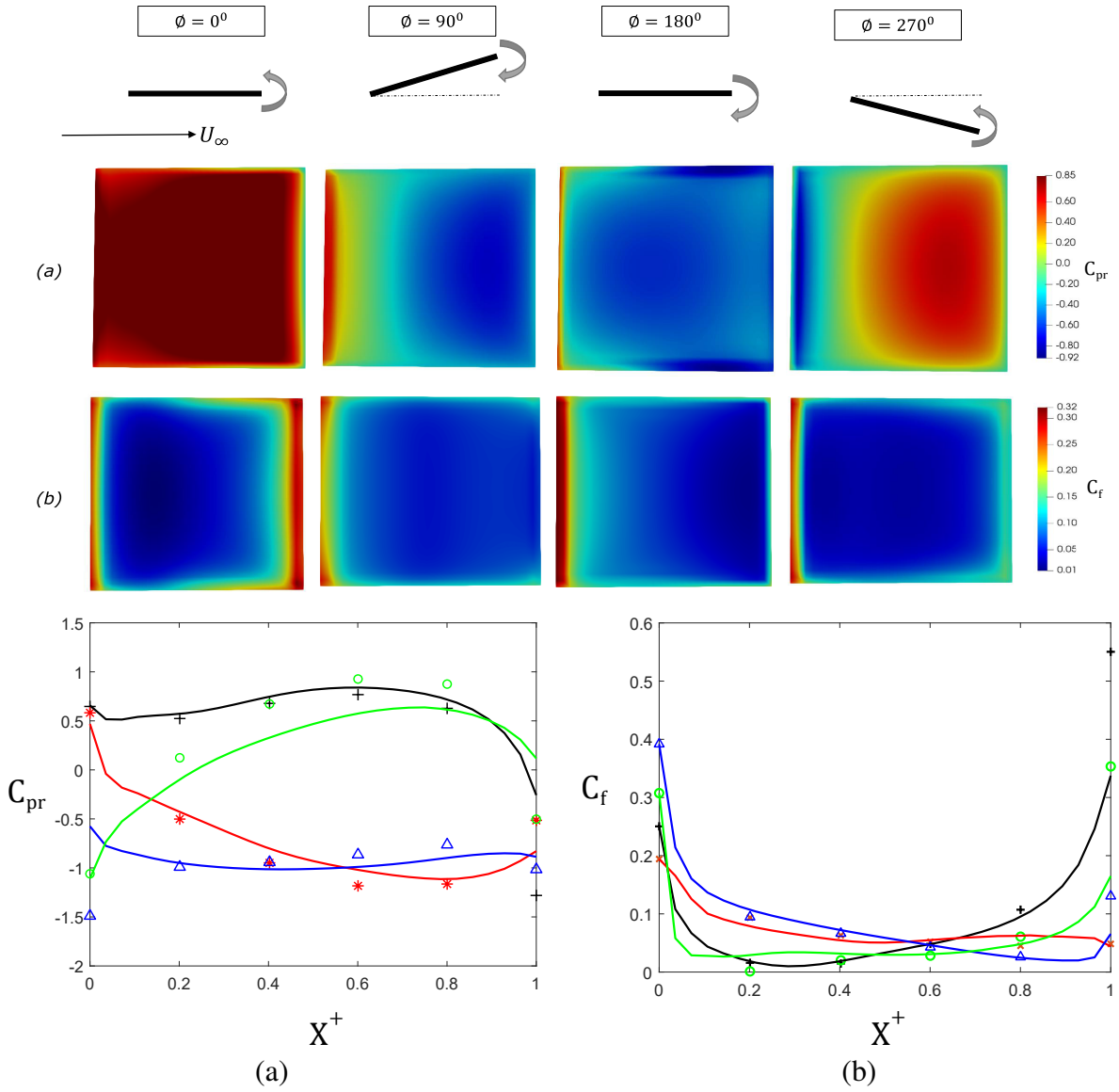

Figure 3.21: Contour plots for (**a**) C_{pr} and (**b**) C_f variation across the top surface of pitching panel for $\psi = 0°, 90°, 180°$ and $270°$, respectively. The Reynolds number is 500. The bottom plots show the variation of C_{pr} and C_f across the midspan in chordwise direction. Black, red, blue and green correspond to the $\psi = 0°, 90°, 180°$ and $270°$, respectively. Colored markers represent the data of Senturk and Smits (2018) at corresponding ψ.

Figure 3.21 shows a chordwise variation of C_{pr} and C_f at midspan of the panel (PanelS6). The leading and trailing edges have higher shear stress coefficient compared to mid chord regions, while pressure coefficient tend to drop at the leading and trailing edges. This is also consistent with the findings of Senturk and Smits (2018). Differences in drag is also observed between different phases of the pitching cycle. A higher pressure is generated as the panel started pitching upwards,

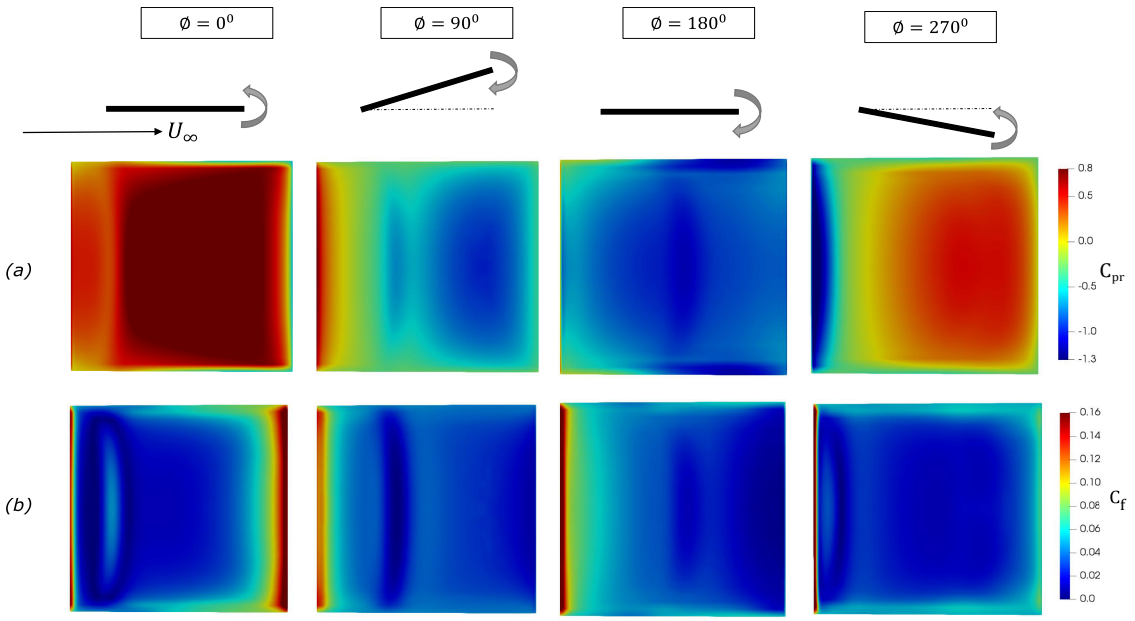

Figure 3.22: Contour plots for (**a**) C_{pr} and (**b**) C_f variation across the top surface of pitching panel for $\psi = 0°, 90°, 180°$ and $270°$, respectively. The Reynolds number is 2000.

thus confirming that a vortex core in the form of a leading edge vortex is forming at the top surface of the panel. As the panel reaches its peak amplitude (i.e., $\psi = 90°$), the vortex separates from the panel leading edge and a low pressure region is formed on the surface. At $\psi = 180°$, the pressure and shear stresses are low, except at the leading edge, where shear stress gradient is still high. As the panel reaches $\psi = 270°$ and move upwards, the pressure increases similar to the start of the pitching cycle. The higher magnitudes of C_{pr} indicate that drag production (or in other cases, thrust production) is dominated by pressure effects.

The low versus moderate Reynolds number effects on the production of drag at low St is further analyzed by looking at the instantaneous C_d and C_l in Figure 3.23a,b. The normalization factor for time is assumed to be the oscillation period (T_o) for the pitching cycle (i.e., $t^+ = T/T_o$). The time-averaged drag coefficient for PanelS7 ($Re = 2000$) is $\approx 70\%$ smaller than PanelS6 at $Re = 500$. The less significant viscous effects at high Re tend to decrease drag, and generally promote thrust generation Senturk and Smits (2018). The higher magnitudes of C_f that are observed along the panel edges (Figure 3.21b) for PanelS6, compared to PanelS7 (Figure 3.22b), verify the increase

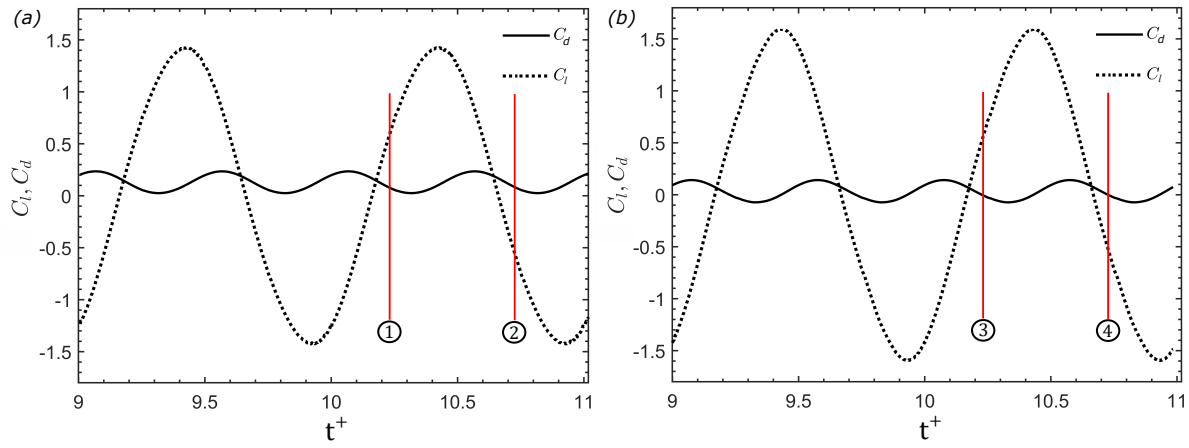

Figure 3.23: Variation of Coefficients of lift (C_l) and drag (C_d) with normalized time t^+, for (**a**) Case 6 and (**b**) Case 7, respectively.

in viscous contribution to drag at lower *Re*. Hemmati et al. (2019a) also explained the effects of surface pressure variation on the nature of thrust and side (lift) forces produced by pitching panels with different trailing edge shapes. For cases presented in our study, we investigated the differences in surface pressure distribution for PanelS6 and PanelS7, at peak trailing edge positions of oscillation cycle. These correspond to $\psi = 90^\circ$ and 270°, respectively. These specific phase positions are also depicted in Figure 3.23 as Instant "1" and Instant "2" for PanelS6, and Instant "3" and Instant "4" for PanelS7. At each of these instants, the distribution of pressure coefficient (C_{pr}) on top and bottom panel surfaces are depicted in Figure 3.24, separately. This further allowed evaluation of any potential similarities or differences in surface pressure distribution at the two *Re*, and its corresponding effects on the nature of drag and lift force at specific phases of the pitching cycle.

The variation of drag produced by the panel did not appear to change as the panel reaches $\psi = 90^\circ$ and 270°. However, the extrema of lift coefficient switched its sign from representing maxima, to a minima, ahead of instant "1" and instant "2" in Figure 3.23a,b, respectively. This trend is similar at the same ψ for both PanelS6 and PanelS7, although the magnitudes of maxima and minima increase at higher *Re*. The change in the sign of the lift force extrema can be further linked to the surface pressure distributions at respective instances shown in Figure 3.24. This depends

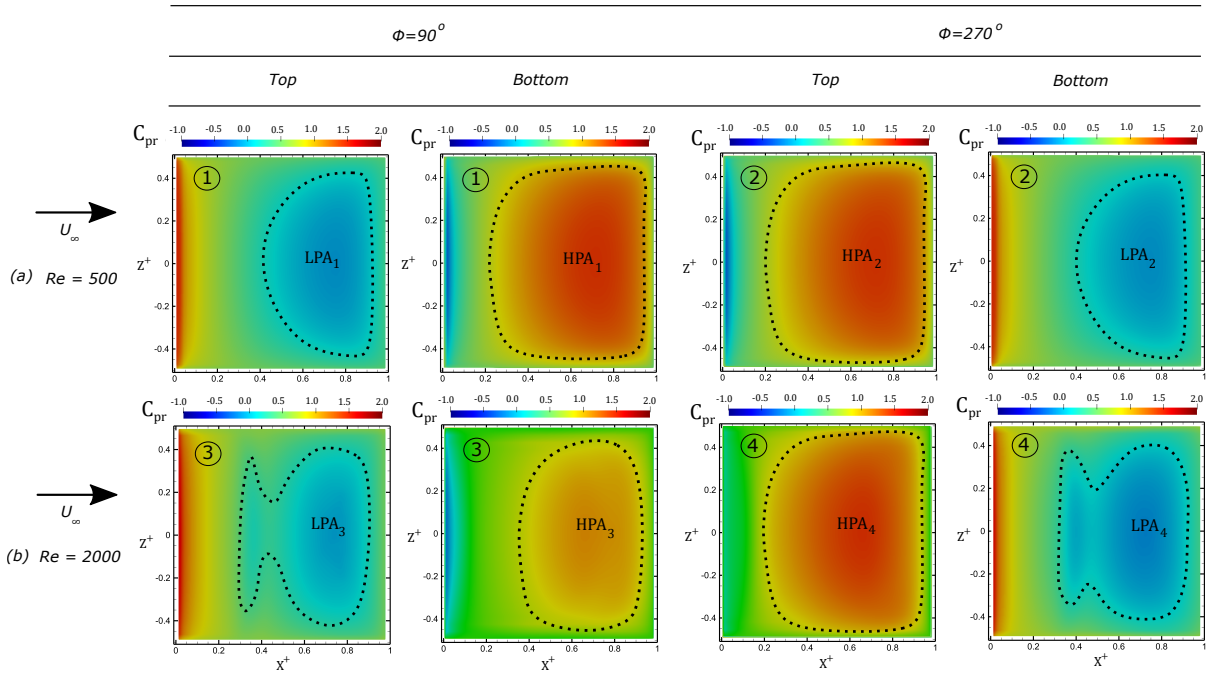

Figure 3.24: Surface pressure contours of C_{pr}, plotted on top and bottom surface of square panel for (**a**) Case 6, and (**b**) Case 7, respectively, at positions of peak trailing edge amplitudes (i.e., $\psi = 90^{\circ}$ and 270°).

on the development and detachment of leading and trailing edge vortex structures Hemmati et al. (2019a). At Instant "1" ($\psi = 90^{\circ}$) for PanelS6, a low pressure region LPA1 exist on the top surface of the panel due to the detachment of a trailing edge vortex structure when the panel reaches its maximum pitch amplitude. The bottom surface, however, correspond to a high pressure region HPA1, where a new trailing edge vortex is still under development. The existence of such large streamwise pressure gradient across the top and bottom surface of panel lead to the local extrema (maxima) in C_l ahead of Instant "1" in Figure 3.23a. The corresponding detachment of the trailing edge vortex structures lead to transfer of momentum from downstream advection of trailing edge vortex structures to the pitching panel. Thus, there exists a minima for C_d ahead of Instant "1". At Instant "2" ($\psi = 270^{\circ}$), the region of higher C_{pr} switch from bottom to the top surface of the panel due to the change in the direction of pitching. However, the streamwise pressure gradients across the surface are quite comparable to Instant "1". This again lead to a local extrema (minima) in both C_d and C_l, after the detachment of the trailing edge vortex structures.

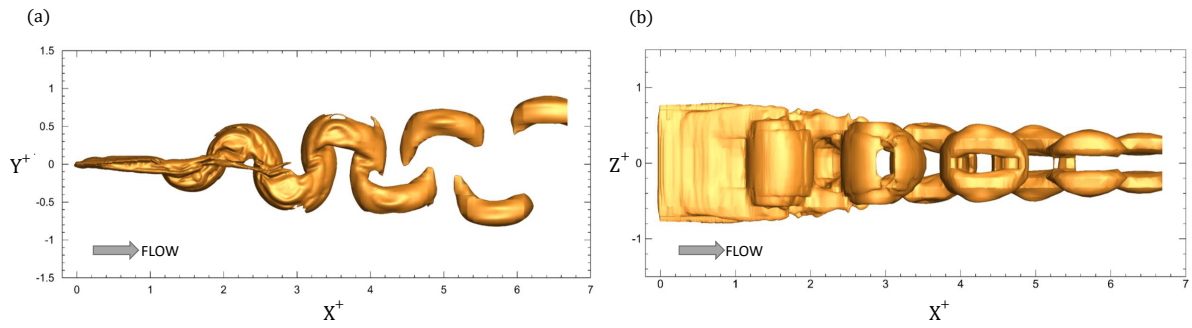

Figure 3.25: Iso-surfaces of vorticity magnitude ($|\omega^+| = 1$) in chordwise (**a**) and spanwise direction (**b**) respectively. The Reynolds number is 2000.

PanelS7 have some noticeable differences from PanelS6 in terms of surface pressure distribution (see Figure 3.24b). At Instant "3" ($\psi = 90°$), there is an increase in size of the low pressure area (LPA3) on the top surface compared to LPA1 in Figure 3.24a for PanelS6. This will increase the integrated streamwise pressure gradient, which exists across the top and bottom surfaces of panel. Thus, there is an increase in magnitude of C_l maxima ahead of Instant "3" (Figure 3.23b) compared to PanelS6. A similar observation is also made at Instant "4" ($\psi = 270°$), where the areal size of LPA4 has increased in comparison to LPA2 in Figure 3.23a for PanelS6. The only difference here is that the increase in streamwise pressure gradient across the panel surfaces promoted an increase in negative minima for C_l (ahead of Instant "4") since the direction of pitching get reversed.

The wake structures are shown using iso-surfaces of vorticity magnitude in Figure 3.25. The chord length and freestream velocity are used to normalize the ω^+. The iso-surfaces correspond to $|\omega^+| = 1$. The vortical pattern are in good agreement with the vortex skeleton model proposed by Buchholz (2006), and further verified by Senturk et al. (2017); Senturk and Smits (2018) and Hemmati et al. (2019a). The vortex street in Figure 3.25a resemble the von Kármán vortex street. The vortex loops are formed and shed from the trailing edge, which generates drag or thrust. However, at low St, the trailing edge vortices (TEVs) are merged with the side shear layers, which inhibit the transfer of momentum from TEVs to the panel. This process lead to the production of drag rather than thrust. Interconnecting vortex rings are observed in the wake

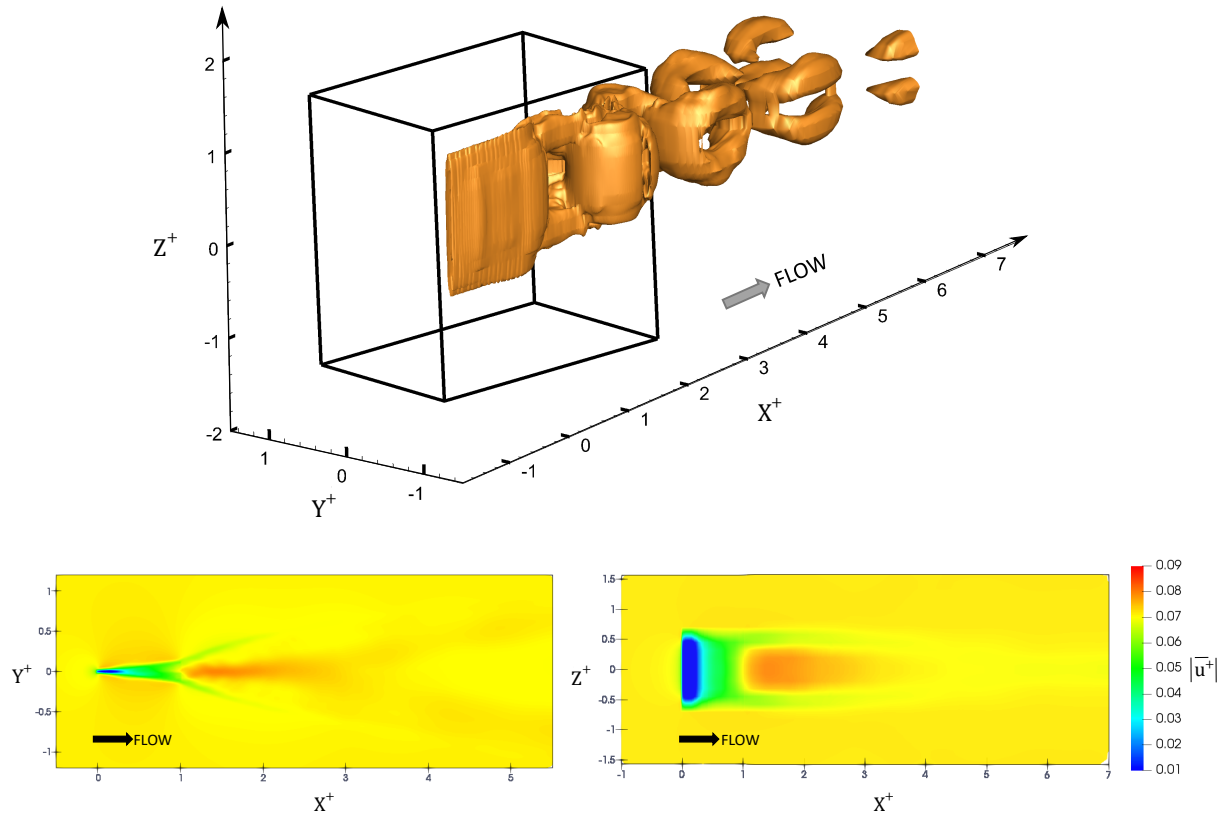

Figure 3.26: Three dimensional isometric view of iso-surfaces corresponding to $|\omega^+| = 1$ (top). Black edges depict the overset grid boundaries. Bottom figures depict two-dimensional Iso-contours for $|\overline{u^+}|$. The *Re* is 2000.

(Figure 3.26 top), which is consistent with the findings of Buchholz (2006) at $Re = 640$. As vortices travel downstream, the interactions weaken between the two vortices, leading to distortion of wake structures. This interaction is stronger for detaching vortices near the trailing edge.

The effect of separation and subsequent downstream movement of vortices are examined using contour of temporal $|\overline{u^+}|$. Figure 3.26 also shows the contour plots of $|\overline{u^+}|$ on the streamwise and spanwise planes. The mean wake is symmetric in both planes and compares well with those of Senturk et al. (2017).

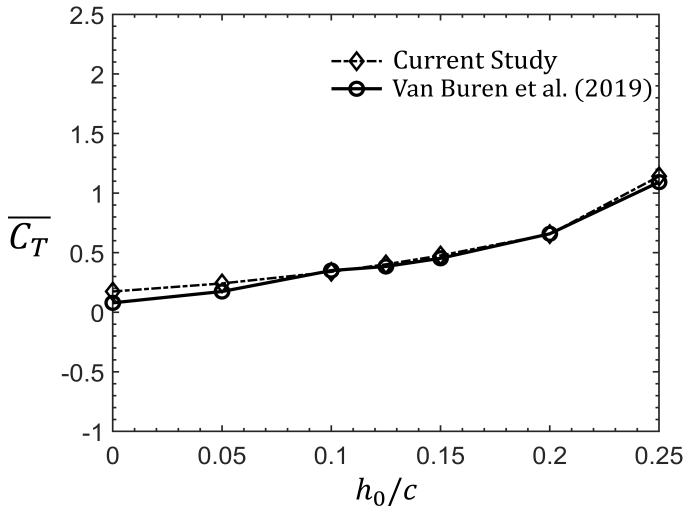

Figure 3.27: Comparison of numerically obtained variation of $\overline{C_T}$ at $St_c = 0.67$, with experiments of Van Buren et al. (2019).

3.6.3 2D Teardrop Foil

Validation of the numerical solver for the case of 2D teardrop foil simulations with experiments of Van Buren et al. (2019) is also depicted in Figure 3.27. Specifically, Figure 3.27(a) shows that the computationally predicted $\overline{C_T}$ for $0< h_o/c <0.25$, $\theta_o = 15°$, $\phi = 270°$ and $St_c = 0.67$, is in good agreement with experimental results.

3.6.4 3D Teardrop Foil

The numerical solutions for the case of 3D teardrop foil are validated by comparing our predicted $\overline{C_T}$ from simulations with the experiments of Van Buren et al. (2019) in Figure 3.28. The reduced frequencies is 1.87 while θ_0 and ϕ is 15° and 270°, respectively. The h_o/c vary from 0 to 0.25. The flow conditions and the parameter space are similar to the experiments of Van Buren et al. (2019), which enable a close comparison of the results. The numerically and experimentally obtained thrust coefficients agree well in Figure 3.28. In an attempt to validate the unsteady force variations, the instantaneous lift and moment components of the total power in an oscillation cycle corresponding to $\phi = 0°$ and 270° are compared, respectively. These results are shown in Figure 3.29a,b. Other parameters such as St_c, h_o/c and θ_o are kept constant at 0.64, 0.375 and

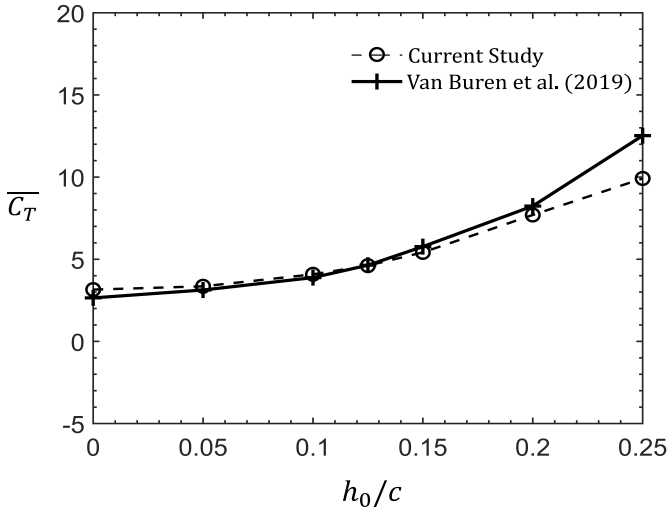

Figure 3.28: Comparison of current numerical results with experiments of Van Buren et al. (2019). Variations of mean thrust are compared at $St_c = 1.87$.

15°, respectively, for this validation study following the parameter space used by Van Buren et al. (2019). It is apparent from the results in Figure 3.29 that the unsteady variations agree well with the experimental results.

3.7 Scalability Results

In order to assess the computational performance and parallel scalability of OGA implementation in OpenFOAM, three performance metrics are evaluated, which are also useful in analyzing and comparing cost of different algorithms. These parameters include the parallel speed-up (S), total execution time (T_p) for the complete simulation in seconds and efficiency (η_S) of parallel computations. These parameters are calculated as:

$$S = \frac{T_s}{T_p} \tag{3.9}$$

$$\eta_S = \frac{S}{pr} \tag{3.10}$$

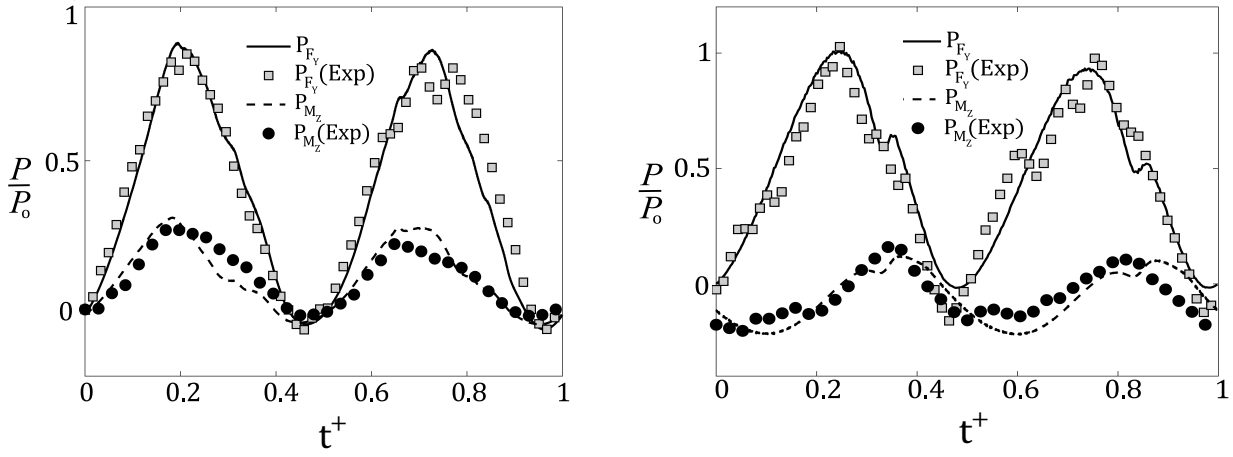

Figure 3.29: Unsteady variations of lift and moment contribution to the total power are compared at (a) ϕ =0° and (b) ϕ =270°. Details of the parameter space are provided in the text.

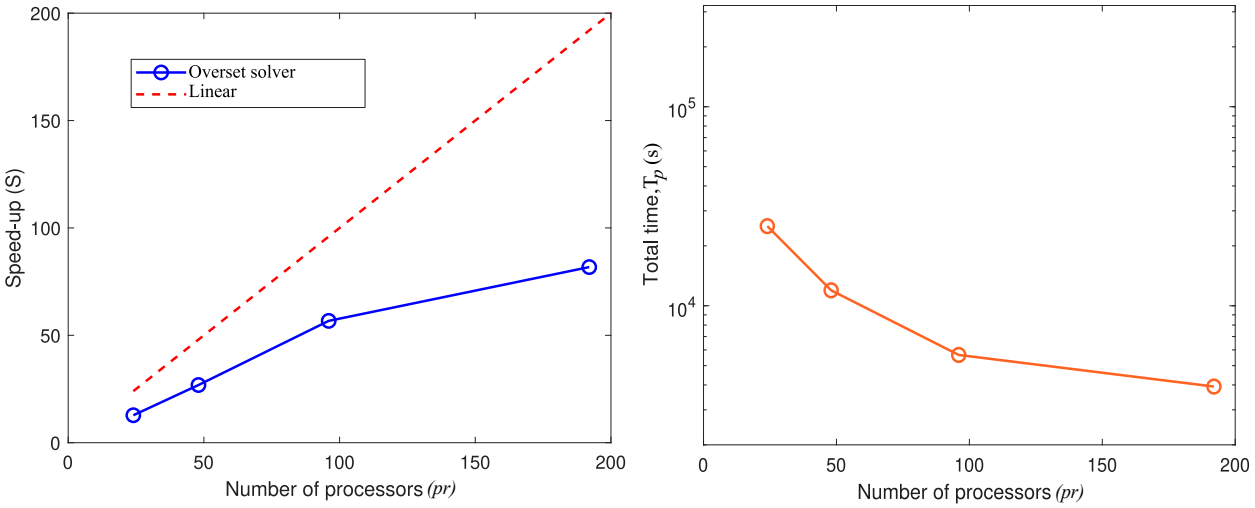

Figure 3.30: Variation of Speed-up (S) and total execution time (Tp) for simulation (in seconds), with increase in number of processors (pr).

where, T_s and T_p denote the total execution time for serial computation and parallel computations, respectively. Here, pr represents the total number of processors used for parallel computation. The assessment is carried out by running a similar pitching panel simulation at $Re = 2000$, as discussed in the previous section, although a coarser grid is constructed for this analysis. Four computations are performed using 24, 48, 96 and 192 processors, respectively. Figure 3.30 presents the results for Speed-up (S) and total execution time for parallel computations (T_p) in seconds. Parallel

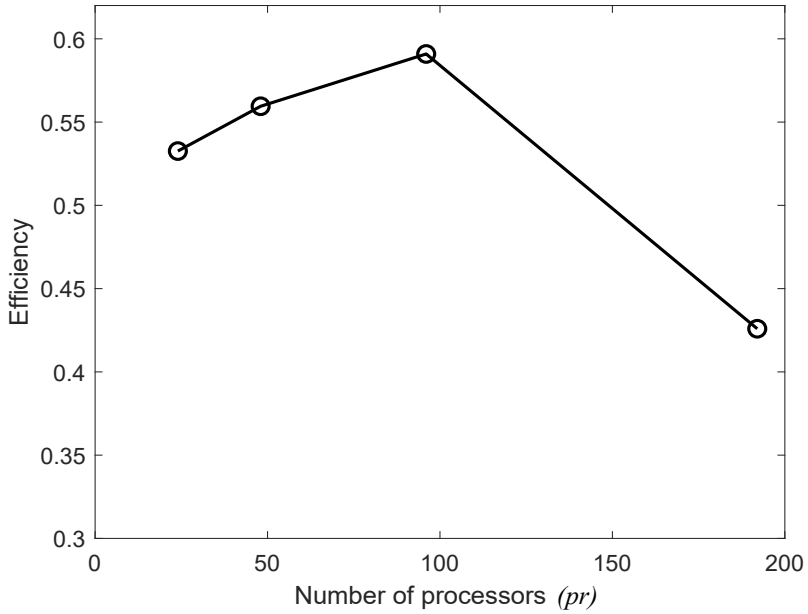

Figure 3.31: Variation of efficiency (η_S) with increase in number of processors (pr).

scalability is observed using OGA as the speed-up increases with increasing pr. The increase in the speed-up from pr = 96 and 192 is only 44.15%, which implies that using processors beyond 192 will also require the problem to be scaled up in order to achieve a higher speed up. The reduction in total execution time with the increase in number of processors is also observed, where the curve approaches an asymptotic region after $p = 96$. The reduction in execution time for pr = 96 and pr = 192 is only 30.63%.

The efficiency for parallel computations is shown in Figure 3.31. An increase in efficiency is observed as pr increases from 24 to 96, beyond which a reduction is observed for pr = 192. Therefore in case of the problem size considered here, the maximum efficiency can be attained for pr = 96. It is important to note that although the computational performance of the simulations increase with using newer versions of OpenFOAM, mainly v1912, the comparability of OGA with other numerical solvers, e.g., IBM, remains the same.

3.8 Summary

A detailed description and algorithm of the OGA method in OpenFOAM was provided in this chapter. The technique offered robust capabilities to model multi-degree of freedom oscillations, which is an essential requirement for this study. Several benchmark studies for verification and validation of the OGA, and to model the wake of stationary and oscillating blunt and bluff bodies, were described. These included 3D square panels (stationary and pitching), 2D and infinite span teardrop foils that oscillate in combined heaving and pitching motion. The computational domain, including boundary and initial conditions, were described in detail for each benchmark case. The numerical accuracy of spatial and temporal discretization schemes were also briefly described. Verification studies in terms of grid independence analysis, time-step and CFL conditions, boundary condition sensitivity and domain size established the optimal setup needed for oscillating foil cases, to accurately capture the 2D and 3D wake evolution.

For validation, the flow characteristics for stationary panels at different angles of attack were quantitatively evaluated first. The average $\overline{C_d}$ for $\alpha = 0^\circ$ to 60° were in good agreement with previous studies (Taira, 2009; Senturk et al., 2017). The maximum difference was 6.36% and it was for the stationary square panel at $\alpha = 60^\circ$. This discrepancy may be overcome by using a higher order interpolation schemes for the overset solver in OpenFOAM (Chandar, 2019) that also required a lower CPU time for computation. The wake of a pitching square panel was numerically examined using the OGA solver. The results were in good agreement with those of Senturk and Smits (2018). The wake structures and dynamics compared well with the experiments of Buchholz (2006). In case of oscillating foils, a rigorous comparative assessment was conducted by comparing mean thrust coefficient at reduced frequency and heave amplitudes, with experimental results of Van Buren et al. (2019). The unsteady force and moment also depicted good agreement with the computational results obtained using OGA.

In terms of parallelization, the efficient scalability of overset method was proven. The reduction in the computational time and increase in speed-up was achieved with increasing number of processors. This presented an advantage over some other dynamic motion solvers such as the Im-

mersed Boundary Method within OpenFOAM, wherein Senturk et al. (2017); Senturk and Smits (2018) indicated that the development of parallelization was in early stages. There was no information provided with regards to parallel scalability for IBM. The Overset method also avoids any remeshing process (at successive timesteps) that is usually noticed for body-fitted mesh approach thereby avoiding any grid quality issues, and saving computational time. Such beneficial features of Overset method highlights its faster applicability for flows wherein other possible solution techniques involve complexities and higher cost of computations.

Chapter 4

GENERALIZING THE SCALING OF PROPULSIVE PERFORMANCE[†]

4.1 Introduction

The variation in thrust generation may depend on Reynolds number. This is numerically evaluated for an oscillating foil with combined pitching and heaving motion at a range of reduced frequencies, amplitudes and phase offsets. As detailed in Section 2.2, the propulsive mechanisms depend on different characteristic parameters, such as translating amplitude of the fin trailing edge, oscillation frequency, motion profiles and its complex multi-degree of freedom dynamics, flow conditions and geometrical constraints (Koochesfahani, 1989; Triantafyllou et al., 1993; Anderson et al., 1998; Smits, 2019). It is therefore necessary to evaluate the linear and non-linear dependence of performance measures (thrust, power and propulsive efficiency) on these parameters to build and operate an optimal swimming system. In this chapter, the physics-based scaling of the propulsive thrust variation with respect to Re is examined in a wider parameter space of St_c, h_0, θ_o and ϕ, which closely resemble the parameter space of Van Buren et al. (2019). We further evaluate the

[†]The content of this chapter has been published in whole or part, in *Physics of Fluids* under the citation (Verma et al., 2022a): "Verma, S., Freeman, B.R.S. & Hemmati, A. (2022a). Effects of Reynolds number and average angle of attack on the laminar scaling of oscillating foils. Phys. Fluids 34 (3), 031905."

scaling laws for increasing average angle of attack, which has a direct dependence on the reduced frequency and trailing edge amplitude. The findings particularly help in enhancing the technology of energy efficient propulsor systems, such as AUV*s*, by incorporating biomimicry of the principal mechanisms of thrust production and locomotion in marine species (Smits, 2019).

Section 2.2 described the inability of individual scaling parameters such as St, St_c, $\omega_n^\star$, A/D, etc to accurately and universally characterize the performance of pitching and heaving foils across a wide range of operating conditions (Floryan et al., 2017). Thus, recent experimental and numerical studies have evaluated the dependence of performance characteristics on multiple scaling parameters (Floryan et al., 2017; Van Buren et al., 2019; Senturk and Smits, 2019a; Ayancik et al., 2019; Simsek et al., 2020) for oscillating foils. The case of kinematics involving combined heaving and pitching motion was recently evaluated by Van Buren et al. (2019) at $Re = 8000$, which proposed novel scaling relations for $\overline{C_T}$ and $\overline{C_P}$. A wide range of St, St_c, h_o,θ_o, and ϕ were considered by Van Buren et al. (2019), which suggested a crucial importance of ϕ between the heaving and pitching motion. However, their study only considered a single Reynolds number. Section 2.2 also highlighted various experimental and numerical studies conducted on pitching or heaving foils (Lau and Kelso, 2016; Das et al., 2016; Floryan et al., 2017; Senturk and Smits, 2019a; Simsek et al., 2020) and finite aspect ratio panels (Senturk and Smits, 2018), which suggested the importance of Re as a scaling parameter. Laminar scaling has been widely observed to hold for these cases, which features inverse square root dependence of $\overline{C_T}$ on Re (Senturk and Smits, 2019a; Simsek et al., 2020; Das et al., 2022). Its validity for foils oscillating in multi-degree of freedom oscillation, however, has not been considered yet. The contents of this chapter comprise quantitative evaluation of laminar scaling using statistical measures for foils oscillating in combined heaving and pitching motion. Average angle of attack ($\overline{\alpha}$) is determined to be a reasonable kinematic parameter that combines the dependence of St, St_c, h_o, θ_o, and ϕ in a single expression. The physical reasoning behind the observations reported on the validity of laminar scaling is also considered, mainly in terms of the dominating pressure or viscous forces on the foil due to the formation of vortical structures. Finally, a modification to the empirical relations for $\overline{C_T}$ and $\overline{C_P}$, proposed by

Van Buren et al. (2019) is introduced and evaluated by incorporation of the *Re* dependence within the scaling relations.

This chapter is arranged such that the problem description and computational setup are briefly discussed in Section 4.2, followed by the discussion of major findings in Section 4.3. The conclusions are summarized in Section 4.4.

4.2 Problem Description

The foil geometry and kinematics has been previously outlined in Section 3.1. The $\overline{\alpha}$ is further calculated here, which represents cycle-average of the foil's α measured at its quarter-chord location, as was given by Van Buren et al. (2019):

$$\bar{\alpha} = f \int_0^{1/f} \left| -\theta - \arctan\left(\frac{\dot{h} + \frac{c}{4}\dot{\theta}}{U_\infty} \right) \right| \mathrm{d}t \tag{4.1}$$

Here, $\overline{\alpha}$ includes contributions from all motion parameters (i.e., h_o, θ_o, St_c and ϕ), so it is an ideal parameter to indicate a range at which the laminar scaling holds well for oscillating foils. Figure 4.1(a,b) depict the motion profile of oscillating foil at a fixed reduced frequency and amplitude while the phase offset increases from 0° to 270°. It is evident in Figure 4.1(b) that $\phi = 90°$ corresponds to the highest peak of α, while $\phi = 270°$ depicts the lowest peak achieved within one cycle. At $\phi = 270°$, the state of pitching foil appears to be in-line with the heaving profile (see Figure 4.1(a)). Thus, this results in the smoothest motion of the foil, and the least disturbance to the flow, as noted previously by Van Buren et al. (2019). The *Re* was also varied in the range of $1,000 < Re < 16,000$. This allowed us to make a comparative assessment with studies that evaluated the laminar scaling ($Re^{-0.5}$), and describe the variation of propulsive performance characteristics with increasing *Re* (Senturk and Smits, 2019a). Godoy-Diana et al. (2008) further suggested that most naturally occurring flapping foils in marine swimming operate in the range of $100 < Re < 10,000$. Table 4.1 summarizes the parameter space employed for the present study along with those of Senturk and Smits (2019a), which evaluated the effects of increasing *Re* for a

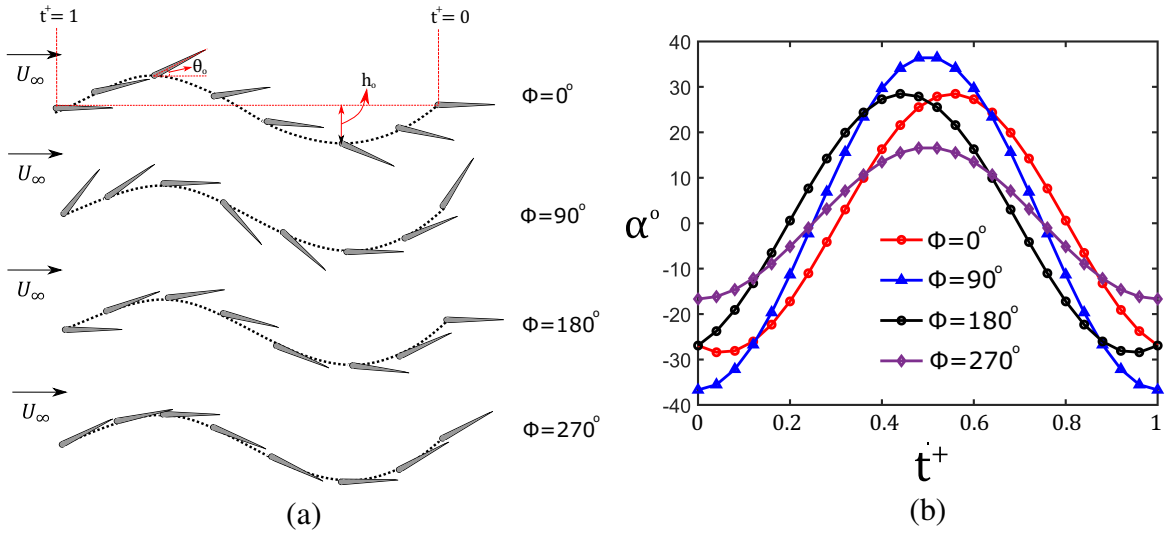

Figure 4.1: (a) Schematic of motion state of foil and (b) Variation of instantaneous α within one oscillation cycle at increasing ϕ. Black dotted line in (a) represent the heave motion profile of the foil.

Table 4.1: Comparison of parameter space employed for the current study and some existing literature.

Study	Senturk and Smits (2019a)	Van Buren et al. (2019)	Present Study
Re	$500-32,000$	$8,000$	$1,000-16,000$
St_c	–	$0.16-0.64$	$0.16-0.64$
St	$0.1-0.6$	$0-0.8$	$0.1-0.8$
a_h	–	$0.125-0.375$	$0.125-0.375$
θ_o	$2^\circ-10^\circ$	$5^\circ-15^\circ$	$5^\circ-15^\circ$
ϕ	–	$0^\circ-360^\circ$	$0^\circ-315^\circ$

purely pitching foil. This parameter space also includes that of Van Buren et al. (2019), the experimental results from which are used to validate the current simulations. It is important to note that an assessment of the specific range of ϕ and Re considered here have not been reported in literature for an oscillating foil with combined heaving and pitching motion.

4.3 Results and Discussion

We first begin by looking at scaling of the thrust generation with Reynolds number in various operating conditions for oscillating foils with combined pitching and heaving motion. This is then extended to evaluate the deviation of the newly identified Reynolds number scaling with changing average angle of attack, heave and pitch amplitude, reduced frequencies and phase offsets. Finally, the physical reasoning for a change in performance of the new scaling is evaluated and discussed thoroughly.

4.3.1 Assessment of laminar scaling

The laminar scaling relationship for oscillating foils corresponds to a dependence on the Reynolds number of the form $a+bRe^{-0.5}$ (e.g. Senturk and Smits (2019a)). This relationship arises out of the laminar Blasius boundary layer solution for a flat plate (Anderson, 1984), and has been successfully adapted to foils oscillating in pure pitching (Senturk and Smits, 2019a; Simsek et al., 2020). We evaluated this scaling by applying it separately to individual motion settings (i.e. combinations of St_c, a_h, and ϕ). The thrust variation was then assessed by performing a linear regression at each motion setting to find the coefficients a and b. The Python package scikit-learn (Pedregosa et al., 2011) was used to perform the regression. Some examples of resulting scaling forms are depicted in Figure 4.2.

For motion settings at increasing St_c and $\phi = 270^\circ$, the simulated time-averaged coefficient of thrust ($\overline{C_T}$) was observed to properly collapse on the regression line up to at least $St_c = 0.48$ (see Figure 4.2a). This collapse was also evident at increasing heave amplitudes (see Figure 4.2b) and heave dominated phase offsets in the range of $90^\circ < \phi < 180^\circ$ (see Figure 4.2c). There is, however, a subtle but increasingly noticeable deviation from the laminar scaling with respect to Re in particular kinematic settings. For example for $\phi = 270^\circ$ in Figure 4.2(a), $\overline{C_T}$ data is observed to deviate at the highest St_c =0.64, compared to the lower St_c. Likewise, these deviations generally follow a pattern with $\overline{C_T}$ being consistently underestimated for $Re = 4000 - 8000$, and

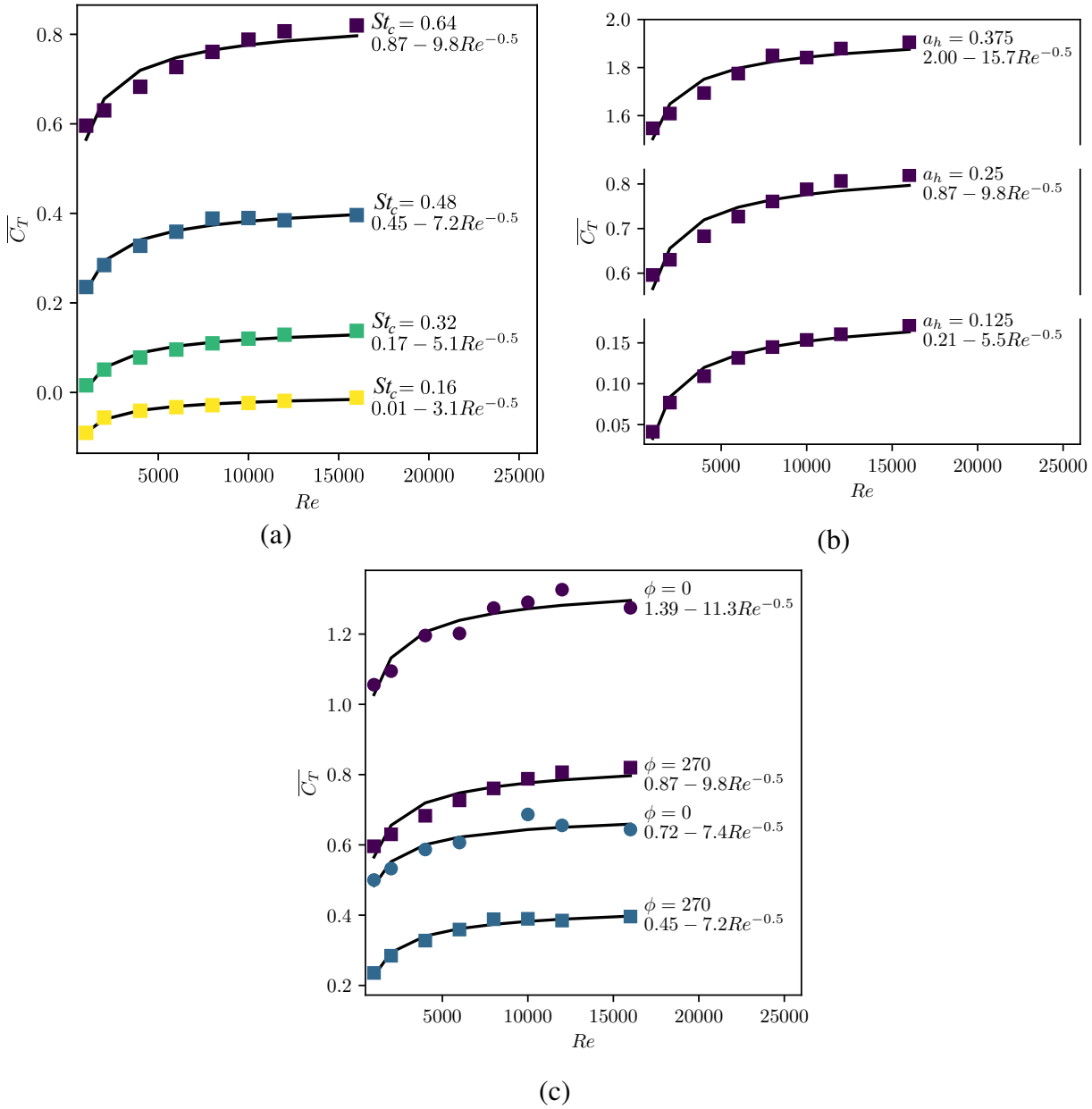

Figure 4.2: Examples of laminar scaling for (a) varying frequency at $a_h = 0.25$, $\phi = 270^\circ$ (b) varying amplitude at $St_c = 0.64$, $\phi = 270^\circ$ (c) varying phase at $a_h = 0.25$, $St_c = 0.48$ and $St_c = 0.64$. Solid lines represent the scaling.

overestimated for $Re = 10000 - 16000$. For example, see $St_c = 0.64$ in Figure 4.2(a) and $\phi = 0$ in Figure 4.2(c). Since these discrepancies appear over a wide range of motion settings, the observed pattern is most likely related to the flow physics and foil kinematics. Such deviations suggest that some of the motion settings for a combined heaving and pitching foil might not perfectly follow the assumptions of laminar scaling relationship (Senturk and Smits, 2019a). This hence leads to inaccuracies in predicting propulsive performance. Although the examples shown in Figure 4.2 suggest qualitatively that the laminar scaling is still a reasonable approximation within a large parameter space for an oscillating foil with combined heaving and pitching motion, it is important to quantify the observed deviations using statistical measures. A quantitative analysis is also useful to strictly understand if they coincide with certain characteristic changes in motion parameters. To the best of our knowledge, this observation for such a broad parameter space has not yet been reported and discussed in literature.

Screening of laminar scaling performance by angle of attack

In order to more rigorously evaluate the deterioration of the laminar scaling across all motion settings, we quantitatively assessed the strength of fit for the individual regressions through the standardized mean squared error κ, which is given by the following expression:

$$\kappa = \frac{\sum_{Re} \delta_i^2}{n_{Re} Var(C_T)} = \frac{\sum_{Re}(C_T - \hat{C}_T)^2}{\sum_{Re}(C_T - \langle C_T \rangle)^2} \tag{4.2}$$

Here, δ_i depicts the deviation of predicted thrust from the laminar scaling based on $Re^{-0.5}$. $\hat{C}_T$ represents the thrust coefficient predicted by the regression and $\langle C_T \rangle$ represents the mean value of computationally predicted C_T across all Re for the particular motion setting. κ represents a normalized estimate of the error across the entire regression, which makes it a natural choice for comparing the accuracy of scaling relations in predicting foil performance. Normalizing by the variance of the data provides a metric that is independent of the range and magnitude of C_T, which

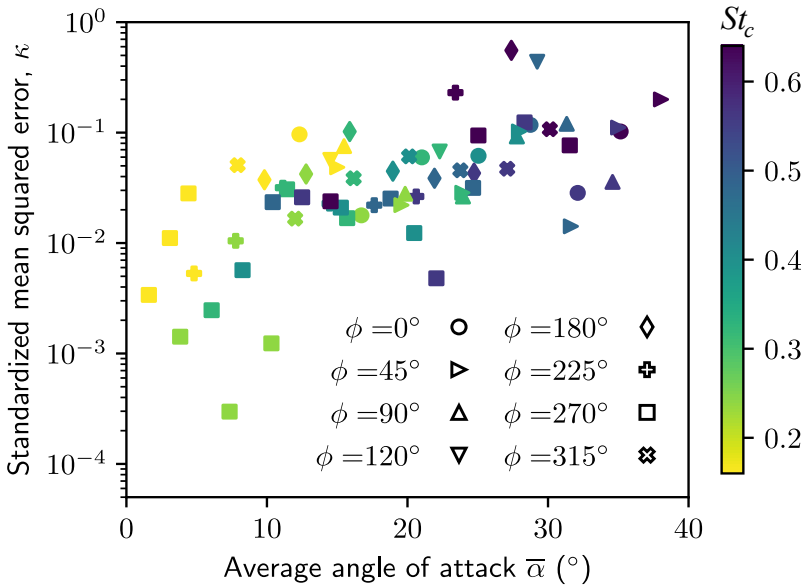

Figure 4.3: Variation of κ with increasing $\overline{\alpha}$.

can vary widely between motion settings. Figure 4.3 depicts the variation of κ with increasing average angle of attack ($\overline{\alpha}$). The results showed that κ increases by nearly two order of magnitude for $\overline{\alpha}$ in the range of $25° \leq \overline{\alpha} \leq 30°$, compared to $0° \leq \overline{\alpha} \leq 10°$. The significant increase in κ, as a measure of the accuracy of the scaling relationship, is suggestive of reduced performance of laminar scaling at high angles of attack. This occurs when the frequency and amplitude of oscillations are large, or when the phase offset deviates from $\phi = 270°$. Higher values of instantaneous angle of attack have been previously observed to coincide with larger pressure gradients in the flow which often lead to non-linearity in vorticity production at the leading and trailing edge of the foil (Cleaver et al., 2012; Visbal, 2009). Further, Lagopoulos et al. (2019) reported that flows at higher α could result in aperiodic wakes, which deviate from the general scaling trends observed in pure pitching or heaving oscillations. Since $\overline{\alpha}°$ is proportional to instantaneous α, this implies that the reasoning for increasing κ with $\overline{\alpha}$ is similar to other reported deviations in previous literature(Cleaver et al., 2012; Visbal, 2009; Lagopoulos et al., 2019). More detailed insights into the

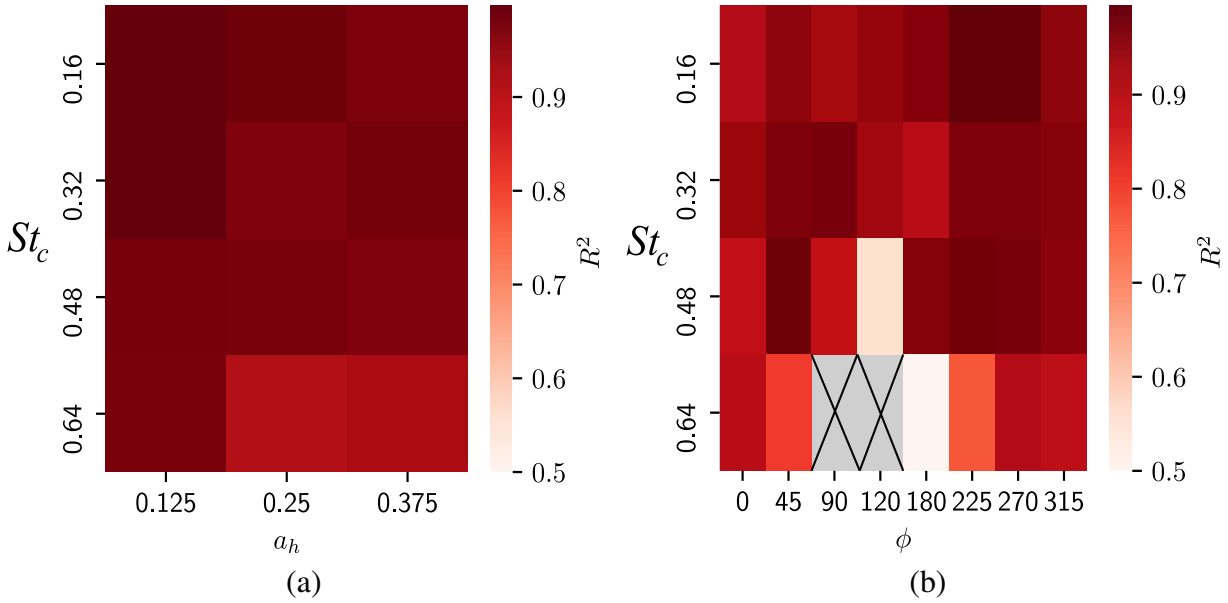

Figure 4.4: R^2 of laminar scaling with varying phase and amplitude. (a) shows the variation with amplitude for $\phi = 270^\circ$ and (b) shows the variations with phase offset for $a_h = 0.25$.

pressure and viscous force distribution will be presented in upcoming sections that will provide more vivid reasoning behind the increased deviation at high $\overline{\alpha}$.

Scaling performance by amplitude, frequency, and phase offset

To further confirm this finding with respect to the validity of laminar scaling to variations in a_h, St_c and ϕ, the coefficient of determination (R^2) was obtained for the scaling at each motion setting. This is shown using heatmaps in Figure 4.4, which depict R^2 values of the laminar scaling that correspond to specific $a_h - St_c$ combinations (Figure 4.4a) and $\phi - St_c$ combinations (Figure 4.4b). At high a_h and St_c, the lower predictive ability of laminar scaling is clearly apparent in terms of lower R^2 values. The $\phi - St_c$ map in Figure 4.4b further confirms that high St_c and phase offsets far from $\phi = 270^\circ$ show reduced predictive capability. These cases correspond to kinematic settings with high angles of attack, as a foil pitching with a phase offset of $\approx 270^\circ$ stays parallel to the effective flow direction. Whereas an offset closer to $\phi = 90^\circ$ results on the foil becoming normal to the flow, which greatly increases the average angle of attack(Van Buren et al., 2019). This was also depicted and described using Figure 4.1 shown previously. Under conditions of coupled motion setting at $\phi = 270^\circ$, studies(Anderson et al., 1998; Lagopoulos et al., 2019) have observed no

significant effects on periodicity of wake structures. This will hence provide a potential reasoning behind the improved accuracy of laminar scaling observed in our study at coupled motion settings corresponding to $\phi = 270°$. The increased accuracy is further evident in Figure 4.4(b), which was discussed earlier. Furthermore, note that the data for crossed tiles in Figure 4.4(b) correspond to $\phi = 90°$ and $120°$, which did not provide a statistically converged numerical state and were hence excluded for this analysis.

4.3.2 Implications of pressure and viscous forces

The trends discussed above provide further motivation to investigate similarities and distinctions that exist with respect to the physical characteristics of propulsive force generation. This includes assessment of the pressure and viscous contribution to the total thrust.

Changes in pressure and viscous contributions to thrust

Using the same motion settings as the results shown before, we evaluated the proportions of pressure and viscous force to the total thrust. Particularly, Figures 4.5a and 4.5b depict the ratio of change in viscous contribution of $\overline{C_T}$ to the change in total $\overline{C_T}$. $\Delta\overline{C_T}$ represents the difference observed between the highest and lowest Re taken in our parameter space, given by the following expression:

$$\Delta\overline{C_T} = \overline{C_{T,Re_{max}}} - \overline{C_{T,Re_{min}}} = \Delta\overline{C_{T,v}} + \overline{\Delta C_{T,p}} \tag{4.3}$$

where $\overline{\Delta C_{T,v}}$ and $\overline{\Delta C_{T,p}}$ represent the changes in $\overline{C_T}$ due to viscous and pressure forces at the highest and lowest Re, respectively. With increasing St_c, all amplitudes depicted a decrease in viscous contribution to the total change in thrust coefficient (Figure 4.5a). This generally coincided with a decreased R^2 for the laminar scaling. Similarly in Figure 4.5b, despite changes in ϕ from $0°$ to $315°$, higher St_c cases still depict a decreased viscous contribution to the total thrust along with a reduced R^2 value of the laminar scaling. This deterioration of the collapse of results based on laminar scaling may be due to the reduced applicability of the laminar boundary layer theory in these regimes. Since scaling with $Re^{-0.5}$ is based on the skin friction coefficient over a flat plate,

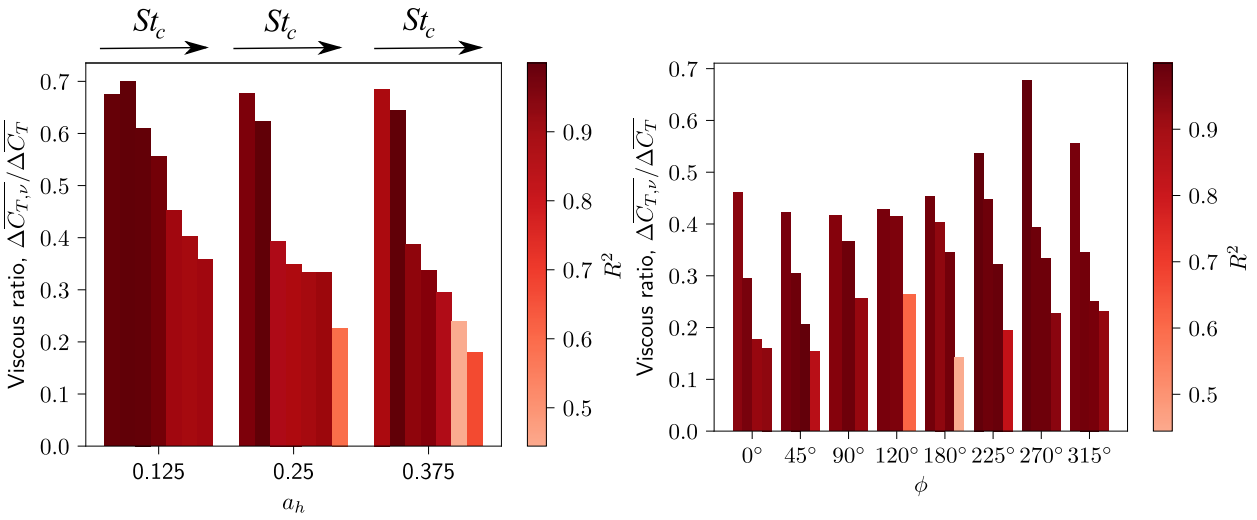

Figure 4.5: Contributions of pressure and viscous forces to the change in $\overline{C_T}$ between low and high *Re* cases based on (a) variations in amplitude for $\phi = 270°$ and (b) variations in phase offset for $a_h = 0.25$.

there is no theoretical argument on the behavior of pressure contributions to thrust generation. Thus, changes in the total force will be more dominated by pressure forces as pressure forces begin to change more rapidly with respect to changes in Reynolds number. Thus, these variations would not necessarily scale with $Re^{-0.5}$. This may attribute to the deteriorating laminar scaling relationship for large-amplitude or fast kinematic settings observed in Figure 8. Furthermore, the oscillating foil motion at high frequency or amplitude features adverse pressure gradients and flow separation(Anderson, 1984). However, it is possible that pressure forces are governed by a relationship that closely approximates laminar scaling, at least in its overall shape. This would allow for this scaling paradigm to at least approximately conform to changes in thrust coefficient, similar to the results in Figure 4.2.

Behavior of the pressure and friction distributions

In order to confirm the behavior of the pressure distribution with changing Reynolds' number, the unsteady force distributions along the foil chord are investigated. Figures 4.6 and 4.7 depict the variation of coefficient of pressure ($C_{pr} = 2p/\rho U_\infty^2$) and skin friction ($C_f = 2\tau_w/\rho U_\infty^2$) along the

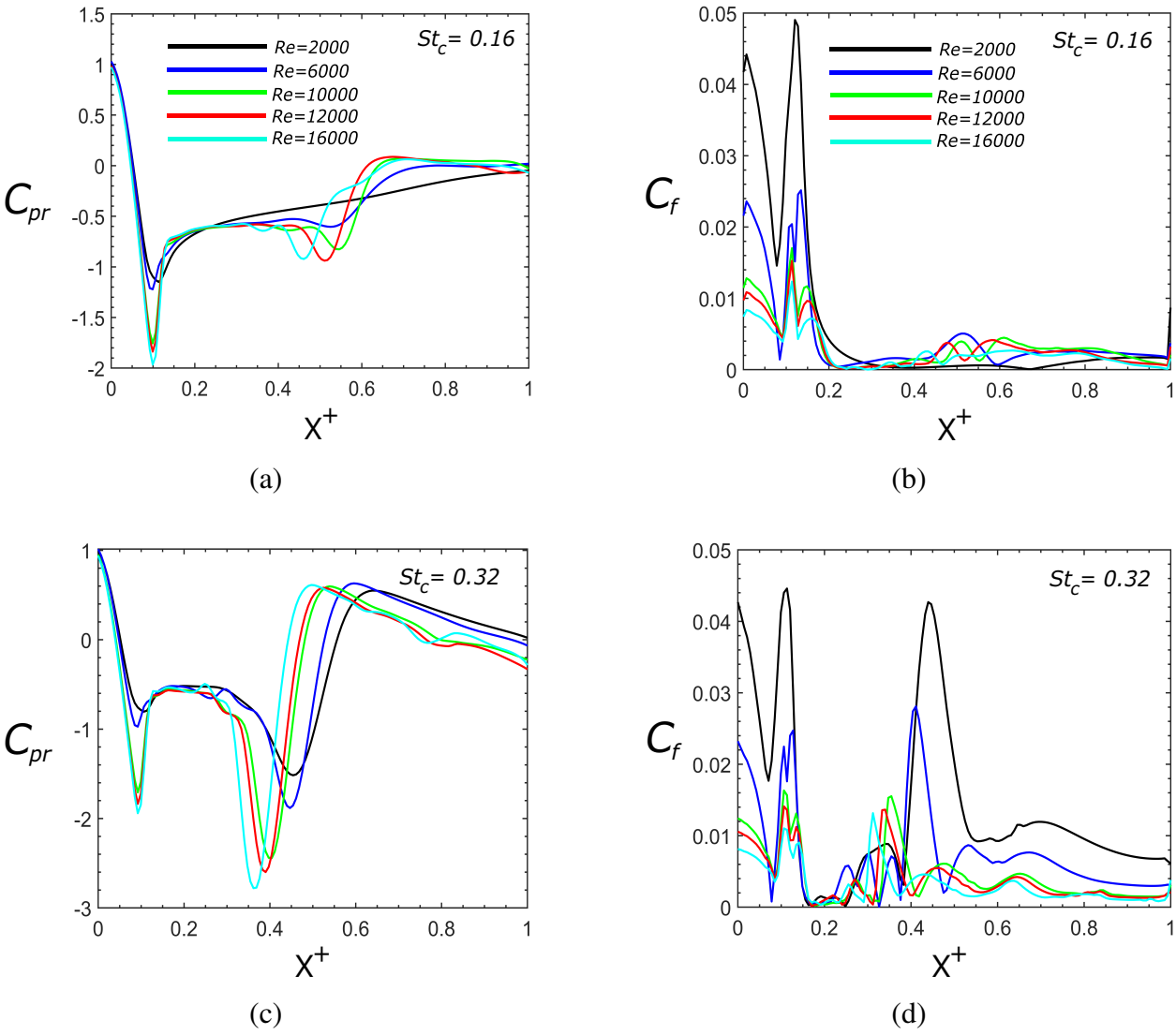

Figure 4.6: Variation of C_{pr} and C_f at increasing Re and $\phi = 270°$, along the chord for $St_c = 0.16$ (a,b) and $St_c = 0.32$ (c,d), respectively.

chord at a range of St_c, Re for $\phi = 270°$. Particularly, Figure 4.6(a,c) and 4.6(b,d) depict C_{pr} and C_f variation, respectively, for $St_c = 0.16$ and 0.32, while Figure 4.7(a-d) correspond to C_{pr} and C_f variations at $St_c = 0.48$ and 0.64. Each profile represents the data obtained at the oscillation phase of $3\pi/4$ (or $t = 0.75T$) following statistical convergence for each numerical simulation.

We also analyzed the effects of increasing Re on distributions of C_{pr} and C_f at a fixed St_c. For $\phi = 270°$, we observed that the variation of C_{pr} at a range of St_c reached a minimum prior to $x^+ = 0.2$ and 0.6, specifically for $St_c = 0.16$ and 0.32, or prior to $x^+ = 0.4$ for $St_c = 0.48$ and

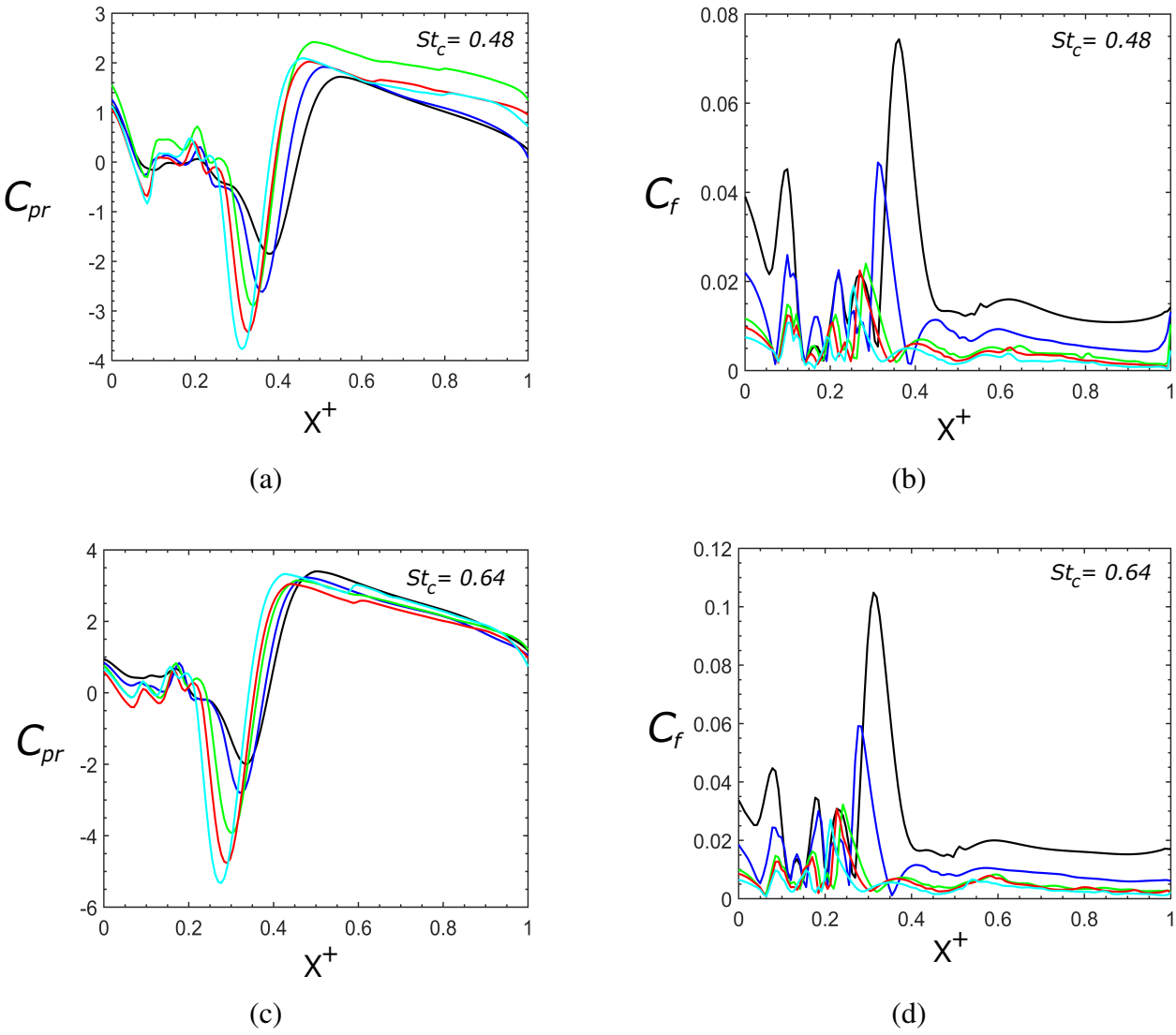

Figure 4.7: Variation of C_{pr} and C_f at increasing Re and $\phi = 270°$, along the chord for $St_c = 0.48$ (a,b) and $St_c = 0.64$ (c,d), respectively.

0.64. These minima locations were characterized by a sudden drop to larger negative values of C_{pr}. For example, the drop was insignificant for the minima location corresponding to $x^+ \approx 0.5$ at a lower St_c of 0.16, but it became increasingly noticeable at higher St_c. Focusing on the minima of C_{pr} at around the mid-chord range, its location was observed to approach the leading edge with increasing St_c. This pressure minima further coincided with leading edge vortex (LEV) structures that advected along the foil. These $LEVs$ are shown in Figure 4.8 for increasing St_c, Re at $\phi = 270°$. At lowest $St_c = 0.16$ and $Re < 10,000$, no imminent formation of LEV or roll up of separated shear

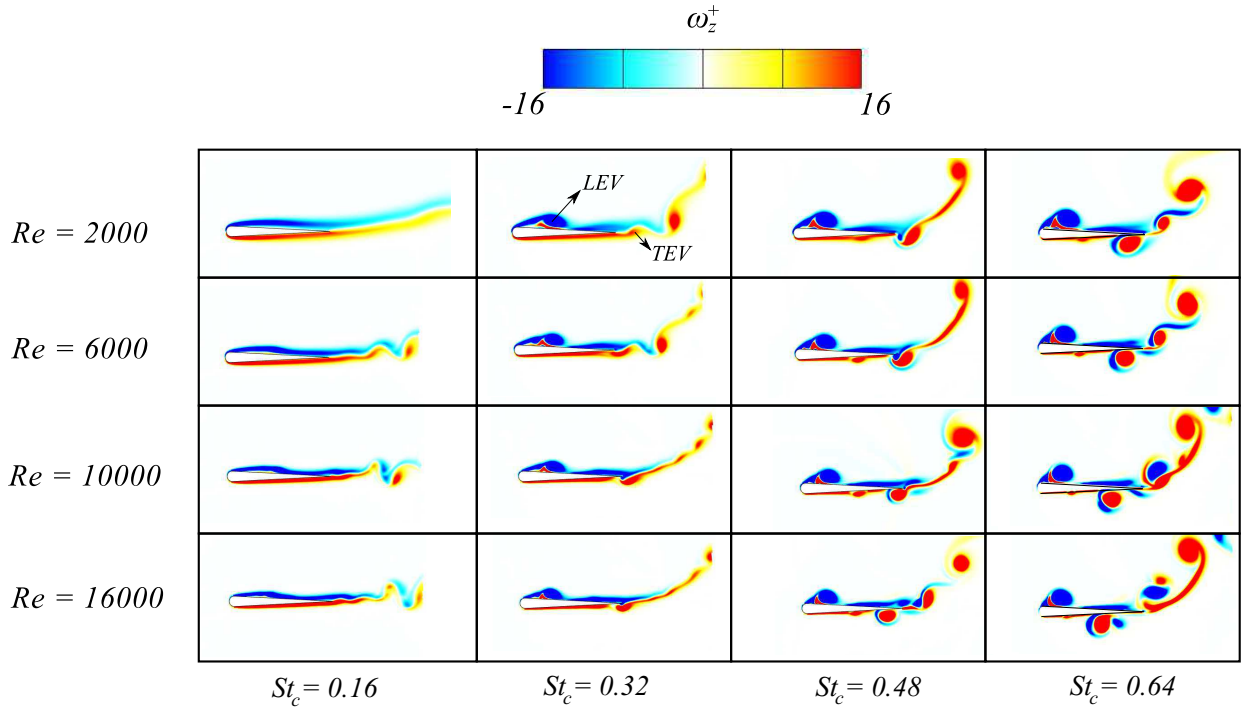

Figure 4.8: ω_z^+ contours at a range of Re and St_c, corresponding to ϕ =270°.

layer was observed. However, a weak *LEV* structure started to form at around the mid-chord at $Re > 10,000$. This structure can also be seen quantitatively via C_{pr} variations in Figure 4.6a for $St_c = 0.16$. As St_c was further increased ($St_c > 0.16$), the *LEV* structure was more prominent even at low Re. Also, the roll up of separated shear layer was achieved earlier with increasing Re, thereby causing the vortex center to move closer to the leading edge. This characteristic was consistent for all St_c. The magnitudes of the pressure minima also increased with increasing Re, as noticed in Figures 4.6(a,c) and 4.7(a,c). This was attributed to the increase in circulation strength of the *LEV*. Even the developing trailing edge vortex structures depicted changes in their spatial configuration with respect to increasing St_c and Re (Figure 4.8).

This characteristic behavior for C_{pr} was in contrast to what was observed for the friction coefficient (C_f) in Figures 4.6(b,d) and 4.7(b,d). We observed that the variations of shear along the chord consistently decrease in magnitude with increasing Re until a self similar state is achieved at higher Reynolds numbers. This was not observed for C_{pr}. This was also consistent for the entire range of St_c considered here. These observations suggested that some apparent reduction in accu-

racy of laminar scaling that was observed earlier may be clearly a consequence of non-asymptotic behavior of pressure with respect to increase in Re. This observation further appear to coincide with changes in the spatial configuration and circulation strength of leading and trailing edge vortex structures, which would promote a non-asymptotic behavior of pressure. Since the change in pressure force at higher St_c was also a larger contributor to total change in thrust (Figure 4.5) for all amplitudes and phase offsets, the R^2 value for the laminar scaling was decreased in predicting the variations in $\overline{C_T}$ with Re at those motion settings.

Effect of phase offset on stress distribution

To ensure that the above analysis is not isolated to $\phi = 270°$, the analysis of the stress distributions and vortex structures was repeated for $\phi = 0°$. Similar variations of C_{pr} were also evident in case of $\phi = 0°$ (see Figures 4.9(a,c) and 4.10(a,c)), where the pressure minima (ahead of x^+ =0.2) moved closer to the leading edge with increasing St_c, and also increase in magnitude with increasing Re. This was confirmed using the spanwise vorticity (ω_z^+) contours shown in Figure 4.11, which depicted the presence of leading and trailing edge vortex structures. However, the vorticity contours showed a large shear layer roll-up, and hence a well-developed LEV structure, even at $St_c = 0.16$. This was attributed to the higher average angle of attack compared to $\phi = 270°$.

4.3.3 Incorporation of laminar scaling into the existing scaling model

The assessment made above focused only on the dependence of propulsive thrust generation on Reynolds number with an otherwise fixed motion setting. Here, we present the incorporation of empirical dependence for Re in the complete scaling model that include all the other motion parameters like frequency, amplitudes and phase offsets. Scaling relationships exist for these parameters independent of the Reynolds number, as investigated by Van Buren et al. (2019). The resulting

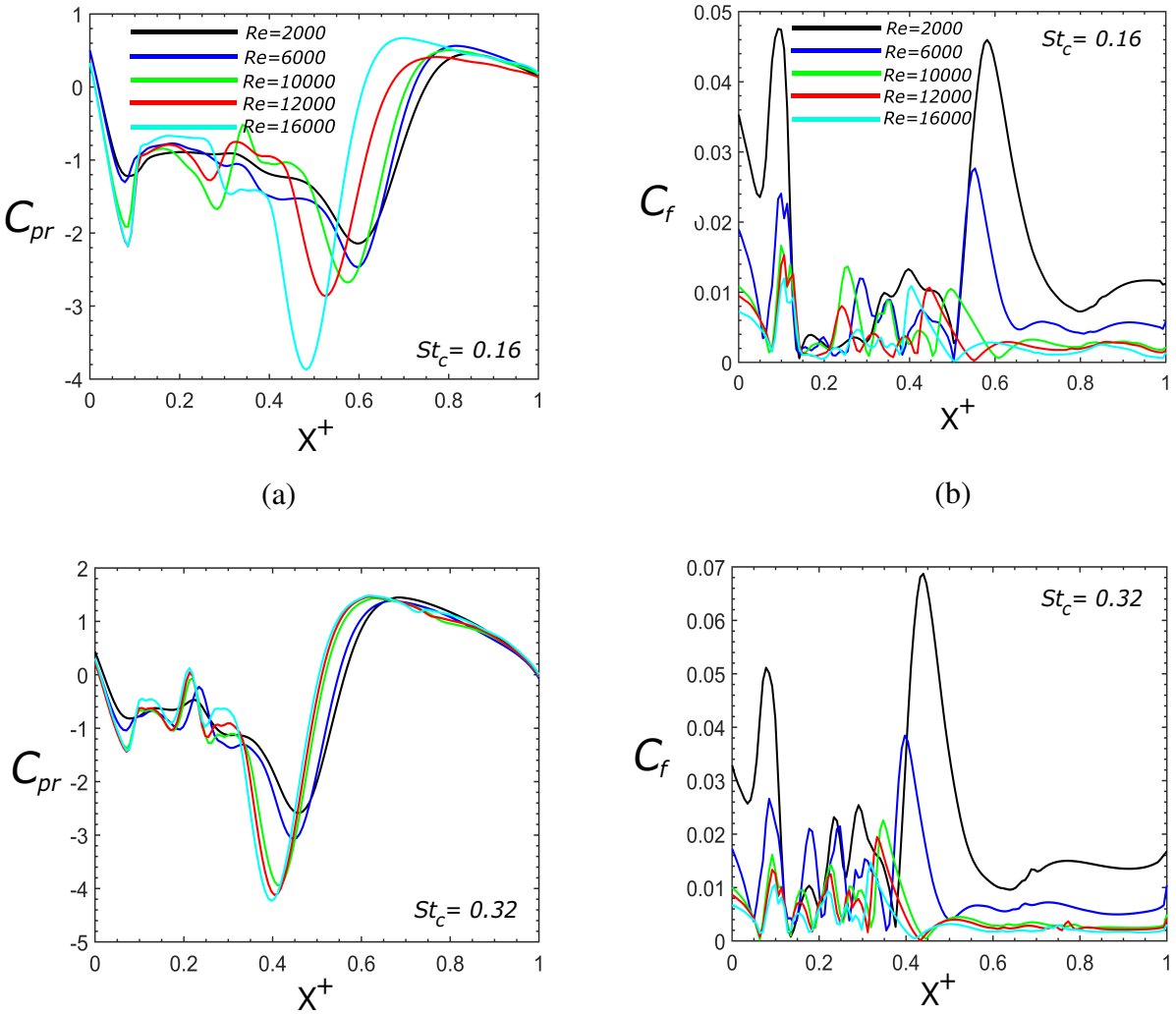

Figure 4.9: Variation of C_{pr} and C_f at increasing Re and $\phi = 0°$, along the chord for $St_c = 0.16$ (a,b) and $St_c = 0.32$ (c,d), respectively.

proposed scaling relationship by Van Buren et al. (2019), for the thrust based on these quantities is:

$$\overline{C_T} = c_1 St^2 + c_2 St_h \theta_0 \sin\phi + c_3 St_\theta \theta_0 - c_4 \theta_0 \tag{4.4}$$

This scaling introduces the nondimensional parameters $St_h = 2h_0 f/U_\infty$ and $St_\theta = 2\theta_0 cf/U_\infty$. In order to incorporate the effect of the Reynolds number into this equation empirically, we employed a similar method as followed by Senturk and Smits (2019a) and Simsek et al. (2020). This method

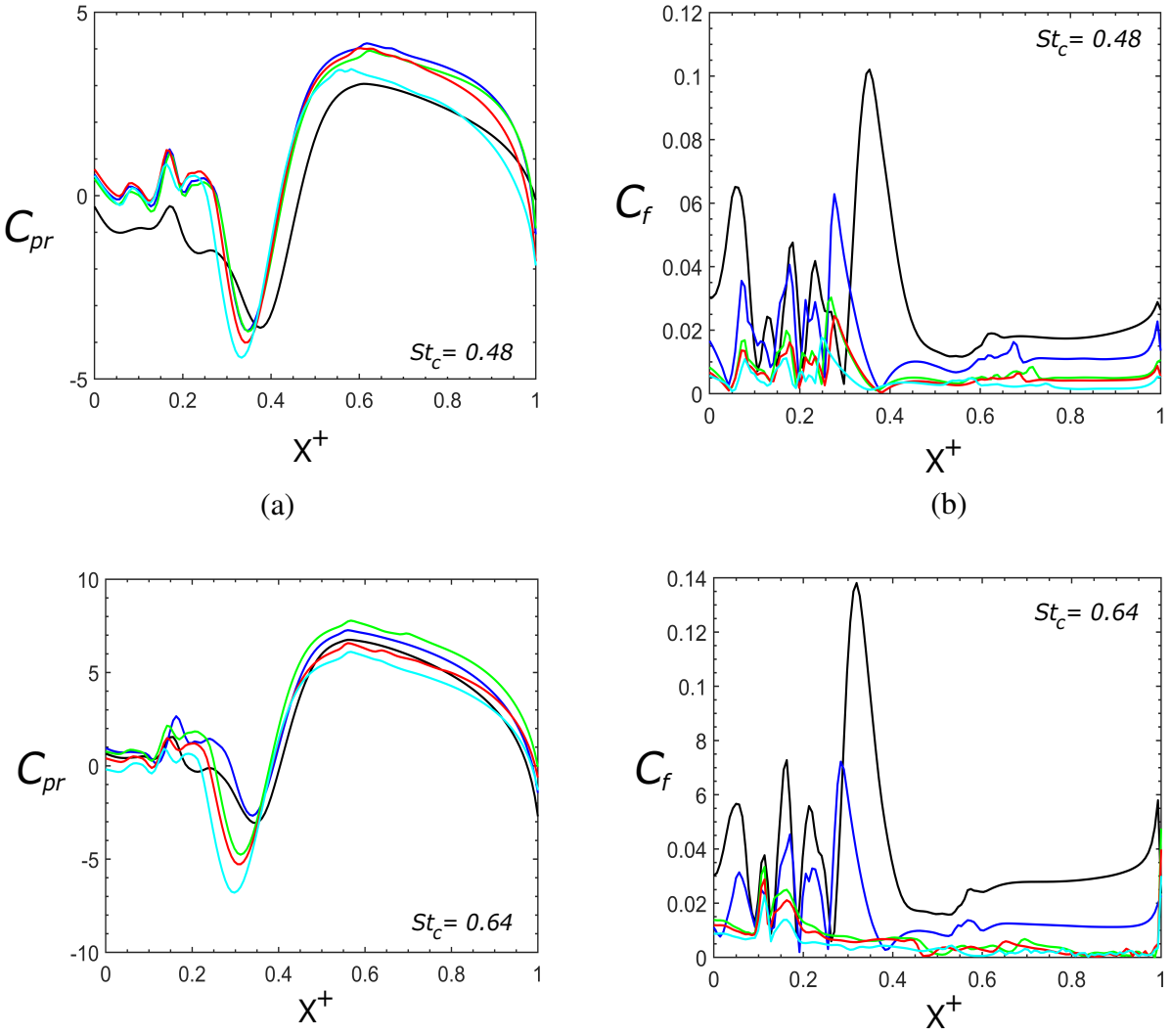

Figure 4.10: Variation of C_{pr} and C_f at increasing Re and $\phi = 0°$, along the chord for $St_c = 0.48$ (a,b) and $St_c = 0.64$ (c,d), respectively.

assumes that the coefficients $c_1 - c_4$ in Eq. 4.4 also follow a laminar scaling relationship. The resulting semi-empirical scaling equation was therefore obtained as:

$$\overline{C_T} = \tau_1 St^2 + \tau_2 St_h \theta_0 \sin(\phi) + \tau_3 St_\theta \theta_0 - \overline{C_D} \tag{4.5}$$

where τ_i and $\overline{C_D}$ are all of the form $a + bRe^{-0.5}$, and $\overline{C_D}$ contains an extra dependence on θ_0 due to the c_4 term of Eq. 4.4. This equation is thus linear with 9 unknown coefficients that can be

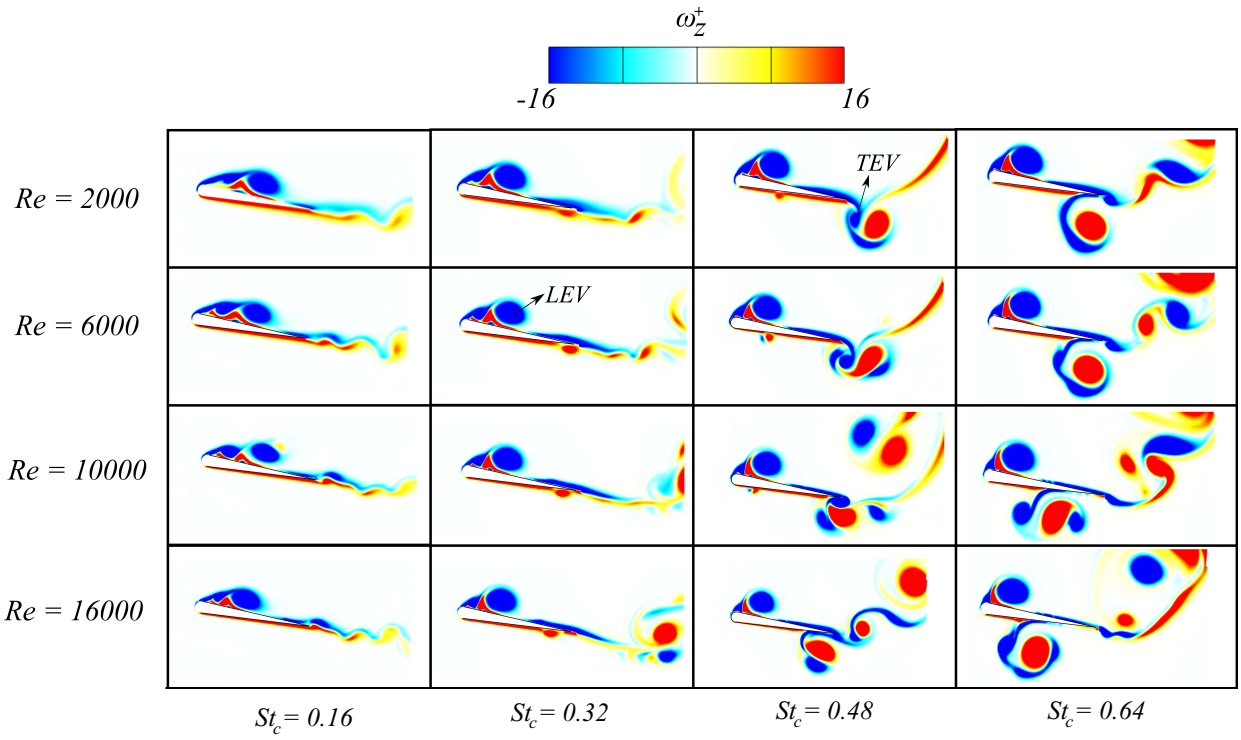

Figure 4.11: ω_z^+ contours at a range of *Re* and St_c, corresponding to ϕ =0°.

determined through ordinary linear regression operations. The result of performing this regression on our full parameter space is depicted in Figure 4.12(a), comparing the predicted value of $\overline{C_T}$ from the scaling (x-axis) to the computationally obtained value (y-axis). The good collapse of performance data are apparent across the expanse of the parameter space considered here with the value of coefficients listed in Table 4.2. Combining the proposed scaling relationship of Van Buren et al. (2019) with the Reynolds number in this way is therefore a reasonable method to obtain a scaling relationship involving both the motion and flow settings of an oscillating foil with combined heaving and pitching motion.

The same methodology can also be used for scaling the power coefficient ($\overline{C_P}$), based on the general scaling proposed by Van Buren et al. (2019). Thus, the following proposed scaling is used

Table 4.2: Results of least squares regression of equation 4.5 over entire parameter space.

Coefficient	Value
τ_1	$5.10 - 25.07Re^{-0.5}$
τ_2	$-4.79 + 22.75Re^{-0.5}$
τ_3	$-3.49 - 15.80Re^{-0.5}$
$\overline{C_D}$	$0.68\theta_0 + 3.36Re^{-0.5} - 0.058$

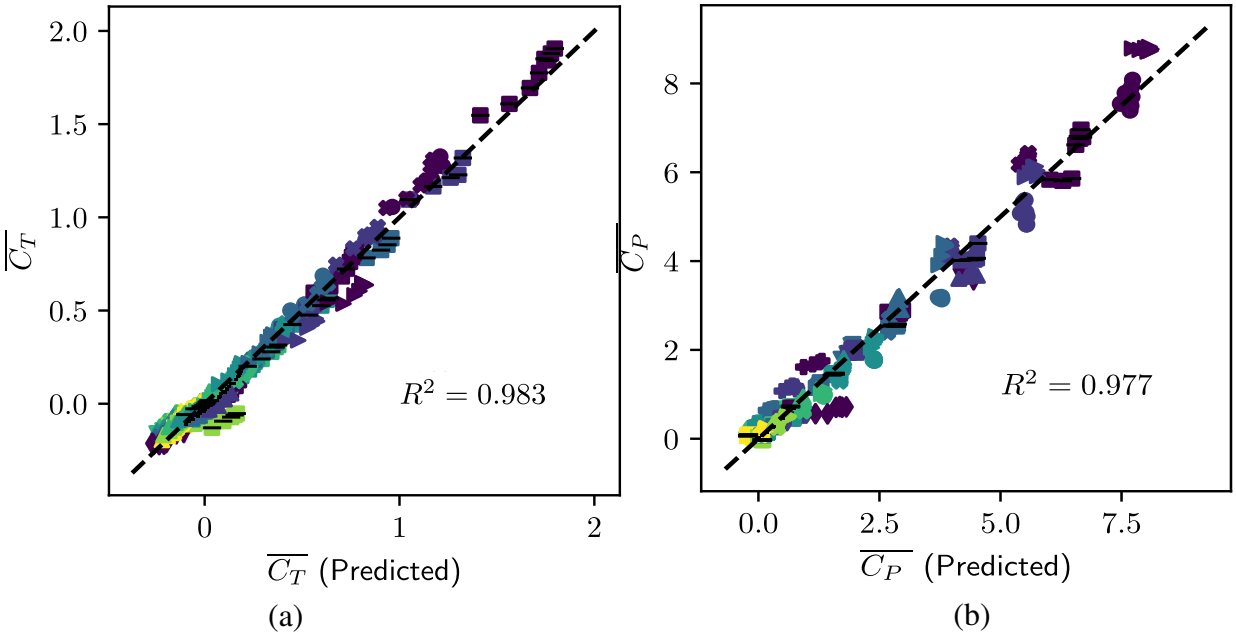

Figure 4.12: Modification of the scaling relationships for (a) $\overline{C_T}$ and (b) $\overline{C_P}$ proposed by Van Buren et al. (2019), to incorporate a laminar scaling dependence on the Reynolds' number. See Figure 4.3 for symbol interpretation.

Table 4.3: Results of least squares regression of equation 4.6 over entire parameter space.

Coefficient	Value
Π_1	$20.2 + 41.9Re^{-0.5}$
Π_2	$50.7 - 250Re^{-0.5}$
Π_3	$-0.413 - 11.8Re^{-0.5}$
Π_4	$87.6 - 803Re^{-0.5}$
Π_5	$-28.0 - 72.0Re^{-0.5}$

across the entire parameter space:

$$\overline{C_P} = \Pi_1 St^2 + \Pi_2 St_c St_h St_\theta \sin(\phi) + \Pi_3 St_h \theta_0 \sin(\phi) + \Pi_4 St_c St_\theta^2 + \Pi_5 St_\theta \theta_0, \tag{4.6}$$

where, once again the coefficients each follow a laminar scaling relationship that may be obtained through linear regression. Note that one term of the original scaling is excluded due to the correlation of a_h and θ_0 in the current dataset. Results of the resultant scaling are shown in figure 4.12(b) and coefficient values are shown in Table 4.3. Once again, a proper collapse is achieved using the modified scaling equation that includes the flow Reynolds number. However, the power coefficient data appears slightly more scatter than the thrust coefficient. A similar effect was observed in the scaling relationship for $\overline{C_P}$ by Simsek et al. (2020). It is possible that the the power coefficient is more strongly driven by pressure due to its dependence on the lift and moment on the foil. This could result in the weakened, but still valid, approximation set by the laminar scaling due to the previously established pressure-driven effect on the thrust coefficient.

4.4 Summary

The propulsive thrust generation of an oscillating foil in combined pitching and heaving motion was assessed numerically at a range of Re, St_c, a_h, θ_o and ϕ. The laminar scaling ($Re^{-0.5}$) for thrust variations was found accurate for the parameter space of our study, although it depicted some deterioration with increase in average angle of attack ($\overline{\alpha}$). Specifically at motion settings that correspond to high reduced frequencies and amplitudes, it was apparent that laminar scaling did reveal deviations in comparison to its predictive capability at lower St_c and amplitudes in terms of strict statistical norms, such as κ and R^2. The quantitative measure that involved κ further revealed that motion settings that correspond to values of $\overline{\alpha} \leq 20°$, depicted the laminar scaling as a good predictor. However, $\overline{\alpha} > 20°$ showed a decreasing accuracy for the laminar scaling of Reynolds

number. This was attributed to the change in contributions of pressure and viscous forces to thrust generation for regimes corresponding to low and high average angles of attack.

At high reduced frequencies, pressure force was the major contributor to the total change in thrust which coincided with the relatively weaker collapse of the data following the laminar scaling. This was similar to observations with variations in ϕ. The chordwise variation of C_{pr} at high St_c also confirmed that an asymptotic trend at higher Re was not achieved. This explained why some apparent deviations in laminar scaling were more prominent in cases with larger pressure contribution to total thrust than viscous forces. These variations were further confirmed qualitatively in terms of identification of leading edge vortex structure using contours of spanwise vorticity at increasing St_c and Re. Contrarily, C_f showed a consistent trend in terms of decrease in magnitude with increased Re. It reached a self-similar state in terms of its chordwise variations at higher Re.

The incorporation of laminar scaling of Re into the proposed scaling model of Van Buren et al. (2019) also depicted its validity in a larger parameter space of combined heaving and pitching motion, similar to that observed for purely pitching cases by Senturk and Smits (2019a). This has not been investigated in the present existing literature. However, the observed statistical deviations of laminar scaling ($Re^{-0.5}$), especially at higher average angle of attack, suggests a potential need to investigate new scaling models that could incorporate the effect of adverse pressure gradients created by the developed LEV structures on oscillating foils, more accurately. We believe that this could be more viable and accurate for various bio-inspired advanced control systems that operate specifically at high reduced frequency and amplitudes, which could hence result in an increased average angle of attack. Despite the implications of changes in kinematics on performance, it is also important to investigate the spatial wake arrangement or topology of the shed vortex structure, ahead of their formation. The correspondence between performance and wake topology at different regimes of kinematics is therefore evaluated in the following chapter.

Chapter 5

ROUTE TO TRANSITION IN PROPULSIVE PERFORMANCE[†]

5.1 Introduction

The teardrop foil closely reflect the geometrical configuration of fins that act as the primary propulsors for fish and marine mammals (Triantafyllou et al., 2000). Several studies discussed in Sections 2.3-2.3.1 highlighted how wake structures generated by su‘ch an oscillating foil, following the same kinematic parameter space as swimming fish, provided insights into their manipulation of the flow yielding an optimum thrust with relatively small power requirements (Anderson et al., 1998; Smits, 2019). Section 4.3 provided qualitative and quantitative evidence on changes in *LEV* and TEV formation as kinematics (St_c, ϕ and h_o/c) and Re vary in the range considered in this study. However, the association of transition in performance and arrangement of shed $LEVs$ and $TEVs$ is still yet to be investigated. These aspects help in developing novel marine propulsion systems, such as autonomous underwater propulsors (AUVs), which could also execute complex and high speed maneuvers with increased propulsive efficiency (Smits, 2019).

[†]The content of this chapter has been published in whole or part, in *Physical Review E* under the citation (Verma and Hemmati, 2022b): "Verma, S. & Hemmati, A. (2022). Route to transition in propulsive performance of oscillating foil. Phys. Rev. E 105 (4), 045102."

Most previous studies that focused on investigating transitions in the performance and wake modes of oscillating foils were either restricted to a single degree of motion, such as pure heaving or pitching, or a fixed phase offset of 90° in a coupled motion kinematics. Detailed review of these studies was provided in Sections 2.3-2.3.1. Meanwhile, experimental observations, e.g., Van Buren et al. (2019), have identified that phase angle dominates performance of oscillating foils with combined pitching and heaving motion. This was even evident based on the observations discussed in Chapter 4. Here, the propulsive performance and wake mode transition are explored for an oscillating foil in coupled motion at a range of phase offset ($0° \leq \phi \leq 315°$) and reduced frequency ($0.16 \leq St_c \leq 0.64$). The range of Re spanned between 1000 to 16000, which aligns with observations that propulsively efficient swimming motion largely occurs within $Re = 100-10000$ (Wang, 2005). Detailed analysis, however, is focused on $Re = 1000$, which is consistent with various studies conducted on transitions in the wake, as highlighted and discussed earlier (Godoy-Diana et al., 2008; Schnipper et al., 2009; Deng et al., 2015; Lagopoulos et al., 2019). This parameter space, therefore, provides a venue to compare current observations with those previously reported in literature for validation and consistency purposes. The transitions will be reflected on maps characterized by increasing St_c and ϕ, termed as $\phi - St_c$ phase space. An important fundamental contribution of this chapter is to investigate if the wake modes and their transition assessments from such phase space diagrams can enable establishing a correlation between performance transition and apparent changes in the vortex synchronization (Godoy-Diana et al., 2008; Schnipper et al., 2009). This is because some experimental, numerical and review studies (Drucker and Lauder, 2001; Fish and Lauder, 2013; Fish et al., 2014; Smits, 2019) had hinted that a propulsively efficient swimming performance could not always correspond to a specific wake pattern. The existence of similar wake modes with significantly different propulsive performance could also suggest that transitions of the wake topology may not always be a reliable tool for understanding propulsive mechanisms of fish swimming or the development of underwater propulsion systems. The phase-space diagrams will further help in recognizing kinematic regimes that sufficiently yield an optimum performance for oscillating foils with combined heaving and pitching motion.

Van Buren et al. (2019) further indicated that a phase offset range between $90^\circ < \phi < 180^\circ$ was not found important propulsively, since no thrust production was evident in this range. However, there has been no attempt for a detailed investigation into the mechanisms and wake dynamics that generally coincides with this range of phase offset, with an aim to explain the drag production dominance. Furthermore, there are no other studies in literature, to the best of author's knowledge, that evaluates the transitions in wake modes at a range of increasing phase offset. The changes posed by increasing ϕ on wake structure interactions could hint at potential mechanisms that limit achieving optimum efficiency in underwater locomotion. The chapter is arranged such that the problem description is explained in Section 5.2, followed by the discussion of results in Section 5.3. A summary of major contributions is then provided in Section 5.4.

5.2 Problem Description

The St_c of oscillation motion varied in the range of $0.16 \leq St_c \leq 0.64$. This corresponds to a Strohaul number variation in the range of $0.2 \leq St_A \leq 0.5$ based on the fixed heaving and pitching amplitude stated above. Andersen et al. (2017) have indicated that interesting and significant transitions in the wake of flapping foils were generally observed within a Strohaul number range of $0.2 < St_A < 0.4$. This range was further observed to coincide with the range that corresponds to optimal propulsive efficiency in swimming mammals (Triantafyllou et al., 1993; Smits, 2019). This range of St_A also preserves the wake two-dimensionality for a flapping foil that involves either a pure pitching, or a pitch dominated coupled motion setting (Zurman-Nasution et al., 2020). This further explains and justifies the parameter space considered in the current study. The ϕ also varied from 0° to 315°, which resulted in variation in trailing edge amplitude. Van Buren et al. (2019) also highlighted that changes in ϕ caused the motion to be either pitch- or heave-dominated, and therefore affected the propulsive performance. However, there has not been any attempts to characterize the effects of ϕ on the transition of propulsive performance and shedding of vortical structures. The chord-based Reynolds number in the current study range from 1000 to 16000, whereas detailed

Table 5.1: Parameter space for studies conducted on transitions in performance and wake of oscillating foil. Studies with a fixed ϕ correspond to the coupled motion while others either considered pure pitching or heaving motion.

Study	Re	St_c	St_D	$a_h(=h_0/c)$	θ_o	A_D	ϕ°
Godoy-Diana et al. (2008)	1173	-	0-0.5	-	-	0-2.2	-
Schnipper et al. (2009)	1320	-	0-0.3	-	-	0-2	-
Kozłowski and Kudela (2014)	100-500	0.2-1.2	-	0.1-1.1	-	-	-
Deng and Caulfield (2015b)	1700	-	0.05-0.5	-	-	0.25-2.5	-
Sun et al. (2018)	1700	-	0.05-0.4	-	-	0.25-2.5	-
Zheng et al. (2019)	1100	-	-	0.05-1.25	$5^\circ-50^\circ$	-	90°
Lagopoulos et al. (2019)	1173,11730	-	0.05-0.35	-	5°-20°	0-3.0	90°
Present study	1000	0.16-0.64	0.016-0.064	0.25	10°	2.5	0°-315°

analyses of the wake and performance are focused on $Re = 1000$ following closely with studies of Godoy-Diana et al. (2008), Schnipper et al. (2009), Deng et al. (2015) and Lagopoulos et al. (2019). As discussed earlier, these studies assessed the transitions in the wake of purely pitching foils, while also describing the quasi-two-dimensional and three-dimensional transitions (Deng et al., 2015). Table 5.1 summarizes the parametric space for some of the prominent oscillating foil studies conducted in the past to investigate the transition in both performance and wake modes. It is also important to note here that the most propulsively efficient phase offset of 90° (Anderson et al., 1998), employed for studies reported in Table 5.1 (Zheng et al., 2019; Lagopoulos et al., 2019), is equivalent to $\phi = 270^\circ$ based on definitions of Van Buren et al. (2019). This was on account of differences in reference coordinate system followed in these studies. The current study will follow the reference system of Van Buren et al. (2019).

5.3 Results and Discussion

The transition of propulsive performance in terms of change from drag dominant flow regime to a thrust producing regime is first mapped on $\phi - St_c$ phase space shown in Figure 5.1(a). The iso-line depicting a zero thrust production clearly differentiates the drag and thrust regimes, where

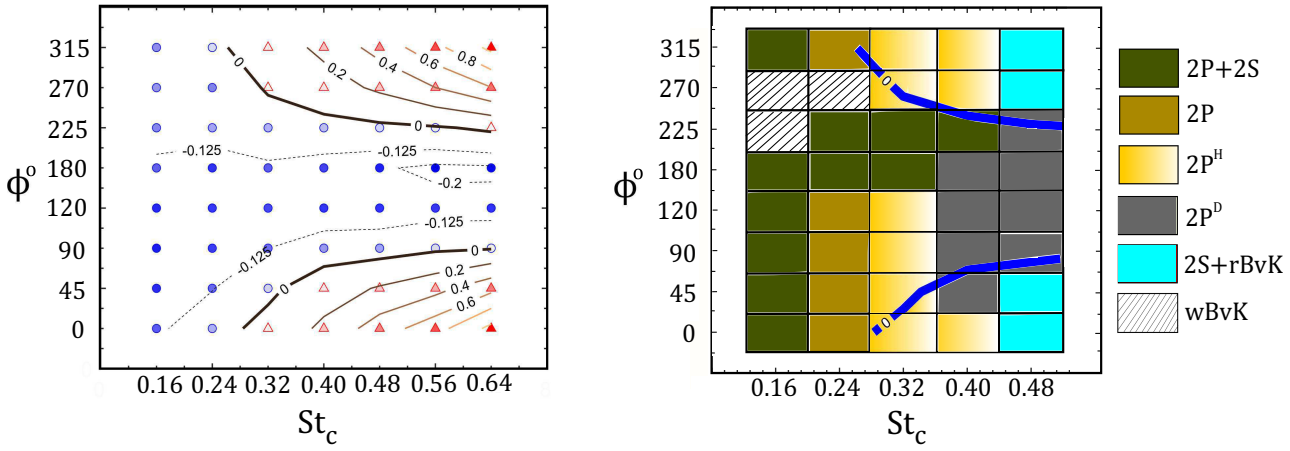

Figure 5.1: The phase-space maps of $\phi - St_c$, depicting the transition of (a) drag to thrust production, and (b) wake modes for $Re = 1000$. Circular and Triangular markers depict the drag and thrust producing cases, respectively. Increasing saturation color levels of filled marker correspond to the increasing the magnitude of thrust or drag. Solid and broken lines represent data points with constant $\overline{C_T}$ and $\overline{C_D}$, respectively.

drag to thrust transition is found symmetric along the phase offset region between $\phi = 120^\circ$ and 180°. For $90^\circ \leq \phi \leq 225^\circ$ in Figure 5.1(a), the phase map depicts an overall drag dominant setting at all reduced frequencies. These findings agree closely with the study of Van Buren et al. (2019), which suggested that there is no propulsive thrust force generation by an oscillating foil in combined heave and pitch motion in the range of $90^\circ < \phi < 180^\circ$. The transition in vortex synchronization or wake modes is further represented on a $\phi - St_c$ phase space in Figure 5.1(b). These wake modes are characterized by the number of vortices shed in one oscillation or shedding cycle, similar to Schnipper et al. (2009). It is important to mention here that most of the previous studies (Godoy-Diana et al., 2008; Schnipper et al., 2009; Kozłowski and Kudela, 2014) that investigated the transition of wake modes were focused on a purely pitching or heaving motion, wherein A_D was directly calculated based on the pitch angle or the heave amplitude (see Table 5.1). However, amplitude is directly dependent on the phase offset between the motions (two degrees of freedom) considered here (Van Buren et al., 2019). Thus, it is more reasonable to study the impact of variations in ϕ for depicting the transitions of vortex synchronization. This follows a similar methodology in using the angle of attack by Zheng et al. (2019) as a threshold to identify the tran-

sition in wake modes and performance of foils. However, here the phase offset is an independent input variable, which is usually provided and controlled in setting up the kinematics of oscillating foils.

Figure 5.1(b) shows that flow developments at the lowest reduced frequency considered here (St_c =0.16) is mostly characterized by a 2P+2S wake mode (Williamson and Roshko, 1988) for $\phi < 225^\circ$ and $\phi > 270^\circ$. However, an undisturbed flow is noticed without any vortex shedding for the case of $\phi = 225^\circ$ and 270°, which is labeled as *wBvK* in Figure 5.1(b). This state of the wake closely resembles the wavy Von Kármán street, which was also observed and discussed by Lentink et al. (2008) in the wake of a flapping foil. In brief, this mode is observed following an instability that emerges downstream of the wake, behind the trailing edge, which lead to an initial roll-up of the shear layer. Further discussions on the flow mechanisms and wake dynamics will be provided in subsequent sections (e.g., Figure 5.3). Comparing this region to the performance transition map in Figure 5.1(a), we observe that the 2P+2S mode and wavy Von Kármán mode, along with their characteristic vortex synchronization near the foil, coincide with drag production. The increase in magnitude of drag production with increasing ϕ from 0° to 120° is also evident at both $St_c = 0.16$ and 0.24 in Figure 5.1(a). However, the wake mode consistently depicts 2P+2S and 2P configurations with increasing ϕ in Figure 5.1(b). Even at higher reduced frequencies in Figure 5.1(a), i.e., $St_c = 0.32$ and 0.4, we observe a drag to thrust transition. For the case of $St_c = 0.32$, transition occurs at approximately $\phi = 45^\circ$ with the wake mode still resembling a $2P^H$ configuration (see Figure 5.1(b)), while transition occurs at 90° for $St_c = 0.4$ with the wake resembling a $2P^D$ configuration. Thus, these observations signify that transition of wake modes may not hold a direct correspondence with transition or changes in propulsive performance, as explained previously by Smits Smits (2019). The symmetric counterpart for the drag-thrust transition boundary presented on the performance and wake map, i.e., region from $\phi = 180^\circ$ to 315°, depicts some apparent similarities with the region lying between $\phi = 0^\circ$ to 120°. For example, a definite increase in thrust occurs at $St_c = 0.32$ and 0.4 (Figure 5.1a), while the wake remains characterized by a $2P^H$ mode. However, a more consistent transition in wake modes is noticeable in the higher phase offset re-

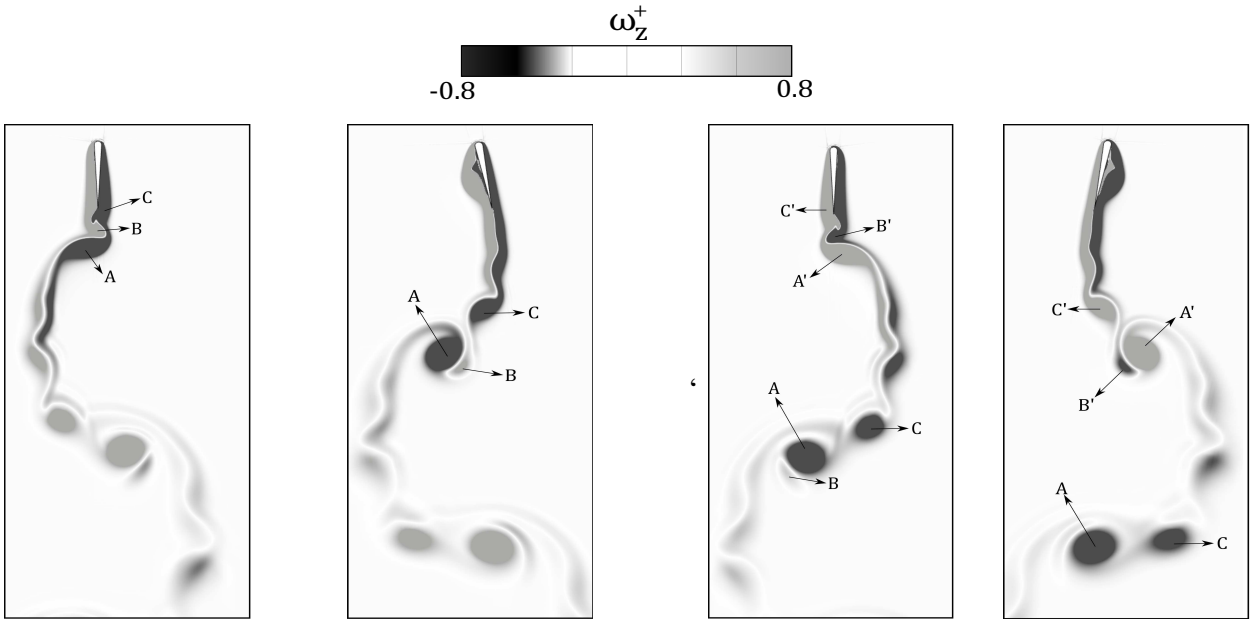

Figure 5.2: Contours of ω_z^+ depicting 2P+2S wake mode at (a) $t = 0$, (b) $t = T/4$, (c) $t = T/2$ and (d) $t = 3T/4$.

gion compared to that observed at lower ϕ. This again demonstrates that even though a symmetry existed for the propulsive performance characteristics in $\phi - St_c$ phase-space diagram, the wake modes do not depict symmetry in their phase-space diagram with respect to their transition features. A more qualitative investigation into visualization of wake modes and mean flow fields could further provide new insights into physical mechanisms that coincide with changes in propulsive performance. This discussion follows below with respect to increase in reduced frequency and phase offset.

We begin by a detailed assessment of the wake at our lowest reduced frequency and aim to understand the dominant wake modes and their transitions that are observable in Figure 5.1(b). The shedding events for a 2P+2S wake formation at $St_c = 0.16$ and $\phi = 0^\circ$ can be qualitatively described using snapshots of spanwise vorticity (ω_z^+) in a single oscillation cycle in Figures 5.2(a)-5.2(d). At the start of the cycle ($t = 0$), a developed TEV structure identified as 'A' forms a couple with a weak counter-rotating TEV structure, 'B'. Note that 'A' was formed in the previous half shedding cycle. Both these structures are then shed at $t = T/4$, which coincides with the formation

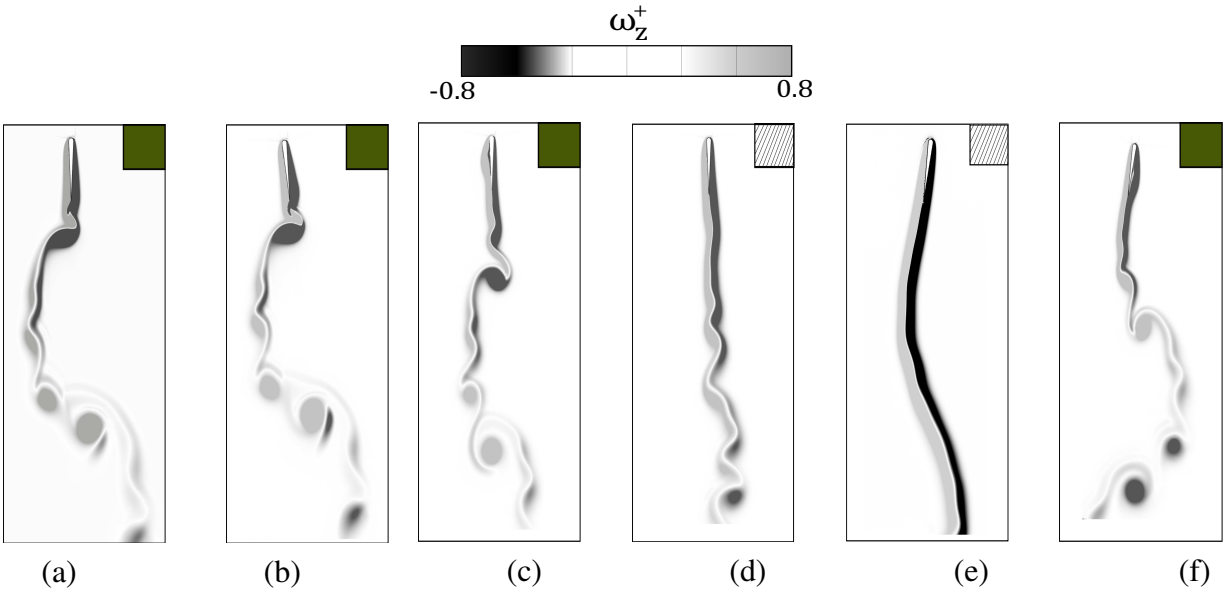

Figure 5.3: Wake modes for increasing ϕ at $St_c = 0.16$. (a)-(f) presents ϕ corresponding to 0°, 90°, 180°, 225°, 270° and 315°, respectively. The color codes refer to the phase map of wake modes, represented in the Figure 5.1(b).

of a *LEV* structure, named 'C' in Figures 5.2. This *LEV* detaches from the foil and follows the couple formed by 'A' and 'B'. These series of events are similarly repeated for the second half of the oscillation cycle, although the sign of vortices are reversed. These are depicted in Figures 5.2(c) and 5.2(d) as structures 'A′', 'B′' and 'C′'. Since there are two paired (or coupled) and two single vortices shed in one oscillation cycle, the wake resembles that of a 2P+2S mode (Williamson and Roshko, 1988). This mode was also observed previously by Schnipper et al. (2009) for a purely pitching foil, where 2P+2S configuration existed far downstream the wake. For the current study, however, the weaker *TEV*s that are formed in their half shedding cycle, namely 'B' and 'B′', diffuse quickly, such that only *TEV*s and *LEV*s with similar direction of rotation (vorticity sign) are advected downstream. This can be an implication of the coupled motion considered here, which lead to the generation of a weaker trailing edge structure in a half oscillation period. Since this motion is directly dependent on the phase offset, it is also intuitive that increasing ϕ poses some effects on the near wake formation. The mid- and far-wake interactions are not considered here since the cases corresponding to this reduced frequency do not depict any major transition in propulsive performance (Figure 5.1a) or the wake (Figure 5.1b).

To further analyze the effects of ϕ at $St_c = 0.16$, Figure 5.3 depicts the near 2P+2S and *wBvK* wake for $0° \leq \phi \leq 315°$. At $\phi = 0°$, $90°$ and $180°$ in Figure 5.3(a-c), we observe an apparent resemblance to the shedding events described earlier in Figure 5.2, although the structures that start to shed have a good alignment with the wake centerline for $\phi > 0°$. Further, the weaker vortex of the 2P pair appears to diffuse much earlier for $\phi = 180°$ in Figure 5.3(c) compared to $\phi = 0°$ and $90°$ in Figure 5.3(a) and 5.3(b)). At $\phi = 225°$ in Figure 5.3(d), a *wBvK* wake is evident, whereas noticeable formation or shedding of near wake structures are not observed. The separated shear layer remains undisturbed until an initial instability starts to develop at some distance downstream of the trailing edge, similar to the mechanism discussed by Lentink et al. (2008). This lack of instability in the wavy shear layer is also apparent for the case of $\phi = 270°$ in Figure 5.3(e), where even the initial instability does not develop as it does for the case of $\phi = 225°$ in Figure 5.3(d). Furthermore, the shedding events at $\phi = 315°$ in Figure 5.3(f) appear to look similar to those observed previously for $\phi < 180°$ in Figure 5.3(c). It is apparent that the heave velocity is quite low at such low St_c, while the foil experiences a decrease in α_o with increasing ϕ from $90°$ to $270°$. Van Buren et al. (2019) also observed a maximum value of α_o corresponding to the phase offset of $90°$, which decreased to a minimum at $\phi = 270°$. Thus, decreasing α_o with increasing ϕ to $270°$ would reduce the possibility of shear layer roll up, and hence lead to the absence of any dominant vortex formations for the *wBvK* wake mode.

Qualitative and quantitative assessment of $\overline{u_x}/U_\infty$ is further presented and described using Figure 5.4(a-c) for increasing ϕ from $0°$ to $90°$. Since this range of ϕ was observed to be characterized by only $2P+2S$ mode, we do not observe substantial differences in the mean flow. The slight velocity excess along the wake centerline, ahead of $X^+ = 3.75$, also appears consistent for increasing ϕ in Figure 5.4(a-c). However, the centerline velocity appears to be slightly lower at $x^+ = 1.875$, compared to the freestream, which coincides with the slight increase in drag production (see Figure 5.1(a)) with increasing ϕ from $45°$ to $90°$. Overall, the velocity excess observed in Figure 5.4(a-c) is not sufficient to counteract the viscous drag of the foil and hence fails to produce a net thrust at $St_c = 0.16$.

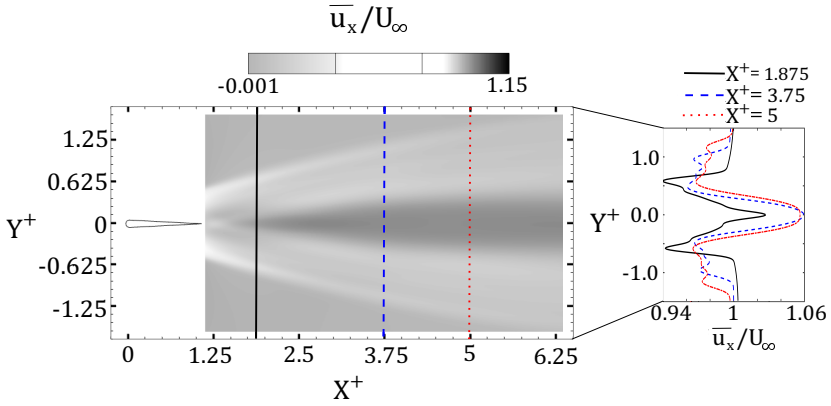

(a)

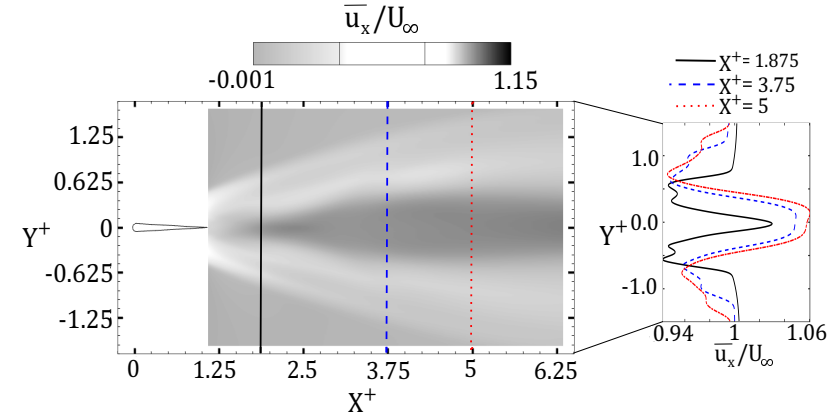

(b)

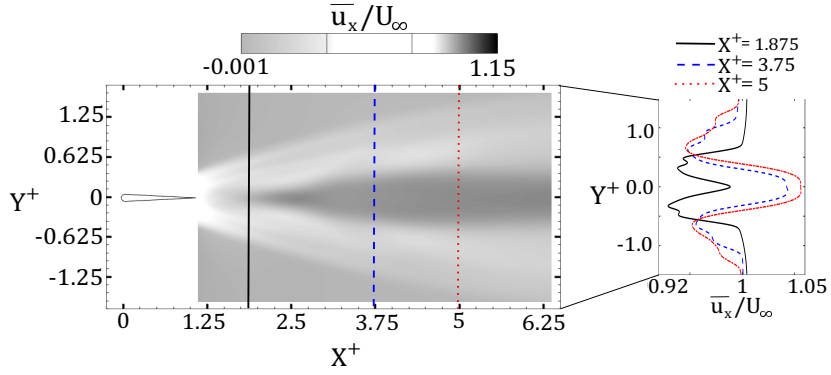

(c)

Figure 5.4: Contours for $\overline{u_x}/U_\infty$ for ϕ = (a) 0°, (b) 45° and (c) 90°, corresponding to $St_c = 0.16$. Variation of $\overline{u_x}/U_\infty$ along the cross-stream direction, at different streamwise locations, are also shown alongside each contour.

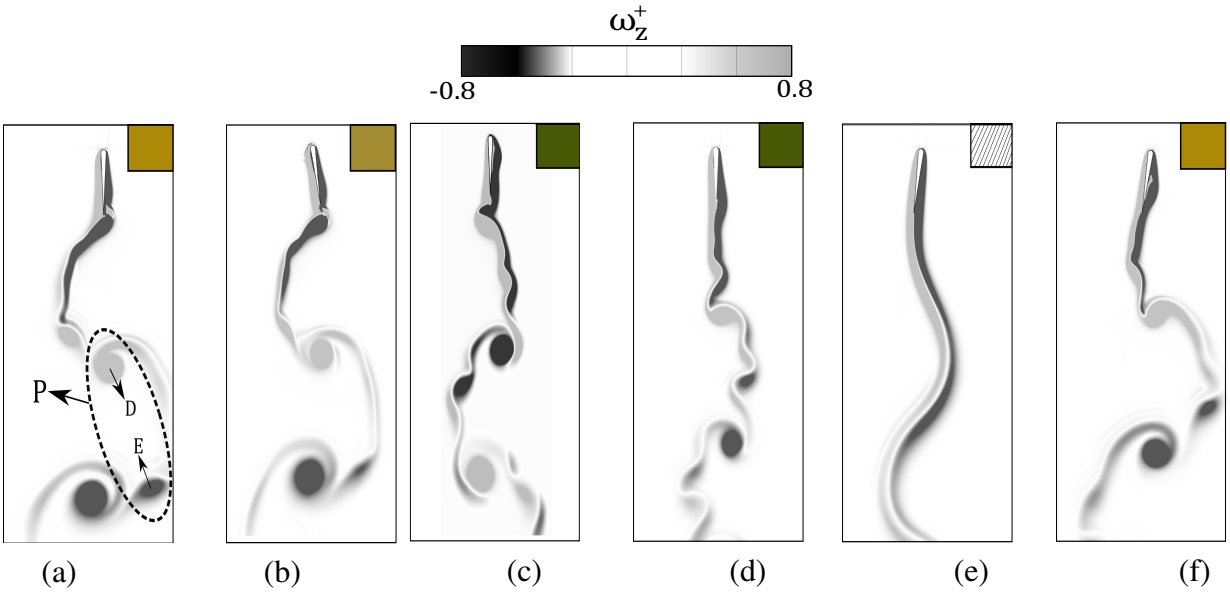

Figure 5.5: Wake modes for increasing ϕ at $St_c = 0.24$. (a)-(f) presents ϕ corresponding to 0°, 90°, 180°, 225°, 270° and 315°, respectively. The color codes refer to the phase map of wake modes, represented in the Figure 5.1(b).

Increasing St_c to 0.24 modifies the wake topology. For example, the wake for the case of $\phi = 0°$ and 90° in Figure 5.1(b) can now be characterized by a 2P mode where two vortex pairs formed by counter-rotating vortices are shed in one oscillation cycle. This mode is visualized in Figure 5.5, where the wake corresponding to increasing ϕ are shown. The formation mechanism for such 2P mode was also explained by Schnipper et al. (2009), and therefore it is not discussed here for brevity. However, the pair of vortices generally formed in a 2P mode can have a downstream or upstream pointed configuration (Schnipper et al., 2009), or they can be horizontally aligned with the wake centerline (Hultmark et al., 2007). Schnipper et al. (2009) indicated that a downstream pointed configuration of paired vortices yields thrust, which could explain why they are employed by biological species for underwater propulsion. They, however, only observed an upstream pointed configuration, which resulted in drag production. Hultmark et al. (2007) later described the existence of downstream and neutral (or horizontal) pointing configuration for the 2P mode in the wake of a robotic lamprey, which resulted in a small thrust generation. Therefore, this could be a unique observation here that reveals the existence of certain phase-space regions, in which foils experience thrust generation with a downstream pointing 2P wake mode.

For the wake modes corresponding to $St_c = 0.24$ in Figure 5.5, the pair 'P' that is formed by vortices 'D' and 'E' has a greater inclination pointing upstream (see Figure 5.5a). This coincides with drag production by the foil which was imminent earlier for all phase-offsets at $St_c = 0.24$ in Figure 5.1(a). For $\phi = 180^\circ$ in Figure 5.5(c), the 2P mode appears to transition back to a 2P+2S mode, as seen previously for $St_c = 0.16$. This transition coincides with the change of motion profile in such a way that the leading edge possesses a greater translating amplitude compared to the trailing edge, while also leading to a lower α_o. This heave dominated motion at low St_c further explains the shedding of vortices in better alignment with the wake centerline. This occurs on account of very weak TEV formation and absence of any dynamic stall separation of LEVs. The wake at $\phi = 270^\circ$ in Figure 5.5(e) resembles a $wBvK$ mode with an undisturbed shear layer without dominant perturbations. For $\phi = 315^\circ$ in Figure 5.5(f), the wake transitions back to a 2P mode. Based on the wake characterization for both $St_c = 0.16$ and 0.24, it is apparent that the flow profile is more streamlined between $90^\circ < \phi \leq 270^\circ$, which is either dominated by a 2P+2S or $wBvK$ mode. The wake mode transition map in Figure 5.1(b) and respective shedding events depicted at $St_c = 0.16$ and 0.24 reveal that α_o does not have a significant impact on transitioning the wake mode for $\phi \leq 180^\circ$. Besides, the wake modes and their characteristic transitions at these lower reduced frequencies do not coincide with any transition to thrust production in Figure 5.1(a). This further demonstrates that differences in shedding of vortex structures, on account of changes in motion profile, does not seem to have a one-to-one correspondence with the transition in propulsive performance of oscillating foils. However, we do observe an increase in drag production with increasing ϕ to 90°. It would therefore be interesting to see if the mean flow fields are affected by changes in ϕ from $0^\circ \leq \phi \leq 90^\circ$, where no substantial changes in the wake mode configuration are apparent.

The quantitative assessments of the $\overline{u_x}/U_\infty$ along the cross-stream wake at three streamwise locations ($X^+ = 1.88$, 3.75 and 5) are shown in Figure 5.6 for $\phi = 0^\circ$, 45° and 90°. At $\phi = 0^\circ$ and 45° in Figure 5.6(a) and 5.6(b), a relatively weak thrust jet is observed along the wake centerline, which reaches an asymptotic value at $X^+ = 5$. This weak jet can be seen even at $X^+ = 1.88$.

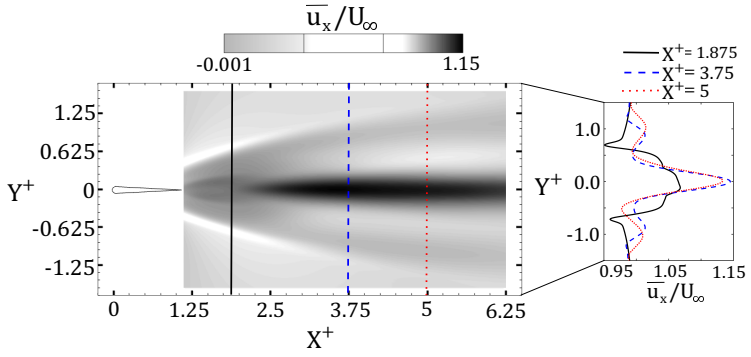

(a)

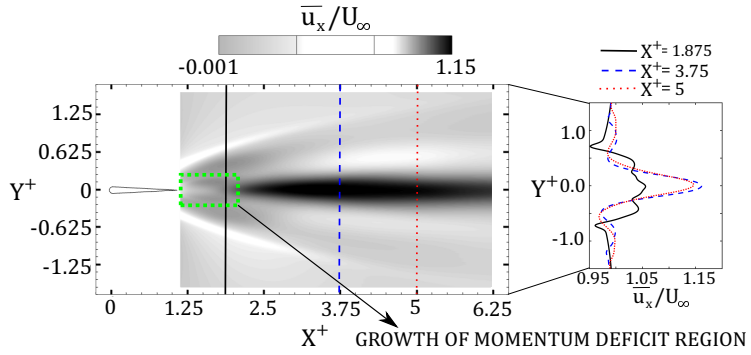

(b)

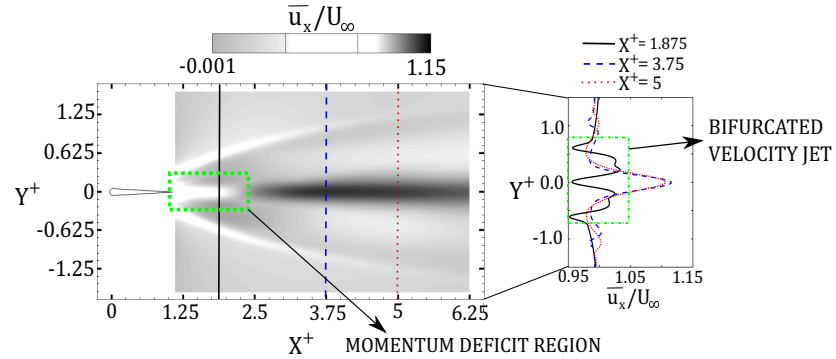

(c)

Figure 5.6: Contours for $\overline{u_x}/U_\infty$ for ϕ = (a) 0°, (b) 45° and (c) 90°, corresponding to $St_c = 0.24$. Variation of $\overline{u_x}/U_\infty$ along the cross-stream direction, at different streamwise locations, are also shown alongside each contour.

However, the velocity excess along the wake centerline reduces at $\phi = 45^\circ$ in Figure 5.6(b), in comparison to that observed for $\phi = 0^\circ$ in Figure 5.6(a). The contour plot of $\overline{u_x}/U_\infty$ also shows the growth of a velocity or momentum deficit region in Figure 5.6(b). At $\phi = 90^\circ$ in Figure 5.6(c), we observe a region that is characterized by a bifurcated jet profile at around $X^+ = 1.88$. This bifurcation results in a large mean momentum deficit just behind the foil trailing edge, as observed in Figure 5.6(c). This deficit, however, is not large enough to counter the viscous drag on the foil. This explains the increase in drag production with increasing ϕ from 0° to 90° at $St_c = 0.24$, which was further apparent from quantitative assessments in Figure 5.1(a). This observation also coincides with a reduction in the trailing edge amplitude as ϕ increases from 0° to 90°. This will provide less time and a shorter distance for the production of vorticity and roll up of the separated shear layer at the tip, on account of the pitching motion. Thus, this contributes towards development of trailing edge vortices that have low circulation strength and small core size in the near wake. As these vortices shed, the transfer of momentum to the foil are not large enough, compared to the existing viscous drag, which favors drag production.

Evolution of the wake development over time is shown in Figure 5.7 for the case of $St_c = 0.24$ at increasing phase-offset from 0° to 90°. A developed vortex-pair formed by counter-rotating structures during the initial stages of an oscillation cycle are depicted and named P_1 for the case of $\phi = 0^\circ$ (Figure 5.7(a)), P_2 for the case of $\phi = 45^\circ$ (Figure 5.7(b)), and P_3 for the case of $\phi = 90^\circ$ (Figure 5.7(c)). The vortex structures that formed the pairs are also identified as D_1 and E_1 for pair P_1, D_2 and E_2 for pair P_2, and D_3 and E_3 for pair P_3. The legs connecting each counter-rotating vortex are observed to bend more drastically towards the wake centerline with increasing ϕ from 0° to 90°. The quantitative estimates of the centers of clockwise rotating vortex structures, i.e. E_1, E_2 and E_3, are $(3.41, 0.72)$, $(3.12, 0.62)$ and $(2.53, 0.58)$, respectively. The procedure to estimate these locations included first finding the coordinates of maximum vorticity magnitude, that is $|\omega^+|$, on a rectangular integration contour window, surrounding the vortex structure. Similar methodology was also followed by Godoy-Diana et al. (2009). This closer and gradual alignment of the pair located nearest to the trailing edge with the wake centerline possibly leads to the growth

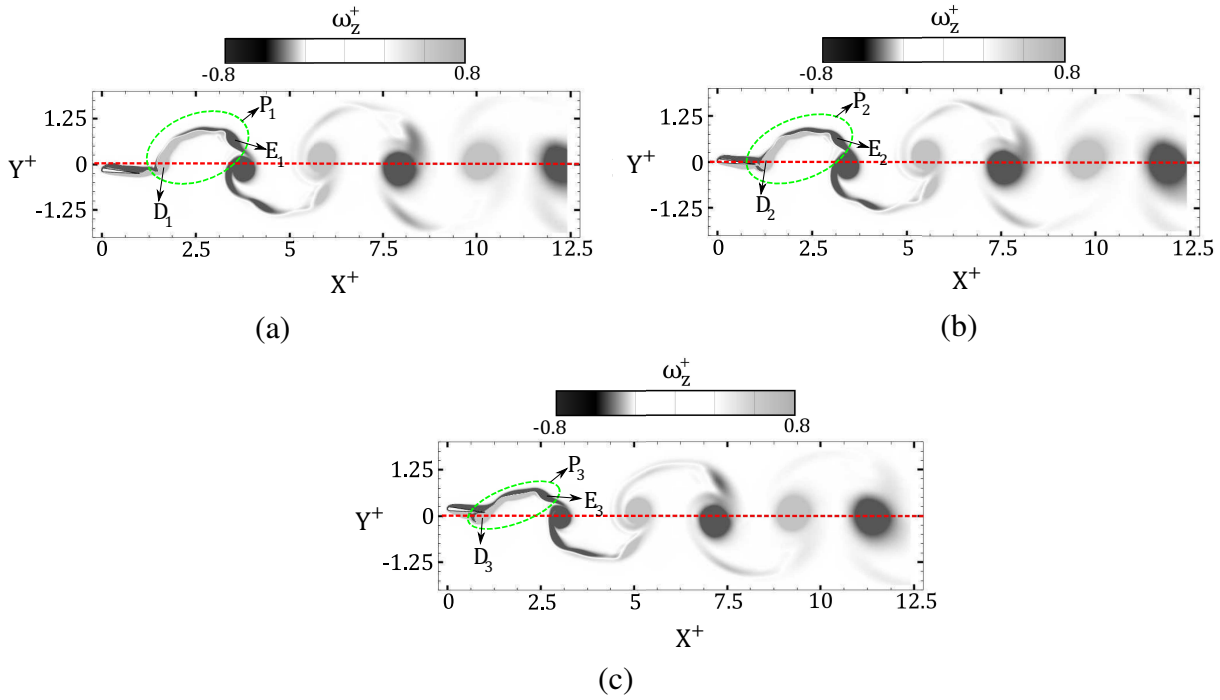

Figure 5.7: Dynamic interactions of vortex structures identified using contours of non-dimensional spanwise vorticity ($\omega_z^+ = \omega_z c/U_\infty$), in the wake corresponding to (a) $\phi = 0^\circ$, (b) $\phi = 45^\circ$ and (c) $\phi = 90^\circ$. St_c corresponds to 0.24. Red dotted line represents the wake centerline.

of a small velocity deficit region in the contours of $\overline{u_x}/U_\infty$ for the case of $\phi = 90^\circ$ in Figure 5.6(c). The vortex E_3 along with the neighboring structure with a similar sense of rotation provided a stronger induced velocity component in the direction opposing that of the freestream. Thus, there is a region formed with a mean momentum deficit. For pairs P_1 and P_2, clockwise vortices E_1 and E_2 are located at a relatively longer separation distance from the wake centerline, compared to E_3. Hence, there is a weaker component of the resultant induced velocity acting in the opposite direction of the freestream, and thereby causing a relative decrease in the mean momentum deficit compared to the case of $\phi = 90^\circ$ in Figure 5.6(c). It is important to note that the weak thrust generating jet observed for all three cases is due to the downstream merger of vortex structures with a similar sense of rotation. This jet begins at a farther streamwise distance from the foil with increasing ϕ from 0° to 90°. This created a velocity excess similar to the mechanism observed for the reverse Von Kármán vortex street (Koochesfahani, 1989).

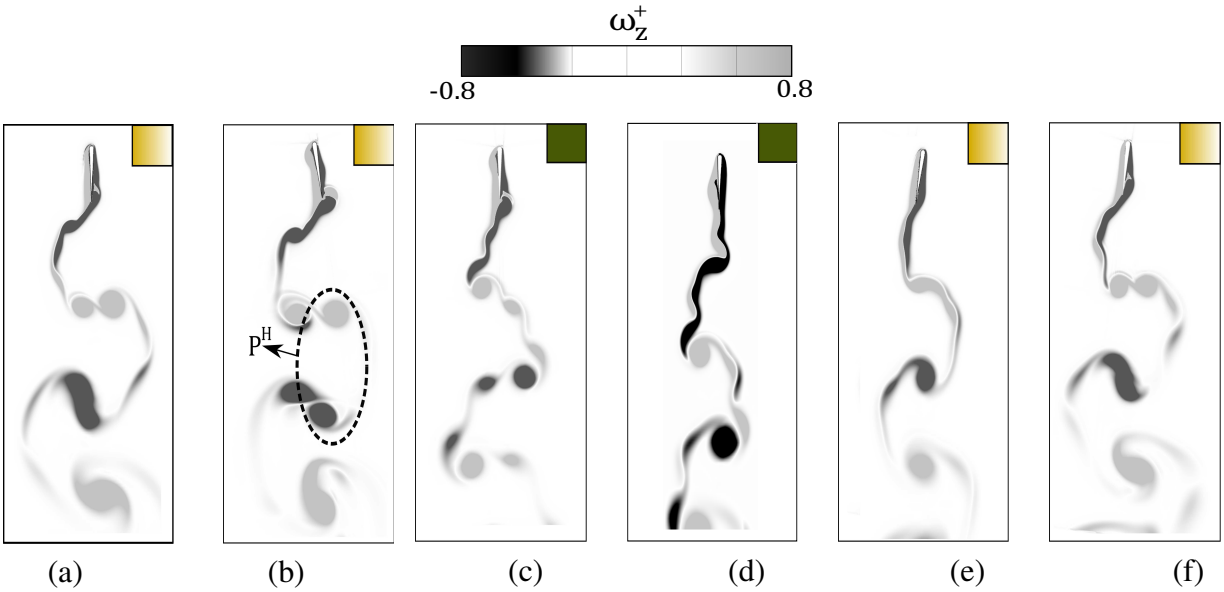

Figure 5.8: Wake modes for increasing ϕ at $St_c = 0.32$. (a)-(f) presents ϕ corresponding to 0°, 90°, 180°, 225°, 270° and 315°, respectively. The color codes refer to the phase map of wake modes, represented in the Figure 5.1(b).

Contour plots in Figure 5.8 show that the wake at $St_c = 0.32$ is still dominated by a 2P mode at $\phi = 0°$ and 90° (see Figure 5.8(a) and 5.8(b)), which was depicted earlier in Figure 5.1(b). However, the spatial configuration of the pairs are horizontally aligned with the wake centerline. We refer to such 2P mode as $2P^H$, which signifies the horizontal pair P^H that is shed per half oscillation cycle in Figure 5.8(b). The performance and wake transition maps (Figures 5.1a and 5.1b) reveal that the $2P^H$ configuration actually results in a thrust generation only for $\phi = 0°$, 45°, 270° and 315°. The oscillations at $\phi = 90°$ and 120° results in drag production, while still depicting a $2P^H$ configuration. This provides further support to our hypothesis that wake modes are not always a good indicator for the propulsive performance of oscillating foils. However, the differences in performance demands more investigation into the dynamics of near wake structures observed in Figures 5.8(a) and 5.8(b). At $\phi = 0°$ in Figure 5.8(a), the clockwise neighboring vortices appear to merge earlier compared to those observed at $\phi = 90°$ (Figure 5.8b). This early merger tilts the pair slightly, which results in a component of induced velocity pointing downstream. Thus, in contrast to the drag production observed for upstream pointed pairs at lower St_c, we now have a $2P^H$ configuration that coincides with thrust production. Further at $\phi = 90°$ in Figure 5.8(b), the merger

of clockwise vortices of neighboring pairs appears to be delayed, which lack any induced velocity component in the downstream direction. This early merger is also observable later for $\phi = 270^\circ$ and 315° in Figure 5.8(e) and 5.8(f), which again yields thrust. At $\phi = 180^\circ$ and 225° in Figure 5.8(c) and 5.8(d), the 2P^H mode transitions back to a 2P+2S mode, as was previously evident for $St_c = 0.24$. It can therefore be deduced that $St_c = 0.32$ act as a threshold, below which the phase offset corresponding to 270° does not lead to any formation of vortical structures, and hence a *wBvK* mode. Zheng et al. (2019) also reported that the α, and its peak, increases with increasing oscillation frequency. This promotes a flow perturbation that is strong enough to form coherent structures. They further described that the growth of the leading edge vortex is more noticeable with increasing α, and contributes to the transition of *wBvK* mode at low frequency to either $2P$, $2P+2S$ or $2S$ mode at higher frequencies of oscillation. We observe a similar feature at $\phi = 270^\circ$ and $St_c < 0.32$, where we do not observe any noticeable growth in the *LEV* (see Figure 5.3(e) and 5.5(e)). However at $St_c = 0.32$, the shear layer roll-up and *LEV* growth along the foil boundary is more evident compared to the cases at lower St_c (see Figure 5.8(e)). It is also important to mention here that although $\phi = 270^\circ$ is a critical case on account of yielding the most propulsively efficient motion profile for biological fin propulsion (Van Buren et al., 2019), we observe no propulsive gain at $\phi = 270^\circ$ for $St_c < 0.32$. Van Buren et al. (2019) provided quantitative evidence that described how the motion profile at $\phi = 270^\circ$ is associated with a lateral acceleration of the oscillating foil. This acceleration contributed to generation of a force component that assisted the foil rotation, and therefore lowered the input power. This was observed to be the primary reason for achieving a higher efficiency at $\phi = 270^\circ$. However, since reduced frequency lower than 0.32 does not reveal any thrust generation at $\phi = 270^\circ$, it is unlikely that the lateral acceleration and its associated positive impacts on lowering the input power would yield any propulsive benefits.

Figure 5.9 depicts useful information regarding the apparent effects on mean streamwise velocity field at $St_c = 0.32$ for increasing ϕ from 0° to 90°. This provides further insights into how mean flow is manipulated by changes in motion profile, thus leading to an increase in drag production (Figure 5.1a). These were also found consistent with observations noted earlier at $St_c =$

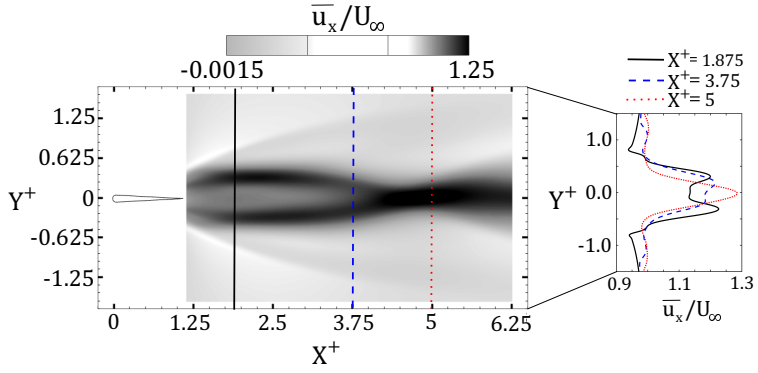

(a)

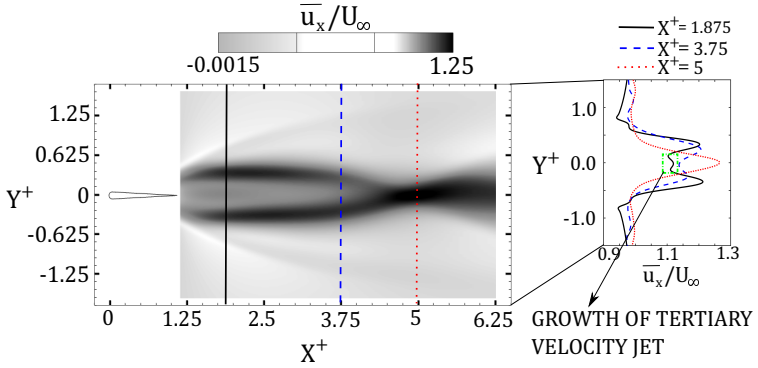

(b)

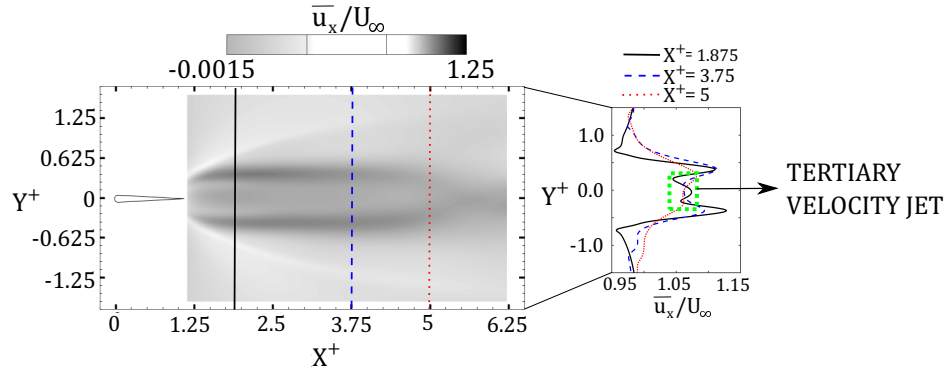

(c)

Figure 5.9: Contours for $\overline{u_x}/U_\infty$ for ϕ = (a) 0°, (b) 45° and (c) 90°, corresponding to $St_c = 0.32$. Variation of $\overline{u_x}/U_\infty$ along the cross-stream direction, at different streamwise locations, are also shown alongside each contour.

0.24. A similar bifurcated thrust jet in the near wake ($X^+ = 1.88$) is apparent for $\phi = 0°$, $45°$ and $90°$ in Figure 5.9(a-c), compared to previous observations for the case of $\phi = 90°$ at $St_c = 0.24$. However, the bifurcation for the new cases appears to be extended and visible even at $X^+ = 3.75$. Increasing ϕ from $0°$ to $90°$ further depicts an increased momentum deficit region near the wake centerline ($Y^+ = 0$), which also extends farther downstream. This also coincides with the thrust to drag transition observed in Figure 5.1(a). Besides, a tertiary peak in the streamwise mean velocity also appears at $X^+ = 1.88$ for the case of $\phi = 45°$ and $90°$ in Figure 5.9(b) and 5.9(c), although the magnitude of this tertiary peak is relatively small compared to the primary bifurcation. We also observed a consistent weakening of the bifurcated velocity jets as ϕ increases from $0°$ to $90°$. This is apparent from the contour plots of $\overline{u_x}/U_\infty$ presented in Figure 5.9.

As described above for the mean flow fields corresponding to $St_c = 0.24$ and 0.32, we observe a consistent behavior in the form of breaking up the thrust jet with increasing ϕ from $0°$ to $90°$. This shows a potential feature of a characteristic route to transition in propulsive performance, while the apparent number of vortex structures that shed and the resulting near wake mode remains the same with increasing ϕ upto $90°$. More details with regards to the changes in vortex interaction and spatial arrangement could hint at mechanisms that lead to the above observed features in the mean flow-field.

Figure 5.10 provides some insights into the dynamics of near wake structures that potentially lead to an extension of the momentum deficit region and a delay in the reattachment of bifurcated velocity jets with increasing ϕ from $0°$ to $90°$. Downstream of $X^+ = 5$, it is evident in Figure 5.10(a-c) that vortex structures with a similar sense of rotation merged for all the three cases. These merged structures are highlighted as 'M_1' and 'N_1' for the case of $\phi = 0°$ in Figure 5.10(a), 'M_2' and 'N_2' for the case of $\phi = 45°$ in Figure 5.10(b), and 'M_3' and 'N_3' for the case of $\phi = 90°$ in Figure 5.10(c). We observe that structures 'M' and 'N', which correspond to the wake of $\phi = 0°$ and $45°$ in Figure 5.10(a) and 5.10(b), do not align perfectly with the wake centerline, and thus result in a configuration resembling *rBvK* mode. However for $\phi = 90°$in Figure 5.10(c), structures 'M_3' and 'N_3' better align with the wake centerline, and hence fail to produce enough momentum

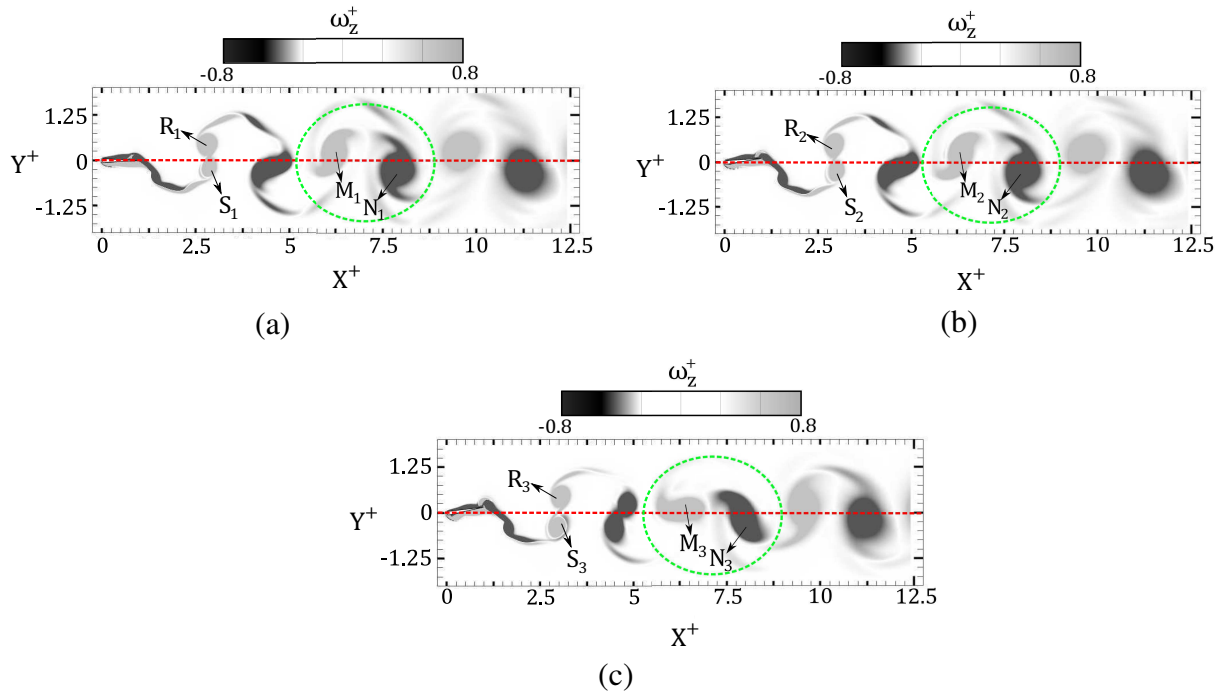

Figure 5.10: Dynamic interactions of vortex structures identified using contours of non-dimensional spanwise vorticity ($\omega_z^+ = \omega_z c/U_\infty$), in the wake corresponding to (a) $\phi = 0°$, (b) $\phi = 45°$ and (c) $\phi = 90°$. St_c corresponds to 0.32. Red dotted line represents the wake centerline.

excess to counter the viscous drag on the foil and produce thrust. Later, however, a configuration similar to the *rBvK* eventually appears as 'M_3' and 'N_3' advect downstream of $X^+ \approx 8.75$ in the case of $\phi = 90°$ in Figure 5.10(c). This also explains the delayed reattachment of mean bifurcated velocity jets, and an relatively extended momentum deficit region for the case of $\phi = 90°$ (see Figure 5.9(c)) compared to $\phi = 0°$ and 45° (see Figure 5.9(a) and 5.9(b)).

As the kinematics extend to $St_c = 0.40$ in Figure 7.4, the $2P^H$ mode is observed for the case of $\phi = 0°$ (see Figure 5.11(a)) with anti-clockwise vortex structures of neighboring pairs near the trailing edge appearing to interact through their vortex legs. This again contributes to merging of vortices with a similar sign of rotation, as observed previously for $St_c = 0.32$. This behavior also helps in transition of the wake towards a *rBvK* mode as the vortex structures advect downstream, which coincides with thrust generation. With increasing ϕ, a new $2P^D$ mode becomes prominent. Here, the counter-rotating vortex structures form and shed in a dipole configuration (P^D shown in Figure 5.11(b)) within one half shedding cycle. Such configurations have been vastly observed for

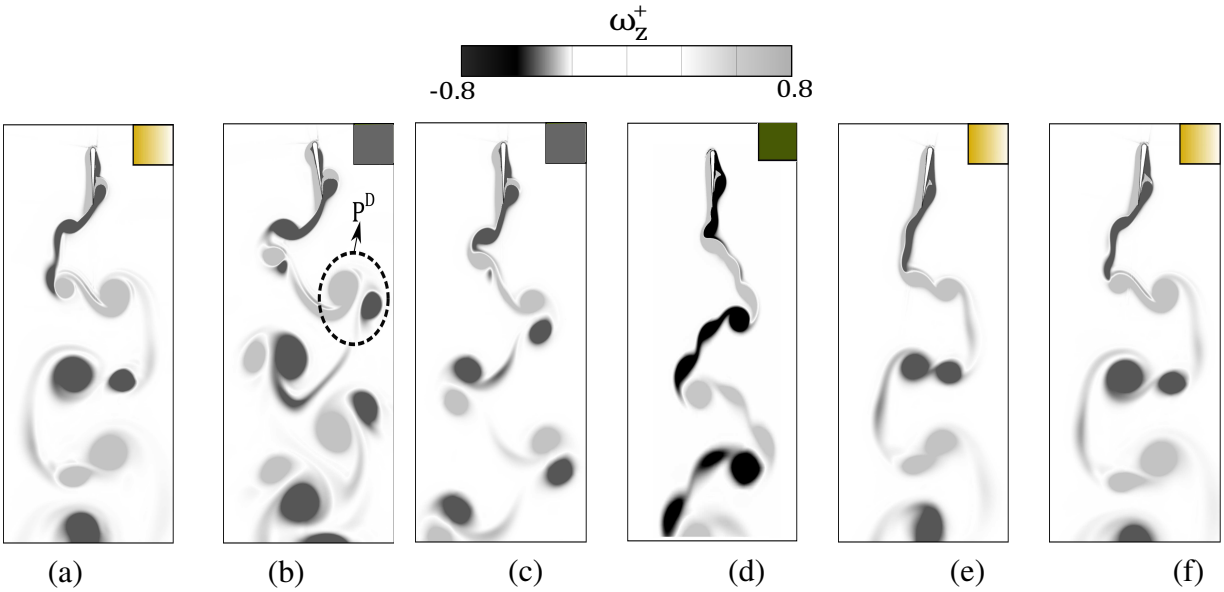

Figure 5.11: Wake modes for increasing ϕ at $St_c = 0.40$. (a)-(f) presents ϕ corresponding to 0°, 90°, 180°, 225°, 270° and 315°, respectively. The color codes refer to the phase map of wake modes, represented in the Figure 5.1(b).

asymmetric wakes (Cleaver et al., 2012; Calderon et al., 2014), although no apparent asymmetry is observed here. Increasing ϕ to 180° in Figure 5.11(c) further show an increased separation between the dipolar structures compared to those observed for $\phi = 90°$ in Figure 5.11(b), which move farther away from the wake centerline. Transition to 2P+2S is again evident for $\phi = 225°$ in Figure 5.11(d), which then transitions back to a $2P^H$ mode at $\phi = 270°$ and 315° in Figure 5.11(e) and 5.11(f). We again notice that the apparent transition of the wake mode from $2P^H$, observed at $\phi = 0°$, to $2P^D$ at $\phi = 45°$ does not coincide with the thrust to drag transition line in Figure 5.1(b). For $\phi = 270°$ and 315°, however, a consistent thrust generation occurs, which coincide with a similarity in terms of the near $2P^H$ wake mode as evident in Figure 5.11(e) and 5.11(f). These observations for $St_c = 0.40$ acts as another indicator that no vivid links are apparent between transitions in propulsive performance and vortex synchronization in the near wake region.

Looking at the profiles of $\overline{u_x}/U_\infty$ in Figure 5.12, there are no bifurcation of the centerline mean velocity jet at St_c= 0.40 for the cases of $\phi = 0°$, 45° and 90° (i.e. Figure 5.12(a-c) respectively). This is in contrast to the observations for lower St_c cases. However, dual momentum deficit regions appear in the very near wake region ($X^+ = 1.88$) with their magnitude increasing with increasing

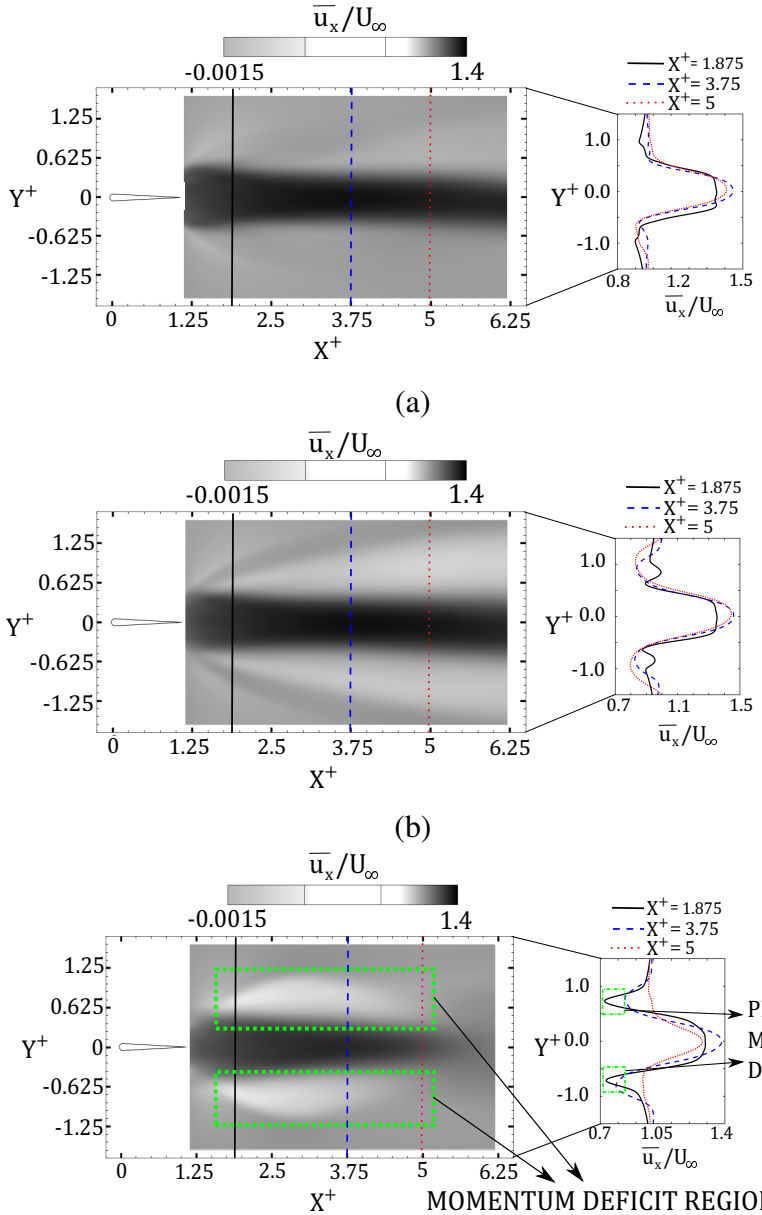

Figure 5.12: Contours for $\overline{u_x}/U_\infty$ for $\phi =$ (a) 0°, (b) 45° and (c) 90°, corresponding to $St_c = 0.40$. Variation of $\overline{u_x}/U_\infty$ along the cross-stream direction, at different streamwise locations, are also shown alongside each contour.

ϕ to 90°. These regions are clearly shown in Figure 5.12(c). At $\phi = 45°$ in Figure 5.12(b), we further observe the presence of two secondary peaks that do not appear for $\phi = 0°$ and 90° in Figure 5.12(a) and 5.12(c). This again signifies a bifurcation of the primary velocity jet, which begins with increasing ϕ above 0°. However, it is not strong or dominant enough compared to the observations from lower reduced frequency cases. The primary thrust generating jet also appears shortened at $\phi = 90°$ in Figure 5.12(c) compared to $\phi = 0°$ and 45° in Figure 5.12(a) and (b), which is not large enough to counter the viscous drag on the foil, thus coinciding with an overall drag production at this motion setting (Figure 5.1a). It is interesting to note the presence of such effects on the mean flow, and their coincidence with the transition in the wake mode from $2P^H$ to $2P^D$. However, further investigation is still needed to explain their characteristic dependence on each other.

Similar to the dynamics of near wake vortical interactions presented for the lower reduced frequency cases, Figure 5.13 depicts apparent dynamics of wake modes and their vortex structures at $St_c = 0.4$ for the cases of $\phi = 0°$, 45° and 90° (i.e. Figure 5.13(a-c) respectively). These further provide physical insights and reasoning behind the characteristic mean flow fields observed in Figure 5.12. For the case of $\phi = 0°$ in Figure 5.13(a), we observe a $2P^H$ mode that is well-evident prior to $X^+ \approx 6.25$. It is further apparent that the structure identified as 'F_1' in Figure 5.13a is stronger in terms of circulation strength and size, compared to the neighboring structure 'G_1' with a similar sense of rotation. Quantitative estimates of normalized circulation magnitude in terms of $|\Gamma^+| = \Gamma/(U_\infty c)$ revealed $|\Gamma^+_{F_1}| = 1.88$ and $|\Gamma^+_{G_1}| = 0.55$, while normalized vortex radii ($a^+ = a/c$) was observed to be $a^+_{F_1} = 0.46$ and $a^+_{G_1} = 0.23$. Here, the surface integral of the vorticity field on the rectangular contour window surrounding the vortex structure provided a reasonable estimate of the circulation strength. Extensive details of the process for estimating the circulation strength and size can also be found in previously published experimental and numerical studies (Godoy-Diana et al., 2009). On account of this significant difference in strength of circulation and presence of the stronger counter-rotating vortex above the wake centerline (i.e. 'F_1'), it is intuitive to see that a mean momentum excess is prevalent at a much earlier advective time, compared to the $2P^H$

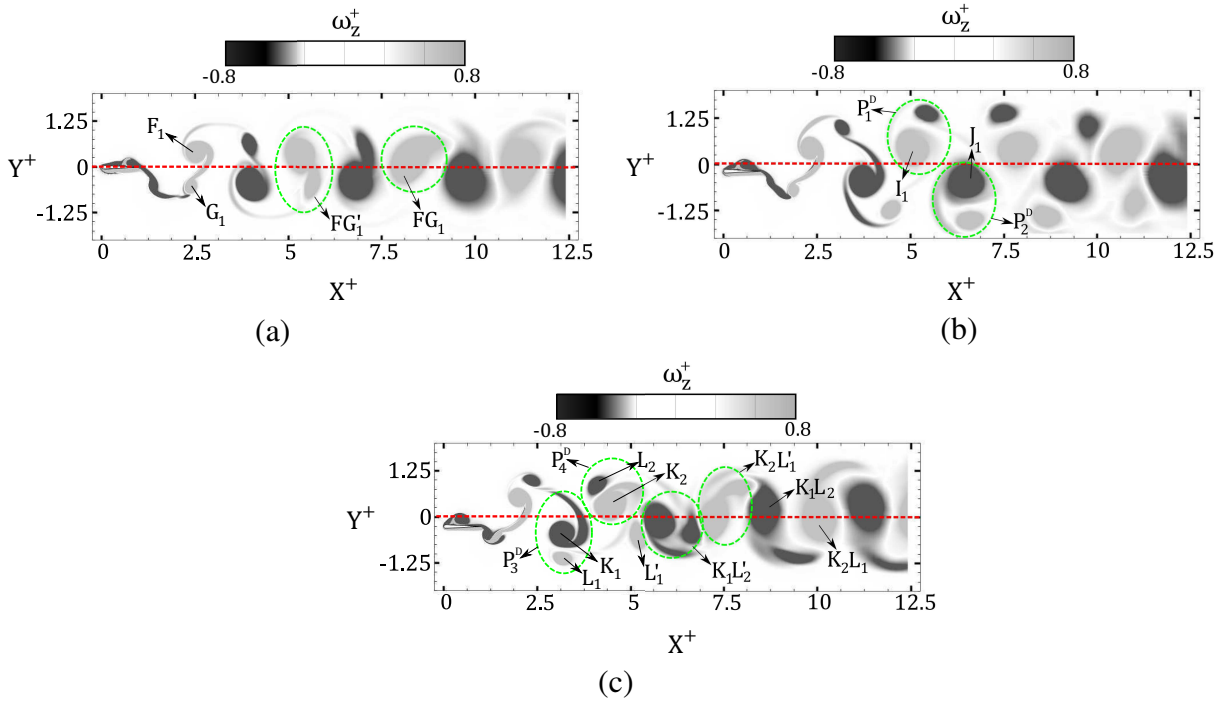

Figure 5.13: Dynamic interactions of vortex structures identified using contours of non-dimensional spanwise vorticity ($\omega_z^+ = \omega_z c/U_\infty$), in the wake corresponding to (a) $\phi = 0°$, (b) $\phi = 45°$ and (c) $\phi = 90°$. St_c corresponds to 0.4. Red dotted line represents the wake centerline.

mode observed previously for $St_c = 0.32$. We observed two vortex structures (i.e. R_i and S_i) of comparable strength, size and sense of rotation for St_c =0.32 in Figure 5.10(a-c), while also maintaining a symmetry in terms of position along the wake centerline. Particularly, the maximum difference between $|\Gamma^+|$ is 30% for structures R_1 and S_1 at $\phi = 0°$ in Figure 5.10(a), while it is below 12% for structures at $\phi = 45°$ and 90° in Figure 5.10(b,c). In comparison to the structures F_1 and G_1 observed here for $St_c = 0.4$, where the difference in $|\Gamma^+|$ is approximately 70%, the similar sign structures at $St_c = 0.32$ possess a lower difference in their circulation strength.

Furthermore, the process of coalescence begins as 'F_1' and 'G_1' advect downstream of $X^+ = 5$ in Figure 5.13(a). These half-merged and fully-merged configurations are termed as 'FG'_1' and 'FG_1', respectively. It is evident that even as the similar-sign structures coalesced, the wake resembles a reverse Von Kármán mode, which has been vastly associated with presence of a sustained mean thrust producing jet in previous studies (Godoy-Diana et al., 2008; Jones et al., 1996). This jet is observed in Figure 5.12(a). For $\phi = 45°$ in Figure 5.13(b), the dipolar configuration of 2P

pairs is clearly evident. It is further interesting to note that even though spatial arrangements of the 2P pairs are found different for $\phi = 0^\circ$ and 45° in Figure 5.13(a) and 5.13(b), the mean thrust producing jet is observed to be approximately similar for both in Figures 5.12(a) and 5.12(b), respectively. However, Figure 5.13(b) shows no apparent merger between vortex structures with similar sense of rotation, at least upto $X^+ = 12.5$. This appears to be in contrast to the early merger observed for the case of $\phi = 0^\circ$(Figure 5.13a). The vortex dipoles 'P_1^D' and 'P_2^D' are also marked in Figure 5.13(b). It is apparent that the vortex structure, marked 'I_1', has a stronger circulation ($|\Gamma_{I_1}^+| = 2.26$) compared to its coupled counter-rotating vortex ($|\Gamma^+| = 0.45$). Similarly, 'J_1' has a larger circulation ($|\Gamma_{J_1}^+| = 2.34$) compared to its coupled counter-part ($|\Gamma^+| = 0.62$) with an opposite sense of rotation compared to 'I_1'. This inherently leads to an induced velocity excess which had minimal contribution from the weaker vortex structure in each dipole. Later, as the dipoles advected downstream, they reorient such that the individual vortex structures with similar sense of rotation approach closer, and eventually merge at a farther downstream distance. At $\phi = 90^\circ$ in Figure 5.13(c), we observe a similar advection of dipolar configuration as seen for the case of $\phi = 45^\circ$ in Figure 5.13(b). However, the merger of vortex structures with a similar sense of rotation occurs much earlier compared to that in $\phi = 45^\circ$ in Figure 5.13(b).

To further understand this interaction, two dipoles are depicted in Figure 5.13(c) named 'P_3^D' and 'P_4^D'. The former is composed of counter-rotating structures 'L_1' and 'K_1', while the latter is composed of 'L_2' and 'K_2'. It is further noted that 'L_1' and 'L_2' have a smaller circulation strength ($|\Gamma_{L_1}^+| = 0.61$ and $|\Gamma_{L_2}^+| = 0.49$), compared to 'K_1' and 'K_2' ($|\Gamma_{K_1}^+| = 1.87$ and $|\Gamma_{K_2}^+| = 1.77$). As these structures advect downstream, an interaction between the clockwise vortices of neighboring dipoles occur. This process is depicted as 'K_1L_2'' at $X^+ \approx 6.25$. The anti-clockwise structures are also observed to interact and the merge later. This interaction is depicted in terms of structures 'K_2' and 'L_1'', which is identified as 'K_2L_1'' in Figure 5.13(c). The intermediary formations 'K_1L_2'' and 'K_2L_1'', which constitutes vortices with a similar sense of rotation, eventually merge to form individual structures, 'K_2L_1' and 'K_1L_1'. These merged vortex structures further contribute to a resulting wake that resembles a standard Von Kármán vortex street. This is observable downstream

of $X^+ \approx 10$ in Figure 5.13(c). Hence, the thrust generating jet loses its strength quite early on in the case of $\phi = 90^\circ$ (see Figure 5.12c). The closer alignment of the dipole structures with the wake centerline in case of $\phi = 90^\circ$ in Figure 5.13(c), compared to $\phi = 45^\circ$ in Figure 5.13(b), results in contraction of the resultant velocity excess region across the cross-stream wake, which is a reasonable justification for the formation of large dual momentum deficit regions in Figure 5.12(c).

Figures 5.14(a)-5.14(f) depicts the wake modes corresponding to $St_c = 0.48$. A $2P^D$ configuration is still apparent for the cases of $\phi = 90^\circ$, 180° and 225° in Figure 5.14(b), 5.14(c) and 5.14(d), respectively. Moreover, a transition of $2P^H$ mode (observed at f^* =0.32 and 0.4) to the *rBvK* mode is observed for $\phi = 0^\circ$, 270° and 315° in Figure 5.14(a), 5.14(e) and 5.14(f), respectively. This behavior is due to increased reduced frequency motivating the early merger of neighboring vortex structures with the same sense of rotation. The mechanism for merger is similar to the description provided by Schnipper et al. (2009), where transition of the 2P to 2S mode occurred with increasing Strohaul number. Discussions with respect to the mean flow fields at $St_c = 0.48$ are not included here since the observations that highlighted the mechanism for drag production are found mostly similar to those observed for $St_c = 0.4$. Moreover, it is important to note here that this reduced frequency is not near the drag-thrust transition boundary, identified in Figure 5.1(a), and hence it is not deemed of much importance within the scope of the present study. The flow fields corresponding to the *rBvK* mode have also been well studied and discussed previously (Godoy-Diana et al., 2008; Deng et al., 2015). It is clearly evident that even at higher reduced frequencies (i.e. St_c =0.40 and 0.48), phase offsets in the range of $\phi < 90^\circ$ and $\phi > 225^\circ$ depict different configuration of wake modes (such as $2P^H$, $2P^D$ and 2S) while showing similarity in terms of thrust production. Thus, a lack of direct correspondence between the transition in propulsive performance and the wake modes is apparent throughout our phase-space representations in Figure 5.1.

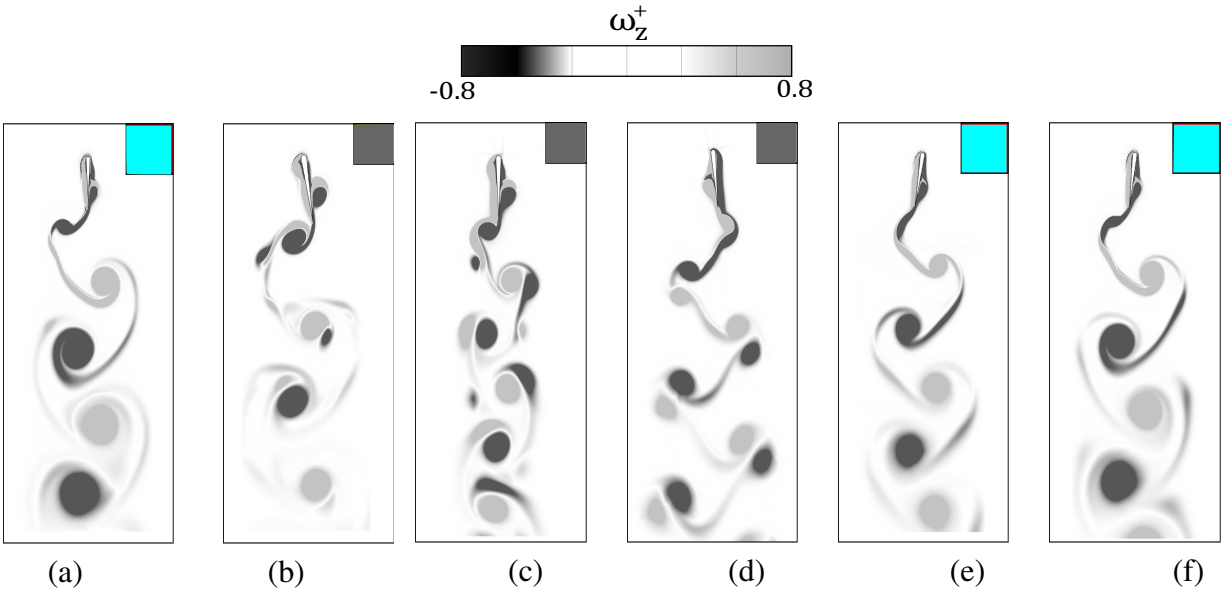

Figure 5.14: Wake modes for increasing ϕ at $St_c = 0.48$. (a)-(f) presents ϕ corresponding to 0°, 90°, 180°, 225°, 270° and 315°, respectively. The color codes refer to the phase map of wake modes, represented in the Figure 5.1(b).

5.4 Summary

This chapter numerically evaluated the transition of propulsive performance and characteristic wake modes for an oscillating foil in combined heaving and pitching motion. The St_c and ϕ were varied in the range of $0.16 \leq St_c \leq 0.64$ and $0° \leq \phi \leq 315°$. The performance maps in the form of $\phi - St_c$ phase space diagram with depicted transition lines showed two drag-thrust transition lines that were symmetric along $\phi = 180°$. Cases corresponding to $\phi > 90°$ and $\phi < 225°$ were mostly dominated by drag production for the entire range of reduced frequency.

Investigation into apparent transitions of wake mode configuration, within our $\phi - St_c$ phase-space, revealed no vivid and direct correspondence with the transitions in propulsive performance characteristics. This was consistent with the recent hypothesis that wake topology described in terms of the number of shed vortex structures per oscillation cycle, was not a good measure for directly evaluating the performance of oscillating foils (Smits, 2019). For the drag dominant settings, several wake mode configurations ranging from 2P+2S, *wBvK* and 2P were identified for increasing phase offset, and reduced frequency less than 0.32. No apparent transition in propulsive

performance was identified to co-exist with changes in the wake modes. This process was also consistent for $St_c > 0.24$ in the range of $90^\circ \leq \phi \leq 225^\circ$, where no transition in drag dominated performance coincided with any visible changes in the wake topology. These changes were evident in the form of different spatial configuration of 2P modes that included $2P^H$ and $2P^D$, which were characterized by either the alignment of vortex pair with the wake centerline or formation of dipoles, respectively. Even while noticing a transition to thrust generation, the wake modes showed similarities with the configurations observable for drag dominated regimes.

The bifurcation in mean centerline velocity jet was observed to coincide with an increased momentum deficit in the near wake. Therefore, it is a characteristic of a plausible route to drag production. The increase in drag was quite noticeable from the performance phase map with increasing ϕ from 0° to 90° for $0.24 \leq St_c \leq 0.40$. This bifurcation further coincided with apparent changes in the dynamic interactions and spatio-temporal evolution of the vortex structures in different wake modes. Lower reduced frequency cases ($St_c = 0.24$ and 0.32) did not show apparent changes in the wake modes. However, vortices that formed a pair, or merged to form individual structures at these reduced frequencies, were found in better alignment with the wake centerline. This feature was similar for cases that showed regions of larger momentum deficit. At $St_c = 0.40$, while a transition from $2P^H$ to $2P^D$ mode occurred, the mean thrust jet did not undergo significant bifurcations. However, dual large momentum deficit region still appeared in the wake that accompany the primary velocity jet. Early merger of vortex structures in the wake further accounted for a decrease in the streamwise extent of thrust generating jet, which also increased the drag production.

A better understanding of the transition mechanisms with increasing ϕ is helpful to enable the development of flow control systems for underwater propulsors and robotic vehicles. It allows them to closely mimic the habits of biological marine swimmers and reduce the break up of mean thrust jet. This would further provide an increased range of phase offsets, where the oscillating foil becomes propulsively efficient without higher power consumption that is generally required at high reduced frequencies. It is also important to evaluate the maneuvering mechanisms of swimmers that is strongly dictated by the lift generation mechanism. The following chapter is therefore

dedicated to investigating coinciding aspects of lift generation and transition of kinematics with changes in ϕ. The corresponding wake topology is also linked with the apparent lift characteristics.

Chapter 6

ON ASSOCIATION OF LIFT GENERATION, WAKE TOPOLOGY AND KINEMATICS[†]

6.1 Introduction

The flapping or oscillatory kinematics of foils provides an effective model to understand insect and bird flights (Wang, 2005). Several experimental and numerical studies described in Sections 2.3-2.3.1 also indicated that pitching or plunging motion closely mimic the biological kinematics within the realm of fish swimming (Smits, 2019). While these studies (Godoy-Diana et al., 2008; Schnipper et al., 2009; Andersen et al., 2017; Floryan et al., 2017; Lagopoulos et al., 2019), and discussion provided in Section 5.3, focused on aspects of thrust generation for an optimal swimming performance, limited work has been conducted in terms of coinciding lift generation. The evaluation of performance features in terms of lift, and its corresponding association with the wake modes, could advance the conceptual designs of propulsors. This includes improving their

[†]The content of this chapter has been published in whole or part, in *International Journal of Micro-Air Vehicles* under the citation (Verma et al., 2022b): "Verma, S., Khalid, M.S.U. & Hemmati, A. (2022b). On association of lift generation, wake topology and kinematics of oscillating foils. International J. of Micro Air Vehicle. 14, 175682932110739"

maneuverability in conditions of collision and enemy avoidance for both aerial and underwater applications.

The main objective of this chapter is to investigate and report on novel findings concerning wake modes that dominate the transitioning (from a heave- to pitch-dominant motion setting) kinematics of an oscillating foil. Additional insights into the coinciding differences in lift characteristics substantiate the observations discussed in Chapters 4 and 5. The changes in kinematics at $1000 \leq Re \leq 4000$ are governed primarily by varying the ϕ between the heaving and pitching motion ($0^\circ \leq \phi \leq 315^\circ$), St_c) of oscillation in the range of $0.16 \leq St_c \leq 0.48$ and St_A, which varies in range of $0.06 \leq St_A \leq 0.34$. Here, the wake and performance evaluation are restricted to $Re = 1000$ similar to Chapter 5, at which case the flow exhibits all necessary coherence features without three-dimensional turbulent flow complexities of higher Reynolds numbers. The association of wake features with temporal lift variations for specific cases of ϕ and St_c can further reveal if a correspondence between kinematics, performance and wake mode formations is existent.

Cleaver et al. (2012) highlighted aspects of lift generation, and their association with wake modes, mostly in cases of oscillating foils with a single degree of plunging motion. Foils with coupled heaving and pitching kinematics have also been investigated in great detail recently (Van Buren et al., 2019), although the performance features were primarily evaluated in terms of propulsive thrust generation and efficiency. This was sufficiently highlighted in Chapter 4. This gap in literature provides enough motivation to investigate the association of lift generation and evolution of wake topology behind an oscillating foil with combined heaving and pitching motion. The chapter is arranged such that the problem description is explained in Section 6.2, followed by the discussion of results in Section 6.3. A summary of major contributions is then provided in Section 6.4.

6.2 Problem Description

Flow around an oscillating teardrop foil is numerically examined at a similar range of St_c, ϕ and Re as highlighted in Section 5.2. h_o/c and θ_o are also fixed at 0.25 and 10°, respectively. Van Buren et al. (2019) highlighted that changes in ϕ dictated the motion setting in terms of pitch- or heave-dominated kinematics. Thus, it could pose apparent effects on the propulsive performance. Despite the aforementioned efforts, there has not been any attempts to characterize the coinciding lift generation and wake topology in the heave-dominated (i.e. $180° \leq \phi \leq 225°$) and pitch-dominated (i.e. $0° \leq \phi \leq 120°$ and $225° < \phi \leq 315°$) regimes. The specified range of ϕ for heave and pitch-dominated kinematics were obtained based on the ratio of peak leading edge to trailing edge amplitude of foil, i.e. h_o/A_T within half oscillation cycle. If the ratio was greater than 1, the corresponding ϕ value would fall under regime of heave-dominated kinematics. In contrast, if the ratio was observed to be lesser than 1, the coinciding ϕ would indicate a pitch dominated motion.

The detailed analyses of the coinciding wake and performance characteristics with the heave- and pitch-dominated kinematics is further limited to a chord-based Reynolds number of $Re = 1000$, where transition of wake modes are more clearly evident (Section 5.3).

6.3 Results and Discussion

First, the wake modes are evaluated along with their coincidence with performance features for oscillating foils, in terms of lift generation, within the heave- and pitch-dominated ranges of ϕ. The observations correspond to a fixed $Re = 1000$. This includes assessments at increasing St_c, where substantial increment in vorticity generation and circulation could contribute towards changes in temporal lift features within an oscillation cycle Cleaver et al. (2012). The instantaneous vortex shedding events within an oscillation cycle for heave- and pitch-dominated regimes of coupled kinematics are considered to reveal apparent association of lift variation with unique wake modes observed at increasing ϕ and St_c.

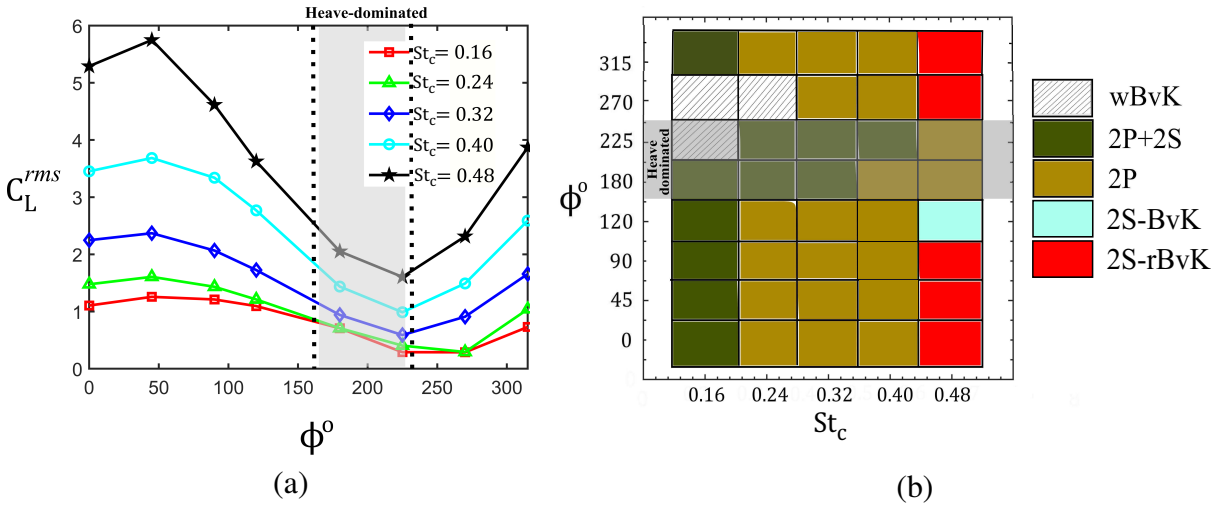

Figure 6.1: (a) Variation of C_L^{rms} with increasing ϕ and St_c, and (b) Wake mode transition depicted on a $\phi - St_c$ phase space.

6.3.1 Lift Generation and Wake Topology

Lift variations are examined in terms of C_L^{rms} in Figure 6.1(a) at increasing ϕ and St_c. Pitch-dominated regime of coupled kinematics coincides with $\phi < 180^\circ$ and $\phi > 225^\circ$, while heave-dominated regime is governed by $180^\circ \leq \phi \leq 225^\circ$. Figure 6.1(a) shows a decreasing magnitude of C_L^{rms} as ϕ transitions from a pitch- to heave-dominated regime. This trend remains consistent at increasing St_c, although the effect appears relatively stronger at higher St_c, where the rate of reduction in C_L^{rms} with increasing ϕ is large compared to observations at $St_c < 0.32$. We further observe that as ϕ increases above 225°, C_L^{rms} depicts an increasing trend that coincides with a reverse transition towards pitch-dominated kinematics regime. Thus, it is evident that heave-dominated regime coincides with low magnitudes of C_L^{rms}, contrary to the features observed in pitch-dominated regime. It will be interesting to evaluate the coinciding changes in wake formation within the heave- and pitch-dominated regimes. This will also help in investigating apparent association of wake topology and lift characteristics.

The wake modes at increasing St_c and ϕ are depicted on a phase-map shown in Figure 6.1(b). For the pitch-dominated regime in the range of $\phi < 180^\circ$, it is evident that the wake associated with $0.24 \leq St_c \leq 0.4$ is wholly dominated by a $2P$ wake mode. This topology is characterized by

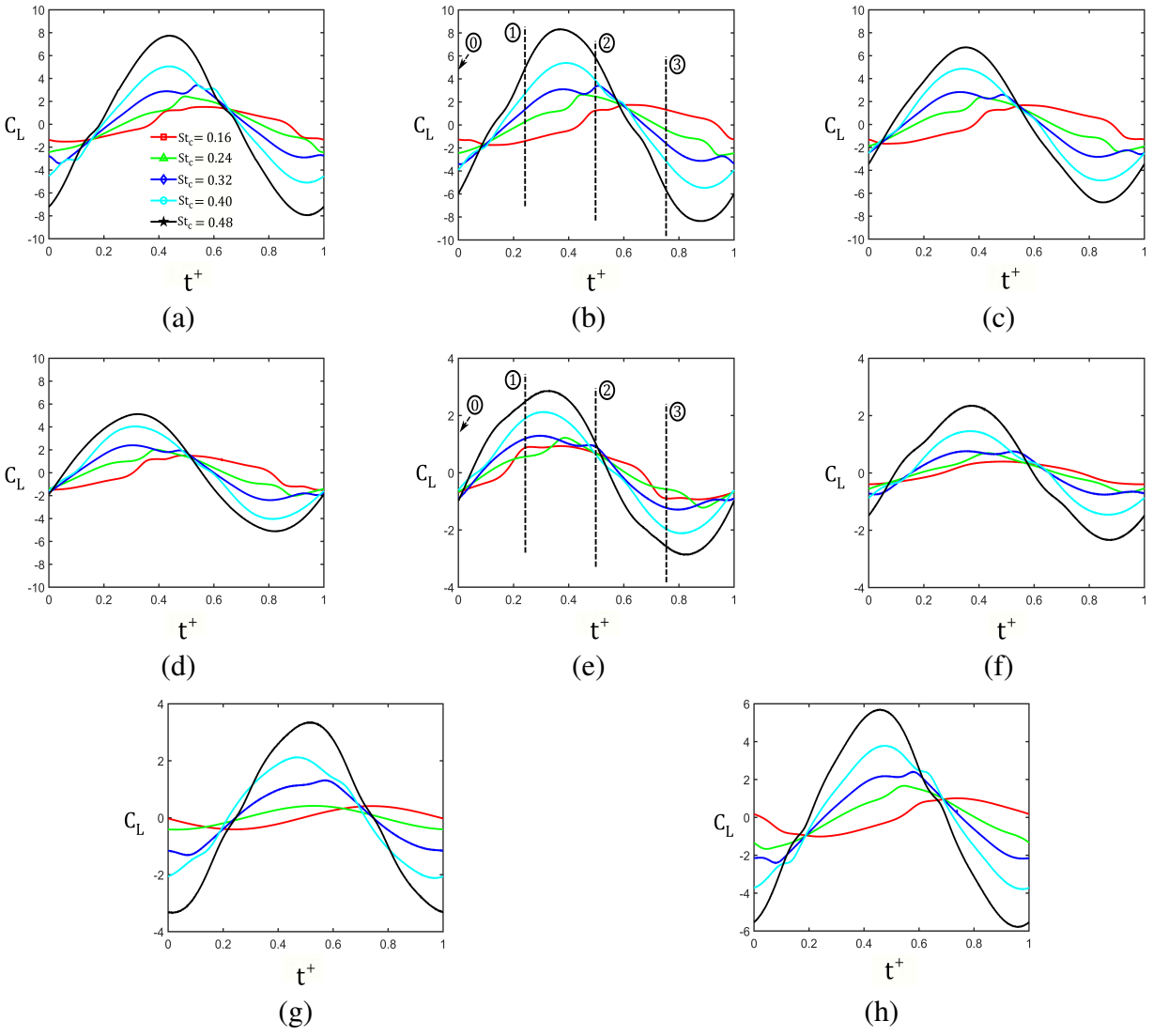

Figure 6.2: Temporal variation of C_L at increasing St_c and ϕ = (a) 0°, (b) 45°, (c) 90°, (d) 120°, (e) 180°, (f) 225°, (g) 270°, (h) 315°.

shedding of two vortex pairs, which comprises of counter-rotating leading and trailing edge vortex structures (Schnipper et al., 2009). Increasing St_c to 0.48 shows a transition to $2S$ vortex modes, including *rBvK* and *BvK*, in which only trailing edge structures dominate the vortex shedding and corresponding wake formation (Koochesfahani, 1989; Schnipper et al., 2009). As the kinematics switch to heave-dominated regime, governed by $\phi \geq 180^\circ$ and $\phi \leq 225^\circ$, we observe that $2P$ wake configuration is retained at the highest St_c of 0.48. This is in contrast to the observations made in pitch-dominated regime discussed earlier. The lack of a wake transition from $2P$ to $2S$ with increasing St_c is attributed to the decreasing trailing edge vorticity relative to the vorticity generated at the leading edge with increasing ϕ to 225°. This further coincides with a decrease in trailing edge amplitude as described by Van Buren et al. (2019). We also observe that the range of St_c between 0.24 and 0.40 shows a delayed wake transition from $2P+2S$ to $2P$ within heave-dominated regime compared to the pitch-dominated regime at $\phi < 180^\circ$, for example. This could again be an implication of weak or no interaction (and merging) near the trailing edge of the foil due to lower strength of generated vorticity. The *wBvK* mode observed at lower St_c, which coincides with both $\phi = 225^\circ$ and 270°, depicts the wavy Von Kármán mode observed in some studies conducted previously (Lentink et al., 2008). Lentink et al. (2008) observed no noticeable shedding of near wake vortex structures for the *wBvK* mode. The separated shear layer remains undisturbed until an initial instability starts to develop at some distance downstream of the trailing edge (Lentink et al., 2008). The pitch-dominated regime above $\phi = 225^\circ$ depicts a similar wake topology and transition as observed for $\phi \leq 180^\circ$.

In order to further evaluate temporal lift features that are pertinent to heave- and pitch-dominated motion kinematics, it is important to consider the variation of C_L within one single oscillation cycle.

6.3.2 Vortex Shedding and Lift Variation

Figure 6.2 depict the variation of C_L within one oscillation cycle. The apparent effect on lift features and its association with transition of pitch- to heave-dominated regimes of coupled kinematics

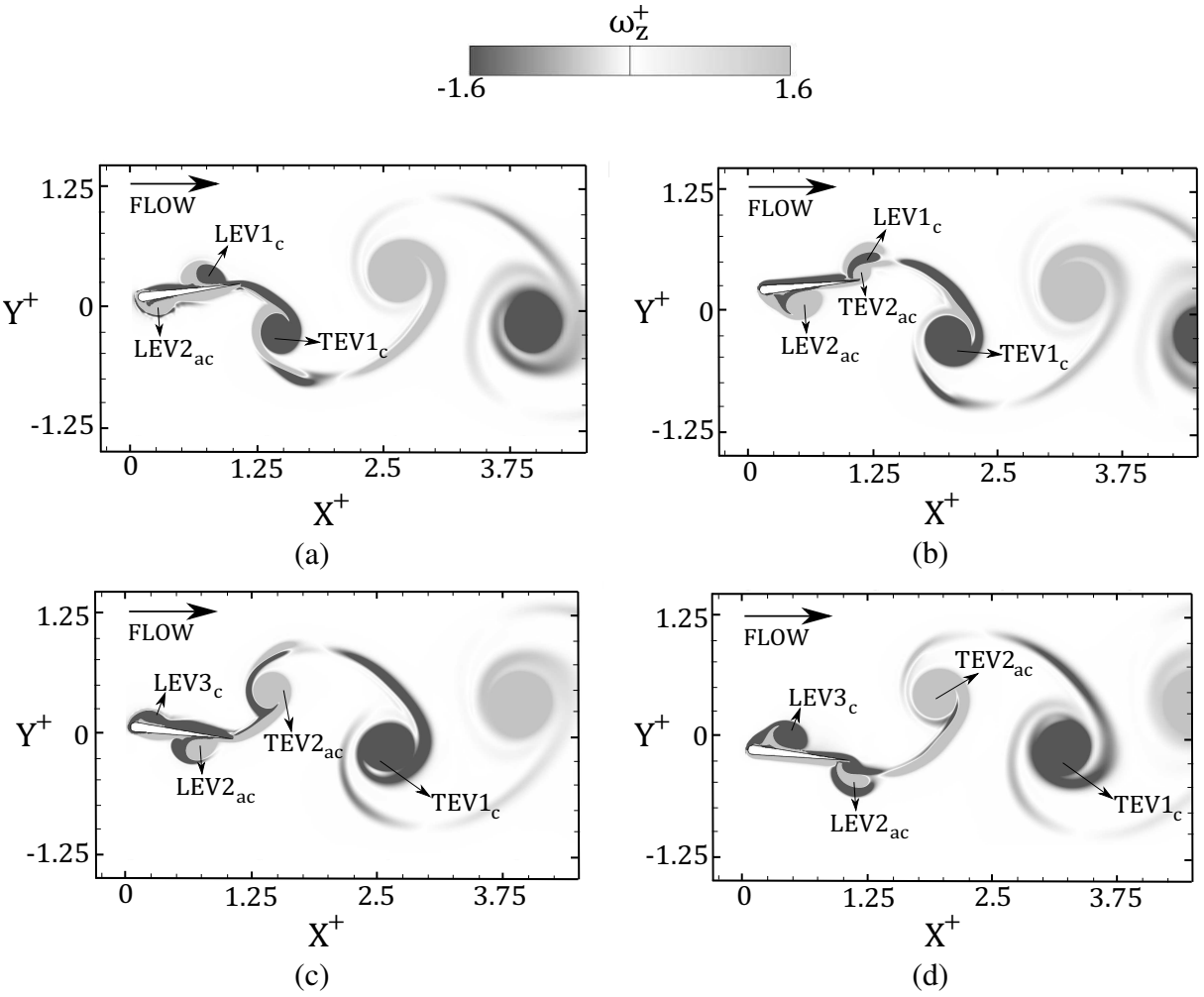

Figure 6.3: Snapshots of ω_z^+ depicting wake formation at $St_c = 0.48$ and $\phi = 45°$, at quarter period of oscillation cycle: (a) $t^+ = 0$, (b) $t^+ = 0.25$, (c) $t^+ = 0.5$ and (d) $t^+ = 0.75$.

are more evident here. At $St_c = 0.16$, the temporal variation in C_L shows a low amplitude within the entire range of ϕ considered in this study. This also supports the observation from Figure 6.1(a) where low C_L^{rms} was evident at $St_c = 0.16$ and increasing ϕ from 0° to 315°. The amplitude of C_L starts to increase as St_c increases above 0.16. While the effects on temporal C_L variation with respect to the shedding period are not clearly identifiable at low St_c, we observe substantial changes at St_c above 0.32. The similarities and association of lift features with pitch- or heave-dominated regimes are also more evident at higher St_c.

With increasing ϕ from 0° to 120° in Figure 6.2, we observe that C_L variation become more symmetric about the half shedding period ($t^+ = 0.5$) and $\overline{C_L} = 0$, in comparison to the trends

observed at $\phi = 0^\circ$ and 45°. This symmetric feature in C_L appears more prominent within the heave-dominated range of ϕ. This characteristic lift variation could also offer capabilities in terms of achieving low amplitude maneuvers in shorter time-period for robotic flights and swimmers which can detect and avoid collisions with obstacles on course. A higher St_c requirement, however, will still be required in order to achieve such lift signature within the heave dominated kinematic regime. Ahead of $\phi = 225^\circ$, we see that this symmetric temporal characteristic is lost, similar to the observations for $\phi < 90^\circ$. A longer proportion of the shedding period is characterized by a rise in C_L towards its local maximum, and followed by its steady decrease as the shedding cycle ends. Contrary to the application posed by lift features of heave dominated kinematics, it appears that pitch-dominated regime offers a high magnitude lift generation capability rather than a short-time directional maneuver. In situations like surface lift-off during strong wind gusts or sudden need of greater side force generation during cyclonic hurricane avoidance in marine robots, such high magnitude lift generation will therefore present greater applications. The wake phase map (Figure 6.1(b)) further showed that heave-dominated regime is largely characterized by a paired wake ($2P$) formation at increasing St_c, while pitch-dominated regimes showed an eventual wake transition to $2S$. Thus in the latter case, only two single counter-rotating vortex structures shed from the trailing edge that dominate the wake. It is important to investigate if any close association exists between temporal lift features and wake formations within the heave- and pitch-dominated regimes.

We proceed by evaluating the instantaneous spanwise vorticity distribution around the foil and in the near wake at each quarter phase ($t^+ = 0.25$) of the oscillation cycle. For brevity, only two specific cases are examined at the highest St_c within this parameter space (i.e. $St_c = 0.48$), while each case represents either a pitch- or heave-dominated regime. Figures 6.3 and 6.4 depict the ω_z^+ distribution at each quarter period of an oscillation cycle, for $\phi = 45^\circ$ and $\phi = 180^\circ$, respectively. As described before, the former represents a case of pitch-dominated regime while the latter corresponds to a heave-dominated kinematics. At $\phi = 45^\circ$ in Figure 6.3, it is evident that the near wake formation is dominated by trailing edge structures (TEV_s) that appear to possess a relatively larger circulation strength compared to the leading edge structure (LEV_s) before shedding

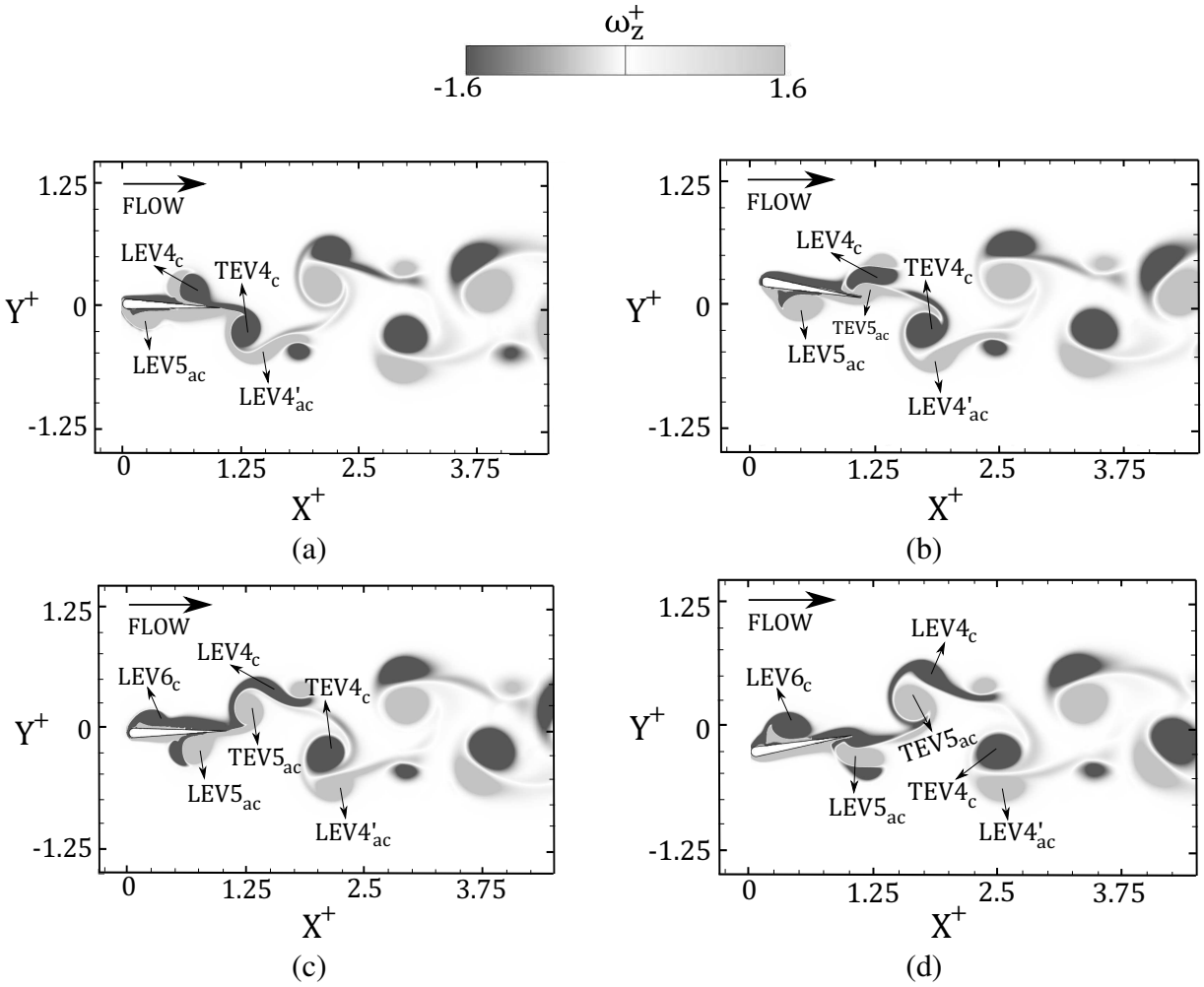

Figure 6.4: Snapshots of ω_z^+ depicting wake formation at $St_c = 0.48$ and $\phi = 180°$, at quarter period of oscillation cycle, i.e. (a) $t^+ = 0$, (b) $t^+ = 0.25$, (c) $t^+ = 0.5$ and (d) $t^+ = 0.75$.

in the wake. This is despite the fact that leading edge structures (LEV_s) are formed and move downstream within each half shedding cycle.

The formation process of the $2S-$rBvK wake at $\phi = 45°$ is quite similar to those described for purely pitching foils (Koochesfahani, 1989; Schnipper et al., 2009). Figure 6.3(a) shows a strong clockwise trailing edge structure ($TEV1_c$) which is almost on the verge of separation from the foil trailing edge. We further observe a weak vortical structure originated at the leading edge ($LEV1_c$), which appears to interact with the attached leg of $TEV1_c$. At $t^+ = 0.25$ in Figure 6.3(b), $LEV1_c$ appears stretched on account of the formation of $TEV2_{ac}$. As $TEV2_{ac}$ grows in circulation strength and size at $t^+ = 0.5$ in Figure 6.3(c), $LEV2_{ac}$ near the trailing edge undergoes stretching

as another anti-clockwise TEV starts to develop. This is evident at $t^+ = 0.75$ in Figure 6.3(d), which is consistent with the observations at $t^+ = 0.25$ in Figure 6.3(b). $LEV3_c$ further grows and reach approximately the mid-chord region of the foil. Overall, the wake is dominated by trailing edge vorticity, while leading edge vorticity disintegrate and diffuse without contributing to the wake formation. Counter-rotating TEV structures grow and shed in the wake during the majority of shedding period, which coincides with lift characteristics depicted in Figure 6.2(b). This shows a more prolonged C_L fluctuation towards extremas within an oscillation period. This rise and fall corresponds to the development and shedding of anti-clockwise and clockwise TEV structures, respectively, shown in Figure 6.3(b,d). Instants 0, 1, 2 and 3 that are marked in Figure 6.2(b) correspond to each quarter phases of oscillation period in Figures 6.3(a), 6.3(b), 6.3(c) and 6.3(d), respectively. It is evident that ahead of instant 1, an extrema of C_L is reached in Figure 6.2(b), which coincides with shedding of $TEV1_c$ in Figure 6.3(b). Similarly, we observe C_L reaching another extrema ahead of instant 3 in Figure 6.2(b) with a negative sign, which coincides with the shedding of an anti-clockwise structure, $TEV2_{ac}$. Similar shedding events are also observed for other cases of ϕ, which depict pitch-dominated regime. However, they are not depicted or discussed here for brevity since they follow a very similar wake formation mechanism as that of $\phi = 45^\circ$ in Figure 6.3.

The wake formation at $\phi = 180^\circ$, which corresponds to a particular case of heave-dominated regime, is shown in Figure 6.4. Similar to the case for pitch-dominated regime, each of the four snapshots in Figure 6.4 corresponds to Instants 0, 1, 2, and 3 in Figure 6.2(e), respectively. At $t^+ = 0$, vortex $LEV4'_{ac}$ has shed into the wake, which appears to start forming a pair with $TEV4_c$. Moreover, $LEV4'_{ac}$ appears stretched on account of straining induced by $TEV4_c$. It is also apparent that $LEV4_c$ and $LEV5_{ac}$ grow in size on the pressure and suction side of the oscillating foil. As the foil reach $t^+ = 0.25$ in Figure 6.4(b), $TEV4_c$ is detached and advects as a counter-rotating pair of $LEV4'_{ac}$. The induced straining by $TEV5_{ac}$, which is just beginning to form, appears to distort $LEV4_c$ in Figure 6.4(b) and 6.4(c). At $t^+ = 0.5$, $TEV5_{ac}$ pairs with the strained $LEV4_c$ near the foil trailing edge, which by $t^+ = 0.75$ sheds from the foil trailing edge and advects into

the wake (see Figure 6.4(d)). This is consistent with the observations made during the first half shedding cycle in Figure 6.4(b). By relating the advection of leading edge structures with lift characteristics for $\phi = 180^\circ$ in Figure 6.2(e), it becomes evident that symmetric C_L variations that are attained with respect to the half shedding period are clearly associated with advected LEV structures for heave-dominated kinematics presented here. Ahead of instant 1 marked in Figure 6.2(e), we observe that $TEV4_c$ grows in strength and size, for example at $t^+ = 0$ in Figure 6.4(a), while C_L increases towards a local extrema. However ahead of instant 2, C_L decreases towards larger negative values. This coincides with advection of $LEV5_{ac}$ in the wake, shown in Figure 6.4(b), and early growth of $TEV5_{ac}$ near the foil trailing edge. At instant 3, which lies just before C_L reaching a local negative extrema in Figure 6.2(e), we notice that $TEV5_{ac}$ is enlarged while $LEV5_{ac}$ has almost reached the trailing edge in Figure 6.4(c). As $LEV5_{ac}$ and $TEV5_{ac}$ shed, the corresponding growth and advection of a new trailing edge structure and $LEV6_c$ again corresponds to an increasing C_L towards positive values as the shedding cycle ends. It is thus apparent that for heave-dominated kinematics, the growth and coherence of advecting LEV structures reveal a more symmetric attainment of C_L extremas in an oscillation cycle. Contrarily, previously discussed pitch-dominated kinematics confirm that LEV_s eventually disintegrates near the foil trailing edge, which therefore corresponds to a lack of symmetry in development of peaks in the profile of C_L at around half the shedding period.

6.4 Summary

The wake topology transition, and its correspondence with lift features, were numerically examined with heave and pitch amplitudes corresponding to $h_o/c = 0.25$ and 10°, respectively. The variation in ϕ between the motions contributed to the changes in trailing edge amplitude, thereby promoting the transition of kinematics between pitch-dominated ($0^\circ \leq \phi < 180^\circ$, $225^\circ < \phi \leq 360^\circ$) to heave-dominated ($180^\circ \leq \phi \leq 225^\circ$) motion regimes.

Assessment of lift variations, in terms of C_L^{rms}, revealed low magnitudes within the heave-dominated regime. The magnitude of C_L^{rms} increased as kinematics switched to a pitch-dominated regime. The $\phi - St_c$ phase map depicting the wake mode transition also revealed that heave-dominated regime does not exhibit wake transition from $2P$ to $2S$ with increasing St_c. This was contrary to the wake features observed for the pitch-dominated kinematics. The reduction of trailing edge amplitude within the heave-dominated regime corresponded to decreasing relative vorticity generated at the trailing edge compared to the leading edge. This characteristic feature thus yields a paired configuration of leading and trailing edge vortical structures, even at high St_c for the heave-dominated kinematics, thereby explaining the $2P$ mode configuration.

The temporal assessments on lift variation within an oscillation cycle provided additional insights into the association of lift characteristics and wake mode transitions identified for the heave- and pitch-dominated regimes. It was evident that heave-dominated regime is characterized by an apparent symmetry in variations of C_L, such that there was a mirror image of the extrema about the half shedding period. The growth and advection of LEV structures followed by their pairing with TEV structures, which yields a $2P$ wake, coincided with unique temporal lift features during the heave-dominated kinematics. The pitch-dominated regimes, however, depicted a lack of symmetry in temporal lift variation, while a major portion of the shedding period was spent in attaining a single extrema. The disintegration of LEV_s, and its lack of contribution towards wake formation, coincided with a change in lift behavior within an oscillation period. The transition in wake topology and the associated lift characteristics thus indicated that the heave-dominated kinematics of coupled motion could offer a more rapid maneuvering control, although the magnitude of lift generation was low. The pitch-dominated cases, however, could yield larger lift, while a rapid maneuvering was not feasible in such a coupled motion regime.

The correspondence between 2P mode formation and its association with thrust and lift characteristics have been quite vivid in Sections 5.3 and 6.3. However, transition in spatial topologies and vortex interactions in the wake governed by $2P$ mode still requires more insights with respect to changes in kinematics of oscillating foil. It is also important to formulate a mathematical rela-

tionship that can describe the LEV and TEV evolution with changes in combined heaving-pitching kinematics.

Chapter 7

CHARACTERIZATION OF BIFURCATED DUAL VORTEX STREETS IN THE WAKE[†]

7.1 Introduction

The theoretical analysis and comprehensive review presented in literature have provided us with fundamental understanding of undulatory motion for slender bodies (Lighthill, 1969), active and passive flow control in biological marine swimmers (Webb, 1975; Colgate and Lynch, 2004), and exploitation of flow in different environments (Fish and Lauder, 2005). More recently, researchers have expanded their studies on locomotion of fish to examine the underlying mechanisms that have also been observed for flight of birds and insects (Li et al., 2020; Bode-Oke and Dong, 2020). These provide insights into the fundamental phenomenon for the generation of dynamic force (i.e., lift, thrust and drag) under different biological conditions and kinematics. The conceptual advancements from these studies have been the prime motivator behind the ongoing innovations

[†]The content of this chapter has been published in whole or part, in *Journal of Fluid Mechanics* under the citation (**?**): "Verma, S., & Hemmati, A. (2022) Characterization of bifurcated dual vortex streets in the wake of an oscillating foil. Journal of Fluid Mechanics 945, A7."

in marine propulsion, aerial flight technologies and novel energy harvesting systems (Wu et al., 2020).

The coupled oscillation with two degree of freedom had gained considerable attention recently on account of its greater complexity with additional motion parameters and their inter-dependence with induced changes in flows (Van Buren et al., 2019). However, as highlighted and explained in Section 2.2, the results only concerned with the propulsive performance scaling of oscillating foils. The essential findings were further expanded through observations discussed in Sections 4.3 and 6.3, that particularly concerned thrust and lift generation, respectively. Recent two-dimensional numerical studies by Lagopoulos et al. (2019) and Zheng et al. (2019) discussed the wake, in addition to the performance metrics, for a foil performing coupled two degree of freedom oscillations, where the ϕ was fixed at 90° (or 270° in the reference frame of Van Buren et al. (2019)). These phase offsets were primarily characterized as a pitch dominated oscillatory motion, where the trailing edge amplitude was higher compared to the leading edge. More details regarding these observations can be found in Sections 2.2-2.3.1.

The major goal in this chapter is to understand the novel wake characteristics when the phase offset between the heave and pitch motion increases from 0° to 180° for a given St_c and Re. The findings reported here supplement the observations discussed in Chapters 5 and 6. This range of phase offset also presents a vivid transition of kinematics of foils from a pitch-to-heave dominated coupled oscillatory motion. Particularly, there are detailed evidence and insights into transition of wake topology towards bifurcated vortex streets characterized by dipole-like paired vortical structures. Quantitative and qualitative characteristics of the evolution are further described for such streets that constitute dipole-like vortical pairs. A mathematical model for the relative circulation strength of counter-rotating structures is then proposed in terms of Strouhal number based on trailing and leading edge amplitudes. This model particularly characterizes the behavior of wake during coupled heaving and pitching kinematics. Lastly, mean flow features associated with the bifurcated dual vortex streets are also highlighted in order to provide detailed insights on time-averaged spatial development of wake under such circumstances. The chapter is arranged such that

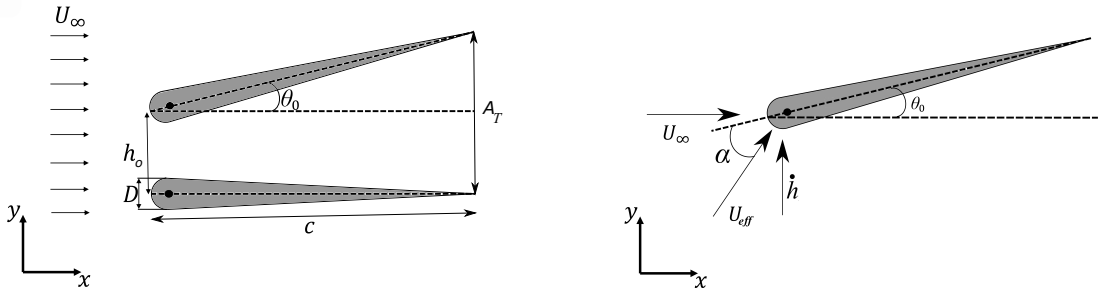

Figure 7.1: Schematics of the foil kinematics and resultant velocity at the leading edge during the motion.

the problem and methodology are explained in Section 7.2, followed by the discussion of results in Section 7.3. Major conclusions are then presented in Section 7.4.

7.2 Problem Description

The range of St_c was 0.16 - 0.48, and St_A was $0.06 \leq St_A \leq 0.34$. The detailed analyses of the wake characteristics are limited to the case of $Re = 1000$ and 4000, where the wake features and transition effects were more profound without the additional complexities associated with higher Reynolds number flows (Zurman-Nasution et al., 2020).

Figure 7.1(a) depicts the oscillating foil, where heave and pitch amplitudes are denoted by h_o and θ_o, respectively. Figure 7.1(b) further depicts the heave ($\dot{h_L}$) and effective (U_{eff}) velocity as seen by the leading edge of the foil. These would be helpful while modeling the vorticity production and circulation strength of vortex structures originating at the leading edge boundary layer. The ϕ varied from 0° to 270°, which directly resulted in a variation of A_T. On account of variation in ϕ and A_T, the St_A also varied in the range specified before. Andersen et al. (2017) have indicated that interesting and significant transitions in the wake of flapping foils were observable within a Strouhal number range of $0.2 < St_A < 0.4$. This also coincides with the range corresponding to optimal propulsive efficiency in swimming mammals (Triantafyllou et al., 1993; Smits, 2019). Further, the specified range of St_A had been observed to preserve the wake two-dimensionality of a flapping foil that involved either a pure pitching, a pitch dominated or a heave-dominated

coupled motion setting (Zurman-Nasution et al., 2020). This further justified the parameter space considered here.

7.3 Results and Discussion

The kinematics of the oscillating foil at an increasing phase offset, chord-based Strouhal number and Reynolds number are examined first. Particularly, these aspects are helpful in evaluating and modeling production of vorticity, and therefore, the circulation strength for vortical structures. The shedding of these structures also coincide with the transition of a pitch-to-heave dominated coupled motion. Then, a qualitative discussion is provided on the transition and formation mechanisms of peculiar wake modes for an increasing ϕ. It reveals the transition to bifurcated dual vortex street characterized by dipole-like paired vortices. Quantification of evolutionary characteristics, such as circulation strength and the separation distance between the shed vortical structures, are then evaluated in order to model the formation of wake mode, and transition in spatial topology with respect to the kinematics of oscillating foil. Initially, the wake analyses are focused on the case of $Re = 1000$, which allows for a more detailed and vivid characterization of coherent structures. This is then expanded to a higher Reynolds number of $Re = 4000$, wherein effects of Reynolds number are expected to be negligible (Das et al., 2016; Senturk and Smits, 2019b; Gungor and Hemmati, 2021). Lastly, the mean flow characteristics are evaluated, which highlight spatio-temporal features of wake that are common to configuration of dual vortex street characterized by dipole-like pairs.

7.3.1 Evaluation of kinematics

The kinematics of oscillating foil in combined heaving and pitching motion is described within a range of $0^\circ \leq \phi \leq 270^\circ$ at $0.16 \leq St_c \leq 0.48$. Instantaneous variations in (a_T^+, h^+), and α° are depicted in Figure 7.2 for one oscillation cycle, whereas the effect of an increasing ϕ on a_T^+ and α° is particularly observable in Figures 7.2(a) and 7.2(c). Figure 7.2(d) further depicts variations in the α_o with respect to increasing phase offset and St_c. The effective angle of attack for a foil

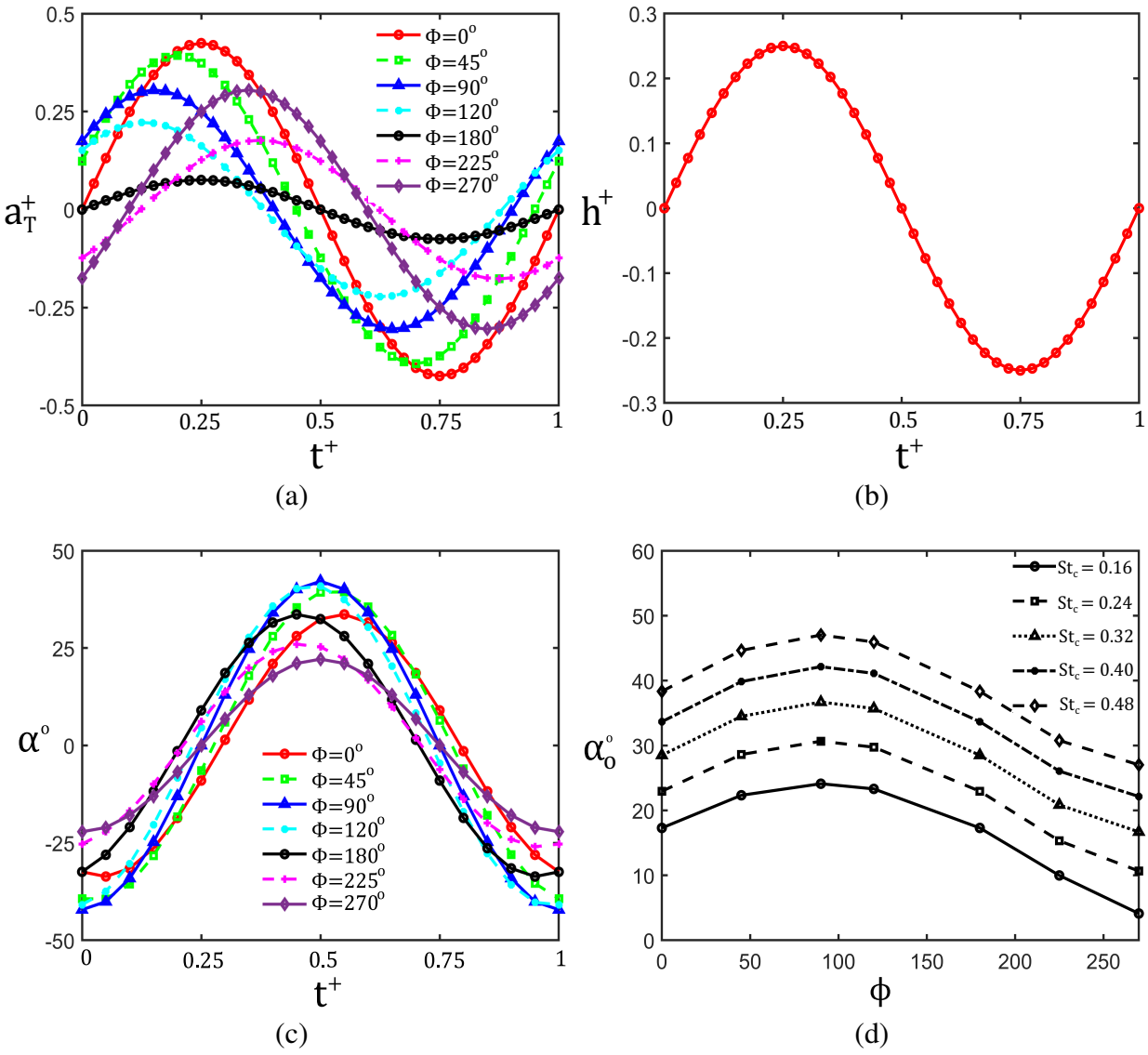

Figure 7.2: Temporal variation of (a) a_T^+, (b) h^+ and (c) instantaneous α°, within one single oscillation cycle. (d) represents variation of peak α with respect to ϕ and St_c.

with combined heaving and pitching motion is the resultant of both pitch and heave induced angle of attack (Lagopoulos et al., 2019). The variation of ϕ, corresponding to the peak angle of attack (i.e. $\phi = 90°$), is consistent for an increasing St_c.

The maximum a_T^+ as observed from Figure 7.2(a) is attained for $\phi = 0°$, which then decreases with ϕ approaching 180°. An increasing ϕ from 180° to 270° results in a higher peak a_T^+ within one oscillation cycle. On comparing the ratio of peak a_T^+ and h^+ with a changing ϕ, it can be deduced that a smooth shift from pitch to heave dominated kinematics occurs with the phase offset

approaching 180°. Then, it reverts back to the pitch dominated motion as ϕ increases beyond 180°. Our understanding about the influence of variations in such kinematics on evolution of wakes is still incomplete and therefore needs more attention. Moreover, the variation in α also depicts an increase in its peak, which then decreases to a minimum at $\phi = 270°$. It is also observed in Figure 7.2(d). The peak angle of attack holds a considerable importance in terms of governing the dynamics of leading edge vortex and stall characteristics of the oscillating foil (Visbal, 2009; Carr, 2012). In order to investigate these aspects, specifically when a transition occurs from pitch to heave dominated coupled motion of a foil, we now discuss newly identified important observations with respect to evolution of wake that coincides with the aforementioned transition in kinematic regimes.

7.3.2 Evaluation of wake mode transition at $Re = 1000$

To understand the configuration of wake and its transition for a range of phase offset, amplitude and St_c at $Re = 1000$, we draw representative wake maps shown in Figure 7.3. Specifically, Figure 7.3(a) and 7.3(b) correspond to phase spaces characterized by $\phi - St_c$ and $A_c - St_c$, respectively. Figure 7.3(b), particularly, allows a comparison of transitions in wake topology with studies conducted on oscillating foils in pure pitching motion (Schnipper et al., 2009). The nomenclature of wake modes is also aligned with the studies conducted by Williamson and Roshko (1988) and Schnipper et al. (2009), which considered the number of shed vortical structures in one oscillation cycle for a cylinder and teardrop foil, respectively. For St_c below 0.32 in Figure 7.3(a), it is observed that three wake modes corresponding to wavy Benard von Kármán or *wBvK* (Lentink et al., 2008), $2P + 2S$ and $2P$, (Schnipper et al., 2009) are prominent at $Re = 1000$. More details of the wake categorization and transition at $Re = 1000$ can also be found in Section 5.3 of Chapter 5. For $St_c = 0.4$ and $Re = 1000$, the heave dominated kinematics corresponding to $90° \leq \phi \leq 180°$ also depicts the dominance of $2P$ mode along with a characteristic bifurcation (marked by B in Figure 7.3(a)) noticed between the two shed vortex pairs of $2P$, particularly at $\phi = 180°$. A transition

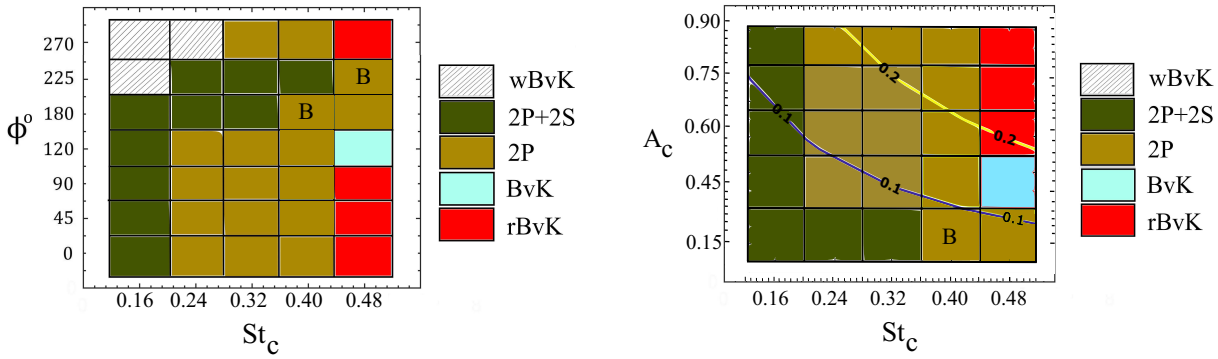

(a) (b)

Figure 7.3: Phase map representation of identified wake modes on (a) $\phi - St_c$ and (b) $A_c - St_c$ phase-space for $Re = 1000$.

from a reverse von Kármán to a Benard von Kármán, followed by the similar bifurcation of $2P$ pairs is further observed at $St_c = 0.48$.

It is worthwhile to observe if such wake mode transitions in terms of number of shed vortex structures, or characteristic bifurcations of shed $2P$ pairs, could coincide with a threshold value of St_A, as investigated by Schnipper et al. (2009), who particularly focused on purely pitching foils. Schnipper et al. (2009) observed that the transition from $2P$ to standard von Kármán ($2S$) mode coincided with the iso-line represented by $St_A = 0.11$. Furthermore, the transition of $2S$ to reverse von Kármán ($rBvK$) mode coincided with the line for $St_A = 0.18$ (Schnipper et al., 2009). In order to evaluate such coinciding transitions of wake modes with iso-lines of constant St_A in our study, we explain the wake modes at $Re = 1000$ on a $A_c - St_c$ phase-space diagram shown in Figure 7.3(b). Here, A_c is the normalized trailing edge amplitude calculated as $2A_T/c$. The product of A_c and St_c yields lines of constant St_A on the phase-space represented in Figure 7.3(b). The two iso-lines drawn on the phase diagram correspond to $St_A = 0.1$ and 0.2, respectively. The range between the observed iso-lines coincides with $2P$ mode. The region beyond $St_A = 0.2$ marks a transition towards $rBvK$ mode. Such findings therefore reveal a close resemblance to the observations reported by Schnipper et al. (2009). The transition from $2P$ mode to $rBvK$ also goes through a BvK type or standard von Kármán wake mode as observed at $St_c = 0.48$. The bifurcation of $2P$ pairs is further found to lie below the line of $St_A = 0.1$, whereas increasing St_A beyond 0.1 does

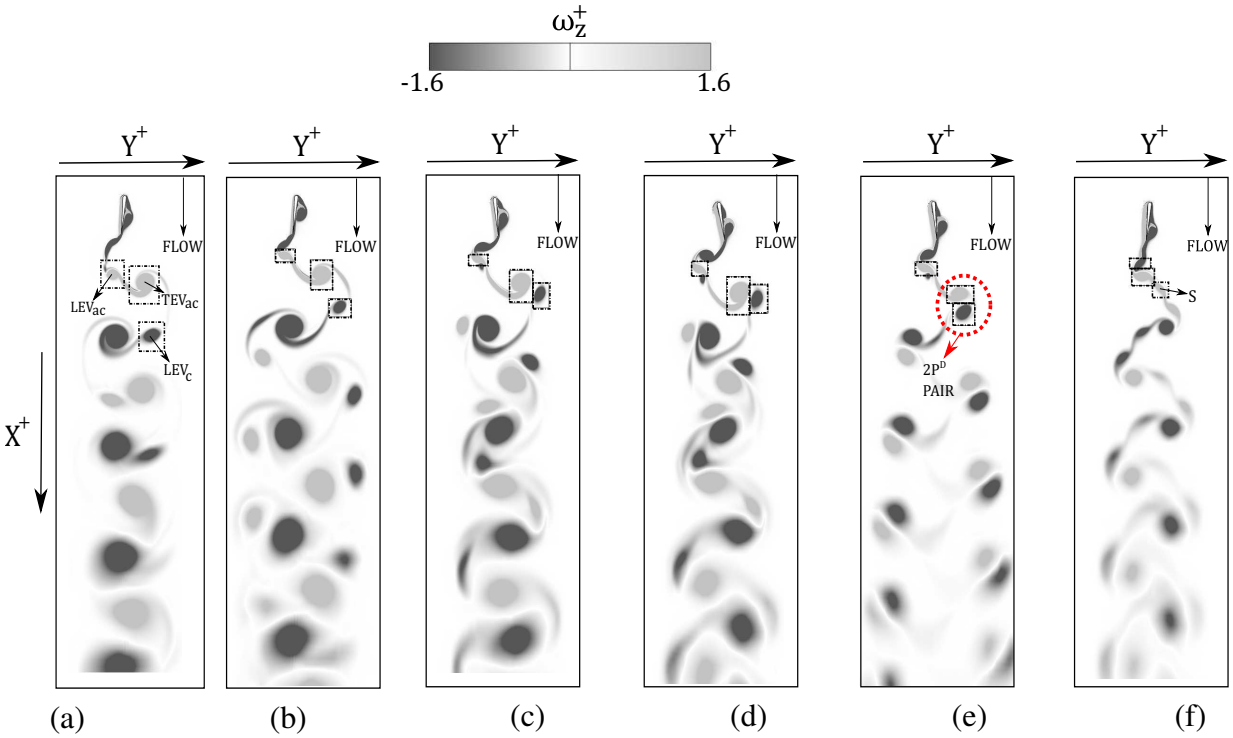

Figure 7.4: Wake modes at increasing ϕ and $Re = 1000$. (a)-(f) represents ϕ corresponding to 0°, 45°, 90°, 120°, 180° and 225°, respectively, while St_c corresponds to 0.4.

not reveal any bifurcations on the phase diagram. Besides the similarity observed in the trends of transition in wake mode configuration, with an increasing St_A, the bifurcation of $2P$ pairs observed at some kinematic settings also reveal a qualitative similarity with the visualizations of $2P$ mode by Schnipper et al. (2009) and Andersen et al. (2017). However, specific details and features of the topological transitions in spatial arrangements of vortex structures, constituting the $2P$ mode, were not identified or investigated. We will therefore provide an in-depth qualitative and quantitative descriptions of the characteristics of evolution while the $2P$ mode undergoes transitions in spatial topologies and encounters bifurcation of shed vortex pairs at certain kinematic settings observed in Figure 7.3.

The wake formations at an increasing ϕ is depicted in Figure 7.4, at $Re = 1000$ and $St_c = 0.4$. A dominant shedding of counter-rotating vortex pairs in each half oscillation cycle is commonly observed for all the cases presented here. However, the changes in spatial configurations of paired structures are observed for an increasing ϕ. At $\phi = 0°$, a $2P$ mode (Williamson and Roshko, 1988;

Schnipper et al., 2009) appears, which is characterized by horizontally pointed pairs. The counter-rotating vortex structures TEV_{ac} and LEV_c, marked on Figure 7.4(a), represent a $2P$ vortex pair. Here, subscripts ac and c denote the anticlockwise and clockwise rotating vortical structures, respectively. Another shed structure, LEV_{ac}, undergoes mutual interaction with the leg of TEV_{ac}. It is important to mention here that the abbreviations TEV_s and LEV_s denote the coherent structures formed at the trailing and leading edge of the foil, respectively. For the pitch-dominated motion profile at $\phi = 0^\circ$ (see Figure 7.2), TEV_{ac} is stronger than LEV_{ac} based on their circulation strength and size in Figure 7.4(a). It eventually results in the merger of similar sign LEV_s and TEV_s of the neighboring pairs, traversing downstream in the wake. A similar $2P$ configuration was observed and discussed previously by Williamson and Roshko (1988), Schnipper et al. (2009) and Hultmark et al. (2007) in the wake of a transversely oscillating cylinder, pitching foil and flexible robotic fins in sinusoidal oscillations, respectively. These $2P$ modes have also presented similarities in spatial configurations of thrust producing wakes by swimming fish (Müller et al., 2008; Schnipper et al., 2009).

In order to further elaborate on the effects of increasing ϕ, we observe that at $\phi = 45^\circ$, $2P$ vortex pairs are tilted and point in the upstream direction. No noticeable merger or interaction is observed between the neighboring structures of these pairs, as shown in Figure 7.4(b). These pairs also advect symmetrically along the wake centerline. The shed TEV possesses higher strength of circulation, in a qualitative sense, similar to the observations made at lower ϕ. Quantitative assessments for circulation are, however, presented in the next section for understanding the effects of changing ϕ on generation of vorticity. Moreover, wake formation at an increasing ϕ up to 90° depicts shedding of counter-rotating vortices with a decreased separation distance (ζ) between their centers compared to the cases with lower values of ϕ. A similar observation can be made for $\phi = 120^\circ$, where resemblance to dipole-like $2P$ pairs now become more vivid. We refer to such vortex pairs as $2P^D$ pairs in order to highlight them as dipole-like paired configuration, which appears in stark contrast to the $2P$ pairs observed at $\phi = 0^\circ$ and 45°, respectively. Also, the wake still possesses a symmetry with respect to its centerline until $\phi = 120^\circ$. Beside mutual interaction and

merger of vortices, we do not observe any bifurcation of the shed pairs and dipole-like ($2P^D$) structures observed at increasing ϕ. However, two vortex streets constituting fully developed $2P^D$ pairs diverge away from the wake centerline with ϕ approaching 180° (see Figure 7.4(e)). Structures forming such fully developed dipole-like configurations possess similar strengths of circulation, and size, which was also reported by Cleaver et al. (2012); Calderon et al. (2014); He and Gursul (2016). Experimental studies of Cleaver et al. (2012) and Calderon et al. (2014) discussed the formation of dipoles and couples behind oscillating foils in purely heaving motion and further explained their prominent association and coincidence with deflected wake modes (i.e. Mode A or Mode B). Here, the dual vortex streets seen at $\phi = 180°$ in Figure 7.4(e) retain a symmetry along the wake centerline. This observation could qualitatively indicate that the entrainment effects of shed dipole-like structures (Calderon et al., 2014) are equally balanced, thus preventing the overall wake deflection in upward or downward direction as noted in previous studies (Cleaver et al., 2012; Calderon et al., 2014). Increasing ϕ to 225°, as shown in Figure 7.4(f), depicts an absence of diverging vortex streets, where $TEVs$ are more stretched in the streamwise direction. An additional single vortex highlighted as S in Figure 7.4(f) also shed with a coincident shedding of a $2P$ pair. This mode therefore falls in the category of $2P + 2S$ (Williamson and Roshko, 1988; Schnipper et al., 2009). It is now evident that while the bifurcation of $2P^D$ pairs resemble the observed $2P$ mode configuration of Schnipper et al. (2009), an elaborate evaluation is still warranted in order to understand the transitioning spatial topologies of $2P$ mode shown in Figure 7.4. Furthermore, the kinematics investigated by Schnipper et al. (2009) followed a pure pitching motion rather than a combined heaving and pitching motion assumed in our current study.

7.3.3 Formation mechanism of $2P^D$ pairs and symmetric bifurcation

We now examine the formation process of $2P^D$ pairs at $Re = 1000$ by assessing the temporal evolution of shed vortical structures for the case of $St_c = 0.4$ and $\phi = 180°$. This parameter space is selected based on observations in Figures 7.3(a) and 7.4(e), which allows for a better examination and characterization of bifurcations observed in $2P$ mode. The snapshots representing contours

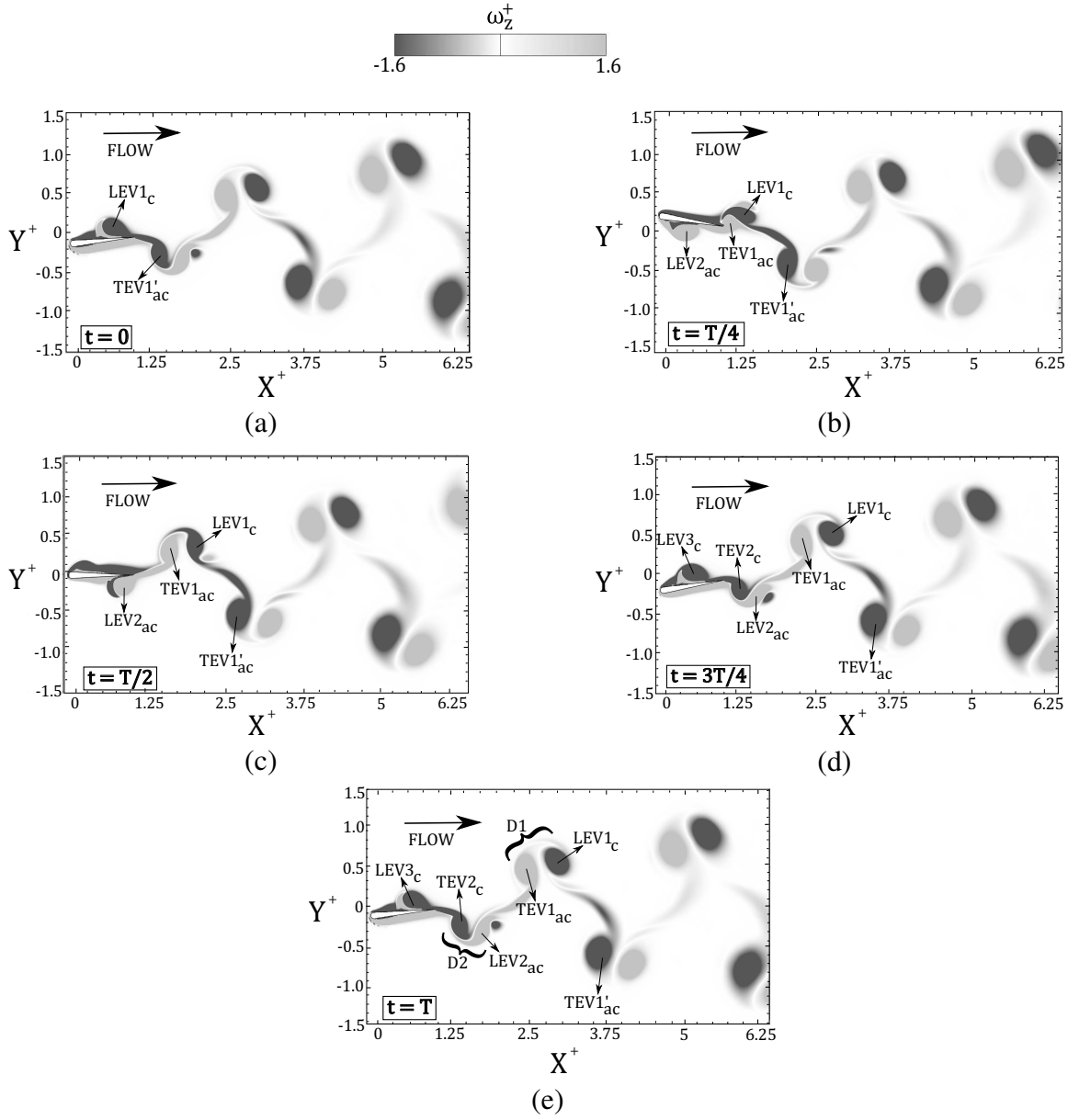

Figure 7.5: Temporal snapshots representing contours of ω_z^+, and depicting formation of $2P^D$ pair and bifurcation within the $2P$ mode at $St_c = 0.4$, $\phi = 180^\circ$ and $Re = 1000$.

of spanwise vorticity (ω_z^+), at each quarter phase of an oscillation cycle, are illustrated in Figure 7.5. At the beginning of an oscillation cycle (i.e. at $t = 0$) in Figure 7.5(a), a developed $LEV1_c$ is located close to the trailing edge, where $TEV1'_{ac}$ is formed in the previous half oscillation cycle. At $t = T/4$ in Figure 7.5(b), $LEV1_c$ is detached from the trailing edge, where a new anti-clockwise $TEV1_{ac}$ starts forming behind the foil. Also, a new $LEV2_{ac}$ appears developed at approximately the mid-chord region. $LEV1_c$ forms a dipole-like paired configuration with $TEV1_{ac}$ at the end of half oscillation cycle (i.e. $t = T/2$) in Figure 7.5(c), while $LEV2_{ac}$ is on the brink of detachment from the trailing edge. With the oscillations proceeding to $t = 3T/4$ in Figure 7.5(d), the first dipole-like pair ($D1$) is observed, which consists of vortical structures $LEV1_c$ and $TEV1_{ac}$. Simultaneously, a new trailing edge structure ($TEV2_c$) begins to form and pairs with $LEV2_{ac}$, which is now detached from the trailing edge. By the end of one oscillation cycle in Figure 7.5(e), $TEV2_c$ and $LEV2_{ac}$ form a second dipole-like pair ($D2$). Both $D1$ and $D2$ are marked in Figure 7.5(e). This description of the formation mechanism of $2P^D$ pairs is quite similar to that of a $2P$ pair observed in the wake of oscillating cylinders (Williamson and Roshko, 1988) and foils (Schnipper et al., 2009; Andersen et al., 2017) with a single degree of freedom motion. Such $2P$ pairs were also seen in wakes corresponding to $\phi = 0^\circ$ in this study, as observed in Figures 7.4(a) and 7.9(a). However, what distinguishes the $2P^D$ pair observed at $\phi = 180^\circ$ from the previously discussed $2P$ pairs is the approximate equality of circulation strength and size of the fully developed leading and trailing edge vortical structures ahead of their complete detachment from the foil's trailing edge. On account of these features, the mutual induced velocity of the dipole-like pair contributes to their movement away from the wake centerline, thus leading to the bifurcated dual vortex streets observed in Figure 7.4(e). The dipole-like formation is also different from the dual branch Mode-1 described by Cleaver et al. (2011) for purely heaving foils. There, the dipole configuration constituted a weak trailing edge structure and another collective structure that was formed on account of a merger between strong leading and trailing edge vortices. This collective structure was formed and shed within one half oscillation cycle. In the case of $2P$ mode characterized by a fully developed $2P^D$ pair, we do not observe the formation of any collective structure similar to those reported

by Cleaver et al. (2011). The above described process, therefore, hints at a spatial wake topology that is unique to foils with a combined heaving-pitching motion with different characteristics in terms of the vortex pair configuration despite similarities in their formation process.

The above mentioned details of formation mechanism further allow us to relate the correspondence of the $2P^D$ pairs to the heave-dominated regime at $Re = 1000$ (see Figure 7.3(a)). As observed here, only heave dominated cases at $Re = 1000$ present a viable scenario, where the generated trailing and leading edge vorticity attains equal circulation strength and size after getting detached from the foil's trailing edge. It results in a net induced velocity of the dipole-like pair, pushing it away from the wake centerline and thus leading to bifurcations. As the kinematics transition to pitch-dominated regime, the trailing edge vorticity gains enough strength relative to the leading edge vorticity that an eventual merger between similar sign structures occur (see Figure 7.4(a)). Hence, it leads to a symmetric *rBvK* wake profile. Quantitative assessments described in the next section provide further evidence for our qualitative observations described above.

7.3.4 Quantitative assessment of evolution characteristics

The quantitative assessment of circulation strength (Γ^+) and separation distance between the centers of vortices ($\zeta^+ = \zeta/c$) can provide deeper insights into changes in evolution characteristics of the shed vortex structures with an increasing ϕ at $Re = 1000$. These would also help understand particular features associated with changes in spatial topology of $2P$ wake, and appearance of bifurcations of $2P^D$ pairs. Specifically, we focus on the computed values of Γ^+ and ζ^+ just at the instance (shown in Figure 7.4), when the counter-rotating vortex structures form pairs ahead of the foil's trailing edge. The estimation process for Γ involves calculating the surface integral of vorticity on a rectangular contour window using:

$$\Gamma = \iint_S (\nabla \times V) \cdot dS \tag{7.1}$$

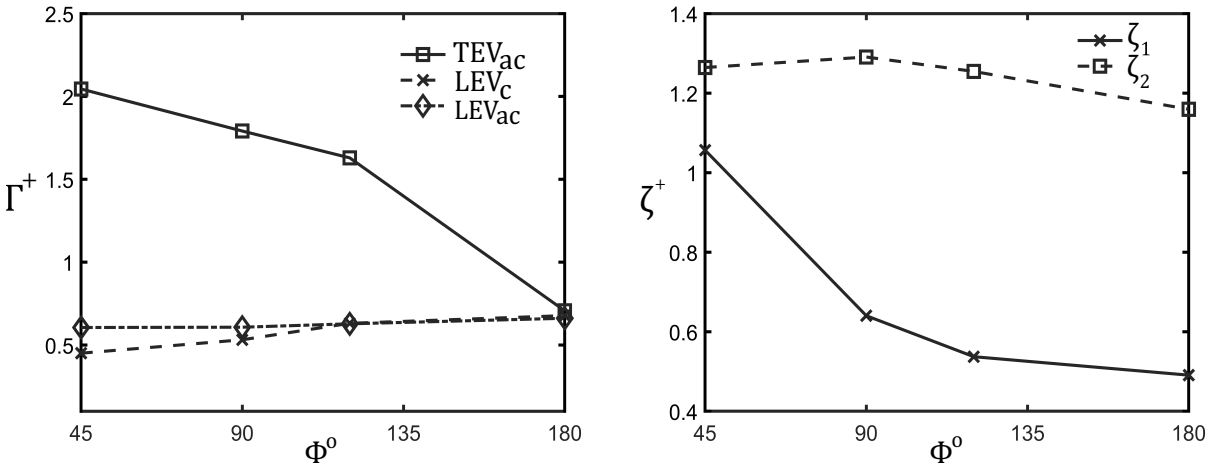

Figure 7.6: Variation of (a) Γ^+ and (b) ζ^+ between counter-rotating and co-rotating vortex structures (highlighted in Figure 7.4), with respect to ϕ.

To calculate ζ, the location of maximum vorticity magnitude, within the rectangular window surrounding the vortex, is evaluated for each structure that form either a co-rotating or counter-rotating pair. The coordinate of centers (X,Y) are then used to find ζ:

$$\zeta = \sqrt{(X_2 - X_1)^2 + (Y_2 - Y_1)^2} \tag{7.2}$$

where, subscripts 1 and 2 depict the center coordinates of two similar sign or counter-rotating vortical structures, respectively. Figure 7.4 presented earlier, depict three windows around vortex structures TEV_{ac}, LEV_c and LEV_{ac}. TEV_{ac} and LEV_c form a pair of counter-rotating vortices, which eventually transitions to a dipole-like configuration as ϕ increases to 180°. TEV_{ac} and LEV_{ac} also undergo mutual interaction on account of their similar sense of rotation. These aspects further motivate us to understand the evolution of marked vortex structures, quantitatively.

Figure 7.6 shows the variation of Γ^+ and ζ^+ with increasing ϕ for the heave-dominated kinematic settings ($\phi = 45° - 180°$), since the major focus is on characterizing the bifurcated vortex street observed for $2P$ mode in this range of ϕ. As seen from Figure 7.6(a), Γ^+ for TEV_{ac} consistently drops as ϕ increases from 45° to 180°. However, the paired vortex structure LEV_c depicts an

opposite trend compared to TEV_{ac}, although the variation of Γ^{+} is not as significant as in case the of TEV_{ac}. Despite the observed variations for these paired vortex structures, the newly shed LEV_{ac} depict no changes with respect to increasing ϕ. This clearly signifies that the dominant evolution characteristics of LEVs remain approximately similar as it attains a paired configuration with the TEV, while kinematics transition from a pitch based motion setting to a heave dominated oscillation. The trailing edge vorticity, however, is greatly influenced by the changes in trailing edge amplitude that was previously discussed in Figure 7.2(a). The variation of ζ_1 and ζ_2, corresponding to the distance calculated between counter-rotating (LEV_c and TEV_{ac}) and co-rotating (LEV_{ac} and TEV_{ac}) vortex structures, is further depicted in Figure 7.6(b). Similar to the qualitative discussion provided with respect to Figure 7.4, we observe a decrease in ζ_1 as ϕ increases from 45° to 180°. On the other hand, ζ_2 shows an increase up to $\phi = 90°$, followed by a slightly decreasing trend towards $\phi = 180°$. The birfurcated vortex streets observed at $\phi = 180°$, which were qualitatively characterized by a fully developed dipole-like configuration, does possess a reduced separation distance between the counter-rotating vortex structures, along with their equal magnitude of Γ^{+}. Comparing these quantitative characteristics to the dipoles observed in deflected wakes of purely heaving and pitching foils (Cleaver et al., 2012; Calderon et al., 2014; He and Gursul, 2016; Deng et al., 2015), the dipole-like $2P^D$ pairs constituting bifurcated wake streets also resemble similar evolution characteristics. However, the resultant wake still possessed a symmetry along the wake centerline, which therefore differs from the deflected wake modes observed previously (Cleaver et al., 2012; Calderon et al., 2014; Deng et al., 2015).

To further understand the transition from a paired configuration of counter-rotating structures with unequal circulation to the dipole-like arrangement characterized by equal strength structures ($2P^D$ pairs), we mathematically model the circulation estimates of a single LEV and TEV at the instant of their shedding from the foil's trailing edge. This will also highlight any existing dependence of vortex evolution characteristics on ϕ. A single LEV structure is formed as a result of boundary layer roll-up near the leading edge, on one side of the foil. Hence, its circulation estimation (Γ_{LEV}) can be obtained by calculating the vorticity transport in the boundary layer (Schnipper

et al., 2009). This transport also assumes no-slip conditions on the foil, while considering contributions from the U_∞ and $\dot{h}$ at the leading edge. Similar assumptions were also in place for the models developed by Schnipper et al. (2009) although their analysis was limited to pitching motion and did not include the dependence on heave velocity. Based on the estimation of vorticity production in the boundary layer, given by Tietjens et al. (1957), we can calculate Γ^+ for *LEV* just at the instant of its shedding in one half oscillation cycle using the following relation:

$$\Gamma_{LEV} = \frac{1}{2}\int_0^{T/2} (U_\infty^2 + \dot{h}^2)\, \mathrm{d}t \tag{7.3}$$

Here, $\dot{h}$ could be evaluated using the time derivative of Eq.2.2. The integral can be subdivided as:

$$\Gamma_{LEV} = \frac{1}{2}\left[\frac{U_\infty^2 T}{2} + \int_0^{\frac{T}{2}} h_o^2 4\pi^2 f^2 \cos^2(2\pi f t) dt\right] \tag{7.4}$$

$$\Gamma_{LEV} = \frac{1}{2}\left[\frac{U_\infty^2 T}{2} + h_o^2 4\pi^2 f^2 \frac{1}{8}\left(\frac{\sin(2\pi f T)}{\pi f} + 2T\right)\right]. \tag{7.5}$$

The *sin* term evaluates to zero in the above equation, which therefore simplifies the above expression to:

$$\Gamma_{LEV} = \frac{U_\infty^2}{4f} + \frac{h_o^2 \pi^2 f}{2} \tag{7.6}$$

Using D and St_D, we can again rewrite the last expression as:

$$\Gamma_{LEV} = \frac{D^2 U_\infty + 2St_D^2 U_\infty h_o^2 \pi^2}{4DSt_D} \tag{7.7}$$

Now, the Γ_{TEV} can be estimated in a way similar to that followed by Schnipper et al. (2009), where

they assumed that the freestream contribution to the vorticity is negligible. The expression can be written as:

$$\Gamma_{TEV} = \frac{1}{2}\left(\int_0^{\frac{T}{2}} U_{TE}^2(t)dt\right) \approx \frac{1}{2}\pi^2 A_T^2 f \tag{7.8}$$

In terms of St_D and A_D, we can further rewrite the above expression as:

$$\Gamma_{TEV} \approx \frac{1}{2}\pi^2 A_D^2 St_D D U_\infty \tag{7.9}$$

Now, in order to obtain an approximate estimate for the ratio of Γ for the LEV and TEV structures, we can divide Eq.7.9 by Eq.7.7. This ratio can be represented in its final form:

$$\frac{\Gamma_{TEV}}{\Gamma_{LEV}} \approx \left[\frac{2\pi^2 A_D^2}{\frac{1}{St_D^2} + \frac{2h_o^2\pi^2}{D^2}}\right] \tag{7.10}$$

Here, the second term in the denominator is a constant value since the heave amplitude is not varying in our study. We can denote it as $\kappa = 2h_o^2\pi^2/D^2$. Also, after making some more simplifications to the above expression, we can also obtain a dependence on the St_A, and thus:

$$\frac{\Gamma_{TEV}}{\Gamma_{LEV}} \approx \frac{1}{2}\left[\frac{\pi^2 St_A^2}{1 + \kappa St_D^2}\right] \tag{7.11}$$

The above expression clearly highlights that at a constant St_D, dependence of the ratio $\Gamma_{TEV}/\Gamma_{LEV}$ on St_A is quite similar to the case of pitching foil developed by (Schnipper et al., 2009), although with a difference in constant of proportionality. We can still modify the above relationship to further obtain a dependence on the heave based Strouhal number $St_h = 2fh_o/U_\infty$. This formulation

can be applied for cases where the variation of heave amplitude is also taken into account. This relationship becomes:

$$\frac{\Gamma_{TEV}}{\Gamma_{LEV}} \approx \left[\frac{\pi^2 St_A^2}{2+\pi^2 St_h^2}\right] \tag{7.12}$$

By relating Eq. 7.12 to the qualitative depiction of wake modes on $A_c - St_c$ phase diagram in Figure 7.3(b), we identify that there is a wake mode transition from $2P$ to $rBvK$ type with increasing St_A from 0.1 to 0.2 and beyond. This is consistent with the observations of Schnipper et al. (2009), who found that a similar rise in relative strength of trailing edge structures was responsible for transition of wake from $2P$ to an $rBvK$ mode. We can also relate this derived model with our quantitative details of kinematics (Figure 7.2) and circulation estimates depicted in Figure 7.6(a), at a constant $St_h = 0.2$ and $St_c = 0.4$. Specifically, the kinematics indicated that with increasing ϕ from 45° to 180°, the peak trailing edge amplitude decreases to a minimum. This would result in a decrease in St_A, which based on Eq. 7.11 and Eq. 7.12 should lead to a decrease in Γ_{TEV}. Ahead of $\phi = 45°$, the variation of Γ_{TEV} in Figure 7.6 confirms this qualitative trend based on the strength of fully developed TEV_{ac}. Note that the parameters St_D and St_h are kept as constants in Eq. 7.11 and Eq. 7.12, respectively. The bifurcation of dipole like vortex pairs ($2P^D$ pairs) within $2P$ mode can be also be linked to Eq. 7.12. As stated, when St_A reduces on account of increasing ϕ, the relative Γ_{TEV} also decreases. At the specific St_A (corresponding to $\phi = 180°$ and $St_c = 0.4$ in our phase space diagram), $\Gamma_{TEV}/\Gamma_{LEV}$ at the instance of shedding is such that the fully developed $2P^D$ pairs, ahead of their complete detachment from foil's trailing edge, constitute vortex structures of equal Γ^+ and lowest ζ. This was quantitatively confirmed in Figure 7.6(a) wherein we see an equal magnitude of $\Gamma^+_{TEV_{ac}}$ and $\Gamma^+_{LEV_c}$ at $\phi = 180°$, $St_c = 0.4$ and $St_h = 0.2$. This contributes towards a transverse induced velocity leading to advection of the $2P^D$ pairs away from the wake centerline, thus causing bifurcation.

It is clear that the approximations for circulation ratio obtained in Schnipper et al. (2009) for purely pitching motion and Eq. 7.12 are quite comparable when St_h is constant. However, Eq. 7.12

still provides a valid and easy extension of the previous approximation (Schnipper et al., 2009) for an oscillating foil in coupled heaving and pitching motion, as considered here. Thus far, the validity of the proposed model is only qualitatively interpreted in terms of its accuracy in predicting the trend between relative circulation strength ($\Gamma_{TEV}/\Gamma_{LEV}$) and St_A for cases corresponding to heave-dominated kinematics at $Re = 1000$ and $St_h = 0.2$ (Figure 7.3). In order to quantitatively evaluate the model's predictive capability at a wider parameter space, an approximate relationship is derived for the relative circulation strength in terms of ϕ, by transforming St_A into heave-based (St_h) and pitch-based (St_θ) Strouhal numbers. This is achieved by evaluating the vector addition of St_h and St_θ (Van Buren et al., 2019), and incorporating ϕ between the pitch and heave motion. This is represented as:

$$St_A^2 = St_h^2 + St_\theta^2 + 2St_h St_\theta \cos\phi \tag{7.13}$$

Here, St_θ is defined as $2fc\theta_o/U_\infty$. Substituting Eq. 7.13 in Eq. 7.12, we will obtain:

$$\frac{\Gamma_{TEV}}{\Gamma_{LEV}} \approx \left[\frac{\pi^2\left(St_h^2 + St_\theta^2 + 2St_h St_\theta \cos\phi\right)}{2 + \pi^2 St_h^2}\right] \tag{7.14}$$

Now we introduce coefficients (c_n) in each term of Eq. 7.14, to account for the multiplicative constants similar to the approach followed by Van Buren et al. (2019) and Section 4.3 of Chapter 4. The resulting expression is therefore written as:

$$\frac{\Gamma_{TEV}}{\Gamma_{LEV}} = \left[\frac{c_1 St_h^2 + c_2 St_\theta^2 + c_3 St_h St_\theta \cos\phi}{c_4 + c_5 St_h^2}\right] \tag{7.15}$$

The coefficients c_n are determined by performing linear regression over the entire parameter space represented in the phase maps (see Figure 7.3). The range of St_h, St_θ and ϕ correspond to $0.08 \leq St_h \leq 0.24$, $0.05 \leq St_\theta \leq 0.17$ and $0^\circ \leq \phi \leq 180^\circ$. Figure 7.7 depicts the plot for calculated

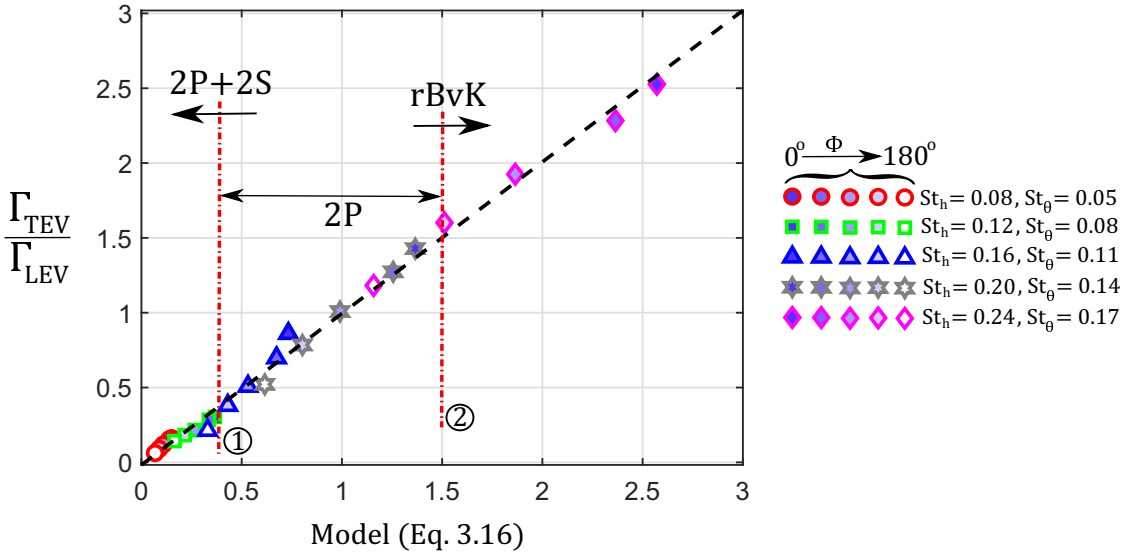

Figure 7.7: Scaling of estimated $\Gamma_{TEV}/\Gamma_{LEV}$ and Model (Eq. 7.15) outputs at increasing St_h, St_θ and ϕ.

estimates of $\Gamma_{TEV}/\Gamma_{LEV}$, determined through numerical simulations, and output of the expression represented by right hand side of Eq. 7.15. The coefficients correspond to $c_1 = 2.02$, $c_2 =$ -0.51, $c_3 = 0.97$, $c_4 = 0.11$ and $c_5 =$ -0.96. As evident in Figure 7.7, we observe a collapse of $\Gamma_{TEV}/\Gamma_{LEV}$ and the model outputs (Eq. 7.15) which therefore indicate a reasonable accuracy of the model at an increasing range of St_h, St_θ and ϕ. We also depict vertical iso-lines in Figure 7.7 that correspond to the model output of ≈ 0.4 and 1.5. These further mark the approximate bounds where a particular wake topology will dominate for a specific combination of St_h, St_θ and ϕ. Kinematic setting corresponding to the left of iso-line 1 shows a dominant $2P+2S$ wake mode, based on the observations from phase maps depicted in Figure 7. Between iso-lines 1 and 2, the $2P$ mode dominates the wake. The specific bounds associated with the $2P$ wake mode with vortex bifurcation ($2P^D$ pairs) occur within the region bounded by iso-lines 1 and 2. Region to the right of iso-line 2 depicts the dominance of *rBvK* wake mode while the $2P$ mode is entirely absent. Overall, Eq. 7.15 constitutes a novel relationship that best describes the transition of wake topology for an oscillating foil with combined motion, based on most critical kinematic parameters including St_θ, St_h, and ϕ.

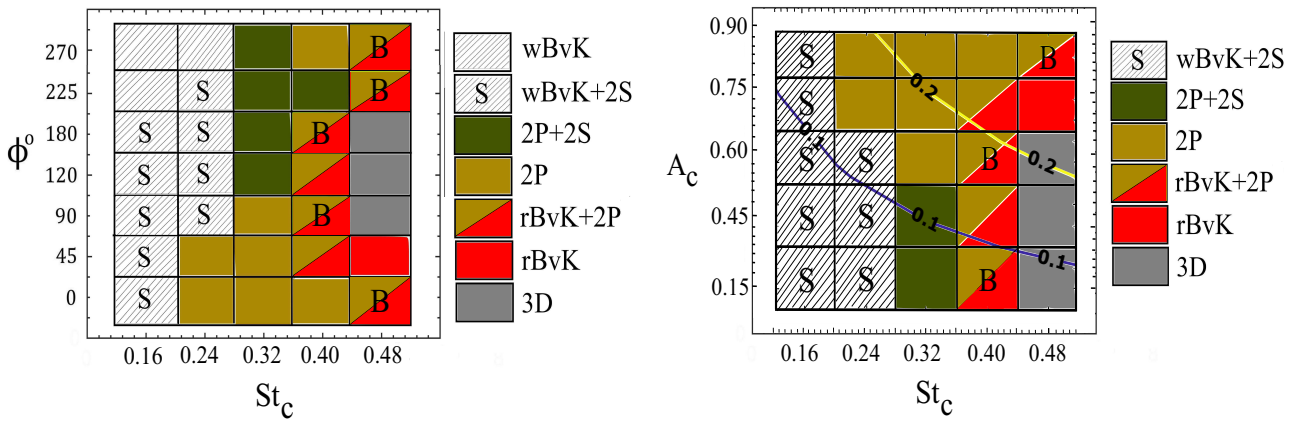

(a) (b)

Figure 7.8: Phase map representation of identified wake modes on (a) $\phi - St_c$ and (b) $A_c - St_c$ phase-space for $Re = 4000$.

7.3.5 Evaluation of wake mode transition at $Re = 4000$

To identify the topological transition features of wake modes, validity of mathematical model (i.e. Eqns.7.12 and 7.14) and existence of bifurcations in $2P$ mode at an increased Re, we now present the phase maps in $\phi - St_c$ and $A_c - St_c$ phase space at $Re = 4000$ in Figure 7.8. We observe that at low $St_c < 0.24$, $wBvK$ mode is supplemented by shedding of two additional single vortical structure, thus representing the configuration as a $wBvK + 2S$ mode. At $St_c > 0.32$, existence of bifurcation is revealed although an additional reverse Von Kármán ($rBvK$) vortex street also co-exists with $2P$ mode. Thus, the resulting wake mode is categorized as $rBvK + 2P$. The $rBvK + 2P$ mode also appears at an increased St_c of 0.48.

On the $A_c - St_c$ phase-space shown in Figure 7.8(b), we observe a transition from $wBvK + 2S$ to $2P$ mode which roughly coincides with the line of $St_A = 0.1$. Beyond $St_A = 0.2$, the $2P$ mode transitions to either $rBvK$ or $rBvk + 2P$ mode. We also observe that the bifurcations in $rBvK + 2P$ mode does not coincide or fall within any threshold St_A, which is in contrast to the observations at $Re = 1000$ (see Figure 7.3(b)). These bifurcations are noticeable at increased St_c and in the entire range of A_c assumed in our study. On account of the above noted observations in $A_c - St_c$ phase space, it can be further deduced that mathematical relationship outlined in Eq. 7.12 and

Eq. 7.14 may not provide an accurate prediction of wake transition at higher Re of 4000. The limitation of our model, as stated above, could also indicate that there are other possible effects on vorticity production at higher Re, besides strengthening of the trailing edge vortex structures with increasing St_A (as suggested by Equation 7.12). This would then make the approximation of LEV and TEV strengths inaccurate in Equation 7.3 and Equation 7.8. These relationships used in Schnipper et al. (2009) have only been validated at Re close to 1000, which were further confirmed in our study as well. Thus, an extensive analysis is still needed to address this limitation in the application of our mathematical model over a range of Re. It is also important to note that studies and models concerning phase space representation of wake modes and their transition (Godoy-Diana et al., 2008, 2009; Deng et al., 2015; Sun et al., 2018; Zheng et al., 2019) were also limited to $1000 < Re < 1500$. The mechanism of transitioning wake topology and bifurcations of vortex pairs in $2P$ mode at $Re = 4000$ could further reveal differences in wake evolution that could hint at weakness of mathematical model in predicting the changes in spatial topologies of $2P$ mode.

In order to highlight the transitions in wake topology and presence of bifurcations in $rBvK+2P$ mode at $Re = 4000$, Figure 7.9 qualitatively depicts the modes in range of $0^\circ \leq \phi \leq 180^\circ$ at $St_c = 0.4$. The wake is dominated by a $2P$ mode at $\phi = 0^\circ$, which is similar to the observations at $Re = 1000$ (see Figure 7.4(a)). The paired trailing and leading edge vortex structure retain coherence only for a short while, after which the similar sign neighboring structures merge to form a single coherent structure shown in Figure 7.9(a). At $\phi = 45^\circ$, a reverse Von Kármán mode is observed in Figure 7.9(b), which is characterized by shedding of strong trailing edge structures that advect close to the wake centerline. In addition, we see dipole-like paired counter-rotating structures ($2P^D$ pairs) that possess weaker strength compared to the trailing edge structures characterizing the $rBvK$ mode. Further, one of the vortical structures constituting this $2P^D$ pair also undergoes stronger stretching in comparison to its counterpart. This $2P^D$ pair, however, do not diverge away from the wake centerline as seen in Figure 7.9(b). On account of the combined presence of features characterizing $rBvK$ and $2P$ modes, the resulting wake configuration was termed as $rBvK+2P$ in Figure 7.8(b).

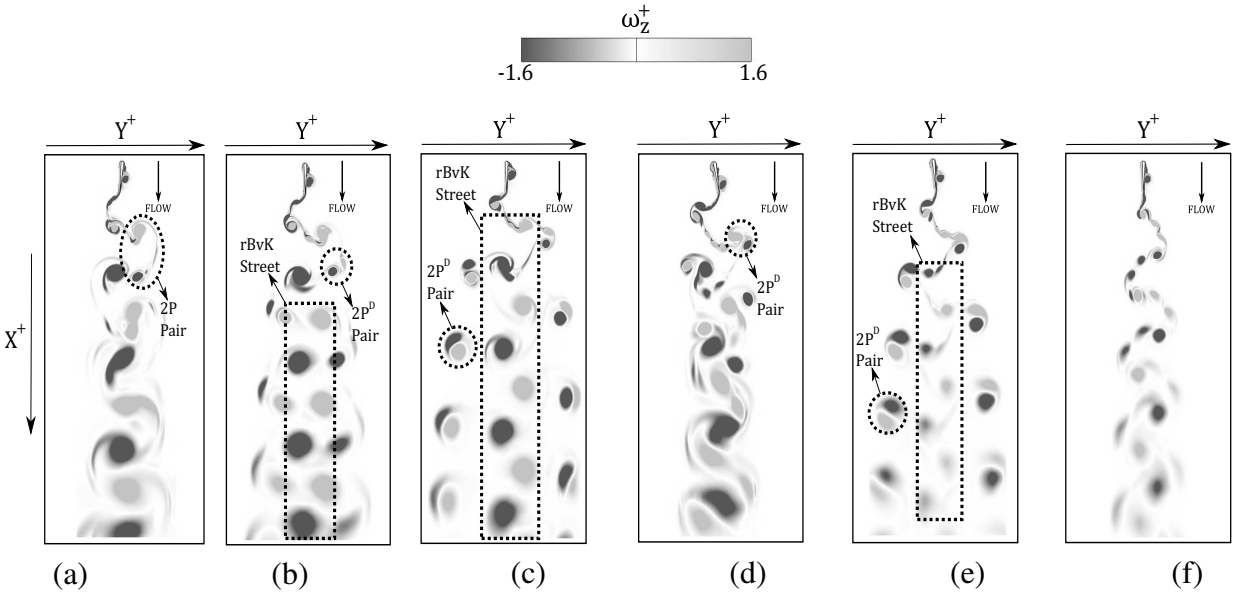

Figure 7.9: Wake modes at increasing ϕ and $Re = 4000$. (a)-(f) represents ϕ corresponding to 0°, 45°, 90°, 120°, 180° and 225°, respectively, while St_c corresponds to 0.4.

Vortex streets that depict clear bifurcation in addition to the advecting *rBvK* structures are observed along the wake centerline with increasing ϕ to 90° (Figure 7.9(c)). The counter-rotating vortical structures constituting these streets also resemble the dipole-like configuration observed previously for $2P^D$ pairs at $Re = 1000$. We further see that the vortical structures associated with *rBvK* mode have more circulation strength and larger size compared to the dipole-like paired structures. This characteristic, however, undergoes a reverse transition at $\phi = 120°$, where the dipole-like paired vortices qualitatively possess a greater strength and size compared to *rBvK* structures. We further see that during this transition at $\phi = 120°$, the similar sign vortices associated with bifurcated vortex streets and *rBvK* street, respectively, merge and form single coherent structures approximately around the middle (streamwise) of the wake. A bifurcation of dipole-like pairs is again visible while increasing ϕ to 180° (Figure 7.9(e)), although the weaker *rBvK* street along the wake centerline is now more vivid compared to $\phi = 120°$. The transition and appearance of bifurcated vortex streets in the wake associated with higher *Re* therefore shows different wake features compared to the wakes identified at lower *Re* in Figure 7.4. Here, we first observe formation of dipole like $2P^D$ pairs in conjunction with *rBvK* structures at $\phi = 45°$. The individual vortices forming the $2P^D$ pair typically possessed lower strength and size compared to the vortical struc-

tures that constitute *rBvK* street. However, the $2P^D$ pairs undergo a consistent increase in their strength and size compared to the *rBvK* structures with increasing ϕ from 45° to 180°. The diverging vortical streets comprising of the $2P^D$ pairs are observed at $\phi = 90°$, which then appeared to resist their movement away from the wake centerline as ϕ increases to 120°. A re-emergence of bifurcated vortex street was then observed at $\phi = 180°$. We believe that this dynamic change in the behavior of bifurcated dipolar streets could be directly associated with the consistent increase, and decrease, in the strength and size of structures, which constitute bifurcated vortex streets and *rBvK* wake, respectively. A more closer attention to the formation mechanism will further reveal details into the transitions of modes observed here. Lastly at $\phi = 225°$ (Figure 7.9(f)), the wake again represents a $2P+2S$ mode, which was even observed and discussed in Figure 7.4(f) at $Re = 1000$. Thus, the unique observations and characterization of bifurcations in $2P$ mode still holds for a higher Reynolds number, although there are additional complexities observed in terms of a combined $rBvK+2P$ mode.

7.3.6 Formation mechanism of $rBvK+2P$ mode and symmetric bifurcations

The wake modes observed for increasing St_c and ϕ at $Re = 4000$ were characterized by a $rBvK+2P$ configuration, where the $2P$ mode observed at $Re = 1000$ is supplemented with a *rBvK* vortex street. Figure 7.10 shows the formation and temporal evolution of wake structures constituting the $rBvK+2P$ mode, along with observed bifurcation of $2P^D$ pairs, at $Re = 4000$. As the oscillation cycle begins (i.e. at $t = 0$) in Figure 7.10(a), we observe a very similar shedding pattern near the trailing edge compared to $Re = 1000$ (see Figure 7.5). The counter-rotating leading and trailing edge structure form an approximate dipole-like paired configuration in each half shedding cycle, which then detaches from the trailing edge. Two dipole-like structures, marked as $D1'$ and $D2'$, are shown in Figure 7.10(a). The dipole-like $2P^D$ pair then moves away from the wake centerline on account of the mutual induced velocity of the pair. However, as the dipole-like structures advect downstream, we observe that an elongated leg of the trailing edge vortex shed in the previous half shedding cycle splits to two structures. This splitting phenomenon was not observed for the

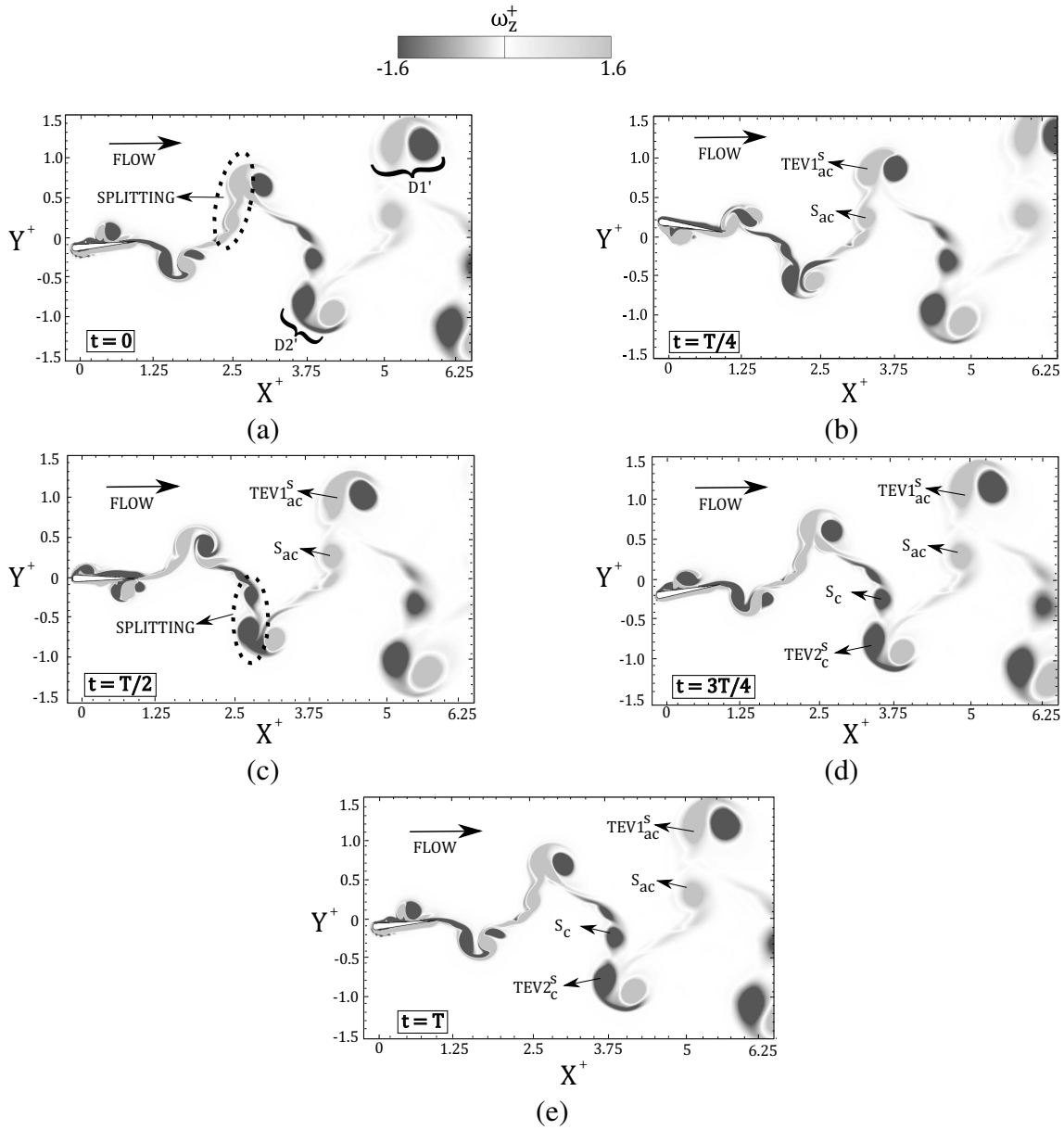

Figure 7.10: Temporal snapshots representing contours of ω_z^+, and depicting formation of $rBvK + 2P$ mode with bifurcation at $Re = 4000$.

$2P$ mode formation at $Re = 1000$. At $t = T/4$ in Figure 7.10(b), we observe vortical structures $TEV1^s_{ac}$ and S_{ac} which form due to the splitting of the vortex leg shown in Figure 7.10(a). It is further seen that $TEV1^s_{ac}$ constitutes a dipole-like configuration of diverging vortex street, while S_{ac} eventually becomes a part of the $rBvK$ wake. A similar splitting process again starts at the end of the first half oscillation cycle, shown in Figure 7.10(c). However, the sense of rotation for the trailing edge vortex leg is opposite to that of the first half shedding cycle. The resulting split structures $TEV2^s_c$ and S_c are shown in Figure 7.10(d). These structures further contributes to the formation of $rBvK+2P$ mode. This characterization constitutes a new wake mode that has not been observed previously for bluff bodies or oscillating foils. It also accounts for a very different wake dynamics observed for oscillating foils with combined heaving and pitching motion, compared to those with either pure-heaving or pitching kinematics.

The shear splitting phenomenon that reasonably explained the formation process of $rBvK+2P$ and coinciding bifurcation, could also provide insights into the disappearance and re-emergence of the birfurcated dipole streets observed and highlighted in the previous section. As ϕ increases from 45° to 180°, we observed (Figures 7.9(b-e)) that a clear bifurcation of dipole-like pairs appear in conjunction with the $rBvK$ structures for $\phi = 90°$. However, at $\phi = 120°$, the bifurcation was not imminent. Further increase in ϕ to 180° depicted a re-appearance of bifurcation for the dipole like pairs. As indicated earlier, there is a consistent decrease in strength of trailing edge vortical structures relative to the structures forming at the leading edge. This change has a direct consequence on the shear splitting phenomenon where a delay in splitting of the trailing edge vortex leg occurs as ϕ increases from 45° to 180°. We qualitatively provide the evidence in Figure 7.11 which depict the shear splitting process for wake observed at $Re = 4000$, and $\phi = 45°$, 90°, 120° and 180°, respectively. At $\phi = 45°$ (Figure 7.11(a)), we see that as the TEV separates from the trailing edge, the dipole-like pair (D) is well detached, devoid of any mutual interaction with the TEV leg. As ϕ increases to 90° (see Figure 7.11(b)), the dipole-like pair (D) now appears close to the detached TEV while also undergoing mutual interaction with its leg. Thus, a delay is observed in the splitting process with weakening of the TEV. Further increasing ϕ to 120°,

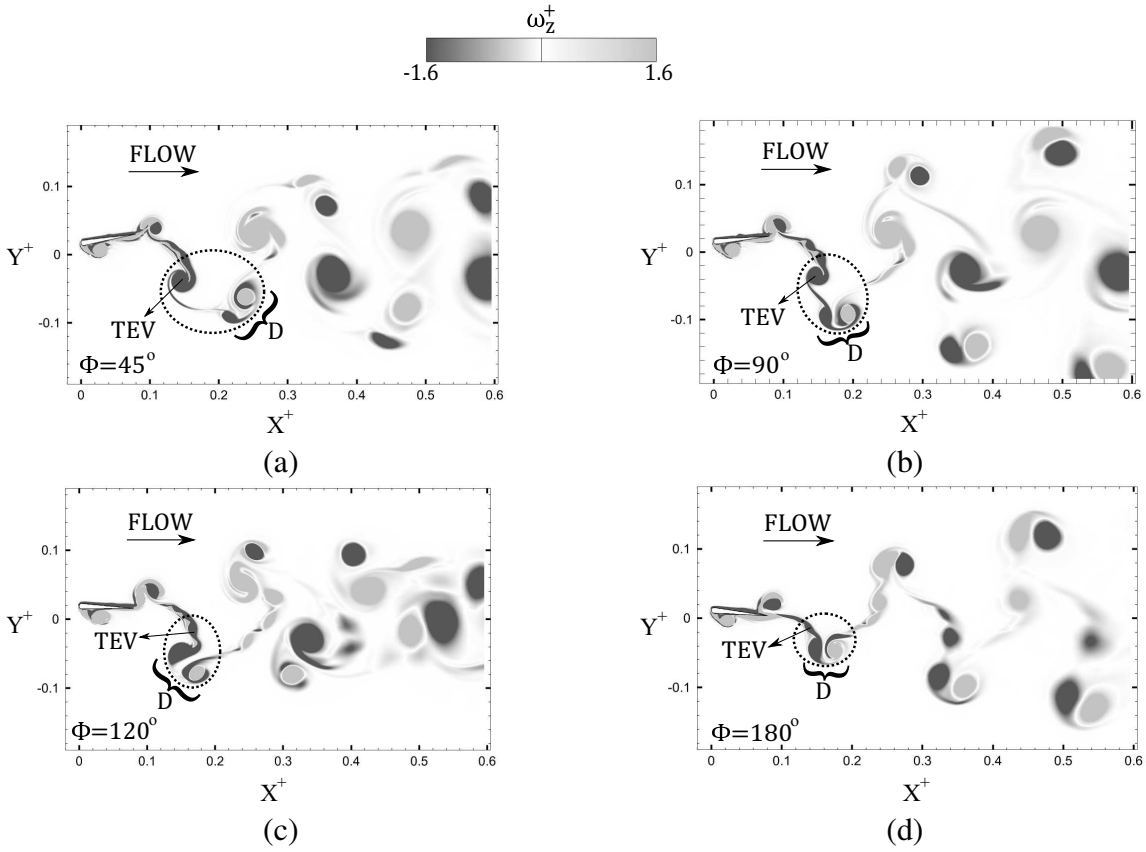

Figure 7.11: Changes in dynamic shear splitting process with increasing ϕ.

the splitting is further delayed compared to $\phi = 90°$. The weaker TEV strength compared to vortical structures constituting D is also observed in Figure 7.11(c). At $\phi = 180°$ (see Figure 7.11(d)), only dipole-like pair D appears well-developed with the splitting process undergoing an even greater delay compared to the cases at lower ϕ. The bifurcation of dipole streets that occur at $\phi < 120°$ could be attributed to the rapid splitting process which happens on account of the longer TEV development. However, bifurcation observed at $\phi > 120°$ could largely be a consequence of higher induced velocity of the dipole-like configuration, which further triggers the shear splitting ahead in the wake.

The lack of bifurcated dipole-like streets at $\phi = 120°$ also needs a closer attention. Figure 7.12 depicts the temporal evolution of the TEV and dipole-like pair D. Even after the shear splitting (at approximately $t = 0.45$T in Figure 7.12) occurs, the short separation distance between the clock-wise vortex, constituting the dipole pair (D), and TEV promotes a merger rather than movement

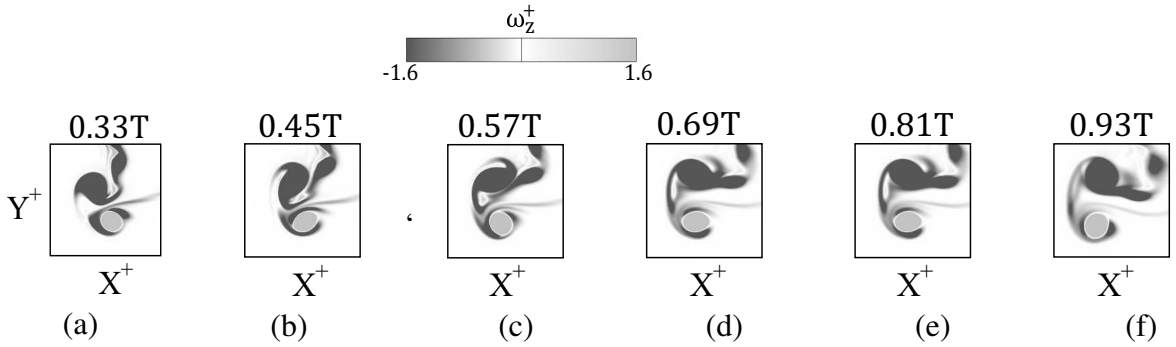

Figure 7.12: Temporal evolution of wake splitting and merging at $\phi = 120°$.

of D away from the wake centerline. Thus we also see in Figure 7.12(c) that the split $TEVs$ eventually merge with the similar sign vortical structures of neighboring dipoles that further undergo a combined interaction near the wake centerline. Besides the determination of critical ϕ (i.e. $\phi = 120°$) where the bifurcation disappears and dipole-induced velocity begins to dominate the wake dynamics, a more detailed investigation is underway in a separate study, which will quantitatively model the above transition process.

The splitting observed at $Re = 4000$ provides additional explanations for the potential limitation of the proposed mathematical model in Equations 7.12 and 7.14 for higher Reynolds numbers. The observations of Schnipper et al. (2009) indicated no splitting in their wake structures near the foil trailing edge at $Re \approx 1200$. The approximation of downward transport of vorticity, as employed in our study similar to that of Schnipper et al. (2009), was based on estimating the vorticity production from Tietjens et al. (1957), which do not account for any effect of splitting mechanism in the wake of bluff bodies. As also detailed in the study by Ramesh et al. (2012), with regards to unsteady effects on leading edge vortex shedding with increasing Re, the vorticity distribution and thereby the circulation is inherently dependent on the wake induced downwash velocity in parallel and normal direction to the foil chord. This wake induced velocity at $Re = 4000$ will not be similar to the approximation (Ramesh et al., 2012) that holds at $Re = 1000$ due to the onset of unsteady splitting mechanisms in the near wake. This directly attributes to the inaccuracy in estimating circulation of the leading edge, or boundary layer, vortices (i.e. Equation 7.3). A similar observation holds for the study of Schnipper et al. (2009). This provides a reasonable

explanation for why our newly proposed mathematical model does not work well in predicting the transition in wake topological characteristics at higher Reynolds numbers, e.g., $Re = 4000$.

The higher complexity of wake dynamics observed at $Re = 4000$ also hint at a reason for the lack of correspondence between the $rBvK + 2P$ mode (and the observed bifurcation) and the pitch- or heave dominated kinematics. The qualitative and quantitative observations of $2P$ mode at $Re = 1000$ suggested that the equalization of strength and size of $LEVs$ and $TEVs$ is the only prominent contributing aspect for the observed bifurcated streets at higher Reynolds numbers, which only coincided with heave-dominated kinematics at low Re. However, the qualitative transition and formation mechanisms at $Re = 4000$ revealed a shear splitting process that was not seen at $Re = 1000$. This phenomenon also depicted varying temporal characteristics as the kinematics switch from pitch- to heave-dominated kinematics based on ϕ. We believe that since the dominance of this splitting process (responsible for formation of bifurcated vortex streets) at $Re = 4000$ is not limited within certain regimes of prescribed kinematics for the foil, such bifurcations in $rBvK + 2P$ wake mode can appear in different kinematic settings that induce similar effects, such as $St_c = 0.48$ at $Re = 4000$ (see Figure 7.8(b)).

7.3.7 Mean flow development in bifurcated dual vortex street wakes

In order to characterize the bifurcated dual vortex streets in $2P$ and $rBvK + 2P$ wake modes, we now evaluate the qualitative and quantitative $\overline{u_x^+}$ distribution in the wake. Figure 7.13 shows the contours of $\overline{u_x^+}$ for increasing ϕ at $St_c = 0.4$ and $Re = 1000$. Although we only depict the contours corresponding to cases of $\phi = 0°$, $90°$, $180°$ and $225°$, the quantitative profiles in Figure 7.14 are shown for all ϕ values ranging from pitch- to heave-dominated motion kinematics. These profiles are further obtained at three streamwise locations corresponding to $X^+ = 1.5$, 3.5 and 5.5, respectively, as shown in Figure 7.13(a). Due to similarities in the mean characteristics for some cases (for example $\phi = 90°$ and $120°$), only contours for some cases are shown for brevity.

The mean velocity excess at the wake centerline ($Y^+ = 0$) is maximum in the case of $\phi = 0°$ and $45°$, at all three X^+ locations (see Figure 7.14). However, a mean velocity deficit region is also

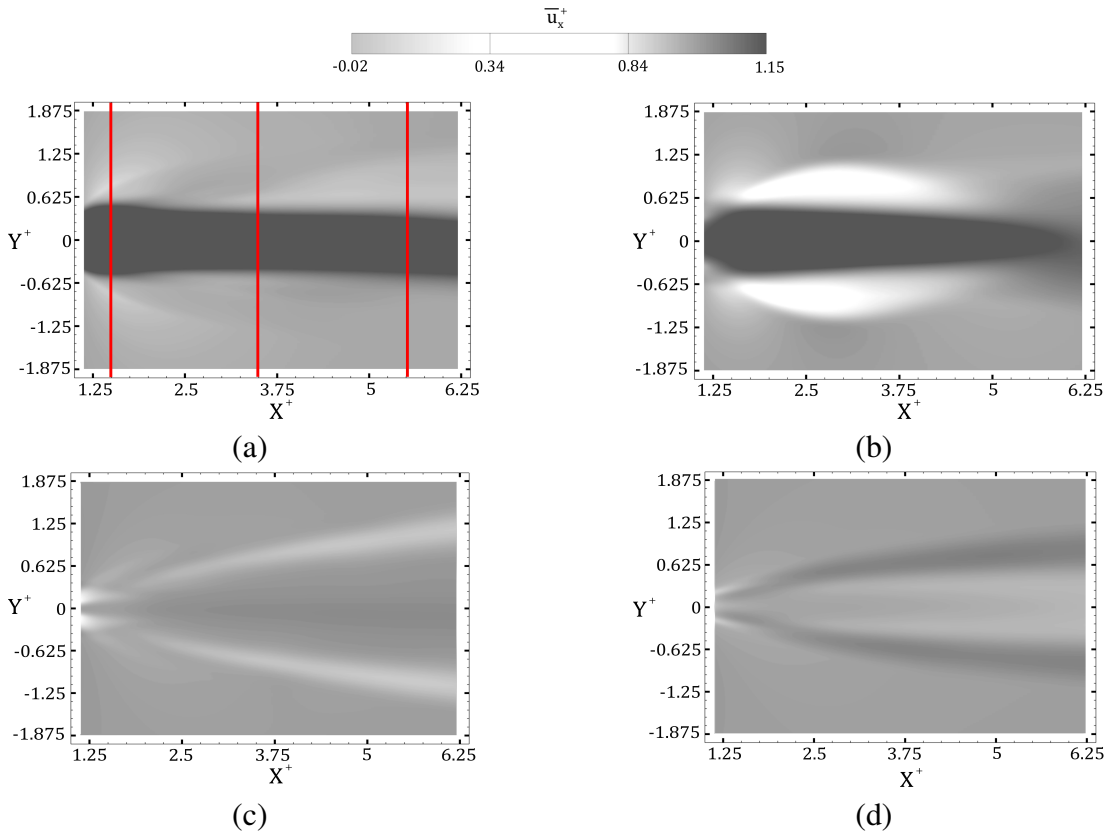

Figure 7.13: Contours of $\overline{u_x^+}$ at (a) $\phi = 0°$, (b) $\phi = 90°$, (c) $\phi = 180°$ and (d) $\phi = 225°$, respectively. Solid red lines depict the streamwise locations where cross-stream profiles of $\overline{u_x^+}$ are extracted and shown in Figure 7.14.

observed for $\phi = 45°$, which further strengthens with increasing X^+. These deficit regions are also observed alongside the mean thrust jet developing in the wake.

Earlier we discussed the upstream tilted vortex pairs depicted for $\phi = 45°$ in Figure 7.4(b), which did not show a significant merger between the neighboring vortex structures with a similar sense of rotation. These tilted pairs promote creation of a resultant induced velocity that acts against the freestream. Therefore, it results in the dual velocity deficit regions observed for the case of $\phi = 45°$. Such tilted pairs, however, were not seen at $\phi = 0°$ in Figure 7.4(a). Increasing ϕ to 90° showed a transition of counter-rotating paired vortex structures to a dipole-like formation in Figure 7.4(c). This clearly coincides with a reduction in the peak magnitude of the mean thrust jet, compared to the lower ϕ cases observed in Figure 7.14. This jet is also shortened in terms of its streamwise extent, as shown in Figure 7.13(b). This is also confirmed by the sharp drop in the peak

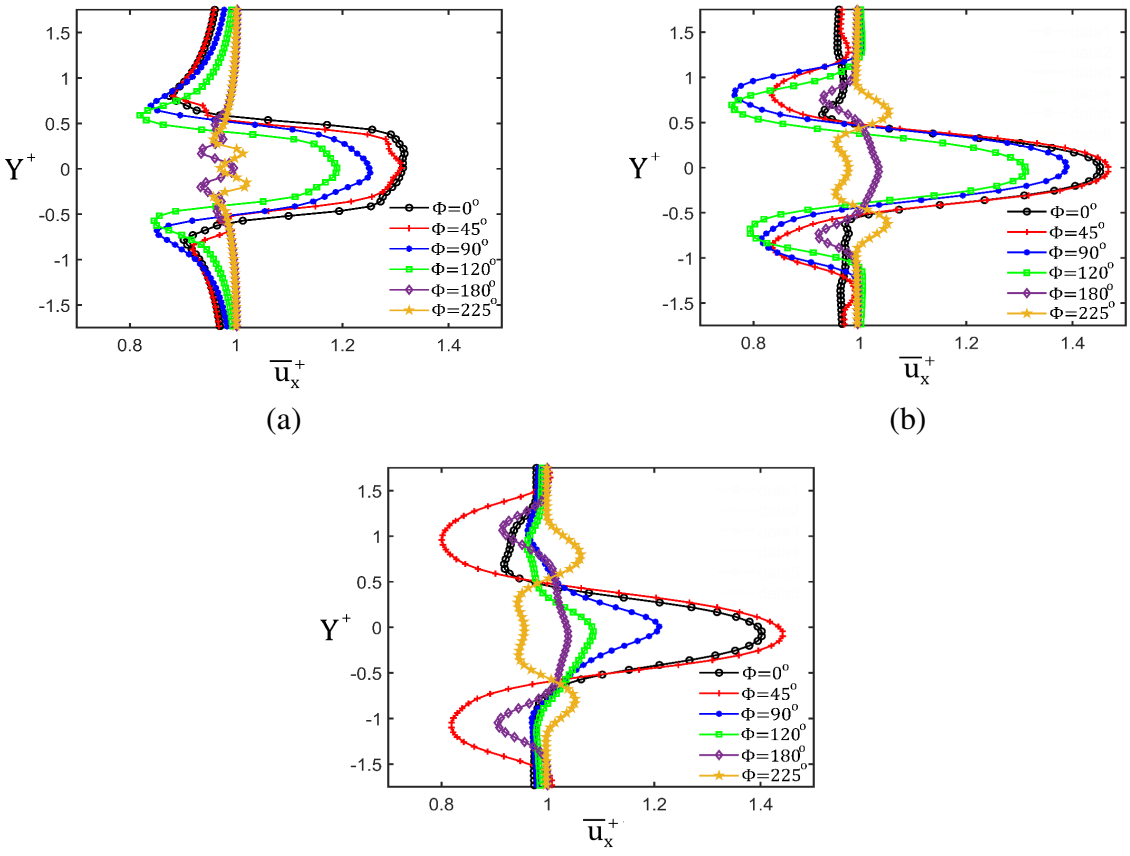

Figure 7.14: Profiles of $\overline{u_x^+}$ along the cross-stream (Y^+) direction at streamwise locations corresponding to (a) $X^+ = 1.5$, (b) $X^+ = 3.5$ and (c) $X^+ = 5.5$, respectively.

velocity at $Y^+ = 0$ in Figure 7.14(c) for the wakes of $\phi \geq 90°$. Despite this decrease along the wake centerline, the neighboring minima decreases further as ϕ increases to 120°. This is specifically observed for the streamwise locations corresponding to $X^+ = 1.5$ and 3.5, respectively. For $X^+ = 5.5$, however, the velocity deficit regions flatten with increasing ϕ to 120°. These observations also coincide with the vortex interaction and merger observed for $\phi = 90°$ and 120° in Figures 7.4(c) and 7.4(d), respectively. Since these merged structures advect closely along the wake centerline in Figure 7.4(c,d), resultant induced velocity must be insignificant. Thus, it leads to flat velocity profiles along Y^+.

At $\phi = 180°$, the cross-stream profiles for $\overline{u_x^+}$ show a different characteristic time-averaged wake. Near the foil, a pair of velocity minimum is observed in Figure 7.14(a) with a relatively

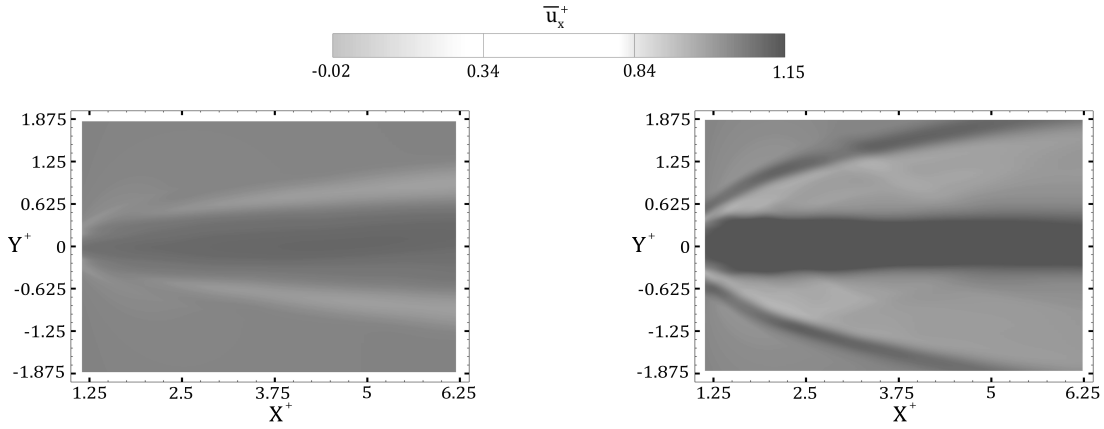

Figure 7.15: Contours of $\overline{u_x^+}$ at (a) $\phi = 225°$, $St_c = 0.48$ and $Re = 1000$ (b) $\phi = 90°$, $St_c = 0.4$ and $Re = 4000$.

minor drop compared to U_∞, which is close to the wake centerline. Assessment at increasing streamwise distance from the foil further reveal that the minima locations disperse away from the wake centerline. This feature coincides with the diverging dual vortex streets seen in Figure 7.4(e). This is qualitatively confirmed in Figure 7.13(c) which identified the presence of diverging velocity deficit streams along the streamwise direction. As ϕ is further increased to 225°, we observe two velocity maximum or peaks that neighbor the wake centerline. This feature, observed from the quantitative profiles depicted in Figure 7.14, is in a definite contrast to the characteristics observed at $\phi = 180°$. However, the twin peaks move away from the wake centerline in a similar fashion as the minima locations observed at $\phi = 180°$. This feature is also noticeable in Figure 7.13(d), where we observe two streams of relatively high mean velocity in the wake. From the above observations, it is seen that the formation of diverging vortex streets at $\phi = 180°$ reflects a critical threshold characteristic, since the mean wake features deviate and follow different spatio-temporal development as ϕ is switched away from 180°. These dual dipole-like vortex streets are also suggestive of a relatively low spatial disturbance near the wake centerline region, compared to mean wake features associated with ϕ values higher or lower than 180°.

Figure 7.15(a) further depicts the contours of $\overline{u_x^+}$ for $\phi = 225°$ at $St_c = 0.48$ and $Re = 1000$. This kinematic and flow configuration corresponded to the $2P$ mode in which bifurcations were evident,

as identified in Figure 7.3(a). It is observable that the mean spatial development coinciding with the bifurcated dual vortex street remains largely unaffected with increased St_c. The diverging velocity deficit streaks appear comparatively similar to the $\overline{u_x^+}$ development observed in Figure 7.13(c), which corresponds to the case of $\phi = 180^\circ$ and $St_c = 0.4$. A spatial uniformity in the cross-stream distribution of $\overline{u_x^+}$ is also retained at this higher St_c setting. Figure 7.15(b), however, depicts the $\overline{u_x^+}$ distribution at higher Re of 4000, while ϕ and St_c correspond to 90° and 0.4, respectively. This setting also coincides with the $rBvK + 2P$ mode identified in Figure 7.8(b), that underwent bifurcation and whose formation was also discussed in a previous section. A relatively strong thrust jet is seen along the wake centerline on account of the $rBvK$ vortex street observed in Figure 7.9(c). We also see two bifurcated streaks that possess a relatively higher velocity compared to the surrounding flow. Such bifurcation in mean flow is again suggestive of an implication posed by dual vortex streets in $rBvK + 2P$ mode. However, these weak jet streaks still appear in contrast to the velocity deficit streaks observed at lower Re, and which only corresponded to a $2P$ mode (see Figures 7.13(c) and 7.15(a)).

7.4 Summary

The wake characteristics were numerically evaluated with respect to increasing phase offset ($0^\circ \leq \phi \leq 270^\circ$), chord based Strouhal number ($0.16 \leq St_c \leq 0.48$) and Reynolds number. Increasing Strouhal number and phase offset within the considered range constitute a transition of kinematics from pitch to heave-dominated oscillatory motion, which brings about a unique transition in wake topology. This transition is characterized by bifurcated dual vortex streets in $2P$ mode. These streets exhibited counter-rotating vortical structures with mutual pairing within half shedding cycle that resembled the mechanism of a $2P$ wake (Williamson and Roshko, 1988; Schnipper et al., 2009). However, qualitative and quantitative characteristics of the wake evolution, such as circulation strength and separation distance, showed resemblance of vortex dipoles or couples. Both leading and trailing edge vortices were further observed to contribute to the formation of dipole-

like configurations ($2P^D$ pairs) that dominated the $2P$ mode. Although this characteristic of $2P^D$ pairs resembled some similarities with the Mode-1 configuration described previously by Cleaver et al. (2011), the $2P$ wake observed here exhibited no merger between similar sign leading and trailing edge vortices. Further, the findings noted here were also in definite contrast to the observations made for typical vortex dipoles that are formed only on account of trailing edge structures(Cleaver et al., 2012; Calderon et al., 2014; He and Gursul, 2016).

This wake mechanism was also modeled mathematically, where the relative circulation strengths of counter-rotating vortical structures was found to depend on the foil kinematics, including St_A, St_h, St_θ and the ϕ between the heaving and pitching motion. The model suggested that at a constant St_h, an increase in ϕ up to 180° would lead to a decrease in St_A, which thereby reduces the relative circulation strength ratio of counter-rotating structures from the trailing and leading edges of the foil. The quantitative estimation of the relative circulation strength from the numerical data confirmed the model findings for ϕ greater than 45°, corresponding to heave-dominated kinematics at a constant $St_h = 0.2$ and $St_c = 0.4$, where the bifurcation in $2P$ mode were observed. The phase map characterized by increasing $A_c - St_c$ also validated the predictions of proposed mathematical model. With increasing St_A, the wake modes qualitatively depicted transition from $2P$ wake topologies to *rBvK* mode. This agreed with previously reported wake dynamics, where increase in St_A corresponded to an increased relative strength in TEV, and hence led to a transition of wake towards a *rBvK* topology. The proposed model was further found accurate in predicting the trends for circulation strength ratio of trailing and leading edge structures, at increasing St_h, St_θ and ϕ, while also providing the approximate bounds (in terms of model output) where the major wake mode configuration like $2P$, $2P+2S$ and *rBvK* are dominant.

The wake mode transition identified at a higher *Re* of 4000 revealed a similar novel wake configuration that is characterized by secondary formation of a *rBvK* vortex street, and accompanied with the bifurcated dual vortex streets of $2P$ mode. Besides the shear splitting phenomenon that is responsible for the growth of *rBvK* street in conjunction with the $2P$ mode, the transition in spatial characteristics of shed vortical structures also showed a distinct signature in the wake. Here, the

coherent structures that dominated the *rBvK* street consistently lost their circulation strength with increasing ϕ to 180°, while the 2*P* mode structures became relatively stronger. This mechanism coincided with a loss and subsequent reappearance of dual bifurcated vortex streets at $\phi = 120°$ and 180°, respectively. Further evaluation of this unique transition mechanism at $Re = 4000$ revealed that with increasing ϕ from 45° to 180°, the shear splitting process undergoes a consistent delay. This coincides with increasing strength of dipole-like paired structures. The contribution of splitting process that was dominant at $\phi < 120°$ reduced with increasing ϕ from 120° to 180°. The induced velocity of the dipole pair was the dominating factor that prompted the formation of bifurcated dipole streets. The mathematical relationship between relative circulation strength of trailing and leading edge vortex structures, and St_A, did not hold well at higher Reynolds numbers (e.g., $Re = 4000$) in qualitative sense. This was possibly on account of changes imposed on approximation for vorticity production at higher Reynolds numbers with increasing St_c. The approximation of circulation of leading edge vortex structures further appears inadequate on account of its failure to include effects of splitting process observed in the near wake at $Re = 4000$. The qualitative result of wake transition thus suggested that a distinct transition among 2*P* and *rBvK* type modes does not coincide within a specific St_A threshold, as observed at $Re = 1000$.

Mean spatio-temporal wake characteristics revealed low disturbance in the cross-stream mean velocity profile associated with the birfurcated dual vortex streets of 2*P* mode. This feature was found consistent with increased streamwise distance along the wake. However, the mean velocity distribution corresponding to ϕ values lower or higher than 180°, appeared in contrast to those associated with the 2*P* mode that experiences bifurcation. For the $rBvK + 2P$ mode observed at a higher *Re*, a mean thrust jet also accompanied the weak bifurcated streaks that were characterized by minor increase in velocity compared to the surrounding flow. The thrust jet was formed on account of the *rBvK* vortex street observed in addition of the 2*P* mode at higher *Re*. Such mean flow characteristics corresponding to bifurcated dual vortex streets are therefore suggestive of novel flow control mechanisms. The dual vortex streets of 2*P* mode can specifically be useful in scenarios where the incoming flow is required to be manipulated such that the wake behind an oscillating

body is free from substantial jet development or a recirculating flow. In situations where segregated mean thrust profile is warranted for design improvements, the bifurcations instilled in $rBvK + 2P$ mode could be useful in flow manipulation.

Overall, increasing Re coincides with significant changes in vortex interaction mechanisms that govern the wake topology of an oscillating foil in combined heaving and pitching motion. However, as highlighted by Zurman-Nasution et al. (2020), onset of three-dimensionality in the wake is apparent at $Re \geq 5300$. Therefore, Chapter 8 examines the evolution of 3D wake features and their underlying association with kinematics.

Chapter 8

EVOLUTION OF THREE-DIMENSIONAL WAKE STRUCTURES AND FEATURES[†‡]

8.1 Introduction

A combination of numerical and experimental studies of flow past oscillating foils has provided a deeper insight into the characteristics of coherent structures in unsteady wakes and their subsequent effects on flow turbulence, e.g., Koochesfahani (1989), Triantafyllou et al. (2004), and Deng and Caulfield (2015b). Fazle Hussain (1986) described coherent structures as any connected turbulent fluid mass over which a certain component of the three-dimensional vorticity is instantaneously coherent over the spatial extent of the fluid mass. The term *vortex* has been since used extensively for flow structures that carry essential aspects of the coherent vorticity (Fazle Hussain, 1986). The

[†]The content of this chapter has been published in whole or part, in *Journal of Fluid Mechanics* under the citation (Verma and Hemmati, 2021b): "Verma, S. & Hemmati, A. (2021). Evolution of wake structures behind oscillating hydrofoils with combined heaving and pitching motion. Journal of Fluid Mechanics 927, A23."

[‡]The content of this chapter has been published in whole or part, in *Progress in Turbulence IX* under the citation (Verma and Hemmati, 2021a): "Verma, S., Hemmati, A. (2021). Asymmetry in Wake of Oscillating Foils with Combined Pitching and Heaving Motion. In: Örlü, R., Talamelli, A., Peinke, J., Oberlack, M. (eds) *Progress in Turbulence IX*. iTi 2021. Springer Proceedings in Physics, vol 267. Springer, Cham."

formation, interaction and merging of vortices is also crucial in studying turbulent wakes. These dynamic behaviors directly influence the flow properties, such as entrainment, heat transfer, hydrodynamic forces (i.e., lift and drag), and fundamental aspects of turbulence modeling. In recent years, the study of bio-inspired propulsors (Gemmell et al., 2015; King et al., 2018; Hemmati et al., 2019a), including wake dynamics analysis, have allowed exploring the mechanisms that govern underwater swimming characteristics in biological species and man-made systems. Here,the focus is on the fundamentals of wake dynamics and secondary vortex structures in underwater swimming that combine heaving and pitching oscillations. These 3D wake features are particularly evident at $Re \geq 5000$ Visbal (2009); Zurman-Nasution et al. (2020); Chiereghin et al. (2020); Son et al. (2022), which is beyond the range investigated within Sections 5.3-7.3. Thus, the wake evolution from here on will be focused at $Re = 8000$, compared to observation discussed in the previous chapters at $Re \leq 4000$.

The inherent complexity and unsteadiness of the vortex formation process had provided a greater motivation for fluid dynamicists to formulate three-dimensional wake models relevant to biological flows. These models not only characterized the vortex structures, but they also discussed the trigger mechanisms, or instabilities, that may be responsible for their individual characteristic features. Extensive details on experimental and numerical studies were covered in Sections 2.4 and 2.5. The major breakthrough in investigating instability for bluff-body wake came with the study of Williamson (1996), who identified two novel mechanisms that derive the formation of secondary vortex structures in the wake of a circular cylinder. These mechanisms were dominant at different ranges of Reynolds number, and they also possessed different spatio-temporal characteristics. The findings were extended by various experimental and numerical studies (Robichaux et al., 1999; Ryan et al., 2005; Deng and Caulfield, 2015b; Gibeau et al., 2018) that concerned different geometries, such as square cylinders, blunt trailing edge cylinders and symmetric oscillating hydrofoils. Their elaborate details are provided in Section 2.5. However, the vortex dynamics and secondary vortex features imposed by combined oscillatory motion of hydrofoils is not yet fully

characterized. This knowledge can facilitate the development of single- and multi-body swimming control systems.

Recently, experiments conducted for high aspect ratio wings in heaving motion Chiereghin et al. (2020), observed the presence of a dominant spanwise instability on the leading edge vortex structures that depicted a wavelength close to 1. The origin of this instability was unclear, and speculated to be either oscillatory wake flow, oscillatory origin or an instability of vortex filament itself. A similar comprehensive analysis of the wake secondary vortex characteristics for oscillating foils undergoing combined heaving and pitching motion is lacking in literature. Such an analysis for specific regimes showing extreme and distinct propulsive performances identified by Van Buren et al. (2019) may reveal new physics on wake three-dimensionality.

In this chapter, the characteristics of vortex structures in the 3D wake of a flapping foil is explored numerically. The propulsive performance results of Van Buren et al. (2019) are used to identify the oscillatory and fluid motion that constitute extreme performance characteristics. The simultaneous plausibility of either high efficiency or large thrust generation in a combined heaving and pitching motion may hint to an association with fundamental differences in the wake. Thus, the wake three-dimensionality and secondary structures are characterized at two very different and extreme oscillatory conditions. Novel wake models are finally introduced based on a complete vivid three-dimensional depiction of coherent wake structures. The chapter is structured such that the methodology is detailed in Section 8.2, which provides a description of governing equations, motion and flow parameters for the simulations. The validation study of the three-dimensional numerical setup is also included in Section 8.2. This is followed by discussion of the results and characterization of the wake in Section 8.3. Main conclusions are summarized in Section 8.4.

8.2 Problem Description

The three-dimensional wake characteristics behind an oscillating teardrop foil is examined at $Re = 8000$. At this Reynolds number, the effects of transitional instability mechanisms are negligible,

Table 8.1: Parameter space for the current studies and the companion experiments.

Study	Re	St_c	St	h_0/c	θ_o	ϕ
SIM0	8000	0.67, 1.87	0.35−0.97	0−0.25	15°	270°
SIM1	8000	0.6	0.21	0.125	10°	270°
SIM2	8000	0.8	0.94	0.375	15°	330°
Van Buren et al. (2019)	8000	0.16-0.64	0.1-0.8	0.125-0.375	5°-15°	0°-330°

which provides stable and consistent wake characteristics for analyzing secondary vortices (Gibeau et al., 2018). The foil is infinitely span across the domain following the experiments of Van Buren et al. (2019), which constitutes an aspect ratio (AR) of infinity. The infinitely span hydrofoil allows us to preserve the characteristics of secondary vortex structures (ribs) formed in the wake. The parameter space (Table 8.1) used in this study closely follows the experiments of Van Buren et al. (2019) to validate the numerical results, provide insight into the wake dynamics associated with the performance observations, and enable practical interpretation of the results in terms of underwater swimming characteristics of fish tail-fins. The range of Strouhal number and reduced frequency considered for evaluating the propulsive performance of the foils were $0.21-0.97$ and $0.6-1.87$, respectively. The wake analysis, however, focused only on the extreme performance conditions. According to Van Buren et al. (2019), which is consistent with our results, the high efficiency locomotion occurs at $St = 0.21$, $St_c = 0.6$ and $\phi = 270°$, while the largest thrust is generated at $St = 0.94$, $St_c = 0.8$ and $\phi = 330°$. These are very different swimming conditions, which hint that there may be fundamentally different wake dynamics coinciding with these conditions that deserve a closer attention.

8.3 Results and Discussion

The propulsive performance of two particular oscillatory motions of an infinite span foil are examined, in which either pitching or heaving motion dominates (SIM1 and SIM2 in Table 8.1). Considering the work of Van Buren et al. (2019), these cases constitute two extreme ends of the performance spectrum when combining pitching and heaving motions. Following the evaluation

Table 8.2: Quantitative evaluation of performance, showing $\overline{C_T}$, C_L^{rms}, $\overline{C_P}$, and η for SIM1 and SIM2 respectively.

Study	$\overline{C_T}$	C_L^{rms}	$\overline{C_P}$	$\eta(\%)$
SIM1	0.14	1.36	0.66	20.77
SIM2	4.95	22.06	38.13	12.98

of the propulsive performance in terms of thrust, power and efficiency, we proceed with examining various primary and secondary wake features.

8.3.1 Propulsive performance

The coefficient of thrust, lift and power are provided in Table 8.2 for SIM1 and SIM2. The η was also calculated based on $\overline{C_T}$ and $\overline{C_P}$, where the time-average C_T, C_L and C_P were calculated over ten oscillation cycles following statistical convergence of the simulations. The higher $\overline{C_T}$ observed for SIM2 compared to SIM1 agreed well with observations of Van Buren et al. (2019), in which the propulsive performance was compared at a range of St_c, St and ϕ. A crucial dependence on ϕ was identified by Van Buren et al. (2019), which also correlated with observations of Anderson et al. (1998) and Wu (2011). Van Buren et al. (2019) described that at $\phi = 330^o$, the combined heaving and pitching motion produced an optimum peak angle of attack, which led to a large thrust generation within their parameter setting. However, the power requirement also went up significantly, thereby lowering the propulsive efficiency of the system. Here, we also observed a similar rise in the $\overline{C_P}$ in SIM2, which tends to lower the predicted efficiency indicated in Table 8.2. The performance estimations for SIM1, however, depicted a corresponding rise in efficiency at the expense of a lowered thrust generation. This was also in agreement with experimental findings of Van Buren et al. (2019) at $\phi = 270^o$. This was attributed to the relative decrease in power requirement (that subsequently increased η) to the production of a supplemental force that is required for pitching. This lowers the external moment applied to the foil. Therefore, the phase difference between the two oscillatory motions play a dominant role in performance of oscillating foils.

Now that we have established there are two very different performances observed by the particular motions imposed on the foil in SIM1 and SIM2, we examine the wake dynamics associated with each of these performance categories: high efficiency and large thrust generation. To this end, we discuss the prominent characteristics of vortex structures observed for SIM1 and SIM2, which highlights the differences and similarities of wake features for high performance regimes identified by Van Buren et al. (2019). Some connections between these and the three-dimensional instability features are also discussed with a comprehensive evaluation presented in subsequent sections.

8.3.2 Primary vortex characteristics

Investigation into primary vortex characteristics for SIM1 and SIM2 is carried out in order to understand the dominant wake mechanisms associated with a high efficiency and large thrust producing wakes, respectively. As mentioned previously, experimental studies conducted by Godoy-Diana et al. (2009), Schnipper et al. (2009) and Calderon et al. (2014) described several wake modes for a pitching or heaving foil by analyzing the spanwise vorticity (ω_z) distribution, which further reflected the two-dimensional nature of primary vortex structures. A vivid dependence on the motion parameters including St, A_D and St_c was also observed (Godoy-Diana et al., 2008, 2009; Calderon et al., 2014; Cleaver et al., 2012). Therefore, we first highlight the vorticity distributions for SIM1 and SIM2 along with a description of respective wake characteristics, based on previously identified modes for pitching (Schnipper et al., 2009) or heaving foils (Cleaver et al., 2012; Calderon et al., 2014). The temporal variation of performance and spanwise pressure variations within one oscillation cycle was also evaluated. Significant differences that exist for SIM1 compared to SIM2 are described qualitatively, which highlight dominant physical mechanisms for wake formation, vortex interactions and temporal variations occurring in the high propulsive performance regimes. We also discuss the quantitative evaluation of specific vortex characteristics as the foil completes an oscillation cycle, e.g., vortex size, separation distance and rate of cross-stream advection in the wake. The apparent association of vortex evolution and spanwise instability characteristics were further assessed in this analysis.

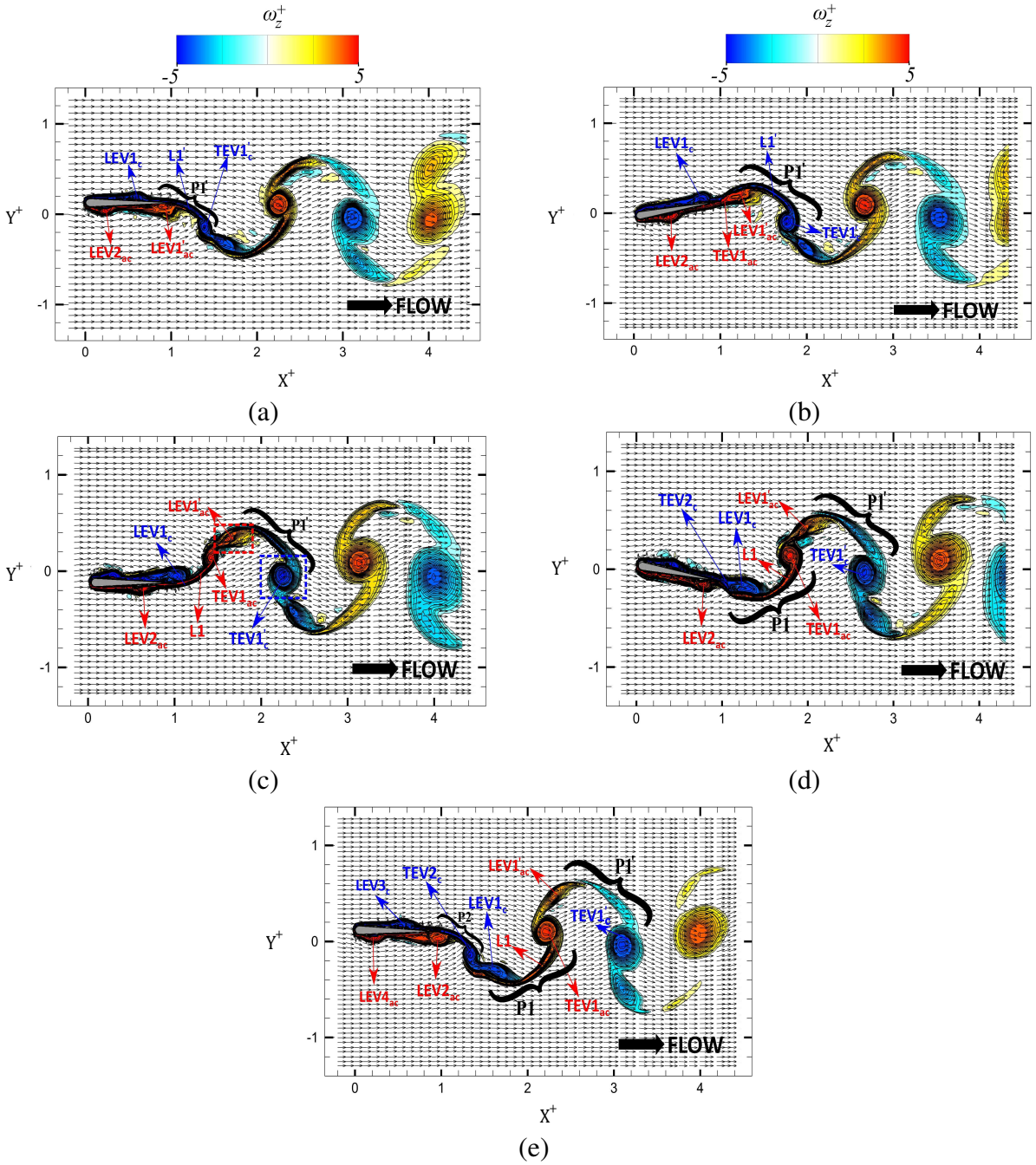

Figure 8.1: Contours of ω_z^+ superimposed by velocity vectors for SIM1. Phases (ψ) of the shedding cycle are (a) $\psi = 0^o$ at $t = 0$, (b) $\psi = 90^o$ at $t = T/4$, (c) $\psi = 180^o$ at $t = T/2$, (d) $\psi = 270^o$ at $t = 3T/4$ and (e) $\psi = 360^o$ at $t = T$.

Formation of 2P^T wake in SIM1 and performance evaluation:

The planar representation of primary vortices was depicted in terms of ω_z^+. Figure 8.1 shows the distribution of ω_z^+ at each quarter phase of the oscillation cycle (i.e. $\psi = 0°$, $90°$, $180°$, $270°$ and $360°$) for SIM1. A symmetric wake was observed for SIM1, which will be referred to as "2P^T" formation. This resembled a "2P" vortex-street mode in the near wake region ($X^+ \leq 4$), whereas a "2S" mode was apparent at $X^+ > 5$. The mechanism for formation of thrust generating "2P^T" wake configuration (Schnipper et al., 2009) is discussed via these spanwise vorticity contours. The instances depict the vortex structures forming at the leading (LEVs) and trailing edges (TEVs) of the foil. These provide the necessary tools to discuss the formation, interaction and merging of LEVs and TEVs in the wake, and identify the particular wake features associated with each case. These are also limited to the initial "2P" wake that extended to $4c$ downstream the trailing edge of the foil. Plots that depict the transition from a nearly "2P" wake to a reverse von Kàrmàn (or "2S") wake are not shown here for brevity, since the vortex coalescence began at $X^+ \geq 4$.

In Figure 8.1a, the foil starts at its peak heaving amplitude when $\psi = 0^o$, during which two LEVs advected downstream along the foil surfaces. The clockwise vortex named $LEV1_c$ was formed above the center line of the foil during the previous shedding cycle, which had already advected $\approx 60\%$ of the chord from the leading edge. There is also a counter-clockwise vortex ($LEV2_{ac}$ in Figure 8.1a) that is below the foil neutral axis (center line) and closer to the leading edge. At $\psi = 90^o$ in Figure 8.1b, the foil leading-edge moves down due to the imposed heaving motion, while the trailing edge moves upward due to the imposed pitching motion, reaching its maximum angle of attack. At this stage of oscillations, $TEV1_{ac}$ was large enough to form a distinct structure near the foil trailing edge. As the foil completed the half-point in its shedding cycle ($\psi = 180^o$ in Figure 8.1c) and reached its maximum heaving amplitude below the wake center line, $TEV1_{ac}$ appeared to pair with $LEV1_c$ that was nearly on the verge of separation from the trailing edge. During the remaining half of the shedding cycle in Figures 8.1(d,e), we observed that $LEV1_c$ and $TEV1_{ac}$ advected downstream as the first pair (P1) of the "2P" wake. Subsequently at $\psi = 270^o$ in Figure 8.1d, a clockwise $TEV2_c$ is formed near the trailing edge, owing to the foil

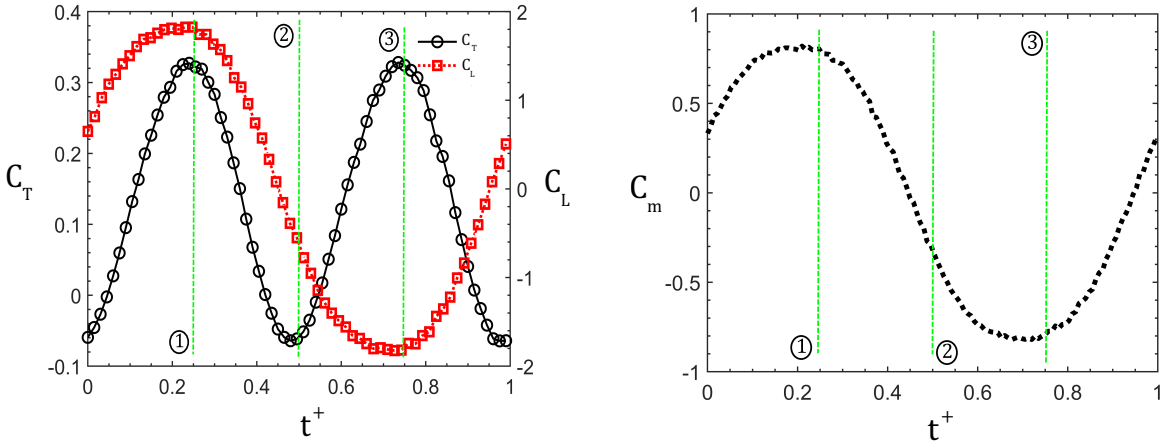

(a) (b)

Figure 8.2: Variation of force (a,b) and moment (c) in one cycle for SIM1.

downward tip movement. At the final stage of the shedding cycle, $TEV2_c$ and $LEV2_{ac}$ separated from the foil and advected downstream as vortex pair P2. This coincided with the formation and advection of $LEV3_c$ and $LEV4_{ac}$ along the foil, respectively. These proceed to become the consecutive counter-part of $LEV1_c$ and $LEV2_{ac}$, which were already discussed for $\psi = 0^o$ in Figure 8.1a.

The performance characteristics, in terms of thrust and lift, for SIM1 are depicted in Figure 8.2. These characteristics were further evaluated with respect to C_{pr}, vortex structures and their dynamics. As the oscillation cycle started ($t = 0$ in Figure 8.2a), lift increased uniformly upto a local maxima at $t = T/4$ (instant 1), which coincided with a local maxima for thrust as well. This corresponded to the same time that TEVs were formed as well as the time that an LEV advected along the foil bottom face. The increase in lift was hence attributed to the gain in the circulation strength of the LEV, which was observed to pair with the TEV and detach just prior to instant 1 (Figure 8.1b). This separation further imparted a forward momentum to the foil. The instantaneous pressure distribution on the suction side of the foil depict $LEV1_c$ near the trailing edge (Figure 8.3a), while $LEV2_{ac}$ is observed approximately at mid-chord on the pressure side of the foil (Figure 8.3a). A distinct low pressure region was also observed near the leading edge depicting the formation of a new LEV structure on account of foil downward motion. Besides identifying

vortex structures, an instability feature was also identified to be prominent on individual $LEVs$, where structures on the suction side exhibited a normalized spanwise wavelength of $\lambda_z/c = 0.98$. Those on the pressure side exhibited a spanwise wavelength of $\lambda_z/c = 0.6$. In terms of normalization with respect to the vortex core radii (a) for $LEV1_c$ and $LEV2_{ac}$, where the core radii of these structures was evaluated later in the wake, the normalized wavelength was λ_z/a =3.16 and 1.93 for structures on the suction and pressure sides, respectively. This estimate of λ_z/a seems close to the numerical estimates of elliptic instability wavelength ($\lambda_z/a = 3.35$ and 1.42) depicted in a study by Dizès and Laporte (2002), where the vortices of unequal circulation strength were considered. Here for the case of SIM1, we would like to note that the paired vortex structures also possessed unequal strengths, where the ratio of circulation magnitude represented as Λ, for a weak LEV structure (for e.g. $LEV1_c$) and its paired TEV structure (for e.g. $TEV1_{ac}$), was found close to 0.478. It is therefore apparent that an interaction between $LEV1_c$ and the developing $TEV1_{ac}$, shown in the Figure 8.1c, would promote a dominant elliptic instability mechanism for a vortex pair (Dizès and Laporte, 2002). Further, in order to compare our results with another study on unequal strength counter-rotating vortex pair, conducted by Ortega et al. (2003), we evaluated the normalized wavelength with respect to the ζ. The estimated value of the ratio λ_z/ζ was found close to 1.88 and 1.15, for $LEV1_c$ and $LEV2_{ac}$, respectively, which lies in range of elliptic instability wavelengths observed for various experimental runs conducted by Ortega et al. (2003). These quantitative evidence therefore suggests that an elliptic instability results in such spanwise undulations on the leading edge vortex filament. For $LEV2_{ac}$, the interaction with the foil boundary could also result in its small amplitude waviness, although a thorough investigation of the exact physical origins is still needed. The characteristic contributions of the associated instability mechanism in the wake would be further discussed in upcoming sections related to the three-dimensionality of spanwise rollers. Ahead of instant 1, a new anti-clockwise TEV structure started to develop, which subsequently lowered the momentum transfer. This coincided with a decreased difference in integrated C_{pr} over the suction and pressure sides of the foil (Figure 8.3b). Thus, the thrust coefficient decreased until $t = T/2$ (instant 2). Also, the coefficient of lift approached its local minimum until

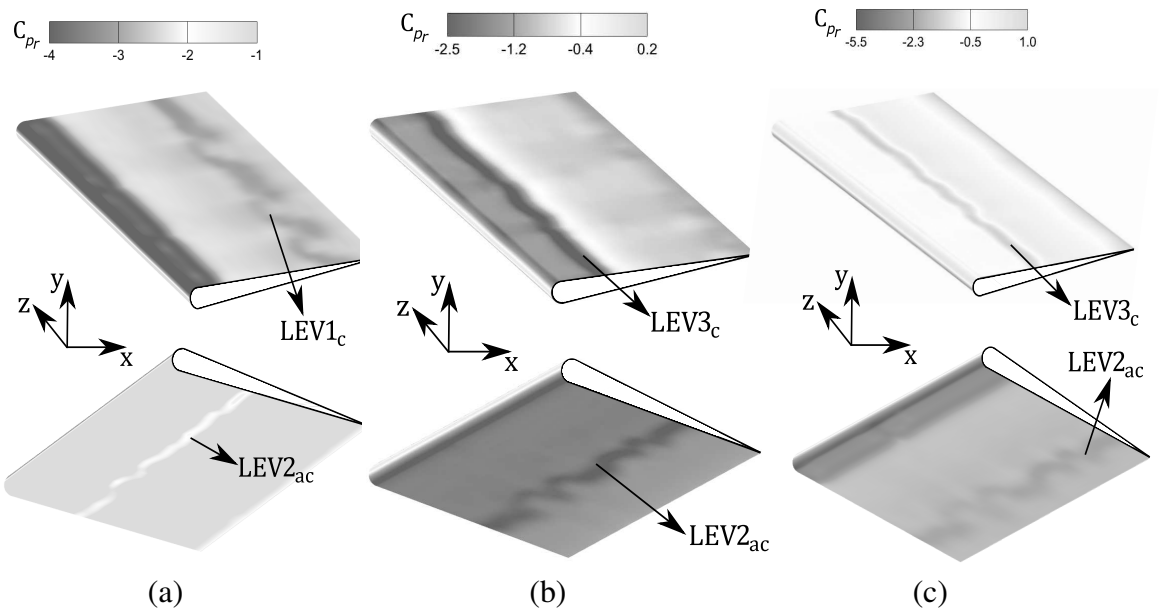

Figure 8.3: C_{pr} distribution on suction side (*top row*) and pressure side (*bottom row*) of the foil at instants (a) 1, (b) 2 and (c) 3 of Figure 8.2.

the *LEV* detached from the foil trailing edge at $t = 3T/4$ (instant 3) because of the advection of an anti-clockwise *LEV* along the bottom boundary of the foil (see Figure 8.1c). Moreover, the vortex pair formed by the new *LEV* and *TEV* (P1) detached and moved into the wake at instant 2. Hence, thrust increased until $t = 3T/4$ (instant 3). This was again well evident from the increased difference in the integrated C_{pr} over the suction and pressure side (Figure 8.3c). Ahead of instant 3, the clockwise *TEV* strengthened (see Figure 8.1d), similar to the previous half cycle, which decreased the thrust until the end of the oscillation cycle ($t = T$). The periodicity (period per cycle) for C_T was double that of the oscillations due to shedding of two vortex pairs per oscillation cycle. Lift increased ahead of instant 3 as a new clockwise *LEV* advected along the upper face of the foil (also evident in C_{pr} distribution). The variations of the C_m in Figure 8.2b was similar to that of C_L.

There exist vivid similarities and differences between the characteristic features of "2P^T" formation identified for SIM1, which resembles the "2*P*" wake observed by Schnipper et al. (2009) for a pitching teardrop hydrofoil. The formation of $LEV1_c$, $LEV2_{ac}$, $TEV1_c$ and $TEV1_{ac}$ had similar origins to those identified by Schnipper et al. (2009). The emergence of vortices $LEV1_c$ and $LEV2_{ac}$ in the boundary layer was also observed by Schnipper et al. (2009), who referred to

them as "boundary layer" vortices. However, $TEV1_{ac}$ and $TEV2_{c}$ were formed solely due to large-tip-speed of the foil trailing edge. The separation distance between $LEV1_{c}$ and $LEV2_{ac}$ was half of the chord length, similar to experiments (Schnipper et al., 2009). These experimental findings also stated that the time it takes for a leading edge structure that contributes to the formation of "2P" wake to travel $1c$ in the streamwise direction is an integral multiple of the oscillation period (T). Thus, the total time (T_c) required for a vortical structure to travel one chord length distance is $2c/U_\infty$ following the assumption of Schnipper et al. (2009) that the traveling speed of an advected structure is $0.5U_\infty$. In terms of St, this advection time (T_c) translates to cSt/fA for SIM1, based on which St is approximately 0.174 if we assume T_c equal to one oscillation period. This falls within the range of $0.17 < St < 0.31$ for vortex synchronization on the phase diagram of Schnipper et al. (2009), in which "2P" mode was prominent. Despite such similarities, the initial wake region of $2P^T$ identified for SIM1 had a different propulsive performance characteristic compared to the wake features identified by Schnipper et al. (2009). According to Schnipper et al. (2009), the vortex pair observed for their "2P" wake mode pointed upstream in the streamwise direction, which leads to a drag producing system. The vortex pair for SIM1 observed in Figure 8.1e, however, pointed downstream in the streamwise direction, which leads to a thrust generating wake configuration. Even the 2P−2S mode discussed by Schnipper et al. (2009) involved shedding of upstream pointed vortex pairs and one single vortex within each half shedding cycle.

The physics of the near wake vorticity distribution is further investigated to understand the possible mechanism for the formation of such downstream pointing vortex pairs. $LEV1_{c}$ at the start of the oscillation cycle (Figure 8.1a) appears connected to $TEV1'_{c}$, which was attached to the foil via its vortex leg L1$'$. This continuous attachment of L1$'$ with the trailing edge of the foil was possible through the downward heaving motion that increases the vorticity fed to $LEV1_{c}$ through the attached shear layer on the foil surface. This process remains until $LEV1'_{ac}$ gains sufficient strength (in terms of vorticity) and motivates vortex leg L1$'$ to separate from the body in Figure 8.1c. Then, $TEV1'_{c}$ and $LEV1'_{ac}$ are advected downstream as a pair (P1$'$ in Figure 8.1c). A similar mechanism was also observed for the latter half of the shedding cycle with respect to $LEV2_{ac}$, L1,

and a subsequent vortex pair P1 formed by $LEV1_c$ and $TEV1_{ac}$. It is important to note that the counter-rotating leading edge vortices, $LEV1'_{ac}$ and $LEV1_c$, cause bending of elongated vortex legs L1′ and L1. This bending results in the vortex pairs P1′ and P1 to point downstream and generate thrust. The description provided by Van Buren et al. (2019) for the foil motion at ϕ =270° also supports our proposed mechanism, wherein the fluid itself strengthens the vorticity generation near the foil which reduces the power requirement, and hence increases the efficiency. Thus, the phase difference (ϕ) between the pitching and heaving oscillations, along with higher A_D for SIM1, are potential contributors to attaining a thrust generating configuration for vortex pairs P1 and P2 observed in the near "2P^T" wake mode of Figure 8.1e.

The vortex pairs observed in Schnipper et al. (2009) also advected away from the wake center line, which was further noticed by Hultmark et al. (2007). The observations made by Hultmark et al. (2007) indicated that the lateral component of mutual advection velocity for each vortex pair resulted in them moving away from the wake centerline, thereby preventing any coalescence. Due to the downstream pointed pairs (P_1, P_2 and P_3) observed in SIM1, there exists a streamwise component for the mutual advection velocity of pairs that promote coalescence of structures with similar vorticity-sign. At higher St, "2P" vortex pairs did appear to merge and form a Von Kàrmàn wake (Schnipper et al., 2009). It was further observed that the wake transitioned from a "2P" wake mode to a "2S" thrust generating wake at $X^+ \approx 5$, which further enhanced the thrust generation mechanism by the oscillating foil while keeping the power requirements low. Thus, a higher overall propulsive efficiency was achieved for the "2P^T" wake of SIM1. This is the first observation of this kind in literature, to our best knowledge, in which the mutual existence of thrust generating "2P" wake and "2S" wake is observed at low St. Experiments by Dewey et al. (2012) suggested that with increasing St, the wake only exhibited characteristics of 2S mode in heaving foils. Quinn et al. (2015) also reported a 2P wake formation at $St = 0.39$ for a flexible streamlined propulsor, which they attributed to their lower flow speeds in order to keep St within an optimum range. However, there was no indication of a 2P^T mode, and any possible influence it may have on propulsive efficiency of the foils. The loss in efficiency was reported only on account of breakdown of vortex

structure very close to the panel (Quinn et al., 2015). This is in contrast to the $2P^T$ mode observed here with vortices coalescing, instead of breaking down, to form an inverse Von Kàrmàn wake with a higher efficiency for SIM1.

Formation of asymmetric wake in SIM2 and performance evaluation

The wake of the pitching-dominated oscillating foil in SIM2 resembles an asymmetric wake. Calderon et al. (2014) described the dependence of such stable deflected wake based on the formation and evolution behavior of trailing edge structures, similar to the vortex system observed in SIM2. The spanwise vorticity contours overlaid with velocity vectors were shown in Figure 8.4, which depicted the near wake formation, evolution or suppression of structures that form the asymmetric wake.

As shown in Figure 8.4a, the foil begins its shedding cycle with simultaneous upward heaving and pitching motion away from the wake center line, that is $Y^+ = 0$. The foil initially had a zero-pitch angle while the leading edge coincided with a cross-flow location at half of the maximum heaving amplitude. At $\psi = 0^o$ (Figure 8.4a), three structures are clearly apparent attached to the foil: $LEV1_{ac}$, $TEV1_c$ and $LEV1'_c$. The former two are formed on the lower side of the wake, while $LEV1'_c$ was initially formed on the upper side in the previous shedding cycle. $LEV1'_c$ appears to pair with $LEV1_{ac}$ and subsequently move to the wake lower side. The foil trailing edge reached its maximum pitching amplitude at $\psi = 90^o$ in Figure 8.4b, during which $LEV1'_c$ appeared diffused or largely distorted due to interactions with the foil boundary layer and $LEV1_{ac}$. Moreover, $TEV1_c$ grew substantially in apparent size to almost $2/3c$, while feeding from the large tip movement of the foil trailing edge at high St_c. As the foil started its downward motion prior to $\psi = 90^o$ (Figure 8.4b), a new structure was formed on the upper surface of the foil trailing edge, $TEV2_{ac}$. At $\psi = 180^o$ in Figure 8.4c, a new leading edge structure ($LEV2_c$) was formed along the upper side of the foil. This coincided with a total disappearance of $LEV1_{ac}$ near the lower side of the trailing edge. The vorticity and momentum associated with $LEV1_{ac}$ merged into $TEV2_{ac}$. Ultimately, $TEV2_{ac}$ joined with $TEV1_c$ at $\psi = 270^o$ to form a vortex couple (Figure 8.4d), which traveled

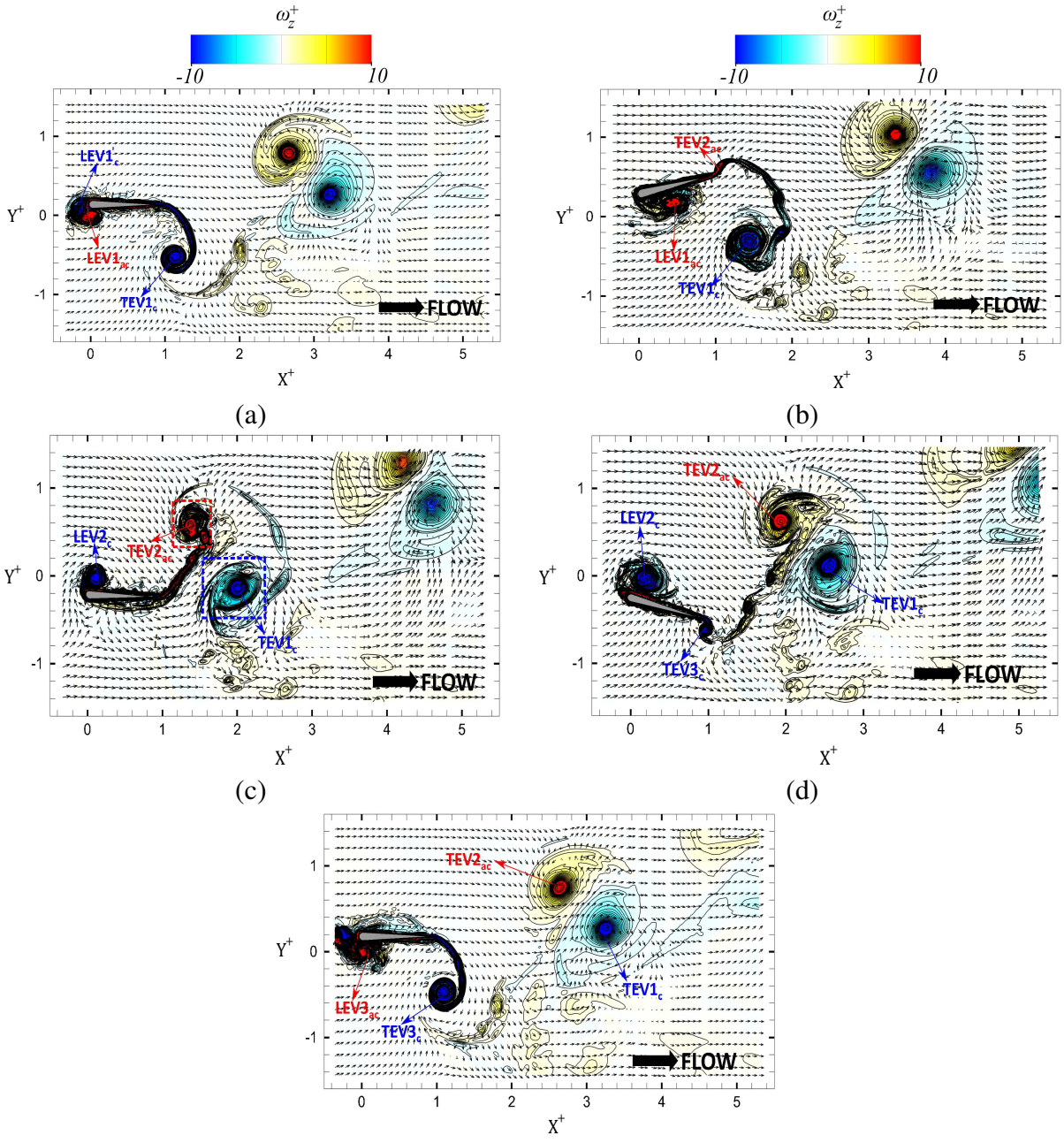

Figure 8.4: Contours of ω_z^+ superimposed by velocity vectors for SIM2. Phases (ψ) of the shedding cycle are (a) $\psi = 0^o$ at $t = 0$, (b) $\psi = 90^o$ at $t = T/4$, (c) $\psi = 180^o$ at $t = T/2$, (d) $\psi = 270^o$ at $t = 3T/4$ and (e) $\psi = 360^o$ at $t = T$.

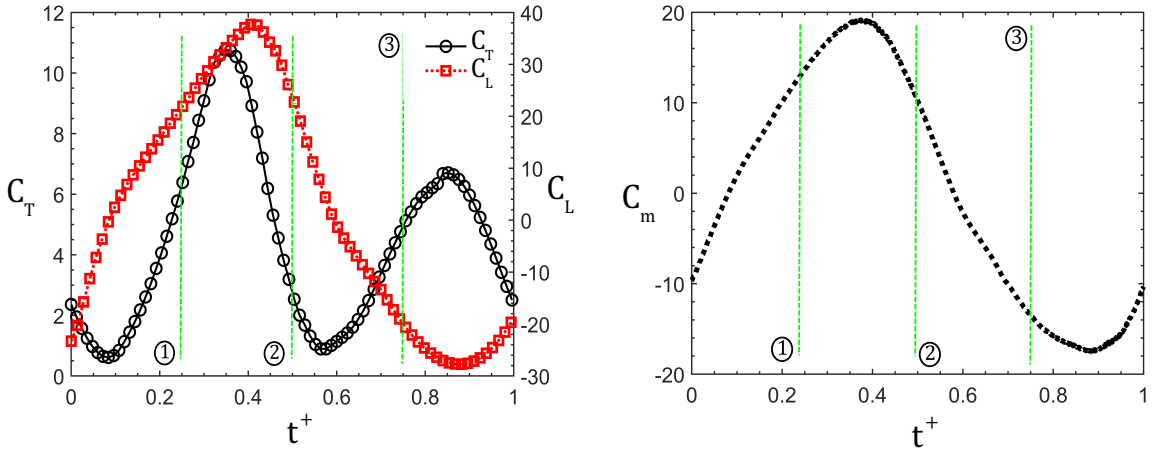

Figure 8.5: Variation of force (a,b) and moment (c) in one cycle for SIM2.

downstream at an angle similar to the upward deflected jet. Meanwhile, $LEV2_c$ grew in its apparent size and strengthened with larger vorticity as the foil started a simultaneous upward heaving and pitching motion. The leading edge structure on the upper surface ($LEV2_c$ in Figure 8.4d) also appeared to undergo a similar pairing and interaction with newly formed $LEV3_c$ in Figure 8.4e at $\psi = 360^o$. It ultimately disintegrate prior to detachment. This coincided with the growth and strengthening of $TEV3_c$ at $\psi = 360^o$ in Figure 8.4e.

Similar to unsteady C_T and C_L variations, and C_{pr} distributions for SIM1, we examine the unsteady variations of these parameters for SIM2 (Figures 8.5a, 8.5b and 8.6) in conjunction with evolution of vortex structures in Figure 8.4. The start of the oscillation cycle ($t = 0$) coincide with the formation of a TEV, the legs of which remain attached to the trailing edge (Figure 8.4a). It is noticed that the thrust decreased as the foil began to heave and pitch upwards. At the same time, a clockwise LEV moved along the foil leading edge and subsequently interacted with the anti-clockwise LEV that formed below the foil. This coincided with C_L ascending towards its local maximum value. At $t = T/4$ (instant 1) in Figure 8.5a, the clockwise LEV was well diffused, while the anti-clockwise LEV gained significant strength, in terms of circulation (see Figure 8.4b). This coincided with thrust approaching a local positive maximum. At instants described above, unsteady lift variations depicted an interesting feature. The rate at which C_L increased dropped

just before reaching instant 1 (approximately $t/T \approx 0.1$). This coincided with the presence of paired LEV structures near the leading edge of the foil (see Figure 8.4a), and just prior to the disintegration of the clockwise LEV structure (see Figure 8.4b). Their presence, therefore, enhanced lift generation at a higher rate compared to a single LEV. This physical process had no meaningful contribution to thrust production or its rate of change. The pressure distributions on the foil pressure side also depicted the localized low pressure region due to the developed anti-clockwise LEV structure (Figure 8.6a). We also observed that the upstream end of this LEV depicted a spanwise instability feature whose value of λ_z/c was equal to 0.8. In terms of normalization with respect to the diameter of invariant streamtube (d_{inv}), whose calculations follow a similar procedure as depicted in Leweke and Williamson (1998); Meunier and Leweke (2005), the ratio λ_z/d_{inv} correspond to 2. We would further like to note here that the dipole configuration in SIM2 comprised of counter-rotating vortex structures of equal circulation strength, similar to the study conducted by Leweke and Williamson (1998). Hence, normalization of spanwise instability wavelength with respect to d_{inv} was reasonable and justified here. An interaction with the clockwise $LEV\,1'_c$ (see Figure 8.4a) before its disintegration would hence promote an elliptic instability mechanism (Leweke and Williamson, 1998) for counter-rotating leading edge structures which will result in the spanwise undulations observed on upstream end of $LEV\,1_{ac}$. The mechanism also seemed evident near the trailing edge for leading edge structure in SIM1 wake. The downstream end, however, did not depict prominent spanwise undulations on account of absence of any neighboring counter-rotating vortex. Following instant 1, we observed that the local maxima of C_L coincided with the local maxima for C_T. This was further attributed to the clockwise TEV that detached from the trailing edge, while a new anti-clockwise TEV was formed. The integrated C_{pr} difference between the suction and pressure side also coincided with the peak in thrust variation (Figure 8.6b). Then, thrust reached its local minima just after instant 2, while the lift coefficient continued to approach its local minimum slowly (smaller slope). This observation was in contrast to the first half shedding cycle, which is attributed to the transfer of vorticity from the anti-clockwise LEV, moving below the foil, to the developing TEV with a similar rotational direction (Figure 8.4c). This vorticity

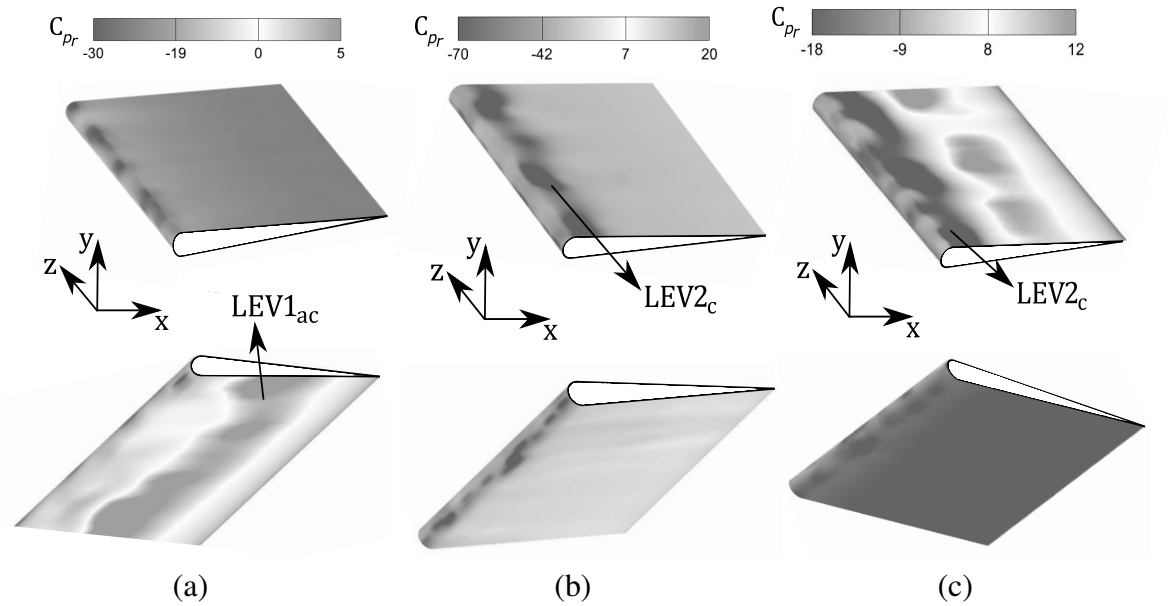

(a) (b) (c)

Figure 8.6: C_{pr} distribution on suction side (*top row*) and pressure side (*bottom row*) of the foil at instants (a) 1, (b) 2 and (c) 3 of Figure 8.5.

transfer reduced the rate of lift production on account of the diffused LEV below the foil. Thrust again started to increase ahead of instant 2, while the anti-clockwise TEV had almost attained its maximum circulation.

We also observed a distinct spanwise instability characteristic for the $LEV2_c$ developed on the suction side of the foil (Figure 8.6b). In contrast to the instability identified on leading edge structures in SIM2 and SIM1 wakes, which was characterized by a shorter wavelength, the undulations observed on $LEV2_c$ appeared to possess a long wavelength with the ratio $\lambda_z/d_{inv} \approx 3.5$. In terms of normalization with respect to the chord length, $\lambda_z/c \approx 1.4$. We hypothesize that there is a potential interaction with the foil boundary that has led to the development of this instability feature due to the lack of any identifiable interactions with other vortices in close proximity of this LEV. The observations discussed by Chiereghin et al. (2020), for the spanwise undulation observed on the isolated leading edge vortex for their purely plunging foil, also depicted a ratio of $\lambda_z/c = 1$. However, the exact source or origin of instability remained unclear. Ahead of instant 3, the anti-clockwise structure was completely detached from the trailing edge and formed a dipole with clockwise TEV from the first half of the oscillation cycle (see Figure 8.4d). The thrust also

approached its maximum value, although with a smaller magnitude compared to its value during the first half of the oscillation cycle. This was also evident in terms of the C_{pr} variation, where we observed that the suction side still had dominant presence of low pressure region on account of the strengthened $LEV2_c$ structure (Figure 8.6c). Thus, the difference in the integrated C_{pr} on suction and pressure side would be quite low. For latter half of the oscillation cycle, vortex couple formed ahead of instant 3 also provided an induced entrainment effect, which reduced the momentum transfer to the foil. A significant part of the resultant force yielded a substantial lift production on account of asymmetry in the wake. This entrainment effect in not as strong in the first half cycle due to the formation of a single vortex. The moment characteristics resembled the variation of C_L (Figure 8.5), as was evident in the case of SIM1.

Looking at the formation mechanism of the asymmetric wake in SIM2, it is apparent that the trailing edge structures are solely contributing to the wake deflection, as was suggested earlier by Calderon et al. (2014) for a similar wake. As trailing edge structures entrain the fluid behind them, newly forming vortex couples are subsequently deflected. The large magnitude of lift generation (or side-force depending on the foil orientation) is also a consequence of the deflected vortex couples. A similar process was observed in the experiments of Calderon et al. (2014) and Cleaver et al. (2012). On the dynamics of leading edge vortex structures, there has been several studies on their transition, disintegration and loss of coherence near the leading edge of a plunging foil (Visbal, 2009; Cleaver et al., 2011). Visbal (2009) indicated that plunging oscillations at high St_c and h_o led to the formation of a system of dynamic stall vortices that moved around the leading edge and experienced an abrupt breakdown at $Re = 10,000$. A similar breakdown was also observed for SIM2, in which the clockwise leading edge structures experience movement and breakdown near the leading edge, while the anti-clockwise structure merged with a developing trailing edge vortex. Cleaver et al. (2011) also described their Mode-2 as a deflected wake with high St_c. The leading edge vortex formed in Mode-2 was also found to lose its coherence due to its interaction with the foil boundary(Cleaver et al., 2011).

There has been many identifiable features of the wake that we have thus far related to the wake three-dimensionality and spanwise instabilities. This hints at the need to provide a through investigation of the wake three-dimensional features, their dynamics, and interactions. These details are provided in the next section for each wake.

Vorticity and evolutionary features of the wake

In order to better characterize the evolutionary features of vortices observed for SIM1 and SIM2, the variation in size (radii), separation distance and cross-stream coordinate for center of counter-rotating structures are examined as they move downstream the wake. A rectangular integration window is constructed over the contour plot, surrounding the clockwise ($TEV1'_c$ and $TEV1_c$) and counter-clockwise ($LEV1'_{ac}$ and $TEV2_{ac}$) vortices (see Figure 8.1c and 8.4c). According to Godoy-Diana et al. (2009), using rectangular contour windows reduces the interpolation errors compared to elliptical windows. The center of these rectangles denoted the location of maximum or minimum ω_z^+ for the counter-clockwise or clockwise structures, respectively. These correspond to vortex pairs in SIM1 (Figure 8.1c) and to vortex couples in SIM2 (Figure 8.4c). The maxima and minima locations of ω_z^+ were easily available via access to three-dimensional velocity fields in the wake. This was followed by a Gaussian fit of ω_z^+ field along a horizontal and vertical axis centered on the maxima and minima locations, respectively. Gaussian fits correspond to the form $e^{(-x_i/a_i)^2}$, where a_i denoted the standard deviation for streamwise and crossflow data of ω_z^+. The radius of the vortex was then quantified as 'a_i', while '$2a_i$' represented the length and width of rectangles surrounding the vortices. Here, t^+ was defined as $t^+ = t/\tau_0$ using the advective time-scale, $\tau_0 = c/U_\infty$.

The variation in the vortex apparent size, that is the normalized radius of counter-rotating vortices ($a^+ = a/c$), is tracked in the wake (Figures 8.7a and 8.7c) to provide additional quantified details on the wake dynamics. Particularly, the trends are indicators of the vortex merger or interactions from previous or subsequent cycles. They also provide evidence regarding the potential association with characteristic three-dimensional spanwise instabilities on primary vortex struc-

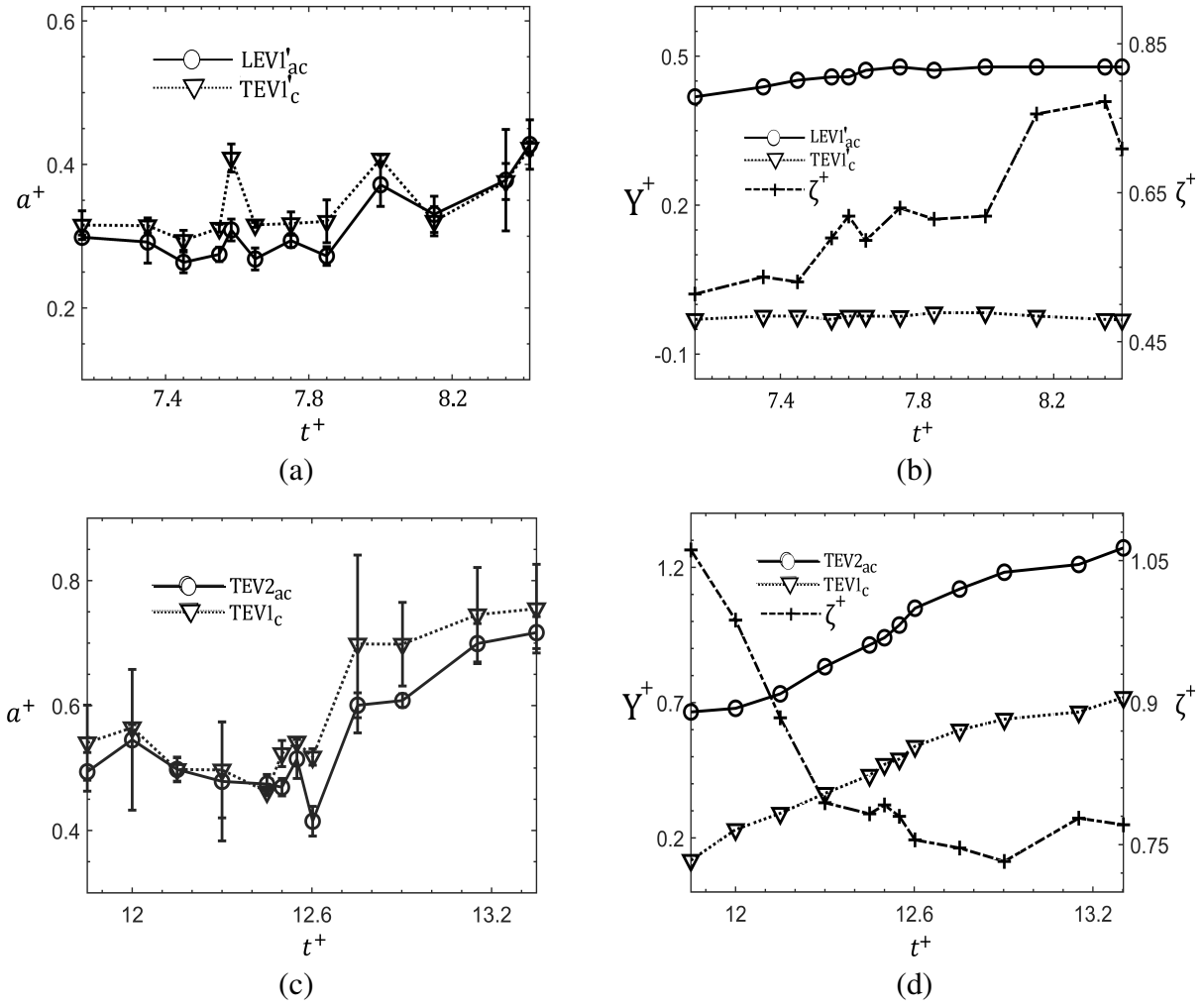

Figure 8.7: Variation of (a,c) vortex radii, a^+, (b,d) cross-stream coordinate of vortex center, Y^+, and (b,d) separation distance between the paired and coupled vortices, ζ^+, with normalized time scale t^+ , for (a,b) SIM1 and (c,d) SIM2, respectively.

tures. The difference of actual values from the mean, i.e. the radius calculated via length and width of the rectangular window, are represented as error bars in Figures 8.7a and 8.7c. For SIM1, $TEV1'_c$ in Figure 8.1c possessed a higher radius compared to $LEV1'_{ac}$ at t^+ =7.2, which is apparent in Figure 8.7a. This was attributed to early merging of neighboring clockwise vortices formed in the previous oscillation cycle. The rate of increase in a^+ was more prominent ahead of t^+ =8.2, as the foil approached $\psi = 270^o$, at which point the merging process appeared accelerated. Circulation (Γ^+) estimations (not shown here for brevity) revealed that $TEV1'_c$ from the vortex pair had a higher magnitude of Γ^+ compared to $LEV1'_{ac}$. This led to merging of the neighboring clockwise vortex $LEV1'_c$ with $TEV1'_c$, while $LEV1'_{ac}$ would subsequently merge with its neighboring counter-clockwise $TEV1_{ac}$. It is important to evaluate if the interaction and merging between neighboring vortices could reveal apparent contribution towards spanwise instability effects on the vortex pair. However as mentioned by Leweke et al. (2016), understanding the phenomenon of merging as a consequence of any instability could be debatable since instabilities were even developed when the gap between two co-rotating vortices decreased below 6% of the two vortex lengths (Cerretelli and Williamson, 2003). This would be further evident in a later section here, which is dedicated to investigating the wakes three-dimensionality. For SIM2, the radii for both counter-rotating coupled structures decreased from t^+ =11.9 to 12.5, followed by an increase until t^+ = 13.2 (Figure 8.7c). Since the magnitude of Γ^+ for individual structures forming a vortex couple in SIM2 were found similar, the decrease in radii of both counter-rotating vortex structures is possibly due to the increased negative straining on each individual structure, which occurs on account of their close proximity. The presence and dependence of growth rates for elliptic instability in primary vortices, with respect to proximity of the counter-rotating vortices was discussed by Leweke and Williamson (1998) and Boustead et al. (2010). While Leweke and Williamson (1998) indicated that the growth rate of [-1,1] Kelvin mode increased as the vortices approached each other, Boustead et al. (2010) discussed about a coupling mechanism for the outer perturbation field of a pair of vortices which intensified as the vortices approached each other. We therefore believe that an increased negative strain field intensity, which coincides with a decreased separation distance, reduced the radii of

vortical structures. Investigation into the change in separation distance (ζ^+) between the center of counter-rotating structures during a similar time provide more insightful observations that are discussed later. This indicate that vortices approaching each other in the near wake experience an increased negative straining. Since merging process was not noticed for SIM2 (in Figure 8.4c), the increase in radii of vortices during t^+ =12.5-13.3 can be attributed to the loss in angular momentum of structures advecting downstream.

The tracking of the Y^+ and ζ^+ in Figures 8.7b and 8.7d, enabled the quantitative evaluation of the advection path of vortex structures ($LEV1'_{ac}$,$TEV1'_c$, $TEV2_{ac}$ and $TEV1_c$) and differences in dynamics of vortex pairs and dipoles. The vortices that formed a pair in SIM1 followed a symmetric path whereas the vortex dipoles clearly followed an asymmetric path. Inviscid models were previously suggested (He and Gursul, 2016), which predict the dipole advection and wake deflection within reasonable agreement with experiments. However, the instability features on individual vortex structures (such as LEVs or TEVs), and their association with temporal evolution of deflected and symmetric wake configuration might not be discussed using those inviscid models. Here, the discussion further provides insights into the association of temporal evolution of individual vortex structures to some prominent instability characteristics and viscous effects, while quantitatively evaluating the advection of pairs and dipoles. The crossflow advection speed of the structures in SIM2 was calculated using the slope of the crossflow coordinate of the vortex centers, that is dy/dt in Figure 8.7d. The slope indicated that the average crossflow velocity of $TEV2_{ac}$ and $TEV1_c$ is approximately $0.56U_\infty$. This provides a substantial lateral momentum, which leads to the asymmetric wake. The separation distance (ζ=$\sqrt{(x_{ac}-x_c)^2+(y_{ac}-y_c)^2}$) between the vortex centers, that is (x_{ac},y_{ac}) and (x_c,y_c), for pairs and dipoles also depict vivid differences in Figure 8.7b,d. For SIM1, an increase in ζ^+ for the paired vortices is observed on account of the merger of weaker LEVs with the neighboring TEVs. Hence, amplitude of instability growth would be more sensitive between the co-rotating vortex structure rather than the counter-rotating vortices of each individual pair. This was briefly discussed in the previous paragraph as well that described the vortex merger and its association with spanwise instability. For SIM2, however, ζ^+ decreased till

approximately $t^+ = 12.9$ and then stayed approximately steady. We suspect that for the initial part, the induced velocity of each vortex, which forms a part of a dipole, was high enough to counteract the viscous diffusion effects, and therefore brought the vortices closer to each other. This could intensify the strain field between the vortices and could thereby lead to growth of instability that has higher amplitudes compared to regions where the dipole vortices are not in such close proximity. Similar assessment was made by Leweke and Williamson (1998) where the amplitude of the short wavelength, or the elliptic instability of the vortex pair, was larger in regions where the paired vortices were closest. More investigation into how this contributes towards dislocations on vortex core and formation of secondary vortex structures will be evaluated in the next section of this paper. Further, as the contribution of opposing centrifugal forces and viscous diffusion became prominent downstream, the induced velocity was not sufficient to further reduce ζ^+, which hence remained approximately steady thereafter. The shorter ζ^+ for dipoles in SIM2 as compared to the pairs in SIM1 had been previously observed by Godoy-Diana et al. (2009), wherein the low frequency oscillatory pitching yielded a higher ζ^+ for counter-rotating vortex structures in comparison to the high frequency pitching. However, the measurement of distance was only made for a single instant when the positive vortex crossed a reference location in the wake. Here, we assessed the changes in ζ^+ with respect to the temporal evolution of the wake and thereby evaluated differences in dynamics of vortex pairs and dipoles. To further connect the advection characteristics with some prominent aspects of propulsive performance, the advection speed of the structures is further calculated using the variation of the streamwise coordinate of the vortex center (X^+) over time (not shown here for brevity). The slope of the data corresponding to the pair of counter-rotating vortices in SIM1 indicate that the wake phase velocity is 7% smaller for $LEV1'_{ac}$ and 9% larger for $TEV1'_c$ relative to the freestream flow. However, the phase velocity of coupled vortices observed for the wake in SIM2 was approximately twice that of SIM1. This should intuitively promote a higher thrust generation in SIM2, which agrees with earlier observations.

8.3.3 The wake three-dimensionality

The three-dimensional wake topology for both cases is examined in terms of spatial dislocations or corrugations observed on the primary spanwise rollers. It is then followed by evaluation of the secondary vortices, or ribs, in the wake. This study expands on the previous work of Deng and Caulfield (2015b), Deng et al. (2015), Moriche et al. (2016) and Sun et al. (2018), who studied the wake of an infinite and finite span oscillating foil. The Floquet stability analysis of Deng and Caulfield (2015b) and Deng et al. (2015) on a pitching foil revealed spatio-temporal characteristics for dominant modes of streamwise vortices that formed in the wake at $Re = 1500$. In another study, Moriche et al. (2016) revealed that net effects of bending and roll-up of TEV around an LEV is minimal with respect to the aerodynamic performance of the oscillating foil. Even for the case of a high aspect ratio plunging foil, Sun et al. (2018) theoretically determined the existence of major instability modes, which were differentiated based on the spanwise wavelength of secondary structures in the wake. Chiereghin et al. (2020) recently observed spanwise deformation and instability on isolated leading edge vortex, shed from a high aspect ratio plunging wing. The wavelength of their observed spanwise undulations showed resemblance to similar instability modes that were previously identified by Sun et al. (2018). Such undulations were also evident from our pressure (C_{pr}) distributions for both wakes, discussed in the previous section. Here, we expand on these findings by detailed examination of the dynamics associated with primary and secondary structures in the wake of oscillating foils with combined heaving and pitching motions.

Primary vortices in high-efficiency wake (SIM1)

Figure 8.1 depicted the mechanism for $2P^T$ wake formation. The pairs of counter-rotating vortices formed appear to move upto approximately $4c$ downstream the foil trailing edge while maintaining their 2P formation (Schnipper et al., 2009). As they moved farther downstream, however, structures with similar sign vorticity merged to form an inverse Von Kàrmàn street, or a 2S wake (Schnipper et al., 2009). Here, we focus on three-dimensional analysis of the wake depicting primary vortices (rollers) using the iso-surface of vorticity components in Figure 8.8. The initial 2P wake depicts the

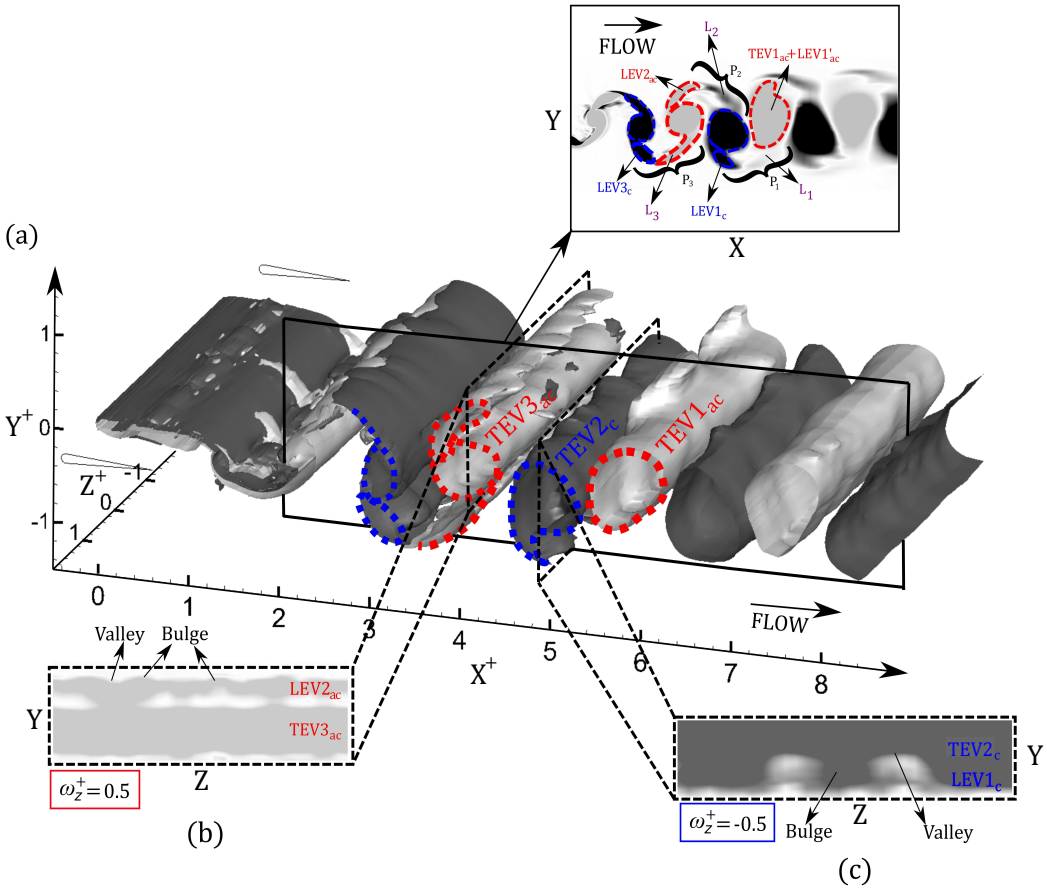

Figure 8.8: Dislocations of primary structures in the wake for SIM1 using (a) iso-surface of $|\omega_z^+| = 0.5$. The iso-contour of $|\omega_z^+|$ on the $yz-$plane are shown at (b) X^+ =4, and (c) $X^+ = 5$. Here, $\omega_z^+ = +0.5$ is colored in grey and $\omega_z^+ = -0.5$ in black.

stretched vortex legs of stronger TEVs that connect the counter-rotating LEVs to form a pair. The legs remain in conjunction with the TEV upto $X^+ \approx 4.2$, after which they start to diffuse by viscous effects. The vortex structures appear to merge with TEVs that have a similar sign vorticity from their neighboring vortex pair. This merger along with continued interaction of paired TEV legs coincided with the corrugations and deformations of weaker LEVs. These so called “dislocations" possessed different spatio-temporal characteristics that are discussed in this section.

Three vortex pairs, namely P_1, P_2 and P_3, are identified in the wake in Figure 8.8a. Each pair is comprised of a vortex formed at the leading edge, which later advects in association with the leg of the TEV formed in the subsequent half shedding cycle. The corresponding vortex legs in each pair were also identified in Figure 8.8a as L_1, L_2 and L_3. Here, L_1 does not appear as prominent

in the wake as L_2 and L_3, partly due to the diffusion caused by viscous effects. Furthermore, L_2 resulted in the stretching of $LEV2_{ac}$, which begins merging with $TEV3_{ac}$ that was shed in the successive shedding cycle. A similar process was also observed for $LEV1_c$ of pair P_1, although the sign of circulation was different. There appears to be a unique mechanism in play here, in which TEVs that possess larger circulation compared to LEVs impose different spanwise dislocation characteristics on the rollers. As observed in Figure 8.8, the corrugations associated with $LEV1_c$ and $LEV2_{ac}$ exhibit noticeable differences in spanwise direction. The quantitative estimate of the circulation for $TEV1_{ac}$ was $\Gamma^+ = 0.81$, which is 11% larger than the estimated value of $\Gamma^+ = 0.732$ for $TEV2_c$, and is likely caused by merging with $LEV1'_c$. The different circulation estimates for $TEV1_{ac}$ and $TEV2_c$ further provide a strong evidence for the mechanism hinted above.

We further describe the evidence to support our proposed mechanism for dislocations, and their associated characteristic differences for subsequent LEVs shed in the wake. The increased axial straining on the legs of TEVs, due to the increasing circulation, formed regions identified as valley and bulge on the rollers (LEVs) in Figures 8.8b, 8.8c and 8.9. Particularly, the valleys and bulges were formed for $LEV1_c$ in pair P_1 and $LEV2_{ac}$ in pair P_2. However, the depth-to-spanwise-width-ratio were different for the identified dislocations. For $LEV2_{ac}$, the associated valleys and bulges had much smaller depth-to-spanwise-width-ratio resulting in finer corrugations compared to those observed on $LEV1_c$. The iso-contours of normalized spanwise vorticity shown on the $yz-$planes of Figures 8.8b and 8.8c (passing through the cores of $LEV1_c$ and $LEV2_{ac}$) depict larger and deeper valleys for $LEV1_c$ compared to $LEV2_{ac}$. This effect was again attributed to the higher straining on $LEV1_c$ caused by $TEV1_{ac}$. We calculated the ratio of spanwise wavelength for the vortex dislocations and the core radii (a), which depicted a value close to 2.68, and appeared to be relatively smaller compared to the ratio λ_z/a that was observed for the leading vortex vortex filament in previous section. However, in terms of normalization with respect to chord, we observed a value of $\lambda_z/c \approx 0.8$, that was quite close to value of $\lambda_z/c \approx 0.98$, estimated for the leading edge vortex ($LEV1_c$). Experimental findings of Zhang et al. (1995) and Brede et al. (1996) also indicated that there exists an instability of primary vortex rollers that result in “tongue-like" formations,

which elongated to form secondary vortex structures. These depicted topological similarities with valley and bulges identified on $LEV2_{ac}$ and $LEV1_c$ for SIM1. Boustead et al. (2010) further discussed “crescent" shaped features observed on primary vortices, which were attributed to the short wavelength elliptic instability growth. Such descriptions, therefore, warrant a need for a thorough Floquet analysis to further confirm, theoretically, if the three-dimensionality is indeed attributed to a dominant instability of the primary vortices. We further observe in Figure 8.8b that spanwise instability was developed even as $LEV2_{ac}$ and $TEV3_{ac}$ were in close proximity of one another, prior to their merger. This also supports our previous discussion with regards to the consequences of vortex merger on the origin of instability. We did not observe any conclusive evidence that would suggest vortex merger between co-rotating vortex structures promote the instability growth. Similar observations were apparent for instability growth in a co-rotating pair which comprised of equal strength vortex structures, in an earlier experimental study by Meunier and Leweke (2005). Moreover, Leweke et al. (2016) described that at high Re flows ($\approx$4000), the diffusive stage in merging of vortices (McWilliams and Zabusky, 1988) often lasted longer, thereby providing sufficient time for the instability to develop and grow. This was ultimately followed by the convective stage of the merger, where the vortices approach each other rapidly, and then merged (McWilliams and Zabusky, 1988). We believe that this non-linear instability growth could indicate the unstable premature merging that was discussed by Leweke et al. (2016). This process will further result in the ejection of vorticity from the outer vortex layer of the weaker co-rotating LEV roller (for instance, $LEV2_{ac}$ in Figure 8.8b).

The accelerated increase in radii observed in Figure 8.7a also coincides with the advective time, which might further be an indication of the convective merging process. However, its consequence on the instability is still debatable. Figure 8.8c depicts a similar asymmetric perturbation growth on $LEV1_c$ and $TEV2_c$, although their merger is almost complete. As shown above, an apparent similarity was observed in terms of λ_z/c when comparing the spanwise instability characteristics and plausible mechanisms observed on $LEVs$ that advected over the foil boundary (Figure 8.3) and the paired vortex structures in the wake. $LEV1_c$ in Figure 8.3(a) depicted a ratio λ_z/c approxi-

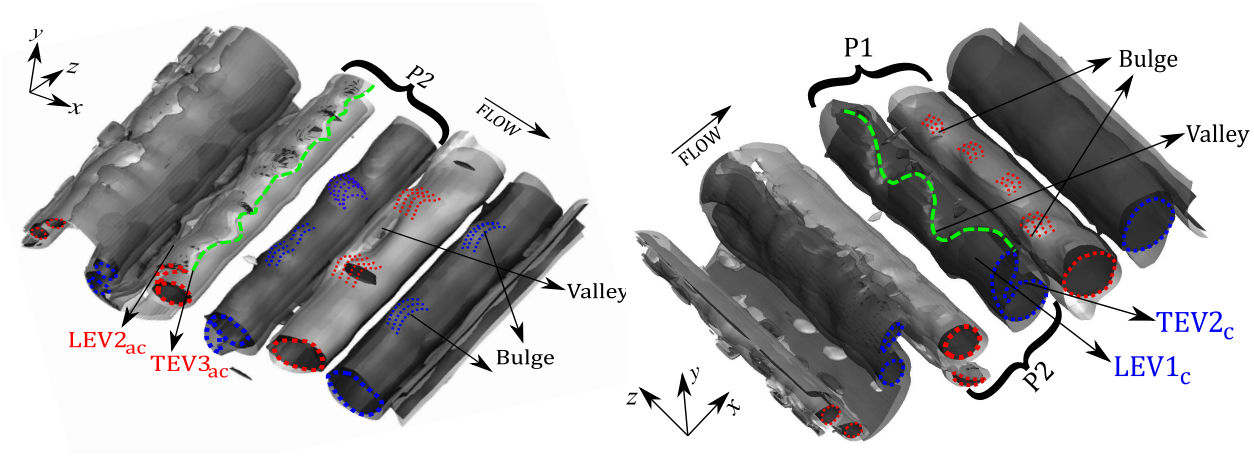

Figure 8.9: Dislocations are highlighted on the iso-surface plots of normalized $Q-$criterion ($Q^+ = Qc^2/U_\infty^2 \approx 0.01$), overlaid with iso-surface of ω_z^+ = 0.5 in grey and ω_z^+ = -0.5 in black shown from spanwise (a) top-view and (b) bottom view.

mately equal to 0.98, which was close to the value estimated for $LEV1_c$ in the wake ($\lambda_z/c \approx 0.8$). However, for the LEV structure located around the mid-chord region ($LEV2_{ac}$ in Figure 8.3b), we observed a 30% difference in its estimated λ_z/c compared to the value observed here in the wake. Thus, quantitative predictions showed that an elliptic instability mechanism of counter-rotating vortex pairs would lead to development of instability feature for vortex structures located over the foil and also those identified in the wake of SIM1. However, the difference in the wavelength predicted for $LEVs$ that were still around the mid-chord length could be on account of the initiation of the elliptic instability that would be in its nascent stages of development. Until the $LEVs$ reach sufficiently close to the developing TEV legs (see Figure 8.1d), the dominant effects of elliptic instability mechanism does not seemed prominent, as those observed in the wake. For the wake structures presented ahead of X^+ =7, the dislocations were not as pronounced as those observed in the near wake. No significant valley or bulge formation was noticed on the primary vortex rollers.

Some of the above highlighted spatial dislocations were also discussed previously by Mittal and Balachandar (1995). For example, similar observations were reported in the wake of stationary cylinders on account of a core instability mechanism where the dislocations were related to the formation of horseshoe structures along the spanwise rollers (Mittal and Balachandar, 1995). As

these rollers advected downstream, the incremental principal strains on braid shear layer between the consecutive rollers elongated the legs of the horseshoe vortex, forming a so called hairpin structure. Further elongation caused streamwise vortex pairs or ribs to form in the wake. Here, to further investigate whether there were any horseshoe or hairpin vortices in the wake of SIM1, we visualized the spanwise vortex cores in terms of isosurface of Q-criterion overlaid with contours of spanwise vorticity (see Figures 8.9). The spanwise view of the rollers in Figure 8.9a (top-view) and Figure 8.9b (bottom-view) provides a vivid visualization of the aforementioned dislocations for $LEV1_c$ and $LEV2_{ac}$. The green dotted lines on $LEV1_c$ and $LEV2_{ac}$ in Figures 8.9 represent the differential spatial topology of valleys and bulges. No imminent formation of horseshoe or hairpin vortices was noted in the wake. This is an important observation since the intermediate vortex structures formed on account of core instabilities of rollers will not contribute towards formation of secondary vortices as was observed by Mittal and Balachandar (1995). The details on qualitative and quantitative characteristics of secondary structures for SIM1 will be further discussed later in this section.

Primary vortices in large-thrust wake (SIM2)

The asymmetric wake of SIM2 had a dominant presence of strong counter-rotating TEVs that advected downstream as vortex couples, at an angle from the free-stream flow. Near wake formation mechanisms and interaction of primary vortices that form the couples had been previously investigated in some experimental studies (Calderon et al., 2014). However, three-dimensional spatial characteristics for coupled rollers in spanwise direction still need further assessment. Similar to depiction of rollers for SIM1, we present the iso-surfaces of spanwise vorticity ($|\omega_z^+|$) for SIM2 in Figure 8.10. Spatial characteristics of dislocations and their differences along the wake are very apparent for the coupled rollers. These characteristics also appear to be different from those observed in the wake of SIM1. The valleys and bulges identified here had much larger depth to width ratio compared to those observed in the wake of SIM1. This is apparent when comparing the deeper dislocations on coupled rollers in Figure 8.10 to their counterpart in SIM1 (Figure 8.9).

This observation also coincides with a decreased separation distance (ζ^+) for SIM2, compared to SIM1, as depicted earlier in Figures 8.7(b) and 8.7(c). Focusing further on SIM2, the valleys and bulges for the vortex couple at X^+ =8 are more flattened in comparison to upstream couple. This can be explained by the elongation of the prominent dislocations, in the form of horseshoe or hairpin vortex structures, under the increased axial straining between the coupled rollers. In order to investigate the presence of these horseshoe and hairpin structures, we look at the iso-surfaces of Q-criterion overlaid with contours of ω_z^+ in Figure 8.11. These plots represent spanwise view of vortex couples at X^+ =6 and 8 respectively, depicting the emergence and development of streamwise dislocations of the rollers.

Three elongated hairpin vortices are identified in Figure 8.11a. The emergence of these hairpin vortices appear to be following the mechanism proposed by Mittal and Balachandar (1995), although the spatial development and elongation for legs of hairpin vortices showed differences compared to the wake of stationary cylinders. The legs of each hairpin structure appear to wrap around the counter-rotating vortex $TEV3_c$, which itself is coupled with $TEV4_{ac}$. An additional insight was on the growth of hairpin vortices, which wherein form a conjoint horseshoe vortex on the head of the hairpin vortices. These conjoint structures, identified in Figure 8.11b, wrap around their counterpart couple, similar to the hairpin structures in Figure 8.11a. However, the legs of horseshoe vortex structures do not elongate to lengths comparable to those of hairpin structure. Similar hairpin vortex structures also appear on couple located downstream.

Although the dislocations in the form of hairpin and horseshoe structures appeared to be in stark contrast with those observed in SIM1, these structures still seem to emerge out of the primary vortex cores thereby hinting at a core instability discussed by Mittal and Balachandar (1995). A similar instability mechanism seemed prominent for SIM1 which led to formation of valleys and bulges (Figure 8.8). Specifically, the ratio of the spanwise wavelength for the observed dislocations and d_{inv} depicts a value of 1.813 that appears relatively close to SIM1. In terms of normalization with respect to chord length, the ratio λ_z/c corresponds to 0.73. We also observed some similarities in the spanwise instability characteristics observed previously on the leading edge primary rollers

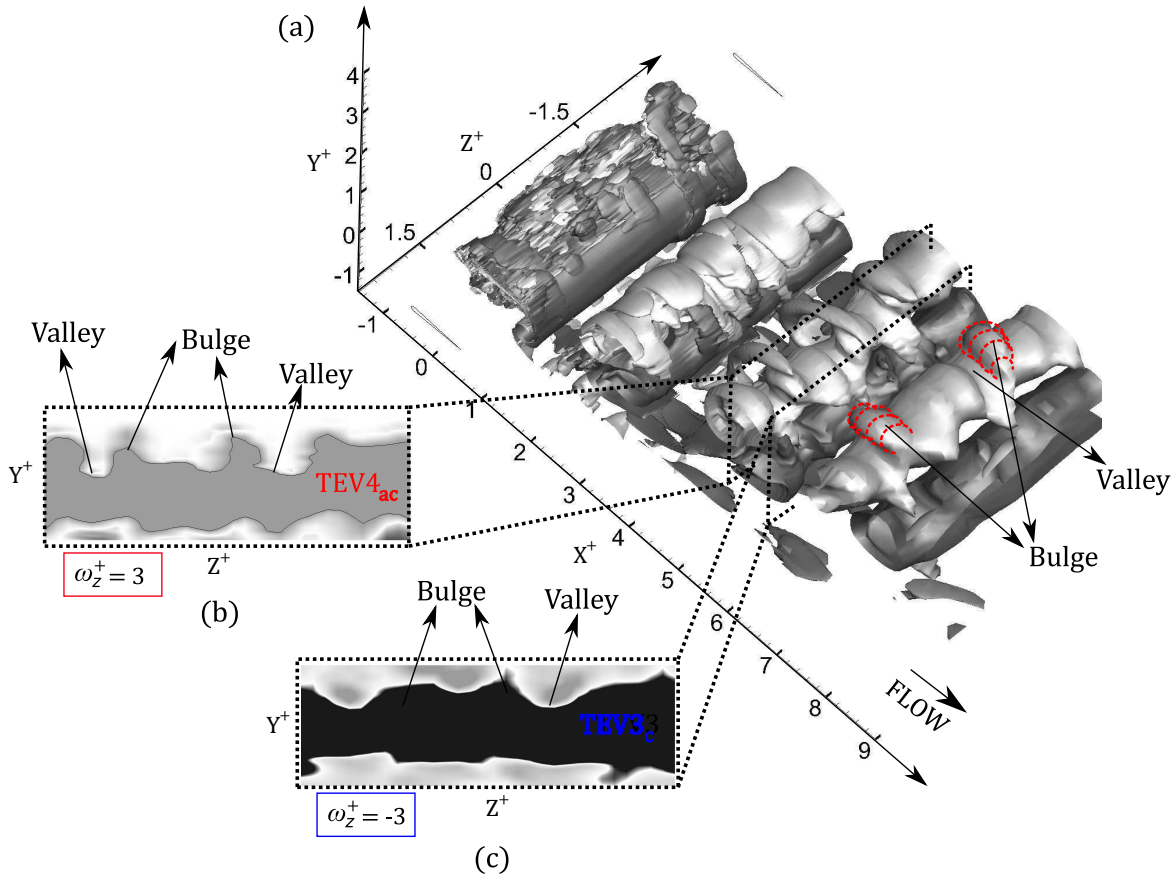

Figure 8.10: Dislocations observed for the primary structures in the wake for SIM2 using (a) isosurface of $|\omega_z^+| = 3$ with valleys and bulges depicted on the $yz-$plane at (b) $X^+ = 5.4$, and (c) $X^+ = 6$. Legends are the same as previous figures.

discussed in the previous section. As noted for $LEV1_{ac}$ on the pressure side in Figure 8.6(a), λ_z/c depicted a value close to 0.8. It was also evident that since $LEV1'_c$ advected along the leading edge and interacted with the developing $LEV1_{ac}$ for a short duration, the elliptic instability mechanism for counter-rotating vortex pair (Leweke and Williamson, 1998) would be responsible for the observed spanwise undulation in 8.6(a). However, Figure 8.6(b) provided evidence that the isolated leading edge vortex ($LEV2_c$) also depicted a spanwise instability whose value of λ_z/c was close to 1.4, in contrast to that observed for $LEV1_{ac}$. Thus, it was speculated that the mechanism for the spanwise instability that occurred for $LEV2_c$ would be different from the elliptic instability mechanism for vortex pairs, and could involve an interaction with the foil boundary. These similarities

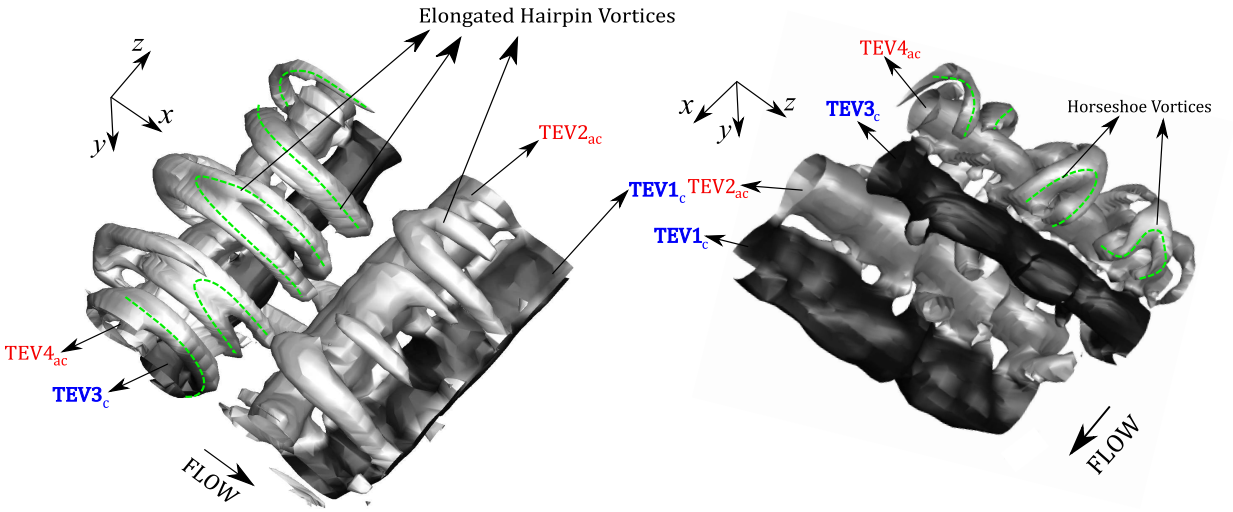

Figure 8.11: Dislocations observed for the primary structures in the wake for SIM2 are highlighted in iso-surface plots of normalized $Q-$criterion ($Q^+ = Qc^2/U_\infty^2 \approx 0.09$) overlaid with colored contours corresponding to ω_z^+ = 3 (grey) and ω_z^+ = -3 (black).

and differences in mechanisms for spanwise instability were therefore evident for $LEVs$ and $TEVs$ in SIM2.

Despite the observations hinting a core instability being imminent on the coupled rollers in wake of SIM2, the interaction of well developed and mature legs of hairpin structures, with the small scale vorticity existing within the braid regions between the coupled rollers is possible. This could also contribute towards the formation of streamwise vortex structures or secondary vortices. Such three-dimensional interaction was discussed as an centrifugal instability by Brede et al. (1996) for stationary cylinder wake, and more recently hinted by Deng and Caulfield (2015b) for oscillatory wake flows behind pitching foils. The ratio of the estimated wavelength associated with spanwise dislocations on SIM2 rollers and the chord length indicated a value approximately equal to 1. A recent experimental study on high aspect ratio wings in plunge oscillations by Chiereghin et al. (2020) predicted a similar ratio for the spanwise instabilities observed on isolated leading edge vortex structures. However, the physical origin of these instabilities was speculated to be due to either oscillating mixing layer, oscillating wake or an individual vortex filament (Chiereghin et al., 2020). Therefore, a stability analysis to identify prominent Floquet modes still seems neces-

sary in order to determine plausible origin of the three-dimensionality and deformation of primary rollers observed for SIM2.

8.3.4 Secondary vortex structures

The identification of instability mechanisms and characteristics of secondary vortices, or “ribs", have been well investigated for wakes of cylinders at low *Re*. Moreover, they have been found to have dominant presence behind normal flat plates (Hemmati et al., 2016), bluff elongated trailing edge cylinders (Ryan et al., 2005; Gibeau et al., 2018) and pitching or heaving foils (Deng and Caulfield, 2015b; Sun et al., 2018) in low to high *Re* regimes. Contrary to the definition of rollers as having constant spanwise vorticity, ribs are identified with a dominant, and in cases constant, streamwise vorticity that occur in pairs. Their orientation typically aligns with the spanwise direction. Periodic spatial and temporal behavior of ribs were observed to vary with ranges of *Re* and shape of the bluff body, although the prominent modes of formation were still explained via characteristic instabilities of vortex rollers (Mode-A) and separated shear layers (Mode-B) (Williamson, 1996). The occurrence and growth of instabilities is often investigated at low *Re*. However, we could relate the dominant features of streamwise vortex shedding to previously identified modes, as described in a recent study by Gibeau et al. (2018). This section therefore focuses on identifying the spatial and temporal evolution of secondary structures in the wake of oscillating foils with unique propulsive performance characteristics (SIM1 and SIM2). The spanwise wavelength (λ) for secondary vortex pairs was calculated using auto-correlation while their periodicity was examined using cross-correlation of $|\omega_x^+|$ across the $yz-$plane. We compared these estimates and features with previously identified rib characteristics for fixed or oscillating cylinders and foils in order to characterize the three-dimensional wake. We further propose a vortex skeleton model for SIM1 and SIM2 that highlights the dominant wake evolution associated with high propulsive performance of oscillating foils.

The wavelength of the ribs, defined as $\lambda_z = \lambda/c$, denote the spacing between two consecutive streamwise vortex pairs aligning along the spanwise direction. In order to calculate λ_z, coefficient

of spatial autocorrelation was determined using Eq. 3.6. For each planar ω_x^+ representation, the value of $C(z)$ is calculated with respect to spanwise lag or shift, Δz. The results of $C(z)$ are then averaged by data obtained from 5 shedding cycles. As the value of $C(z)$ is plotted with respect to $\Delta z^+ (= \Delta z/c)$ along the spanwise direction, an extrema for $C(z)$ occurred on account of the rib periodicity. The distance between the maxima of $C(z)$ and the first minima provides an estimated value of half of λ_z for ribs in the wake. The periodicity in temporal evolution of ribs in the streamwise direction is further determined using spatial cross-correlation applied between two subsequent streamwise locations, corresponding to centers of primary vortex rollers. These vortices are shed at fixed time intervals with respect to shedding period (T_{shed}) in different locations in the wake. This presents an ideal temporal data for analyzing the evolution of ribs. The formulation for cross-correlation coefficient is given as:

$$\rho(\Delta z) = \frac{\langle \omega_x^+(y_o, z_0, t_i) \cdot \omega_x^+(y_o, z_0 + \Delta z, t_i + T_{shed}) \rangle}{\omega_{x,rms}^+(y_o, z_0, t_i)\, \omega_{x,rms}^+(y_o, z_0 + \Delta z, t_i + T_{shed})}. \tag{8.1}$$

Similar to the analysis of auto-correlation data discussed earlier, we examine the variation of $\rho(z)$ with respect to the spanwise shift (Δz) to gain a quantitative understanding of the ribs characteristics. The sign-switch for ribs between consecutive full or half shedding cycles are determined based on whether $\rho(z)$ began with a positive value and subsequently dropped towards a local minima, or vice versa. If former condition holds, then it implies that ribs maintain their direction of rotation as the shedding cycles progress. However if there is any change or reversal in the streamwise vortex sign, this implies that the curve for $\rho(z)$ tends towards a local maximum value from an initial starting value. The results for the cross-correlation are then averaged for five shedding cycles.

Secondary vortex structures in SIM1

We first assessed the spatial location for alignment of secondary vortices with respect to turbulent streamwise velocity fluctuations (u') on $yz-$planes. The streamwise location of each plane was

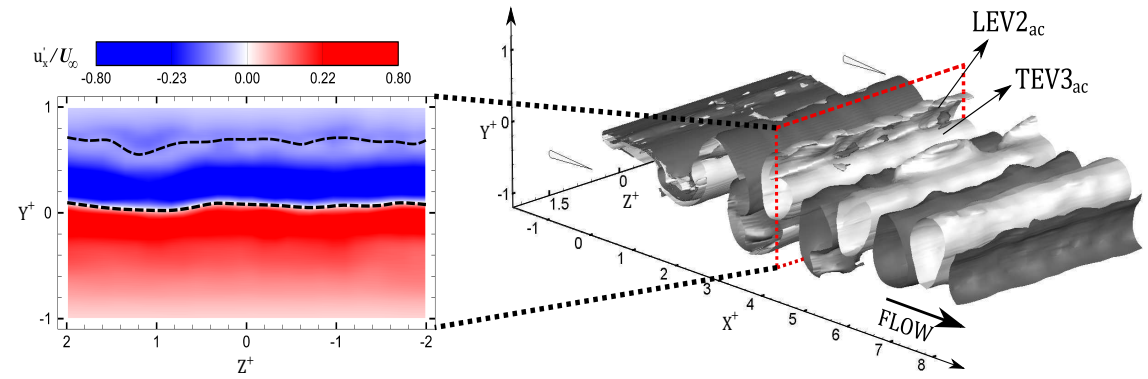

(a)

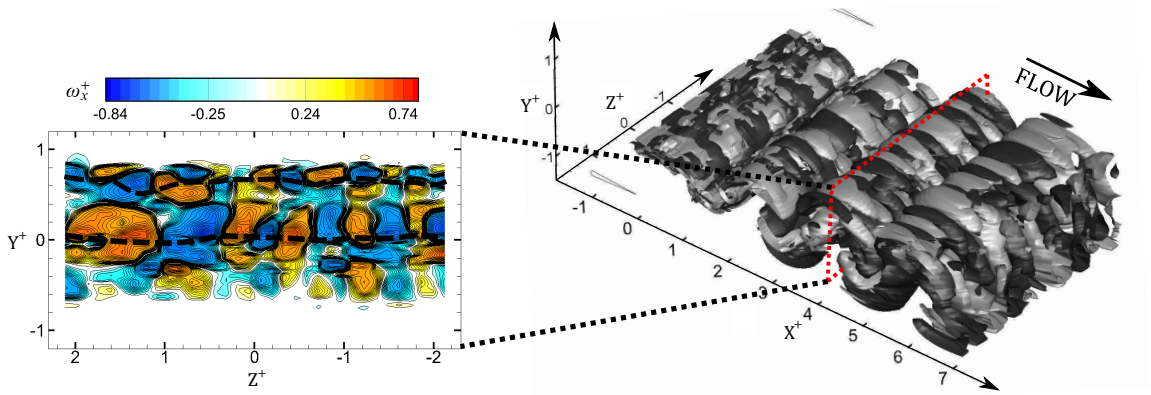

(b)

Figure 8.12: (a) Iso-surface of $\omega_z^+ = +0.5$ (grey) and $\omega_z^+ = -0.5$ (black) along with $yz-$planar contour of u' at $X^+ = 4$. (b) The depiction of ribs using iso-surface of $\omega_x^+ = +0.055$ (gray) and $\omega_x^+ = -0.055$ (black) along with the $yz-$planar contour of streamwise vorticity at $X^+ = 4$.

governed by the position of counter-rotating primary vortex rollers. A similar analysis was also carried out by Gibeau et al. (2018), who reported that a dominant alignment of secondary vortices was observed in the region where u' distribution was negative. They further linked this characteristic to the model for Mode B instability proposed earlier by Brede et al. (1996), wherein the streamwise vortices always passed on the side of rollers with negative u' distribution with respect to the advecting frame of reference.

Figure 8.12a depicts the $yz-$plane corresponding to location of the center of the primary vortex rollers $TEV3_{ac}$ and $LEV2_{ac}$. Since $TEV3_{ac}$ had a counter-clockwise circulation, the value of u' was negative with respect to the advecting frame of reference in the region above $TEV3_{ac}$. The black dotted lines depicted on the u' spatial distribution represent the region where values of u'

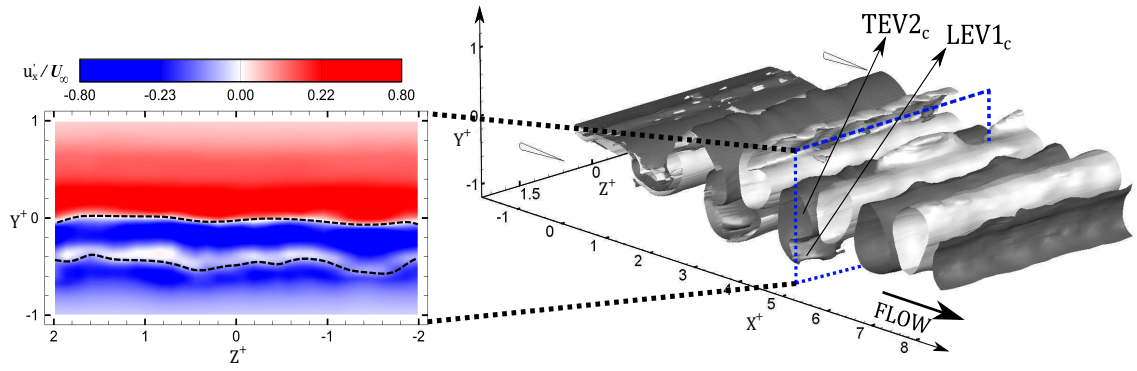

(a)

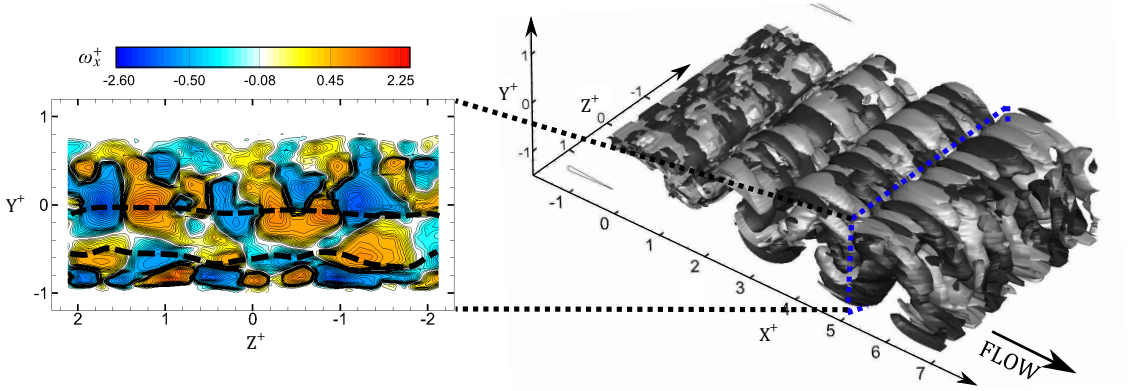

(b)

Figure 8.13: (a) Iso-surface of $\omega_z^+ = +0.5$ (grey) and $\omega_z^+ = -0.5$ (black) along with the $yz-$planar contour of u' at $X^+ = 5$. (b) The depiction of ribs using iso-surface of $\omega_x^+ = +0.055$ (grey) and $\omega_x^+ = -0.055$ (black) along with the $yz-$planar contour of streamwise vorticity at $X^+ = 5$.

were close to zero. Please note that the $yz-$plane passes through both $TEV3_{ac}$ and $LEV2_{ac}$, hint the existence of two lines of $u' \approx 0$. Figure 8.12b depicts the iso-surfaces of $|\omega_x^+|$ =0.055 that provides a vivid three-dimensional representation of continuous rib pairs as they passed over each roller. In order to determine the precise spanwise location of the ribs with respect to the rollers, we look at the planar iso-contours of ω_x^+ at the same location as in Figure 8.12a. The contours clearly show an alignment of streamwise vortex pairs specifically in regions where $u' < 0$, with respect to the free-stream flow. In addition to alignment of rib pairs in regions of $u' \lessapprox 0$, we also observed streamwise vorticity distribution along spanwise locations where $u' > 0$. However, it is important to note that the distribution in these locations are within the core regions of rollers. Thus, they should not be interpreted in terms of dominant streamwise vortices that align and extend through

the braid regions between consecutive vortex couples. Deng and Caulfield (2015b) reported a similar observation on the existence of opposite signed streamwise vortex structures within coupled rollers.

Figure 8.13a shows the contour of u' on a plane passing through rollers $TEV2_c$ and $LEV1_c$, although the region of negative u' now falls below the rollers. The alignment of the dominant streamwise vortex pairs appear below $LEV1_c$ in Figure 8.13b. The combination of these observations indicate that the ribs in SIM1 closely follow the model proposed by Brede et al. (1996) for the streamwise vortex arrangement of Mode B. However, further analysis is needed to validate the dominant mode characteristics for the secondary structures with respect to λ_z and streamwise periodicity.

In order to further characterize the rib pairs in terms of their spanwise spacing (λ_z), the auto-correlation coefficient ($C(z)$) was calculated for ω_x^+ along the span. Figure 8.14 shows $C(z)$ plotted against the spanwise shift (Δz). Particularly, the variation of $C(z)$ for the rib pairs identified on different $yz-$planes (previously shown in Figures 8.12 and 8.13) is presented in Figure 8.14a. The distance between the initial maximum value and the first minima of $C(z)$ hints at $\lambda_z \approx 0.7$. Farther downstream the wake at $X^+ = 6.65$ and 7.65, which is after the wake transition from 2P to 2S, the variation of $C(z)$ in Figure 8.14b hints at a similar λ_z. Extending our study of the ribs arrangement into the mid wake allows investigating the spatio-temporal changes that could have occurred due to the wake transitioning from 2P to 2S arrangement. Figures 8.15a and 8.15b show the iso-contour plots of ω_x^+ at the mid-wake locations, where the dominant alignment of rib pairs was still evident. This suggested that as the primary vortex rollers undergo a mode transition from 2P to 2S, the streamwise vortices maintain their spatial distribution and periodicity along the spanwise direction. The spanwise wavelength of ribs is in close agreement with the prediction of Williamson (1996), Zhang et al. (1995), Brede et al. (1996), and Gibeau et al. (2018) for streamwise vortex arrangement in Mode B. The study of Ortega et al. (2003) further highlighted that the ratio of spanwise wavelength of the streamwise undulations, and separation distance ζ between the unequal strength counter-rotating vortex pair, was approximately in range of 1 to 1.2 for several

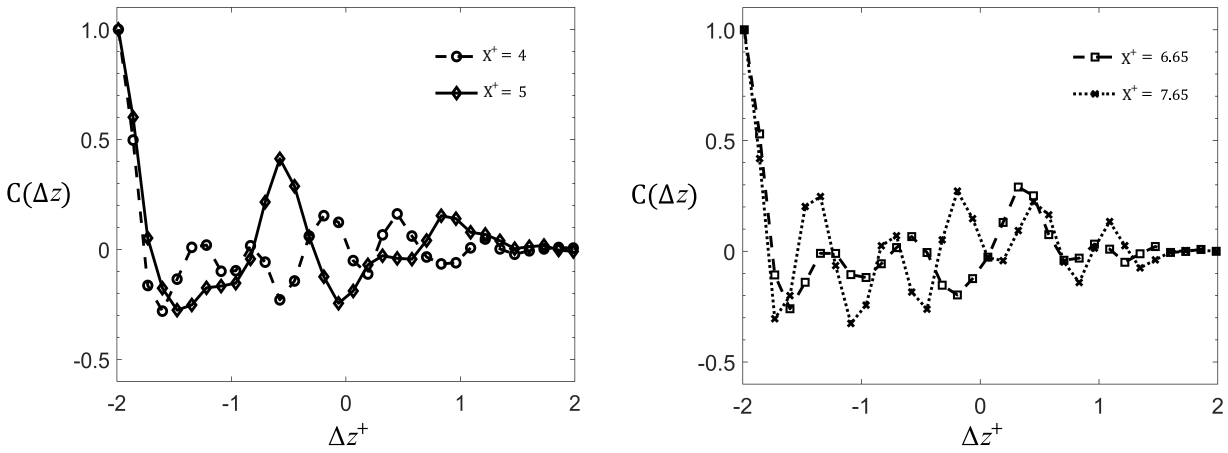

Figure 8.14: Variation of $C(\Delta z)$ with respect to spanwise shift (Δz^+) during (a) 2P wake at $X^+ = 4$ and 5, and (b) 2S wake at $X^+ = 6.65$ and 7.65 for SIM1.

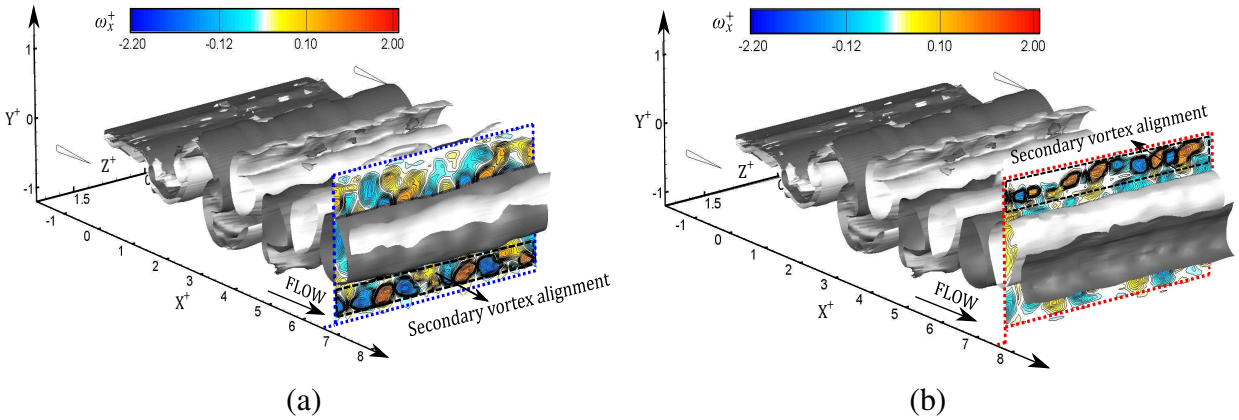

Figure 8.15: Alignment of streamwise vortex pairs on the $yz-$plane at (a) X^+ =6.65, and (b)X^+ =7.65 for SIM1.

experimental runs. For the secondary structures identified for SIM1, this ratio (λ_z/ζ) was estimated to be approximately 1.22, which hints that the instability of the unequal strength primary vortex pairs is associated with development and interaction of the secondary vortex pairs.

Temporal evolution of ribs and their streamwise periodicity with respect to shedding period was investigated using cross-correlations of ω_x^+ on the $yz-$plane for two consecutive full (Figure 8.16a) and half (Figure 8.16b) shedding cycles. It was evident that ribs maintain their direction of

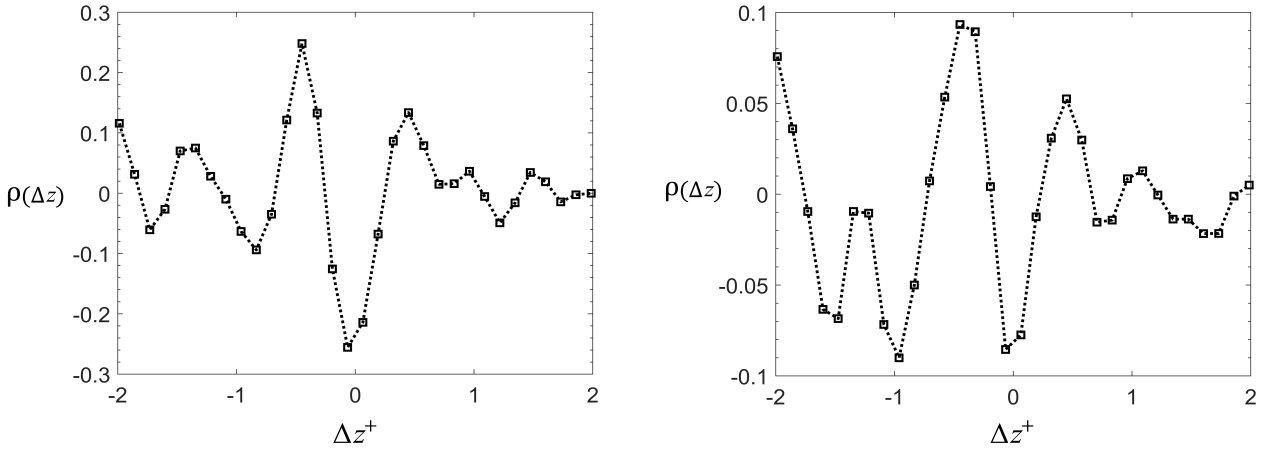

Figure 8.16: Variation of $\rho(\Delta z)$ obtained from cross-correlations of ω_x^+ between (a) Full and (b) Half shedding cycles for SIM1.

rotation, i.e. temporal periodicity, in each full and half shedding cycle. Based on the observations made above, the ribs follow the Mode B arrangement and its corresponding characteristics.

Secondary vortex structures in SIM2

We now assess the asymmetric wake of SIM2 to determine the characteristics of its dominant secondary structures. The procedure follows that described for SIM1. We first evaluated the location of the secondary vortex alignment with respect to u' distribution on the $yz-$planes passing through the cores of spanwise rollers. This is followed by determining λ_z and streamwise periodicity of ribs in the wake.

Figure 8.17a (left) depicts the $yz-$plane passing through vortex roller $TEV4_{ac}$. Since $TEV4_{ac}$ has a counter-clockwise circulation, u' has a negative value in regions located above the roller. In Figure 8.17a (left), the black dotted line represents spanwise locations where $u' \approx 0$ with respect to the advecting frame of reference. From the distribution of ω_x^+ in Figure 8.17b (left), it is apparent that the dominant rib pairs align in regions where u' is both negative and positive. Thus, there is a significant difference observed on the spatial topology of ribs in SIM2 compared to SIM1. The three-dimensional structure of the ribs was qualitatively evaluated using iso-surfaces of $\omega_x^+(=0.5)$ in Figure 8.17b (right). The ribs clearly appear to wrap around the counter-rotating vortices that

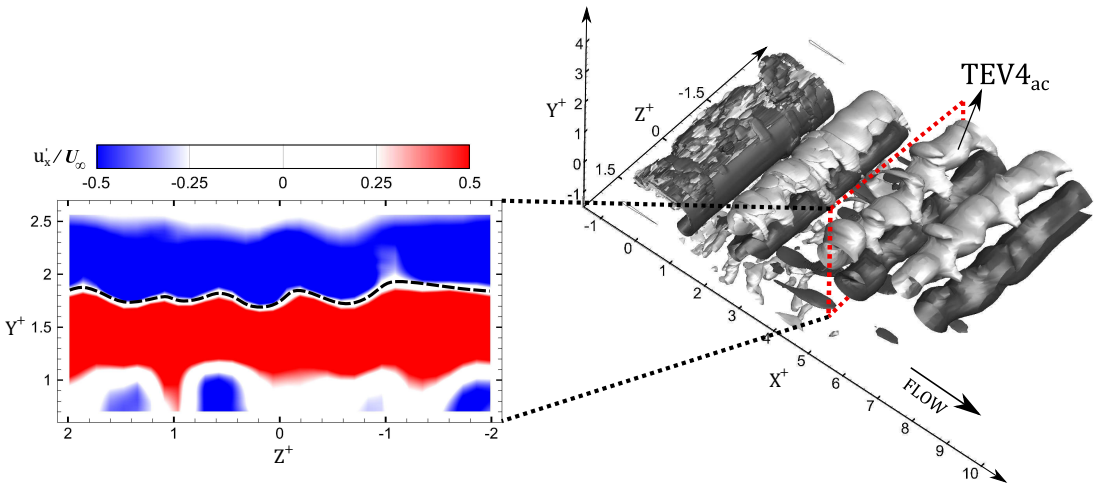

(a)

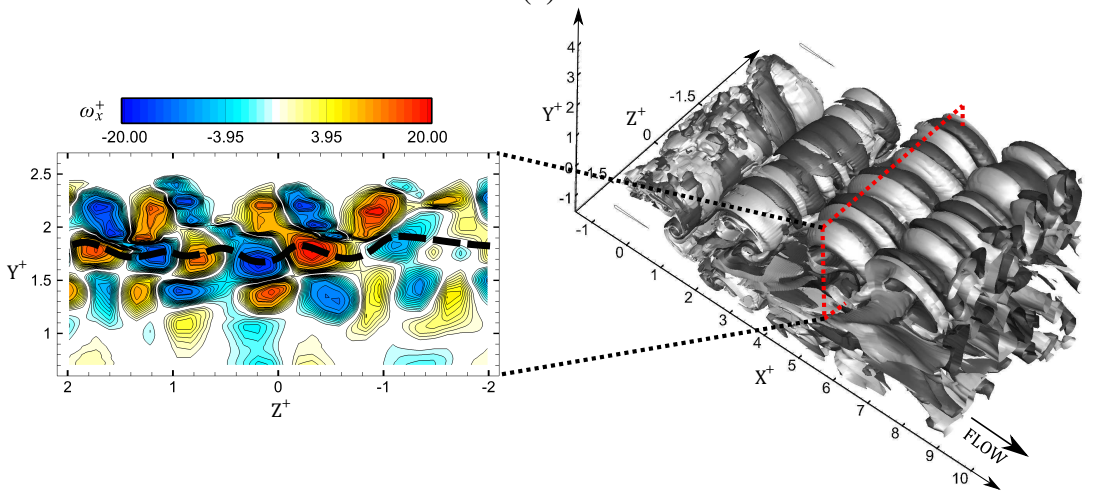

(b)

Figure 8.17: (a) Iso-surface of $\omega_z^+ = +3$ (grey) and $\omega_z^+ = -3$ (black) along with the $yz-$planar contour of u' at $X^+ = 5.4$. (b) The depiction of ribs using iso-surface of $\omega_x^+ = +0.5$ (grey) and $\omega_x^+ = -0.5$ (black) along with the $yz-$planar contour of streamwise vorticity at $X^+ = 5.4$.

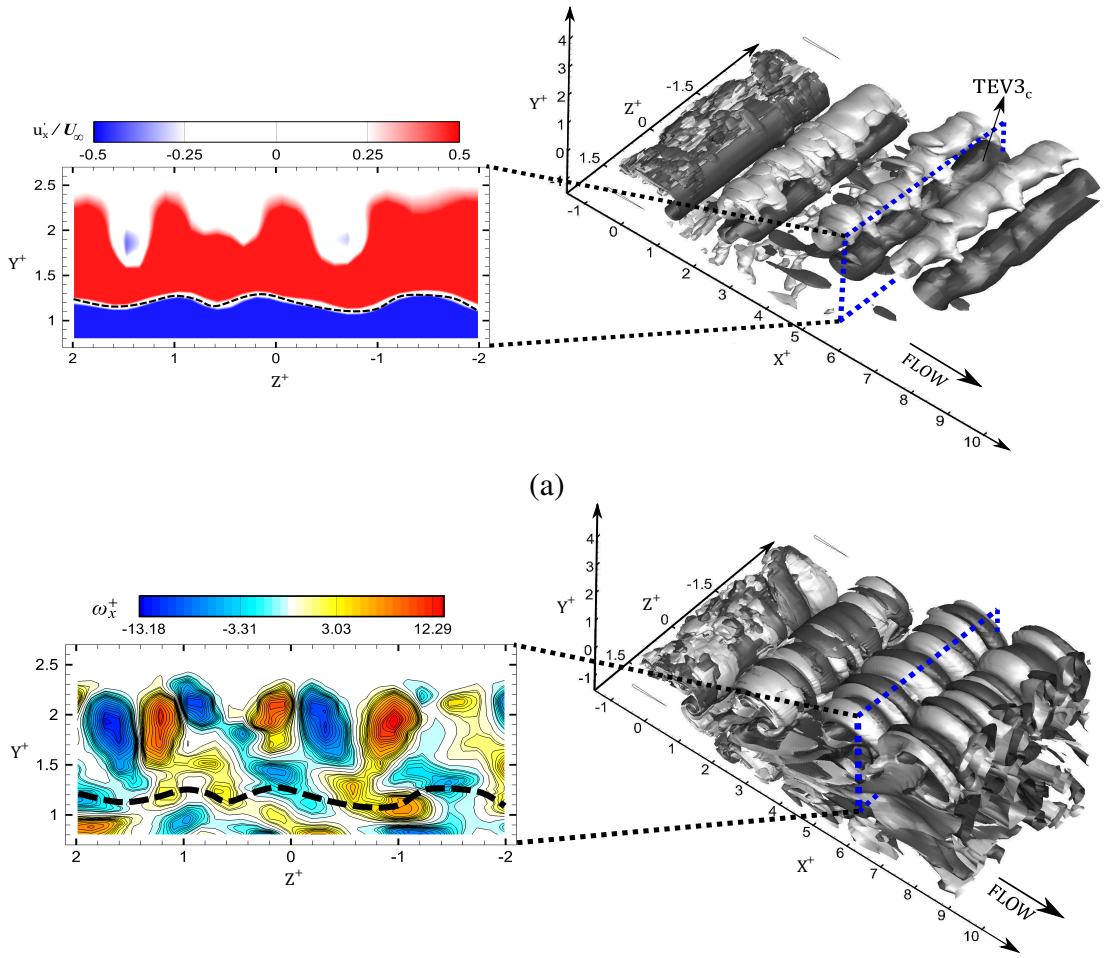

Figure 8.18: (a) Iso-surface of $\omega_z^+ = +3$ (grey) and $\omega_z^+ = -3$ (black) along with the $yz-$planar contour of u' at $X^+ = 6$. (b) The depiction of ribs using iso-surface of $\omega_x^+ = +0.5$ (grey) and $\omega_x^+ = -0.5$ (black) along with the $yz-$planar contour of streamwise vorticity at $X^+ = 6$.

advect as a couple. The observations of Deng and Caulfield (2015b), Deng et al. (2015) and Sun et al. (2018) revealed similar distribution for streamwise vortex pairs in the wake of pitching and heaving foils, although some differences exists that are mainly due to their lower *Re* range of 1500-1700. The long wavelength mode for pitching foil and Mode-A for a heaving foil did not reveal a continuous rib structure (Deng and Caulfield, 2015b; Sun et al., 2018). However, the short wavelength mode for pitching foil depicted continuity only for two successive shedding cycles after which the structures decayed on account of viscous dissipation (Deng and Caulfield, 2015b). Comparing the current wake with the observations of Deng and Caulfield (2015b), Deng et al. (2015) and Sun et al. (2018), the ribs maintained a continuous profile for three subsequent

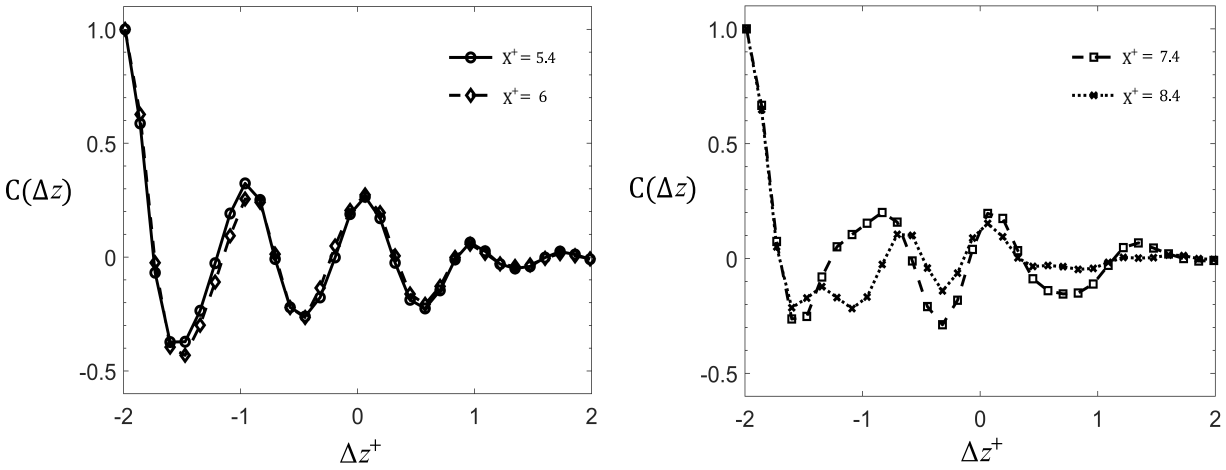

Figure 8.19: Variation of $C(\Delta z)$ with respect to normalized spanwise shift (Δz^+) in the (a) Near wake and (b) Mid wake of SIM2.

shedding cycles (i.e. approximately $9c$ downstream of the foil trailing edge). The orientation and appearance of coherent structures in mid-wake hints at increased axial straining within braid vorticity regions due to newly forming vortex couples in the near wake. Statistical characteristics of secondary structures, such as λ_z and periodicity, can provide more clues on whether structures retain their coherence in the wake. The nonuniform distribution of u' was attributed to the effects of dislocation on primary vortices previously discussed as part of Figure 8.11. However, this does not appear to have made a major impact on the arrangement of secondary structures or ribs. Furthermore, the distributions of u' in Figure 8.18a (left) and ω_x^+ in Figure 8.18b (left) indicated that the alignment of secondary vortices follow a similar trend to that described for Figure 8.17a (left) and ω_x^+ in Figure 8.17b (left). This provides qualitative evidence that counter-rotating rib pairs, along the spanwise direction, enclose and wrap each vortex couple. This topology will be further described using a skeleton model in Section 8.3.5.

Deng and Caulfield (2015b) and Deng et al. (2015) found two different estimates for λ_z that correspond to the Short and Long wavelength modes described earlier in this section. The Long wavelength mode was characterized by $\lambda_z = 1$, whereas the Short mode was characterized by $\lambda_z = 0.21$ (Deng and Caulfield, 2015b). The Mode A and Mode B predicted by Sun et al. (2018)

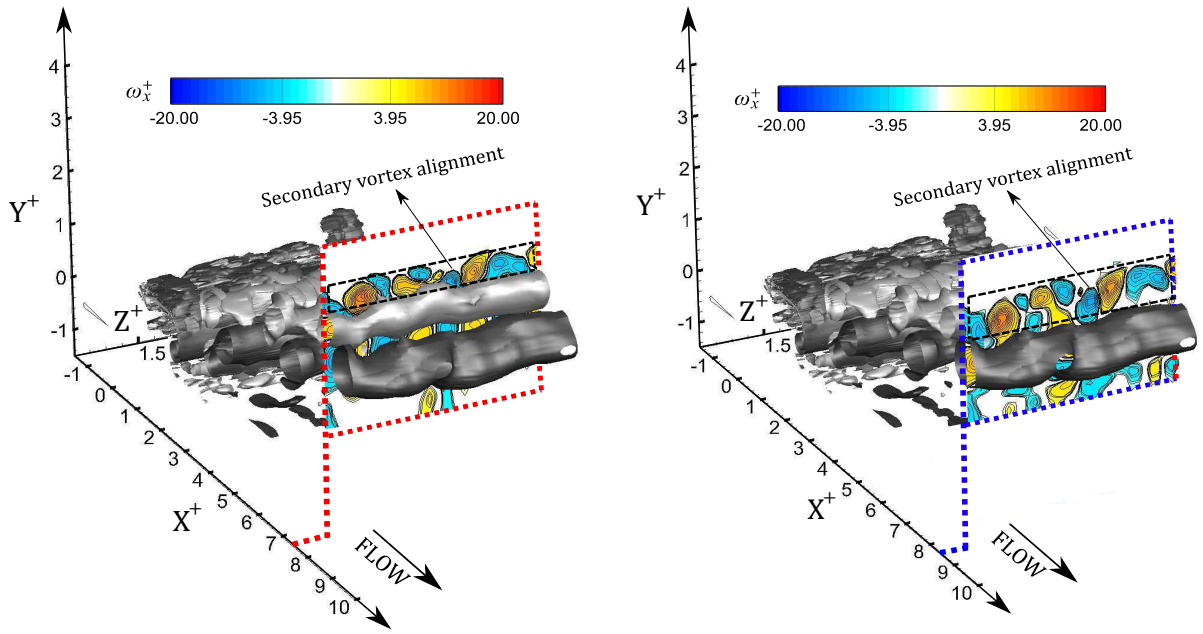

Figure 8.20: Iso-surface of ω_z^+ with the alignment of streamwise vortex pairs shown on $yz-$plane at (a) $X^+ = 7.4$ and (b) $X^+ = 8.4$.

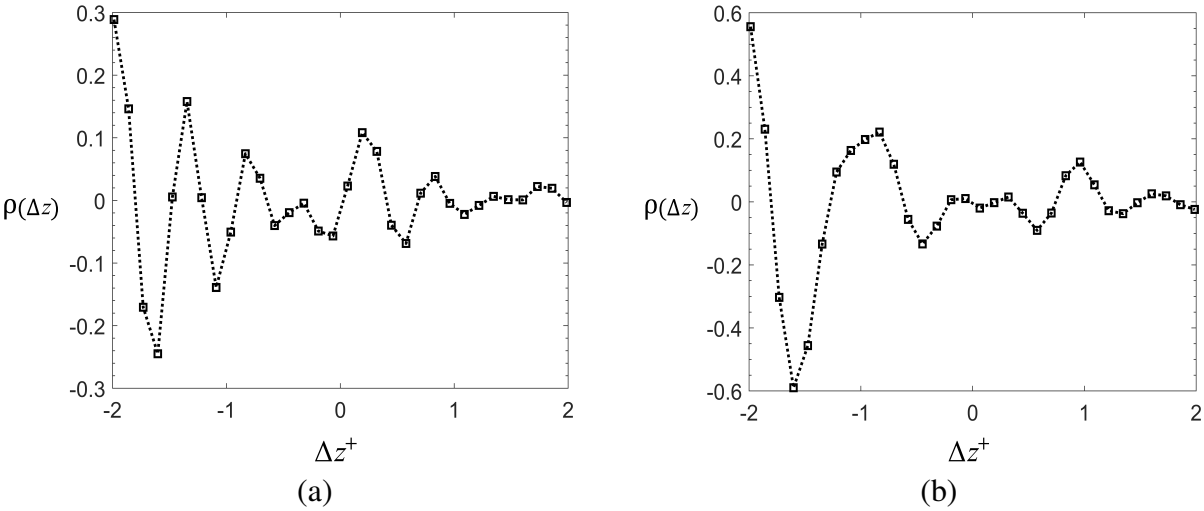

Figure 8.21: Variation of $\rho(\Delta z)$ with respect to normalized spanwise shift (Δz^+) based on cross-correlations of ω_x^+ between (a) Full and (b) Half shedding cycles for SIM2.

for a heaving foil also had a $\lambda_z = 1.05$ and 0.196, respectively. The spatial auto-correlation of ω_x^+ is presented in Figure 8.19a, which corresponds to $\lambda_z = 0.72$, similar to the value estimated for SIM1. Moreover, λ_z falls within the range of $\lambda_z = 0.7h - 0.8h$ for Mode B that was estimated for BTE cylinder by Gibeau et al. (2018). It also resembles the predicted Long-Wavelength-Mode and Mode A ($\lambda_z = 1c$) for pitching and heaving foils, respectively, that was characterized by Deng and Caulfield (2015b) and Sun et al. (2018). Investigation into the ratio of spanwise wavelength of counter-rotating rib-pairs to the d_{inv} revealed a value close to 1.813. This suggests a core instability mechanism, which was also discussed earlier for SIM1. However, the discussion presented for the identified horseshoe and hairpin structures in previous section, linked their interaction with the pre-existing vorticity in the braid region. This interaction is now evident in the form of matured secondary vortices observed between two vortex couples, which therefore indicates an instability feature of the braid region. The asymmetric streamwise spatial development of ribs in Figures 8.17b and 8.18b further hint at a need for a vortex skeleton model that provides a complete topological structure for the wake.

We further investigate λ_z at different locations in mid wake (e.g., $X^+ = 7.4$ and 8.4). This enables analyzing the consistency in characteristics of coherent streamwise structures. As apparent from Figure 8.20b, the wavelength in the wake changes from $\lambda_z = 0.7$ to 0.75 as you move closer to $X^+ = 8$. The corresponding iso-contour of ω_x^+ in Figure 8.20 also identify that the alignment of rib pairs do not change significantly in mid wake. The temporal periodicity for the ribs is further assessed using cross-correlation of ω_x^+ between two consecutive full and half shedding cycles. The variation of $\rho(z)$ in Figures 8.21a and 8.21b show that the ribs maintain their spanwise periodicity with respect to shedding cycles, and their periodic characteristics remains similar to that observed for SIM1.

8.3.5 Vortex skeleton models for high propulsive performance regimes

The simplified vortex skeleton model representing all observations outlined thus far is presented in Figure 8.22a for SIM1, which coincides with highly efficient propulsive performance of an

oscillating foil. Similarly, the simplified model of the wake for SIM2 is presented in Figure 8.22b, which coincides with large thrust generation for an oscillating foil with combined heaving and pitching motion. These schematics depict the overall spatio-temporal arrangements for primary (rollers) and secondary (ribs) vortex structures based on the quantitative and qualitative analysis presented in previous sections. Each model represents the wake region from $2c$ downstream of the trailing edge of the foil to $\approx 7c$, where the dominant three-dimensional characteristics were observed in the flow. For SIM1, the initial $2P^T$ wake mode comprised of rollers in the form of pairs. The weaker vortices of a pair interacts with the stronger structure with similar vorticity-sign of the neighboring pair, and they eventually merge to form an inverse Von-Kàrmàn, or 2S, wake configuration. The counter-rotating streamwise vortices or ribs are observed to pass over the rollers while maintaining their direction of rotation with successive shedding cycles. The model also shows the pairing of counter-rotating ribs in the spanwise direction. Despite the transition of the wake from 2P to 2S mode for rollers, the paired ribs do not get affected in terms of their spatio-temporal characteristics.

For the asymmetric wake of SIM2, the rollers advect downstream in the form of vortex couples and they do not show dominant interaction or merger between them. The rib configuration depicts a different topology compared to SIM1, wherein the secondary vortex pairs wrap around the couple to form a vortex loop. The conjoint horseshoe vortex dislocations (in Figures 8.10 and 8.11) and their subsequent elongations lead to the formation of these vortex loops, which enclose the roller couples. This mechanism in combination with the large axial straining within the braid region of consecutive vortex couples could explain the peculiar rib topology observed in the wake. The rib pairs align along the spanwise direction and maintain their circulation as they move downstream.

8.4 Summary

The evolution of coherent structures and vortex arrangements were examined numerically in the wake at $Re = 8000$ and $St = 0.21 - 0.94$. Two extreme performance settings were observed at low

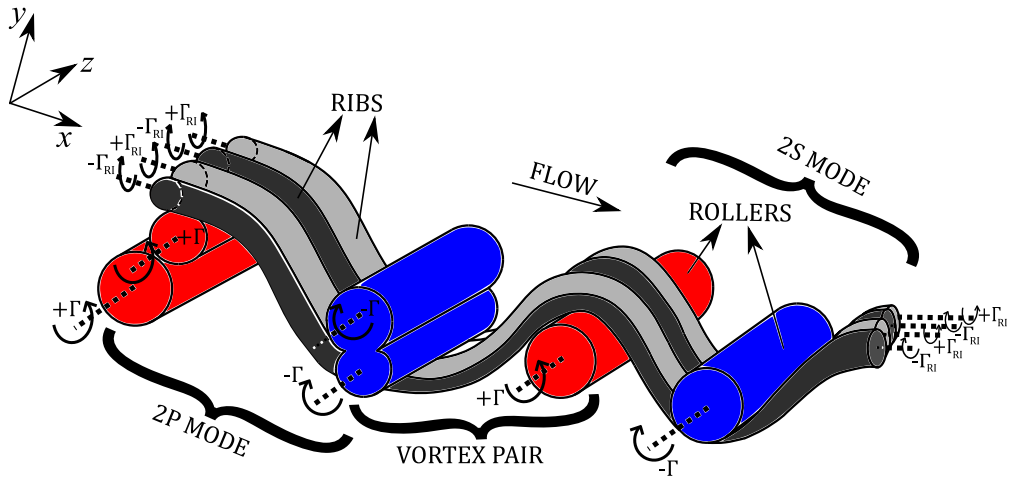

(a)

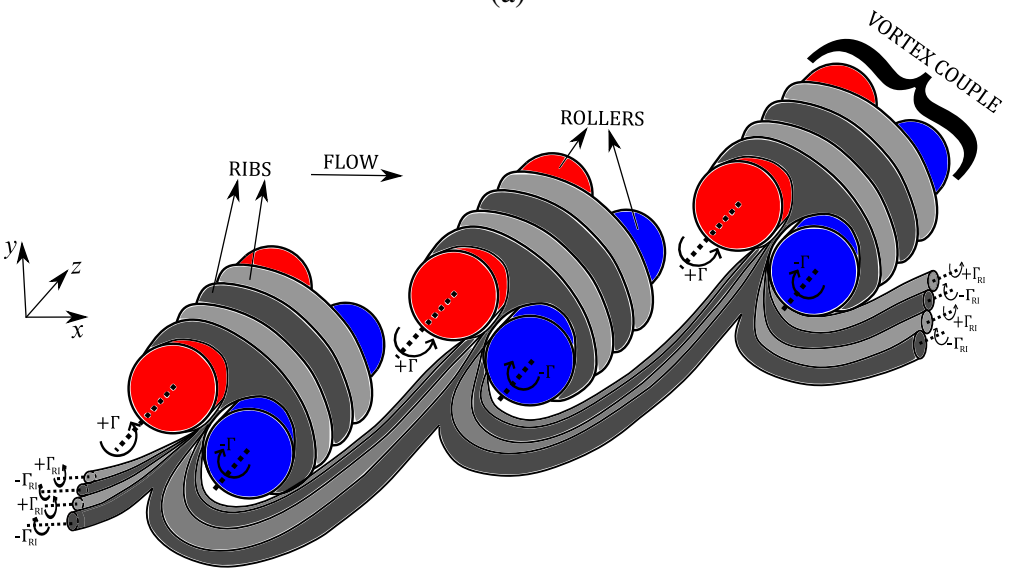

(b)

Figure 8.22: Vortex skeleton models for (a) SIM1 and (b) SIM2. $+\Gamma$ and $-\Gamma$ denote the circulation for counter-clockwise and clockwise rollers, respectively. $+\Gamma_{RI}$ and $-\Gamma_{RI}$ denote the circulation for counter-clockwise and clockwise ribs, respectively.

and high St. The foil exhibited high efficiency and small thrust generation at low St, or SIM1. Contrarily, larger thrust generation was observed at high St (SIM2), which coincided with a lower propulsive efficiency. These performance characteristics agreed well with experimental findings of Van Buren et al. (2019), which motivated a detailed study of the wake to identify any major alterations that coincide with such performance variations.

The higher efficiency wake ($2P^T$) in SIM1 coincided with coalescence and interaction of vortex structures in neighboring pairs. Vortices that formed a pair (2P mode) possessed different magnitudes of circulation. This supported our hypothesis that weaker LEVs merge with stronger TEVs of the neighboring pair, thereby promoting transition of the wake to 2S or inverse Von Kàrmàn mode. However, the phenomenon of merger of co-rotating vortices did not show any major consequence on the characteristics of instability where the spanwise corrugations developed on account of strengthening strain field, as the co-rotating vortices approached one another. The increase in the separation distance of counter-rotating vortices of a pair was further prominent due to vortex coalescence (or merger) observed for 2P pairs. Near the foil, the apparent straining exerted by counter-rotating LEVs, which formed on the opposite side, eventually bent the elongated legs of TEVs. This resulted in downstream pointed pairs, which themselves formed a thrust producing momentum jet near the foil trailing edge. Pressure distribution along the suction and pressure surface of the foil further showed imminent spanwise instability features on leading edge rollers, whose ratio of spanwise wavelength (λ_z) and chord length (c) depicted a value close to 0.98, as they approached the developing trailing edge structures. This further showed resemblance to elliptic instability of counter-rotating vortex pair whose mechanism and description was described previously by Dizès and Laporte (2002); Ortega et al. (2003).

The high-efficiency wake of SIM1 did not incorporate any hairpin vortex formations, contrary to the wake of stationary cylinders. Moreover, the wake exhibited spanwise dislocations, which possessed different spatial characteristics with respect to temporal evolution of primary vortex rollers. Particularly, there existed valleys and bulges in the spanwise direction on the weaker LEV rollers that interacted and merged with the stronger TEV rollers. The depth-to-spanwise-width-

ratio of these corrugation-type dislocations on LEVs was further dependent on the circulation of their neighboring TEVs, such that TEVs with larger circulation led to a relatively larger ratio. The estimated ratio of spanwise wavelength to chord length revealed a value of 0.8, which again hinted at a dominant elliptic instability of primary vortices, similar to that observed for $LEVs$. The tongue like formations on shed $LEVs$ further provided evidence for the instability features, although theoretical analysis in terms of Floquet modes are still needed to confirm these findings. Statistical correlation techniques combined with qualitative examination of the wake revealed that secondary vortex arrangements resemble the Long-Wavelength-Mode and Mode-A for pitching and heaving foils, respectively, and Mode B for stationary circular and BTE cylinders. The presence of $2P^T$ mode in the wake did not significantly alter the secondary vortex arrangements, such that they retained their continuity. A new vortex skeleton model was introduced that detail salient features of the spatial wake topology for the high efficiency wake of oscillating foils with combined pitching and heaving motion.

The larger-thrust-generating wake of SIM2 resembled an asymmetric configuration, which was dominated by shedding of vortex couples that possessed a similar magnitude of circulation, and no mutual interactions. The asymmetry mode observed was in line with Mode-2 and Mode-A observed in studies of heaving foils. However, the variation of separation distance between the coupled vortices of a dipole, with the advective time, exhibited a decrease in the first half oscillation period as the induced velocity overcomes the opposing centrifugal forces and viscous diffusion, while bring the counter-rotating vortices closer. The higher negative straining due to close proximity of coupled vortices coincided with a decrease in their radii. This stronger strain field also coincided with the appearance of large scale dislocations on the coupled vortex structures. The corresponding pressure distribution revealed similar spanwise instability features on leading edge rollers as those shown for SIM1. However, it was speculated that the stronger vortex$-$foil interactions near the leading edge led to the early development of long wavelength spanwise undulation with $\lambda_z/d_{inv} \approx 3.5$ or $\lambda_z/c \approx 1.4$.

Investigating the wake three-dimensional features for the large thrust generating wake of SIM2 also revealed similar dislocations and instability features in the spanwise direction compared to SIM1. The ratio of spanwise wavelength to diameter of the invariant streamtube was observed to be approximately 1.813. However, the wake for the former was dominated by hairpin vortex structures, which further contributed to strongly deformed TEV rollers. The legs of conjoint hairpin-horseshoe vortices, which emanated from the primary vortex cores, wrapped around each vortex couple. Hence, they provided a distinct dislocation feature for the asymmetric wake. The interaction of these conjoint hairpin-horseshoe structures with the braid vorticity region further hinted at a braid instability mechanism that also contributed to the formation of secondary structures in SIM2. Statistical correlation techniques provided an estimated spanwise wavelength (λ_z) in range of $0.7c$ to $0.75c$, similar to SIM1. The temporal periodicity assessment also revealed that ribs maintained their direction of circulation during the shedding cycles. The secondary vortex arrangements resembled those of Mode B for cylinders and Long Wavelength Mode for pitching foils. The asymmetric topology of the wrapped *rib* pairs around dipoles also indicated an influence of the large scale dislocations observed for the wake in large thrust generation configuration. However, these dislocations did not affect the spanwise wavelength or temporal periodicity of *rib* pairs in both propulsive wakes. A novel skeleton model was introduced that incorporated a continuous rib profile, where the ribs wrapped around each primary vortex couple up to at least three consecutive oscillation cycles.

The current chapter discussed the qualitative and quantitative evidence for the onset of elliptic instability (Leweke et al., 2016). However, the association of the instability features such as undulations of LEV filaments over the foil boundary, and the presence of secondary vortex structures in the wake, is not entirely clear. Chapter 9, therefore, evaluates the mechanisms that could interlink the growth of spanwise instability and the secondary vortex as LEV and TEV structures shed from the foil.

Chapter 9

IMPLICATIONS OF SPANWISE WAKE INSTABILITY ON THE FORMATION OF SECONDARY WAKE STRUCTURES[†]

9.1 Introduction

The mechanisms of formation, evolution and early dismantlement of straight vortical filaments, especially in the wake of aircrafts and submarines, are greatly important for minimizing wake hazards and noise propagation (Leweke and Williamson, 1998; Dizès and Laporte, 2002; Ortega et al., 2003; Meunier and Leweke, 2005). Jacquin et al. (2003) briefly outlined the critical role of increasing turbulence and promotion of the cooperative instability, in terms of an increased radius for a system of vortices, that contributed to a decreased rolling moment on the aircraft. Characterization of instabilities on wake structures have further gained motivation in terms of their association with the propulsive performance of natural bird flights and swimming mammals (Deng and Caulfield, 2015b; Deng et al., 2016; Sun et al., 2018). Section 8.3 also provided details on the

[†]The content of this chapter has been published in whole or part, in *Proceedings of the twelfth International Symposium on Turbulence and Shear Flow Phenomena (TSFP12)* under the citation: "Verma, S., Hemmati, A. (2022). Implications of spanwise wake instability on formation of secondary structures behind oscillating foils.*TSFP12* 1-6."

dominant elliptic instability and dislocation characteristics on rollers that contributed towards high performance wakes. This chapter further expands on the present understanding of the association between vortex instability characteristics and three-dimensionality in turbulent wakes of oscillating rigid foils. Since the foil kinematics closely mimic the motion of biological propulsors (e.g., insect wings, bird wings, and fish tail fins) and robotic maneuvering systems in underwater applications, the understanding gained here will present unique insights for advancement of highly efficient micro-aerial vehicles and marine robotic swimmers.

Extensive investigations done on the wake of stationary bluff bodies, such as circular cylinders, square cylinders, bluff elongated trailing edge airfoils revealed the presence of primary and secondary instabilities that were associated with either outflux of core vorticity or the straining of braid shear layer (Mittal and Balachandar, 1995; Zhang et al., 1995; Williamson, 1996; Brede et al., 1996; Robichaux et al., 1999; Ryan et al., 2005; Gibeau et al., 2018). The details regarding these topics were provided in Section 2.5. While some studies have conducted assessments on oscillating foils mimicking kinematics of bird wings and fish tail fins (Deng and Caulfield, 2015b; Sun et al., 2018; Chiereghin et al., 2020), the association of spanwise instabilities and turbulence in the wake, however, needs a more detailed investigation. Quantitative estimations of spanwise instability wavelengths for several modes in the wake of purely pitching or heaving foils, have been made. These include 'long' and 'short' wavelength modes for purely pitching foils (Deng and Caulfield, 2015b; Deng et al., 2015). Sun et al. (2018) characterized the instability modes A, B, QP and S, for purely heaving foils. More information and characteristics of these modes are highlighted in Section 2.5. However, extensive characterization of the instability features were mostly concerned with deflected wake topology. The qualitative insights into the presence or evolution of spatial dislocations, and their association with the leading edge vortex (LEV) dynamics in particular, was also limited. The observations discussed in Chapters 8 presented detailed quantitative and qualitative evidence for the possible association of spanwise undulation of $LEVs$ to the elliptic instability of vortex pair for foils that executed coupled pitching and heaving kinematics. It also discussed the spanwise dislocation features and the formation of conjoint hairpin-horseshoe

structure for different wake topologies. These provided unique insights into the association of spanwise instability and growth of streamwise vortical structures in the wake of oscillating foils.

In this chapter, we particularly expand on the implications of characteristic spanwise instability of the leading edge vortex on the formation and evolution of secondary wake structures for foils. The observations will provide fundamental insights and hints with regards to the association of *LEV* dynamics and growth of secondary structures in the wake. We discuss the effects of increasing ϕ between the heaving and pitching, on the evolution of *LEV* instability and secondary wake structures that has not been assessed for oscillating foils. The problem setup closely follows that of Chapters 8, although some details are briefly highlighted in Section 9.2. This followed by assessment of major observations in the Results & Discussion (Section 9.3). A brief summary of important findings is presented in Section 9.4.

9.2 Problem Description

Three-dimensional wake evolution of an oscillating hydrofoil is assessed by solving the Navier-Stokes equations directly at $Re = 8000$. The infinite span of the oscillating teardrop foil preserves the developing spanwise instability on primary vortex (*rollers*) and secondary structures (*ribs*) in the wake (Mittal and Balachandar, 1995). The oscillation frequency can be expressed in terms of the St_c, which varied as $0.32 \leq St_c \leq 0.64$. This corresponds to an St_A in the range of $0.2 \leq St_A \leq 0.8$, which further coincide with highly propulsive wakes observed for foils in coupled motion at a similar range of St_A (Schnipper et al., 2009). The ϕ was varied in the range of $90^\circ \leq \phi \leq 270^\circ$, which ensured a heave dominated kinematics, and thereby allowing *LEVs* to develop and advect along the foil boundary. Contrarily, pitch dominated kinematics coincided with either a weak *LEV* formation or their apparent disintegration during an early stage of the oscillation cycle (see Section 8.3). Here, the results are limited to the case of $St_c = 0.32$ to mainly detail the changes in evolution of instability and secondary structures at increasing ϕ. For details on computational

domain, boundary and initial conditions, verification and validation studies, the readers are referred to Sections 3.4, 3.5 and 3.6.

9.3 Results and Discussion

The time evolution and advection of the leading edge vortex structures are initially evaluated in an oscillation cycle for kinematics corresponding to $\phi = 90^\circ$ and $St_c = 0.32$. The origination of spanwise undulations and its links to instability mechanisms are qualitatively evaluated, along with their implications on growth of secondary streamwise structures. The quantified λ_z of paired *rib* filaments is estimated using autocorrelation of ω_x at increasing streamwise distance, which will highlight their growth and rearrangement process. The effects of increasing ϕ from 90° to 270° is then evaluated qualitatively, primarily depicting the delay and a gradual disappearance of secondary structures.

Figures 9.1a-9.1e depict the formation and advection of *LEV rollers* at successive quarter phases of one oscillation cycle, that are visualized using λ_2 criterion. λ_2 is further normalized with respect to U_∞ and c ($\lambda_2^+ = \lambda c^2/U_\infty^2$). This method had been proven effective and accurate to extract vortex cores (Jeong and Hussain, 1995). At $t = 0$, the anti-clockwise roller $LEV1_{ac}$ is formed near the leading edge of the foil with no visible spanwise undulation. At $t = T/4$ in Figure 9.1b, however, $LEV1_{ac}$ depicts a low amplitude spanwise undulation. We further notice a counter-rotating secondary *roller* ($LEV1_c^s$) that forms on account of the vorticity outflux resulting from the mutual interaction of $LEV1_{ac}$ and the foil boundary. It is reasonable to speculate that the presence of two counter-rotating *rollers* will initiate an elliptic instability mechanism featuring the spanwise undulations observed on $LEV1_{ac}$ (Leweke et al., 2016).

As $LEV1_{ac}$ and the paired secondary vortex ($LEV1_c^s$) approach the trailing edge at $t = T/2$, it is apparent that a few paired streamwise vortex filaments start to grow. The amplitude of undulation on *rollers* also appears enhanced, which coincides with the appearance of paired *rib* filaments. It is important to mention here that the origin of *rib* filaments appears associated with the developing

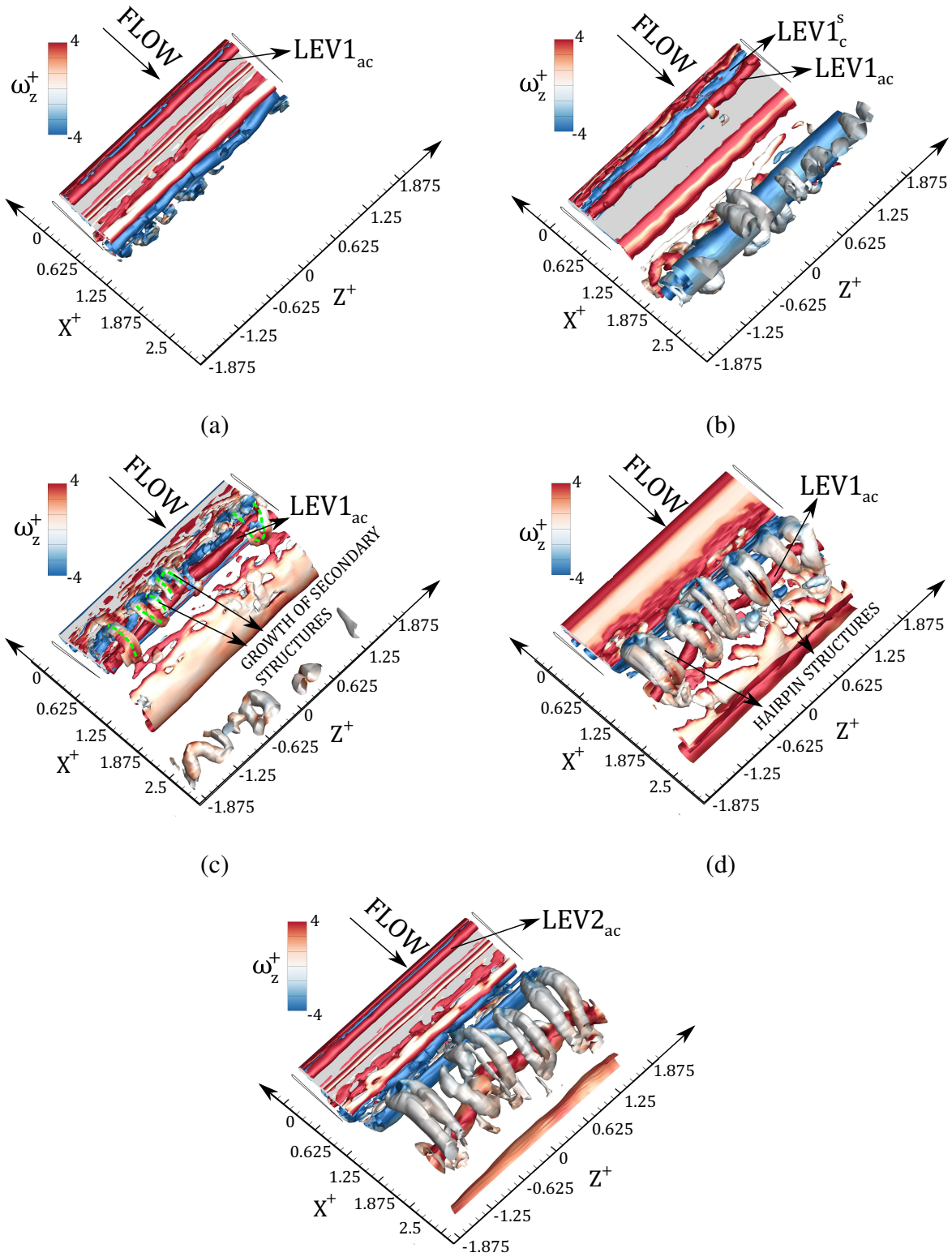

Figure 9.1: Time evolution of *LEVs* for $\phi = 90^\circ$ at (a) $t = 0$, (b) $t = T/4$, (c) $t = T/2$, (d) $t = 3T/4$ and (e) $t = T$. The vortical structures are identified using iso-surfaces of $\lambda_2^+ = \lambda_2 c^2/U_\infty^2$ = -0.032, colored with spanwise vorticity ($|\omega_z^+| = \omega_z c/U_\infty = 4$).

elliptic instability feature on $LEV1_{ac}$ and $LEV1_c^s$. As the weaker $LEV1_c^s$ experiences straining in the presence of the stronger $LEV1_{ac}$, a core vorticity outflux occurs from $LEV1_c^s$. This grows to form *rib* filament pairs along the spanwise direction. At $t = 3T/4$, a more vivid alignment of stronger hairpin structures is observed, which coincides with large amplitude undulations of $LEV1_{ac}$. $LEV1_c^s$ eventually loses its coherence on account of the consistent vorticity outflux and straining due to elongation of secondary hairpin structures. The hairpin legs further elongate in the streamwise direction at $t = T$, which eventually result in paired *rib* alignment along the spanwise direction.

Formation of the secondary roller (i.e. $LEV1_c^s$) and its interaction within the neighborhood of primary $LEVs$ (i.e., $LEV1_{ac}$) is also captured using contours of coefficient of pressure, $C_{pr} = P/(0.5\rho U_\infty^2)$. This is presented on the pressure side of the foil in Figures 9.2a and 9.2b. The low magnitude pressure signature for weaker secondary $LEV1_c^s$ is observed alongside a stronger pressure dominated region that highlights $LEV1_{ac}$ at $t = T/4$ (Figure 9.2a). Faint undulations of both primary and secondary rollers are also visible, which indicate the onset of elliptic instability for the vortex pair. At $t = T/2$, the diffused secondary $LEV1_c^s$ is captured on account of its core vorticity outflux, thus forming the *rib* filaments shown in Figure 9.1c. While the primary $LEV1_{ac}$ shed at $t = T/2$, the instability feature is amplified compared to the undulations captured at $t = T/4$.

We now estimate the spanwise wavelength (λ_z) for the *rib* filaments at increasing streamwise distance (i.e. $x^+ = 0.875$, 1.75 and 2.5) to highlight the evolution features of secondary structures in the wake. Autocorrelation of streamwise vorticity ($\omega_x^+ = \omega c/U_\infty$) on specific spanwise slices is used to estimate λ_z, following Section 8.3 of Chapter 8.

Figure 9.3(a) depicts the variation of $C(\Delta z)$ for spanwise slices at $x^+ = 0.875$, 1.75 and 2.5, respectively. The estimated λ_z will correspond to twice the distance of first minimum observed for $C(\Delta z)$ in Figure 9.3a (see Section 8.3 of Chapter 8). At $X^+ = 0.875$, λ_z is close to $0.86c$ which then decreases to $0.71c$ and $0.57c$ at $X^+ = 1.75$ and 2.5, respectively. The qualitative visualization of the counter-rotating hairpin legs and the spanwise slice at $X^+ = 0.875$, 1.75 and 2.5, respectively,

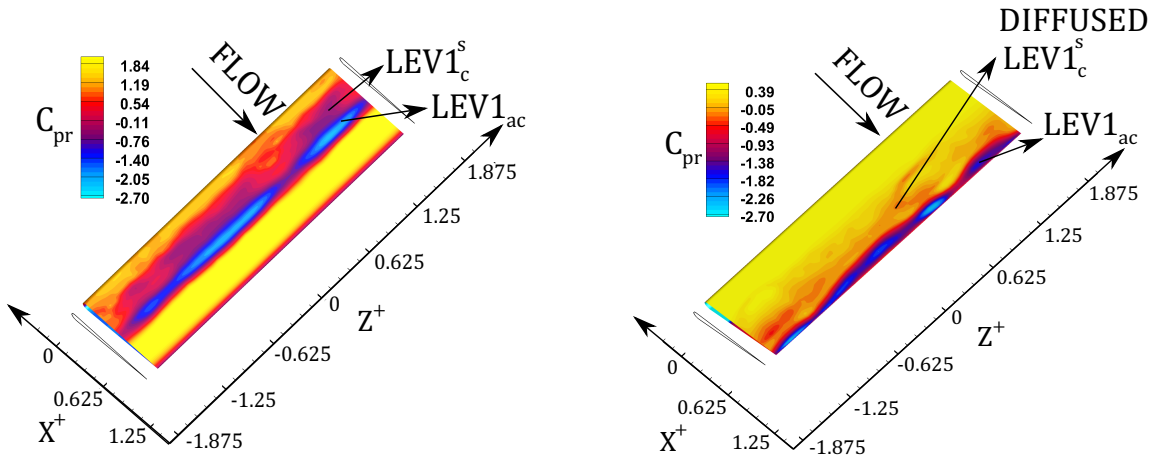

(a) (b)

Figure 9.2: Surface pressure (C_{pr}) distribution on foil for $\phi = 90^\circ$ at (a) $t = T/4$ and (b) $T/2$.

are also shown in Figure 9.3b. The counter-rotating ω_x^+ pairs at $X^+ = 0.875$ appear to be in their early stages of spatio-temporal development while the core vorticity outflux occurs via mechanism of elliptic instability (Leweke and Williamson, 1998). At $X^+ = 1.75$ and 2.5, the ω_x^+ pairs become more symmetric and developed compared to those observed at $X^+ = 0.875$, while supporting the smaller λ_z observed in Figure 9.3a. The decreasing λ_z with increasing X^+ can therefore be linked to the rearrangement mechanism for the evolving hairpin legs, which depends on the action of continuous straining within the braid vorticity region between two successive *rollers*. Qualitative observations in Figure 9.1c further provide a vivid indication that the newly formed hairpin legs continuously feed upon the core vorticity outflux from the secondary *LEV roller* ($LEV1_c^s$) before attaining a strong coherence at some distance downstream of the trailing edge.

The onset of elliptic spanwise instability on *LEVs* and its association with the growth of secondary hairpin structures at $\phi = 90^\circ$ provided unique insights into the wake three-dimensionality behind oscillating foils. We now evaluate the effects of increasing ϕ on the spanwise instability features and the associated growth of secondary structures. Figure 9.4 depicts the evolution of *LEV rollers*, spanwise undulations and growth of secondary hairpin structures for the cases corresponding to $\phi = 180^\circ$, 225° and 270°, respectively. The instantaneous snapshots of wake evolution are shown at each quarter phase of one oscillation cycle (i.e. from $t = T/4$ to $t = T$). At

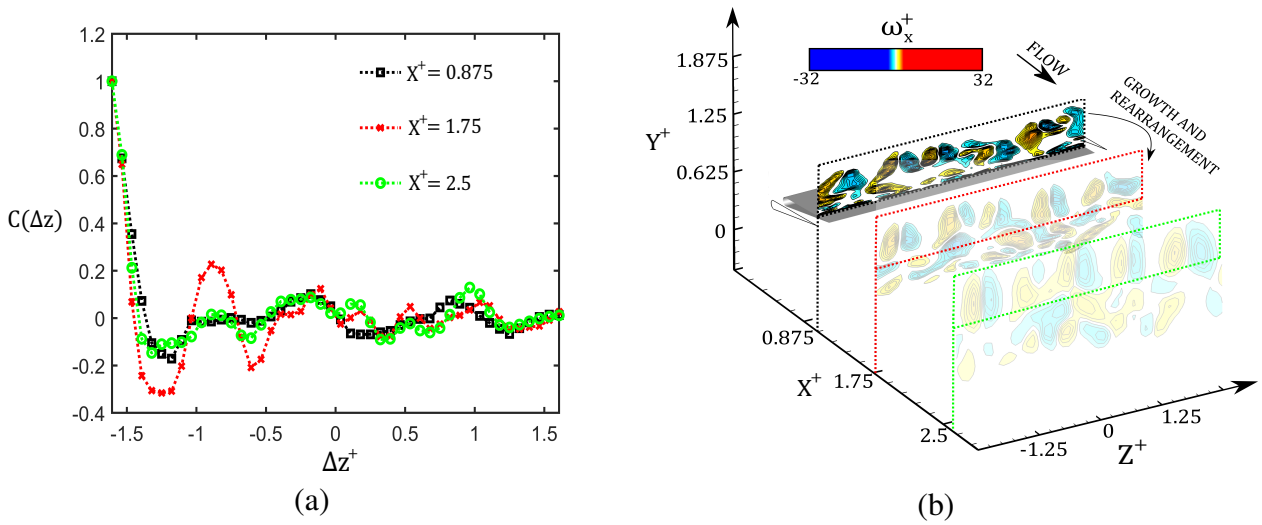

Figure 9.3: (a) Variation of $C(\Delta z)$ with $\Delta z^+ = \Delta z/c$ and (b) Depiction of ω_x^+ pairs on spanwise slices at increasing X^+. Here, decreasing opacity of *rib* pairs ensures a complete streamwise and spanwise views in the wake.

$\phi = 180°$ (Figures 9.4a, 9.4d, 9.4g and 9.4j), we observe a primary $LEV3_{ac}$ along with remnants of a disintegrated secondary LEV neighboring $LEV3_{ac}$. We also observe a tertiary $LEV3_{ac}^T$ that remains in close vicinity of $LEV3_{ac}$. This tertiary LEV did not appear to have a coherent presence at $\phi = 90°$ (Figure 9.1). At $t = T/2$ (Figure 9.4d), we now observe a secondary $LEV3_c^s$ which forms on account of the combined vorticity outflux of $LEV3_{ac}$ and $LEV3_{ac}^T$. The spanwise undulations on $LEVs$ also become evident at $t = T/2$, while mutual straining of $LEV3_c^s$ from $LEV3_{ac}$ and $LEV3_{ac}^T$, leads to core vorticity outflux and subsequent growth of small hairpin legs observed at $t = 3T/4$ (Figure 9.4g). These small *rib*-like formations evolve further downstream and form strong coherent hairpin structures at $t = T$ (Figure 9.4j). In comparison to the growing secondary structures at $\phi = 90°$, which became evident at an earlier streamwise distance and advective time ($t = T/2$ in Figure 9.1(c)), a delayed growth of secondary structures is quite clear for the case of $\phi = 180°$. This delay is attributed to an early disintegration and regeneration of the secondary *roller* (i.e. $LEV3_c^s$) noticed for $\phi = 180°$ at $t = T/4$ and $t = T/2$, respectively.

At $\phi = 225°$, Figure 9.4b depicts a peculiar series formation of primary ($LEV4_{ac}$), secondary ($LEV4_c^s$) and tertiary ($LEV4_{ac}^T$) $LEVs$ at $t = T/4$. Besides a localized inception of an instability feature at $t = T/2$ (Figure 9.4e), an initial disintegration of secondary $LEV4_c^s$ is not apparent here.

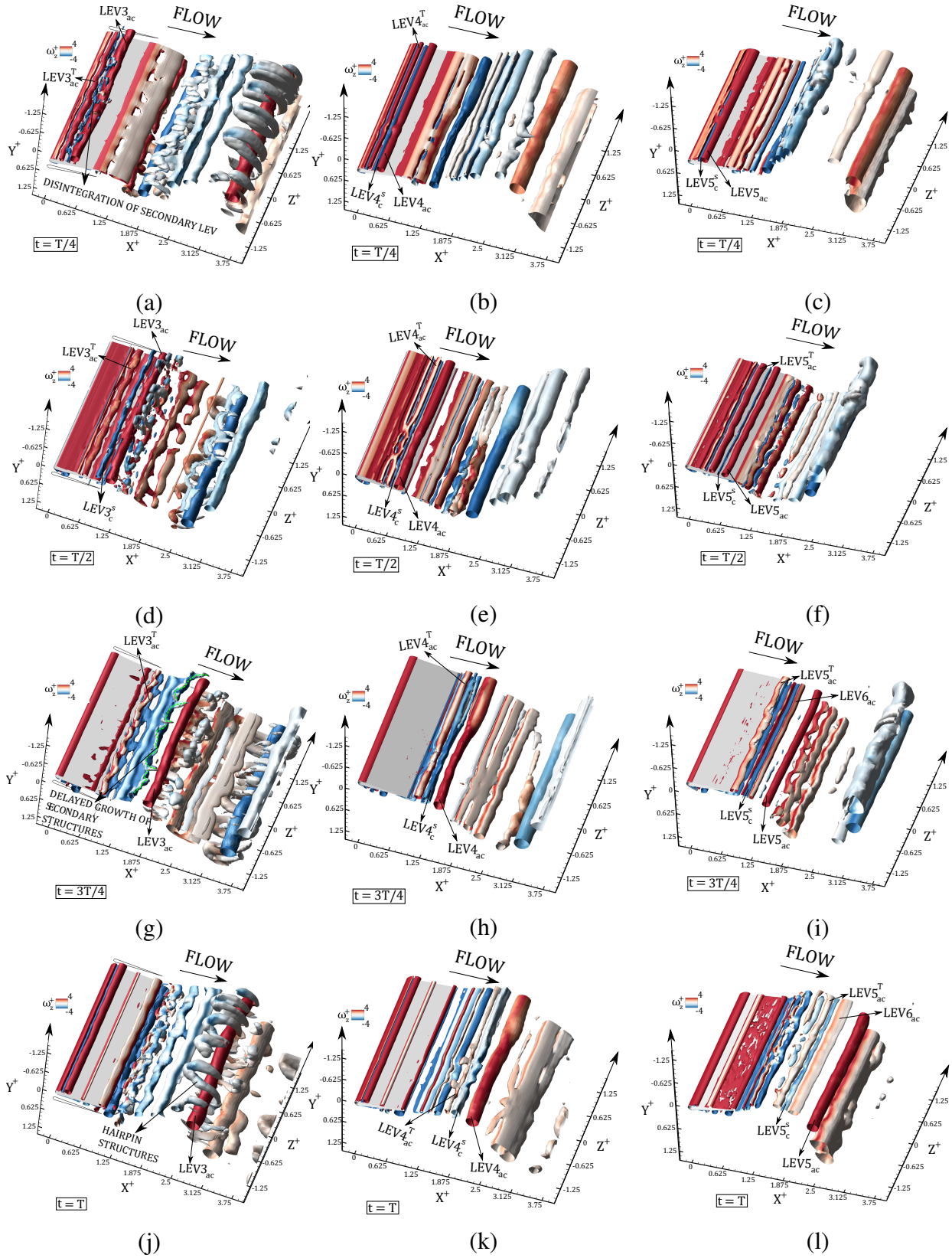

Figure 9.4: Iso-surfaces of $\lambda_2^+ =$ -0.032 criterion colored with $|\omega_z^+| = 4$, for $\phi = 180^\circ$ (a,d,g,j), 225° (b,e,h,k) and 270° (c,f,i,l). The instantaneous snapshots correspond to $t = T/4$, $T/2$, $3T/4$, T, respectively.

At $t = 3T/4$ (Figure 9.4h), while $LEV4_{ac}$, $LEV4_c^s$ and $LEV4_{ac}^T$ shed from the trailing edge of the foil, there seems to be no evident growth of secondary structures. This absence also remains persistent at $t = T$ (Figure 9.4k). We further observe a similar evolution process of $LEVs$ at $\phi = 270°$ (Figures 9.4c, 9.4f, 9.4i, and 9.4l)). A series formation of counter-rotating $LEVs$ ($LEV5_{ac}$, $LEV5_c^s$ and $LEV5_{ac}^T$) is observed at $t = T/2$ (Figure 9.4f), which evolve and shed in the wake at subsequent phases of the oscillation cycle. Although spanwise instability features remain dominant on $LEVs$, the growth of secondary structures is entirely absent for $\phi = 270°$ as well. We speculate that an inherent dependence between the circulation strength of *rollers* and the growth of secondary structures must hold. Wherein, the former plausibly decreases with increasing ϕ, which thereby lower the intensity of straining in the braid shear layer. The quantitative measurements are currently underway and will be presented in upcoming studies. Overall, there is vivid evidence that the association of spanwise instability features and growth of secondary structures is most dominant at $\phi = 90°$, while it successively fades away with increasing ϕ to 270°.

9.4 Summary

Three-dimensional wake assessments were described at $St_c = 0.32$ and $Re = 8000$, while ϕ varied in the range of 90° to 270°. The spatio-temporal wake evolution revealed an association of elliptic spanwise instability characteristics on primary, secondary and tertiary $LEVs$ that formed over the foil boundary, and the growth of paired secondary streamwise structures in the form of hairpin vortices. These hairpin structures are the result of core vorticity outflux, particularly from the secondary LEV, via a mechanism detailed previously by Mittal and Balachandar (1995). The concerned association was strongly dominant at $\phi = 90°$ where the secondary LEV, located in close vicinity of the primary LEV, encountered strong straining on account of the existing spanwise instability. However, the dominant association faded away as ϕ increased above 90°. At $\phi = 180°$, the LEV evolution depicted a disintegration and re-emergence of the secondary LEV, which coincided with a delay in the growth of secondary hairpin structures with respect to advective time.

Further increase in ϕ towards 225° and 270° showed a complete absence of secondary structures despite the presence and inception of spanwise instability features on *rollers*. Possibly, an increasing ϕ from 90° to 270° promotes a weaker *LEV* formation (e.g., circulation strength), which leads to an insufficient core vorticity outflux necessary for the growth of secondary structures. Quantitative assessment of the circulation of *LEV* is presented later in Chapter 11, which supports the qualitative observations presented here. Chapter 11 further presents investigation into effects of St_c at $\phi = 90°$ on the evolution mechanisms of secondary wake structures, such that a universal perspective is developed on the association of kinematics and 3D wake evolution of oscillating foils.

Chapter 10

INFLUENCE OF REDUCED FREQUENCY ON EVOLUTION OF SECONDARY WAKE STRUCTURES[†]

10.1 Introduction

Unsteady dynamics of *LEV*s can have considerable influence on the operation of bio-inspired robotic swimmers and micro UAVs (Mueller and DeLaurier, 2003). As outlined in Chapter 9, the spanwise instability of the *LEV* promotes the growth of secondary vortex structures that eventually lead to wake three-dimensionality. The understanding of mechanisms that explain the spatio-temporal dynamics of such instabilities is important since they can directly influence the force and rolling moments generated on the lifting surface of, for example, wings (Son et al., 2022). Instability characterization also helps in establishing an association between the unsteady vortex dynamics and propulsive performance of swimming mammals (Deng and Caulfield, 2015b; Deng et al., 2016; Sun et al., 2018). However, influence of varying kinematics on the 2D wake topology

[†]The content of this chapter are under review, in *International Journal of Heat and Fluid Flow* under the citation: "Verma, S., Hemmati, A. (2023). Influence of reduced frequency on evolution of secondary wake structures of oscillating foils."

and propulsive performance was immense (see Chapter 4-7). Chapter 9 provided elaborate description for the evolution features of secondary instabilities and intermediate secondary structures, at $\phi = 90^{\circ}$ and $St_c = 0.32$. However, the effects of varying kinematics setting, in terms of St_c, was not discussed in detail. This chapter extends the findings of Chapter 9 by assessing the influence of varying St_c on the spanwise instability mechanisms and growth of secondary structures.

Details that are relevant to the instability and secondary structures associated with stationary and oscillating rigid bodies have been explained in Section 2.5. Results in Chapter 8 presented detailed quantitative and qualitative evidence for the possible association of spanwise undulation of $LEVs$ to the elliptic instability of vortex pair for foils with coupled pitching and heaving kinematics. It also discussed the spanwise dislocation features and the formation of conjoint hairpin-horseshoe structure for different wake topologies. The changes coincided with low and high reduced frequencies, where the former only depicted fine scale corrugations on the shed vortex structures while the latter showed large scale hairpin-horse shoe vortex structures in the wake. Calderon et al. (2013b,a) and Visbal et al. (2013) have further outlined the major implications of varying reduced frequency, on the aspects of LEV dynamics for low aspect ratio wings. Particularly, higher reduced frequencies result in the LEV undergoing large deformations into arch type vortex undulation (Calderon et al., 2013a). Son et al. (2022) recently evaluated LEV instabilities for a high aspect ratio wing, and an infinite span airfoil, in heaving oscillations. It was observed that at increasing reduced frequency, the strength of the primary LEV and TEV changed, which coincided with the changes in onset mechanisms of the instability. Here, we further elaborate on the features associated with secondary vortex structures that possess an association with reduced frequency.

In this chapter, the kinematic settings include a range of reduced frequency ($0.32 \leq St_c \leq 0.56$) while the phase offset is fixed at $\phi = 90^{\circ}$. The Reynolds number is $Re = 8000$. The mechanisms and characteristics of secondary hairpin structures have already been outlined at $St_c = 0.32$, within Chapter 9. Here, the discussion will be extended to higher St_c to mainly detail the changes in

evolution of instability and secondary structures at increasing St_c. The problem setup closely follows that of Chapters 8 and 9.

10.2 Results and Discussion

The mechanisms responsible for the onset of secondary vortex growth at increasing St_c from 0.32 to 0.56 are discussed qualitatively. Detailed investigation for the case of $St_c = 0.32$ was discussed in Chapter 9. However, a brief summary is still provided initially for a comparison with higher St_c cases. The evolution of spanwise undulations on primary LEV and its contribution towards secondary structures is further explored, which particularly highlights the existence of supplementary mechanisms at higher St_c. These also contribute towards the growth of secondary structures in the wake of oscillating foil.

10.2.1 $St_c = 0.32$

It was discussed in Chapter 9 that the growth of a secondary LEV roller leads to an elliptic type instability of the counter-rotating primary, and secondary, LEVs. The streamwise vorticity filaments emanated from the secondary LEV, which initially arranged in the spanwise configuration of nascent hairpin vortices. Under continuous strain fields, the legs of hairpins extended as the rollers shed in the wake, which ultimately led to the formation of rib pairs downstream of the foil trailing edge. Figures 10.1(a-c) depict the wake at three consecutive time instants in an oscillation cycle. Particularly, the focus is on the primary LEV ($LEV1_{ac}$ or $LEV1'_{ac}$ from previous oscillation cycle), as it simultaneously advects with other shed TEVs and secondary vortex structures. At $t^+ = 0.5$ and 0.75 in Figures 10.1(a) and 10.1(b), respectively, $LEV1_{ac}$ undergoes an increase in undulation amplitude just ahead of its separation, while the hairpin vortex legs grow and form rib pairs. R1′ demonstrates this configuration based on the evolution observed in the previous oscillation cycle. As the current cycle ends in Figure 10.1(c), $LEV1_{ac}$ does not show any substantial increase in its undulation amplitude. $LEV1'_{ac}$ further provides visible evidence that even at $X^+ >$

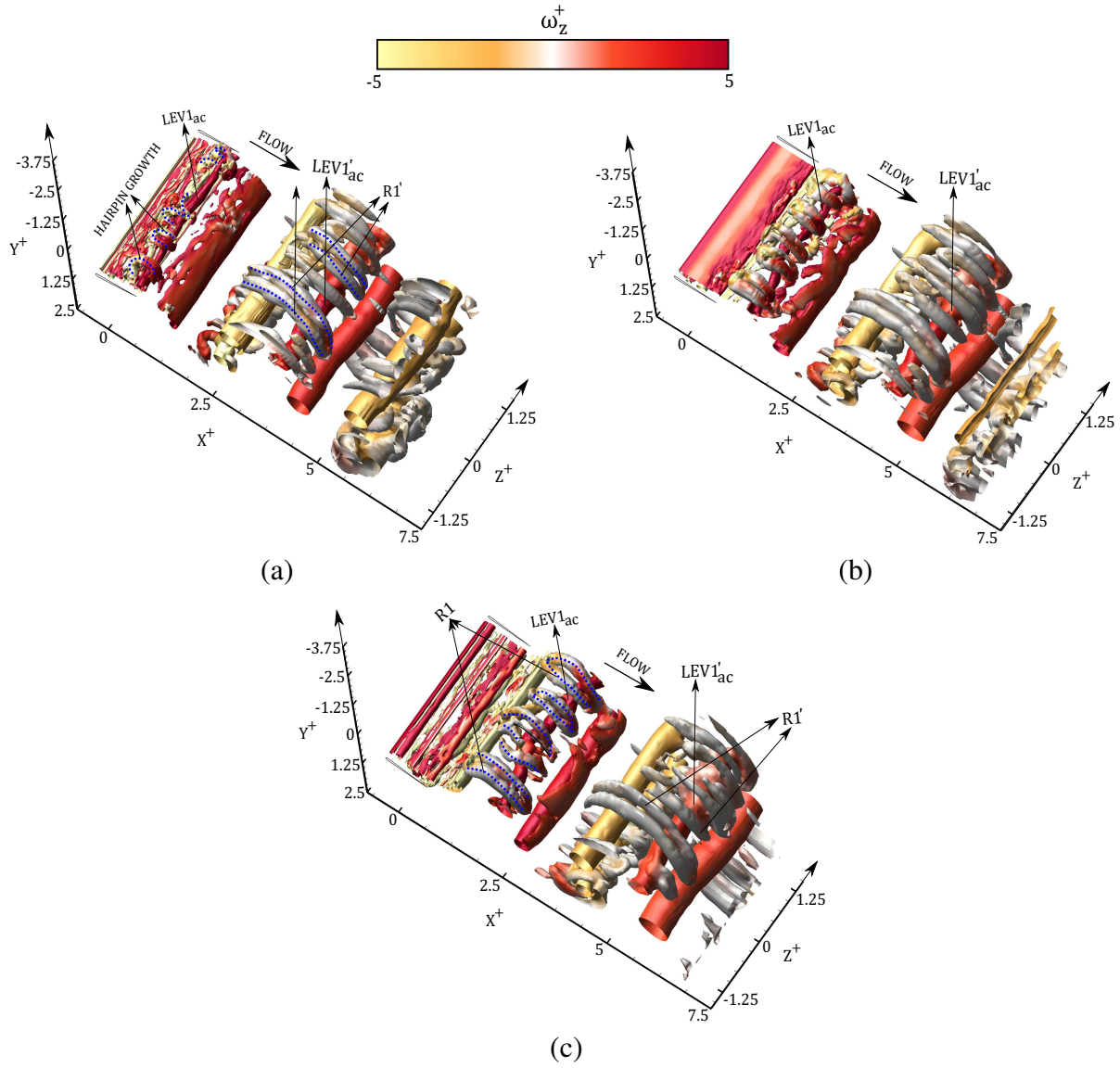

Figure 10.1: Stages of wake evolution at $\phi = 90^\circ$ and $St_c = 0.32$. (a-c) correspond to quarter phases of an oscillation cycle, beginning from (a) $t^+ = 0.5$, (b) $t^+ = 0.75$ and (c) $t^+ = 1$. Each stage is represented using iso-surfaces of $\lambda_2^+ = -0.05$, which are colored based on $|\omega_z^+| = 5$.

5, no prominent bending occurs despite the consistent elongation of rib pairs. Therefore, the only contribution to the growth of secondary wake structure is attributed to the streamwise vorticity outflux from the secondary *LEV* roller (see details in Section 9.3).

10.2.2 $St_c = 0.40$

At $St_c = 0.40$, Figures 10.2(a-c) depict the evolution of primary $LEV2_{ac}$ along with the growth of streamwise hairpin filaments near the foil trailing edge. The onset of these secondary vortex filaments follow a similar mechanism outlined before for $St_c = 0.32$. However, at $t^+ = 0.5$, $LEV2_{ac}$ shows a larger bending amplitude compared to $LEV1_{ac}$ at $St_c = 0.32$ (see Figure 10.1(a)). This also coincides with consistent elongation of hairpin legs to form rib pairs in the wake. To further detail the behavior of $LEV2_{ac}$ downstream, Figure 10.2(a) highlights the growth of dominant horseshoe vortex structures (HS1$'$ and HS2$''$) along the spanwise direction, at $X^+ > 2.5$. The growth of these structures is on account of the strong bending and apparent dislocations on the primary LEVs ($LEV2'_{ac}$ and $LEV2''_{ac}$) shed in previous oscillation cycles, which closely resemble the observations discussed by Mittal and Balachandar (1995) in the wake of a stationary circular cylinder. Mittal and Balachandar (1995) highlighted the mechanism for horseshoe formations in terms of vortex core instability, and simultaneous spanwise dislocations triggered by existing rib structures. The rib pairs are also noted in Figures 10.2(a-c), which evolve in conjunction with horseshoe structures (HS$'$ and HS$''$). Although results shown in Figures 10.2(a-c) are currently limited to $X^+ = 7.5$, it is reasonable to extrapolate that their long term evolution will follow the discussion presented in Mittal and Balachandar (1995). The legs of horseshoe vortex will elongate and resemble an intermediate hairpin-like configuration. The head of this structure could then bifurcate and form a supplemental rib pair in the wake (Mittal and Balachandar, 1995; Williamson, 1996). This process also follows the mechanism of core instability, and its resulting secondary vortex arrangement, noted by Williamson (1996) and Brede et al. (1996). In comparison to the observations at $St_c = 0.32$, it is clear that an increased deformation and bending of primary LEV at $St_c = 0.4$ lead to the growth of dominant horseshoe configuration ahead of $X^+ = 5$.

10.2.3 $St_c = 0.48$ and 0.56

The evolution of wake at $St_c = 0.48$ and 0.56 is shown in Figure 10.3(a-b) and Figure 10.4(a-c), respectively. The onset of secondary hairpin growth near the foil trailing edge, and LEV instability,

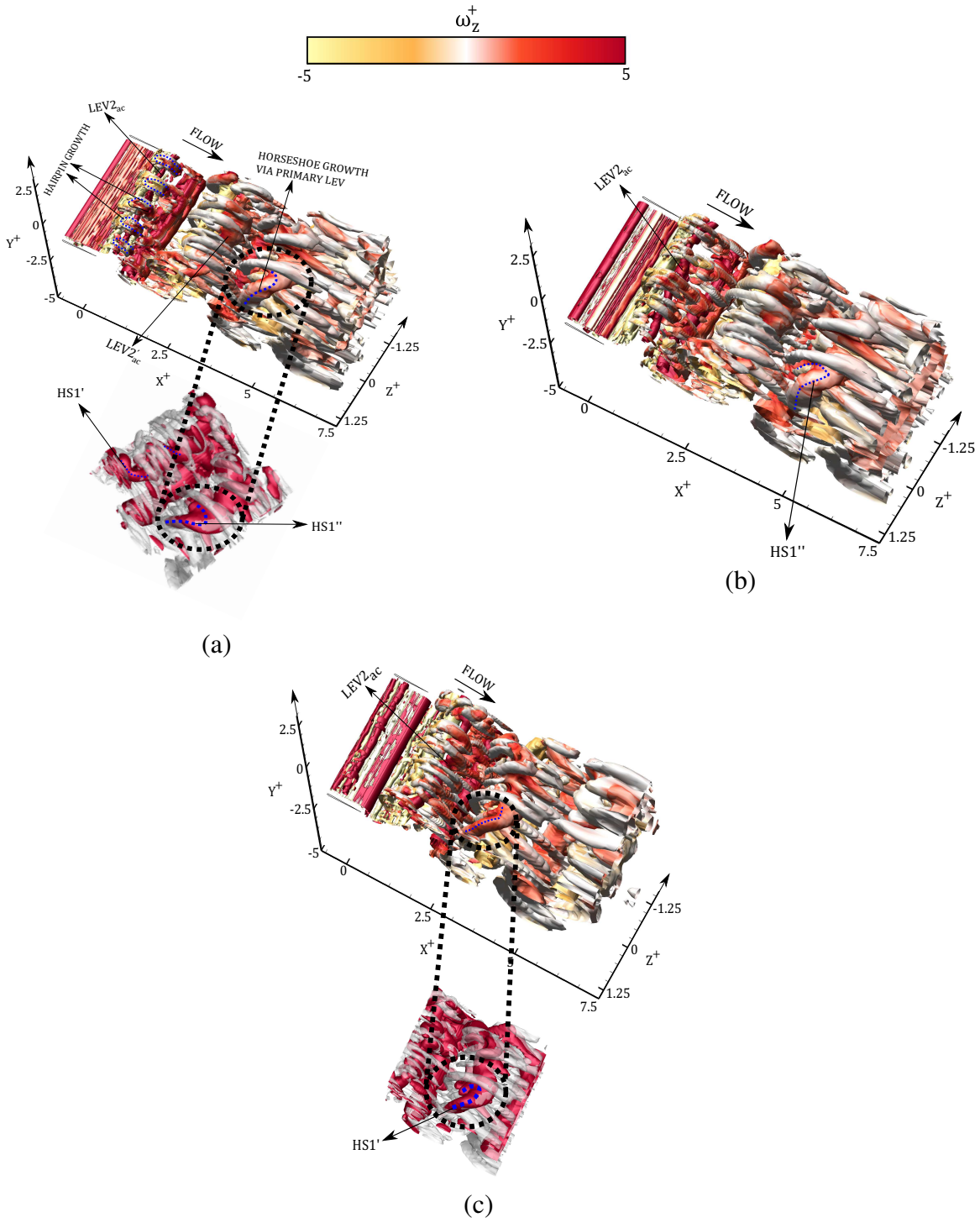

Figure 10.2: Stages of wake evolution at $\phi = 90^\circ$ and $St_c = 0.40$. (a-c) correspond to quarter phases of an oscillation cycle, beginning from (a) $t^+ = 0.5$, (b) $t^+ = 0.75$ and (c) $t^+ = 1$. Each stage is represented using iso-surfaces of $\lambda_2^+ = -0.05$, which are colored based on $|\omega_z^+| = 5$.

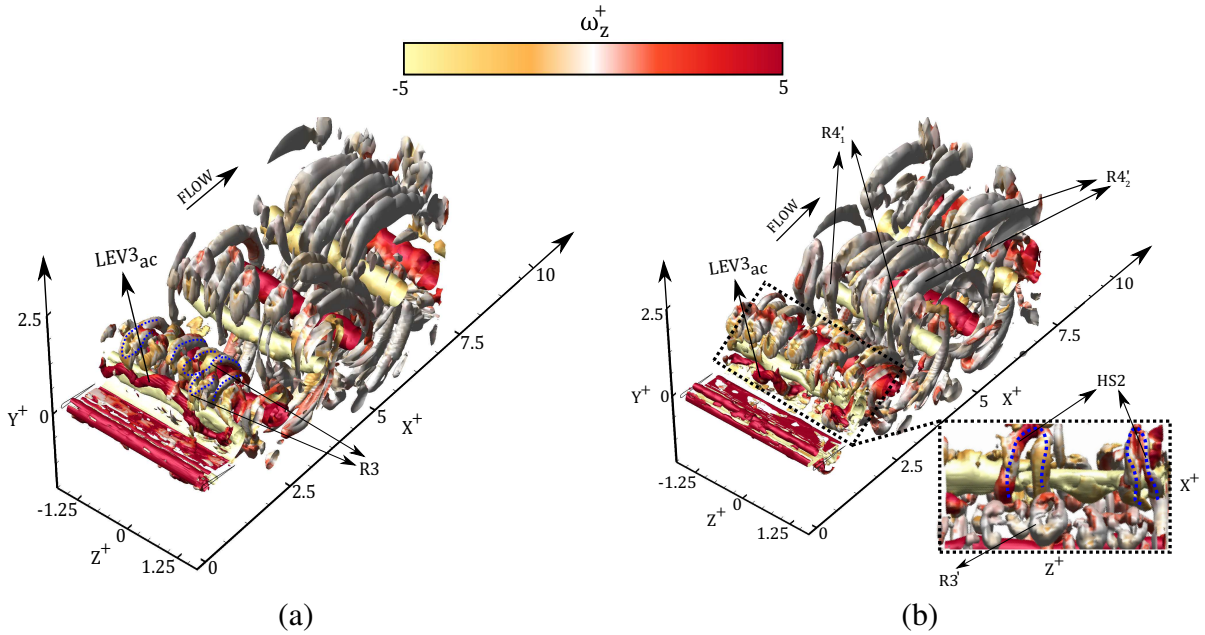

Figure 10.3: Stages of wake evolution at $\phi = 90^\circ$ and $St_c = 0.48$. (a-b) correspond to quarter phases of an oscillation cycle, beginning from (a) $t^+ = 0.75$ and (b) $t^+ = 1$. Each stage is represented using iso-surfaces of $\lambda_2^+ = -0.05$, which are colored based on $|\omega_z^+| = 5$.

still remain prominent. However, the legs of hairpin vortices appear to be more elongated (see Figures 10.3(a) and 10.4(b)) at the instance of shedding, compared to the observations at $St_c = 0.32$ and 0.40.

The bending of separated $LEV3_{ac}$ is imminent at $St_c = 0.48$, in Figure 10.3(a). The maximum bending amplitude is approximately at the mid-span ($Z^+ = 0$), with two identical arches forming at the neighboring ends of the center arch. As the $LEV3_{ac}$ evolve downstream, dual horseshoe structures become evident when viewed from the bottom side of the wake. These are marked as HS2 in Figure 10.3(b), which emerge on account of the eventual amplification of the arch's amplitude, that was initially observed on $LEV3_{ac}$ in Figure 10.3(a). Compared to HS1′ and HS1″ observed at $St_c = 0.40$, the legs of HS2 at $St_c = 0.48$ appear to undergo a relatively faster elongation, which consequently wrap around the shed TEV roller. A consequence of this process is therefore observed in terms of an early transition of horseshoe to a hairpin vortex, which then tears around its head to form ribs. This rib pair originating via primary LEV (marked as $R4'_2$ in Figure 10.3(b)) bound to possess a larger circulation and size (in qualitative sense), compared to the pairs that originate

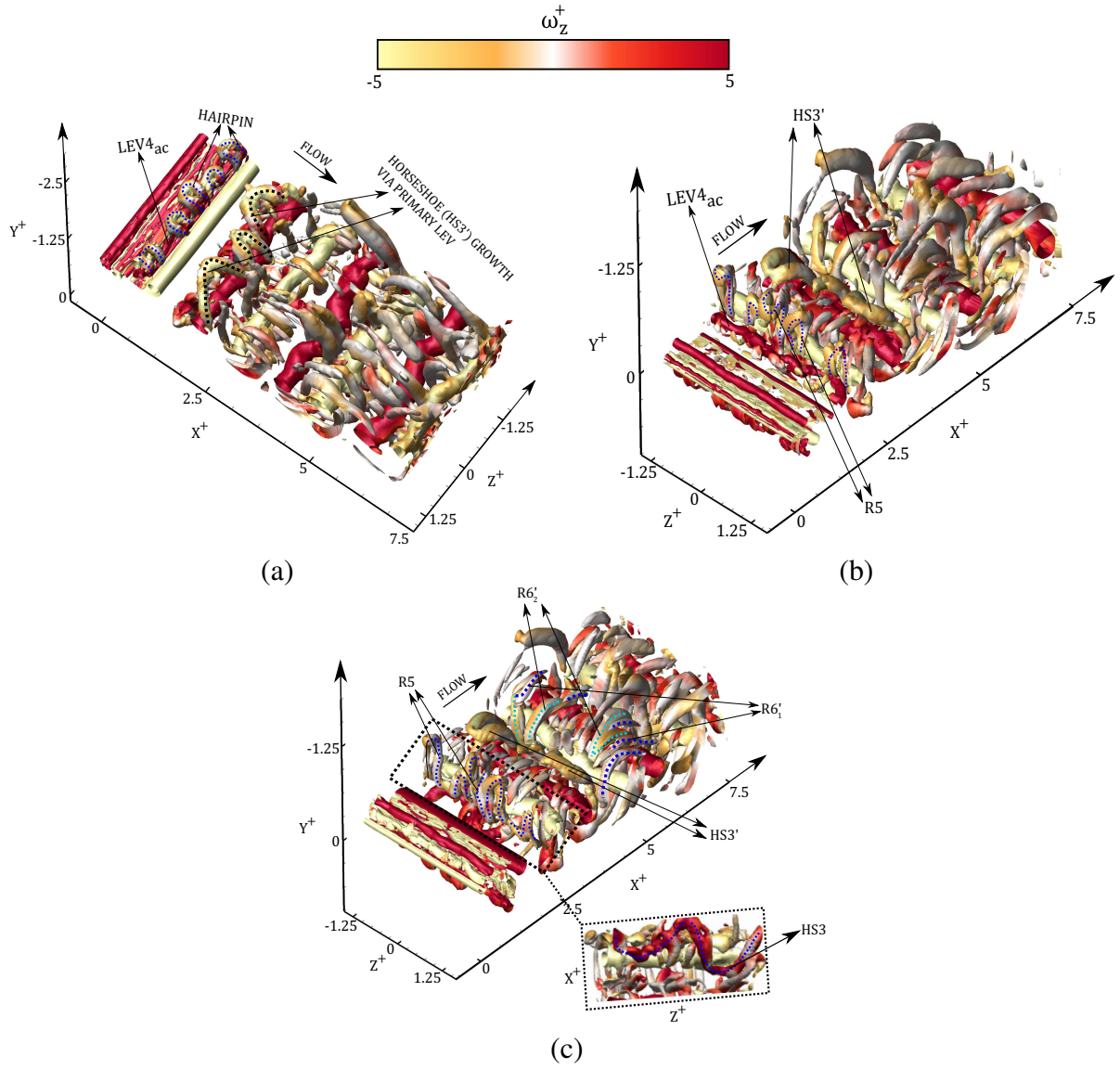

Figure 10.4: Stages of wake evolution at $\phi = 90^\circ$ and $St_c = 0.56$. (a-c) correspond to quarter phases of an oscillation cycle, beginning from (a) $t^+ = 0.5$, (b) $t^+ = 0.75$ and (c) $t^+ = 1$. Each stage is represented using iso-surfaces of $\lambda_2^+ = -0.05$, which are colored based on $|\omega_z^+| = 5$.

via hairpin evolution from the secondary *LEV* vorticity outflux over the foil boundary (marked as $R4'_1$). Such stronger and weaker rib pairs coexist in the wake, while originating through different evolution mechanisms in the wake.

The simultaneous presence of secondary hairpins and horseshoe vortex is also consistent in the wake at $St_c = 0.56$ (see Figure 10.4). Three dominant horseshoe structures (HS3′) are marked in Figure 10.4(a). These evolve via bending of the *LEV* shed in the previous cycle from the

bottom side of the foil. A similar bending and transition to a dual horseshoe system is again evident for $LEV4_{ac}$ (shed from the foil's top side) in Figures 10.4(b) and 10.4(c). These structures are marked as HS3 in Figure 10.4(c). Elongated legs of hairpin structures formed on account of the vorticity outflux from secondary *LEV* are also marked (R5), since they eventually extend to rib pairs downstream, forming $R6'_1$ structures (see Figure 10.4(c)). Upon further evolution, the HS3 structures tear up from their head and form a supplementary system of paired rib structures downstream. These are marked as $R6'_2$ in Figure 10.4(c), which elongate through the HS3′ system of horseshoe vortex structures.

Overall, a close resemblance to the observations at $St_c = 0.48$ is noted here, where the presence of secondary structures in the wake is uniquely attributed to two separate mechanisms. It is also interesting to note that the bending of primary *LEV* and resulting horseshoe structure formation is accelerated at $St_c > 0.40$. For example, the horseshoe legs in case of $St_c = 0.48$ and 0.56 are observed to be highly elongated around $X^+ = 2.5$, although for $St_c = 0.40$, these structures still lack elongation even at $X^+ = 5$. It is further evident that for cases presented at $St_c > 0.40$, the rib pairs originating from the primary *LEV*, and those evolving through secondary *LEV* near the foil trailing edge (hairpins), become coherent at a shorter streamwise distance from the foil trailing edge.

To summarize and understand the implications of increasing St_c mode clearly, Figure 10.5 qualitatively describes a typical wake model that highlight the transition process and growth of secondary wake structures. At approximately $t^+ = 0.25$, a secondary *LEV* remain persistent for the entire St_c range under consideration. This *LEV* forms a counter-rotating vortex pair of unequal strength with the primary *LEV*. At $St_c = 0.32$, the primary *LEV* does not undergo any substantial deformation, while the hairpin legs elongate and evolve on account of the braid vorticity straining (Williamson, 1996), thus transforming to counter-rotating rib pairs. With increasing St_c (e.g. $St_c = 0.40$), the primary *LEV* core begin to undergo high amplitude undulation, compared to those observed at lower St_c. A plausible physical explanation is the increasing strength of primary *LEV* as St_c increases from 0.32 to 0.56. Studies conducted by Calderon et al. (2014) and Son et al. (2022)

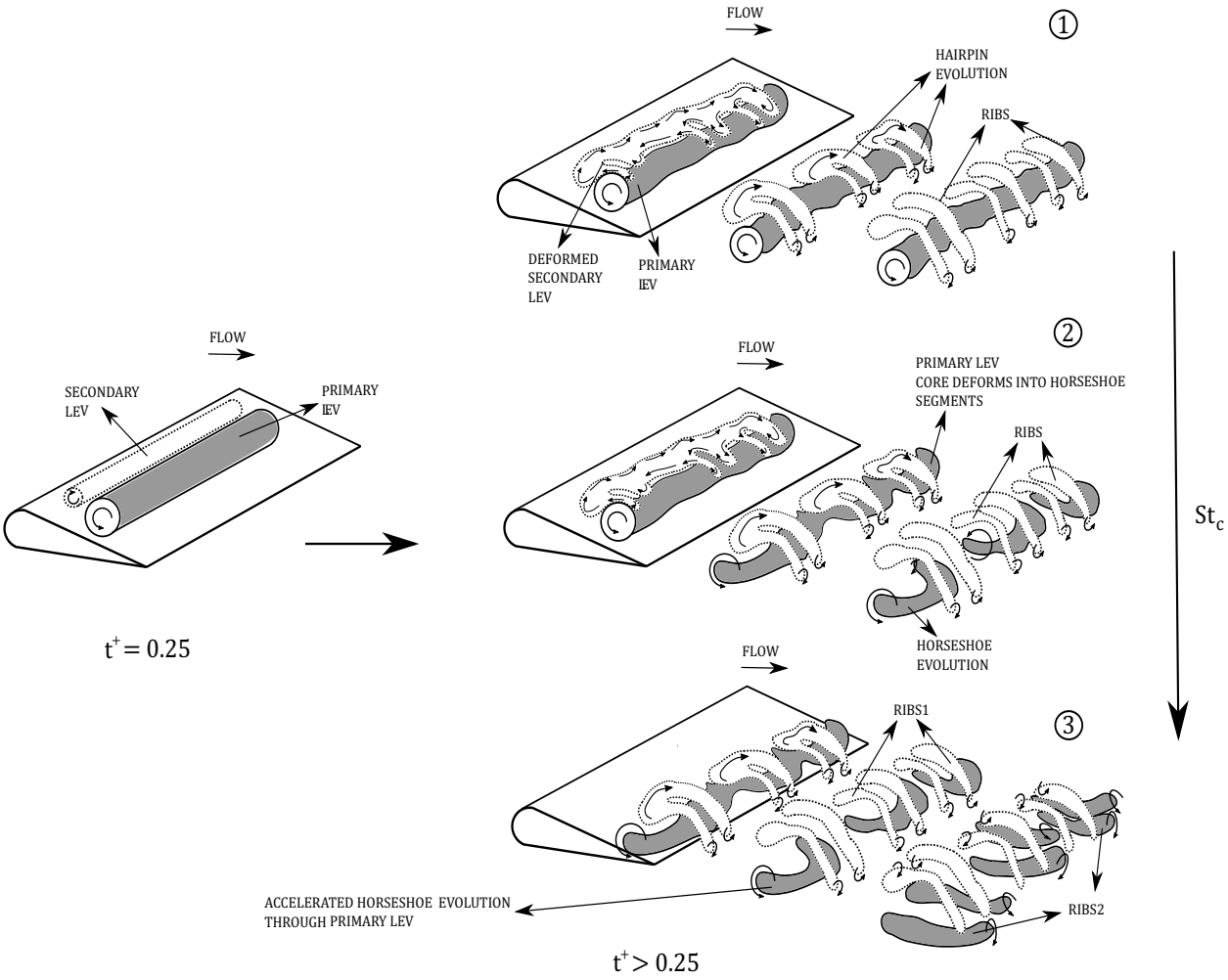

Figure 10.5: Vortex skeleton model depicting the transition of wake topology at increasing St_c.

had provided evidence that an increasing St_c accompanies strong vortical rollers (i.e. LEVs and TEVs). The strong primary LEV could lead to a higher secondary vorticity outflux which leads to an increase in strength of the streamwise hairpin filaments. Hence, this causes a stronger core deformation of the primary LEV. The bends on LEV eventually tear, and form the visible horseshoe vortex structures downstream of the wake. Elongation of hairpin legs (that evolved from secondary LEV) and their eventual transition to rib pairs is still consistent with the details observed for lower St_c.

With further increase in St_c (i.e. $St_c = 0.48$ and 0.56), the process of horseshoe formation is accelerated, where these structures gain coherence at a relatively shorter distance from the trailing edge, compared to the lower St_c cases. It is clear that an early amplification of the undulating

arches of primary *LEV* is the prominent cause for an early segmentation and transformation to horseshoe structures. Subsequently, the continuous straining of the existing secondary vortex pairs and braid vorticity lead to the transition of horseshoe structures to additional rib pairs (marked as RIBS2 in Figure 10.5). Qualitatively, it was vivid in Figures 10.3 and 10.4 that RIBS2 did possess a greater size in comparison to RIBS1, which possibly lost strength on account of viscous effects. The long term and far wake evolution is still yet to be investigated. Besides, it will also be interesting to evaluate the existence and characteristics of these co-existing mechanisms as ϕ increases beyond 90°. It was also highlighted in Section 9.3 that secondary hairpin structures disappear as ϕ increased from 90° to 270° at $St_c = 0.32$. Hence, a more rigorous quantitative assessment would reveal deeper insights into the universal association of kinematics and growth of secondary structures in the wake of an oscillating foil.

10.3 Summary

The initial findings of this chapter demonstrated that the primary *LEV* roller at this kinematics setting does not undergo a substantial bending as it advects downstream. The evolution of the rib configuration is attributed to only one mechanism, as identified and described in Chapter 9. However, a supplementary mechanism behind the characteristic growth of secondary vortex structures became evident as St_c increased beyond 0.32. This mechanism followed a substantial bending of the primary *LEV* in the wake, which also link to the core instability mechanism of primary rollers (Mittal and Balachandar, 1995; Williamson, 1996). This strongly deformed primary *LEV* also depicted a dual arch configuration near the foil trailing edge, particularly for St_c above 0.40. These bends ultimately transformed into a horseshoe vortex configuration, whose legs elongated as the structures advected downstream. This elongation eventually created a second system of rib pairs that remained coherent in conjunction with the ribs formed on account of the streamwise vorticity outflux of secondary *LEV* roller. Based on the findings reported here and within Chapter 9, a col-

lective outlook on the association of kinematics, spanwise instability and secondary hairpin growth will be elaborated in terms of quantitative aspects in the next chapter.

Chapter 11

ON THE ASSOCIATION OF KINEMATICS, SPANWISE INSTABILITY AND GROWTH OF SECONDARY VORTEX STRUCTURES[†]

11.1 Introduction

Achieving fast decay of vortical structures is crucial in modern high-speed aircraft and tactical submarines to reduce the risk of incidents during take-off or landing, while also improving stealth through reduced noise propagation (Leweke and Williamson, 1998; Ortega et al., 2003; Bristol et al., 2004). Such aspects are also useful in technologies that improved the propulsive lift and thrust generation of bio-inspired robotic swimmers during marine surveillance (Meunier and Leweke, 2005), operations of conventional helicopter rotors (McCroskey, 1982), and flight performance of micro air vehicles (MAV*s*) (Mueller and DeLaurier, 2003). As discussed in Sec-

[†]The content of this chapter are under review, in *Proceedings of the Royal Society A* under the citation: "Verma, S., Khalid, M.S.U. & Hemmati, A. (2023). On the association of kinematics, spanwise instability and growth of secondary vortex structures in the wake of oscillating foils."

tion 2.5, the origins of wake instabilities garnered sufficient attention besides characterizing their spatio-temporal development stages during the evolution process (Mittal and Balachandar, 1995; Williamson, 1996). This revealed intricate physical connection to the formation of secondary vortical structures as well (Mittal and Balachandar, 1995), whose role in promoting wake three-dimensionality was immense. Such secondary vortical structures had been largely characterized in wakes of stationary and oscillating bluff bodies including cylinders (with varying cross-sectional shapes) and hydro- or airfoils (Mittal and Balachandar, 1995; Brede et al., 1996; Robichaux et al., 1999; Ryan et al., 2005; Deng et al., 2015; Sun et al., 2018). Chapters 8 and 9 also described the spatio-temporal evolution characteristics of secondary structures and spanwise instabilities in wake of foil oscillating in coupled heaving and pitching motion. However, association of secondary wake structures with prevailing spanwise instability on the primary vortex still require more attention. This study extends our knowledge by characterizing the origins of secondary wake structures, including their inherent association with the governing spanwise instability and prescribed coupled kinematics of an oscillating foil.

The details on mechanism of instability and secondary structure evolution is provided for low to high St_c, which provide reasonable evidence for the strong association of spanwise vortex instability, secondary wake structures and kinematics. The onset of spanwise instability on oscillating foils have also gained considerable attention recently. Few studies (Chiereghin et al., 2020; Hammer et al., 2022; Son et al., 2022) have already been highlighted in Section 2.5. Particularly, Chiereghin et al. (2020) observed the origins of sinusoidal undulation on the shed *LEV* filament in the wake of a high aspect ratio heaving swept wing remained unclear in the study conducted by Chiereghin et al. (2020). They speculated to be either an instability of oscillating shear flow, mixing layer, or the vortex filament itself. The presence of secondary structures and their association with the *LEV* dynamics was also not evident in the study of Chiereghin et al. (2020). Son et al. (2022) and Hammer et al. (2022) recently expanded upon the association of *LEV* instability with St_c and $A.R$ of oscillating foil, although they were limited to only heaving, and a single motion or geometrical parameter (i.e. St_c or $A.R$). The details of the respective studies can be found in Section 2.5. Thus,

there is an imminent need for an adequate extension of this particular association to more complex prescribed kinematics, and its relationship to eventual growth of secondary wake structures.

In this chapter, detailed insights on specific mechanisms that govern the onset of a spanwise instability on primary rollers, and its association with the growth of secondary wake structures, are provided. The work particularly expands on the previously reported results of Chapters 8 and 9, by looking at a wider kinematic parameter (i.e. St_c and ϕ). As identified in Chapter 8, spanwise undulations observed on rollers near the leading edge held key details for the induced spanwise instability, that consequently promoted the growth of secondary wake structures. Thus, to ensure that a strong *LEV* generation is captured in our numerical study, we specifically focus on the oscillations that govern heave dominated coupled kinematics (see Chapter 7 for details). A brief preliminary discussion was presented in Chapter 9, which outlined the association of spanwise wake instability and the growth of secondary wake structures at $St_c = 0.32$ and $\phi = 90^\circ$. This chapter elaborates on those findings, while also revealing the effects on spanwise instability and secondary wake structures, as kinematics slowly undergoes transition and enters a pitch-dominated regime of foil motion.

The flow around an infinite span foil is examined numerically at similar range of kinematics, as highlighted in Section 9.2. The Reynolds number is also consistent with Chapters 8-10. In order to present a broader association of spanwise instability, secondary wake structures and kinematics, the ϕ between heaving and pitching motion in the range of 90° and 270°. This leads to changes in A_T relative to a fixed h_o/c (= 0.25) and $\theta = (10^\circ)$ (see Section 7.3). ϕ below 225° are suggestive of a heave-dominated kinematics, based on the relatively higher h_o compared to A_T (see Section 6.3). At $\phi \geq 225^\circ$, the oscillating foil kinematics starts transitioning towards pitch dominated motion settings (see Section 6.3). On account of variation in ϕ and A_T, St_A is varied in the range specified earlier, where the maximum St_A corresponds to both $\phi = 90^\circ$ and 270°, while the least St_A is observed at $\phi = 180^\circ$ (see Section 7.3). Andersen et al. (2017) indicated that significant transitions in the wake of flapping foils were observable at $0.2 < St_A < 0.4$. This also coincides with the range

corresponding to optimal propulsive efficiency in swimming mammals (Smits, 2019; Triantafyllou et al., 1993).

11.2 Results and Discussion

The qualitative wake visualization is initially discussed at a lower St_c of 0.32, at $\phi = 90^\circ$ and 180°. Here, the relative leading to trailing edge amplitude is the greatest (see Section 7.3). In a way, the cases are representative of kinematics where the heave domination is maximum for oscillating foils executing a coupled heave-pitch motion. These particularly showcase the developed spanwise instability and secondary hairpin structures behind the oscillating foil, specifically for the kinematics settings considered in this study. We then evaluate differences in mechanisms that govern the growth of secondary wake structures in both cases. Since the elaborate details for the case of $\phi = 90^\circ$ have already been presented in Section 9.3, the discussion here focuses on wake characteristics at $\phi = 180^\circ$ more comprehensively. The observations are then extended to $\phi = 225^\circ$ and 270°, which mark the onset of transition towards pitch-dominated kinematics. Quantitative discussions are presented in terms of the variations in primary LEV strength that hint at a physical reasoning behind the manipulated spanwise instability aspects and growth of secondary structures in the wake of an oscillating foil. This is followed by quantitative analysis of spanwise instability wavelength to evaluate the coinciding aspects of primary vortex undulation, growth of secondary structures and changing kinematics. The above investigation is finally extended to higher St_c in order to provide a more generalized fundamental outlook on the observed physics.

Figures 11.1(a) and 11.1(b) present the three-dimensional instantaneous wake structures for the cases corresponding to $\phi = 90^\circ$ and 180°, respectively, while $St_c = 0.32$. The normalized time instant ($t^+ = t/T$) in Figure 11.1 corresponds to $t^+ = 0.75$. The primary vortex (or rollers) and secondary wake structures in terms of hairpin-like formations are well identifiable for both cases using iso-surfaces of λ_2 criterion (Jeong and Hussain, 1995). In terms of the spatial features, the dominant spanwise undulation is evident on the roller highlighted at $\phi = 90^\circ$ (i.e. Figure 11.1(a)).

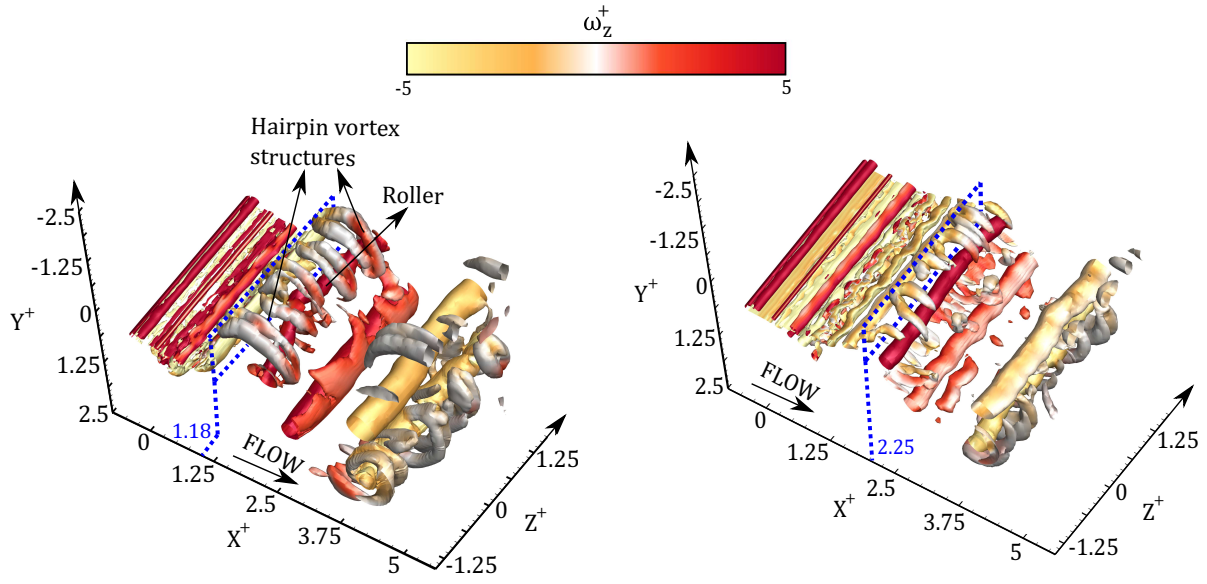

(a) (b)

Figure 11.1: Wakes corresponding to (a) $\phi = 90^\circ$ and (b) $\phi = 180^\circ$, at $St_c = 0.32$. The oscillation time corresponds to $t^+ = 0.75$. Each stage is represented using iso-surfaces of $\lambda_2^+ = -0.05$, which are colored based on $|\omega_z^+| = 5$.

However, such spanwise dislocations are characterized by finer scales and much smaller amplitude for $\phi = 180^\circ$. It is also noticeable that the hairpin secondary structures observed at $\phi = 90^\circ$ possess elongated legs, which eventually grow to form ribs usually observed in wakes of stationary bluff bodies (Williamson, 1996; Mittal and Balachandar, 1995; Brede et al., 1996). Contrary to this case, the hairpin structures at $\phi = 180^\circ$ possess shorter legs, and thus indicate that their growth encounters a temporal lag compared to the wake evolution at $\phi = 90^\circ$. The spatio-temporal delay is marked in Figure 11.1, where the streamwise location corresponding to the initial emergence of hairpin head at $t^+ = 0.75$, are identified as $X^+ = 1.18$ and 2.25 for $\phi = 90^\circ$ and 180°, respectively. Such preliminary wake observations illustrates the fact that spanwise wake instability of *LEV* filaments and the successive growth of secondary wake structures can be attributed to different onset mechanisms that govern the wake evolution at $\phi = 90^\circ$ and 180°.

In order to highlight the mechanism of spanwise instability development and the formation of secondary wake structures at $\phi = 90^\circ$, we plot the contours of ω_z^+ distribution along the mid-span at different time instants (t^+) within an oscillation cycle in Figures 11.2(a-e). For brevity, three-

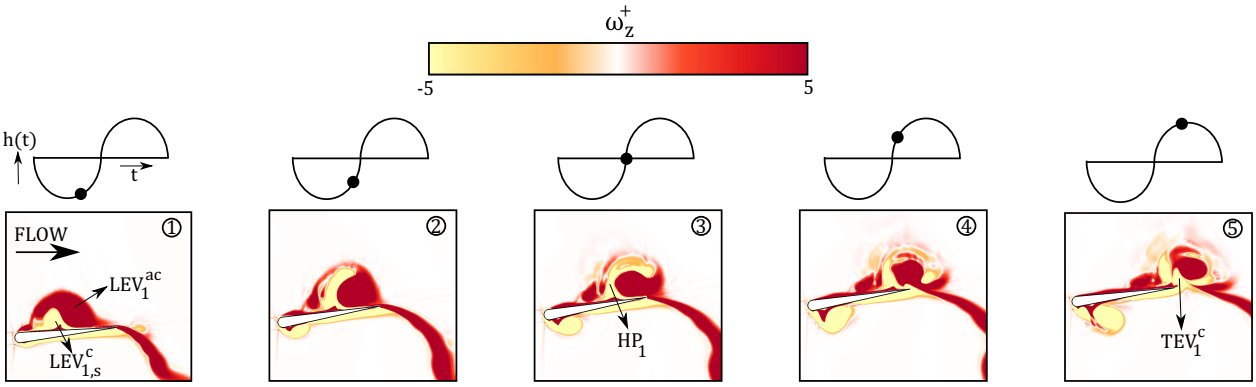

Figure 11.2: Stages of primary and secondary *LEV* evolution at $\phi = 90°$ and $St_c = 0.32$. Each stage is represented using iso-contours of ω_z^+ at the foil mid-span ($Z^+ = 0$).

dimensional wake visualizations are not included within this paper since they have been extensively discussed in Section 9.3 of Chapter 9. The iso-contours in Figure 11.2 provide a summarized depiction of the wake evolution at $\phi = 90°$. In Figure 11.2(a), we observe that as the primary LEV_1^{ac} gains strength and grow in size, a secondary roller ($LEV\,1_s^c$) begin to form in close vicinity of LEV_1^{ac}. The outflux of counter-rotating vorticity via vortex-foil interaction is likely the cause of this secondary *LEV* formation, as was also suggested by Visbal (2009) and Son et al. (2022). However, as $LEV\,1_s^c$ further evolve downstream, the cooperative elliptic instability (Leweke and Williamson, 1998; Ortega and Savas, 2001) starts developing on these unequal strength, counter-rotating vortex structures, which then lead to undulations of both *LEV* filaments. This is followed by a secondary streamwise vorticity outflux via $LEV\,1_s^c$, owing to its relatively weak strength compared to LEV_1^{ac}, which subsequently reveals weak hairpin-like structures (marked as HP_1 in Figure 11.2(c)). The legs of these hairpin-like structures elongate to form ribs, downstream of the foil trailing edge due to the braid vorticity straining, similar to the mechanism outlined by Mittal and Balachandar (1995) in the wake of a stationary circular cylinder. The trailing edge structure TEV_1^c is also seen in its early stages of growth (see Figure 11.2(e)). As it grows in strength and size, the strong primary *LEV* and secondary hairpin-like structures have already advected sufficiently downstream in the wake. Therefore, there are no mutual interactions with the developing *TEV* near the foil trailing edge.

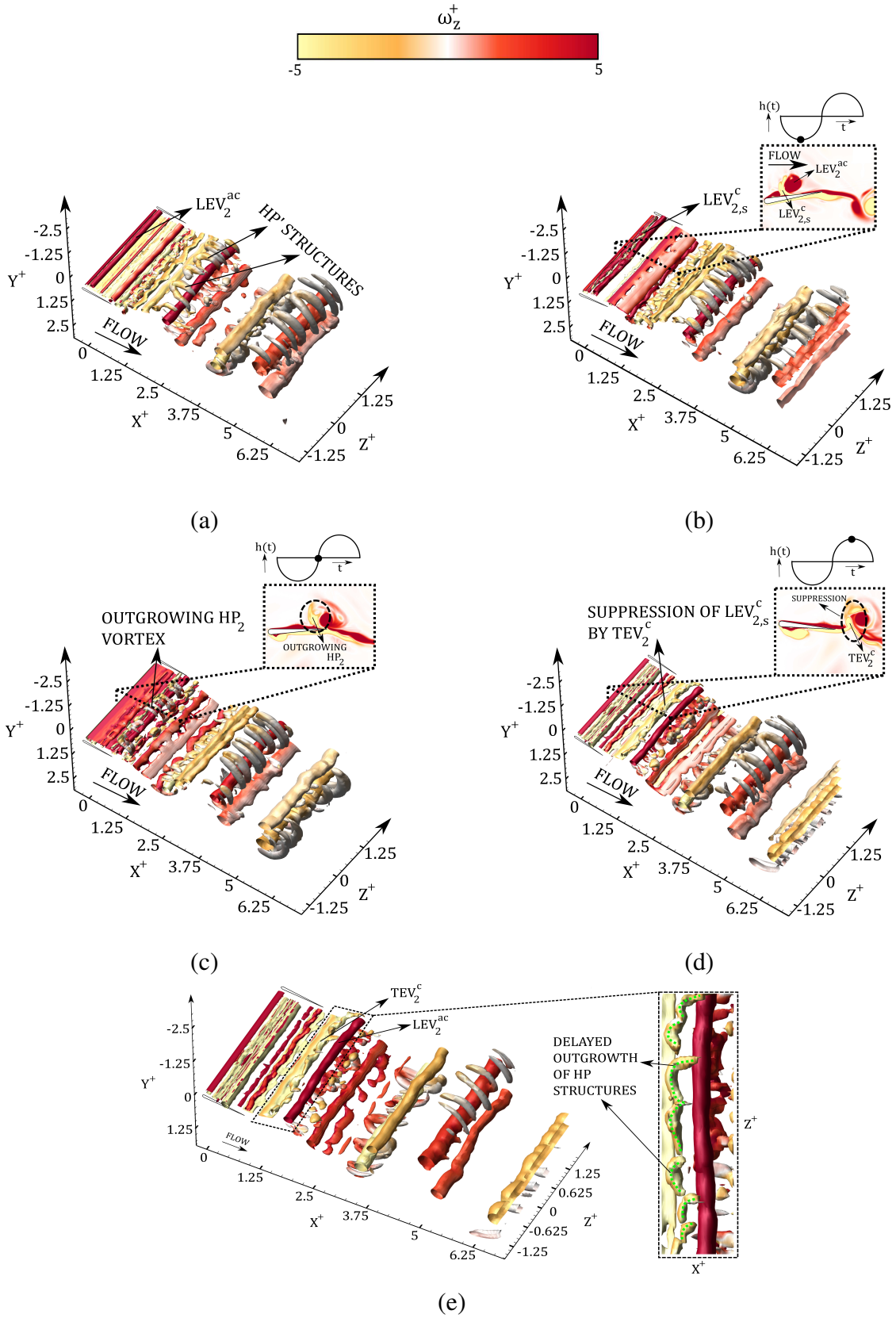

Figure 11.3: Stages of wake evolution at $\phi = 180^\circ$ and $St_c = 0.32$. Each stage is represented using iso-surfaces of $\lambda_2^+ = -0.05$, which are colored based on $|\omega_z^+| = 5$.

The stages of wake evolution at $\phi = 180^{\circ}$ are now discussed to understand the distinct changes in characteristics of spanwise instability and secondary structures, as kinematics change compared to $\phi = 90^{\circ}$. Section 7.3 reported that there is a clear decrease in trailing edge amplitude relative to the leading edge, which coincided with a decrease in peak effective angle of attack (α_o) within an oscillation cycle. However, both cases still represent a heave-dominated kinematic regime for oscillating foils in coupled motion.

Figures 11.3(a-e) depicts three-dimensional iso-surface (λ_2 = -0.05) plots at every quarter of the oscillation cycle. At $t^+ = 0$, development of a primary roller (LEV_2^{ac}) is observed near the leading edge while hairpin-like structures (marked HP') are evident downstream of trailing edge. These secondary structures are formed through a similar process of core vorticity outflux and subsequent shear straining of streamwise filaments that emanated from rollers during the oscillation cycle (Williamson, 1996; Mittal and Balachandar, 1995). However, it is still important to investigate if these streamwise vorticity filaments remain associated with a secondary *LEV*, as observed in the case of $\phi = 90^{\circ}$. At $t^+ = 0.25$, a thin neighboring filament ($LEV_{2,s}^{c}$) appears besides LEV_2^{ac}, although in a partially diffused form. This is attributed to the reduction in normalized circulation, $\Gamma^+ = \Gamma/(U_\infty c)$, of the primary *LEV* ($LEV_2^{ac}$) at $\phi = 180^{\circ}$, compared to LEV_1^{ac} observed at $\phi = 90^{\circ}$. This further contributes to a reduction in intensity of vortex-foil interaction that subsequently decrease the outflux of secondary spanwise vorticity. The quantitative assessment of Γ^+ is also discussed below. Spanwise undulation of primary roller (LEV_2^{ac}) emerge at $t^+ = 0.25$, owing to the cooperative instability induced by the neighboring paired vortex $LEV_{2,s}^{c}$. As the primary and secondary *LEV* pair approach the trailing edge at approximately $t^+ = 0.5$ (see Figure 11.3(c)), the outgrowth of thin streamwise hairpin-like filaments (HP_2) is evident. However at $t^+ = 0.75$, the coincident growth of TEV_2^{c} from the bottom part of the foil (see Figure 11.3(d)) inhibits the continued elongation and straining process of streamwise filaments seen in Figure 11.3(c). Thus, it is important to note here that although the growth of streamwise filaments from a secondary *LEV* is consistent with the observations at $\phi = 90^{\circ}$, the suppression mechanism by the early TEV actually lead to distinct changes in spatio-temporal evolution of secondary hairpin-like structures.

This is observed as the oscillation cycle ends in Figure 11.3(e), besides the visible cooperative instability that retains its form due to the presence of counter-rotating vortex rollers (LEV_2^{ac} and TEV_2^c). This subsequently promotes core vorticity outflux from TEV_2^c, which then demonstrates valley and bulge like features (Mittal and Balachandar, 1995) along the spanwise direction. Such dislocations eventually evolve into secondary hairpin-like structures, as the next oscillation cycle begin at $\phi = 180^\circ$ (see Figure 11.3(e)). The detailed evaluation of the evolution stages certainly provides a fundamental reasoning behind the spatio-temporal delay observed in the formation of secondary wake structures in Figure 11.1(b), compared to their formation at $\phi = 90^\circ$ in Figure 11.1(a). It is further established that the origins of secondary wake structures is not necessarily associated with the formation of secondary *LEV* roller, despite the heave dominated kinematics. However, the presence of spanwise cooperative instability is consistent during distinct evolution mechanisms discussed within the heave dominated kinematics at $\phi = 90^\circ$ and 180°, respectively.

Interestingly, increasing ϕ further towards 225° and 270° reveals the absence of secondary hairpin structures, as shown in Figures 11.4(a) and 11.4(b), respectively. This observation surfaces despite the presence of spanwise undulations on the primary rollers (LEV_3^{ac} and LEV_4^{ac}) in the wake of foils. These small amplitude undulations are attributed to the weak foil-vortex interactions that occur during the *LEV* advection over the foil boundary. The much weaker secondary *LEV* is observed to either diffuse or merge with the shear layer separating from the bottom part of the foil, as observed earlier at $\phi = 180^\circ$ (see Figure 11.3(d)). The temporal evolution of vortex structures are not presented here for brevity, since the observations that concerned growth and advection of the primary $LEVs$ and $TEVs$ are mostly similar to $\phi = 180^\circ$. The lack of secondary wake structures certainly demands a quantitative assessment in terms of Γ^+ for the primary rollers, which should reveal an appropriate physical reasoning. Chiereghin et al. (2020) also speculated in their study that a larger deformation of the *LEV* filament could be attributed to an increased circulation strength, which occurs due to an increase in reduced frequency. However, no plausible association with the growth of secondary wake structures were presented in the study (Chiereghin et al., 2020). Figure 11.5 exhibits variation in $|\Gamma^+|$ for one oscillation cycle, in the ϕ range as-

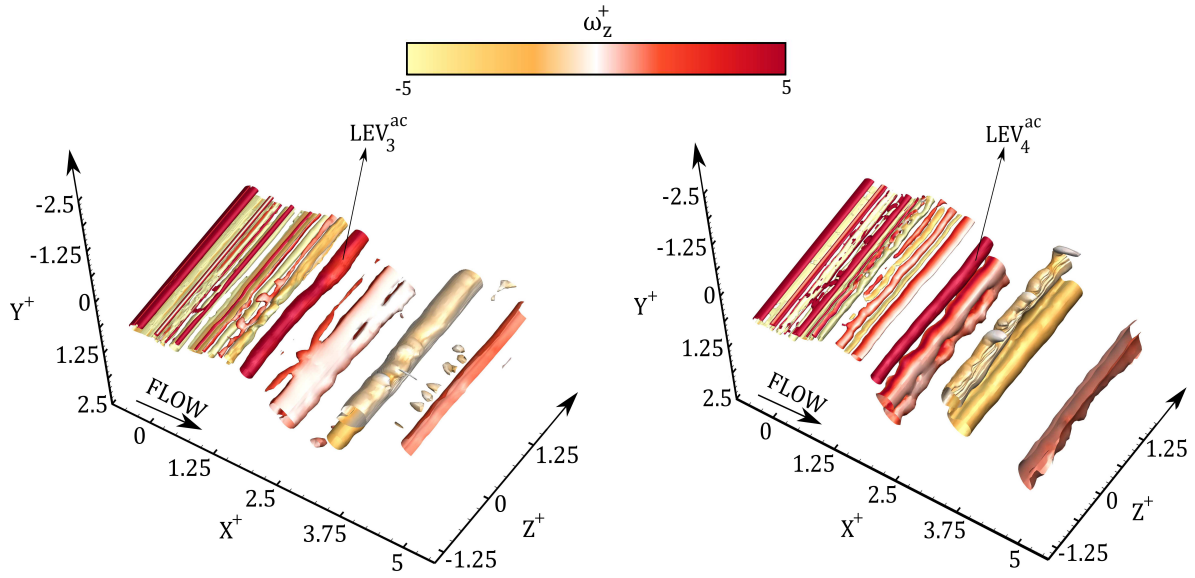

(a) (b)

Figure 11.4: Wakes corresponding to (a) $\phi = 225°$ and (b) $\phi = 270°$, at $St_c = 0.32$. The oscillation time corresponds to $t^+ = 0.75$. Each stage is represented using iso-surfaces of $\lambda_2^+ = -0.05$, which are colored based on $|\omega_z^+| = 5$.

sessed till now. Evidently, $|\Gamma^+|$ depicts a reduction in the peak magnitude with increasing ϕ from 90° to 270°, which coincides with $t^+ = 0.4$. This characteristic peak magnitude further coincides with the generation of secondary streamwise vorticity filaments observed in the wake at $\phi = 90°$ and 180°. These observations therefore suggest that intensity of core vorticity outflux mechanism (Williamson, 1996; Mittal and Balachandar, 1995), which is inherently responsible for the generation of streamwise vorticity filaments, and thus growth of hairpin-like secondary structures, is commensurate with the strength of the primary *LEV* that advects over the foil boundary.

In addition to the above observations, it is also worthwhile to discuss the changes in spanwise instability characteristics of the primary *LEV*, which coincides with the heave dominated kinematic regime and the emergence (or absence) of secondary wake structures. We particularly compare the temporal development of spanwise instability in terms of the quantified estimate of its wavelength, represented by λ_z. The estimation process follows Sections 8.3 and 9.3, where a spatial autocorrelation coefficient ($C(\Delta z)$) is calculated with respect to the streamwise vorticity (ω_x^+) distribution on a planar spanwise slice that passes through the core of primary *LEV*.

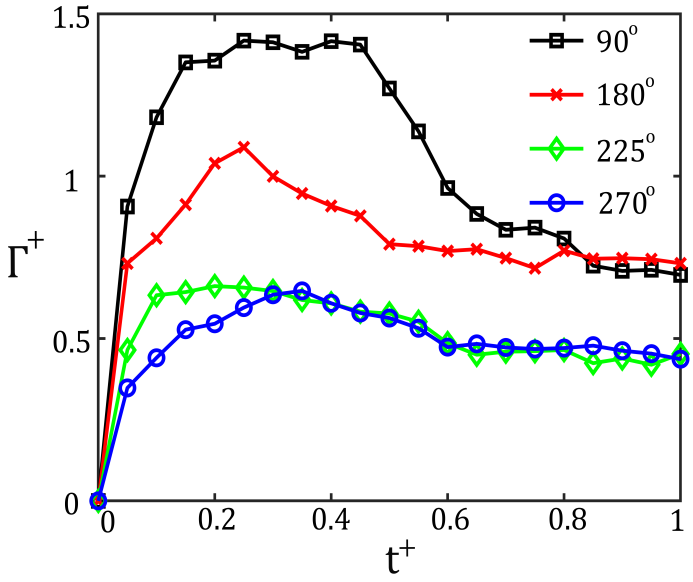

Figure 11.5: $|\Gamma^+|$ variation of primary *LEVs* as they advect in an oscillation cycle corresponding to cases of $\phi = 90°$-$270°$.

As an example, Figure 11.6 presents the process of calculating λ_z for a primary *LEV* (LEV_1^{ac}) shed in the case of $\phi = 90°$. t^+ corresponds to 0.75, where instability features are quite dominant in terms of the spanwise undulation amplitude. The variation of $C(\Delta z)$ with respect to normalized lag ($\Delta z/c$) is also shown, where $C(\Delta z)$ is obtained via spanwise ω_x^+ distribution on a slice passing through the center of primary roller LEV_1^{ac} at $X^+ \approx 1.25$. The estimated distance to the first minima of $C(\Delta z)$ is equal to $\lambda_z/2$, which characterize the spanwise instability. For instance, the distance to the minima (shown in Figure 11.6) is approximately 0.43, which thus yields $\lambda_z = 0.86$ for LEV_1^{ac}.

Figure 11.7 shows the comparative assessment of λ_z for the primary *LEV*, as it advects in each case (i.e. $\phi = 90°$-$270°$). The results suggest that the estimated λ_z remains below 1 for the cases corresponding to $\phi = 90°$ and $180°$, where the relative amplitude of leading edge, with respect to the trailing edge, is the largest within the heave dominated motion setting. Particularly for $\phi = 90°$, it is found that λ_z slightly increases from 0.57 to 0.86, at approximately the mid-cycle, during which a dominant growth of secondary hairpin structures is also observed. The decrease in λ_z at the end of the oscillation cycle is possibly an implication of braid vorticity interaction in the region between consecutive rollers, which introduce fine scale dislocations (Williamson, 1996),

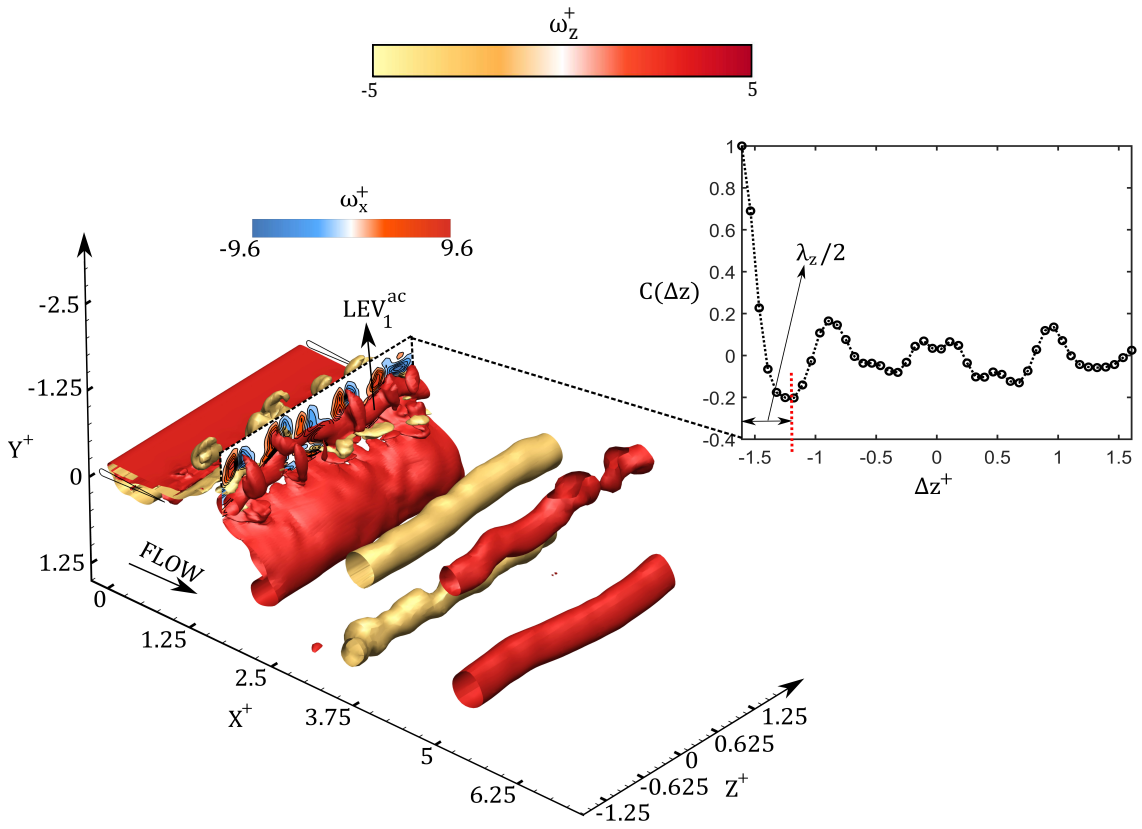

Figure 11.6: Estimation process of λ_z characterizing the spanwise instability of primary *LEV*.

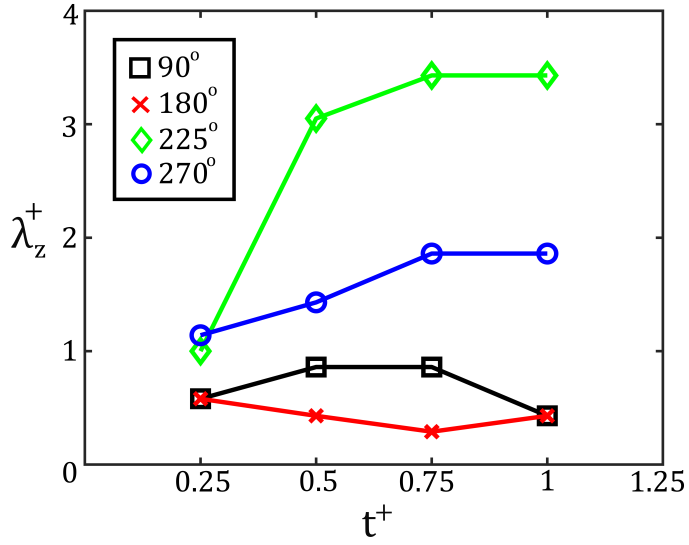

Figure 11.7: Variation of λ_z in an oscillation cycle corresponding to $\phi = 90°$-$270°$.

and hence, a reduction in λ_z. For $\phi = 180°$, however, a slight decrease in λ_z is evident until t^+ = 0.75, which implies a greater association with fine scale vorticity interactions occurring during vortex advection over the foil boundary. Growth of hairpin structures via strained TEV, ahead of t^+ = 0.75, coincides with a minor increase in λ_z until the oscillation cycle ends. Thus, close association between the spanwise instability characteristics and the growth of secondary structure seem apparent for both $\phi = 90°$ and 180°, wherein the heave domination is maximum.

In cases of $\phi = 225°$ and 270°, λ_z variation depicts a relatively higher value compared to the lower ϕ cases during the entire oscillation cycle. This further coincides with a transition from heave to pitch dominated motion regime, which begins ahead of $\phi = 270°$. Specifically, advection of the primary LEV at $\phi = 225°$ demonstrates an increase in λ_z to 3.43, as the oscillation cycle ends. For $\phi = 270°$, however, an overall reduction of $\lambda_z(\approx 1.86)$ is noticeable, compared to $\phi = 225°$. The higher λ_z at $\phi = 225°$ also coincides with a lowering Γ^+ (Figure 11.5), while exhibiting no interaction with any secondary hairpin-like structure. Qualitatively, wake visualizations in Figure 11.4(a) reveals no imminent neighboring roller of counter-rotating vorticity to LEV_3^{ac}, which may contribute to a spanwise instability characterized by a longer wavelength compared to λ_z for $\phi = 90$ and 180°, respectively. Besides the observation concerning higher λ_z^+, the amplitude of undulation in LEV filament is much smaller compared to lower ϕ cases that supports the speculation presented by Chiereghin et al. (2020) with respect to the decreased Γ^+. At $\phi = 270°$ (Figure 11.4(b)), however, the presence of co-rotating vortex rollers in close proximity of one another contributes to a reduced λ_z compared to $\phi = 225°$, given the observation that Γ^+ is approximately similar in both cases (see Figure 11.5).

11.3 Impacts of variation in reduced frequency (St_c)

The close association of spanwise instability characteristics with secondary hairpin structures is evident from the observations discussed thus far. However, it is still necessary to evaluate the impacts of increasing St_c on the mechanisms governing evolution of spanwise instability and sec-

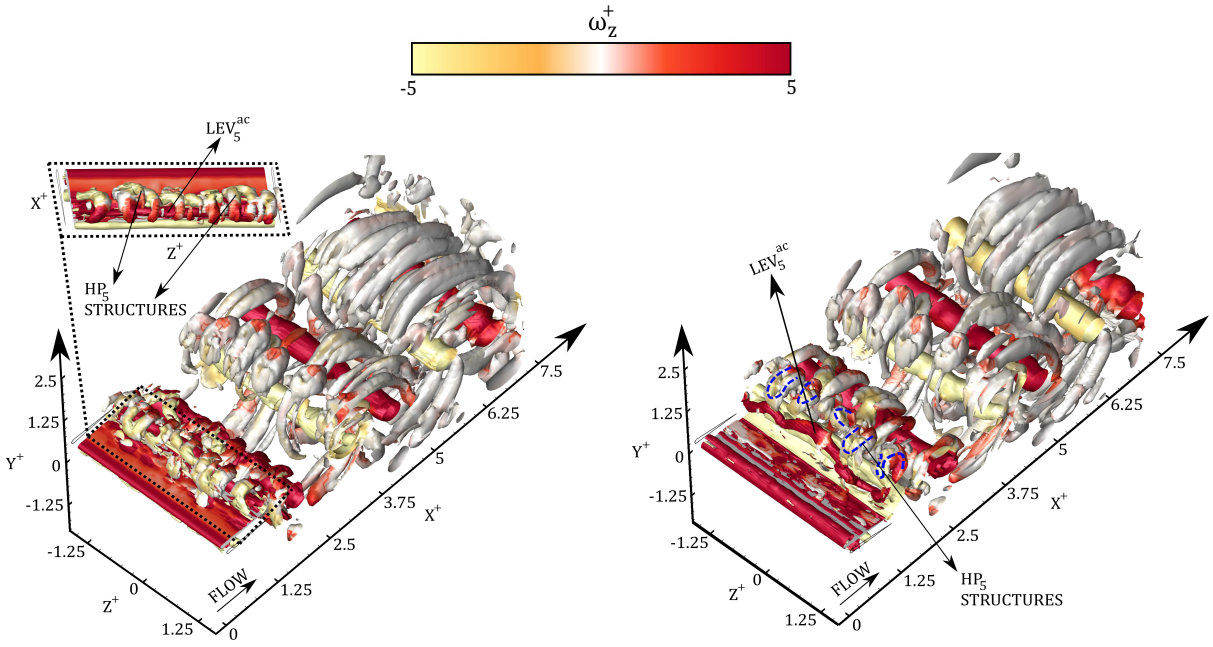

(a) (b)

Figure 11.8: Wake snapshots corresponding to $\phi = 90°$, at $St_c = 0.48$. The oscillation time corresponds to (a) $t^+ = 0.5$ and (b) $t^+ = 0.75$. Each stage is represented using iso-surfaces of $\lambda_2^+ = -0.05$, which are colored based on $|\omega_z^+| = 5$.

ondary wake structures for the heave-dominated motion regime (i.e. $\phi = 90°$-$270°$). An increasing St_c usually accompanies stronger vortical rollers (i.e. $LEVs$ and $TEVs$) shed from the oscillating foil (Calderon et al., 2014; Son et al., 2022). Section 8.3 depicted that the wake topology characterized by the arrangement of primary rollers was different at low and high St_c, and it further coincided with different spatio-temporal features, in terms of spanwise dislocations and secondary hairpin formation. Son et al. (2022) also analyzed the impacts of modified reduced frequency (k) of a heaving foil, so that the strength of LEV and TEV rollers could be manipulated to study their impacts on the LEV instability characteristics.

Figures 11.8(a) and 11.8(b) presents the evolution of primary LEV (LEV_5^{ac}) along with the visible secondary hairpin structures at $\phi = 90°$ and $St_c = 0.48$. t^+ corresponds to 0.5 and 0.75, respectively. Overall, the growth mechanism of spanwise instability on LEV_5^{ac} remains consistent with the observations at $St_c = 0.32$ (see Figure 11.2, and Section 9.3). The growth of secondary hairpin (HP_5) structures and their eventual elongation to rib formations, downstream of the foil

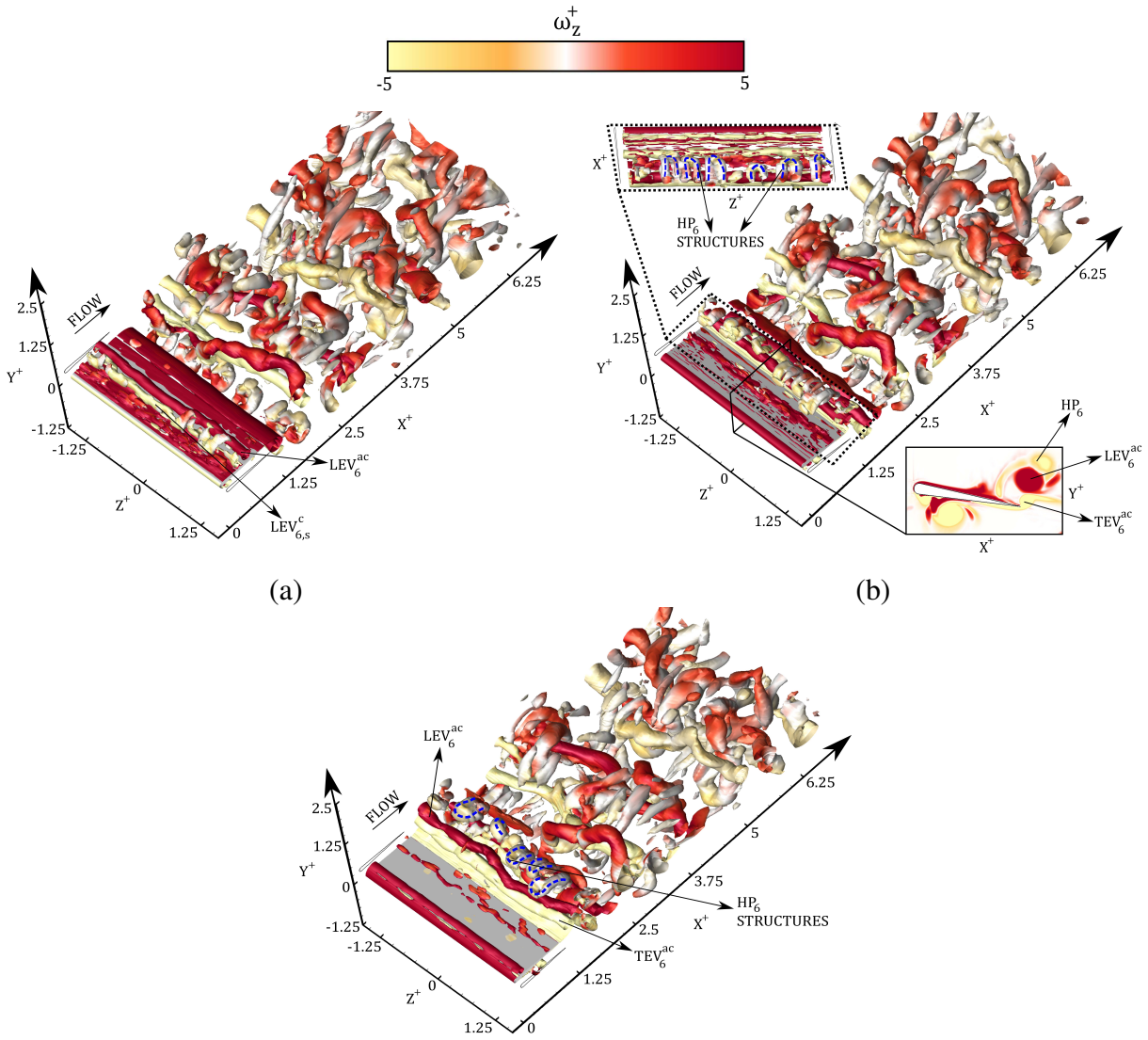

Figure 11.9: Wake snapshots corresponding to $\phi = 180°$, at $St_c = 0.48$. The oscillation time corresponds to (a) $t^+ = 0.25$, (b) $t^+ = 0.5$ and (c) $t^+ = 0.75$. Each stage is represented using iso-surfaces of $\lambda_2^+ = -0.05$, which are colored based on $|\omega_z^+| = 5$.

trailing edge, is further visible in Figures 11.8(a) and 11.8(b). However, LEV_5^{ac} depicts a much larger spanwise undulation amplitude after its shedding at $t^+ = 0.75$ (Figure 11.8(b)), compared to the LEV undulations seen previously at $\phi = 90^\circ$ and $St_c = 0.32$. This is attributed to the increased strength of the primary LEV (Chiereghin et al., 2020), which further contributes to a much stronger secondary hairpin formations over the foil boundary. Based on quantitative assessments for the case of $\phi = 90^\circ$ at $St_c = 0.48$ and 0.32, it is found that at $t^+ = 0.5$, LEV_5^{ac} has a $|\Gamma^+| = 1.29$, that is approximately 20% greater compared to LEV_1^{ac}. Even for the secondary hairpin (HP_5) structures that grow around $t^+ = 0.5$, the associated counter-clockwise rotating leg, corresponding to the case of $St_c = 0.48$, possess a $|\Gamma^+|$ that is 58% higher relative to the strength of hairpin leg (with similar sense of rotation) that develops at $St_c = 0.32$ (HP_1). Enhanced amplitude of LEV undulation at the higher St_c is also evident as ϕ increases to 180°. Snapshots of wake evolution at $t^+ = 0.25$, 0.5 and 0.75 are shown in Figures 11.9(a), 11.9(b) and 11.9(c), respectively. The larger deformation of LEV_6^{ac}, compared to LEV_2^{ac} in Figure 11.3(e) (for lower St_c), is evident in Figure 11.9(c). Apart from the changes seen in visible undulations and deformations of LEV filaments, a coincident change in the mechanism of secondary hairpin growth is further noticed here. At $t^+ = 0.25$ (Figure 11.9(a)), the secondary $LEV_{6,s}^c$ is stronger compared to its companion structure ($LEV_{2,s}^c$) observed at lower St_c (see Figure 11.3(b)). Quantitative estimation reveals $|\Gamma^+| = 0.37$ and 0.25 for $LEV_{6,s}^c$ and $LEV_{2,s}^c$, respectively. Due to this stronger secondary LEV, the outgrowth of stronger hairpin (HP_6) structures also occurs relatively earlier, as seen in Figure 11.9(b). It is further apparent that the newly forming TEV_6^c has not grown enough (in terms of size) to hinder the advecting HP_6 structures. Therefore, we see that the origin of hairpin growth remain the same at $\phi = 90^\circ$ and 180°.

At $\phi = 225^\circ$, however, the wake evolution (shown at $t^+ = 0.5$ and 0.75 in Figures 11.10(a) and 11.10(b), respectively) demonstrates changes in the origin of secondary hairpin structures compared to $\phi = 90^\circ$ and 180°, discussed above. We observe that the counter-rotating secondary LEV is not evident in the vicinity of primary LEV_7^{ac}. However, the nascent growth of TEV_7^c is apparent in the immediate neighborhood of LEV_7^{ac}, which also depicts valley and bulge formations

due to the developed spanwise instability. These vortex dislocations eventually grow and form the hairpin (marked as HP_7) and rib structures, downstream in the wake. This mechanism is therefore in accordance with the evolution process we had observed at lower St_c, although ϕ corresponded to 180°. The wake evolution corresponding to $\phi = 270°$ closely resembles our findings at $St_c = 0.32$ (Figure 11.4(b)). Hence, we do not present the snapshots here at $St_c = 0.48$ for brevity. In relation to the observations presented here, it is clear that mechanisms governing the growth of secondary wake structures and spanwise *LEV* instability in the heave dominated kinematics remain consistent within the range of increasing St_c considered here.

Quantitative estimation of λ_z for the higher St_c also reveal values close to the observations noted before at $St_c = 0.32$, which again implies that the characteristics of spanwise instability, coinciding growth of secondary wake structures, and their associations remain consistent. Specifically for $\phi =$ 90° and 180°, λ_z is 0.43 for the primary rollers LEV_5^{ac} and LEV_6^{ac}, respectively. We will note here that the estimations are conducted just before *LEVs* undergo large scale deformation, as shown in Figures 11.8(b) and 11.9(c). For LEV_7^{ac}, corresponding to $\phi = 225°$, the estimated λ_z is in the range of 0.43 to 0.57 at both instants presented in Figures 11.10(a) and 11.10(b). The similarity in terms of λ_z, for $\phi = 90° - 225°$, is attributed to the fact that the growth of secondary hairpin is evident in all these cases at $St_c = 0.48$. This follows the argument presented at lower St_c, where the growth of secondary hairpin structures at $\phi = 90°$ and 180° also coincided with $\lambda_z < 1$.

11.4 Summary

The association between coupled kinematics and the wake three-dimensionality is numerically investigated in this study. The foil kinematics modify based on changing phase offset (ϕ) between coupled heave and pitch motion, and an increasing reduced frequency (St_c), while $Re = 8000$. The considered range of ϕ is largely representative of a heave-dominated kinematics, which also enables a dominant leading edge vortex formation that undergoes deformation on account of the spanwise instability. It concurrently plays a role in the evolution of secondary wake structures.

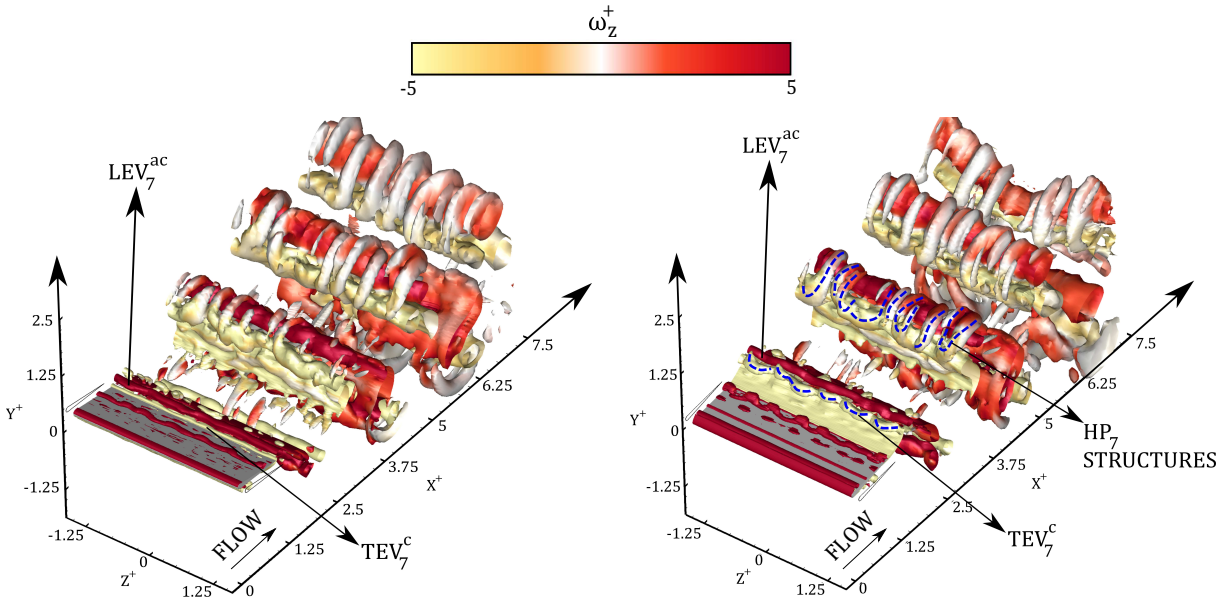

(a) (b)

Figure 11.10: Wake snapshots corresponding to $\phi = 225°$, at $St_c = 0.48$. The oscillation time corresponds to (a)$t^+ = 0.5$ and (b) $t^+ = 0.75$. Each stage is represented using iso-surfaces of $\lambda_2^+ = -0.05$, which are colored based on $|\omega_z^+| = 5$.

At lower St_c, spanwise undulations of the primary roller remained evident on account of the developed instability. But, the quantitative estimation of its wavelength (λ_z) reflected substantial changes with increasing ϕ from 90° to 270°. The primary roller for $\phi = 90°$ and 180°, where the relative leading to trailing edge amplitude was greatest within the heave-dominated kinematics considered here, depicted a shorter instability wavelength of the characteristic undulation ($\lambda_z < 1$), along with a dominant growth of secondary hairpin-like structures. These hairpins were essentially an outcome of core vorticity outflux from either the formation of a secondary *LEV*, that neighbors a primary *LEV* ($\phi = 90°$), or a *TEV* interacting with a primary *LEV* shed behind the foil ($\phi = 180°$). Contrary to these cases, it was observed that at $\phi = 225°$ and 270°, the primary roller is characterized by a longer instability wavelength ($\lambda_z > 1$), while the wake coincided with the absence of hairpin-like structures. This range of ϕ also coincided with a decreasing leading edge amplitude relative to the trailing edge, thus presenting the onset of pitch domination at $\phi = 270°$. Overall, the changes in λ_z and origins of secondary hairpin vortex, on account of increasing ϕ,

reflected a unique association of kinematics and induced three-dimensionality of wake that features the development of spanwise instability and secondary vortex structures. The above noted observations also remained consistent with increasing St_c. The range of ϕ presented here show a dominant growth of secondary wake structures (i.e. $\phi = 90^\circ$-225°) that were characterized by $\lambda_z <$ 1 for the primary roller, following the arguments proposed at lower St_c. Quantitative assessment on circulation of primary *LEVs* further indicated that the reduction in their strength coincided with a lower possibility of core vorticity outflux, as ϕ increases from 90° to 270°. This explains the disappearance of secondary wake structures for $\phi = 225^\circ$ and 270° at lower St_c, and $\phi = 270^\circ$ at higher St_c. The absence of secondary wake structures, which also coincided with the longer instability wavelength of primary *LEVs*, is still under investigation.

Chapter 12

CONCLUSION

The objectives of this research study were concerned with the investigation of wake dynamics for an oscillating teardrop foil that executed combined heaving and pitching motion. OGA technique was employed to directly solve the unsteady and incompressible form of the Navier-Stokes equations. The first aim revolved around characterizing the coincident transitions in propulsive performance and spatial topology of two-dimensional coherent rollers shed behind an oscillating foil at low *Re*. A new physics-based model was developed based on quantitative and qualitative observations of vortex features that included circulation. This mathematical relationship presented a unique framework to predict transitions in the wake topology with changes in foil kinematics, while also characterizing their mutual association. The identification and characterization of three-dimensional wake topology formed the second major objective of this study. The characteristics of spanwise instability and the onset mechanisms of secondary structures were evaluated for heave- and pitch-dominated regimes of kinematics. Their underlying fundamental association was ultimately established in detail.

Changes in propulsive performance, specifically thrust and input power, with respect to varying kinematic settings were adequately described using scaling relationships. However, the applicability of laminar scaling for thrust generation which incorporated dependence on $Re^{-0.5}$, was limited to $\overline{\alpha^{\circ}} \leq 20^{\circ}$. The non-asymptotic behavior of pressure forces, in contrast to the viscous force,

further coincided with the observed deviation. In terms of the association with vortex dynamics, a large adverse pressure gradient created by the leading edge vortex was evident under kinematic regimes that particularly reflected deviation. On the aspects that concerned transition of propulsive performance and wake mode configuration, it was demonstrated that the number of vortex structures shed in an oscillation cycle does not hold a one-to-one correspondence with the changes in performance from thrust to drag. On the $\phi - St_c$ phase map, it was identified that several different wake configurations ($2P+2S$, *wBvK* and $2P$) coincided with a drag dominated performance at increasing range of ϕ and $St_c < 0.32$. The mechanisms governing thrust to drag transition in the wake also revealed that either the mean momentum jet underwent bifurcations, or shortened on account of dynamic vortex interactions and merging in the wake. The characteristics of temporal lift variation were evaluated within a similar range of $\phi - St_c$, as assumed for the observations summarized above. It was noted that within a heave dominated regime (i.e. $90^\circ \leq \phi \leq 225^\circ$), the lift signature within an oscillation cycle depicted a symmetry such that a mirror image of the extreme for C_L existed about the half shedding period. In contrast, for the pitch dominated oscillation regime (i.e. $\phi < 90^\circ$ and $\phi > 225^\circ$), no associated symmetry in the C_L variation became evident. The presence of $2P$ mode, which highlighted shedding of vortex pairs (constituting LEV and TEV) rather than single isolated structures in the wake, was further evident in the heave-dominated regime. Within a pitch-dominated kinematics, the LEV*s* either disintegrated or merged with the TEV that was under development. Thus, the wake topology depicted a transition from $2P$ to $2S$, as St_c increased for pitch dominated kinematics.

The evaluation of the transitions in wake topologies, at an increasing range of Re, ϕ and St_c, was finally culminated by the development and validation of a novel physics based model. This provided a mathematical relationship between some vortex features (e.g. ratio of circulation strength for vortex structures) and foil kinematics (e.g. St_h, St_θ and ϕ), which ultimately established a unique framework to predict transitions in wake topology. Within the range of kinematics considered here, it was evident that at $Re = 1000$, the model was able to predict the transition of $2P$ to $2P+2S$ or $2S$ modes, respectively. Overall, wake assessments of an oscillating foil revealed

several insights with respect to the association of transitions in propulsive performance and spatio-temporal evolution of two-dimensional rollers. The incorporation of spanwise effects, however, became important at $Re = 8000$ on account of the associated three-dimensionality of wake structures. Therefore, an infinite span teardrop foil model was considered in order to address the second major objective of this dissertation.

Spanwise instability of rollers and growth of secondary structures in the wake became imminent at $Re = 8000$. Their inherent interlinked dynamics provided crucial evidence on the mechanisms that govern the wake transition towards three-dimensionality. The initial assessment was conducted at two extremes of St_A variations (i.e., low and high St_A, respectively). This enabled a vivid characterization of the fundamental three-dimensional wake topology, and vortex instabilities, of foils oscillating in mixed motion. The case represented by low St_A depicted a $2P^T$ wake mode, which characterized shedding of a single vortex pair within a half cycle. Each vortex in the pair possessed an elliptic spanwise instability feature, which grew in amplitude as the vortex shed into the wake. Instability wavelength also revealed close resemblance to the elliptic type instability associated with counter-rotating vortex pairs (Leweke et al., 2016). No secondary hairpin structures were observed although vortex dislocation features in form of tongue-like corrugations became evident along the spanwise extent of the LEV. Contrary to the observations at low St_A setting, the wake at high St_A depicted an asymmetric topology characterized by dipole like shedding. No imminent role of LEV was observed on account of its early disintegration near the foil leading edge. In terms of the instability features, the characteristic wavelength still resembled an elliptic type. However, secondary hairpin structures were found dominant, whose legs further wrapped around the dipoles and thereby resulted in stronger roller deformations. The interaction of hairpin legs with braid vorticity was hypothesized to result in the formation of rib-like secondary vortex pairs in the wake. This also indicated a combined presence of centrifugal and core roller instability. Based on similarities in the quantitative estimates of wavelengths associated with spanwise instability and secondary vortex pair, it was also evident that large scale dislocations (like conjoint hairpin-horseshoe vortex) do not influence the spatial and temporal periodicity of secondary

structures. However, the presence of such structures could influence the wake topology in terms of spatial asymmetry in the arrangement of rollers (as associated with large thrust generation wake).

A detailed investigation on the dominant role of LEV was conducted in order to outline the global association of spanwise vortex instability, growth of secondary structures and combined oscillatory kinematics of the foils. It was observed that as the kinematics change from heave- to pitch-dominated at a low $St_c = 0.32$, the spanwise instability features and the growth of secondary vortex structures experienced substantial changes in terms of their formation mechanisms in the wake. Two dominant mechanisms were identified, the first of which involved a secondary LEV that paired with the primary LEV, and thereby resulted in a spanwise elliptic instability. The second mechanism, however, included a LEV-TEV pair that subsequently resulted in the temporal delay in the development of elliptic instability. Growth of secondary vortex structures was associated with the deformed secondary LEV, or the TEV, that possessed a relatively weaker circulation compared to the paired primary LEV. A complete absence of the growing secondary structure became evident during the onset of pitch dominated motion at $\phi = 270^{\circ}$. The changes in mechanisms that governed the growth of secondary wake structures, while the foil motion transitioned from heave- to pitch dominated kinematics, was also consistently observed at an increasing range of St_c. However, the amplified undulations of the primary LEV coincided with this increase in St_c. As these undulations evolved in the wake, growth of a strong horseshoe vortex system became evident in conjunction with the usual elongation of hairpin legs to ribs, observed at low St_c. An accelerated elongation of horseshoe legs was also observed with increasing St_c beyond 0.48, which therefore contributed to the existence of supplemental rib pairs in the wake. Thus, this evaluation elaborated upon the close association between the three-dimensional wake topology and kinematics of oscillating foil.

In summary, the novelty of this work is reflected on its comprehensive numerical evaluation of the wake evolution behind an oscillating foil with combined heaving and pitching motion. The transition of two-dimensional wake topology reveals unique primary vortex interaction mechanisms that modify the mean flow signatures within certain kinematics regimes. However, a direct correspondence of topological transitions and changes in propulsive performance may not exist.

Further, the kinematics parameter including Strouhal number, based on heave and pitch amplitudes, and the phase offset are sufficient to represent a unique relationship with circulation of trailing and leading edge vortex structures. The onset of three-dimensionality is characterized by elliptic instability of the primary vortex, which also reveals a correspondence with the formation of secondary vortices that resemble multiple hairpin and horseshoe structures. However, the mechanisms that govern their growth are directly associated with heave or pitch dominated kinematics of oscillating foils.

The interdependence of the wake dynamics, kinematics and performance was uniquely expressed in this study that concerned oscillating foils with combined heaving and pitching motion. Improvement of swimming mechanisms for man-made underwater robots, and energy harvesters, can be achieved by application of specific kinematics that induce certain vortical interactions to manipulate the mean wake features. These features contributes towards an increased thrust generation while having a low input power requirement. The three-dimensional onset of secondary wake structures can be further triggered or modified based on specific changes in ϕ between heaving and pitching motion, and through variation of St_c. The corresponding delay or accelerated disintegration of vortical rollers through interactions of secondary wake structures can ultimately prove effective in active flow control for reducing induced wake effects and noise propagation.

Chapter 13

FUTURE WORK

The evaluation of 2D and 3D wake features of an oscillating foil in combined heaving and pitching motion revealed several fundamental insights relevant to transitions in topological arrangement of rollers, their spanwise instability features and growth of secondary vortex structures. The knowledge gained here plays a crucial role in understanding aspects of turbulence that are universally exploited in nature, and can help in advancement of man-made engineering systems. However, there remains unexplored areas that will need further investigation. These revolve around the implications of varying flexural stiffness or rigidity of the oscillating foil, on (A) validity of the propulsive performance scaling for thrust and power, which could reveal a universal formulation capable of modeling both rigid and flexible propulsors; (B) controlling or inhibiting the shedding of vortex structures that could lead to a drag based wake signature within some kinematic settings; (C) evaluating and modifying the circulation model developed here such that the flexural rigidity can be directly incorporated in conjunction with kinematic parameters (St_h, St_θ, St_A and ϕ); (D) changes in the growth mechanisms of three-dimensional wake instabilities and evolution of secondary wake structures.

In view of the several points highlighted above, the evaluation of 2D aspects can be extended from the studies that were conducted for single degree of pitching or heaving plates, and foils, respectively. However, the three-dimensional wake evolution and the details of mechanisms as-

sociated with spanwise instabilities and secondary vortex structures is sufficiently difficult to investigate, both experimentally and numerically. Despite the fact that physical insights into primary vortex topology of 3D flexible fins that mimic swimming style of biological mammals had been provided experimentally (Hultmark et al., 2007; Dewey et al., 2012, 2013; Smits, 2019), no detailed work have yet reported on the wake physics of infinite span flexible bodies. The experimental setups also encounter difficulties while capturing flow physics near a moving boundary, where the information relevant to onset of spanwise instability and secondary vortex structures remains concentrated. Computational techniques like DNS and LES does offer an accurate and robust way to investigate the complex wake physics of flexible foils, owing to the advancement in computing power. However, an integration of OGA method with the discretized equations of solid displacement is still not established. Computational software packages does exist for handling fluid structure interaction through non-overset approaches (for e.g. mesh morphing). However, the major issue in terms of non-orthogonality emerge during large amplitude motion.

There is interest for evaluating wake of finite aspect ratio oscillating foils in the community. Numerous experimental studies have began investigating the three-dimensionality effects associated with tip vortex formation on foils that oscillate in pure heaving or pitching. However, the influence of combined heaving and pitching motion on the three-dimensional wake aspects, especially the dynamics of tip vortex remain unexplored. Such addressable gaps present a more closer analogy with practical applications and biological swimming mechanics, since the actual fins are always subjected to tip vortex interaction with the developing or shed $LEVs$, and $TEVs$, respectively.

Bibliography

Aarnes, J. R., Jin, T., Mao, C., Haugen, N. E. L., Luo, K., and Andersson, H. I. (2020). Treatment of solid objects in the pencil code using an immersed boundary method and overset grids. *Geophysical & Astrophysical Fluid Dynamics*, 114(1-2):35–57.

A.J., G. M. S. (2008). Effects of three-dimensionality on thrust production by a pitching panel. *Journal of Fluid Mechanics*, 615:211–220.

Andersen, A., Bohr, T., Schnipper, T., and Walther, J. H. (2017). Wake structure and thrust generation of a flapping foil in two-dimensional flow. *Journal of Fluid Mechanics*, 812:R4.

Anderson, J. D. (1984). *Fundamentals of aerodynamics.* McGraw-Hill, New York City.

Anderson, J. M., Streitlien, K., Barrett, D. S., and Triantafyllou, M. S. (1998). Oscillating foils of high propulsive efficiency. *Journal of Fluid Mechanics*, 360:41–72.

Ayancik, F., Zhong, Q., Quinn, D. B., Brandes, A., Bart-Smith, H., and Moored, K. W. (2019). Scaling laws for the propulsive performance of three-dimensional pitching propulsors. *Journal of Fluid Mechanics*, 871:1117–1138.

Barkley, D. and Henderson, R. D. (1996). Three-dimensional Floquet stability analysis of the wake of a circular cylinder. *Journal of Fluid Mechanics*.

Birch, J. M. and Dickinson, M. H. (2001). Spanwise flow and the attachment of the leading-edge vortex on insect wings. *Nature 2001 412:6848*, 412(6848):729–733.

Bishop, R. E. D. and Hassan, A. Y. (1964). The Lift and Drag Forces on a Circular Cylinder Oscillating in a Flowing Fluid. Technical Report 1368.

Blondeaux, P., Fornarelli, F., Guglielmini, L., Triantafyllou, M. S., and Verzicco, R. (2005). Numerical experiments on flapping foils mimicking fish-like locomotion. *Physics of Fluids*, 17(11):113601.

Bode-Oke, A. T. and Dong, H. (2020). The reverse flight of a monarch butterfly (Danaus plexippus) is characterized by a weight-supporting upstroke and postural changes. *Journal of the Royal Society Interface*, 17(167).

Boustead, N., Ryan, K., and Sheard, G. J. (2010). Short-wave instability growth in closely spaced vortex pairs. *Progress in Computational Fluid Dynamics*.

Bratt, J. B. (1950). Flow Patterns in the Wake of an Oscillating Airfoil. *Aeronautical Research Council*, page p. 2773.

Brede, M., Eckelmann, H., and Rockwell, D. (1996). On secondary vortices in the cylinder wake. *Physics of Fluids*.

Bristol, R. L., Ortega, J. M., Marcus, P. S., and Savas, . (2004). On cooperative instabilities of parallel vortex pairs. *Journal of Fluid Mechanics*, 517:331–358.

Buchholz, J.H.J.; Smits, A. (2006). On the evolution of the wake structure produced by a low-aspect-ratio pitching panel. *Journal of Fluid Mechanics*, 546:433–443.

Calderon, D. E., Cleaver, D. J., Gursul, I., and Wang, Z. (2014). On the absence of asymmetric wakes for periodically plunging finite wings. *Physics of Fluids*.

Calderon, D. E., Wang, Z., and Gursul, I. (2013a). Lift-enhancing vortex flows generated by plunging rectangular wings with small amplitude. *AIAA Journal*, 51(12):2953–2964.

Calderon, D. E., Wang, Z., Gursul, I., and Visbal, M. R. (2013b). Volumetric measurements and simulations of the vortex structures generated by low aspect ratio plunging wings. *Physics of Fluids*, 25(6):067102.

Carr, L. W. (2012). Progress in analysis and prediction of dynamic stall. *https://doi.org/10.2514/3.45534*, 25(1):6–17.

Carrica, P. M., Wilson, R. V., Noack, R. W., and Stern, F. (2007). Ship motions using single-phase level set with dynamic overset grids. *Computers & Fluids*, 36(9):1415–1433.

Cerretelli, C. and Williamson, C. H. (2003). The physical mechanism for vortex merging. *Journal of Fluid Mechanics*.

Chandar, D. D. (2019). On overset interpolation strategies and conservation on unstructured grids in openfoam. *Computer Physics Communications*, 239:72–83.

Chandar, D.; Gopalan, H. (2016). In *Comparative Analysis of the Arbitrary Mesh Interface(AMI) and Overset Methods for Dynamic Body Motions in OpenFOAM*. In Proceedings of the 46th AIAA Fluid Dynamics Conference, Washington, DC, USA, 13–17 June.

Chao, L.-M., Alam, M. M., and Ji, C. (2021). Drag–thrust transition and wake structures of a pitching foil undergoing asymmetric oscillation. *Journal of Fluids and Structures*, 103:103289.

Chatelain, P., Curioni, A., Bergdorf, M., Rossinelli, D., Andreoni, W., and Koumoutsakos, P. (2008). Billion vortex particle direct numerical simulations of aircraft wakes. *Computer Methods in Applied Mechanics and Engineering*, 197(13):1296–1304.

Chiereghin, N., Bull, S., Cleaver, D. J., and Gursul, I. (2020). Three-dimensionality of leading-edge vortices on high aspect ratio plunging wings. *Phys. Rev. Fluids*, 5:064701.

Cleaver, D. J., Wang, Z., and Gursul, I. (2012). Bifurcating flows of plunging aerofoils at high Strouhal numbers. *Journal of Fluid Mechanics*.

Cleaver, D. J., Wang, Z., Gursul, I., and Visbal, M. R. (2011). Lift enhancement by means of small-amplitude airfoil oscillations at low reynolds numbers. *AIAA Journal*, 49(9):2018–2033.

Colgate, J. E. and Lynch, K. M. (2004). Mechanics and control of swimming: A review. *IEEE Journal of Oceanic Engineering*, 29(3):660–673.

Corrsin, S. (1944). investigation of the behavior of parallel two-dimensional air jets.

Cros, A., Franco Llamas, B., and Sandoval Hernández, E. (2018). Vortical patterns generated by flapping foils of variable ratio chord-to-thickness. *Experiments in Fluids*, 59(10):152.

Crow, S. C. (1970). Stability theory for a pair of trailing vortices. *AIAA Journal*, 8(12):2172–2179.

Das, A., Shukla, R. K., and Govardhan, R. N. (2016). Existence of a sharp transition in the peak propulsive efficiency of a low-Re pitching foil. *Journal of Fluid Mechanics*, 800:307–326.

Das, A., Shukla, R. K., and Govardhan, R. N. (2022). Contrasting thrust generation mechanics and energetics of flapping foil locomotory states characterized by a unified *st-re* scaling. *Journal of Fluid Mechanics*, 930:A27.

Dee, F. B., Nicholas, O. P., Dept, A., and Bedford, R. A. E. (1968). Flight measurements of wing-tip vortex motion near the ground.

Delaurier, J. and Harris, J. (1982). Experimental study of oscillating-wing propulsion. *Journal of Aircraft - J AIRCRAFT*, 19:368–373.

Deng, J. and Caulfield, C. P. (2015a). Three-dimensional transition after wake deflection behind a flapping foil. *Phys. Rev. E*, 91:043017.

Deng, J. and Caulfield, C. P. (2015b). Three-dimensional transition after wake deflection behind a flapping foil. *Physical Review E - Statistical, Nonlinear, and Soft Matter Physics*.

Deng, J., Sun, L., Lubao Teng, Pan, D., and Shao, X. (2016). The correlation between wake transition and propulsive efficiency of a flapping foil: A numerical study. *Physics of Fluids*, 28(9).

Deng, J., Sun, L., and Shao, X. (2015). Dynamical features of the wake behind a pitching foil. *Phys. Rev. E*, 92:063013.

Dewey, P. A., Boschitsch, B. M., Moored, K. W., Stone, H. A., and Smits, A. J. (2013). Scaling laws for the thrust production of flexible pitching panels. *Journal of Fluid Mechanics*, 732:29–46.

Dewey, P. A., Carriou, A., and Smits, A. J. (2012). On the relationship between efficiency and wake structure of a batoid-inspired oscillating fin. *Journal of Fluid Mechanics*.

Dizès, S. L. and Laporte, F. (2002). Theoretical predictions for the elliptical instability in a two-vortex flow. *Journal of Fluid Mechanics*, 471:169–201.

Dong, H., Mittal, R., and Najjar, F. M. (2006). Wake topology and hydrodynamic performance of low-aspect-ratio flapping foils. *Journal of Fluid Mechanics*.

Drucker, E. G. and Lauder, G. V. (2001). Locomotor function of the dorsal fin in teleost fishes: experimental analysis of wake forces in sunfish. *Journal of Experimental Biology*, 204(17):2943–2958.

Duponcheel, M. (2009). Direct and large-eddy simulation of turbulent wall-bounded flows : further development of a parallel solver, improvement of multiscale subgrid models and investigation of vortex pairs in ground effect.

Durbin, P. A. and Reif, B. A. (2010). Statistical Theory and Modeling for Turbulent Flows: Second Edition. *Statistical Theory and Modeling for Turbulent Flows: Second Edition*.

Ellenrieder, K.D.V.; Parker, K. S. J. (2003). Flow structures behind a heaving and pitching finite-span wing. *Journal of Fluid Mechanics*, 490:129–138.

Fage, A. and Johansen, F. C. (1927). On the flow of air behind an inclined flat plate of infinite span. *Proceedings of the Royal Society of London. Series A, Containing Papers of a Mathematical and Physical Character*, 116(773):170–197.

Fazle Hussain, A. K. (1986). Coherent structures and turbulence. *Journal of Fluid Mechanics*, 173:303–356.

Fish, F. and Lauder, G. (2005). Passive and active flow control by swimming fish and mammals. *http://dx.doi.org/10.1146/annurev.fluid.38.050304.092201*, 38:193–224.

Fish, F. and Lauder, G. (2013). Not just going with the flow. *American Scientist*, 101(2):114–123.

Fish, F. E., Legac, P., Williams, T. M., and Wei, T. (2014). Measurement of hydrodynamic force generation by swimming dolphins using bubble DPIV. *Journal of Experimental Biology*, 217(2):252–260.

Floryan, D., Van Buren, T., Rowley, C. W., and Smits, A. J. (2017). Scaling the propulsive performance of heaving and pitching foils. *Journal of Fluid Mechanics*, 822:386–397.

Friedlander, S. and Lipton-Lifschitz, A. (2003). Chapter 8 - localized instabilities in fluids. volume 2 of *Handbook of Mathematical Fluid Dynamics*, pages 289–354. North-Holland.

Garrick, I. (1936). Propulsion of a flapping and oscillating foil, NACA Tech. Rep. 567.

Gemmell, B. J., Colin, S. P., Costello, J. H., and Dabiri, J. O. (2015). Suction-based propulsion as a basis for efficient animal swimming. *Nature Communications*.

Gibeau, B., Koch, C. R., and Ghaemi, S. (2018). Secondary instabilities in the wake of an elongated two-dimensional body with a blunt trailing edge. *Journal of Fluid Mechanics*.

Godoy-Diana, R., Aider, J. L., and Wesfreid, J. E. (2008). Transitions in the wake of a flapping foil. *Physical Review E - Statistical, Nonlinear, and Soft Matter Physics*, 77:016308.

Godoy-Diana, R., Marais, C., Aider, J. L., and Wesfreid, J. E. (2009). A model for the symmetry breaking of the reverse Bénard-von Kármán vortex street produced by a flapping foil. *Journal of Fluid Mechanics*.

Grinstein, F., Hussain, F., and Boris, J. (1991). *Dynamics and Topology of Coherent Structures in a Plane Wake*, pages 34–41.

Gullberg, P., Sengupta, R., and Horrigan, K. (2013). Transient fan modelling and effects of blade deformation in a truck cooling fan installation. In *Vehicle Thermal Management Systems Conference Proceedings (VTMS11)*, pages 219–227. Woodhead Publishing.

Gungor, A. and Hemmati, A. (2021). The scaling and performance of side-by-side pitching hydrofoils. *Journal of Fluids and Structures*, 104:103320.

Hakvey, J. K. and Perry, F. J. (2012). Flowfield produced by trailing vortices in the vicinity of the ground. *https://doi.org/10.2514/3.6415*, 9(8):1659–1660.

Hammer, P. R., Garmann, D. J., and Visbal, M. R. (2022). Effect of aspect ratio on finite-wing dynamic stall. *AIAA Journal*, 0(0):1–13.

Harris, D. M. and Williamson, C. H. (2012). Instability of secondary vortices generated by a vortex pair in ground effect. *Journal of Fluid Mechanics*, 700:148–186.

He, X. and Gursul, I. (2016). Point vortex model of deflected wakes of oscillating airfoils. *AIAA Journal*, 54(11):3647–3651.

Hemmati, A. and Smits, A. J. (2019). The Effect of Pitching Frequency on the Hydrodynamics of Oscillating Foils. *Journal of Applied Mechanics*.

Hemmati, A., Van Buren, T., and Smits, A. J. (2019a). Effects of trailing edge shape on vortex formation by pitching panels of small aspect ratio. *Physical Review Fluids*, 4:033101.

Hemmati, A., Van Buren, T., and Smits, A. J. (2019b). Effects of trailing edge shape on vortex formation by pitching panels of small aspect ratio. *Phys. Rev. Fluids*, 4:033101.

Hemmati, A., Wood, D. H., and Martinuzzi, R. J. (2016). Characteristics of distinct flow regimes in the wake of an infinite span normal thin flat plate. *International Journal of Heat and Fluid Flow*.

Hemmati, A., Wood, D. H., and Martinuzzi, R. J. (2018). On simulating the flow past a normal thin flat plate. *Journal of Wind Engineering and Industrial Aerodynamics*, 174:170–187.

Hobeika, T., Löfdahl, L., and Sebben, S. (2014). Study of different tyre simulation methods and effects on passenger car aerodynamics. In Park, H., editor, *The International Vehicle Aerodynamics Conference*, pages 187–195. Woodhead Publishing, Oxford.

Hu, Q. Q. and Yu, Y. L. (2021). Hydrodynamic scaling law in undulatory braking locomotion. *Science China Physics, Mechanics and Astronomy 2021 64:7*, 64:1–12.

Hultmark, M., Leftwich, M., and Smits, A. J. (2007). Flowfield measurements in the wake of a robotic lamprey. *Experiments in Fluids*, 43(5):683–690.

Hussain, A. K. (1998). Coherent structures—reality and myth. *The Physics of Fluids*, 26(10):2816.

Jacquin, L., Fabre, D., Sipp, D., Theofilis, V., and Vollmers, H. (2003). Instability and unsteadiness of aircraft wake vortices. *Aerospace Science and Technology*, 7(8):577–593.

Jeong, J. and Hussain, F. (1995). On the identification of a vortex. *Journal of Fluid Mechanics*, 285:69–94.

Jones, K. D., Dohring, C. M., and Platzer, M. F. (1996). Wake structures behind plunging airfoils: A comparison of numerical and experimental results. In *34th Aerospace Sciences Meeting and Exhibit*.

Jones, K. D., Dohring, C. M., and Platzer, M. F. (1998). Experimental and computational investigation of the Knoller-Betz effect. *AIAA Journal*.

Kerswell, R. R. (2002). Elliptical instability. *Annual Review of Fluid Mechanics*, 34(1):83–113.

Kim, D., Strom, B., Mandre, S., and Breuer, K. (2017). Energy harvesting performance and flow structure of an oscillating hydrofoil with finite span. *Journal of Fluids and Structures*, 70:314–326.

Kim, Y. and Xie, Z. T. (2016). Modelling the effect of freestream turbulence on dynamic stall of wind turbine blades. *Computers and Fluids*.

King, J. T., Kumar, R., and Green, M. A. (2018). Experimental observations of the three-dimensional wake structures and dynamics generated by a rigid, bioinspired pitching panel. *Physical Review Fluids*.

Klein, R., Majda, A. J., and Damodaran, K. (1995). Simplified equations for the interaction of nearly parallel vortex filaments. *Journal of Fluid Mechanics*, 288:201–248.

Kline, S. J., Reynolds, W. C., Schraub, F. A., and Runstadler, P. W. (1967). The structure of turbulent boundary layers. *Journal of Fluid Mechanics*, 30(4):741–773.

Koochesfahani, M. M. (1989). Vortical patterns in the wake of an oscillating airfoil. *AIAA Journal*, 27:1200–1205.

Kozłowski, T. and Kudela, H. (2014). Transitions in the vortex wake behind the plunging profile. *Fluid Dynamics Research*, 46(6):061406.

Kármán, T. (2013). On the mechanism of the drag a moving body experiences in a fluid, communicated by f. klein, september 14th, 1911. translated by e. krause and a. henze, institute of aerodynamics, rwth aachen university. *Progress in Aerospace Sciences*, 59:13–15. Special issue: Theodore von Kármán.

Lagopoulos, N. S., Weymouth, G. D., and Ganapathisubramani, B. (2019). Universal scaling law for drag-to-thrust wake transition in flapping foils. *Journal of Fluid Mechanics*, 872:R1.

Lamb, H. (1945). *Hydrodynamics*. Dover publications, New York.

Lau, T. C. and Kelso, R. M. (2016). A scaling law for thrust generating unsteady hydrofoils. *Journal of Fluids and Structures*, 65:455–471.

Lentink, D., Muijres, F. T., Donker-Duyvis, F. J., and Van Leeuwen, J. L. (2008). Vortex-wake interactions of a flapping foil that models animal swimming and flight. In *Journal of Experimental Biology*.

Leweke, T., Le Dizès, S., and Williamson, C. H. (2016). Dynamics and Instabilities of Vortex Pairs.

Leweke, T. and Williamson, C. H. (1998). Cooperative elliptic instability of a vortex pair. *Journal of Fluid Mechanics*.

Leweke, T. and Williamson, C. H. K. (2011). Experiments on long-wavelength instability and reconnection of a vortex pair. *Physics of Fluids*, 23(2):024101.

Li, C., Dong, H., and Zhao, K. (2020). Dual functions of insect wings in an odor-guided aeronautic navigation. *Journal of Fluids Engineering*, 142(3).

Lighthill, M. J. (1969). Hydromechanics of Aquatic Animal Propulsion. *http://dx.doi.org/10.1146/annurev.fl.01.010169.002213*, 1(1):413–446.

Liu, H. (2009). Integrated modeling of insect flight: From morphology, kinematics to aerodynamics. *Journal of Computational Physics*, 228:439–459.

Liu, J., Akay, H. U., Ecer, A., and Payli, R. U. (2010). Flows around moving bodies using a dynamic unstructured overset-grid method. *International Journal of Computational Fluid Dynamics*, 24(6):187–200.

Luton, J. A. and Ragab, S. A. (1994). The three-dimensional interaction of a vortex pair with a wall. *Phys. Fluids*, 9:114102.

Ma, P., Yang, Z., Wang, Y., Liu, H., and Xie, Y. (2017). Energy extraction and hydrodynamic behavior analysis by an oscillating hydrofoil device. *Renewable Energy*, 113:648–659.

Mannam, N. P. B., Krishnankutty, P., Vijayakumaran, H., and Sunny, R. C. (2017). Experimental and Numerical Study of Penguin Mode Flapping Foil Propulsion System for Ships. *Journal of Bionic Engineering*, 14(4):770–780.

McCroskey, W. J. (1982). Unsteady airfoils. *Annual Review of Fluid Mechanics*, 14(1):285–311.

Mcnaughton, J., Afgan, I., Apsley, D., Rolfo, S., Stallard, T., and Stansby, P. (2014). A simple sliding-mesh interface procedure and its application to the cfd simulation of a tidal-stream turbine. *International Journal for Numerical Methods in Fluids*, 74.

McWilliams, J. C. and Zabusky, N. J. (1988). Symmetric vortex merger in two dimensions: Causes and conditions. *Journal of Fluid Mechanics*.

Meunier, P. and Leweke, T. (2001). Three-dimensional instability during vortex merging. *Physics of Fluids*, 13(10):2747–2750.

Meunier, P. and Leweke, T. (2005). Elliptic instability of a co-rotating vortex pair. *Journal of Fluid Mechanics*.

Mittal, R. and Balachandar, S. (1995). Generation of streamwise vortical structures in bluff body wakes. *Physical Review Letters*.

Mo, W., He, G., Wang, J., Zhang, Z., Gao, Y., Zhang, W., Sun, L., and Ghassemi, H. (2022). Hydrodynamic analysis of three oscillating hydrofoils with wing-in-ground effect on power extraction performance. *Ocean Engineering*, 246:110642.

Moin, P. and Mahesh, K. (1998). Direct numerical simulation: A tool in turbulence research. *Annual Review of Fluid Mechanics*, 30(1):539–578.

Moriche, M., Flores, O., and García-Villalba, M. (2016). Three-dimensional instabilities in the wake of a flapping wing at low Reynolds number. *International Journal of Heat and Fluid Flow*.

Morris, M.J.; Dutton, J. A. A. (1987). In *Peak torque characteristics of butterfly valves*, volume 54, pages 63–66. In Proceedings of Forum Ind. Appl. Fluid Mech.

Mueller, T. J. and DeLaurier, J. D. (2003). Aerodynamics of small vehicles. *Annual Review of Fluid Mechanics*, 35(1):89–111.

Müller, U. K., Smit, J., Stamhuis, E. J., and Videler, J. J. (2001). HOW THE BODY CONTRIBUTES TO THE WAKE IN UNDULATORY FISH SWIMMING. *Journal of Experimental Biology*, 204(16):2751–2762.

Müller, U. K., Van Den Boogaart, J. G., and Van Leeuwen, J. L. (2008). Flow patterns of larval fish: Undulatory swimming in the intermediate flow regime. In *Journal of Experimental Biology*.

Najjar, F.M.; Balachandar, S. (1998). Low-frequency unsteadiness in the wake of a normal flat plate. *Journal of Fluid Mechanics*, 370:101–147.

Narasimhamurthy, V. D. and Andersson, H. I. (2009). Numerical simulation of the turbulent wake behind a normal flat plate. *International Journal of Heat and Fluid Flow*, 30(6):1037–1043.

Nazarinia, M., Lo Jacono, D., Thompson, C. M., and Sheridan, J. (2009). The three-dimensional wake of a cylinder undergoing a combination of translational and rotational oscillation in a quiescent fluid. *Physics of Fluids*.

Noack, R.; Boger, D. K. R. C. P. (2009). In *Sugar++: An improved general overset grid assembly capability*. In Proceedings of the 19th AIAA Computational Fluid Dynamics Conference, San Antonio, TX, USA, 22–25 June.

Ohmi, K., Coutanceau, M., Daube, O., and Loc, T. P. (1991). Further experiments on vortex formation around an oscillating and translating airfoil at large incidences. *Journal of Fluid Mechanics*, 225:607–630.

Ohmi, K., Coutanceau, M., Loc, T. P., and Dulieu, A. (1990). Vortex formation around an oscillating and translating airfoil at large incidences. *Journal of Fluid Mechanics*.

Ortega, J. M., Bristol, R. L., and Savas, Ö. (2003). Experimental study of the instability of unequal-strength counter-rotating vortex pairs. *Journal of Fluid Mechanics*, 474(474):35–84.

Ortega, J. M. and Savas, O. (2001). Rapidly growing instability mode in trailing multiple-vortex wakes. *AIAA Journal*, 39(4):750–754.

Panahi, R. and Shafieefar, M. (2009). Application of overlapping mesh in numerical hydrodynamics. *Polish Maritime Research - POL MARIT RES*, 16:24–33.

Parker, K., von Ellenrieder, K. D., and Soria, J. (2003). Flow visualization of the effect of pitch amplitude changes on the vortical signatures behind a three-dimensional flapping airfoil. In *Optical Technology and Image Processing for Fluids and Solids Diagnostics 2002*.

Peace, A. J. and Riley, N. (1983). A viscous vortex pair in ground effect. *Journal of Fluid Mechanics*, 129:409–426.

Pedregosa, F., Varoquaux, G., Gramfort, A., Michel, V., Thirion, B., Grisel, O., Blondel, M., Prettenhofer, P., Weiss, R., Dubourg, V., Vanderplas, J., Passos, A., Cournapeau, D., Brucher, M., Perrot, M., and Duchesnay, E. (2011). Scikit-learn: Machine learning in Python. *Journal of Machine Learning Research*, 12:2825–2830.

Petra, T. (2019). In *Description of the overset mesh approach in ESI version of OpenFOAM*. Proceedings of the CFD with OpenSource Software, Nilsson, H., Ed.; Chalmers University of Technology: Gothenburg, Sweden.

Piellard, M. and Coutty, B. (2011). Application of a hybrid computational aeroacoustics method to an automotive blower. In *Vehicle Thermal Management Systems Conference and Exhibition (VTMS10)*, pages 447–455. Woodhead Publishing.

Pope, S. B. (2000). *Turbulent Flows*. Cambridge University Press, Cambridge.

Quinn, D. B., Lauder, G. V., and Smits, A. J. (2015). Maximizing the efficiency of a flexible propulsor using experimental optimization. *Journal of Fluid Mechanics*.

Ramesh, K. K., Ke, J., Gopalarathnam, A., and Edwards, J. R. (2012). Effect of airfoil shape and reynolds number on leading edge vortex shedding in unsteady flows. pages 1505–1515. American Institute of Aeronautics and Astronautics Inc.

Read, D., Hover, F., and Triantafyllou, M. (2003). Forces on oscillating foils for propulsion and maneuvering. *Journal of Fluids and Structures*, 17(1):163–183.

Robichaux, J., Balachandar, S., and Vanka, S. P. (1999). Three-dimensional Floquet instability of the wake of square cylinder. *Physics of Fluids*.

Roget, B. and Sitaraman, J. (2014). Robust and efficient overset grid assembly for partitioned unstructured meshes. *Journal of Computational Physics*.

Roshko, A. (1954a). In *On the drag and shedding frequency of two-dimensional bluff bodies*. National Advisory Committee for Aeronautics technical note 3169; California Institute of Technology: Pasadena, CA, USA.

Roshko, A. (1954b). on the development of turbulent wakes from vortex streets.

Roshko, A. (1961). Experiments on the flow past a circular cylinder at very high reynolds number. *Journal of Fluid Mechanics*, 10(3):345–356.

Ryan, K., Thompson, M. C., and Hourigan, K. (2005). Three-dimensional transition in the wake of bluff elongated cylinders. *Journal of Fluid Mechanics*.

Schnipper, T., Andersen, A., and Bohr, T. (2009). Vortex wakes of a flapping foil. *Journal of Fluid Mechanics*.

Sedov, L. I., Chu, C. K., Cohen, H., Seckler, B., and Gillis, J. (1965). Two-dimensional problems in hydrodynamics and aerodynamics. *Physics Today*, 18:78–79.

Senturk, U., Brunner, D., Jasak, H., Herzog, N., Rowley, C. W., and Smits, A. J. (2017). Benchmark simulations of flow past rigid bodies using an open-source, sharp interface immersed boundary method. *Progress in Computational Fluid Dynamics*, 19:205–2019.

Senturk, U. and Smits, A. J. (2018). Numerical simulations of the flow around a square pitching panel. *Journal of Fluids and Structures*, 76:454–468.

Senturk, U. and Smits, A. J. (2019a). Reynolds number scaling of the propulsive performance of a pitching airfoil. *AIAA Journal*, 57:2663–2669.

Senturk, U. and Smits, A. J. (2019b). Reynolds number scaling of the propulsive performance of a pitching airfoil. *AIAA Journal*, 57(7):2663–2669.

Shenoy, R., Smith, M. J., and Park, M. A. (2014). Unstructured overset mesh adaptation with turbulence modeling for unsteady aerodynamic interactions. *Journal of Aircraft*, 51(1):161–174.

Simsek, E., Freeman, B., Senturk, U., and Hemmati, A. (2020). Effect of In-Line Tandem Configuration on Performance and Scaling of Pitching Hydrofoils. *AIAA Journal*, 58:4620–4628.

Sitorus, P. E. and Ko, J. H. (2019). Power extraction performance of three types of flapping hydrofoils at a Reynolds number of 1.7E6. *Renewable Energy*, 132:106–118.

Smits, A. J. (2019). Undulatory and oscillatory swimming. *J. of Fluid Mechanics*, 874:P1.

Son, O., Gao, A.-K., Gursul, I., Cantwell, C., Wang, Z., and Sherwin, S. (2022). Leading-edge vortex dynamics on plunging airfoils and wings. *Journal of Fluid Mechanics*, 940:A28.

Srigrarom, S. and Vincent, C. W. S. (2008). Effect of pitching and heaving motions of SD8020 hydrofoil on thrust and efficiency for swimming propulsion. In *38th AIAA Fluid Dynamics Conference and Exhibit*.

Sun, L., Deng, J., and Shao, X. (2018). Three-dimensional instabilities for the flow around a heaving foil. *Physical Review E*.

Taira, K.; Colonius, T. (2009). Three-dimensional flows around low-aspect-ratio flat-plate wings at low reynolds numbers. *Journal of Fluid Mechanics*, 623:187–207.

Tay, W. B., Bijl, H., and van Oudheusden, B. W. (2013). Biplane and tail effects in flapping flight. *AIAA Journal*, 51(9):2133–2146.

Theodorsen, T. (1935). General Theory of Aerodynamic Instability and the Mechanism of Flutter, NACA Report 496, 1935.

Tietjens, O. G. O. G., Prandtl, L., and Rosenhead, L. (1957). Fundamentals of hydro- and aeromechanics. page 270.

Triantafyllou, G. S., Triantafyllou, M. S., and Grosenbaugh, M. A. (1993). Optimal thrust development in oscillating foils with application to fish propulsion. *Journal of Fluids and Structures*, 7:205–224.

Triantafyllou, M. S., Hover, F. S., Techet, A. H., and Yue, D. K. (2005). Review of hydrodynamic scaling laws in aquatic locomotion and fishlike swimming. In *Applied Mechanics Reviews*, volume 58, pages 226–237.

Triantafyllou, M. S., Techet, A. H., and Hover, F. S. (2004). Review of experimental work in biomimetic foils. *IEEE Journal of Oceanic Engineering*.

Triantafyllou, M. S., Triantafyllou, G. S., and Yue, D. K. (2000). Hydrodynamics of fishlike swimming. *Annual Review of Fluid Mechanics*, 32:33–53.

Vagianos, Nicholas J. Thurston, D. B. (1970). Hydrofoil Seaplane Design. *THURSTON AIRCRAFT CORP SANFORD ME*.

Van Buren, T., Floryan, D., and Smits, A. J. (2019). Scaling and performance of simultaneously heaving and pitching foils. *AIAA Journal*, 57:3666–3677.

Van Buren, T., Floryan, D., Wei, N., and Smits, A. J. (2018). Flow speed has little impact on propulsive characteristics of oscillating foils. *Physical Review Fluids*, 3:013103.

Verma, S., Freeman, B. R. S., and Hemmati, A. (2022a). Effects of Reynolds number and average angle of attack on the laminar scaling of oscillating foils. *Physics of Fluids*, 34(3):031905.

Verma, S. and Hemmati, A. (2020). Performance of Overset Mesh in Modeling the Wake of Sharp-Edge Bodies. *Computations*, 8:66.

Verma, S. and Hemmati, A. (2021a). Asymmetry in wake of oscillating foils with combined pitching and heaving motion. In Örlü, R., Talamelli, A., Peinke, J., and Oberlack, M., editors, *Progress in Turbulence IX*, pages 97–102, Cham. Springer International Publishing.

Verma, S. and Hemmati, A. (2021b). Evolution of wake structures behind oscillating hydrofoils with combined heaving and pitching motion. *Journal of Fluid Mechanics*, 927:A23.

Verma, S. and Hemmati, A. (2022a). Characterization of bifurcated dual vortex streets in the wake of an oscillating foil. *Journal of Fluid Mechanics*, 945:A7.

Verma, S. and Hemmati, A. (2022b). Route to transition in propulsive performance of oscillating foil. *Physical Review E*, 105(4):045102.

Verma, S., Khalid, M. S., and Hemmati, A. (2022b). On association of lift generation, wake topology and kinematics of oscillating foils:. *International Journal of Micro Air Vehicle*, 14:175682932110739.

Videler, J. J. (1993). Fish swimming. 10:260.

Visbal, M., Yilmaz, T. O., and Rockwell, D. (2013). Three-dimensional vortex formation on a heaving low-aspect-ratio wing: Computations and experiments. *Journal of Fluids and Structures*, 38:58–76.

Visbal, M. R. (2009). High-fidelity simulation of transitional flows past a plunging airfoil. *AIAA Journal*, 47:11.

von Ellenrieder, K. D., Parker, K., and Soria, J. (2003). Flow structures behind a heaving and pitching finite-span wing. *Journal of Fluid Mechanics*.

Wang, J.; Wan, D. (2017). In *Wave effects on free running ship in standard zig-zag maneuver*. In Proceedings of the 32th Workshop on Water Waves and Floating Bodies, Dalian, China, 23–26 April.

Wang, Y., Huang, D., Han, W., YangOu, C., and Zheng, Z. (2017). Research on the mechanism of power extraction performance for flapping hydrofoils. *Ocean Engineering*, 129:626–636.

Wang, Z. J. (2005). DISSECTING INSECT FLIGHT. *Annu. Rev. Fluid Mech*, 37:183–210.

Webb, P. (1975). Hydrodynamics and Energetics of Fish Propulsion. *Bulletin of the Fisheries Research Board of Canada*, 190:1–156.

Williamson, C. H. (1996). Three-dimensional wake transition. *Journal of Fluid Mechanics*.

Williamson, C. H., Leweke, T., Asselin, D. J., and Harris, D. M. (2014). Phenomena, dynamics and instabilities of vortex pairs. *Fluid Dynamics Research*, 46(6):061425.

Williamson, C. H. and Roshko, A. (1988). Vortex formation in the wake of an oscillating cylinder. *Journal of Fluids and Structures*.

Winckelmans, G., Cocle, R., Dufresne, L., and Capart, R. (2005). Vortex methods and their application to trailing wake vortex simulations. *Comptes Rendus Physique*, 6(4):467–486. Aircraft trailing vortices.

Wu, T. Y. (2011). Fish swimming and bird/insect flight. *Annual Review of Fluid Mechanics*, 43(1):25–58.

Wu, X., Zhang, X., Tian, X., Li, X., and Lu, W. (2020). A review on fluid dynamics of flapping foils. *Ocean Engineering*, 195:106712.

Xia, J., Tian, S., and Wu, Y. (2009). Numerical simulation of parachute inflation process using an overset deforming grids method. *Modern Physics Letters B*, 23(03):305–308.

Xu, L., Baglietto, E., and Brizzolara, S. (2018). Extending the applicability of RANS turbulence closures to the simulation of transitional flow around hydrofoils at low Reynolds number. *Ocean Engineering*, 164:1–12.

Yang, C. and Mao, Z.-S. (2014). Chapter 3 - multiphase stirred reactors. In Yang, C. and Mao, Z.-S., editors, *Numerical Simulation of Multiphase Reactors with Continuous Liquid Phase*, pages 75–151. Academic Press, Oxford.

Yu, Y.-L. and Huang, K.-J. (2021). Scaling law of fish undulatory propulsion. *Physics of Fluids*, 33(6):061905.

Zhang, H. Q., Fey, U., Noack, B. R., König, M., and Eckelmann, H. (1995). On the transition of the cylinder wake. *Physics of Fluids*.

Zhang, C.; Liu, X. F. S. W. D. W. J. (2018). In *Implementation of Overset Grid in OpenFOAM and its validation to PMM model test of a container ship*. In Proceedings of the 13th OpenFOAM Workshop (OFW13), Shanghai, China, 24–29 June.

Zheng, H., Xie, F., Zheng, Y., Ji, T., and Zhu, Z. (2019). Propulsion performance of a two-dimensional flapping airfoil with wake map and dynamic mode decomposition analysis. *Physical Review E*, 99(6):063109.

Zheng, Z. C. and Wei, Z. (2012). Study of mechanisms and factors that influence the formation of vortical wake of a heaving airfoil. *Physics of Fluids*.

Zurman-Nasution, A. N., Ganapathisubramani, B., and Weymouth, G. D. (2020). Influence of three-dimensionality on propulsive flapping. *Journal of Fluid Mechanics*, 886.